NASA Contractor Report 166616

Mathematical Analysis Study for Radar Data Processing and Enhancement

Part I: Radar Data Analysis

Robert James and James D. Brownlow

Contract NAS2-11491
August 1985

National Aeronautics and
Space Administration

NASA Contractor Report 166616

Mathematical Analysis Study for Radar Data Processing and Enhancement

Part I: Radar Data Analysis

Robert James and James D. Brownlow
GMD Systems, Lancaster, California

Prepared for
Ames Research Center
Dryden Flight Research Facility
Edwards, California
under Contract NAS2-11491

1985

National Aeronautics and
Space Administration
Ames Research Center
Dryden Flight Research Facility
Edwards, California 93523

TABLE OF CONTENTS

APPENDIX A - A DESCRIPTION OF THE NASA AN/FPS-16 INSTRUMENTATION RADAR AND FACTORS AFFECTING SYSTEM ACCURACY

APPENDIX B - NOISE DATA ANALYSIS TECHNIQUE

APPENDIX C - AN ANALYSIS OF FILTERING TECHNIQUES

MATHEMATICAL ANALYSIS STUDY
FOR
RADAR DATA PROCESSING AND ENHANCEMENT

PART I - RADAR DATA ANALYSIS

1.0 INTRODUCTION

In accordance with requirements set forth in contract NAS2-1149, an analysis program was undertaken to evaluate the fundamental performance parameters of the NASA AN/FPS-16 radar installed at Edwards Air Force Base, California. The project was planned as a one man-level overall effort which was to span a six month period beginning 1 March 1984 and ending 1 September 1984. During this time, efforts by GMD Systems were to be directed toward four tasks which were delineated in the Statement of Work. Three of these tasks are addressed in Part I of the report. The fourth is addressed in Part II.

1. Data from six flight support missions were analyzed. The missions used were F-104 flights 811, 814, 855, and 856, the STS-41C approach and Edwards landing, and the STS-41D launch orbit (Rev 2). Detailed data and discussions relating to these analyses are provided in sections 2 through 8 of this report. In addition, software from the Cyber radar data reduction program was reviewed to determine the accuracy and suitability of the processing methods used for post-mission reduction of radar tracking data. Results of this analysis are provided in section 9 of this document.

2. Noise and bias errors in raw tracking data were analyzed for each of the tracking missions. These missions are considered to be representative of the types of operations supported by the NASA AN/FPS-16 (34) radar. Detailed data and discussions pertinent to the noise analyses are provided in sections 3 through 8 for the six missions analyzed. In addition, a discussion of an altitude bias error observed during all of the missions is provided in section 10 of the report. Additional information about the AN/FPS-16 radar and a discussion of typical noise and bias errors in the range and angle measurements are provided in appendix A. The specific methods used for estimating the noise in the measurement data are described in appendix B.

3. Four separate filtering methods, representative of the most widely used optimal estimation techniques for enhancement of radar tracking data, were analyzed for suitability in processing both real-time and post-mission data. Inputs to each filtering method included data from both steady-state and highly dynamic flight profiles.

Results and detailed discussions pertinent to these analyses are provided in section 11. In addition, mathematical descriptions of each of the filters, along with certain test case conditions, are provided in appendix C.

Conclusions reached during the various analyses are provided in section 12, and recommendations for future study are provided in section 13.

2.0 AN ANALYSIS OF SIX TRACKING MISSIONS

During the period from 1 March 1984 through 1 September 1984, an analysis was made of radar tracking data obtained during four air data calibration flights and two Shuttle support missions. The air data calibration flights were conducted using a highly instrumented F-104 aircraft which was tracked by the NASA AN/FPS-16 (34) radar. The shuttle support missions included the approach and Edwards landing of STS-41C and the launch orbit (Rev 2) of STS-41D.

The primary objective of these analyses was to determine the overall performance capabilities of the NASA radar as shown by the quality of the tracking data and the accuracy with which air data parameters such as Mach number and altitude could be derived. During the F-104 missions, flight data were recorded on-board the aircraft, and radar tracking data were recorded both at the radar site and in the Varian area. Data capture on site was accomplished using a hard disc recording system provided with the A900 computer. Data capture in the Varian area was accomplished in duo-binary form using an FR-2000 analog recorder. Immediately prior to or following each of the air data calibration missions, except flight 811, a rawinsonde balloon was released and tracked by the radar. Data from the balloon track was recorded on disc at the radar site, and atmospheric data from the rawinsonde measurements were obtained from the Air Weather Service Unit at Edwards.

Prior to each mission, the radar was subjected to the same type of pre-mission tests and calibrations as are normally used prior to any flight in which tracking data is required for post-mission analysis. This included both skin and beacon calibrations using various surveyed radar range and angle calibration targets on the lakebed and in the surrouding hills, as well as the usual angle calibrations and r-f and optical collimations using the boresight tower signal source and optical targets. Angle calibrations on the boresight tower were performed with the antenna in both the normal and plunge (upside down) configurations.

2.1 Analysis Methods

The following procedures were used to reduce data from aircraft missions.

Following the mission, disc recordings, made on the A900 computer system at the radar site, were copied onto tape cartridges and transported to the GMD facility in Lancaster. FR-2000 duo-binary analog recordings of real-time data were digitized and formatted on to 9-track NRZI tapes using the Varian computer system. The tapes were then sent to the Cyber area where they were reduced using the Cyber radar data

reduction program. Flight data were also reduced using the Cyber flight data reduction program. From these two sets of data a composite tape was prepared which contained Mach number, pressure altitude, temperature, and free-stream pressure as derived from the Cyber flight data reduction program, and Mach number and geometric altitude as derived from the Cyber radar data reduction program. This composite tape was used at the GMD facility where software was written to read the Cyber tapes and to compare the Cyber results with those from the GMD data reduction program.

Software was also prepared to read the Varian tapes used by the Cyber radar data reduction program. The Varian tapes contained only those segments of the flight which were specified for reduction by the NASA engineers. The A900 recordings contained the same type of data for the entire period from takeoff to touchdown. In order to insure that no errors were present in the raw Varian data, which might be carried though into the reduced data from the Cyber program, special software was prepared by GMD to compare the data segments contained on the Varian tapes with data for the same time intervals from the A900 recordings made at the radar site. The comparison test, accomplished on data from the first and second air data calibration flights, revealed no discrepancies in the data being furnished to the Cyber.

Wind and weather data were obtained for the period of the flight. This included both synoptic reports, furnished by NASA, and local rawinsonde measurements made by the Air Weather Service Unit at Edwards Air Force Base. The synoptic reports were based on an extensive analysis of measurements from several upper-air stations surrounding the Edwards operating area.

Since the atmosphere is subject to significant movement and change over even short periods of time, and since the path over which data can be collected is spatially separated from the flight path of the test aircraft, a certain amount of error will always be present in both the measured and derived weather parameters, in spite of the accuracy of the measurement devices or the care taken in the analysis process. The error is likely to become greater on days when atmospheric activity is high. In the case of the upper air wind measurements obtained by balloon tracks, the wind data obtained is generally subjected to heavy smoothing to obtain wind vectors that are free from anomalies due to momentary gusting or shear conditions. The effects of variations in both wind and weather data were included in this analysis.

A composite wind profile was prepared from the wind data and entered into the GMD computers. The wind files thus prepared were available for callup during playbacks of the data so

that different wind profiles could be evaluated without the need to repeat the entire data reduction process. Special routines were prepared to generate the wind files from either manually entered synoptic or rawinsonde data, or from filtered data reductions of the radar balloon tracks. Wind data from all of these sources were analyzed.

From the weather data, a weather file was prepared for each mission. This file included temperature, dew point, and pressure for altitude intervals of 1000 or 2000 feet. From these discrete points, a cubic spline curve fit was used to provide continuous weather data for the main data reduction program. In order to provide an additional check on the weather data, recordings of dry bulb temperature, wet bulb temperature, and pressure were made at the radar site during the course of each mission. From these observations, the dew point temperature was calculated and all three of the weather parameters thus obtained were compared with the surface weather measurements shown in the rawinsonde printouts and in the NASA synoptic data. Surface comparisons, corrected for elevation differences between the various surface measurement locations, showed no significant variations. Dew point values, computed for specific dry bulb, wet bulb, and pressure conditions, also correlated with values contained in psychrometric tables published by the U.S. Department of Commerce in reference 1.

Software was also prepared to generate atmospheric parameters identical to those contained in the U.S. Standard Atmosphere, 1976 (Ref. 2). This was provided for use in when comparisons were made using standard atmospheric parameters. Standard atmosphere data were used for the analysis of both of the Shuttle missions.

From the weather data, the modulus of refraction for r-f energy was computed for the entire altitude range of the flight. This was accomplished by supplying temperature, dew point, and pressure to subroutines which first computed the partial pressure of water vapor, and; from the partial pressure of water vapor, the total pressure, and the temperature; the index of refraction. Extensive validations of the results were made to insure that the correct modulus of refraction was computed. This was accomplished by direct comparisons of results, over the complete range of values encountered in this analysis, with values contained in reference 3 as well as with results computed by the rawinsonde computer. The partial pressure of water vapor, needed as one of the inputs for the calculation of refractivity, was computed from the Claperon-Clausius equations using the method described in reference 4.

2.1.1 Data Reduction

Data reduction was accomplished using several high-accuracy software routines furnished by GMD Systems for this application. This included a series of programs which read the 20 pps raw data files and performed atmospheric refraction corrections, digital filtering, geodetic conversions, and various air data calculations needed for the analysis tasks.

Included as run time selections were:

1. The starting and ending times of the segment to be reduced.

2. The filtering method to be used, or no filtering at all. The filter selection included:

   a. A one-by-eight-state Kalman filter (Ref. 5)
   b. A three-by-three-state Kalman filter (Ref. 6)
   c. A second order alpha-beta-gamma filter (Ref. 7)
   d. A second order QD filter (Ref. 7)

   Keyboard entries of filter constants could also be made depending on the nature of the mission. For example, during aircraft missions where it was desirable to retain frequencies sufficiently high to show minor movements induced by the pilot in attempting to remain on the test profile or by gust loadings on the aircraft, a higher bandwidth was required than for orbital missions where the flight path was known to be smooth and where the frequency cut-off point could be significantly lower without loss of important data.

3. The selection of any one of three refraction correction methods, or no refraction correction at all. The refraction methods provided were:

   a. The gradient refraction solution (Ref. 8)
   b. The spherical slab refraction solution (Ref. 9)
   c. A White Sands (Pearson) refraction solution (Ref. 10)

   The gradient method is currently used on the A900 to support real-time mission operations, the spherical slab refraction method is used on the Varian computer to drive real-time control room displays, and the White Sands method is used as part of the post-mission radar data reduction program operated on the NASA Cyber system. Comparisons were also made of all three methods using tabulated results from a highly accurate non-real-time ray tracing solution used by the Johnson Space Center (Ref. 9)

4. The selection of geodetic conversion or no geodetic conversion. Geodetic equations from reference 8 were implemented to convert refraction corrected position data defined in the spherical coordinate system of range, azimuth, and elevation into geodetic coordinates of latitude, longitude, and altitude.

5. The selection of wind source. During all flights except 811, wind data was available from three sources: rawinsonde soundings, radar tracks of the rawinsonde balloons, and a synoptic analysis of upper-air data from Edwards and other nearby weather stations.

Data to be reduced were read from disc files containing the exact 20 pps data frames as recorded by the A900 computer in real time. After reduction, the data were stored in files which contained:

1. GMT, binary seconds
2. Uncorrected range, counts
3. Uncorrected azimuth, counts
4. Uncorrected elevation, counts
5. Range refraction correction, counts
6. Elevation refraction correction, counts
7. Target altitude, feet
8. Filtered X position, feet
9. Filtered Y position, feet
10. Filtered Z position, feet
11. Filtered X velocity, feet per second
12. Filtered Y velocity, feet per second
13. Filtered Z velocity, feet per second
14. Range noise sigma, counts
15. Azimuth noise sigma, counts
16. Elevation noise sigma, counts
17. Event status bits (on/off target, skin/beacon mode)
18. Target latitude, degrees
19. Target longitude, degrees

Numerous routines were provided to print and plot data in formats best suited for the various analytical tasks. The printout formats included:

1. Printouts of unprocessed time, range, azimuth, and elevation data, and event status flags. Keyboard entries were provided to select starting and ending times, counts or engineering units, and so forth. As the printouts were being made, software routines continuously kept track of frame counts to detect the loss of any frame or subframe data. Also shown were the status of the ON BEACON and ON TARGET radar flags along with the site address, frame count, an error flag to indicate invalid

data or data dropouts, and a record number identifying the location of the specific frame in the disc file.

2. Printouts of processed data containing both measured and derived parameters. The printout formats included one which was identical to the output from the Cyber radar data reduction program as well as abbreviated listings which contained only those parameters pertinent to this evaluation.

3. Either time history or rectangular plots of any of the raw or reduced data parameters used in this analysis were also available. These plots were accomplished by computer-to-computer links between the GMD A600 and A900 data reduction computers and an HP-9845 computer used for data plotting purposes. Software was prepared which allowed data from the Cyber air data reduction program and the Cyber radar data reduction program to be plotted together with similar parameters from the GMD data reduction routines. This greatly facilitated the analysis process by highlighting both similarities and differences in data from the three sources.

The analysis of the data from the four air data calibration flights and the two shuttle missions included time history plots of: raw range, azimuth, and elevation measurement data; derived altitude, Mach number, and true course; range, azimuth, and elevation noise, and so forth.

For the air data calibration missions, individual test points were analyzed by using time history blow-ups for the specific time interval of interest. These blow-up plots provided comparisons between on-board measurements of pressure altitude and Mach number. Other plots provided the radar-derived true course, flight path heading, slant range, and elevation angle for each test point.

Individual test points were designed to provide information in several areas of interest. First, and probably most important, were 'survey' runs. Survey runs were legs flown at constant Mach number, constant heading, and constant pressure altitude. Ideally they were planned to start and end approximately equidistant from the radar and to pass close by the radar at the near point. The distances at the start and end of the run were selected so that, in a typical case, the measured elevation angle would range from about 1 to 3 degrees at the start, up to possibly 30 to 40 degrees at the near point, and then continue on down to 1 to 3 degrees by the end of the run.

Other types of test points analyzed included constant-Mach-number climbs and descents; both level and push-pull

accelerations and decelerations; low-level runs with terrain or multipath interference; and low-level arcing legs. Also included were several high-g turns, rolls, and similar maneuvers conducted for the purpose of analyzing the accuracy and smoothness of the track during highly dynamic flight conditions. Tests of this type were performed using both skin and beacon modes on the radar.

During the survey runs, altitude commands were uplinked to the aircraft and displayed on a horizontal flight director bar so that the pilot needed only keep the bar centered in order to remain on the desired altitude profile. During the first and second flights, the altitude error signals were generated from real-time radar data in the Varian computer. For subsequent flights, the altitude commands were derived from downlinked on-board pressure data. During the run, on-board measurements of pressure altitude and Mach number were recorded and used for post-mission comparisons with radar derived geometric altitude and Mach number. Radar derived Mach number was adjusted and compared using upper air winds from the three sources previously described.

To obtain a better plotting correlation, the on-board pressure altitude was adjusted to roughly eliminate local differences between geometric altitude (Z) and pressure altitude (Hp) resulting from day-to-day variations in atmospheric pressure. The amount of adjustment was determined by comparison of pressure altitude data derived from on-board measurements with radar-derived geometric altitude for periods when the elevation angle was sufficiently high or when the range was sufficiently close that the amount of refraction correction was small and thus the errors in the corrections were negligible. Using the differences between the Z and Hp values obtained at these points, the synoptic Z-Hp curves were adjusted so that the best plotting correlations could be achieved.

It is important to note that design specifications for the AN/FPS-16 radar required bias errors of less than 0.1 mil (about 2 LSB values) in the angle measurements, and less than 5 feet in the range measurements. Since that time, many tests have been conducted both by the manufacturer and by the Department of Defense to substantiated these accuracies. Thus, if the radar is properly calibrated, the geometric altitude computed during high angle passes should provide very high accuracy. For example, at a 35 degree elevation angle, an elevation bias error of 2 LSB values would only contribute 4.6 feet of error to the altitude computation. An error of 1 LSB in the range measurement would only cause a 3.3-foot altitude error. Similarly, during close-in measurements made during takeoff and landing (range of about 22,000 to 23,000 feet), 2 LSB values of elevation bias error

would cause an error of only 1 foot in the derived geometric altitude, and 1 LSB of range error would have no perceptible effect because of the near-level travel of the r-f beam. Even if the angle calibration errors were double or triple the maximum typical errors, both types of measurements would still be reasonably good.

The Z-Hp horizontal gradients used in this analysis were as provided in the synoptic data. For this work, no attempt was made to provide automatic corrections for different distances and azimuth angles. This was performed manually in the few cases where needed. Also note that, in all cases, the Z-Hp corrections were applied to the on-board pressure measurements so that comparisons could always be made using geometric altitude. This required that Z-Hp tables supplied by NASA, which were computed to convert geometric altitude to pressure altitude, be revised to convert pressure altitude to geometric altitude.

Although radar measurements provide strictly geometric position data, in this analysis, the comparison between Z-Hp corrected on-board pressure altitude and radar-derived geometric altitude was important since it offered a method by which it was possible to determine how well the radar data followed minor flight path changes induced by pilot stick movements, gust loadings, and so forth. It was also provided a good method for determining the optimum values for filter constants which would balance the need to retain the true aircraft movements while maximizing the removal of random measurement noise. Without the on-board measurements, it is impossible to determine if an oscillation in the radar-derived position data is due to noise or to an aircraft movement. In addition, by applying horizontal pressure gradients from the synoptic analysis to the on-board pressure data, it was possible to estimate the magnitudes of bias errors which existed at long tracking ranges and low elevation angles.

Although altitude comparisons were used as the primary method for determining the quality of the radar track, it was also important to determine the accuracy with which secondary (derived) parameters, such as Mach number, could be determined from the radar data alone. In order to accomplish this, the radar derived ground speed was adjusted for upper level winds obtained from synoptic data, from rawinsonde measurements, and from radar balloon tracks. In the data reduction program aircraft horizontal velocity and vertical velocity were first computed separately. Next, the horizontal velocity component was adjusted for wind (from the selected source), so that both uncorrected and wind-corrected total velocities could be computed. The total velocity was then converted to Mach number as the ratio of aircraft

velocity to speed of sound for the particular altitude. The speed of sound, A, was computed from the relation

$$A = Asl(Ta/288.16K)^{0.5}$$

where Asl was taken as 661.48 knots and Ta was the ambient temperature in Kelvin. Upper air temperatures used for these calculations are tabulated at the beginning of each of the mission analysis sections in this document.

Time taken for the reduction of data by the various A900 routines was dependent on filtering and refraction correction methods selected. The three-by-three and eight-state Kalman filters required more processing time than did the simpler alpha-beta-gamma and QD filters. However, both of the Kalman filters had the advantage of being adaptive so that more or less credence was placed on the measurement data depending on the amount of agreement achieved between the extrapolated and the measured values. Similarly, gradient refraction, used on the real-time A900 system installed at the radar site, is by far the most time-consuming refraction correction method. The White Sands refraction correction method is the fastest. In general, it was found that the data reduction program ran at speeds from about three times faster than real-time for software with heavier computational loads to about four times faster than real-time for software with lighter computational loads. However, the GMD software routines used on this project were designed for accuracy rather than speed. Many speed improvements would be possible in software designed strictly for the usual post-mission reduction tasks.

Discussions of each of the four air data calibration flights are provided in sections 3 through 6 of this document. The discussions include a general description of the mission and its objectives, a summary of flight day wind and weather conditions, an analysis of the individual test points, an analysis of the wind data used for the Mach number calculations, an analysis of the noise content of in the raw measurement data, and a summary of results and conclusions from each specific flight. In the analysis section, an overview of each test point is provided followed by plots showing altitude and Mach number data derived for the test point as well as plots of true course, flight path angle, slant range, and elevation angle for the same time period.

Sections 7 and 8 analyze data from two Shuttle support missions. Data in both of these cases were reduced using standard atmospheric conditions.

Section 9 provides findings and recommendations related to the Cyber radar data reducton software, and section 10 discusses

a low-elevation-angle anomaly observed on the four air data calibration flights. Section 11 discusses the performance of the four filters used in this analysis. Section 12 provides general conclusions resulting from all of the analysis tasks.

The technical contract monitor for this project was Mr. Terry J. Larson. Synoptic data for each of the air data calibration flights were prepared by Mr. L. J. Ehernberger. NASA attendees at the various technical reviews included Mr. Larson, Mr. Ehernberger, and Mr. Stephen A. Whitmore, all of whom are members of the Aeronautics Branch at the Dryden Flight Research Facility.

3.0 AIR DATA CALIBRATION FLIGHT 811

Air data calibration flight F811 was flown on 5 April 1984 using F-104 tail number 826. The pilot was Mr. Ed Schneider. During the flight, six specific test conditions or runs were conducted for the air data calibration tests; other tests were also performed on a non-related project. Figures 3-1 through 3-3 provide time history plots of radar-measured range, azimuth, and elevation from takeoff to landing. The takeoff track was performed in AIDED EL; however, at close ranges, such as during takeoff and landing, the optical track point is calibrated to be close to the r-f track point, so both the takeoff and landing data are considered valid, subject to some manual elevation tracking errors and some errors in establishing an optical aim point on the video monitor.

3.1 Summary of Flight Day Wind and Weather Conditions

Synoptic interpolations were made for 2200Z (1400 PST).

On the flight day, local cool temperatures were observed with strong westerly or west-northwesterly flow in the upper troposphere. Pressure contour patterns for the flight period were consistent, giving a high degree of confidence in the synoptic pressure analysis; however, it was expected that significantly strong wind shear zones could be present even though they were not clearly defined in the weather analysis for the flight.

No semi-diurnal correction was applied to the pressure analysis. Surface data showed deviations of about 34 feet from the 12-hour straight-line trend, and the changes in the 12-hour time period were relatively small, considering the strength of the winds aloft.

Specific estimates for the temperature, dew point, pressure, and wind profiles for 1400 PST are given in table 3-I along with the derived index of refraction for each altitude. Local synoptic Z-Hp values and radar adjusted values are provided in table 3-II. Note that these corrections are computed so as to be applied to the on-board pressure altitude data.

It should be noted that Edwards rawinsonde data was not available for flight 811, and it was considered to be a "high wind" day with estimated winds up to about 100 knots at 40,000 feet. Also, during flight 811, the local Z-Hp values obtained from the synoptic data showed poor agreement with values obtained by comparison of high angle radar-derived altitude with on-board pressure altitude. At 33,000 feet, the radar derived altitude appeared to closely match the on-

board altitude, indicating a Z-Hp value near zero for that altitude. Synoptic data estimated the local value of Z-Hp for 33,000 feet to be about 191 feet. Plots comparing Z-Hp values from the synoptic data with the radar-adjusted values used for this analysis are provided in figure 3-4.

Figure 3-5 provides data from the AIDED EL track used as an approximate check of the radar derived geometric altitude during takeoff. The elevation of the runway, estimated from nearby taxiway survey point NRP 4, is approximately 2280 feet. Allowing about 3 to 4 feet for the elevation of the beacon above the surface of the runway, the 2283 value shown in figure 3-5 is the expected value.

Figures 3-6 through 3-9 show the close range and/or high-angle points used to obtain Z-Hp checks for altitudes of 5,000 to 10,000 feet, 11,000 feet, 25,000 to 28,000 feet, and 33,000 feet. Some additional adjustments to these values were made using longer time segment shown in figure 3-12.

It is also important to understand that prior to each flight, the optical and r-f axes of the antenna are collimated. This is accomplished by locking the radar on to the r-f feedhorn on the boresight tower, then establishing an optical track point which falls directly on the offset optical targets. This is accomplished in both normal and plunge modes. The optical track point determined by this procedure is marked with a small dot on the face of the video monitor. At close ranges, where the effects of refraction are slight, the r-f and optical aim points should coincide, except that allowances must be made for the 5-foot lateral offset of the camera from the feed horn assembly. Thus, during both takeoff and landing operations, the radar is locked on in range and in azimuth, but, because of multipath, the operator controls elevation by using the AIDED EL rate mode. To be consistent with the FULL AUTO track mode, the operator generally selects the position of the beacon antenna as his aim point on the aircraft. From many observations made during takeoffs and landings, the track in AIDED EL is generally good enough to provide target altitude information that is within about plus or minus 5 or so feet. However, this will vary somewhat, depending on operator attention and workload at the time.

TABLE 3-I. FLIGHT 811 WEATHER DATA

WEATHER DATA FOR FLIGHT 811

ALTITUDE (FT)	TEMPERATURE (DEG C)	DEW POINT (DEG C)	PRESSURE (MB)	N X 10E6	WIND (DEG/KTS)
2300	17.0	1.1	931.82	278.9	235.0/ 7.0
3000	14.6	1.0	908.12	274.9	215.0/ 11.0
4000	11.4	.9	876.00	269.4	195.0/ 13.0
5000	8.8	.8	843.50	263.0	175.0/ 15.0
6000	6.5	0.0	812.00	254.9	180.0/ 18.0
7000	4.5	-5.6	781.00	238.1	182.8/ 20.0
8000	2.7	-12.0	752.62	223.9	185.0/ 22.0
9000	.8	-12.2	722.00	216.6	185.0/ 23.0
10000	-1.2	-18.0	696.82	213.5	185.0/ 24.0
11000	-3.3	-8.4	671.47	210.0	189.4/ 25.3
12000	-5.6	-7.5	644.41	205.3	195.0/ 27.0
13000	-7.8	-9.2	620.63	198.0	199.9/ 28.4
14000	-10.2	-12.0	595.24	189.0	205.0/ 30.0
15000	-12.6	-14.5	571.80	181.3	209.7/ 31.1
16000	-14.9	-18.0	549.15	173.5	215.0/ 32.0
17000	-17.0	-23.9	527.24	165.3	221.0/ 33.2
18000	-19.0	-30.0	506.00	157.5	225.0/ 35.0
19000	-21.0	-32.6	485.50	151.6	223.1/ 37.8
20000	-22.9	-33.0	465.63	146.7	220.0/ 41.0
21000	-24.8	-31.5	446.47	142.2	219.6/ 43.7
22000	-26.6	-30.0	427.92	137.9	220.0/ 46.0
23000	-28.6	-32.0	410.03	132.8	220.9/ 48.2
24000	-30.8	-35.0	392.71	127.8	222.0/ 51.0
25000	-33.3	-37.3	376.02	123.3	223.1/ 55.7
26000	-36.1	-40.0	359.89	119.1	224.0/ 61.0
27000	-39.0	-44.5	344.39	115.0	224.9/ 65.6
28000	-41.9	-50.0	329.32	111.0	226.0/ 70.0
29000	-44.4	-55.5	314.69	107.0	227.4/ 74.3
30000	-46.8	-60.0	300.90	103.3	228.0/ 79.0
31000	-49.1	-60.7	288.74	100.1	226.6/ 84.6
32000	-51.0	-60.0	277.29	97.0	225.0/ 90.0
33000	-52.1	-60.0	265.50	93.4	224.8/ 92.7
34000	-53.0	-60.0	253.68	89.6	225.0/ 94.0
35000	-54.3	-60.0	241.80	85.9	226.3/ 94.7

TABLE 3-II. FLIGHT 811 Z-Hp DATA

SYNOPTIC Z-Hp DATA FOR FLIGHT 811

Altitude (feet)	Syn. Z-Hp (feet)	Radar Z-Hp (feet)	Change in Z-Hp (feet/n.mi.)	Direction of decrease
36,000	+187	+ 40		
34,000	+198	+ 42	2.20	310
32,000	+185	+ 57		
30,000	+173	+ 71	1.94	310
28,000	+174	+ 77		
26,000	+174	+ 78		
24,000	+174	+ 74	1.13	309
22,000	+161	+ 65		
20,000	+146	+ 49		
18,000	+128	+ 29	0.83	306
16,000	+ 93	+ 1		
14,000	+ 59	- 23		
12,000	+ 25	- 49		
10,000	- 10	- 70	0.40	270
8,000	- 39	- 90		
6,000	- 69	-110		
5,000	- 84	-119	0.25	345
4,000	-104	-128		
3,000	-125	-138		
2,000	-147	-148	0.30	035

Add Z-Hp values to pressure altitude to obtain geometric altitude

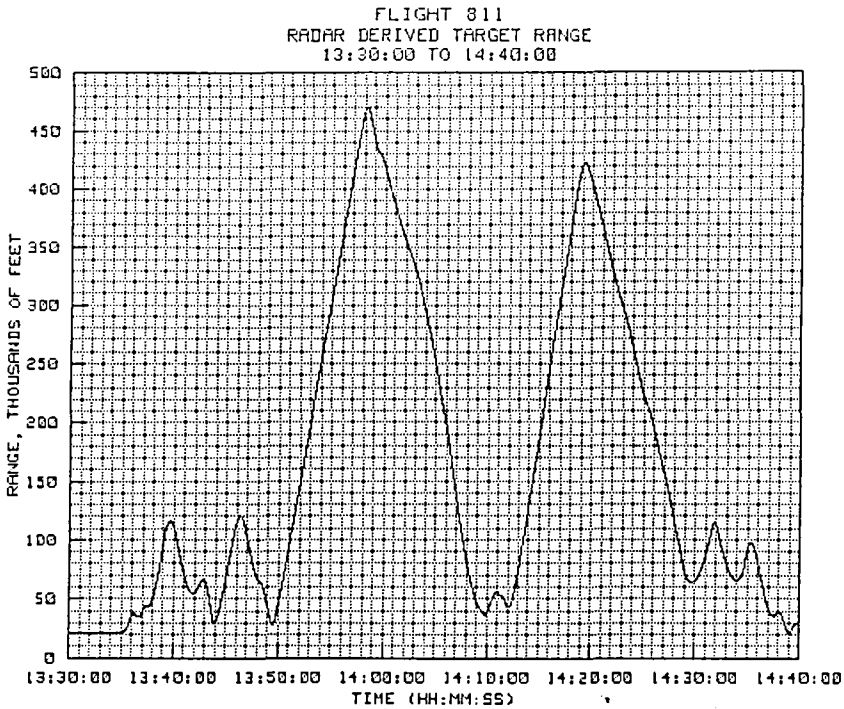

Figure 3-1. Flight 811 Radar-derived target range.

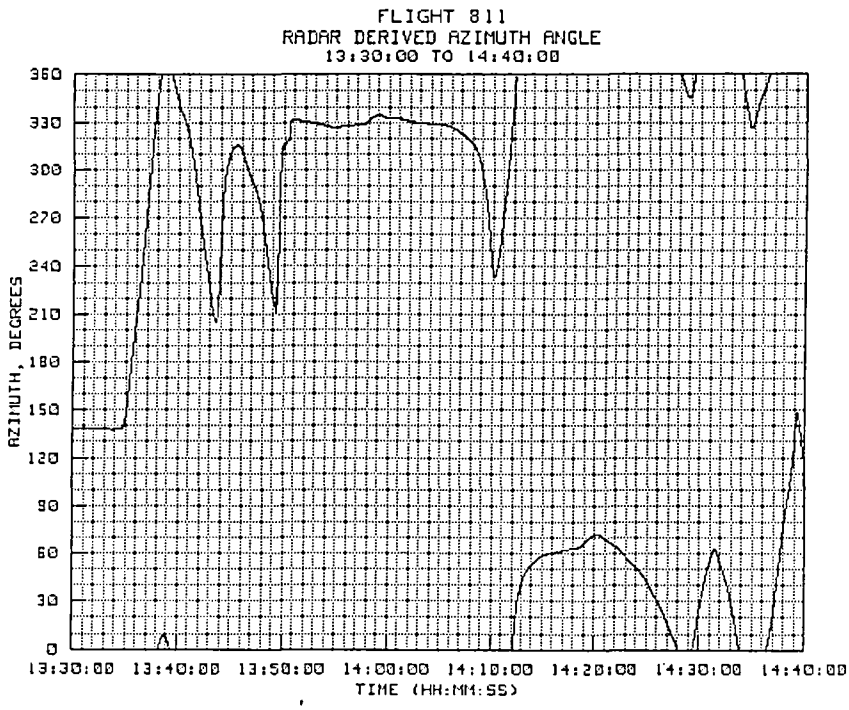

Figure 3-2. Flight 811 Radar-derived target azimuth angle.

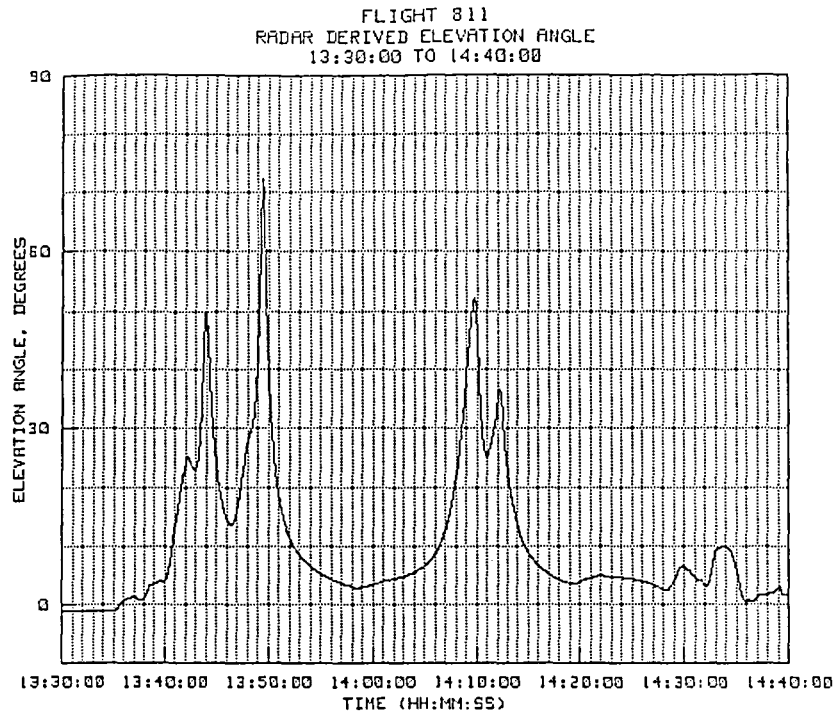

Figure 3-3. Flight 811 radar-derived target elevation.

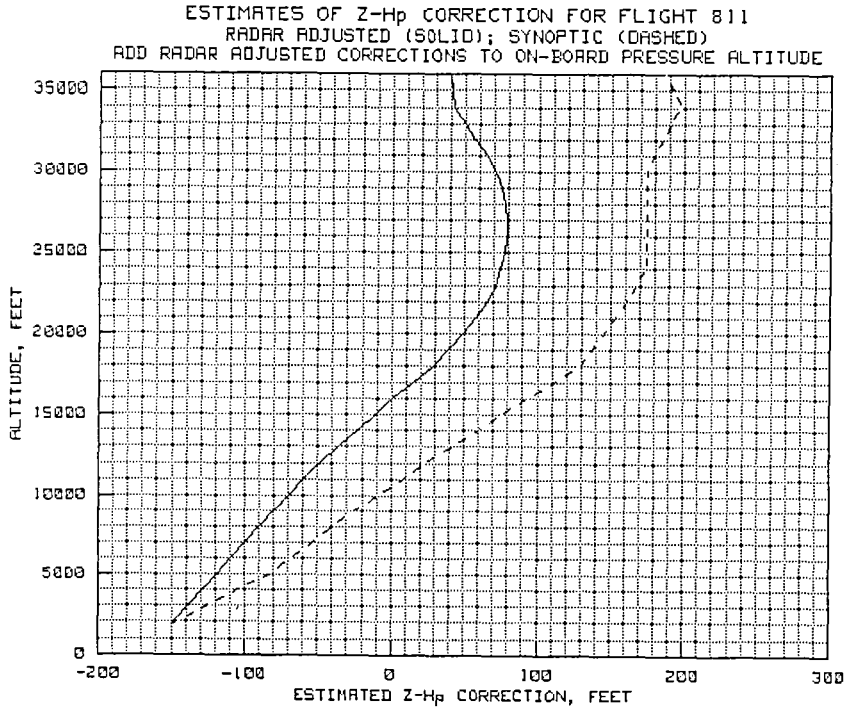

Figure 3-4. Flight 811 synoptic and radar derived Z-Hp plots.

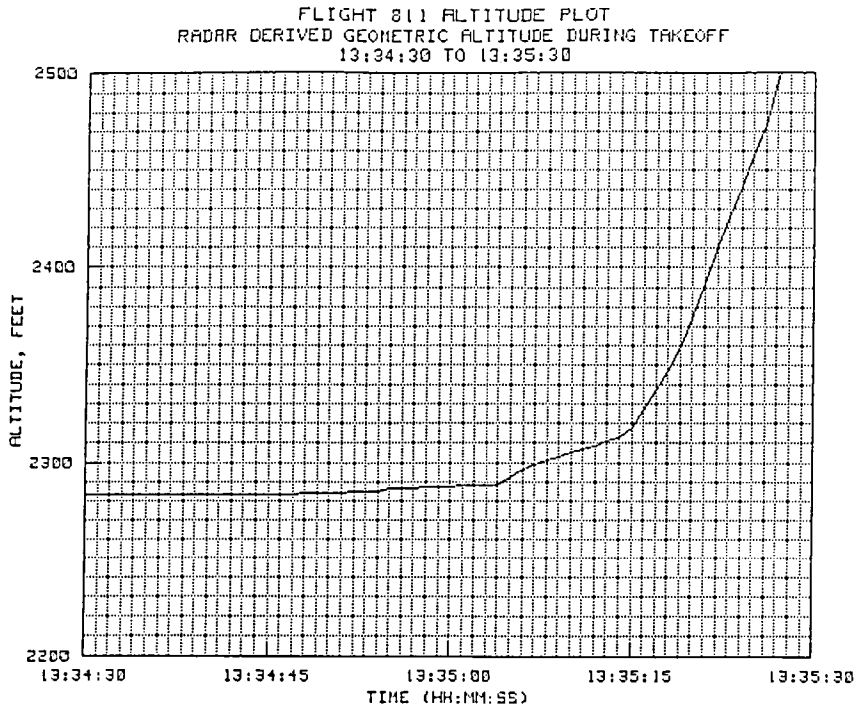

Figure 3-5. Flight 811 radar geometric altitude on takeoff.

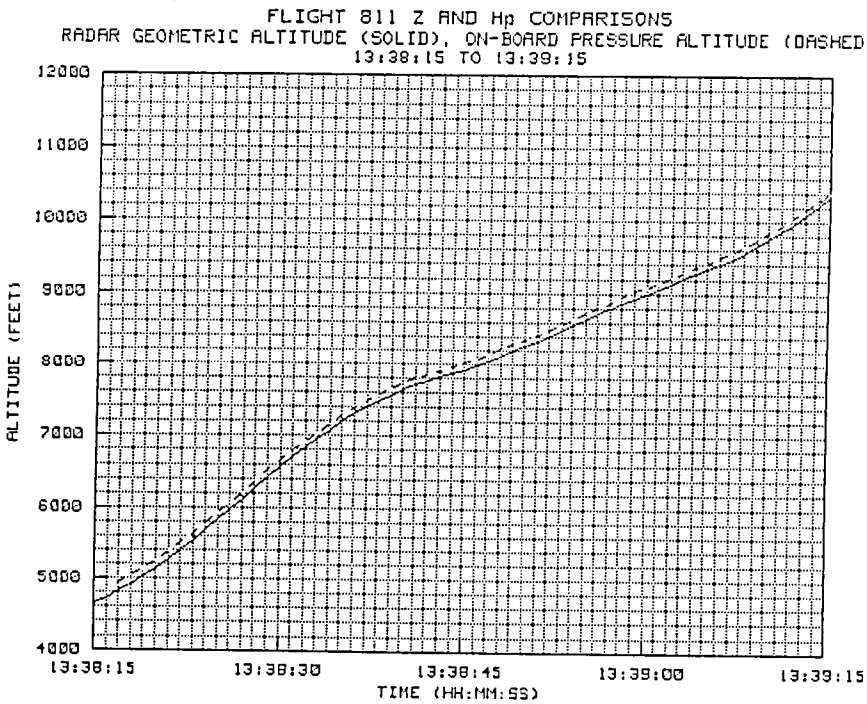

Figure 3-6. Flight 811 Z-Hp comparisons 5,000 to 10,000 feet.

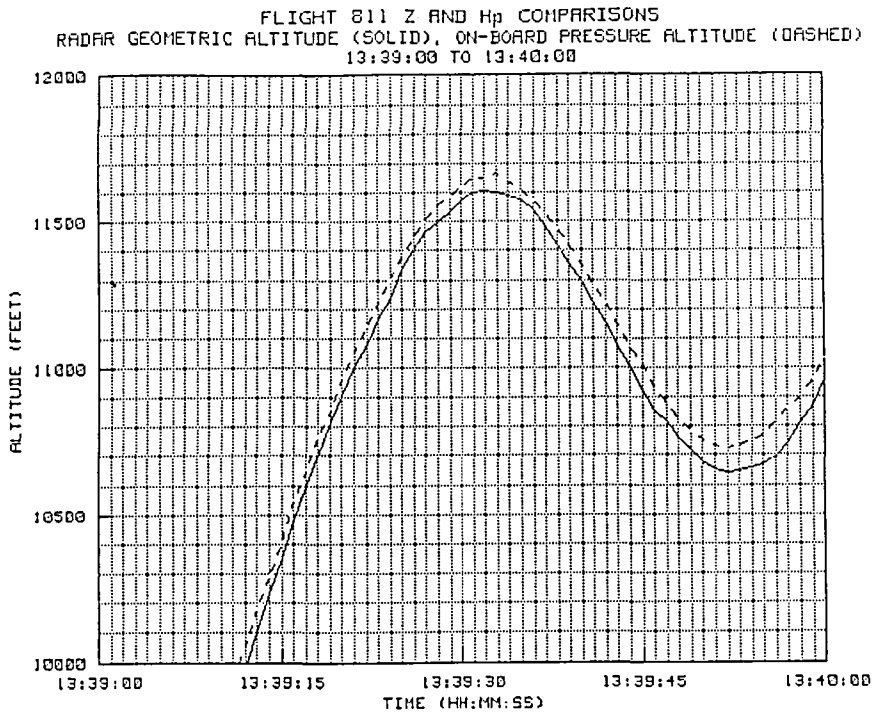

Figure 3-7. Flight 811 Z-Hp comparisons 11,000 feet.

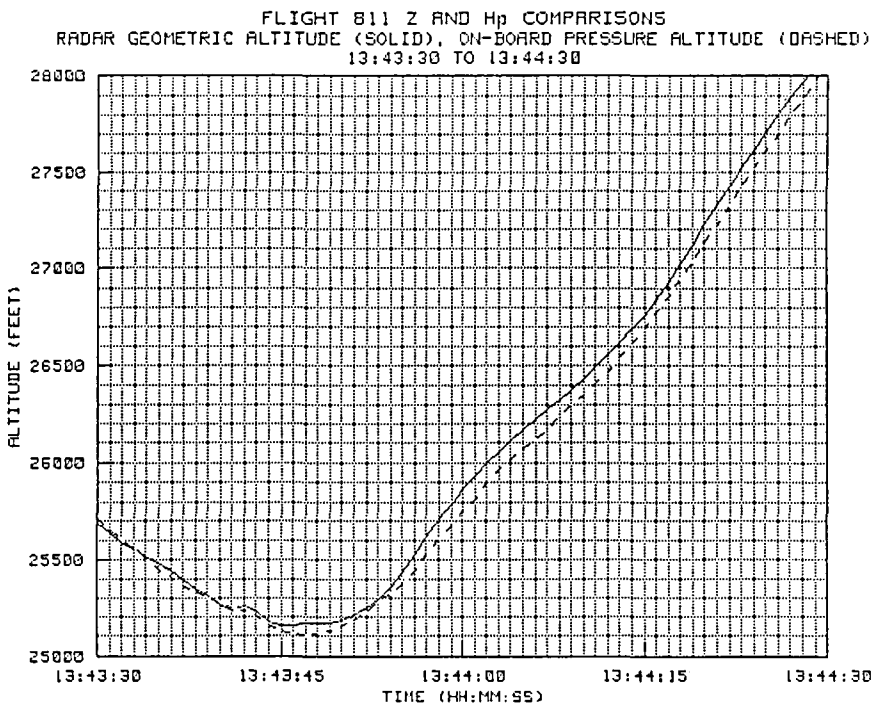

Figure 3-8. Flight 811 Z-Hp comparisons 25,000 to 28,000 feet.

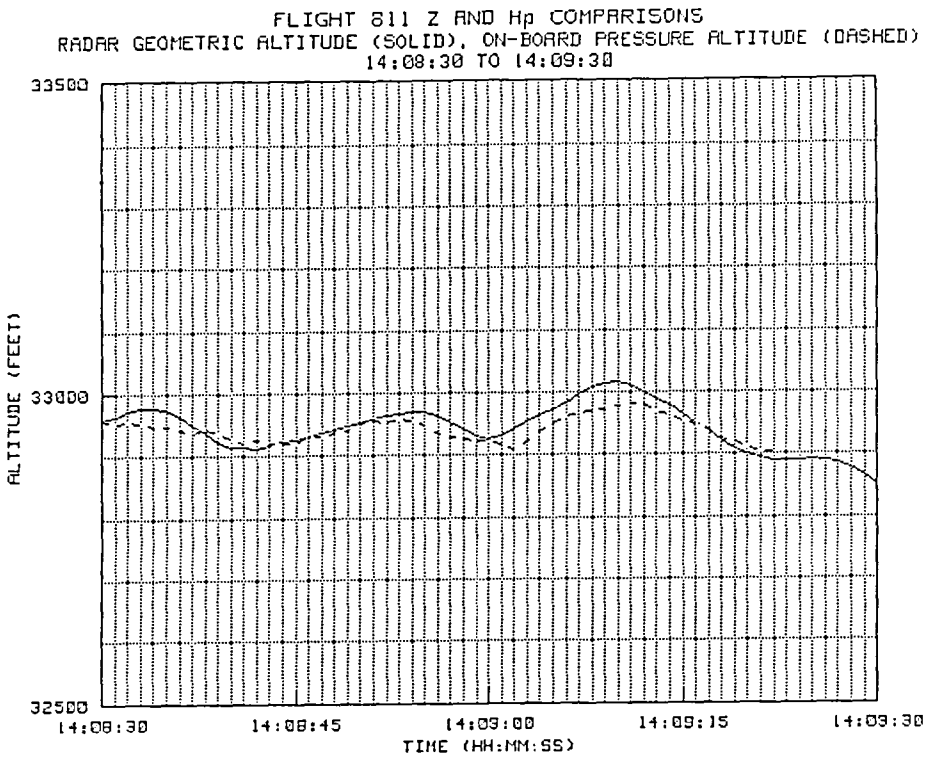

Figure 3-9. Flight 811 Z-Hp comparisons 33,000 feet.

3.2 Analysis of Test Points

When flight 811 was being planned, uncertainty existed as to how to measure the accuracy of the radar data in a way which would provide a high level of confidence in the results. Shortly after the analyses were started, GMD personnel recognized that concurrent on-board data would be essential to this task. The use of high-angle (higher accuracy) radar-derived altitude data to tie in on-board pressure measurements seemed to be the only practical way to provide a comparison parameter needed to identify true short term aircraft movements as well as overall trends in the radar data at longer tracking ranges.

After the flight, comparative plots were made of radar derived geometric altitude and pressure altitude recorded on board the aircraft. In all cases, the pressure altitude values were "corrected" for the local Z-Hp values determined by high-angle or close-in portions of the tracks. The correction curve for flight 811 is shown in figure 3-4.

Also provided are time history Mach number plots in which wind-corrected, radar-derived Mach number is shown as a solid line, and on-board Mach number is shown as a dashed line. Wind corrections for flight 811 are taken directly from the synoptic analysis.

In addition, plots of radar derived true course and flight path angle, along with measured range and elevation, are also included for cross-reference purposes. Note that the flight path angles were referenced to local vertical at the radar site, as is the case in the Cyber data reduction program.

The test points from flight 811 include the following time segments:

1. 13:36:57 to 13:37:30 - 0.6 Mach level run at 3500 feet.

2. 13:38:00 to 13:48:00 - 0.9 Mach climb; surface to 33,500 feet.

3. 13:51:00 to 13:57:30 - 0.9 Mach level survey run at 33,000 feet.

4. 14:02:50 to 14:09:30 - 0.55 to 1.2 Mach, 33,000-foot level acceleration and deceleration.

5. 14:13:30 to 14:18:15 - 0.9 Mach, 33,000-foot level cross survey run.

6. 14:21:45 to 14:28:15 - 0.9 Mach descent from 33,500 feet to 8500 feet.

3.2.1 Test Point #1

The altitude plot for test point #1 is shown in figure 3-10(a), and the Mach number plot is shown in figure 3-10(b). Plots of true course and flight path angle are provided in figures 3-10(c) and 3-10(d), and plots of slant range and elevation angle for the test point are provided in figures 3-10(e) and 3-10(f).

The test point was started at a slant range of 37,260 feet (6.13 n.mi.) and an elevation angle of 1.48 degrees. It ended at a slant range of 43,535 feet (7.16 n.mi.) and an elevation angle of 0.95 degrees. Both the altitude and the Mach number data were well behaved for this time period; however, on-board data were not provided for this test point, so no comparisons were made.

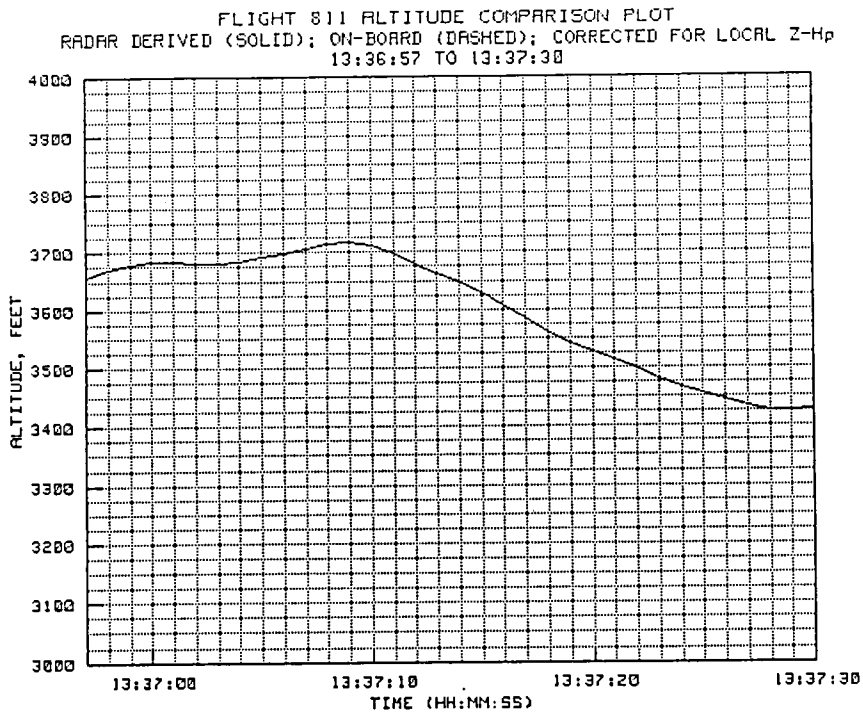

Figure 3-10(a). TP #1 radar-derived and on-board altitude.

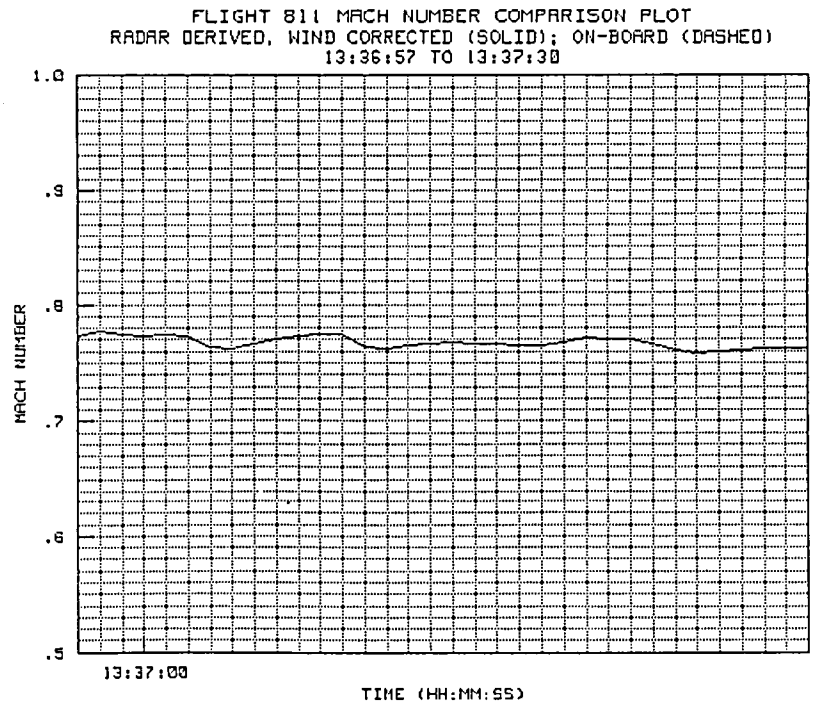

Figure 3-10(b). TP #1 radar-derived and on-board Mach number.

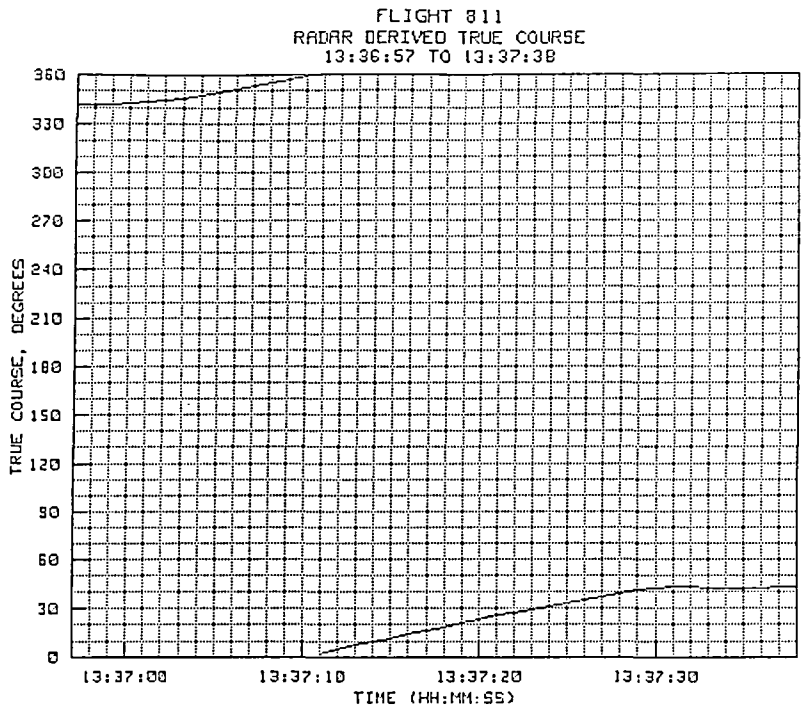

Figure 3-10(c). TP #1 radar-derived true course.

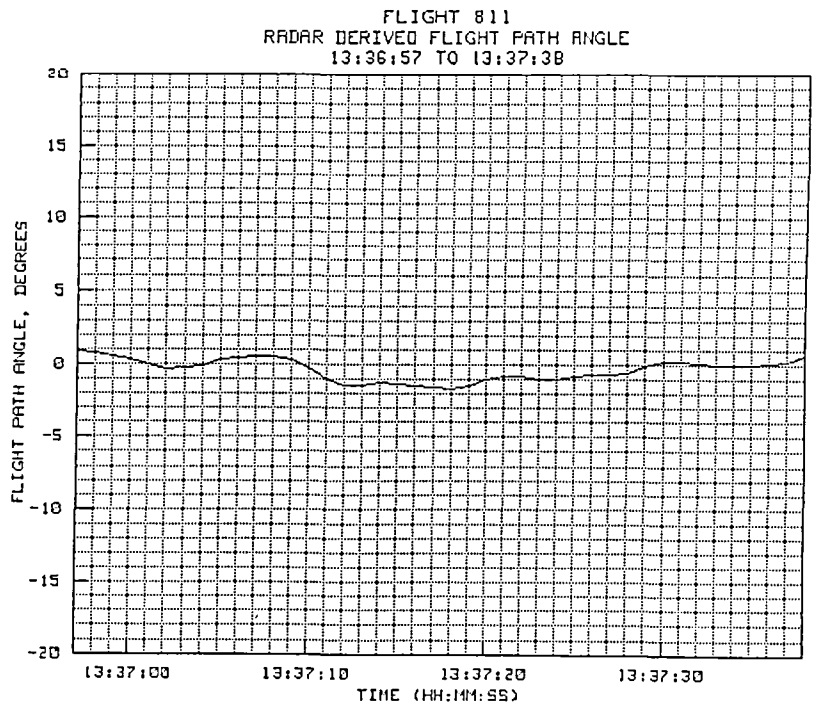

Figure 3-10(d). TP #1 radar-derived flight path angle.

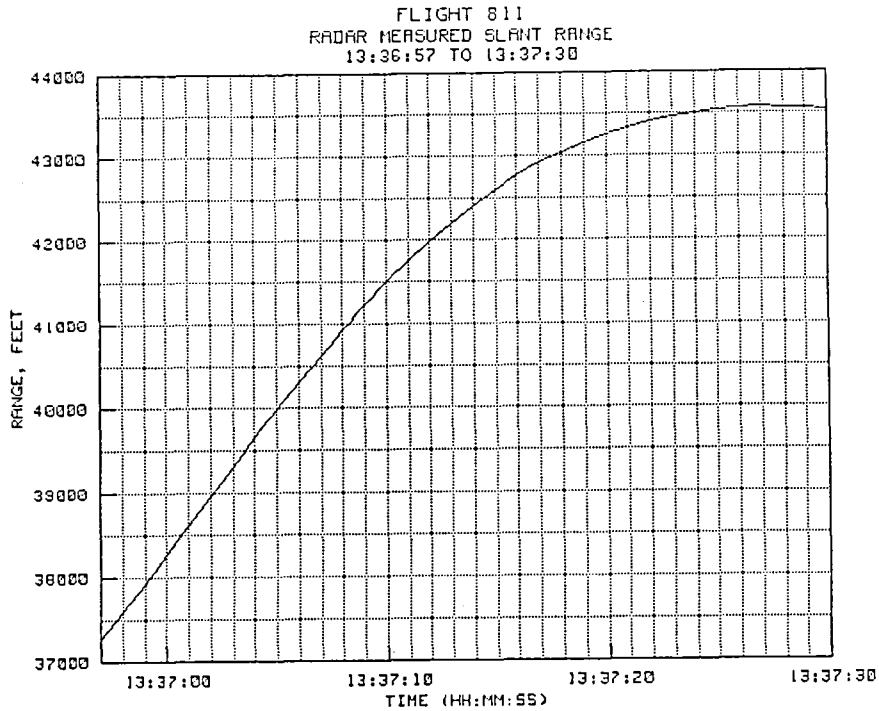

Figure 3-10(e). TP #1 radar-derived slant range.

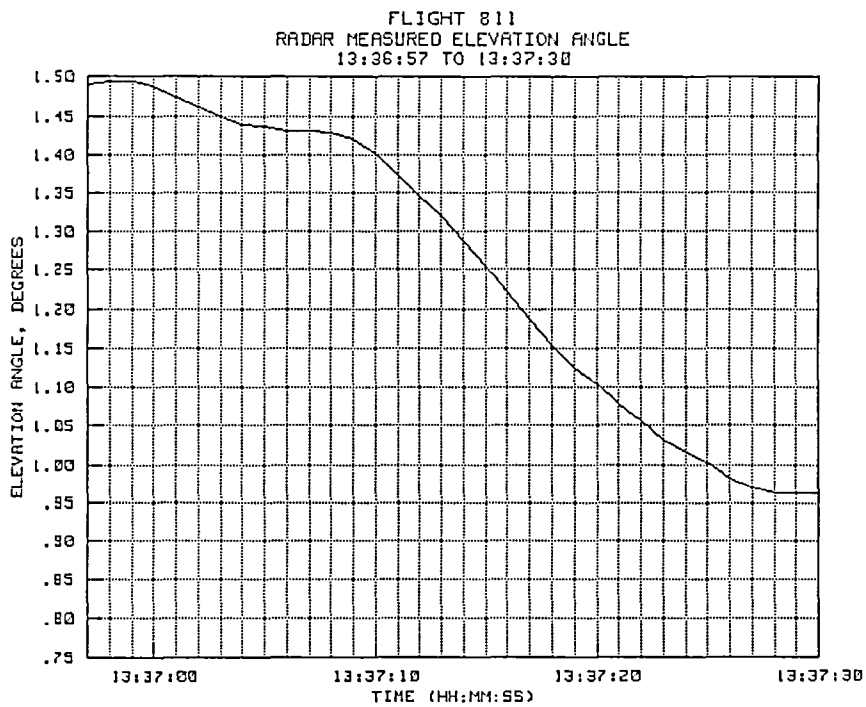

Figure 3-10(f). TP #1 radar-derived elevation angle.

3.2.2 Test Point #2

The time history plots for test point #2 are shown in figures 3-11(a) to 3-11(f). This test point was a 0.9 Mach number climb from the surface to 33,500 feet. The slant range at the start of the climb was 50,256 feet (8.27 n.mi.) with an elevation angle of 1.18 degrees. At the end of the climb the slant range was 66,498 feet (10.94 n.mi.) at an elevation angle of 27.82 degrees. The on-board pressure altitude measurements were corrected for the high-angle radar-adjusted Z-Hp values. In Figure 3-11(a), the radar derived geometric altitude plot (solid line) overlays the adjusted on-board pressure altitude plot (solid line).

An overcast condition existed during the time of this flight. The inconsistent climb pattern shown in figure 3-11(a) resulted from pilot attempts to remain in visual flight rule (VFR) conditions. Because of this, a number of heading changes were made during the climb so that the aircraft range from the radar remained within 5 to 20 nautical miles and the elevation angle varied from 1 degree to to as high as 50 degrees about the time the aircraft was passing the 25,000-foot level.

The Mach number plot for test point #2 shows some significant differences, even with the synoptic wind correction applied. Since the climb was made in essentially a continuous left turn, except for three short periods of wings level flight, the Mach data is subject to variations as a result of both altitude and heading changes. The maximum error, 0.04 Mach is considered to be about as good as could be expected for the high wind conditions that existed on the flight day. It is also possible that some of the Mach number variations may have been due, in part, to the effect of target glint resulting from maneuvering to avoid clouds.

It might also be noted that the Mach number values derived for altitudes above 25,000 feet appeared to be better than those derived for the lower altitudes, even though the aircraft was still turning. Differences between on-board and radar derived Mach above 25,000 feet were less than 0.01 Mach throughout the high altitude portion of the climb.

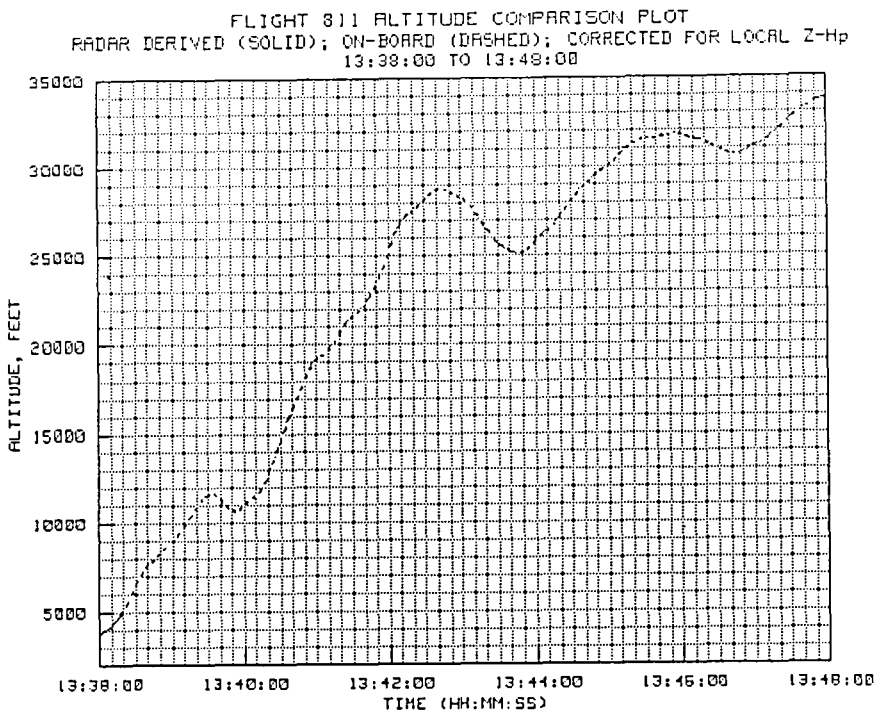

Figure 3-11(a). TP #2 radar-derived and on-board altitude.

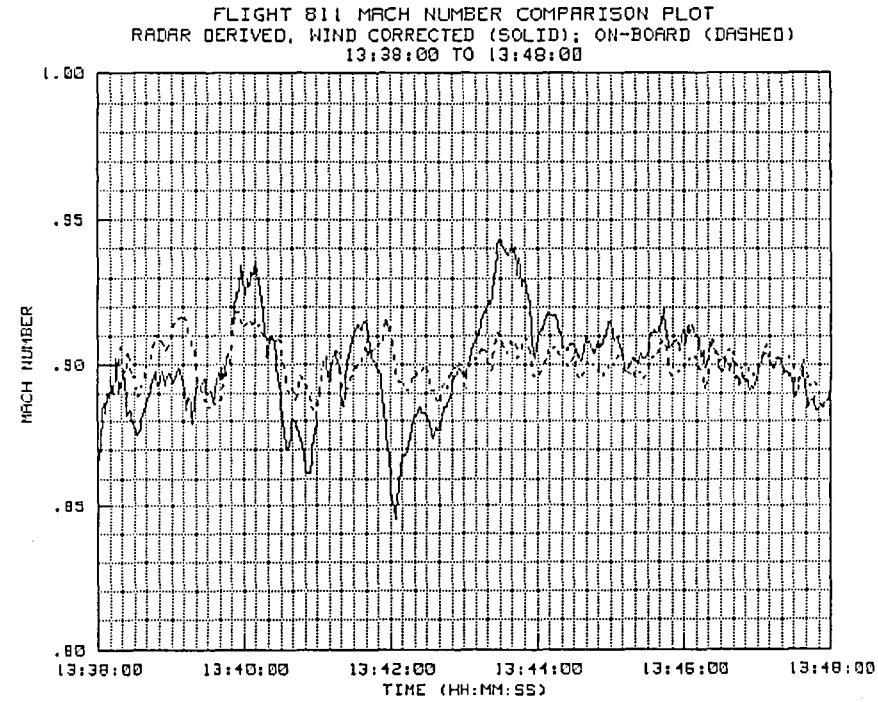

Figure 3-11(b). TP #2 radar-derived and on-board Mach number.

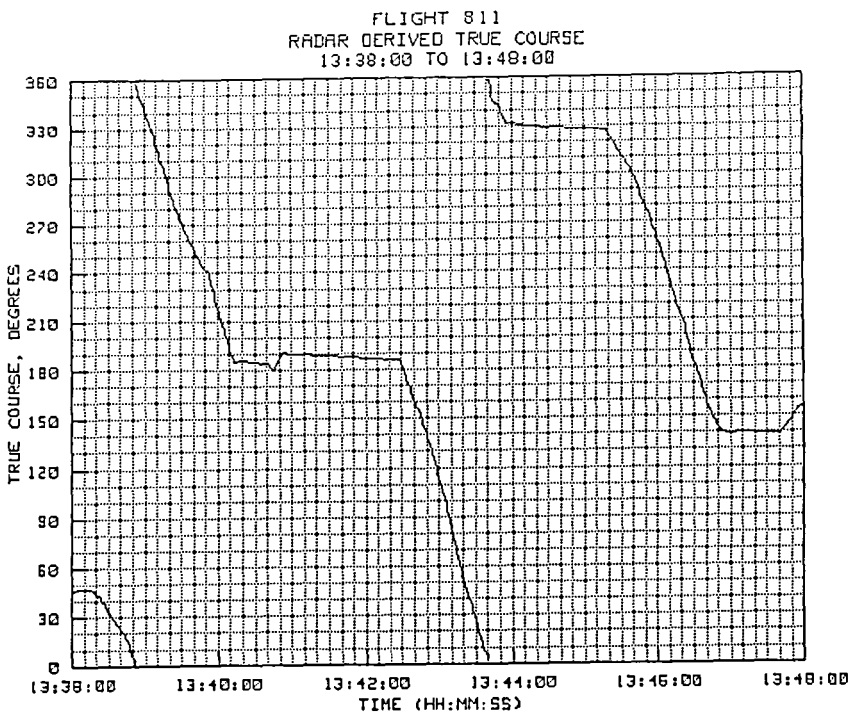

Figure 3-11(c). TP #2 radar-derived true course.

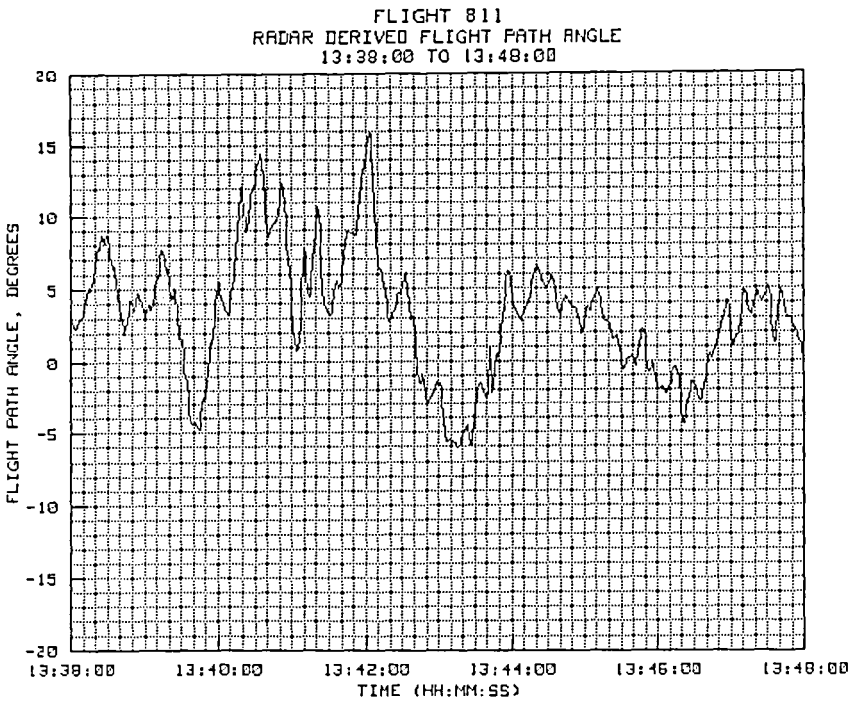

Figure 3-11(d). TP #2 radar-derived flight path angle.

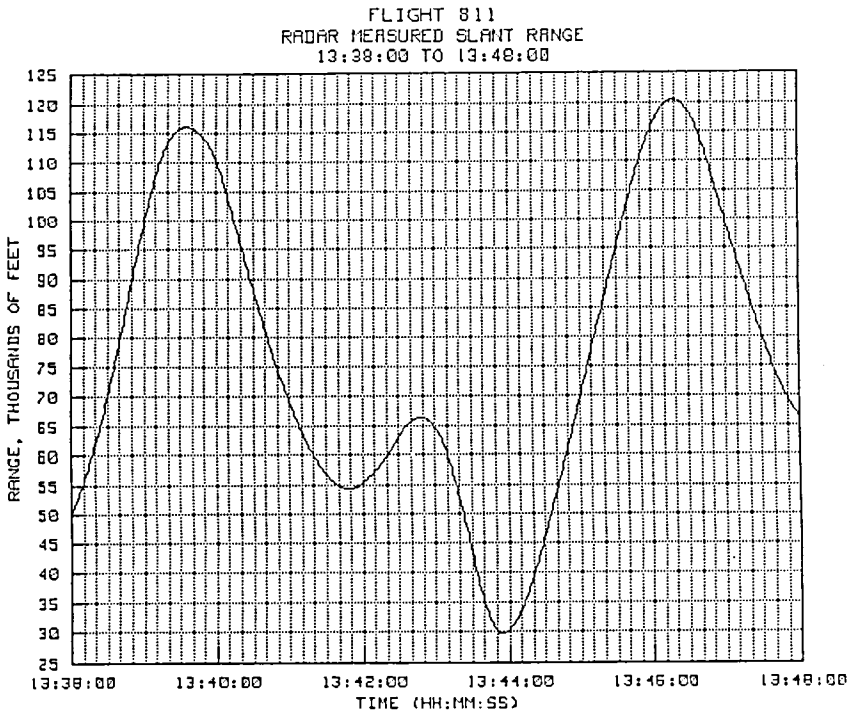

Figure 3-11(e). TP #2 radar-derived slant range.

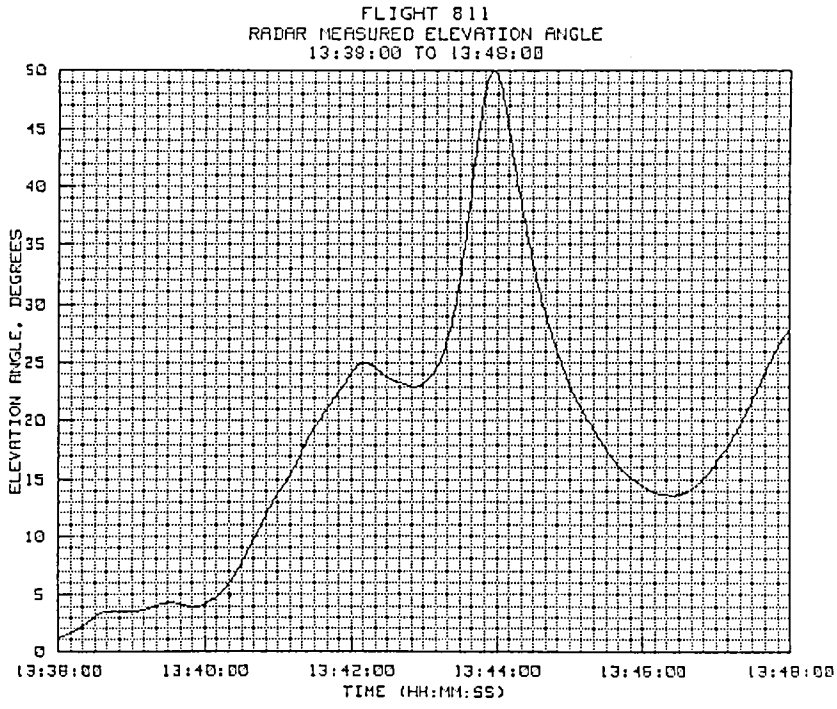

Figure 3-11(f). TP #2 radar-derived elevation angle.

3.2.3 Test Point #3

The time history plots for test point #3 are shown in figures 3-12(a) to 3-12(f). This was a "survey" run which started at 95,548 feet slant range (15.72 n.mi.) on an azimuth of 330 degrees and continued outbound until reaching 443,145 feet slant range (72.92 n.mi.) on approximately the same azimuth angle. The near point was the start of the run at 13:51:00. The elevation angle was 18.34 degrees at the start of the run and continually decreased until reaching about 3.31 degrees at the end of the run. Altitude commands from the real-time radar data program on the Varian computer were uplinked to the aircraft and displayed on the horizontal flight director bar. The pilot used this display as his reference for maintaining the desired altitude along the entire leg.

Two important factors affected the pressure altitude of the aircraft during this run. First, a strong pressure gradient existed along the direction of flight. According to the synoptic data, assuming an approximate linear behavior in the horizontal pressure gradient over the extent of this leg, the Z-Hp value along the direction of flight was expected to decrease by about 2.2 feet per nautical mile. Thus, with essentially no Z-Hp correction at the start of the run, the pressure altitude at the end of the run could be expected to read about 160 feet above the true geometric altitude.

Secondly, the altitude computations in the Varian computer are performed using the spherical slab refraction correction method. In the Varian program, a standard refractivity value of 0.000302 is always used. Low altitude inaccuracies in the spherical slab solution, combined with a 23 N-unit error in surface refractivity on the test day, probably resulted in significant errors in the altitude commands being uplinked. While this probably caused a certain amount of geometric altitude change, it should have no effect on this analysis since the principal concern, as far as these data, was to determine how well the true geometric altitude of the target could be computed from radar data alone, regardless of the pressure altitude.

In figure 3-13, a solid line has been drawn on the plot indicating the averaged values of the pressure altitude adjusted for the estimated local values of Z-Hp. A second solid line has been drawn to indicate the averaged values of radar derived geometric altitude for the same test point. A dashed line has been drawn to indicate the amount of variation in the pressure altitude which could be attributed to the horizontal Z-Hp gradient on the test day, based on the synoptic analysis. Thus, the interval labeled with an "a" at the right of the plot is the amount of variation between pressure altitude and geometric altitude that could be

expected as a result of the horizontal pressure gradient for the test day. The interval labeled with a "b" at the right of the plot is believed to be an error in the calculation of the radar-derived geometric altitude. Note that the amount of this error appears to be non-linear and appears to increase as the elevation angle decreases. The unaccountable difference at a maximum range of 73 miles was on the order of 190 feet, with the radar-derived altitude being lower than the pressure altitude.

A great deal of effort was expended during this analysis in attempting to identify the source of this error. Calibration procedures used on the NASA AN/FPS-16 radar ruled out error sources such as antenna droop, multipath, and so forth. The analysis of this portion of the flight was repeated using all the available refraction correction methods (White Sands, spherical slab, and gradient solutions) and using all available filters. The error was present, in virtually the same magnitude, in all cases. Other tests were run using different surface N-unit values, and, with the gradient method, using different vertical N-unit profiles. Within the reasonable range of N-unit uncertainty (about 5 percent), the majority of the error was still present in all cases.

To insure that the correct surface weather, and hence N-unit values, was used; pressure, temperature, and dew point data were cross checked with psychrometric measurements made at the site during the flight. All of these cross checked well. Computed values of the index of refraction obtained from the measured psychrometric data were cross checked against tables of r-f refractivity contained in Bean and Dutton (Ref. 3). Almost perfect agreement was obtained.

The possibility that an erroneous earth curvature value was being used was checked, however the values used in the software were correct. Variations in the computed altitude resulting from different earth models was checked. Differences in this case were found to be insignificant; on the order of 0.01 foot in altitude.

After considerable analysis of possible error sources which could be manifested in this way, it was concluded that if a systematic elevation bias error was present, it was not detected by the extensive calibration and test procedures used. At the same time, no errors were found in any of the data reduction programs, nor in the refractivity profile used for the test. Yet, long range, low elevation-angle data from later flights also exhibited the same behavior. Considerably more attention will be given to anomaly later in the analysis.

Other than for the difference observed between radar-derived geometric altitude and on-board pressure altitude, figure

3-12(a) indicates a good correlation between the short term behavior of the on-board and radar-derived altitude data. Note, however, that the noise in the radar-derived altitude increases as the target range increases. While this was first thought to result from reduced signal strength and hence greater dispersion in the measurement data, it was found that there was no appreciable difference in the amount of noise present in the raw measurement data when the target was at short ranges or at the maximum ranges encountered during this flight. (See Sec. 3.3) Instead, the increase in the magnitude of the noise in the altitude calculations at longer ranges was found to be due to the fact that small antenna movements had greater influence at longer ranges. For example, at the maximum range on this run, a change of one LSB in elevation resulted in a difference of 21 feet in the altitude calculation. At the start of the run, a change of 1 LSB accounted for only 4.5 feet.

The Mach number time history for test point #3 is shown in figure 3-12(b). On this run, a good correlation was achieved between the radar derived and the on-board measured Mach number values. The maximum difference at any point in the run was about 0.01 Mach. Since the true course throughout the run only varied by plus or minus 10 degrees, and since the Mach number and altitude were reasonably constant, the variation in the two Mach number calculations are probably due to the variability of the wind in combination with bias errors in the synoptic wind vectors.

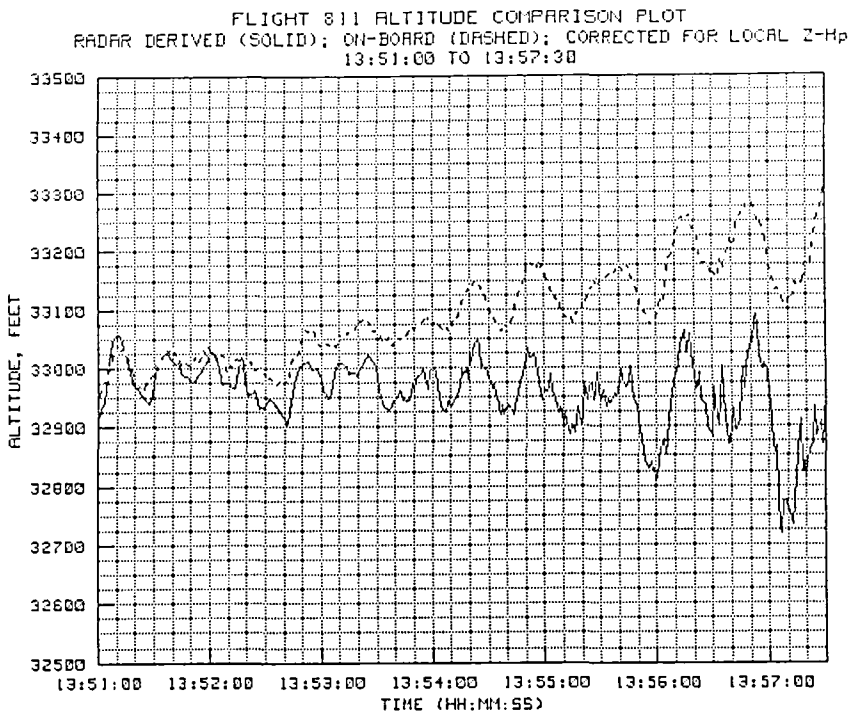

Figure 3-12(a). TP #3 radar-derived and on-board altitude.

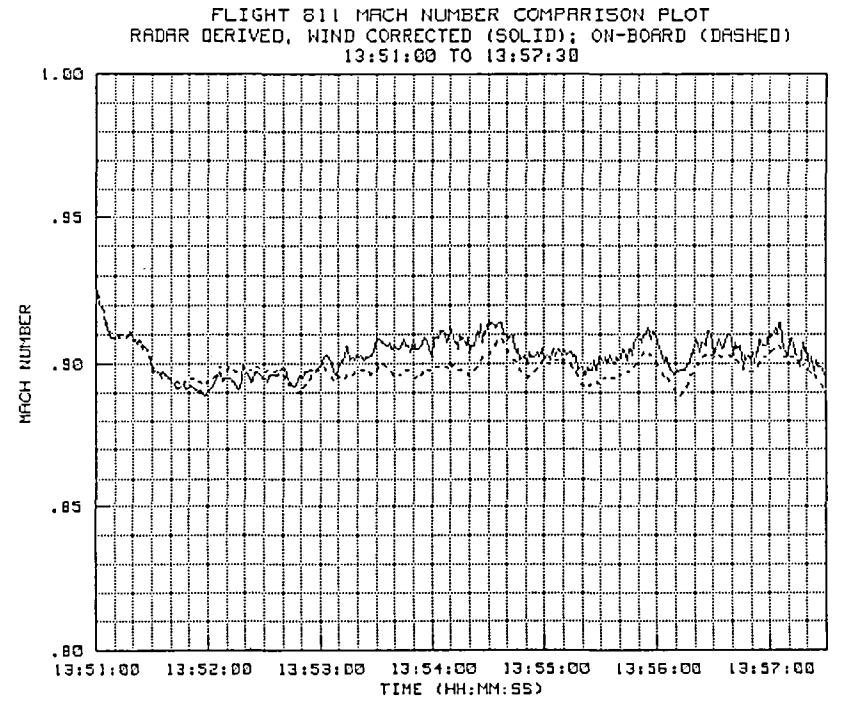

Figure 3-12(b). TP #3 radar-derived and on-board Mach number.

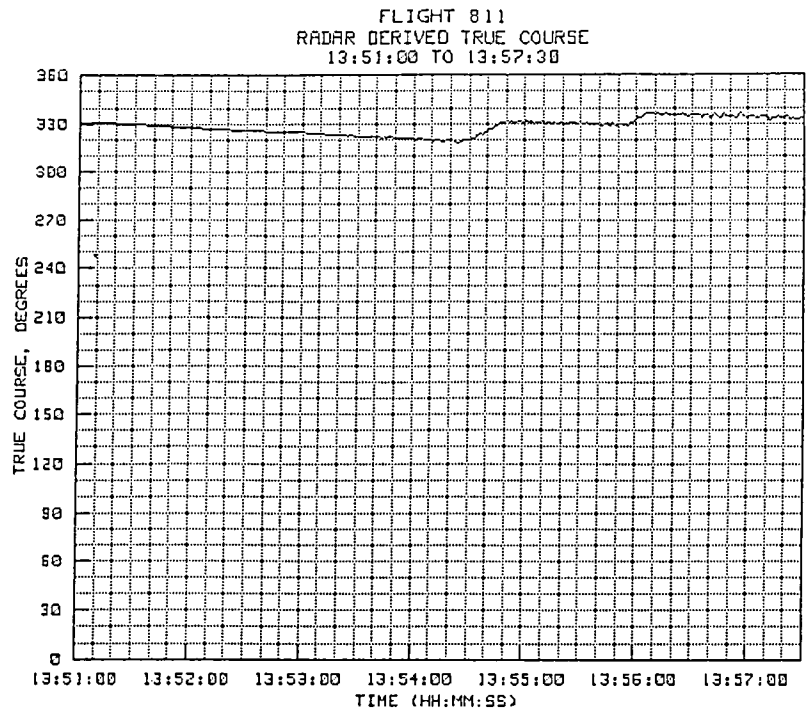

Figure 3-12(c). TP #3 radar-derived true course.

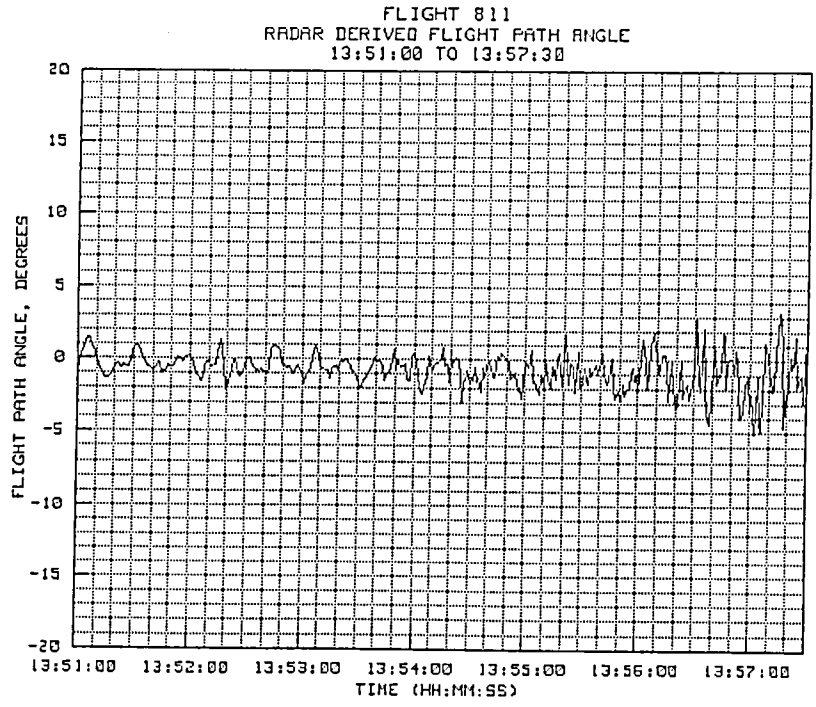

Figure 3-12(d). TP #3 radar-derived flight path angle.

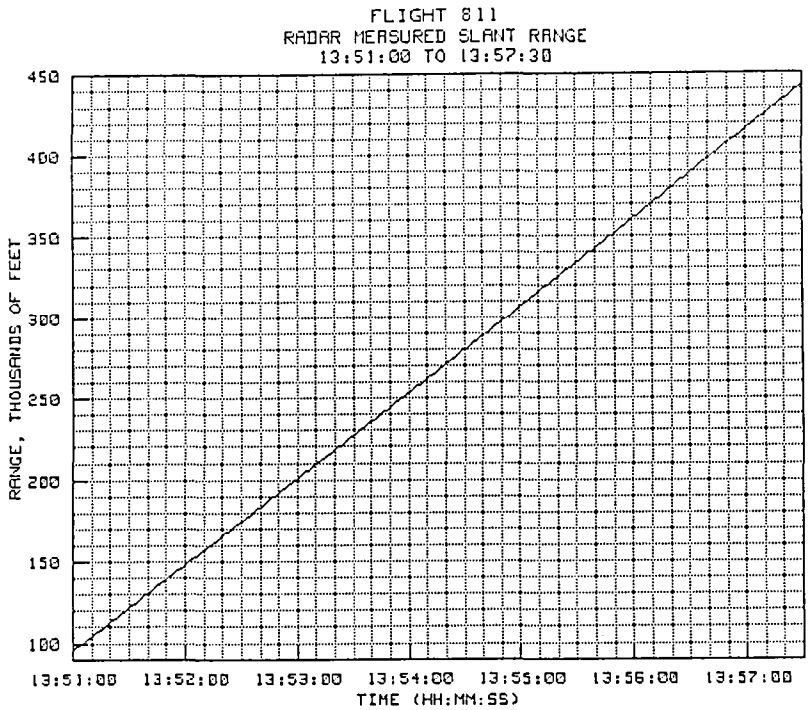

Figure 3-12(e). TP #3 radar-derived slant range.

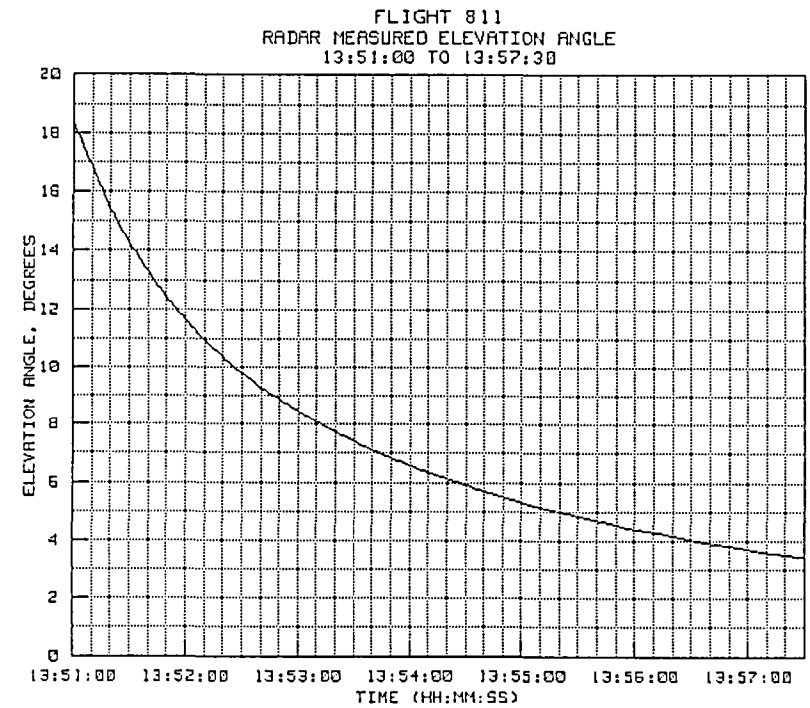

Figure 3-12(f). TP #3 radar-derived elevation angle.

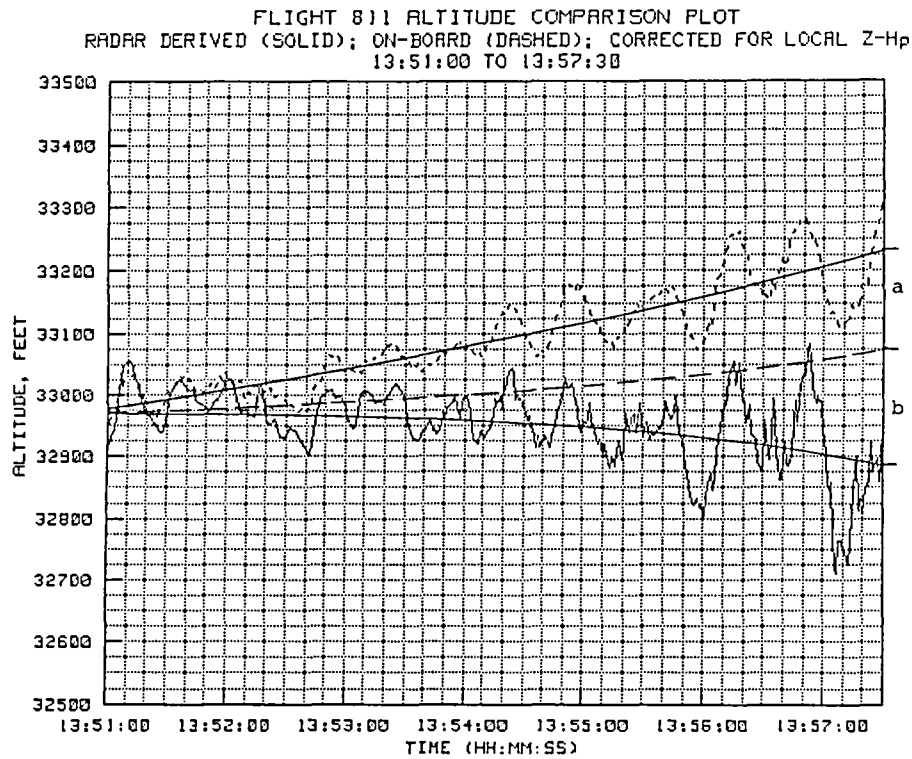

Figure 3-13. TP #3 error in altitude derivation.

3.2.4 Test Point #4

The time history plots for test point #4 are provided in figures 3-14(a) to 3-14(f). This was a level acceleration and deceleration with the Mach number starting at 0.55, increasing up to 1.22, and then decreasing back to about 0.6. The run was entered at a slant range of 334,735 feet (55.09 n.mi.) with a measured elevation angle of 4.71 degrees and an azimuth angle of 330 degrees. The leg was flown inbound on a southerly heading to a range of 39,738 feet (6.54 n.mi.), at which point the elevation angle had increased to 49.41 degrees. At the start of the leg, a comparable difference to that of test point #3 was observed between the pressure altitude and the radar-derived altitude. The transition to supersonic flight can be seen clearly in the flight (dashed) data; however, shortly after the acceleration through Mach 1, an anomaly occurred in the on-board data when an instantaneous decrease in the measured pressure altitude was observed at 14:05:50. The maximum Mach point was achieved at 14:06:39, after which the aircraft was decelerated back through Mach 1 and on down to about 0.6 Mach. No comparable jump in the measured pressure altitude was observed during the decelerating portion of the run, except at the supersonic and subsonic transition points where anomalies in the data occurred because of uncorrected effects of the shock wave on the aircraft pressure sources.

During this run, a good correlation can be seen in the short term altitude movements; however, the jump in the pressure altitude masks the true geometric versus pressure altitude differences that may have exsisted, except for data at the maximum ranges. The amount of difference at the start of the run is approximately the same as the amount of difference found in test point #3 at 15:55:30 where the target range and elevation angle were about the same.

Mach number data for test point #4, shown in figure 3-14(b), appears to be well behaved. Aircraft true course during this run ranged between 150 and 160 degrees. Throughout the run, the on-board and wind-corrected radar-derived Mach numbers agreed to within about 0.01 Mach or less, except at the supersonic transition point where a slight "hump" in the on-board data brought the difference close to 0.02 Mach. The "hump" was also due to uncorrected effects of the shock wave on the pressure sensing ports.

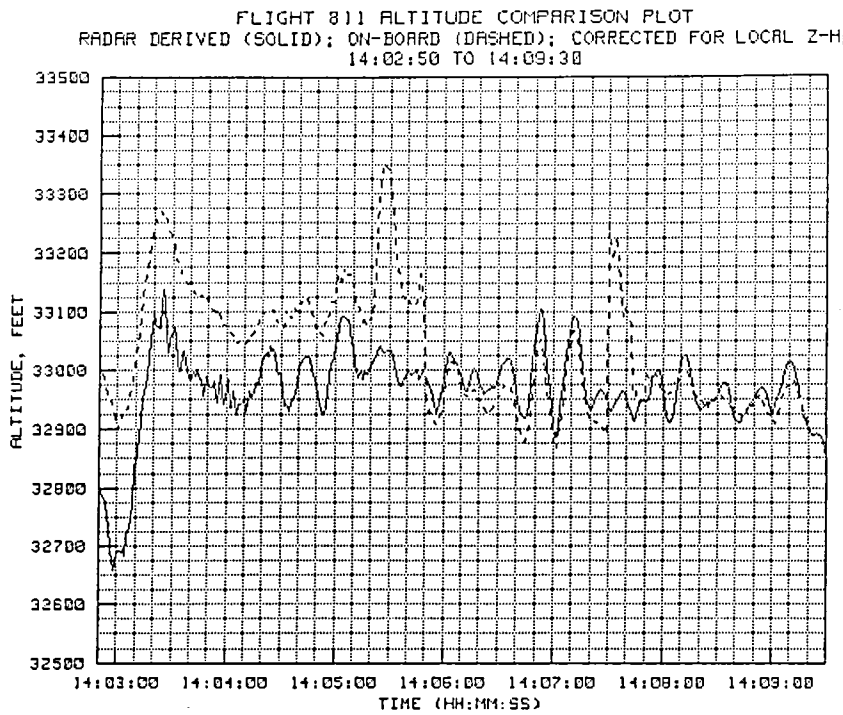

Figure 3-14(a). TP #4 radar-derived and on-board altitude.

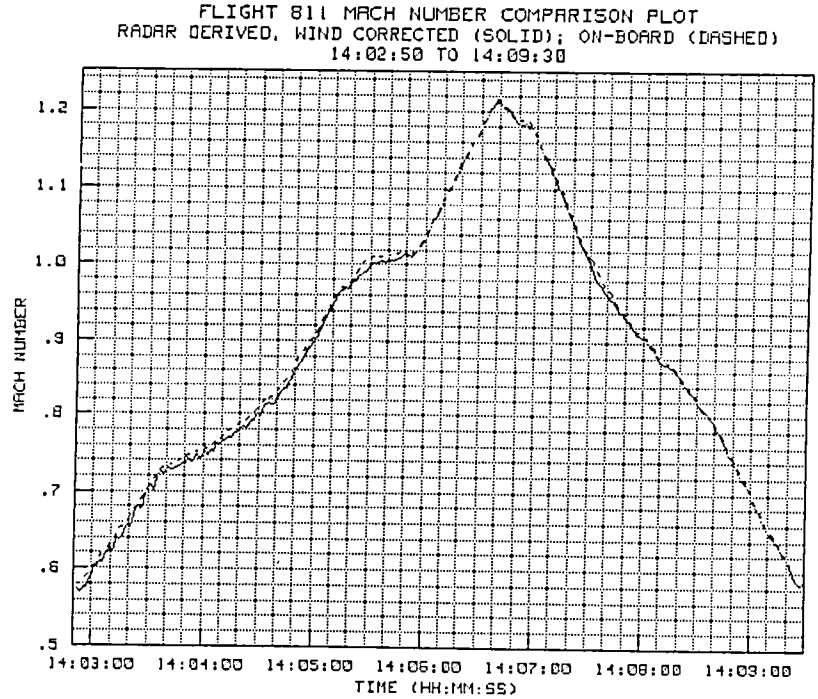

Figure 3-14(b). TP #4 radar-derived and on-board Mach number.

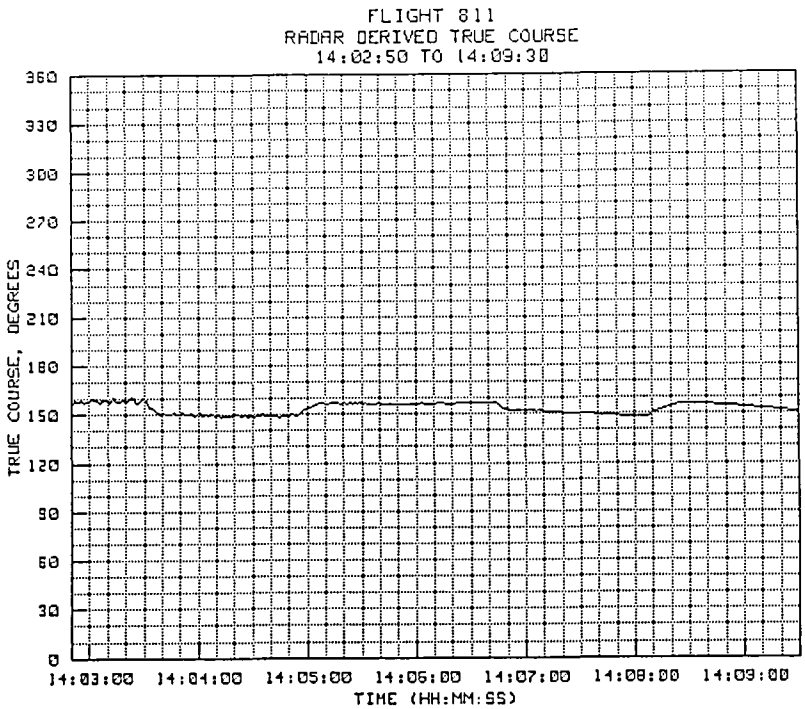

Figure 3-14(c). TP #4 radar-derived true course.

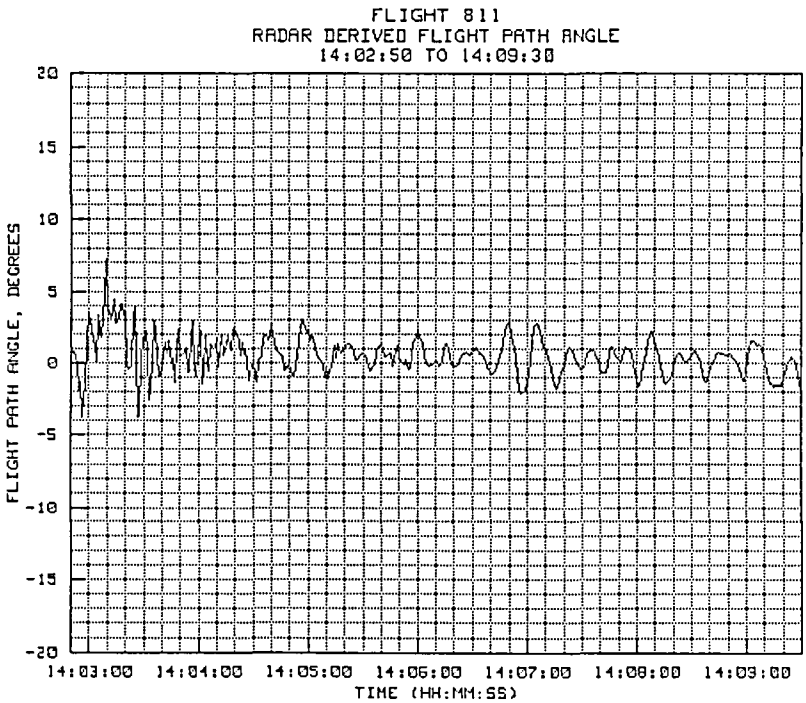

Figure 3-14(d). TP #4 radar-derived flight path angle.

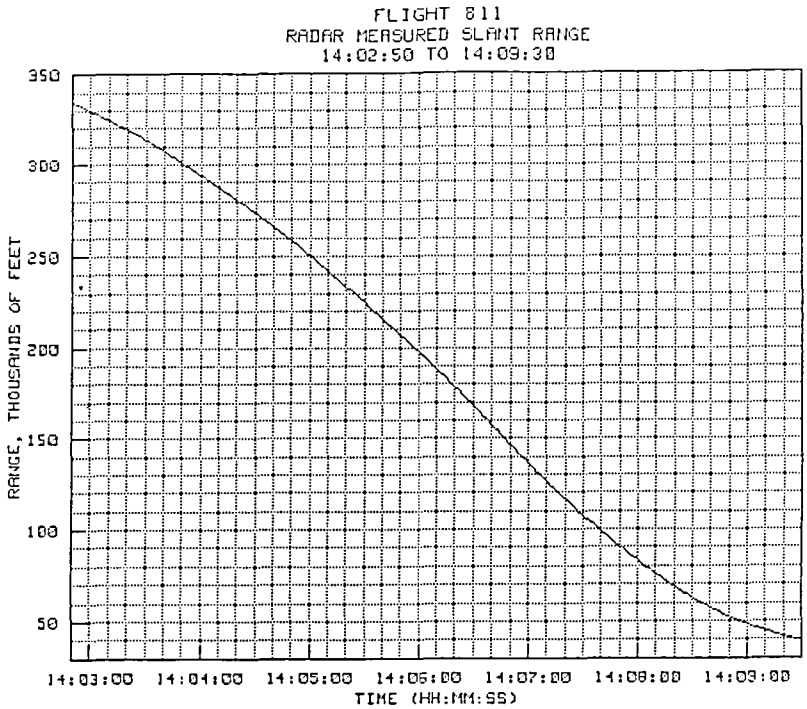

Figure 3-14(e). TP #4 radar-derived slant range.

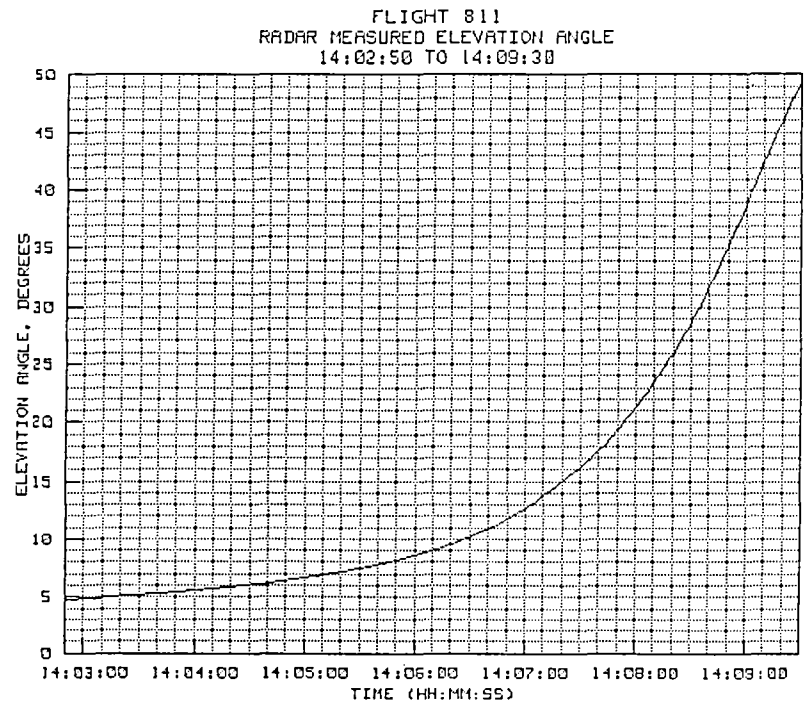

Figure 3-14(f). TP #4 radar-derived elevation angle.

3.2.5 Test Point #5

The time history plots for test point #5 are shown in figures 3-15(a) to 3-15(f). The run started at a slant range of 101,051 feet (16.63 n.mi.) and an elevation angle of 17.26 degrees on a azimuth of 40 degrees. The pass was flown at a constant 0.9 Mach on a true course that ranged from 060 to 070 degrees, or approximately perpendicular to the first survey run. The run was concluded at 385,254 feet slant range, about 63.41 nautical miles, with an elevation angle of 4.09 degrees at 062 degrees azimuth. The near point was the start of the run at 14:13:30.

At the start of the run, the corrected pressure altitude appeared to be about 25 feet below the radar-derived geometric altitude. By the end of the run, the pressure altitude was about 25 feet above the geometric altitude. This run was in a direction along which a low pressure gradient had been predicted. Therefore, the nearly 50 foot change observed between geometric and pressure altitude can not be accounted for by the pressure gradient. Thus, it is likely that the same type of error as observed on test point #3 was also present in these data, except that the ranges were shorter, therefore the error was smaller.

Again, good correlation can be seen in the short term altitude oscillations, and again the noise in the altitude data can be seen to increase with greater target range.

The time history Mach number plot for this run, figure 3-15(b), shows excellent correlation between the on-board Mach number and the radar derived Mach number. The maximum difference throughout the run was on the order of 0.007 Mach with most values falling within 0.003 Mach.

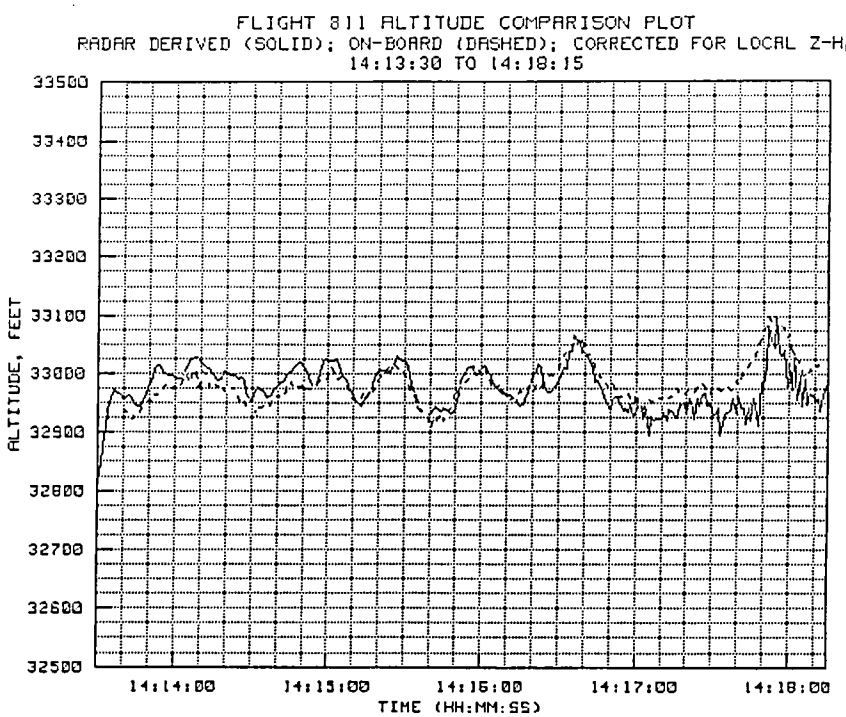

Figure 3-15(a). TP #5 radar-derived and on-board altitude.

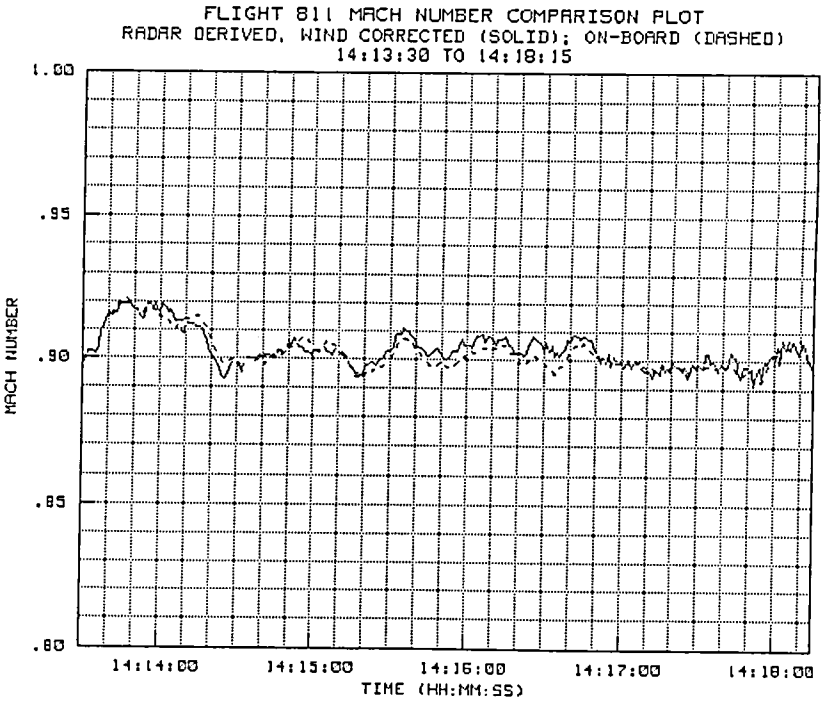

Figure 3-15(b). TP #5 radar-derived and on-board Mach number.

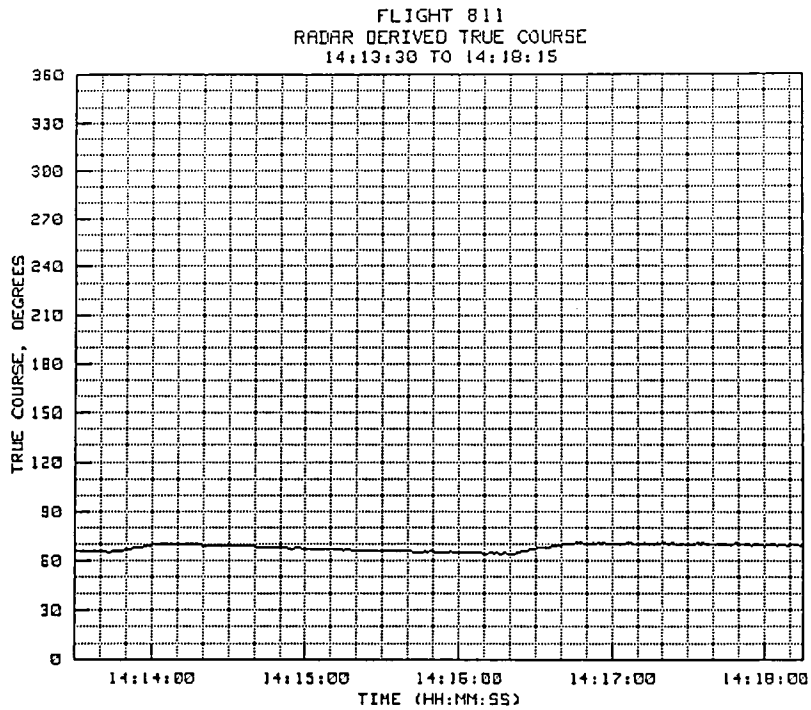

Figure 3-15(c). TP #5 radar-derived true course.

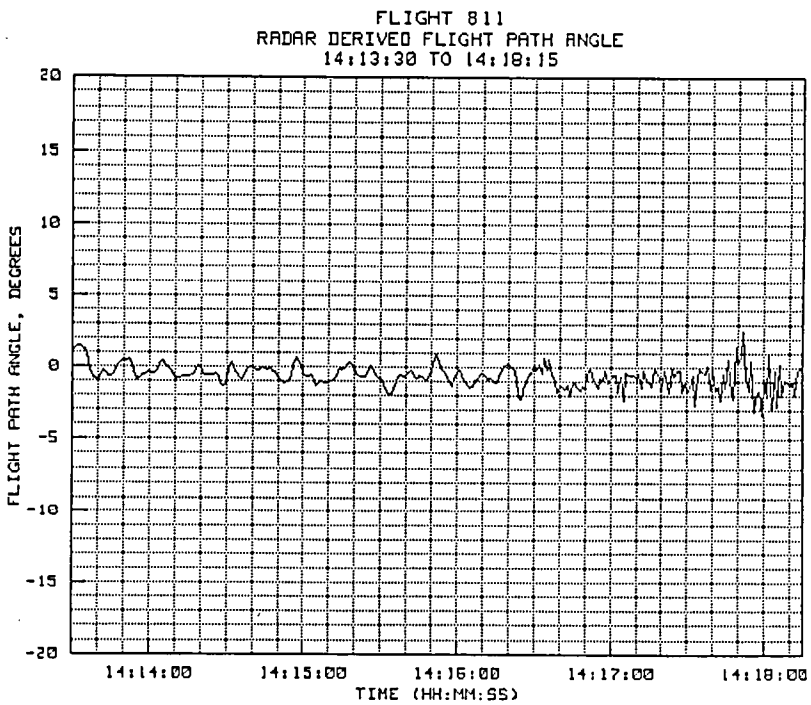

Figure 3-15(d). TP #5 radar-derived flight path angle.

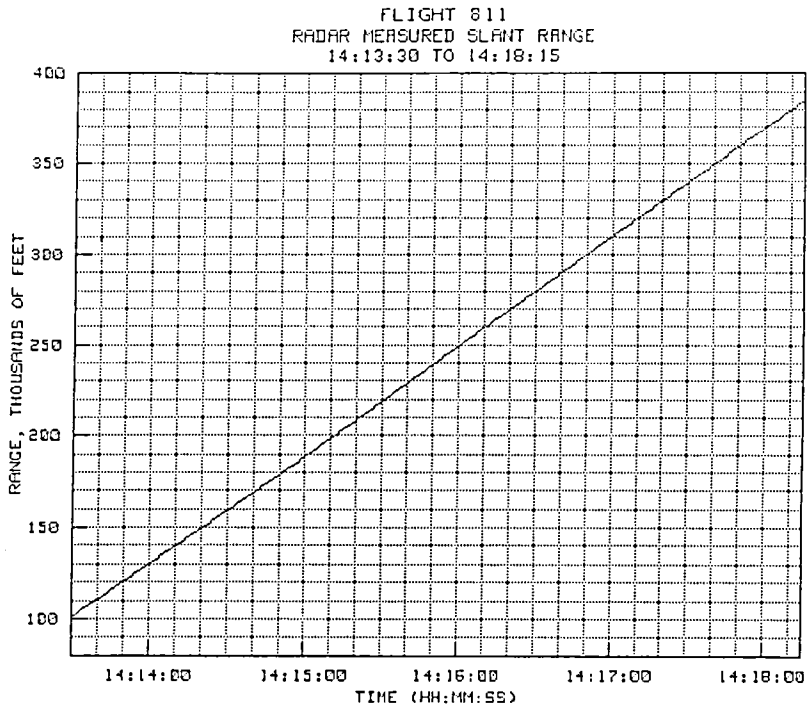

Figure 3-15(e). TP #5 radar-derived slant range.

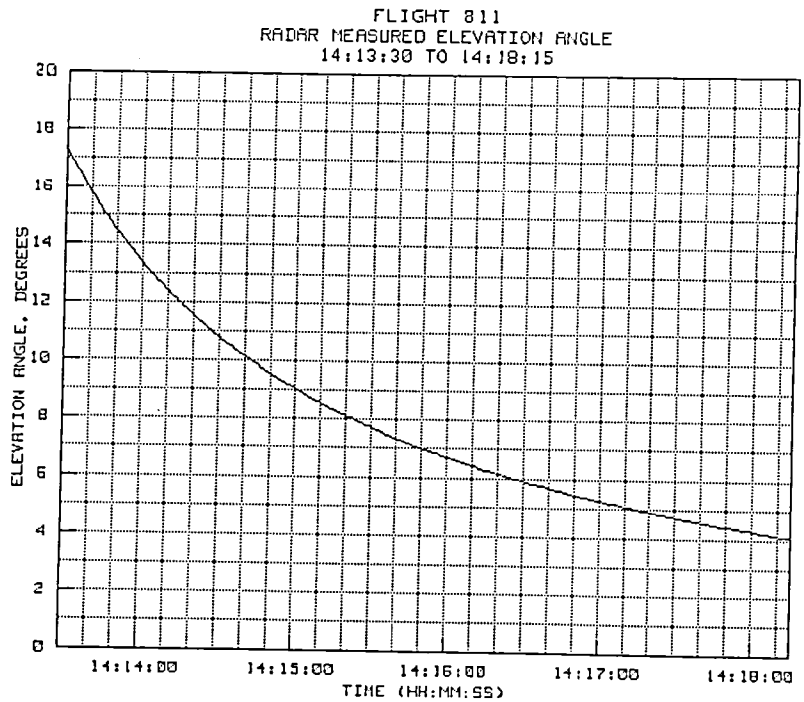

Figure 3-15(f). TP #5 radar-derived elevation angle.

3.2.6 Test Point #6

The time history plots for test point #6 are shown in figures 3-16(a) to 3-16(f). The run consisted of a descent from 34,000 feet down to 7000 feet MSL at a constant 0.9 Mach. The descent was made in a westerly direction, toward the radar site. The aircraft was at 337,329 feet (55.52 n.mi.) at the start of the descent and at 104,338 feet slant range (17.17 n.mi.) at level off. The starting elevation angle was 4.83 degrees; the ending angle was 2.57 degrees.

For this run, the geometric altitude plot shows good correlation between the altitude derived from the on-board pressure data and the altitude derived from the radar measurements. In fact, the radar-derived data (shown as a solid line) completely masks the on-board data over which it was plotted. Even so, differences of up to 25 or so feet might not be noticeable because of the plot scale.

Mach number during the descent, shown in figure 3-16(b), shows some variations. The first, at about 14:23:40 occurred during a heading change (see Fig. 3-16(c)). The next, at about 14:27:30, also occurred during another heading change. Both of these variations persist for a fairly long period of time (30 to 40 seconds) suggesting differences between the actual and the synoptic wind vectors.

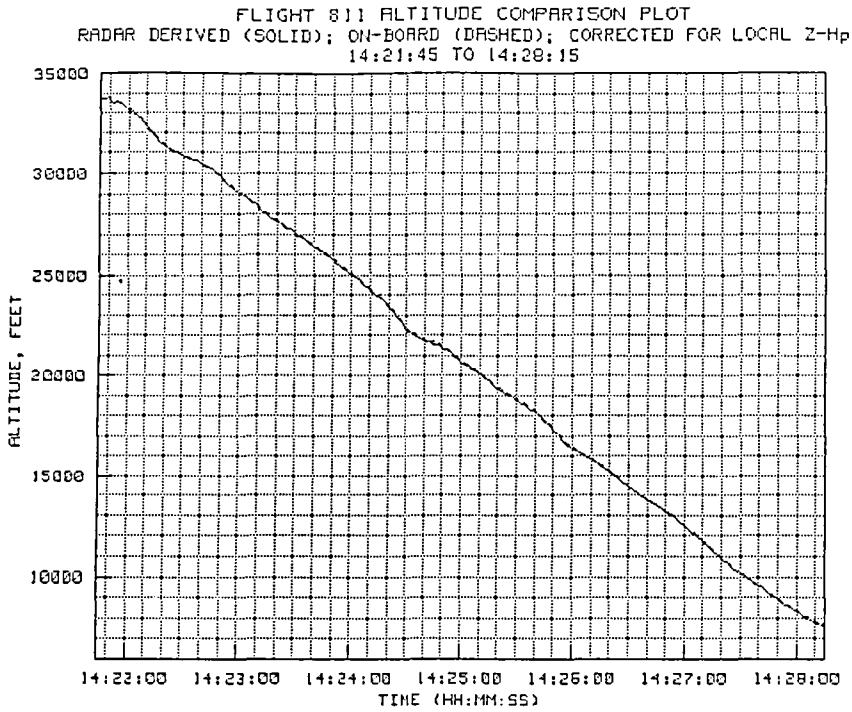

Figure 3-16(a). TP #6 radar-derived and on-board altitude.

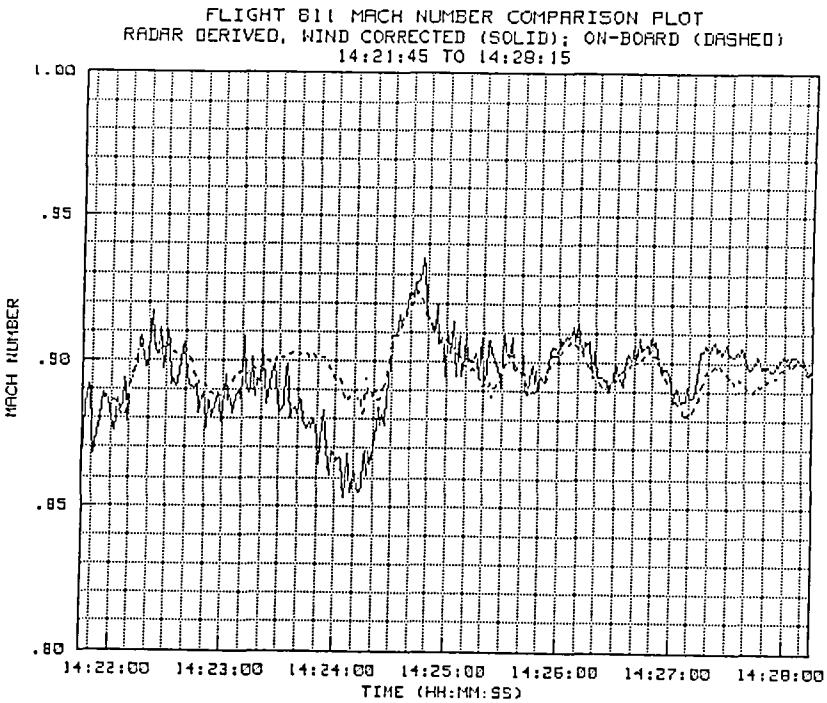

Figure 3-16(b). TP #6 radar-derived and on-board Mach number.

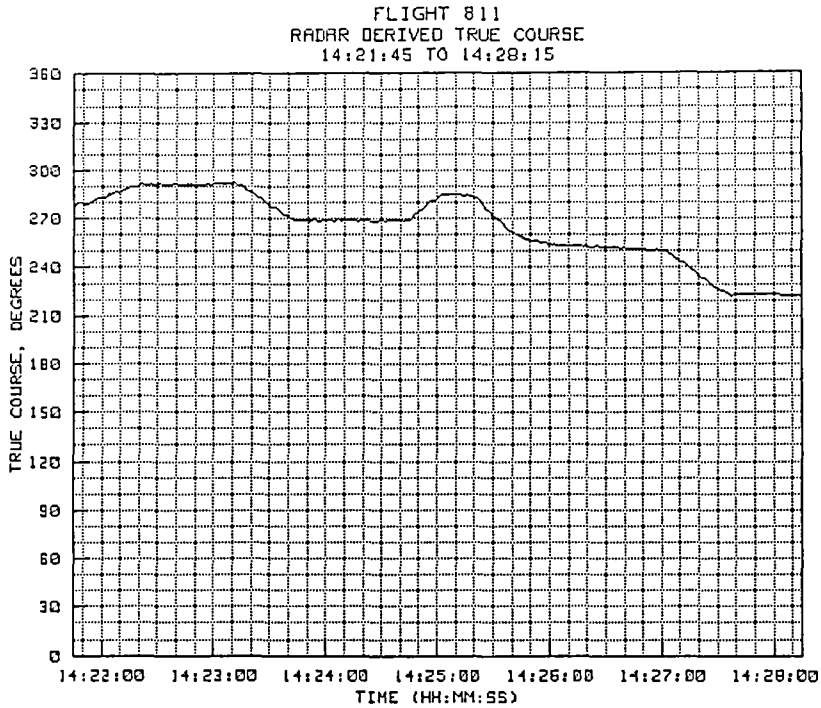

Figure 3-16(c). TP #6 radar-derived true course.

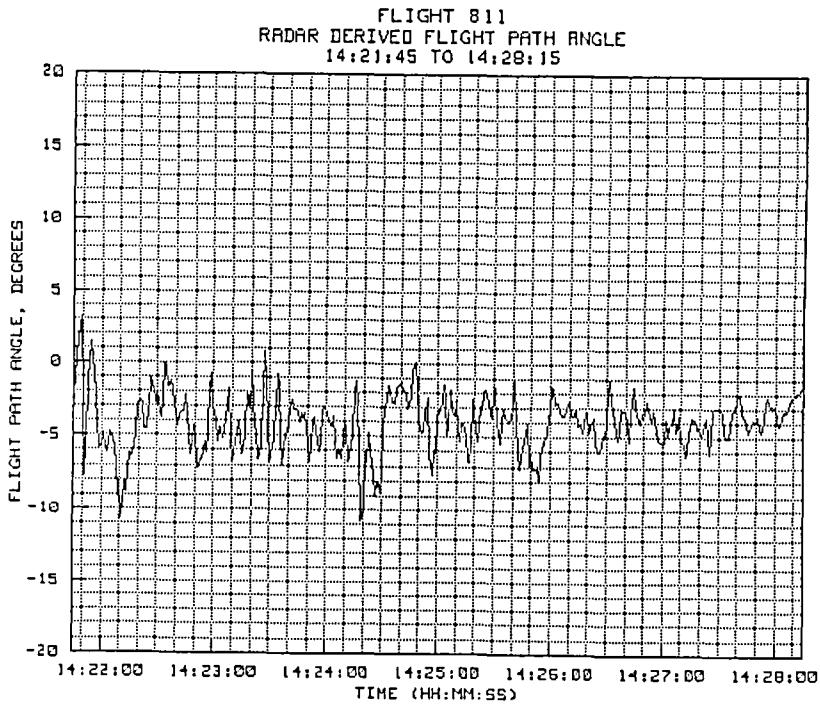

Figure 3-16(d). TP #6 radar-derived flight path angle.

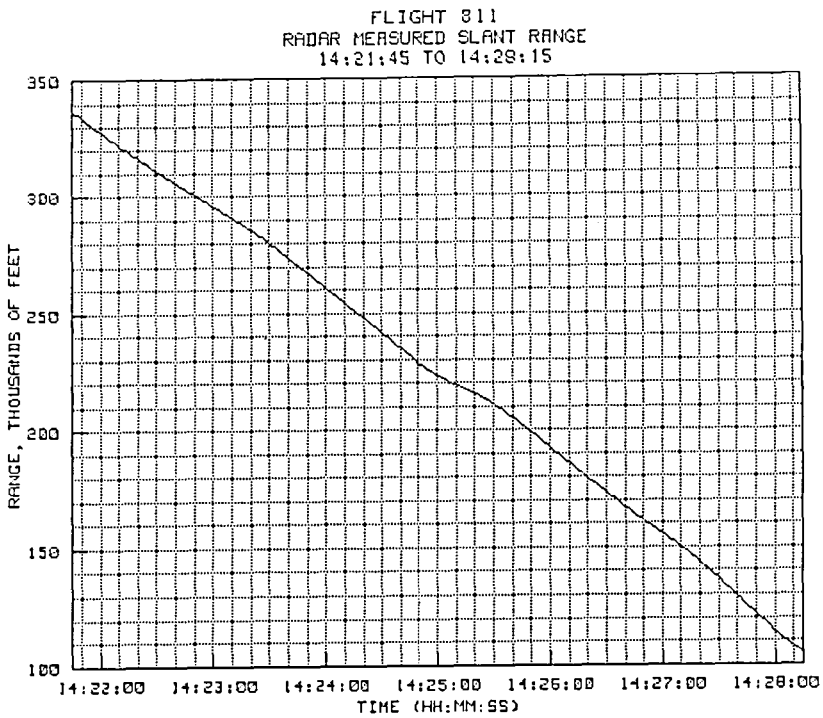

Figure 3-16(e). TP #6 radar-derived slant range.

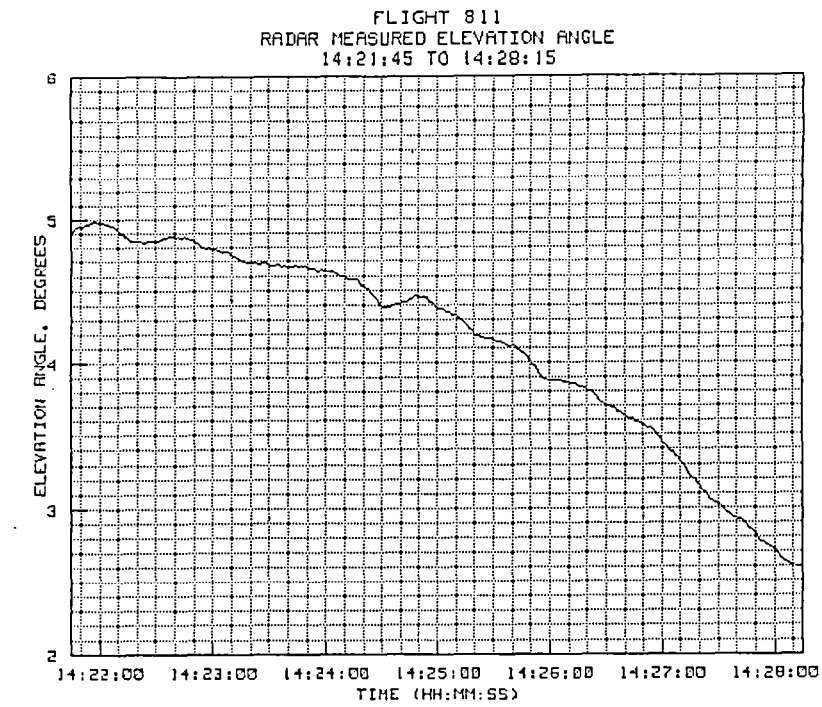

Figure 3-16(f). TP #6 radar-derived elevation angle.

3.3 Noise Analysis for Flight 811

Figures 3-17, 3-18, and 3-19 provide time history plots of random noise in the range, azimuth, and elevation channels of the radar. The scale is given in terms of 1 sigma of noise standard error in LSB count values.

In general, the range noise was relatively low during this flight. However, a number of spikes in the range noise plot can be seen from about 13:35 to 13:37. Takeoff was at 13:35 and the track was performed in the AIDED EL mode throughout this period. Some noise spikes can be expected during takeoff and landing due to spurious reflections and side lobing from nearby hangars, buildings, towers, etc. Noise is also induced when manual corrections are made to keep on the target. It is also possible that, at the shift from the AIDED track mode to FULL AUTO, some momentary noise may be induced in the measurement circuits of the radar due to relay closures etc.

Both the azimuth and elevation noise plots show a small noise spike at about 13:43:40 as the aircraft was passing an altitude of 16,000 feet. The true course plot shows the initiation of a turn occurring at this same time, therefore the noise probably resulted in a momentary glint effect. The 1-sigma noise level at this spike was about 1.5 LSB values in azimuth and about 1.2 LSB values in elevation; not enough to cause a discernable jump in the filtered output.

A serious off-target situation occurred at about 13:49:00 when the aircraft passed over the radar at an elevation angle in excess of 70 degrees. Dynamic lag caused the lock to transfer to a side lobe. This condition was immediately recognized by both the radar operator and by the triplexed antenna operator. The radar was unlocked and the target was reacquired shortly thereafter.

The angle noise at 14:10:00 occurred at the end of test point #4 when the elevation angle increased to over 45 degrees. In this case the angle noise did not reach the levels which caused the earlier off target situation, but it was clearly apparent on both the azimuth and elevation plots. Higher levels of angle noise are typically present at the very high-elevation points on close-in passes.

Some additional noise was present on the landing approach. This was during the aided track mode and was therefore not analyzed further.

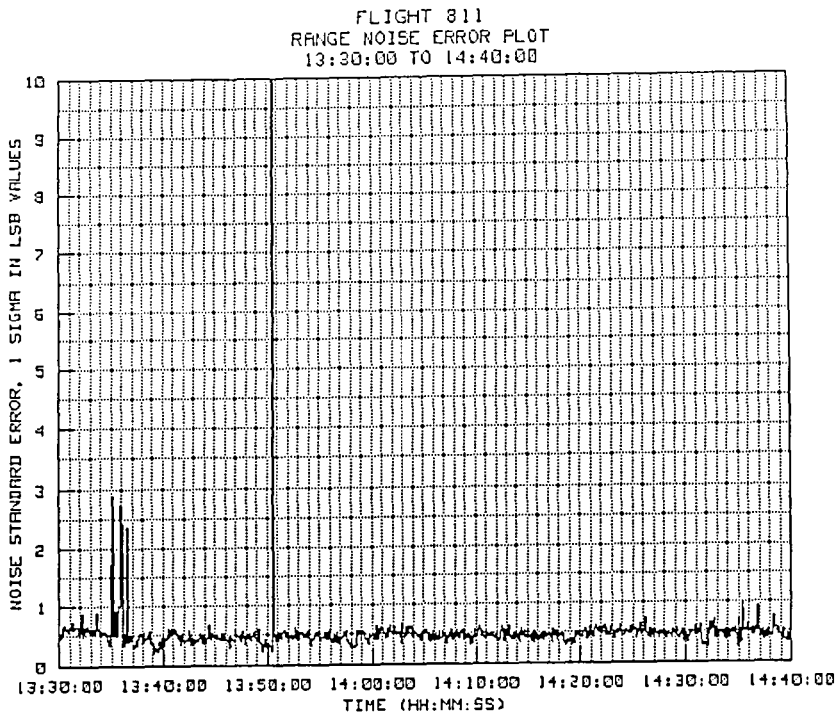

Figure 3-17. Flight 811 range noise analysis.

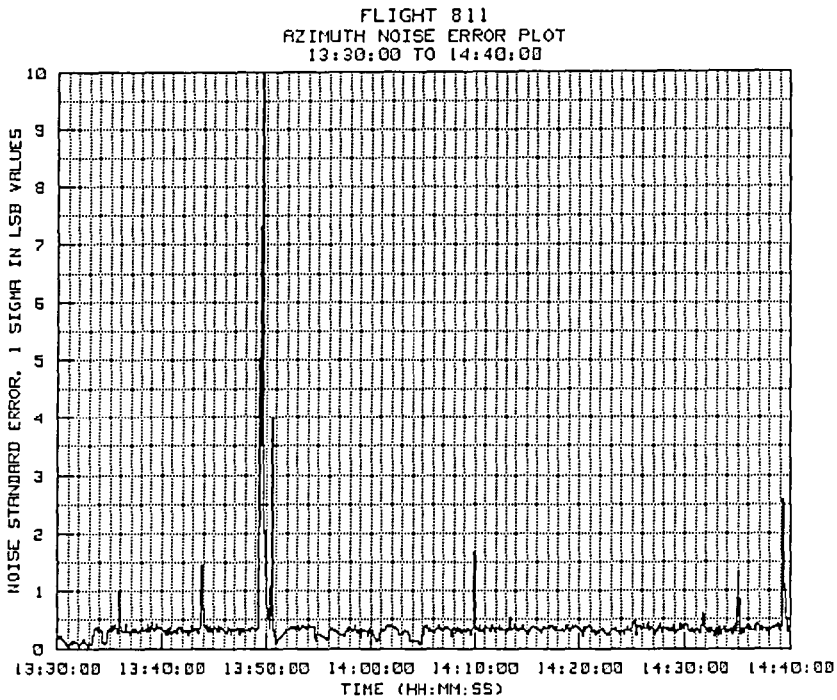

Figure 3-18. Flight 811 azimuth noise plot.

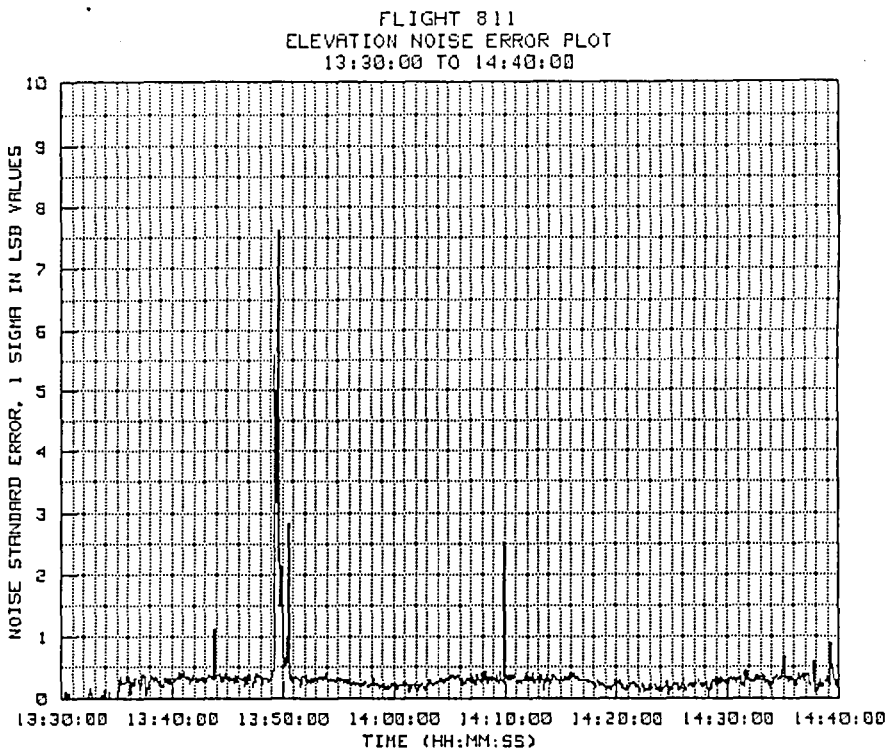

Figure 3-19. Flight 811 elevation noise plot.

3.4 Summary of Results from Flight 811

Flight 811 was conducted on a "high wind" day when high pressure gradients existed. Only synoptic wind and weather data was provided since local rawinsonde data were not available due to other circumstances.

Altitude data were compared with pressure altitude recorded on board, after Z-Hp corrections had been applied. Z-Hp corrections for this flight were determined from comparisons of on-board pressure altitude recordings with radar derived geometric altitude data obtained during high angle and/or close range tracking periods, when the atmospheric refraction corrections were small. After the correction, the altitude data agreed to within about twenty-five feet for all portions of the flight except for the long leg to the north. On this leg, a bias between the on-board, Z-Hp corrected altitude and the radar-derived geometric altitude developed as the range increased and as the elevation angle decreased. The amount of the difference, after compensating for the estimated horizontal Z-Hp gradient, appeared to be on the order of 190 feet at a maximum range of 73 nautical miles.

Although the same difference appeared to be present at the start of the inbound leg, an anomaly in the on-board data acquisition system prevented a precise measurement of the altitude difference over the full extent of the inbound run.

A second "survey" run was made on a northeast heading, approximately 90 degrees to the first run. On this run, the geometric altitude ranged from about twenty-five feet above the pressure altitude at close range to about twenty-five feet below the pressure altitude at the maximum range of 64 nautical miles. While this was not as large a difference as observed on the northerly leg, the leg itself was considerably shorter and the elevation angles were higher.

Radar derived Mach number, corrected for synoptic winds, agreed well with on board Mach number for all tests conducted at constant altitude. Agreement was usually within 0.01 Mach with some short periods in which the variation grew to about 0.02 Mach. Greater differences in the Mach numbers were observed during the climb and descent portions of the flight. These differences, up to about 0.05 Mach, are believed to have been mainly due to local temporal differences between the true wind vectors and those from the synoptic wind data used for Mach number corrections. Another factor which may have contributed to short term Mach differences was target glint effects as a result of maneuvering to avoid clouds during the climb and descent.

4.0 AIR DATA CALIBRATION FLIGHT 814

Air data calibration flight 814 was flown on 3 May 1984 using F-104 tail number 826. Ten specific test conditions or runs were planned. The pilot was Mr. Rogers Smith. Figures 4-1 through 4-3 provide time history plots of radar-measured range, azimuth, and elevation data from takeoff to landing.

4.1 Summary of Flight Day Wind and Weather Conditions

The flight day was classifed as "nominal" on the basis of wind speed magnitudes between 10,000 and 30,000 feet and on the basis of the synoptic scale (Z-Hp) changes over the 12-hour period.

However, in view of a lee wave motion observed in the lower troposphere, the atmosphere was considered to be active. Z-Hp perturbations on the order of plus or minus twenty feet were observed as a result of the mountain wave activity. The associated fluctuations in horizontal wind speed and in the pressure gradient near the surface were not well defined by the available data.

Measurements from the Edwards rawinsonde released just prior to the flight provided dew point measurements that were consistent with other Edwards rawinsondes earlier in the day and with expectations for the clear sky conditions which were observed. Other nearby locations, such as Vandenberg and Desert Rock, did show a slightly different humidity structure.

Winds for the flight were generally out of the west at speeds of from 20 knots at the surface to sixty knots at 40,000 feet. The surface temperature was 27 degrees C, and the surface pressure was 932.51 millibars. Surface r-f refractivity, as determined from the rawinsonde measurements, was 277 N-units.

Specific wind and weather values, and the computed r-f index of refraction used for analysis purposes, are provided in table 4-I. Local synoptic values for Z-Hp and radar adjusted Z-Hp values are provided in table 4-II. Radar adjustments to the synoptic Z-Hp values are based on radar derived geometric altitudes at times when the ranges were short or the elevation angles high. Plots showing a comparison of the synoptic and radar-adjusted Z-Hp values are provided in figure 4-4. Differences between on-board pressure altitude and radar-derived geometric altitude during several short range or high angle periods are shown in figures 4-5 through 4-8. These differences, along with high-angle data from test point #2 were used to determine the amount of adjustment to be made to the synoptic data.

Figure 4-5 provides a check of the radar-derived geometric altitude during the takeoff roll, rotation, and liftoff. The hard copy data shows a radar measured elevation just prior to brake release as about 2285 feet. A survey reference marker, NRP 4, located on the taxiway adjacent to the hold point is 2280 feet. This would indicate that the optical aim point being used was approximately on the nose of the aircraft.

Figures 4-6 and 4-8 provide comparisons of radar derived geometric altitude and on-board pressure altitude for high-angle tracks when the target was at 18,000 feet, and figure 4-7 shows close-in comparison data for the altitude range from 3500 to 4500 feet. Note that only very slight adjustments were made to the synoptic Z-Hp data provided for this flight.

A rawinsonde balloon was released immediately prior to the flight and tracked by the radar to an altitude of 20,000 feet. This allowed comparisons to be made between synoptic winds, rawinsonde winds, and winds derived from the radar track of the rawinsonde balloon. However, since rawinsonde winds were immediately available, they were used for the Mach number comparisons in section 4.2. Subsequent comparisons of radar-derived Mach numbers using all three wind sources are provided in section 4.3.

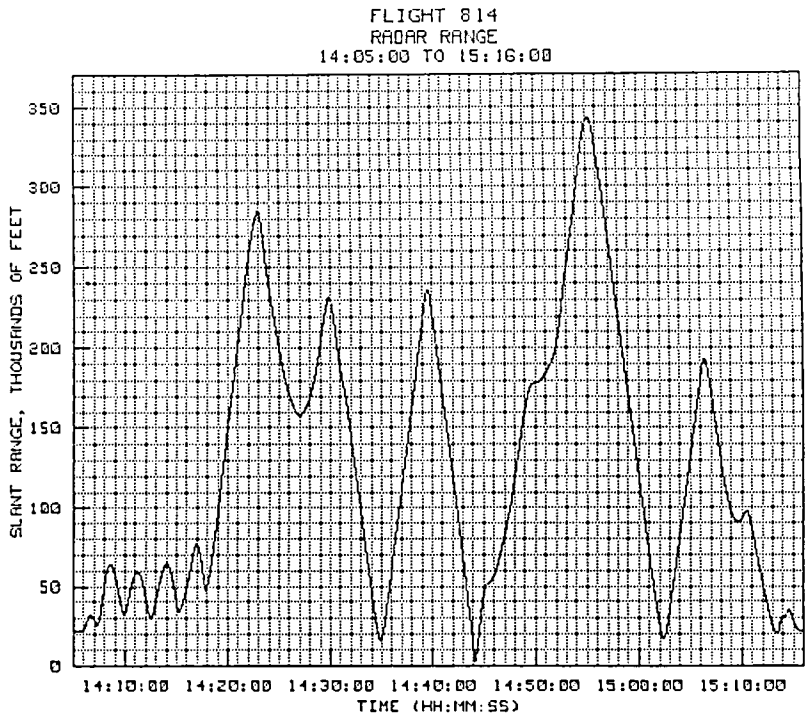

Figure 4-1. Flight 814 radar-derived slant range.

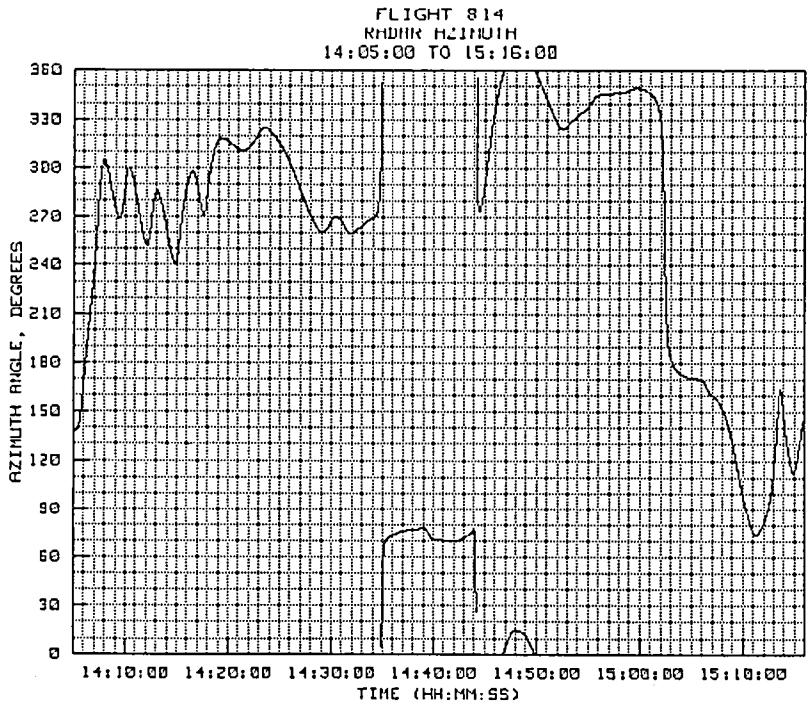

Figure 4-2. Flight 814 radar-derived azimuth angle.

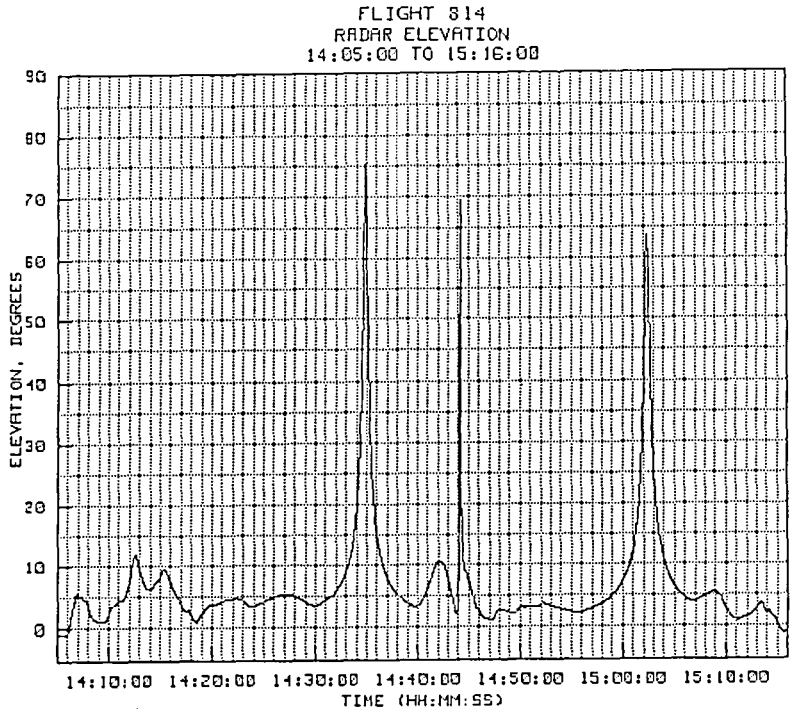

Figure 4-3. Flight 814 radar-derived elevation angle.

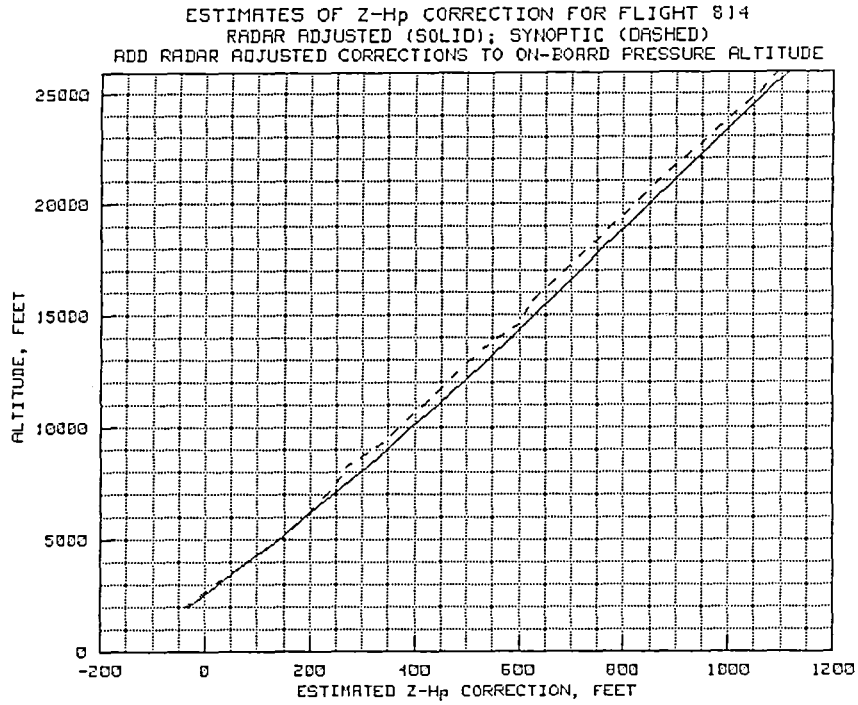

Figure 4-4. Flight 814 synoptic and radar derived Z-Hp plots.

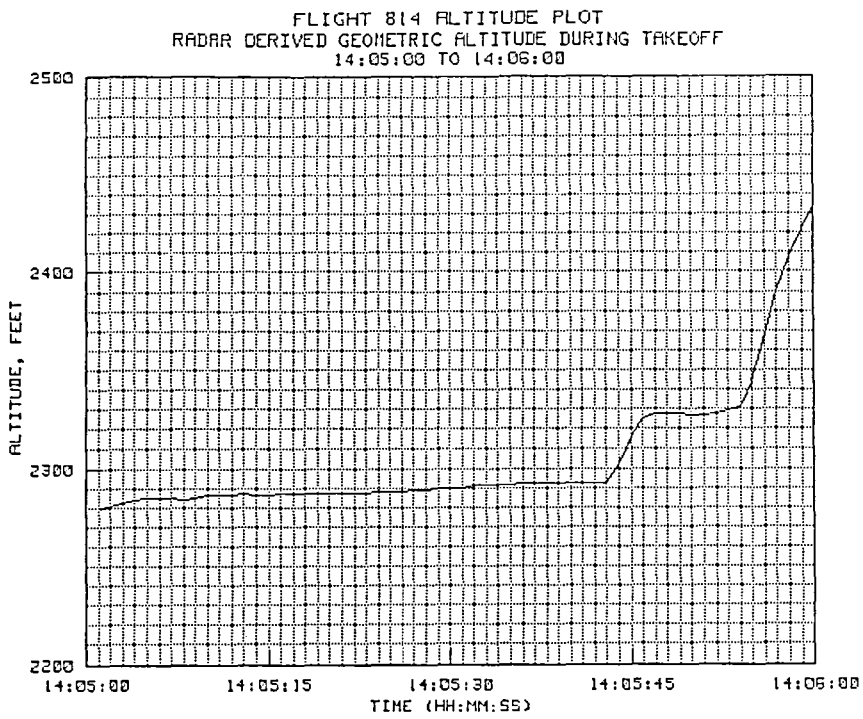

Figure 4-5. Flight 814 radar-derived takeoff altitude.

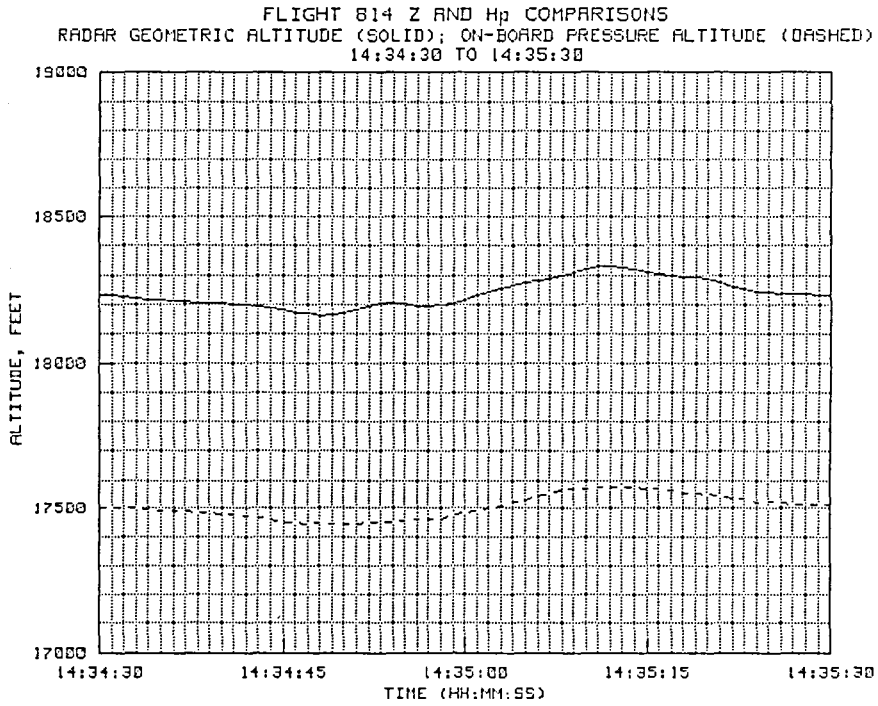

Figure 4-6. Flight 814 Z and Hp comparison at 18,000 feet.

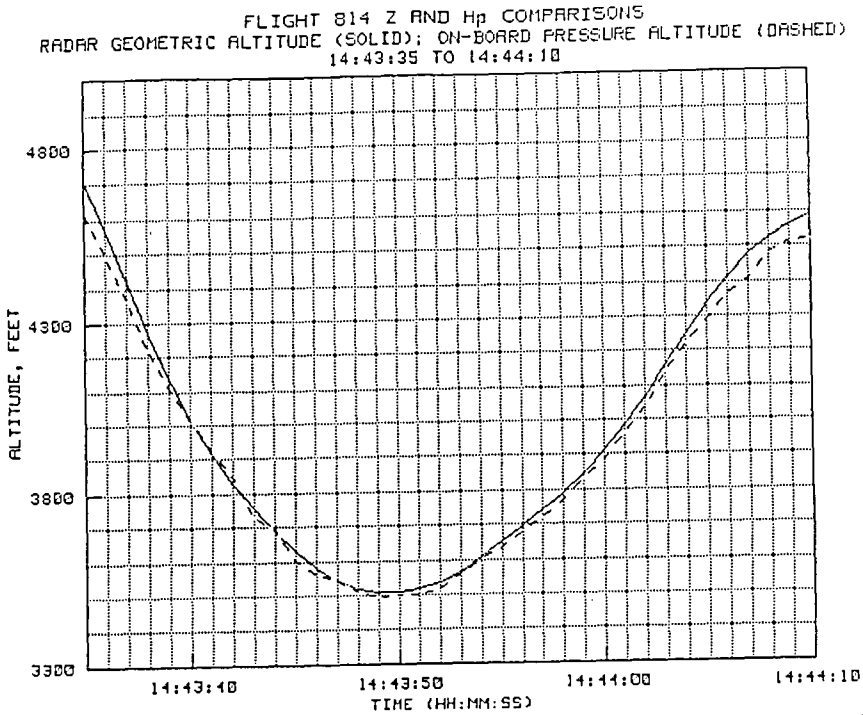

Figure 4-7. Flight 814 Z and Hp comparison 3500 to 4500 feet.

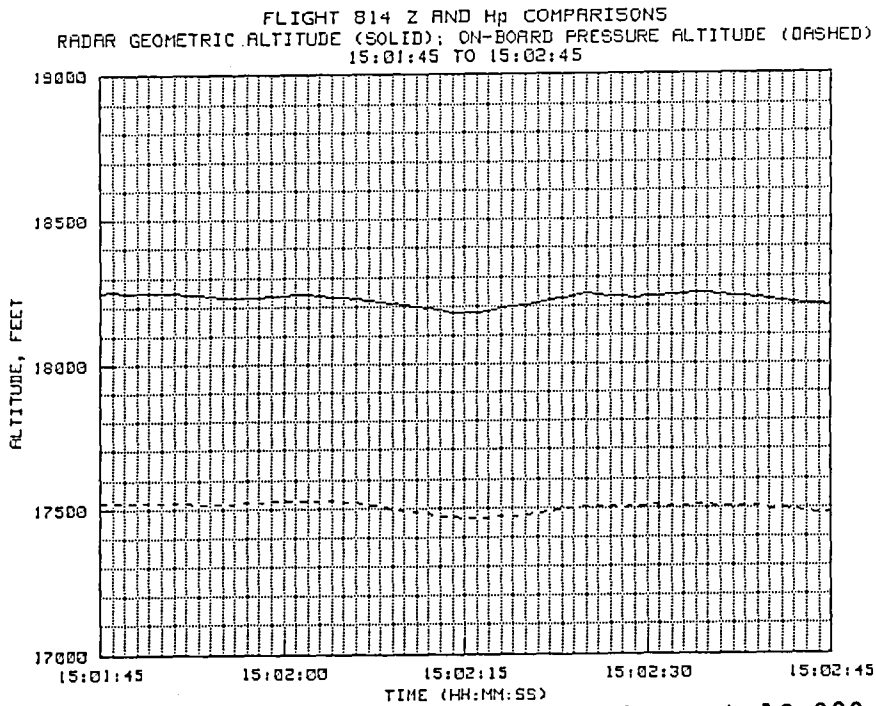

Figure 4-8. Flight 814 Z and Hp comparison at 18,000 feet.

TABLE 4-I. FLIGHT 814 WEATHER DATA

WEATHER DATA FOR FLIGHT 814

ALTITUDE (FT)	TEMPERATURE (DEG C)	DEW POINT (DEG C)	PRESSURE (MB)	N X 10E6	WIND (DEG/KTS)
2300	27.0	5.3	932.51	278.5	260.0/ 20.0
3000	24.5	3.4	912.42	271.2	288.0/ 28.0
4000	21.6	1.9	880.94	262.4	304.0/ 25.0
5000	18.8	-1.8	850.38	249.8	310.0/ 18.0
6000	16.3	-3.0	820.67	242.1	341.0/ 14.0
7000	14.2	-4.2	791.73	234.3	337.0/ 7.0
8000	12.5	-5.8	763.56	225.8	318.0/ 11.0
9000	11.0	-12.6	736.37	212.0	315.0/ 24.0
10000	9.5	-14.1	710.05	204.7	306.0/ 21.0
11000	7.4	-15.9	684.48	197.9	299.0/ 20.0
12000	5.3	-18.1	659.70	191.1	292.0/ 20.0
13000	3.1	-19.9	635.49	184.8	289.0/ 25.0
14000	.9	-21.4	612.07	178.9	289.0/ 29.0
15000	-1.1	-22.6	589.35	173.2	291.0/ 35.0
16000	-3.3	-24.4	567.29	167.6	297.0/ 40.0
17000	-5.6	-26.3	545.90	162.1	301.0/ 43.0
18000	-7.9	-28.1	525.09	156.9	293.0/ 38.0
19000	-10.3	-30.1	504.88	151.8	285.0/ 40.0
20000	-12.6	-31.9	485.27	146.9	278.0/ 41.0
21000	-15.0	-33.6	466.27	142.2	275.0/ 42.0
22000	-17.3	-35.5	447.88	137.6	274.0/ 42.0
23000	-19.7	-37.9	430.03	133.1	276.0/ 41.0
24000	-22.0	-39.7	412.71	128.7	275.0/ 41.0
25000	-24.5	-41.0	395.93	124.6	274.0/ 43.0

TABLE 4-II. FLIGHT 814 Z-Hp DATA

Synoptic Z-Hp Data for Flight 814

Altitude (feet)	Syn. Z-Hp (feet)	Radar Z-Hp (feet)	Change in Z-Hp (feet/n.mi.)	Direction of decrease
26,000	+1093	+1115		
25,000	+1060	+1070	1.22	007
24,000	+1016	+1026	1.20	008
23,000	+ 960	+ 985	1.18	009
22,000	+ 913	+ 942	1.16	010
21,000	+ 866	+ 899	1.13	011
20,000	+ 819	+ 851	1.11	012
19,000	+ 777	+ 809	1.09	013
18,000	+ 732	+ 760	1.02	017
17,000	+ 685	+ 720	0.96	021
16,000	+ 641	+ 677	0.90	025
15,000	+ 597	+ 630	0.83	029
14,000	+ 583	+ 585	0.77	033
13,000	+ 496	+ 541	0.71	037
12,000	+ 461	+ 492	0.64	042
11,000	+ 417	+ 445	0.58	046
10,000	+ 372	+ 392	0.52	050
9,000	+ 326	+ 348	0.52	052
8,000	+ 254	+ 295	0.53	054
7,000	+ 238	+ 245	0.53	055
6,000	+ 186	+ 187	0.53	057
5,000	+ 141	+ 142	0.54	059
4,000	+ 80	+ 80	----	---
3,000	+ 20	+ 26	----	---
2,300	- 35	- 30	0.95	040

Add Z-Hp values to pressure altitude to obtain geometric altitude

4.2 Analysis of Test Points

During flight 814, ten test points were planned. The first three test points were part of the radar evaluation, as was test point #10. The interim points, #4 through #9, were part of an unrelated project. At the end of the flight, additional flight data were recorded just prior to touchdown. The times and descriptions of the radar test points are provided below. Note that the radar test points have been consecutively renumbered to provide better continuity for this analysis.

1. 14:18:30 to 14:22:25 - Constant 0.9 Mach climb to 25,000 feet.

2. 14:32:20 to 14:38:34 - Level run at 17,500 feet and Mach 0.75.

3. 14:41:41 to 14:44:13 - 0.9 Mach descent, 25,000 feet to surface.

4. 14:56:36 to 15:05:57 - Level run at 17,500 feet and Mach 0.75.

5. 15:11:51 to 15:16:00 - Level run at 4,000 feet and Mach 0.50, followed by landing.

Note that the flight data for test point #5 were only provided up to 15:13:30, however the radar data plot was extended to 15:16:00 in order to provide a radar-derived geometric elevation on landing.

4.2.1 Test Point #1

The time history plots for test point #1 are shown in figures 4-9(a) to 4-9(f). The test point consisted of a climb which started at a slant range of about 69,826 feet (11.49 n.mi.) and continued outbound on a northerly course with some heading adjustments which ended the climb on a true course of about 300 degrees at a range of 272,625 feet (44.87 n.mi.). At the start of the climb the elevation angle was 1.0 degree and at the end of the climb it was 4.7 degrees. It should be noted that the pressure altitude, adjusted for the Z-Hp difference, starts out slightly above the radar altitude, then comes into fair agreement at around 17,000 feet, and then goes slightly above again at the higher altitudes. This correlates with the trends observed during flight 811 in which the radar appeared to read increasingly low as range increased and elevation angle decreased. The confidence in the Z-Hp values in the 17,000-foot range are very good since data from the high-angle track periods around 14:34:50 and 15:02:18 indicated a Z-Hp value of 710 feet to 730 feet. This fell within the 40 to 50 foot range of uncertainty in the 685-foot difference estimated in the synoptic analysis.

The Mach number plot for this same time segment (Fig. 4-9(b)) shows variations of up to 0.05 Mach at the lower altitudes with agreement down to about 0.01 Mach at altitudes above 20,000 feet. The airborne data had a bad segment at about 14:17:50, probably due to a telemetry dropout. This dropout occurred about the same time that the left turn off 342 degrees was initiated (see Fig. 4-9(c)). The variations between radar derived and on-board altitude for this segment are probably due to the variability of the true winds during the climb.

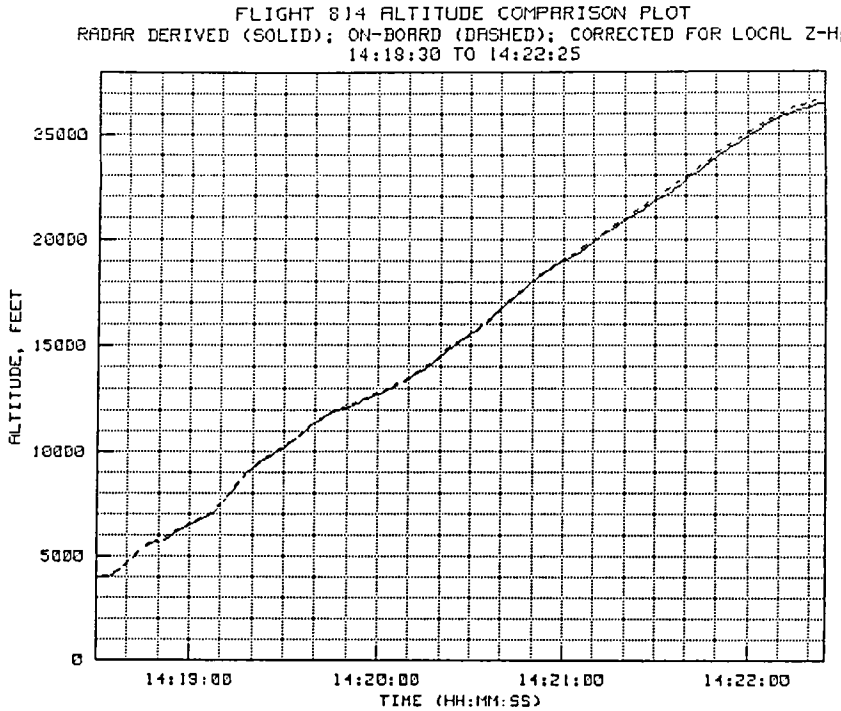

Figure 4-9(a). TP #1 radar-derived and on-board altitude.

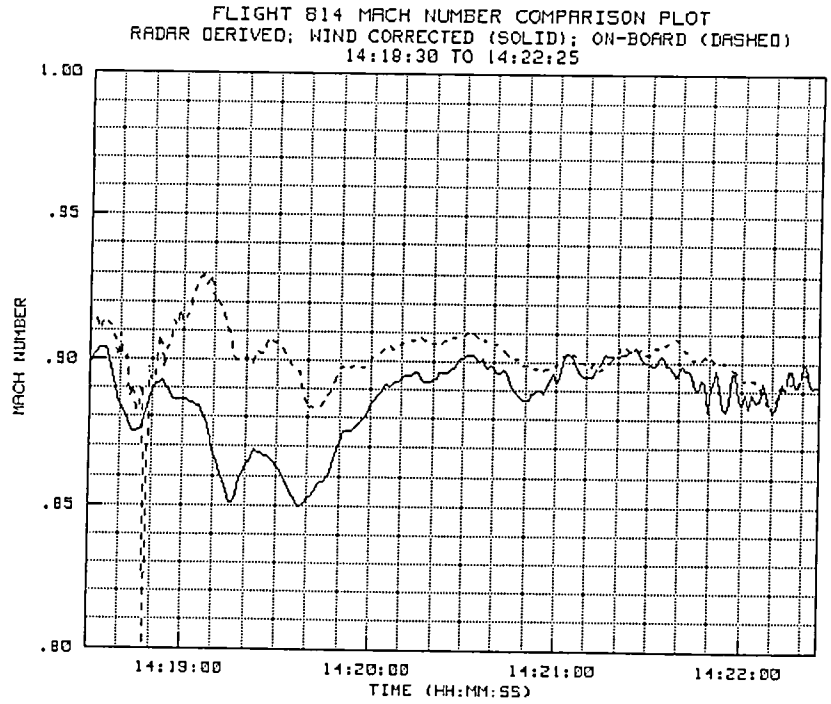

Figure 4-9(b). TP #1 radar-derived and on-board Mach number.

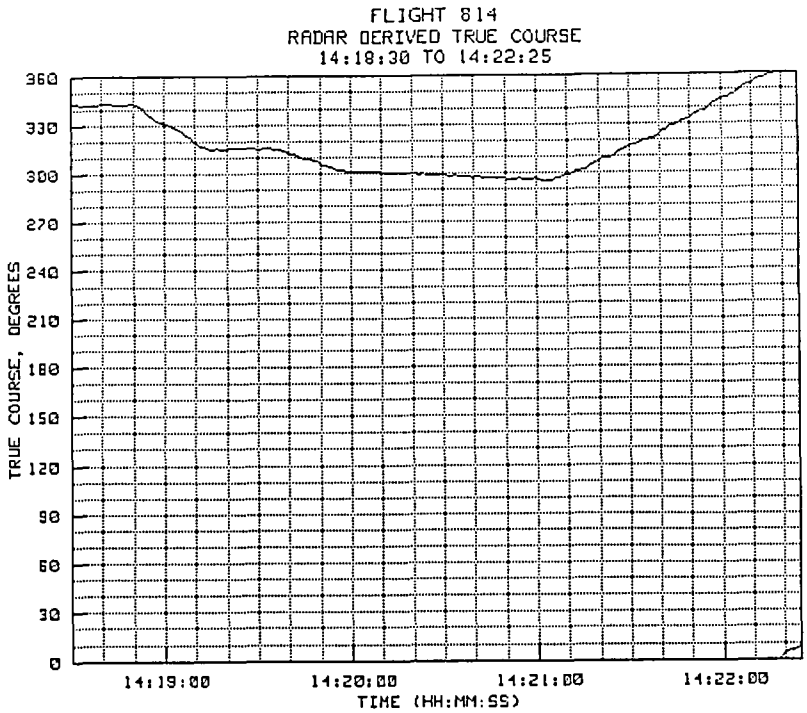

Figure 4-9(c). TP #1 radar-derived true course.

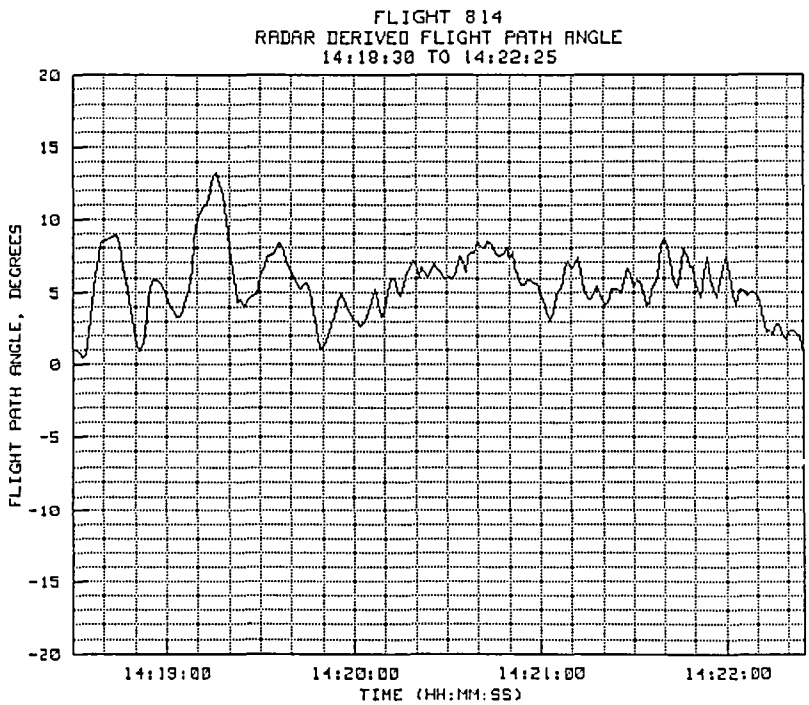

Figure 4-9(d). TP #1 radar-derived flight path angle.

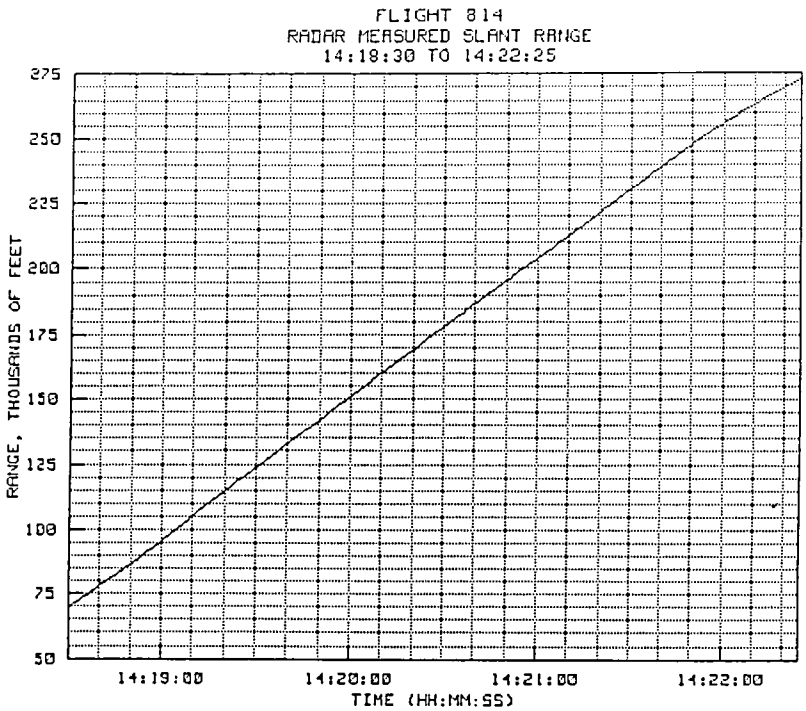

Figure 4-9(e). TP #1 radar-derived target slant range.

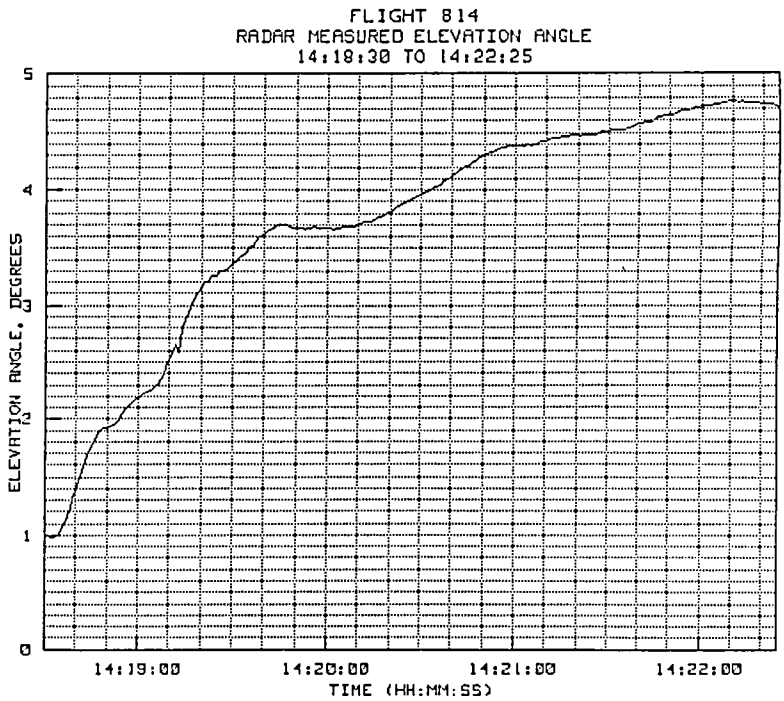

Figure 4-9(f). TP #1 radar-derived elevation angle.

4.2.2 Test Point #2

The time history plots for test point #2 are provided in figures 4-10(a) to 4-10(f). Test point #2 was a level survey run made on an easterly course, starting at a slant range of 129,720 feet (21.35 n.mi.) and at an elevation angle of 6.78 degrees. The near point occurred at 14:34:53 at which time the range was 16,078 feet and the elevation angle was in excess of 75 degrees. The ending range was 190,722 feet (31.39 n.mi.) at an elevation angle of 4.474 degrees.

The Z-Hp analysis for this altitude shows the maximum gradient to be about 1 foot per nautical mile at 17 degrees true. Thus, on the easterly heading used for this leg, the expected gradient would be on the order of 0.3 foot per nautical mile. This would put the expected pressure altitude about 7 feet lower than the geometric altitude at the start of the run and about 10 feet higher at the end of the run. From the altitude plot (Fig. 4-10(a)), the pressure altitude appears to be about 10 feet low at the start of the run and about 35 feet high at the end of the run. However, at equidistant points on each side of the near point, the apparent gradient can be roughly determined by the asymmetrical behavior of the altitude. Over these ranges, the Z-Hp gradient seemed to agree well with the synoptic value. However, as the run continued down to the final elevation of 4.47 degrees, the difference between the pressure altitude and the geometric altitude appeared to increase rapidly. As a result, a difference of about 20 feet was present after allowances were made for the Z-Hp gradient. The difference is in the same direction as noted during flight 811.

The Mach number plot (Fig. 4-10(b)) for the same leg shows variations of about 0.1 Mach at the start of the run, decreasing to about 0.05 Mach at the end of the run. This is probably due to errors in the rawinsonde wind vectors used in the reduction of the data. As noted in figure 4-10(c), during the early part of the run, heading changes were made and it is in this part of the run that the greatest differences are seen. Finally, about half way through the run, the course held steady at 080 degrees and the Mach difference appeared to be about the same magnitude from that point until the end of the run.

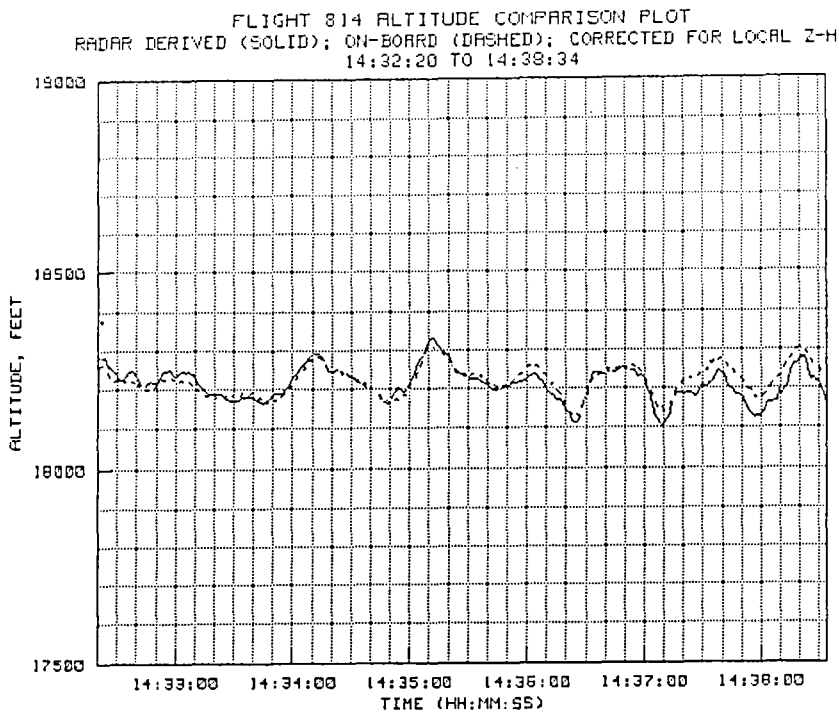

Figure 4-10(a). TP #2 radar-derived and on-board altitude.

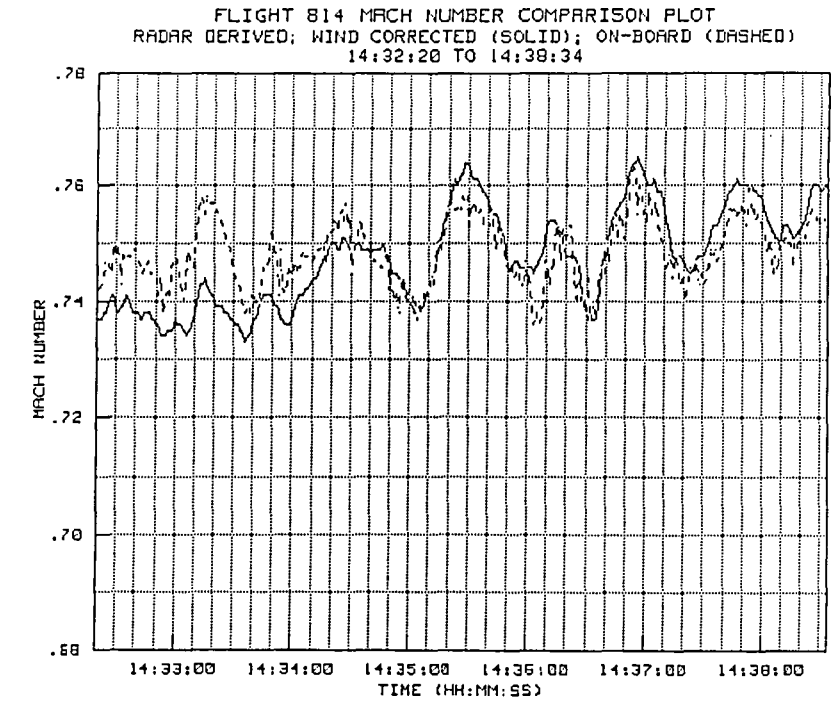

Figure 4-10(b). TP #2 radar-derived and on-board Mach number.

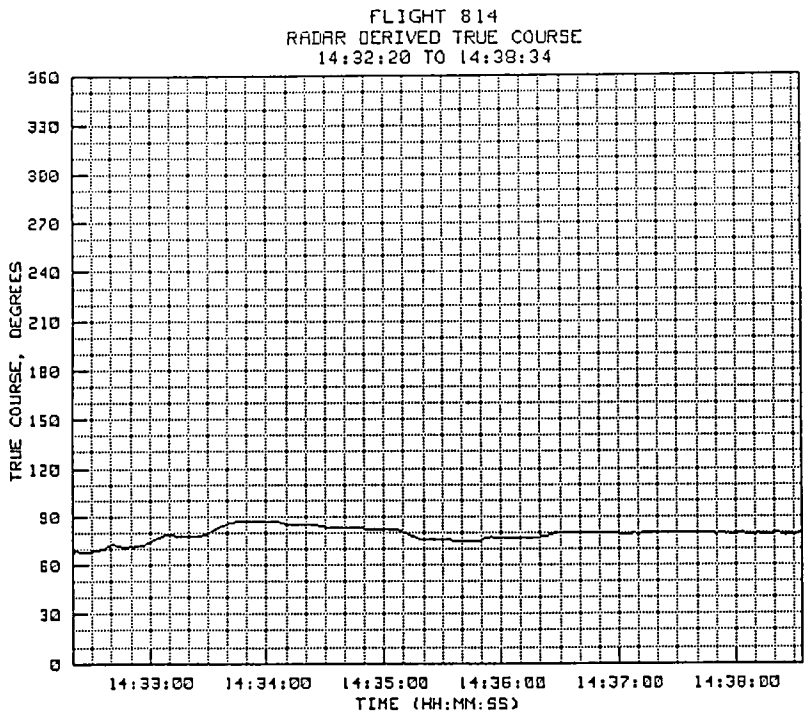

Figure 4-10(c). TP #2 radar-derived true course.

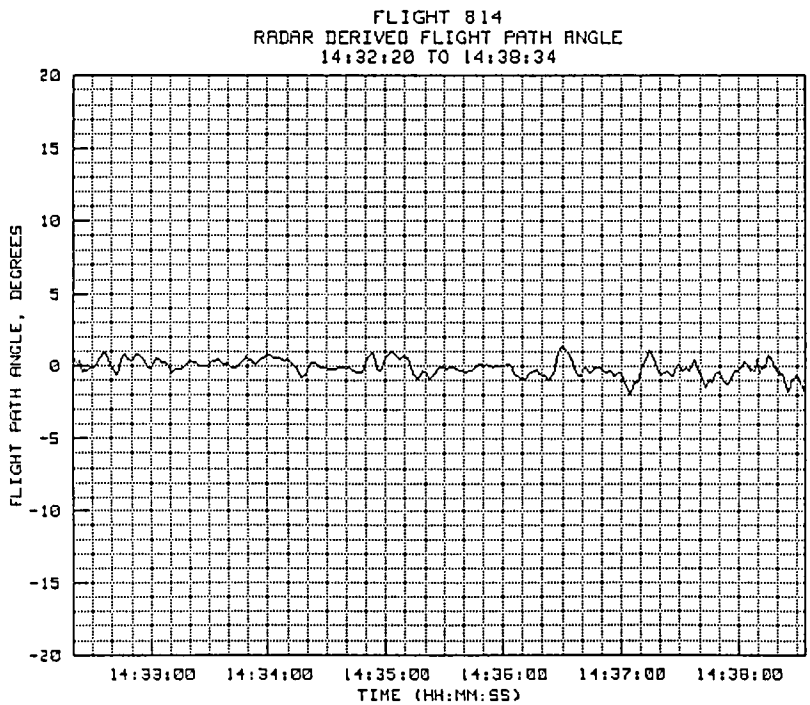

Figure 4-10(d). TP #2 radar-derived flight path angle.

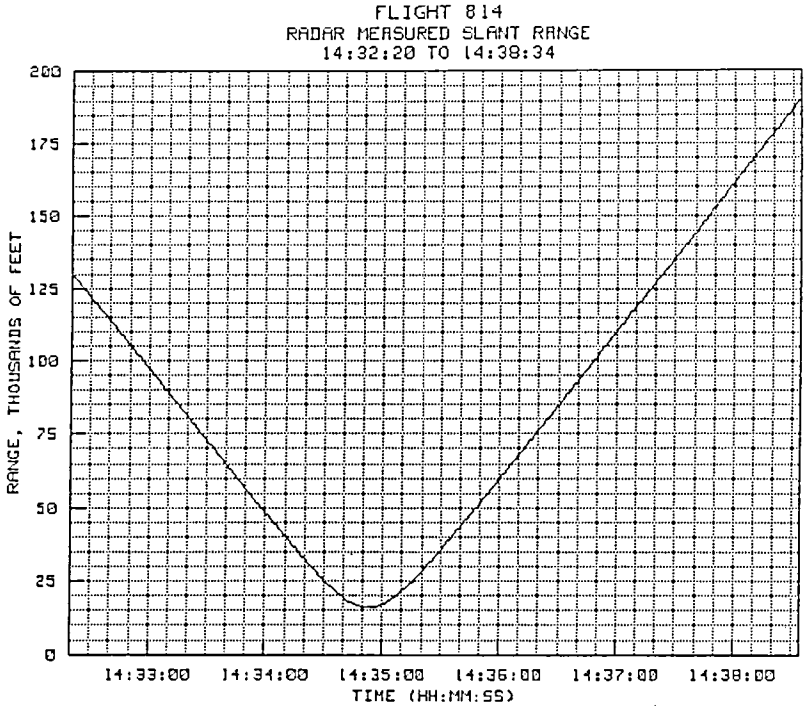

Figure 4-10(e). TP #2 radar-derived slant range.

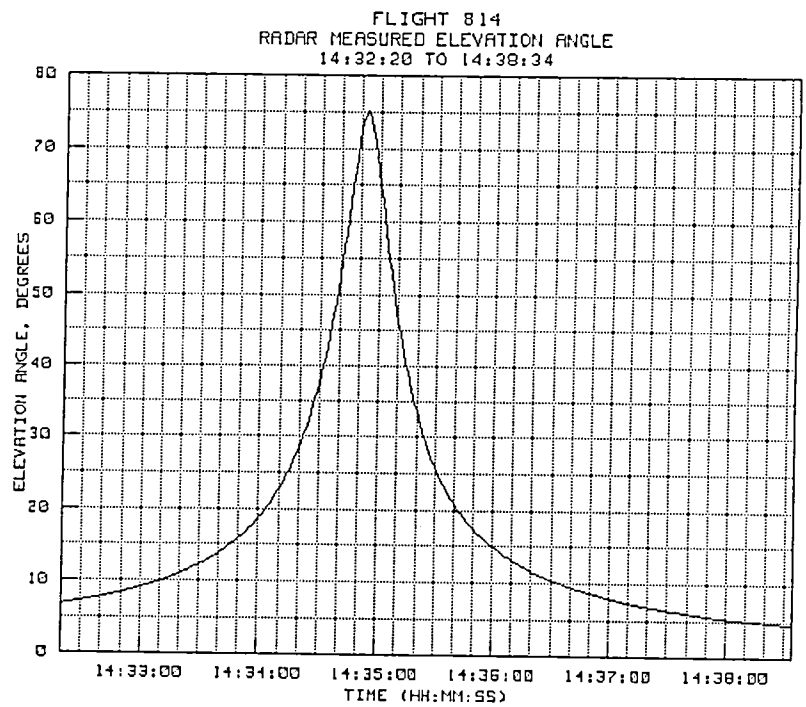

Figure 4-10(f). TP #2 radar-derived elevation angle.

4.2.3 Test Point #3

The time history plots for test point #3 are shown in figures 4-11(a) to 4-11(f). This test point was a descent made toward the radar on a course of 250 degrees true, followed by a slight right turn in the last 30 seconds. The starting slant range was 137,988 feet (22.71 n.mi.) at an elevation angle of 9.68 degrees; the near point in the descent was at the end of the run when the target aircraft nearly passed over the radar. The altitude correlation during the descent is very good; however, some slight Z-Hp differences are detectable.

The Mach number plot for the same run, shown in figure 4-11(b), has errors on the order of 0.02 Mach at the higher altitudes, decreasing to near zero close to the surface. Except for the wind bias errors, the correlation of the short term movements in the Mach number is very good. A spike in the radar derived Mach Mach number can be observed at the end of the run. This was due to a momentary off-target condition that occurred when the aircraft passed over the radar.

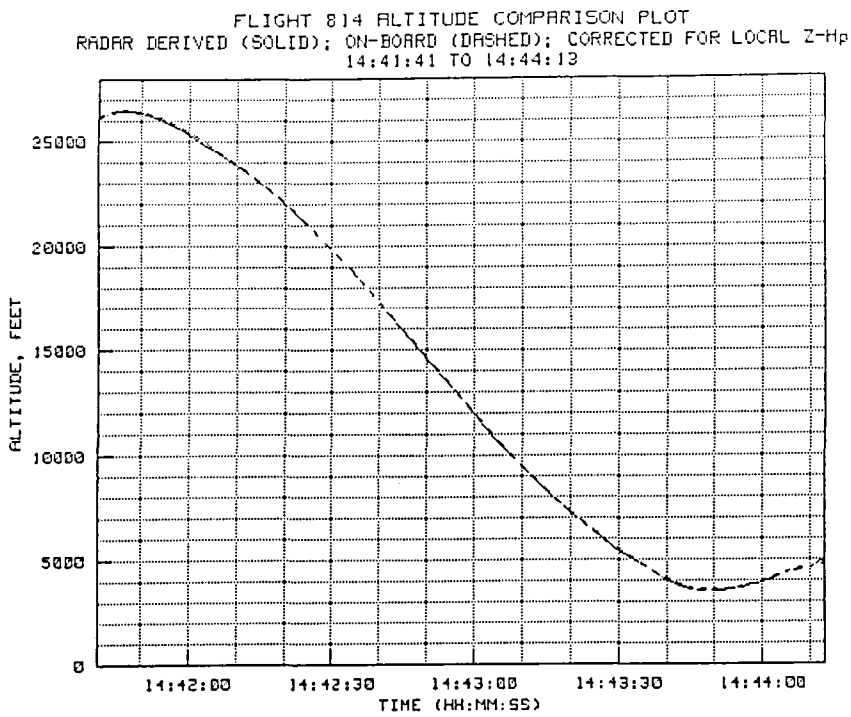

Figure 4-11(a). TP #3 radar-derived and on-board altitude.

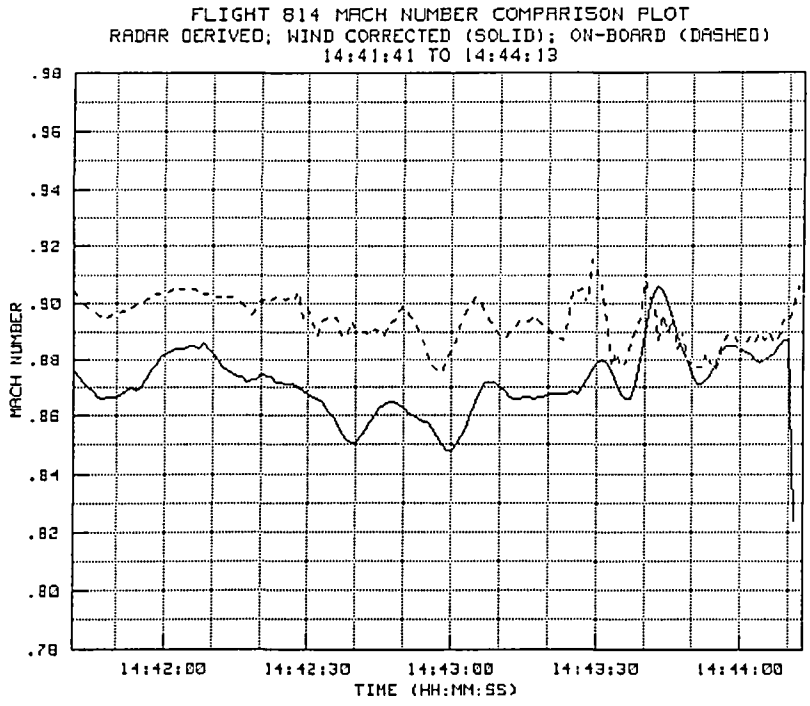

Figure 4-11(b). TP #3 radar-derived and on-board Mach number.

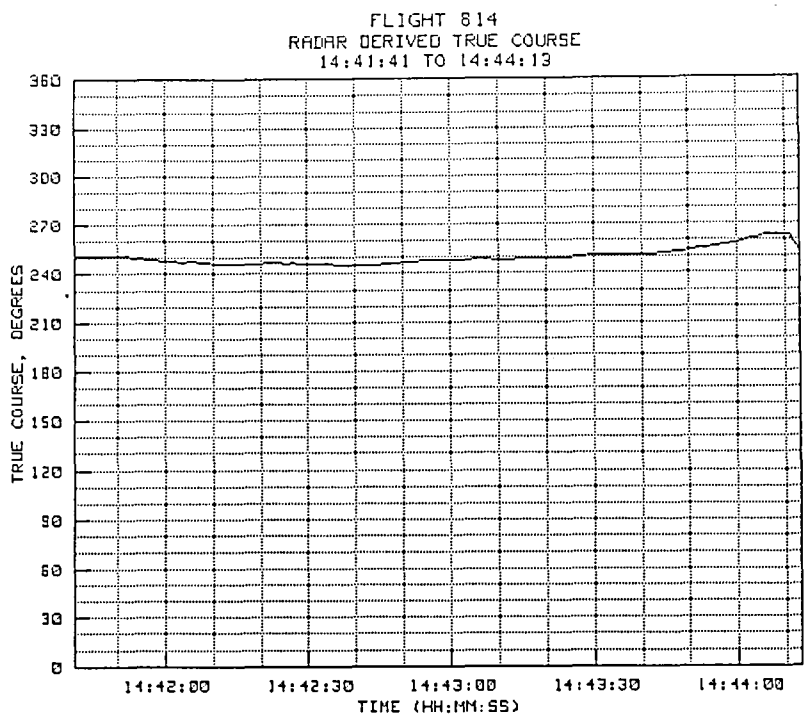

Figure 4-11(c). TP #3 radar-derived true course.

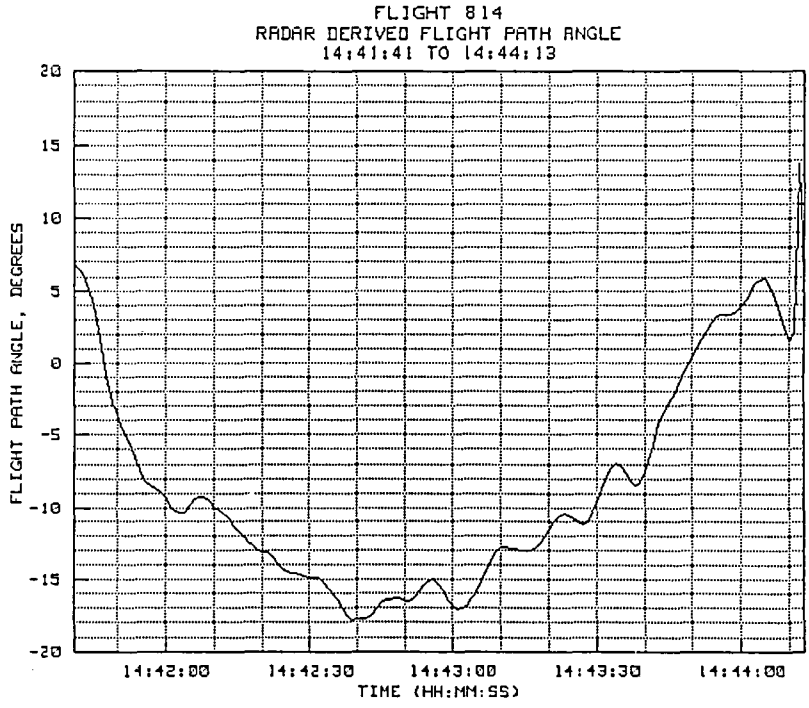

Figure 4-11(d). TP #3 radar-derived flight path angle.

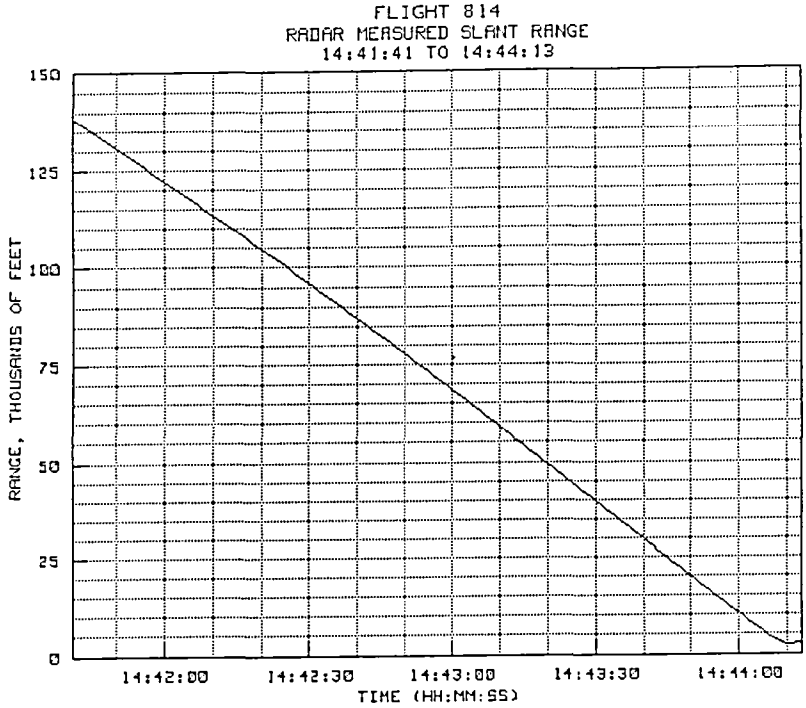

Figure 4-11(e). TP #3 radar-derived slant range.

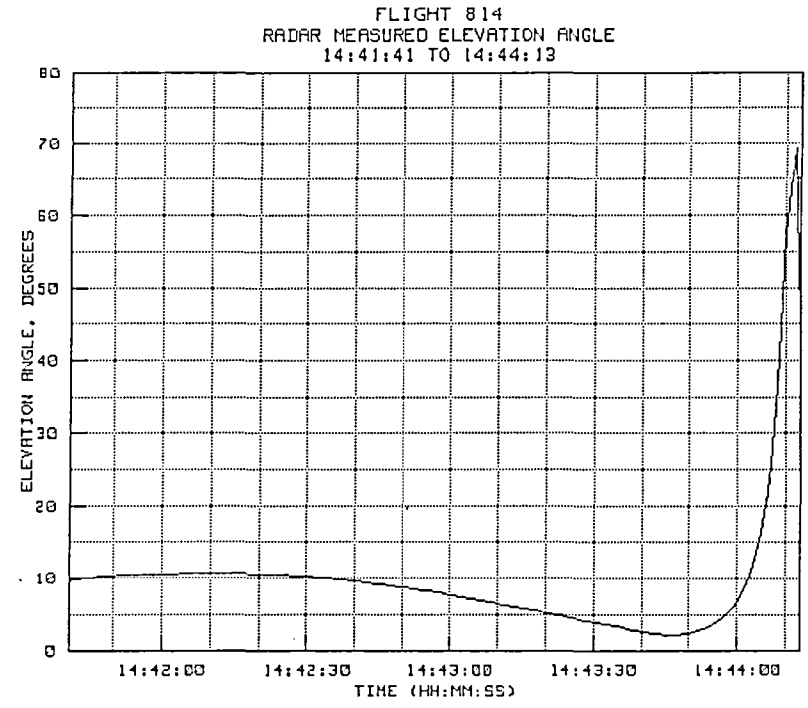

Figure 4-11(f). TP #3 radar-derived elevation angle.

4.2.4 Test Point #4

Test point #4, a level survey leg for the radar evaluation, was actually shown as test point #10 on the flight plan since other intermediate tests were run for an unrelated project. The time history plots for this test point are shown in figure 4-12(a) to 4-12(f). The run was made on an approximate southerly heading (165 degrees) commencing at a slant range of 291,504 feet (47.98 n.mi.) at an elevation angle of 2.7 degrees. The closest point of approach occurred at 15:02:23 when the slant range closed to 17,367 feet and the elevation angle increased to 63 degrees. At the start of this run, the anomaly in the calculation of geometric altitude is clearly apparent. Over the course of the run the Z-Hp gradient would have caused a decrease of about 0.5 foot per nautical mile in the pressure altitude. Instead, at the start of the run, where the range was large and the elevation angle quite small, almost a 200 foot difference was present, and at the near point, the difference was negligible. Although some bias errors may be present in the Z-Hp data, they would not account for this amount of difference. Note that the altitude calculations for this run show the same type of behavior as observed during flight 811 and, to a lesser extent, as observed in the test point #2 data from this same flight.

Radar Mach number, provided in figure 4-12(b), shows good correlation with the short term changes observed in the on-board data. However, the same bias errors are present as previously observed. In this case the errors are on the order of 0.01 to 0.02 Mach, with some overshooting clearly detectable. Since velocity is a first derivative of position, more noise can be expected in the Mach number calculations than in the position calculations, and this is reasonably evident in all of the Mach number plots.

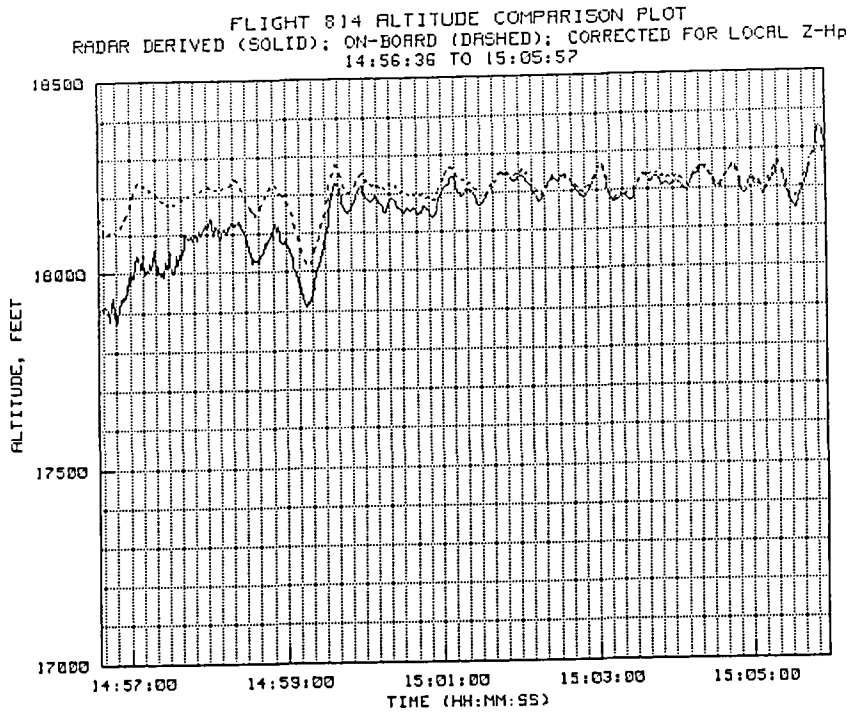

Figure 4-12(a). TP #4 radar-derived and on-board altitude.

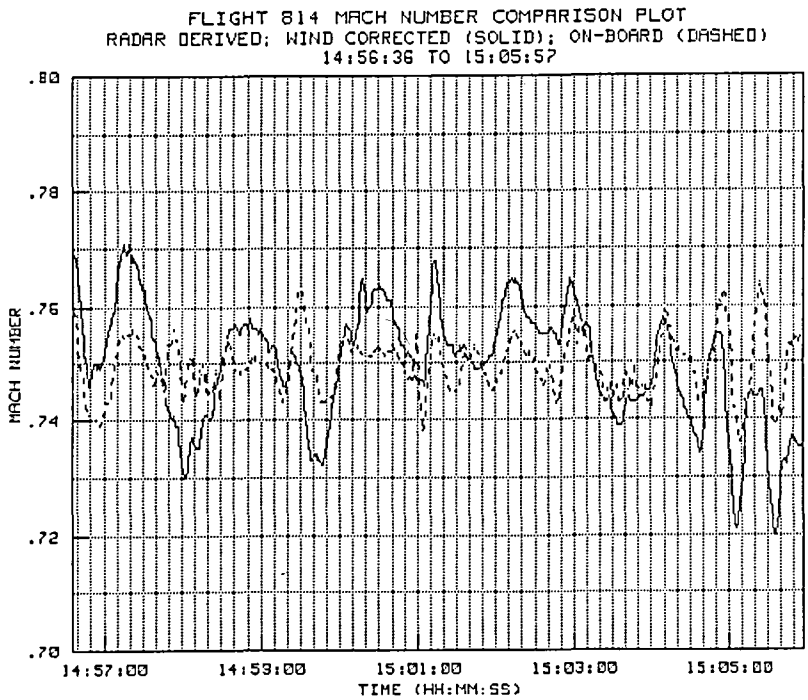

Figure 4-12(b). TP #4 radar-derived and on-board Mach number.

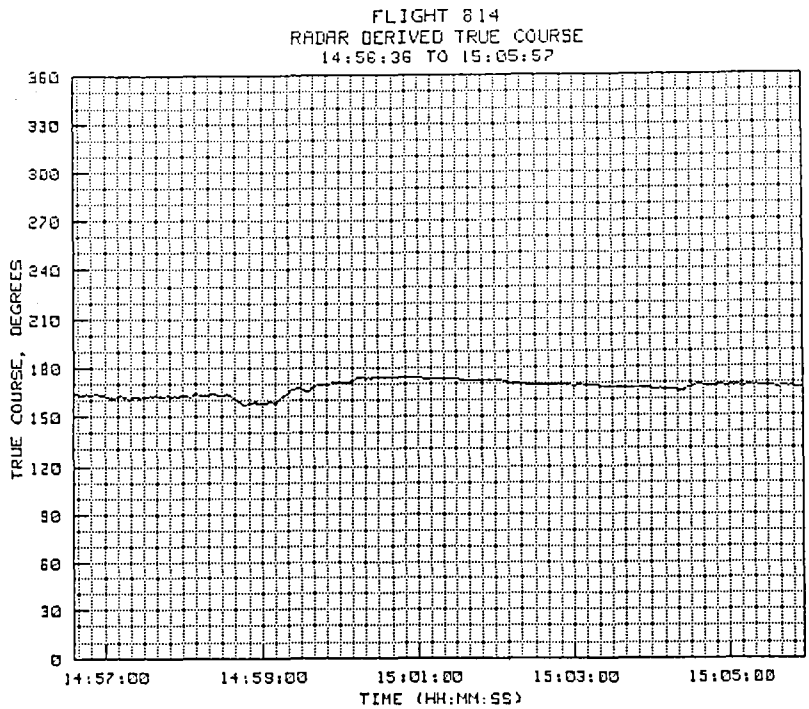

Figure 4-12(c). TP #4 radar-derived true course.

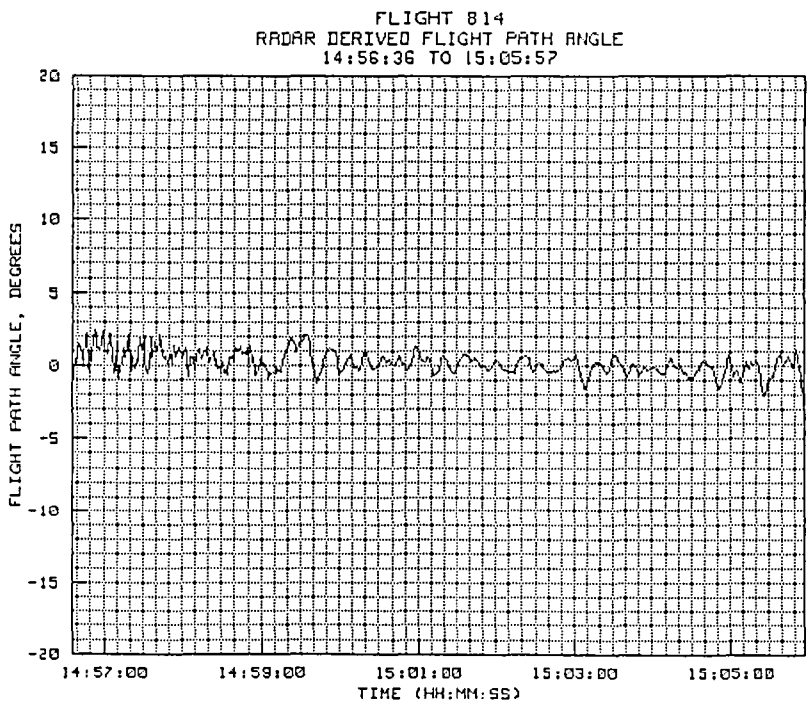

Figure 4-12(d). TP #4 radar-derived flight path angle.

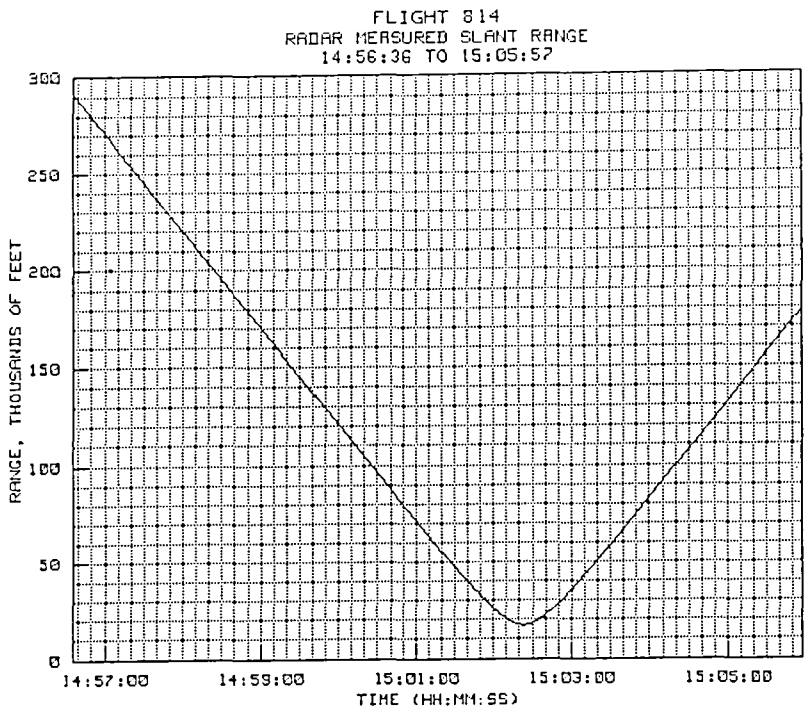

Figure 4-12(e). TP #4 radar-derived slant range.

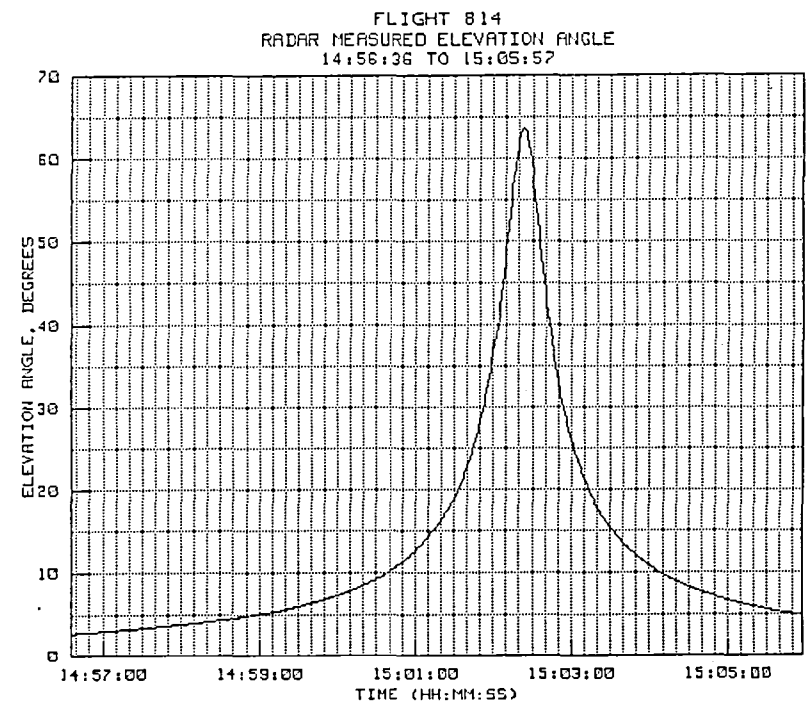

Figure 4-12(f). TP #4 radar-derived elevation angle.

4.2.5 Test Point #5

The final run for which airborne data was provided is shown in figures 4-13(a) to 4-13(f). The plot was continued past the point where the airborne data ended in order to obtain an estimate of the geometric altitude at touchdown, however, the scale of the plot prevented an accurate value from being determined. Therefore, data was examined in hardcopy form. This showed the radar-derived altitude to be 2284 feet at the touchdown point.

Good correlation can be seen between the behavior of the radar and the on-board altitude data prior to touchdown, except that an apparent Z-Hp difference of about 80 feet is present. Since the radar altitude agrees with the runway elevation after touchdown, it is probable that the difference may be due to an error in the Z-Hp adjustment used for this time segment. Also, this test point was taken just prior to touchdown, therefore the higher angle of attack may have had some effect on the on-board pressure measurements.

Note that a slight overshoot in the radar data occurred just prior to touchdown. This is fairly common when the target is being tracked in the AIDED EL rate mode, because a large rate input adjustment must be made by the radar operator at the flare point. Since the video tape recordings did not include the touchdown point, it was not possible to determine the exact behavior of the optical track during the landing.

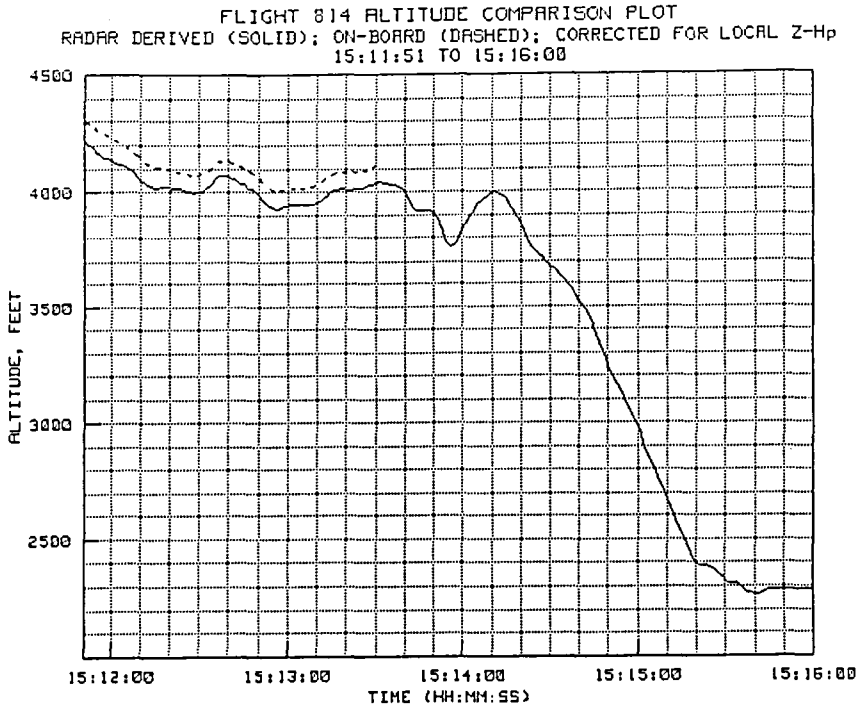

Figure 4-13(a). TP #5 radar-derived and on-board altitude.

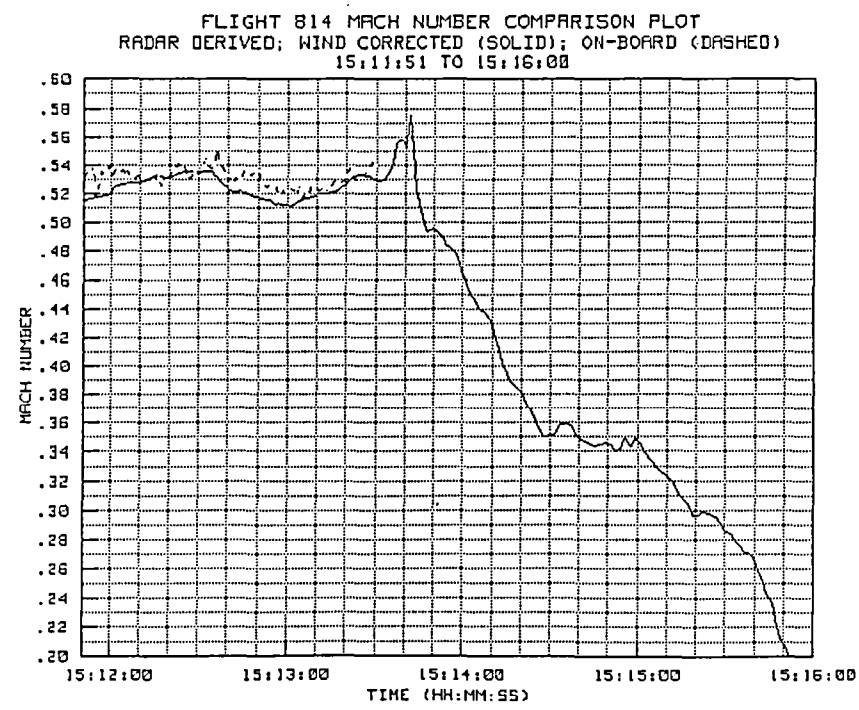

Figure 4-13(b). TP #5 radar-derived and on-board Mach number.

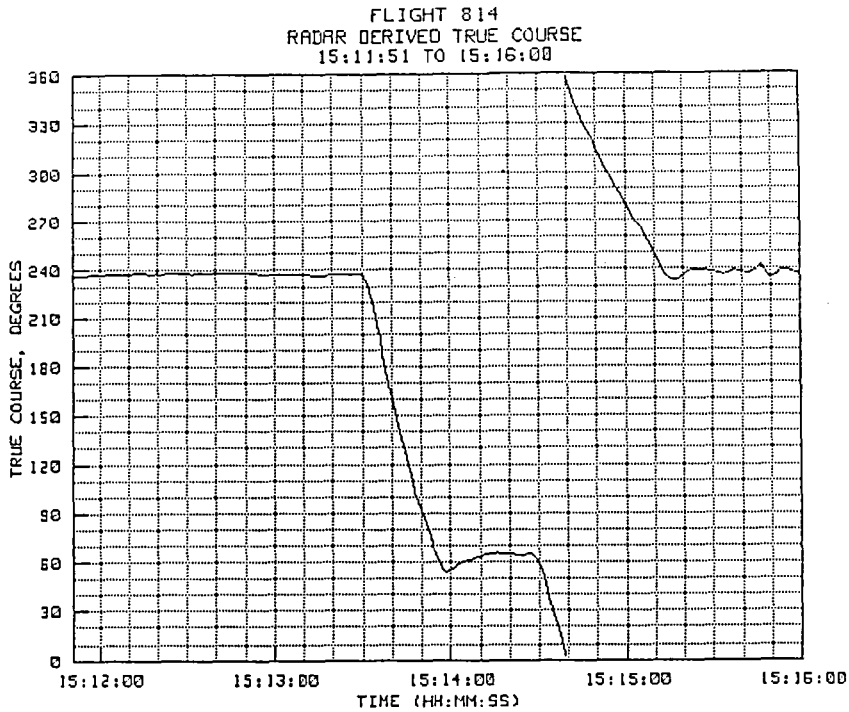

Figure 4-13(c). TP #5 radar-derived true course.

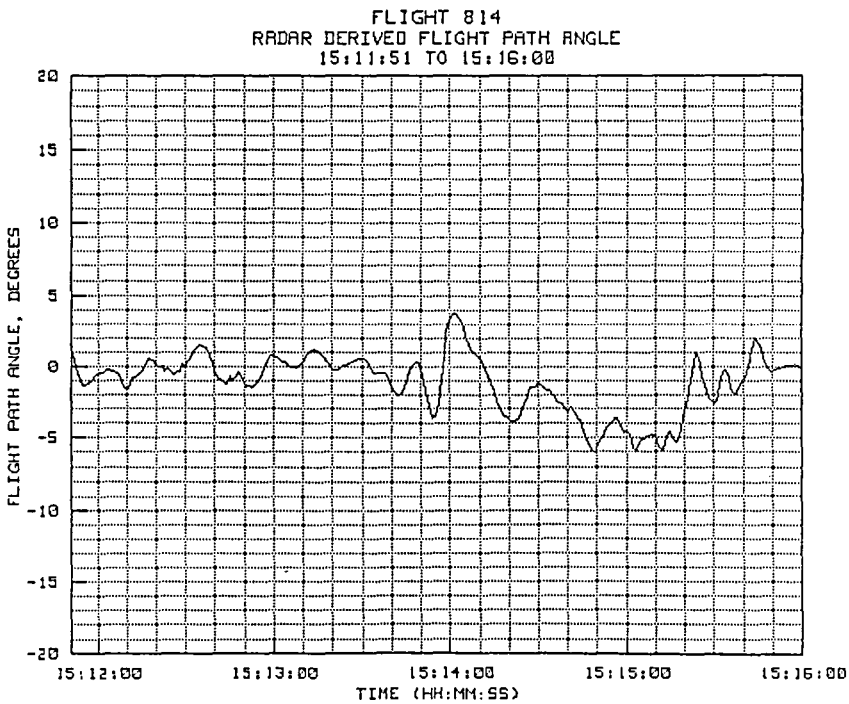

Figure 4-13(d). TP #5 radar-derived flight path angle.

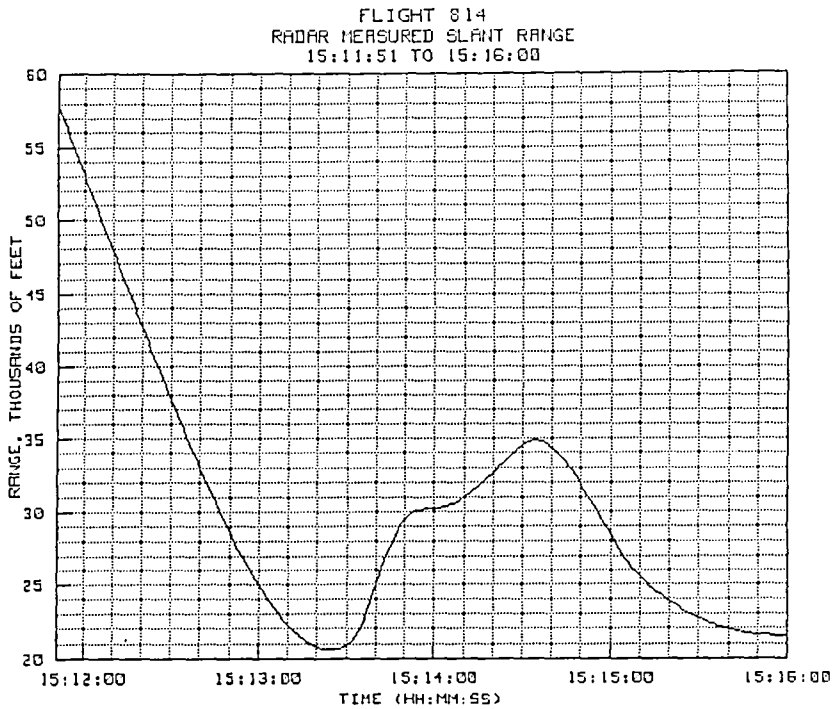

Figure 4-13(e). TP #5 radar-derived slant range.

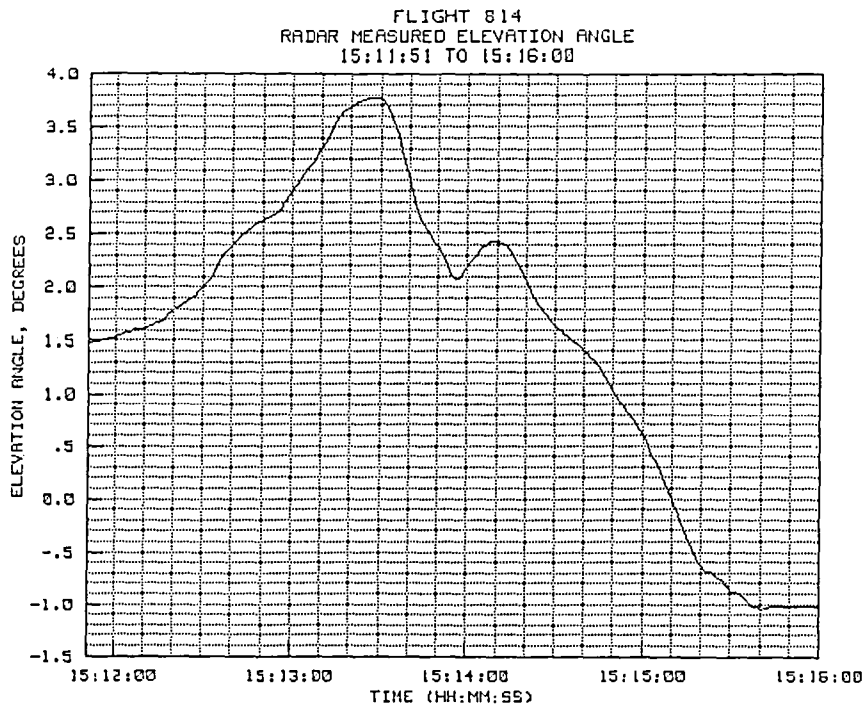

Figure 4-13(f). TP #5 radar-derived elevation angle.

4.3 Analysis of Wind Data for Flight 814

Three sources of reduced wind data were available for the analysis of flight 814. Immediately before the flight, a rawinsonde balloon was released. Wind data from this balloon track was obtained from both radar measurements and from the normal rawindonde data reduction program. In addition, winds from the post mission synoptic analysis were provided for comparison purposes.

Figures 4-14(a) and 4-14(b) show plots of wind data from all three sources. Unfortunately, the small reflector used on the rawinsonde weather package provides a very poor radar target. Therefore, the balloon was tracked optically (using the M-3 optics) until it reached sufficient altitude where a lock-on could be achieved. In this particular case, a consistent lock-on was not achieved until the balloon was at 8000 feet.

Data from the radar track, shown as solid lines on the two plots, agrees reasonably well with the rawinsonde measurements. However, it is necessary to apply very heavy damping to the data in order to eliminate gust effects and a pendulum motion which is readily evident on the visual monitor during all rawinsonde tracks. The pendulum motion is due to the fact that there is a long tether between the weather package and the balloon itself. On this track, gusting conditions caused the weather package (and radar reflector) to oscillate back and forth with about a ten second period. This, in turn, caused velocity oscillations of about 10 to 35 feet per second as shown in figures 4-15(a) and 4-15(b). The oscillating trace in these plots resulted when the data were reduced using the same damping as used for the reduction of aircraft data. The stable trace was made with very heavy damping.

When rawinsonde balloons are tracked, a small radar reflector is attached to the weather package. A far superior track could be obtained by using a radar reflective surface on the balloon itself. This should greatly reduce the periodic motion during a radar track and allow less damping in the data reduction process. When reflective balloons, such as the gemisphere, are tracked, lockons are generally obtained prior to launch and held solidly throughout all of the track.

Figures 4-16 through 4-19 show comparisons between on-board Mach number measurements and radar-derived velocity data adjusted using all three wind sources. In all three figures the on-board data are represented with a solid line, and the Mach numbers derived using radar, rawinsonde, and synoptic winds are shown by a short dashed line, a longer dashed line, and a dotted line, respectively.

In figure 4-16, which provides Mach number data during a climb from 4000 feet to 26,500 feet, values derived using all three wind sources show considerable differences from the on-board data at the lower altitudes. These differences decrease as the altitude increases until, at about 20,000 feet (at 14:21:10), the Mach calculations all agree with the on-board data to within about 0.01 Mach. In the regions of greatest difference, none of the wind sources show any distinct advantage.

Figure 4-17 shows Mach number comparison data for a level survey leg at an altitude of about 18,200 feet. In this case reasonably good agreement is obtained using all three sources. Maximum differences are on the order of 0.01 Mach throughout the run. Mach numbers computed from the radar derived winds show slightly better comparisons at the start of the run, and worse comparisons at the end of the run. Mach numbers computed from both the rawinsonde winds and the synoptic winds show nearly the same variations from the on-board data, with both having greater differences at the start of the leg and less differences at the end.

Figure 4-18 compares the on-board Mach number data with the radar derived data for a descent from 26,500 to 3500 feet. Again, Mach numbers derived using all three wind sources show approximately the same difference from the on-board data throughout most of the run. The greatest differences, at about 14:43:00, amount to 0.03 to 0.04 Mach.

Since Mach numbers during all three plots were reasonably constant, it is probable that the differences are due to the variability of the wind and errors in the wind vectors used for analysis purposes and not due to variations in the on-board measurements. Based on the Mach number comparisons made using data from the three test points, no distinct advantage could be found in any of the three wind sources.

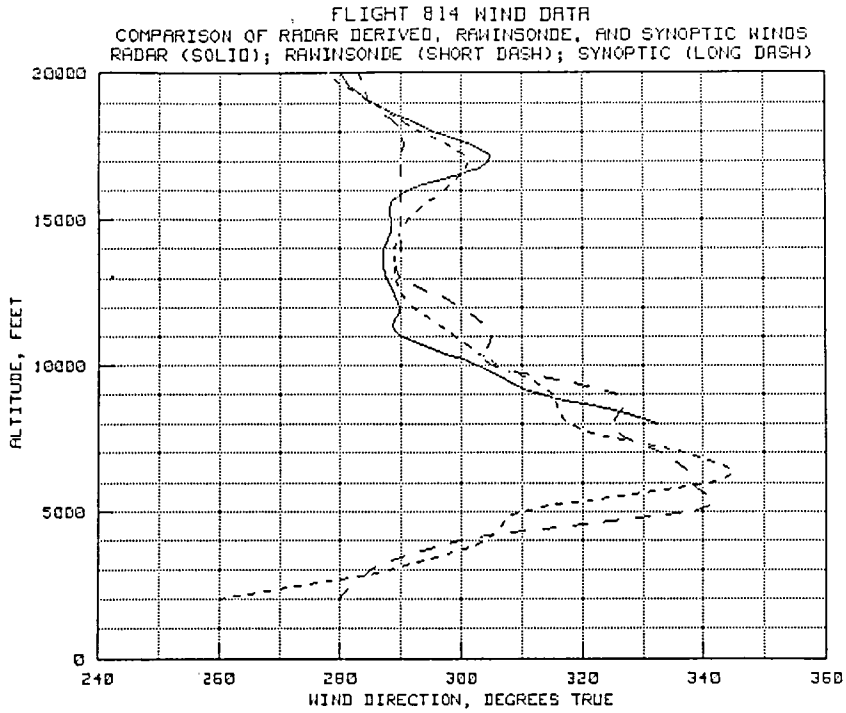

Figure 4-14(a). Flight 814 wind direction.

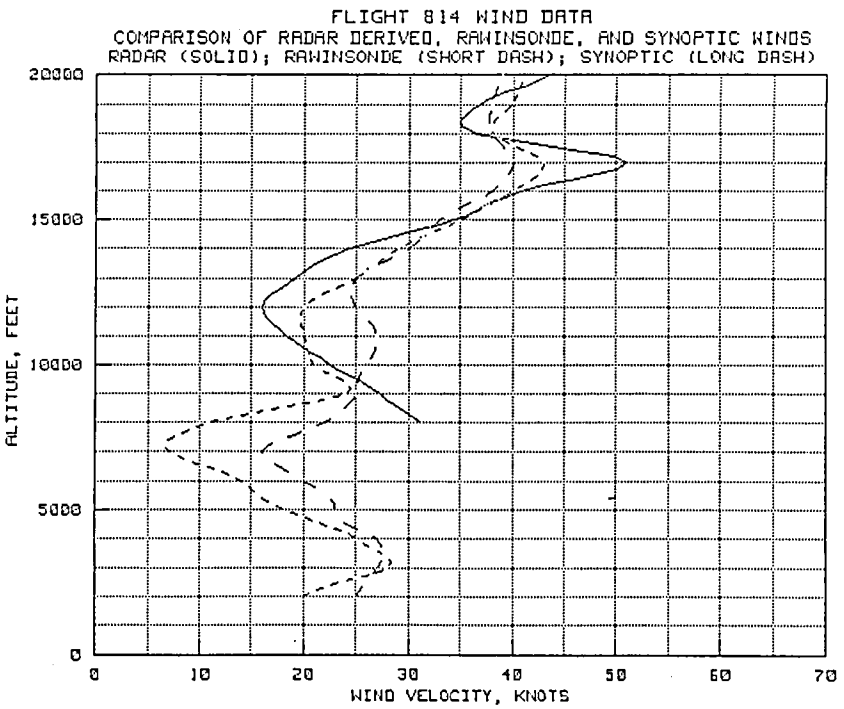

Figure 4-14(b). Flight 814 wind velocity.

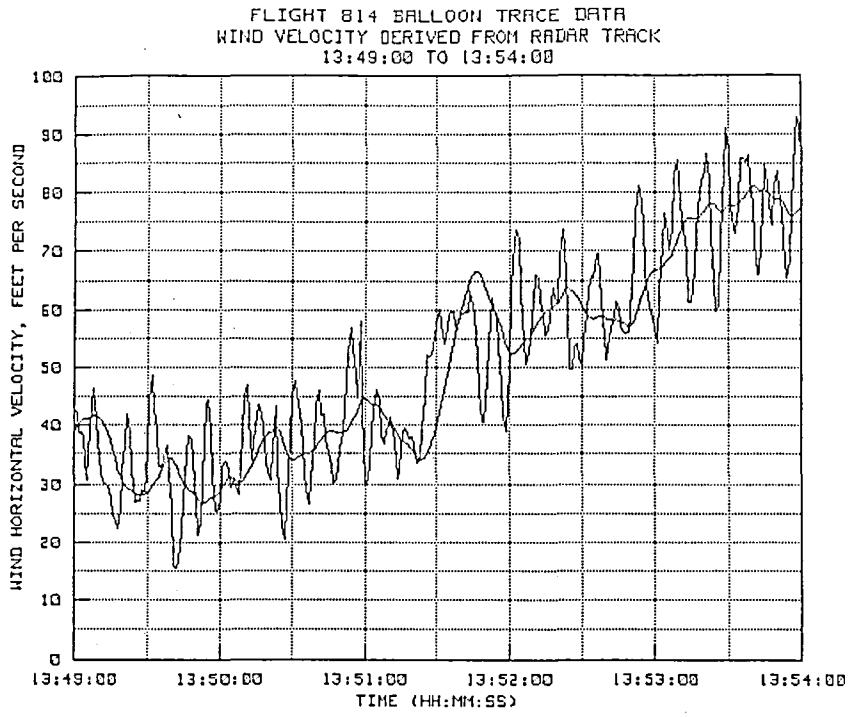

Figure 4-15(a). Flight 814 periodic character of wind velocity.

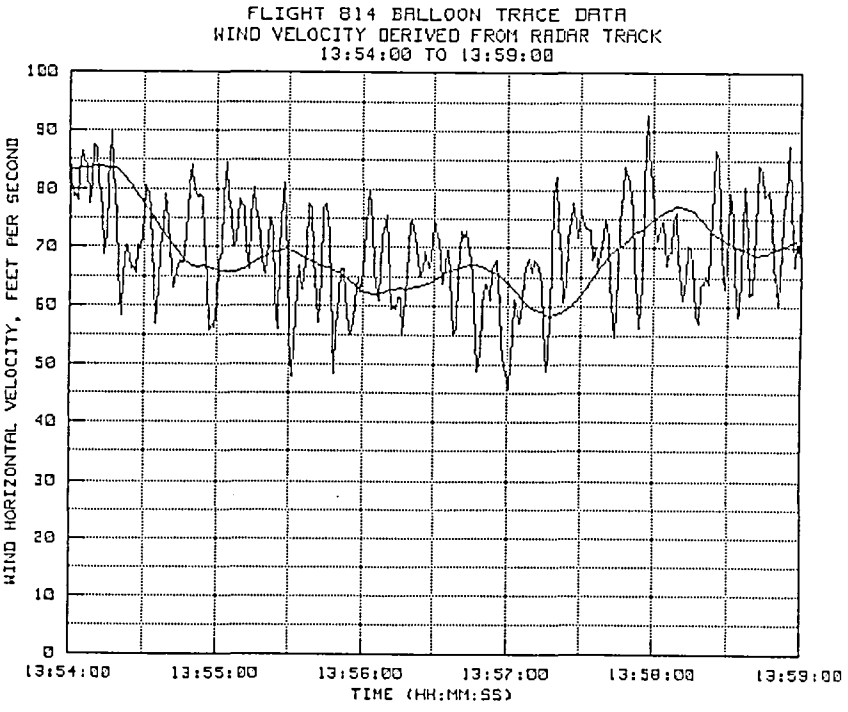

Figure 4-15(b). Flight 814 periodic character of wind velocity.

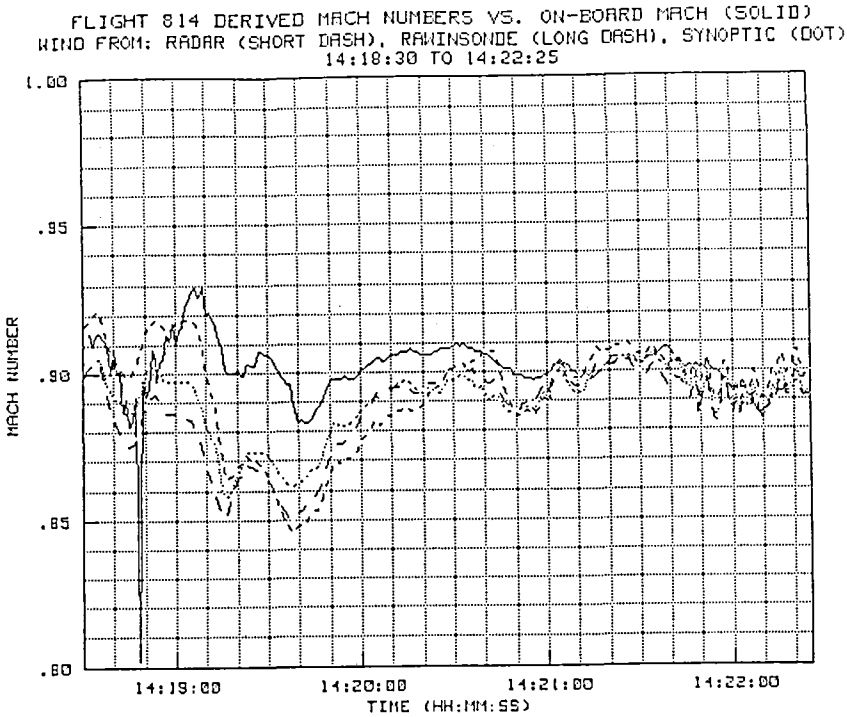

Figure 4-16. Mach comparison using three wind sources.

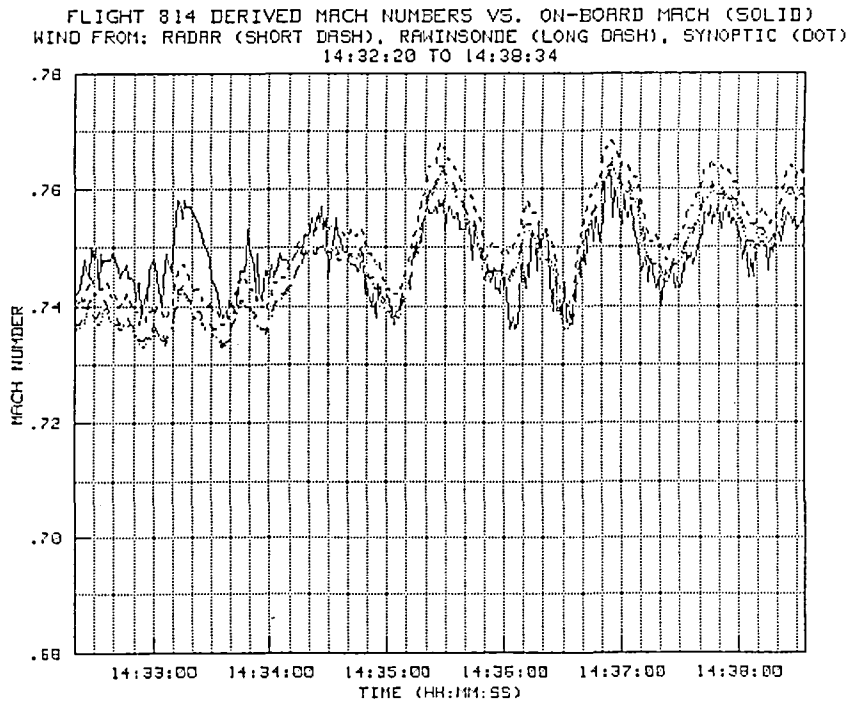

Figure 4-17. Mach comparison using three wind sources.

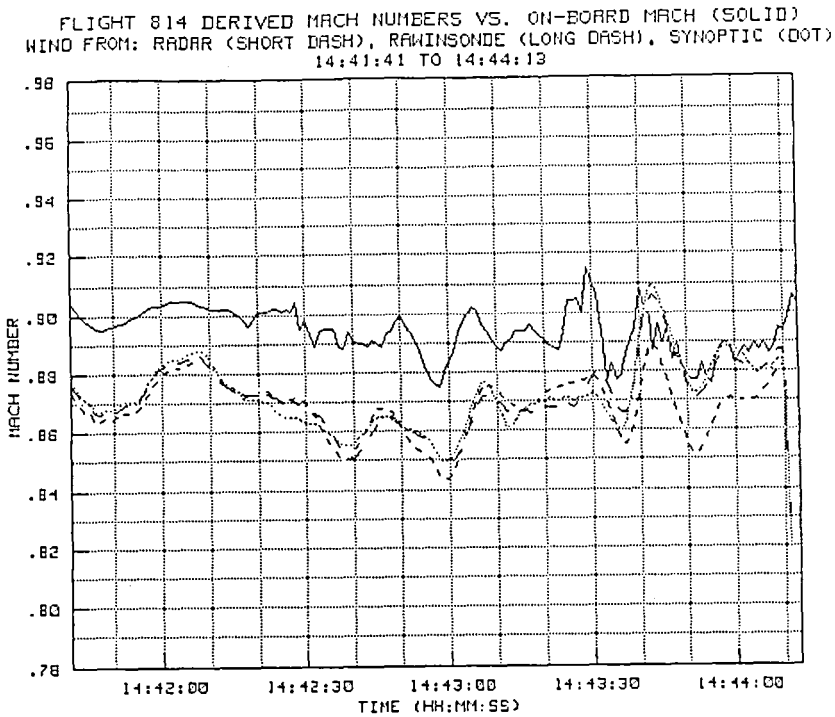

Figure 4-18. Mach comparison using three wind sources.

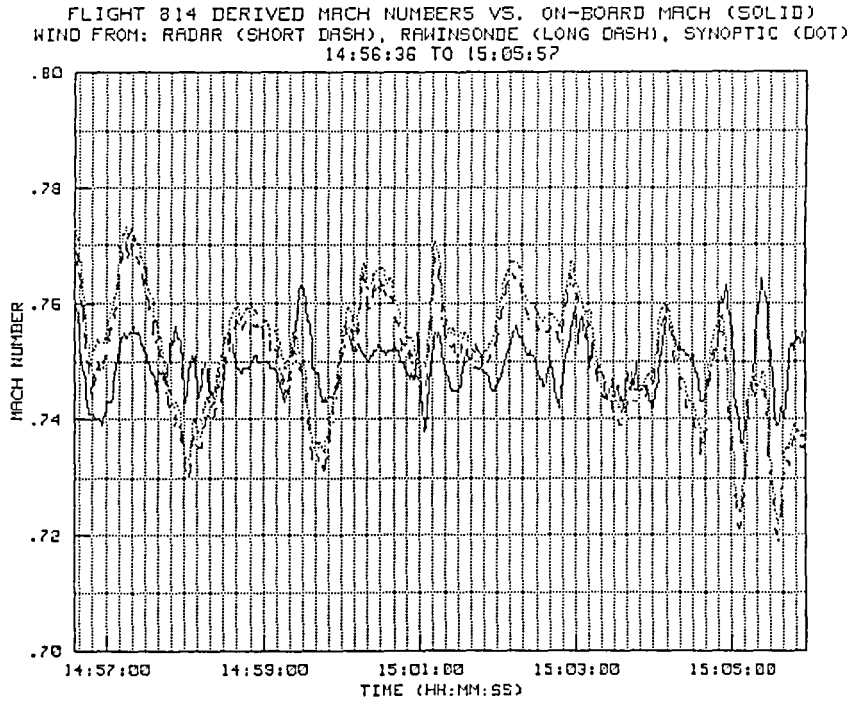

Figure 4-19. Mach comparison using three wind sources.

4.4 Noise Analysis for Flight 814

Noise plots for flight 814 are provided in figures 4-20(a), 4-20(b), and 4-20(c).

Shortly after takeoff it was learned that the ground telemetry system had malfunctioned. The pilot was instructed to circle to await a reboot of the system. As a result, a holding pattern was entered at low altitude with the chase aircraft flying a close wing position. Numerous jumps in the azimuth data were observed during this close-in track. Just before 14:10:00, with the system in skin mode, the lock transfered from the test aircraft to the chase aircraft. The operator immediately went to manual mode and reacquired the test aircraft. This resulted in the noise at 14:10:00. After that, the track was continued in beacon mode, however, a number of small jumps, primarily in range and azimuth, occurred due to reflections from the chase aircraft. About 14:18:00 the telemetry problems were resolved and normal tracking operations were resumed.

A small spike can be seen in the azimuth and elevation noise plots about 14:35:00. This was during the period when non-related tests were being performed, therefore the data was not reduced for that time segment. However, the sharp appearance and low magnitude of the noise spike would indicate that it also resulted from a momentary return from the chase aircraft.

A large noise spike appears in all three of the noise plots about 14:44. This was caused by an off-target condition that occurred when the aircraft flew almost directly over the radar site.

In general, the noise in the raw data measurements falls below one-half an LSB value in all three channels throughout all of the mission. Except for the few noise spikes discussed above, the overall range and angle noise for this mission was less than half that expected for a typical AN/FPS-16 radar in similar tracking circumstances.

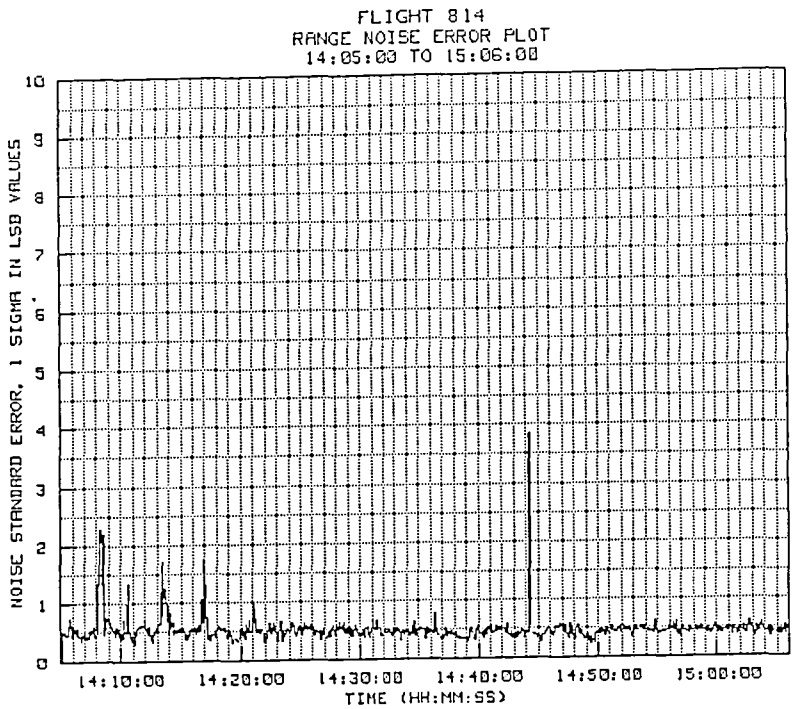

Figure 4-20(a). Flight 814 range noise plot.

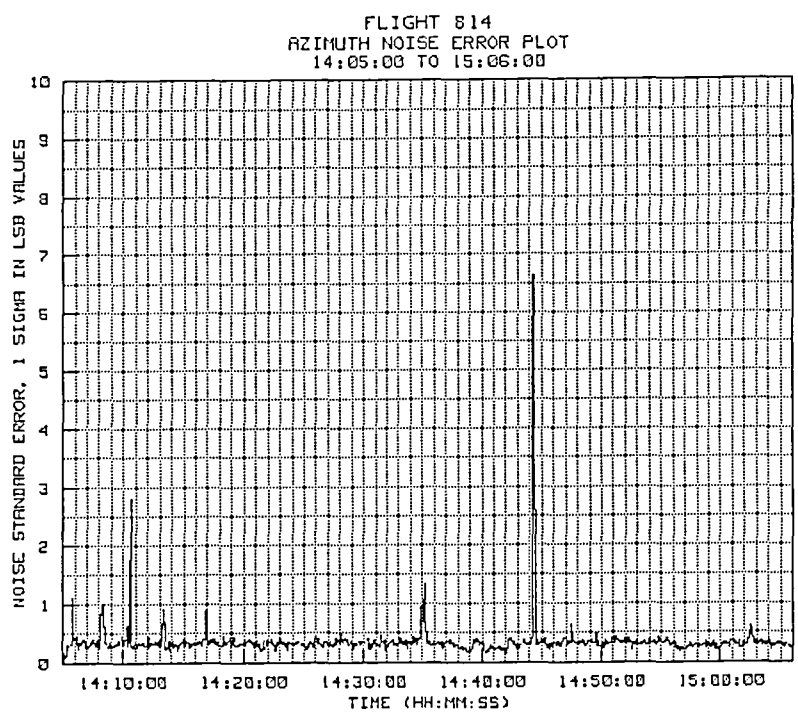

Figure 4-20(b). Flight 814 azimuth noise plot.

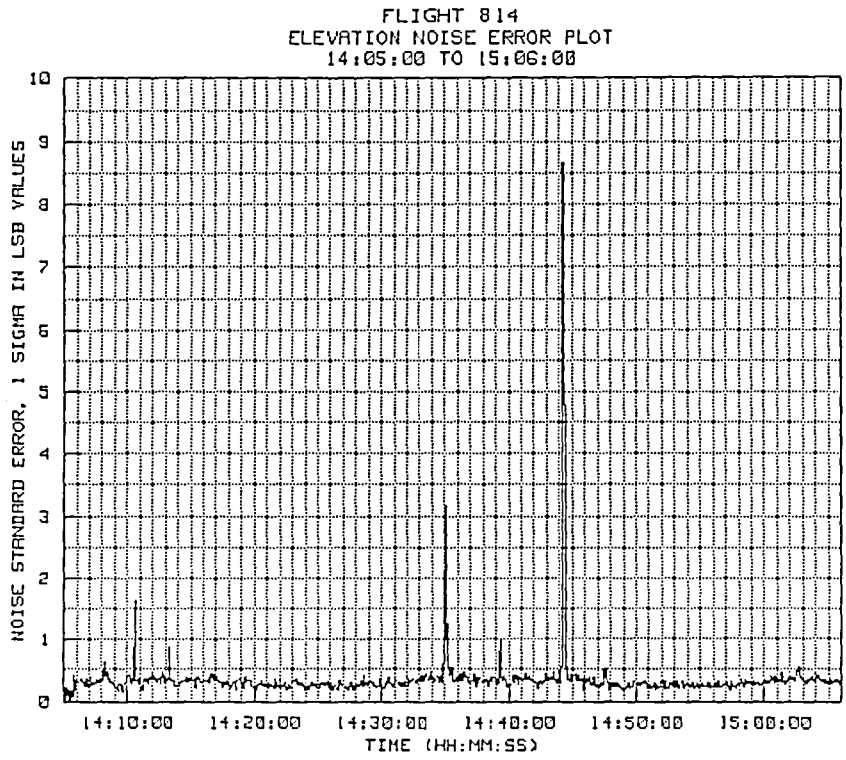

Figure 4-20(c). Flight 814 elevation noise plot.

4.5 Summary of Results from Flight 814

Flight 814 was conducted on a moderately windy day that was classified as nominal for the Edwards area. Radar adjusted synoptic estimates of Z-Hp and the horizontal Z-Hp gradient were used to adjust pressure altitude, and pre-mission rawinsonde measurements were used for the reduction of the radar data. All data appeared to be accurate throughout the flight, although some small Z-Hp differences were present, especially just prior to touchdown. This may have been due to atmospheric variations which occurred over the time of flight. It is also possible that some uncompensated variations in the on-board pressure measurements may have occurred due to the reduced airspeed and higher angle of attack just prior to landing.

During most of the flight, radar altitude data closely correlated with on-board pressure altitude measurements such that short term altitude changes were clearly evident in the test point altitude plots. However, the same type of long range, low elevation anomaly was found to be present in the altitude calculations on this flight as found during flight 811. After this difference was detected in flight 811, a careful alignment of the radar was made. The calibration procedures appear to rule out droop, encoder zero-set, r-f axis shift, and so forth as probable causes.

Mach number predictions on this flight had the same characteristics as they did on flight 811. Inaccuracies in predicting the wind vectors, as well as dynamic changes occurring in the wind over even short periods of time, seem to preclude consistent high accuracy derivations of Mach number during either high or moderate wind conditions. Errors on the order of 0.01 to 0.02 Mach appear to be commonplace, with even higher errors easily possible. No wind source (radar balloon track, rawinsonde, or synoptic analysis) showed any distinct accuracy advantage during flight 814.

5.0 AIR DATA CALIBRATION FLIGHT 855

Air data calibration flight 855 was flown on August 20, 1984 using F-104 tail number 826. The pilot was Mr. Ed Schneider. Fourteen specific test maneuvers were scheduled and successfully carried out. Figures 5-1 through 5-3 provide time history plots of the raw range, azimuth, and elevation measurements taken from takeoff until touchdown.

5.1 Summary of Flight Day Wind and Weather Conditions

The flight day was classified as "benign" from the standpoint of wind and other atmospheric activity. The surface temperature was 28.8 degrees C, and the surface winds were light and variable. Relative humidity was 48 percent, giving an r-f index of refraction of 316 N-units, some thirty to forty N-units higher than on the previous two flights. This was considered important since additional facts might be learned about the low-elevation, long-range altitude differences experienced on flights 811 and 814.

On the test day, the flow pattern was weak and relatively stationary, and the wind conditions at the surface remained below 7 knots from sunrise to sunset. The flight was conducted before noon, with sky condition reported as 20,000-foot scattered. Towering cumulus developed in the mid-afternoon, and both thunder and lightning were observed in the early evening. Cloud coverage remained scattered with isolated cumulo-nimbus observed at sunset.

The surface semi-diurnal effect at 1800Z was 72 feet above the Z-Hp values interpolated linearly from synoptic analyses for 1200Z and 2400Z on 20 August. The Z-Hp data from the linear interpolation was checked against Z-Hp calculated from temperature-aloft measurements and from surface pressures measured at test time. This showed semi-diurnal Z-Hp increases of less than 30 feet at flight levels below 20,000 feet. Therefore, the semi-diurnal adjustments applied to the linearly interpolated data were limited to 20 to 25 feet. However, the semi-diurnal effects substantially increased the total uncertainty in the Z-Hp profiles. The surface Z-Hp peaked just before takeoff and reached a rate of decrease equal to -13 feet per hour at landing time.

Specific wind and weather values used for this analysis are provided in table 5-I. Note that again three sources of wind data were available for this analysis: (1) radar derived winds from the rawinsonde track, (2) winds from the rawinsonde system, and (3) winds from the synoptic analysis. Because of time constraints, the rawinsonde winds, which were immediately available after the flight, were used for the Mach calculations in section 5.2. However, comparisons of

radar derived Mach numbers using all three sources are provided in section 5.3.

Table 5-II provides Z-Hp values from the synoptic analysis along with the adjusted Z-Hp values based on comparisons of the on-board pressure altitude with radar-derived geometric altitudes for high-angle or close-in tracking periods. In order to obtain the best plotting correlation, the radar-adjusted values of Z-Hp were used for analysis purposes. Figure 5-4 provides plots of both the synoptic Z-Hp values and the same values as adjusted by measurements made during highest-accuracy periods of the radar track.

In order to check the radar elevation data for close-in conditions, the takeoff portion of the flight (AIDED EL) was plotted (Fig. 5-5). Brake release occurred at 10:04:49 as indicated by the first event mark on figure 5-5. At that point the computed geometric altitude was 2273 feet or about 7 feet below the elevation of the runway surface estimated from the nearby taxiway marker, NRP 4. An analysis of the video tape recordings of the takeoff revealed that the optical aim point during takeoff may have been slightly low at the start of the roll. At about 10:05:05, indicated by the second event marker, the operator made an elevation adjustment which brought the optical aim point closer to the position of the aircraft beacon antenna. This increased the computed geometric altitude to 2282 feet. At about 10:05:17, indicated by the third event marker, the nose wheel was observed to break ground and shortly thereafter the main gear also left the runway. The optical aim point used for the post-mission analysis was determined from the r-f track point after the switch to FULL AUTO track. It was also noted that the lighted reticule was not turned on until after the takeoff. After the reticule was turned on, the quality of the optical track appeared to improve. Therefore, it was concluded that the computed geometric altitude during the first part of the takeoff roll was about 10 feet low, and this may have been due in part to using a slight error in establishing the optical aim point on the TV monitor. It is also possible that some of the difference noted may have been due to an error in the elevation encoder setting.

High angle and/or close-in range measurements of the aircraft trajectory during the flight period are provided in figures 5-6 through 5-8. In figure 5-6, the difference between radar derived geometric altitude and on-board pressure altitude was approximately 85 to 90 feet. By 5000 feet, the difference appeared to increase to about 130 feet. In figure 5-7, the difference for a pressure altitude of 17,500 feet appears to be about 830 feet. And, in figure 5-8, the difference, again for a pressure altitude of 17,500 feet, appears to be about

825 to 830 feet. All of the radar adjusted values fall well within the error tolerances estimated for the synoptic values.

Another check on the radar-derived geometric altitude was made at touchdown as shown in figure 5-9. Touchdown occurred at 10:28:09 and, at that time, the video recordings showed the track point to be approximately at the position of the beacon antenna. From the data in figure 5-9, it appears that the elevation calculations on touchdown were about 6 feet lower than the true position of the beacon. Since the optical track point on touchdown appeared to be within one or two feet of the position of the beacon antenna, it is possible that some error may have been present in the optical aim point, in addition to a small error in the elevation encoder setting.

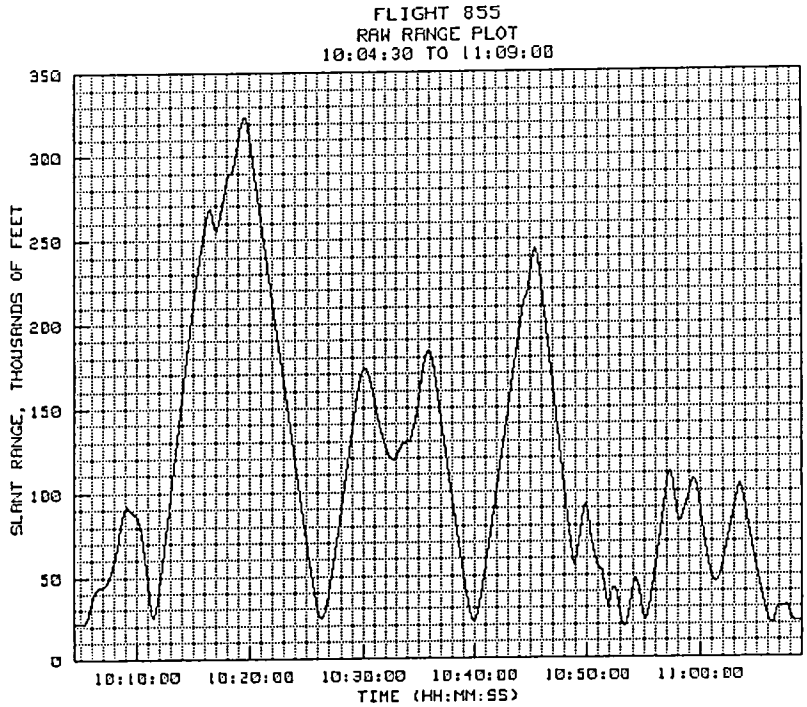

Figure 5-1. Flight 855 radar-derived slant range.

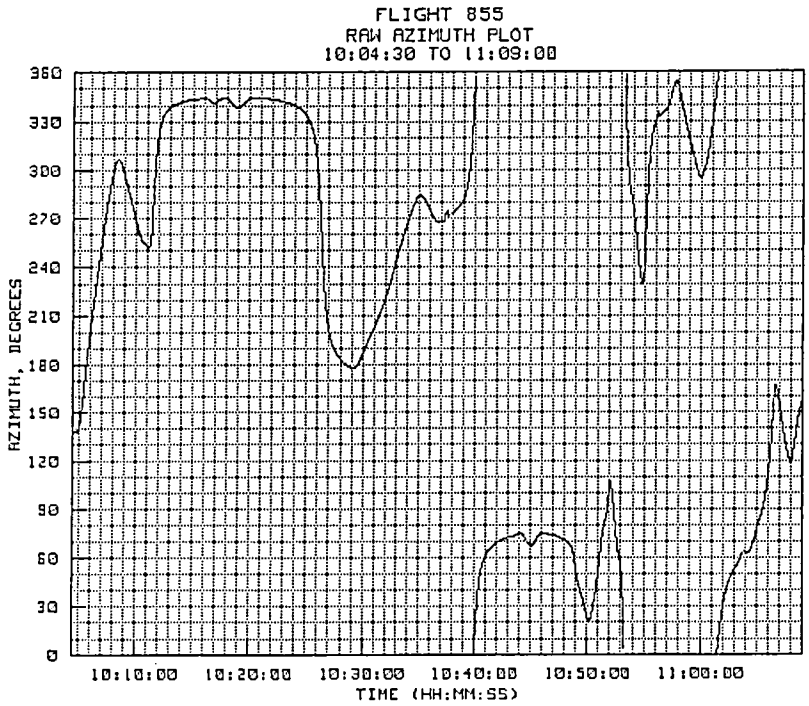

Figure 5-2. Flight 855 radar-derived azimuth angle.

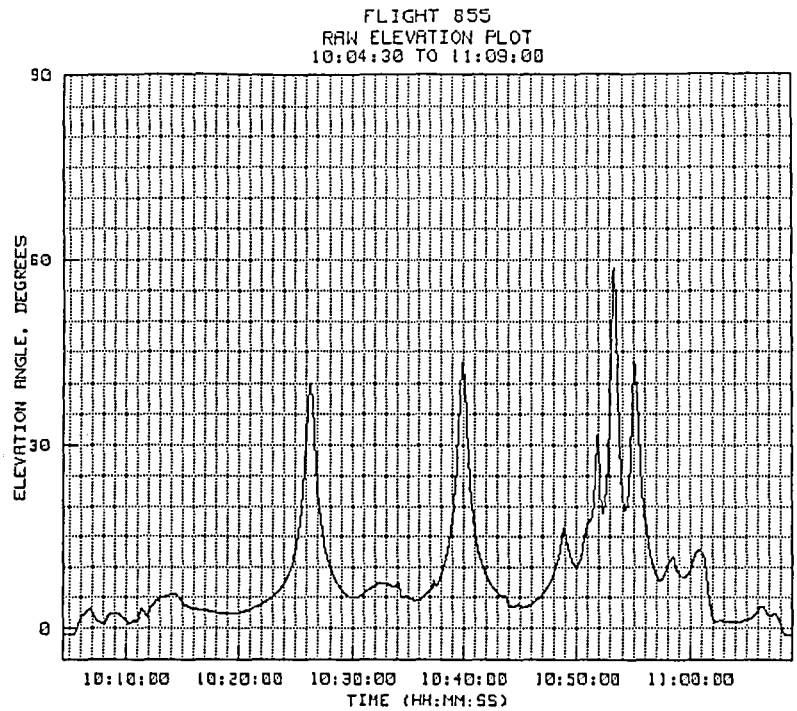

Figure 5-3. Flight 855 radar-derived elevation angle.

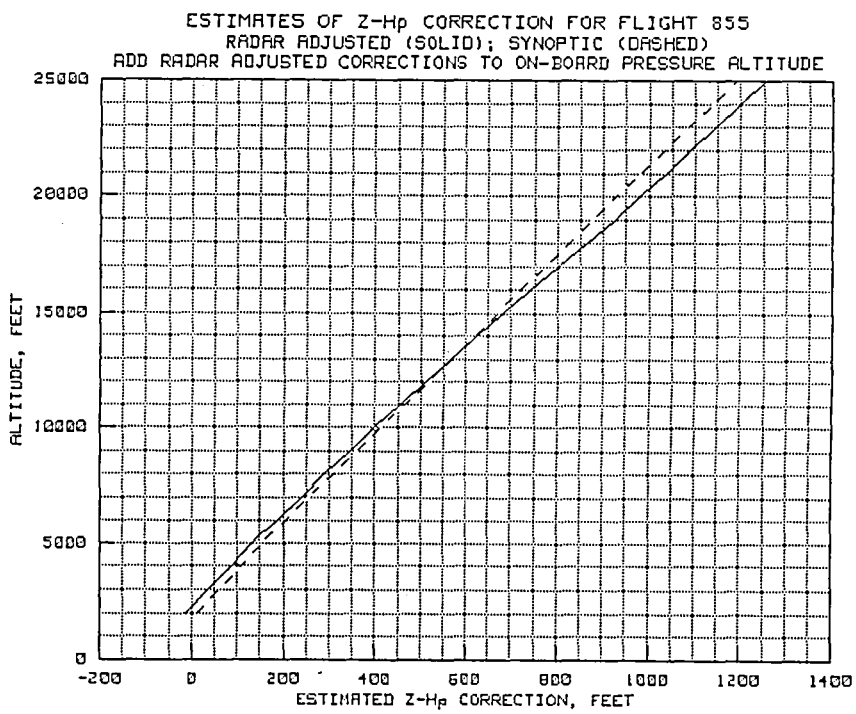

Figure 5-4. Flight 855 synoptic and radar derived Z-Hp plots.

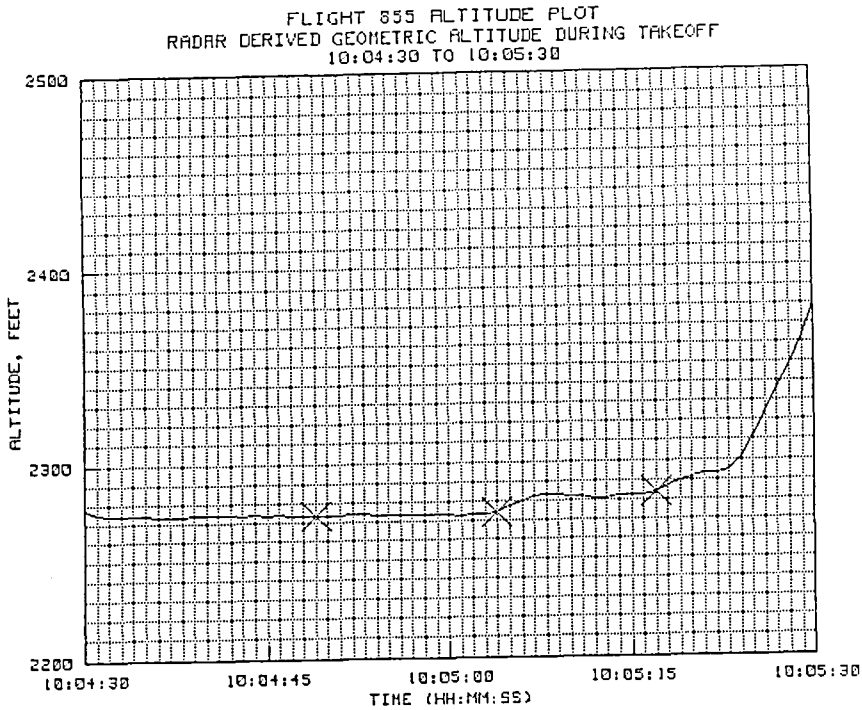

Figure 5-5. Flight 855 geometric altitude on takeoff.

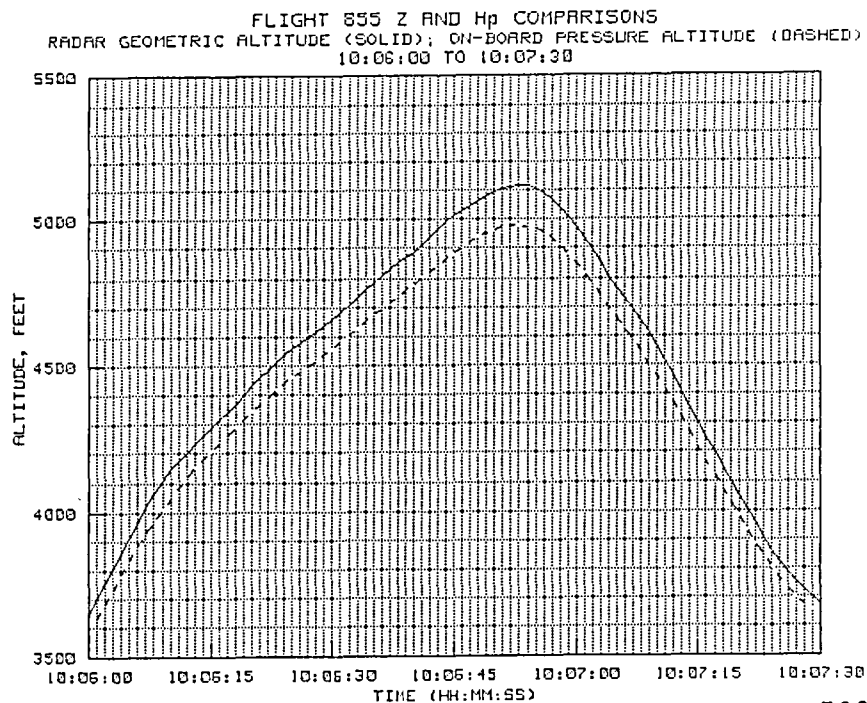

Figure 5-6. Flight 855 Z and Hp comparison 4000 to 5000 feet.

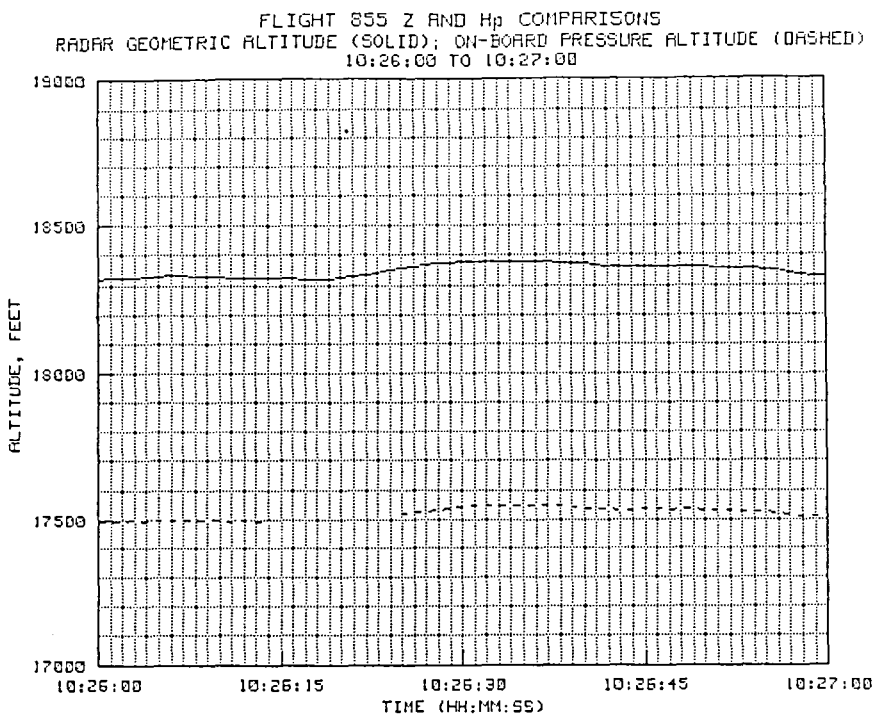

Figure 5-7. Flight 855 Z and Hp comparison 18,000 feet.

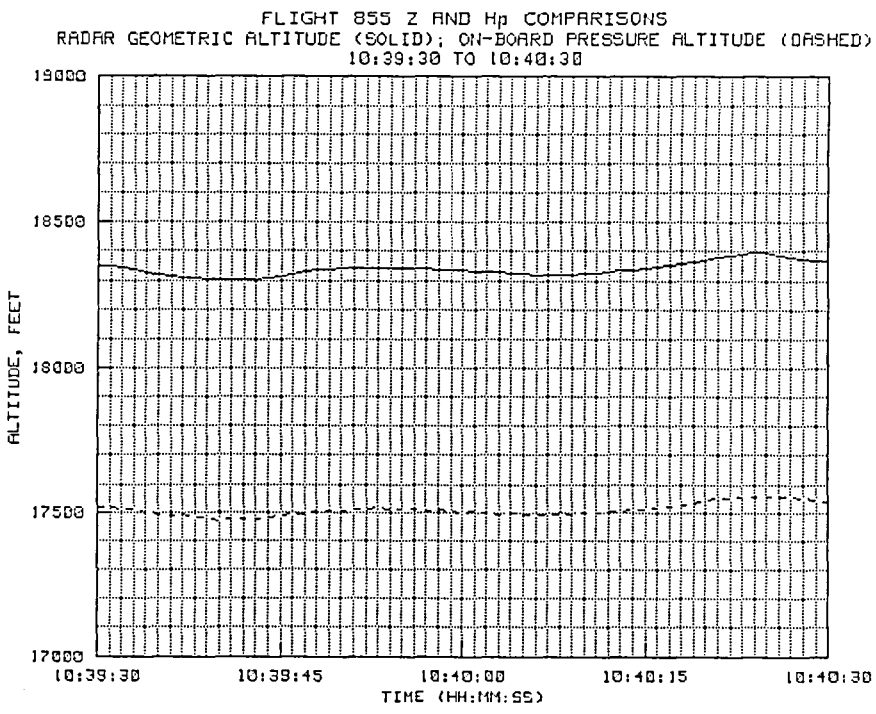

Figure 5-8. Flight 855 Z and Hp comparison 18,000 feet.

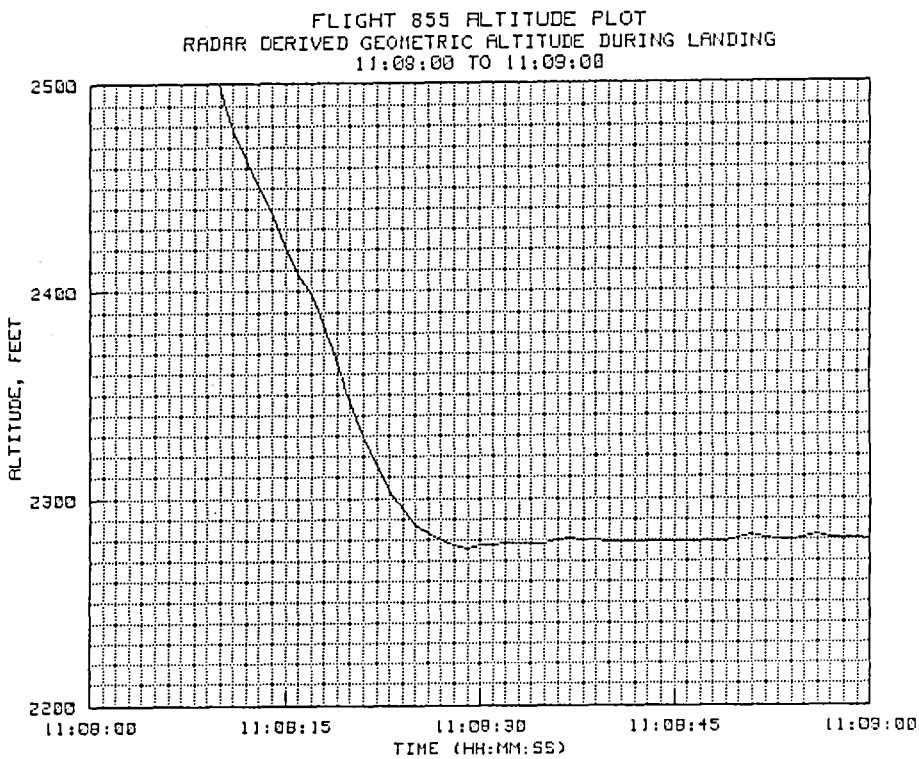

Figure 5-9. Flight 855 geometric altitude on landing.

TABLE 5-I. FLIGHT 855 WEATHER DATA

JEATHER DATA FOR FLIGHT 855

ALTITUDE (FT)	TEMPERATURE (DEG C)	DEW POINT (DEG C)	PRESSURE (MB)	N X 10E6	WIND (DEG/KTS)
2300	28.0	16.7	931.19	318.1	60.0/ 6.0
3000	24.8	11.1	911.33	293.6	59.0/ 10.0
4000	21.9	10.8	880.09	287.7	65.0/ 9.0
5000	20.0	10.6	849.78	281.2	69.0/ 8.0
6000	18.1	10.7	820.17	275.9	82.0/ 7.0
7000	16.1	11.6	791.50	274.1	78.0/ 8.0
8000	13.8	10.6	763.63	265.2	69.0/ 9.0
9000	12.5	7.7	736.57	248.8	59.0/ 7.0
10000	10.5	7.2	710.32	242.1	47.0/ 8.0
11000	8.3	6.0	684.82	233.5	36.0/ 11.0
12000	7.1	3.1	660.07	219.5	36.0/ 13.0
13000	5.0	.2	636.06	207.8	30.0/ 16.0
14000	2.6	-2.2	612.72	198.3	31.0/ 15.0
15000	.5	-4.8	590.06	189.0	16.0/ 12.0
16000	-2.0	-7.2	568.06	180.9	358.0/ 10.0
17000	-4.8	-10.0	546.68	172.6	345.0/ 6.0
18000	-5.7	-18.8	525.96	160.0	352.0/ 5.0
19000	-7.0	-25.8	505.90	151.5	357.0/ 6.0
20000	-8.7	-28.1	486.51	146.1	2.0/ 6.0
21000	-10.1	-29.4	467.74	140.9	350.0/ 6.0
22000	-11.9	-30.7	449.59	136.2	316.0/ 6.0
23000	-14.0	-32.3	432.01	131.7	308.0/ 8.0
24000	-16.3	-34.1	415.00	127.4	315.0/ 8.0
25000	-18.1	-35.6	398.52	123.0	322.0/ 7.0

TABLE 5-II. FLIGHT 855 Z-Hp DATA

Synoptic Z-Hp Data for Flight 855

Altitude (feet)	Syn. Z-Hp (feet)	Radar Z-Hp (feet)	Change in Z-Hp (feet/n.mi.)	Direction of decrease
25,000	+1255	+1255	0.20	007
24,000	+1134	+1200		
23,000	+1082	+1145		
22,000	+1030	+1090		
21,000	+ 978	+1035		
20,000	+ 926	+ 980		
19,000	+ 874	+ 925	0.28	100
18,000	+ 822	+ 865		
17,000	+ 772	+ 801		
16,000	+ 719	+ 741		
15,000	+ 669	+ 682		
14,000	+ 618	+ 625		
13,000	+ 565	+ 568		
12,000	+ 515	+ 512		
11,000	+ 462	+ 456		
10,000	+ 411	+ 400	0.16	103
9,000	+ 359	+ 346		
8,000	+ 307	+ 291		
7,000	+ 255	+ 240		
6,000	+ 203	+ 188		
5,000	+ 151	+ 130		
4,000	+ 107	+ 88		
3,000	+ 61	+ 36		
2,000	+ 15	- 13		

Add Z-Hp values to pressure altitude to obtain geometric altitude

5.2 Analysis of Test Points

During flight 855, fourteen test points yielded data suitable for analysis. The starting and ending times and the description of each test point are given below. All times shown are Pacific Daylight Time (PDT). Note that some of these points combine two of the original test points shown on the pilot's flight card, and the test point numbers used in the descriptions below have been sequentially renumbered for clarity.

1. 10:06:00 to 10:07:30 - A low level close-in leg at stable Mach.

2. 10:11:50 to 10:14:23 - Mach 0.9 climb 4000 feet to 21,000 feet.

3. 10:16:00 to 10:17:25 - 360 degree tight left turn (beacon check).

4. 10:20:50 to 10:30:00 - Survey leg at 0.75 Mach, 18,350 feet.

5. 10:33:30 to 10:35:00 - Right roll (beacon check).

6. 10:35:45 to 10:37:45 - Left turn followed by left roll (beacon check).

7. 10:38:45 to 10:43:30 - Cross survey leg at 0.75 Mach, 18,350 feet.

8. 10:43:15 to 10:44:30 - Right roll (beacon check).

9. 10:48:00 to 10:49:15 - Deceleration and 3-g 90-degree right turn.

10. 10:51:00 to 10:52:30 - High-g maneuvering flight (beacon check).

11. 10:53:45 to 10:56:30 - High-g maneuvering flight (beacon check).

12. 10:56:45 to 10:58:45 - Right roll (beacon check).

13. 11:00:15 to 11:02:45 - Mach 0.85 descent to 4000 ft level-off.

14. 11:02:45 to 11:03:15 - Trimmed-up, hands-off flight.

The data for this flight were analyzed using psychrometric values and wind profiles from rawinsonde data which was available immediately after the flight. However, comparisons

of winds from the rawinsonde radar track, from the rawinsonde measurements, and from the synoptic analysis are provided in section 5.3. As shown in figures 5-24(a) and 5-24(b), the synoptic wind estimates agreed reasonably well with the rawinsonde measurements for this test mission.

5.2.1 Test Point #1

The time history plots for test point #1 are shown in figures 5-10(a) to 5-10(f). This test point was to have been a stable Mach and altitude pass within 35 miles of the radar. A 1.5 minute leg was entered on a true course of about 249 dgrees, and a nearly constant right bank angle was held so that the leg ended on a true course of about 348 degrees. Altitude at the start of the run was 3654 feet, increasing to about 5118 feet at 10:06:53, then dropping to 3673 feet at the end of the run. Starting slant range was 33,820 feet (5.57 n.mi.) increasing to 48,064 feet (7.91 n.mi.) by the end of the run. The starting elevation angle was 1.63 degrees, increasing to 3.15 degrees at the high point, then decreasing to 1.34 degrees at the end of the leg. During this leg, the pressure altitude agreed well with the radar derived altitude. As noted in figure 5-10(a), the difference between the two at 5000 feet was very close to zero. At altitudes below 4000 feet, a difference of possibly 10 to 15 feet can be observed, with the radar-derived altitude falling slightly below the pressure altitude.

Mach number for the same run is shown in figure 5-10(b). Some antenna movement was present at the start of the run, about the same time the right bank was initiated. By about 20 seconds into the run, the radar-derived Mach number settled down and followed the general pattern shown in the on-board data; however, a bias error appeared to build up as the aircraft course became more northerly. The greatest amount of difference appeared at 10:07:15 when it reached about 0.012 Mach.

Since the onset and buildup of the Mach bias did not correlate with the heading changes made during the leg, it is believed that the differences are probably due to variations between the actual winds encountered on the leg and the rawinsonde wind vectors used for the reduction of the data.

No tracking anomalies occurred during the time of this run.

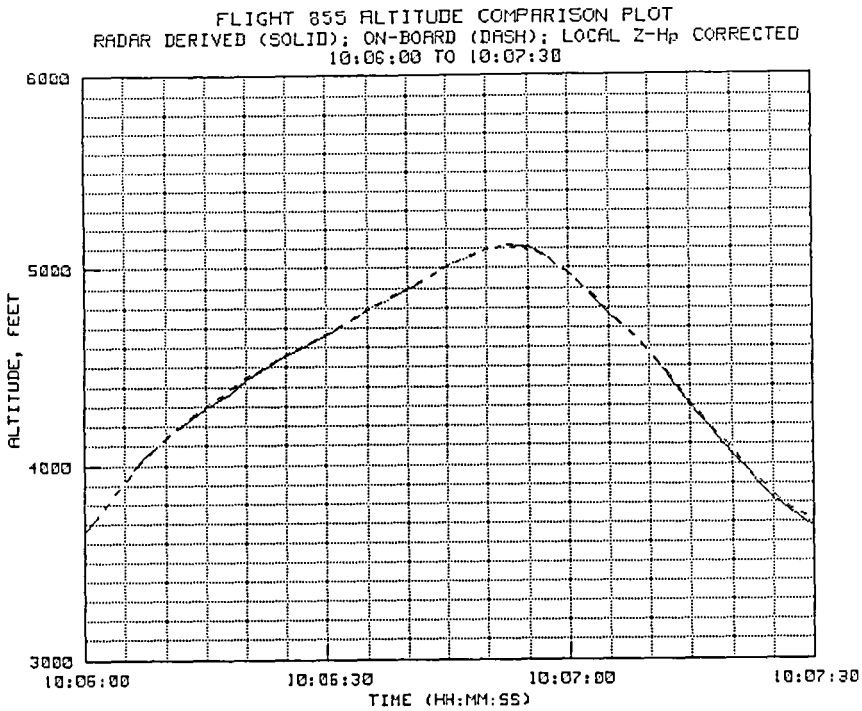

ıre 5-10(a). TP #1 radar-derived and on-board altitud

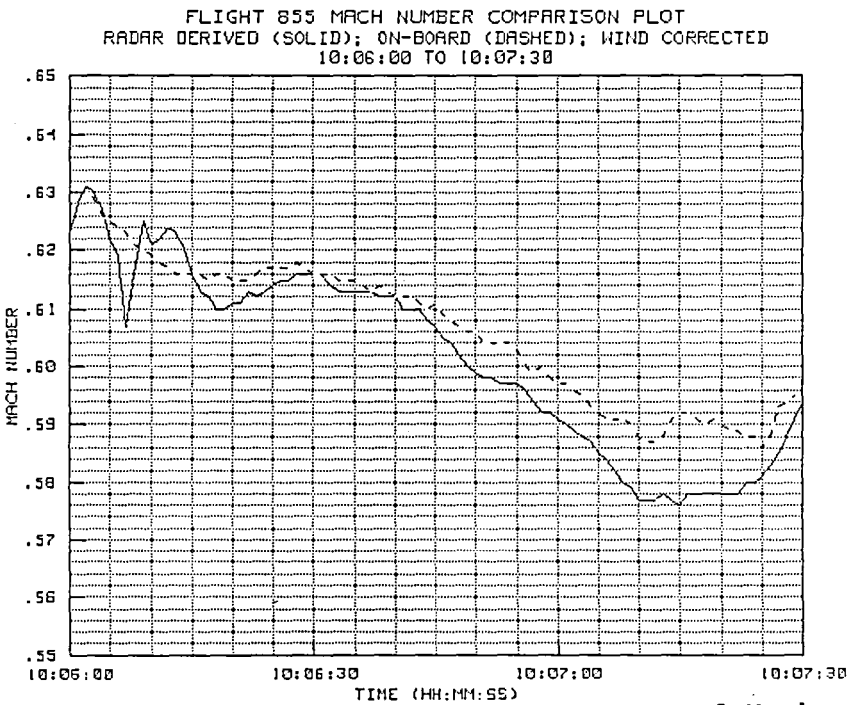

Figure 5-10(b). TP #1 radar-derived and on-board Mach numl

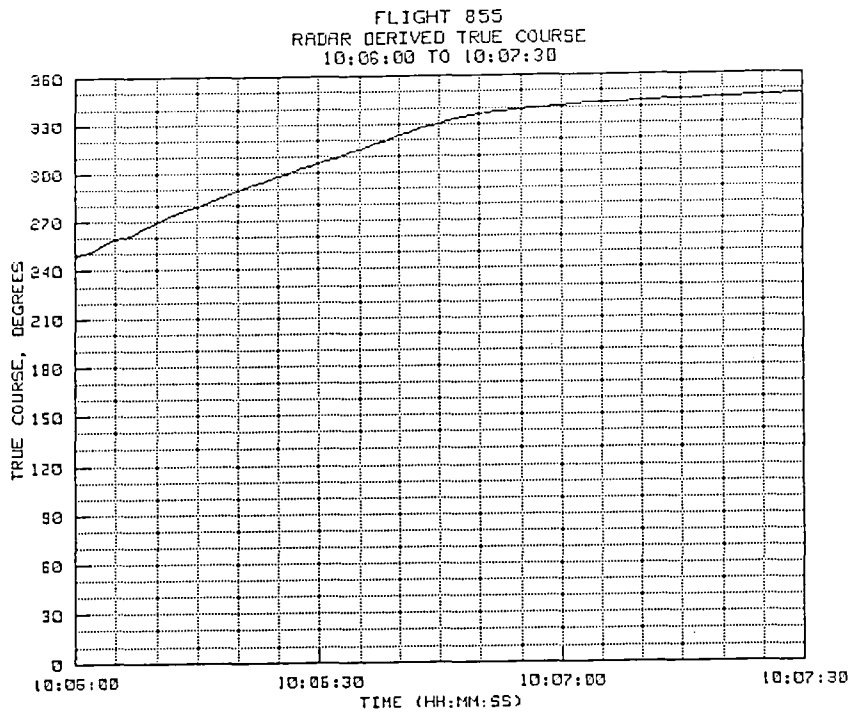

Figure 5-10(c). TP #1 radar-derived true course.

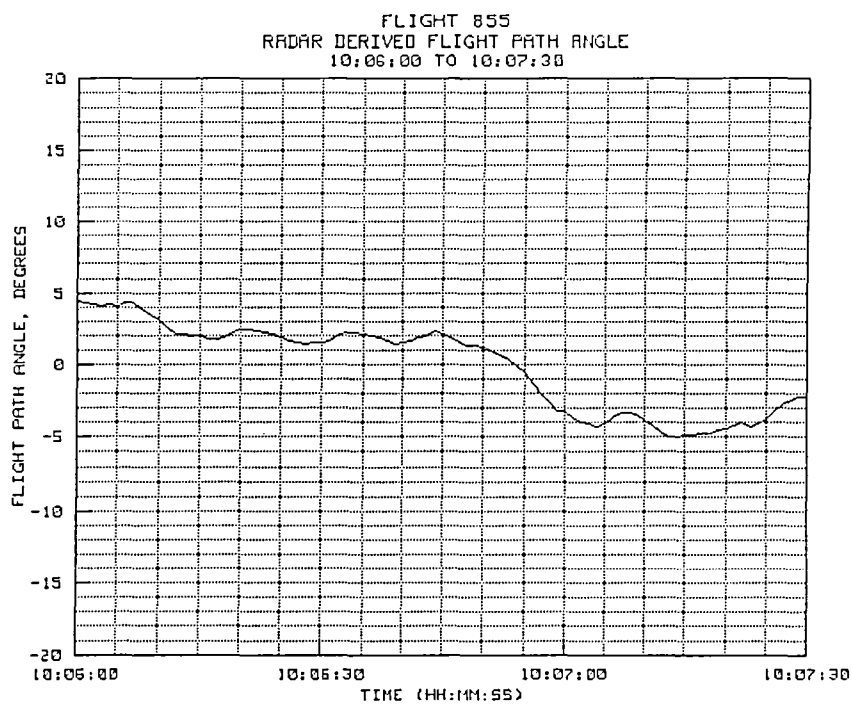

Figure 5-10(d). TP #1 radar-derived flight path angle.

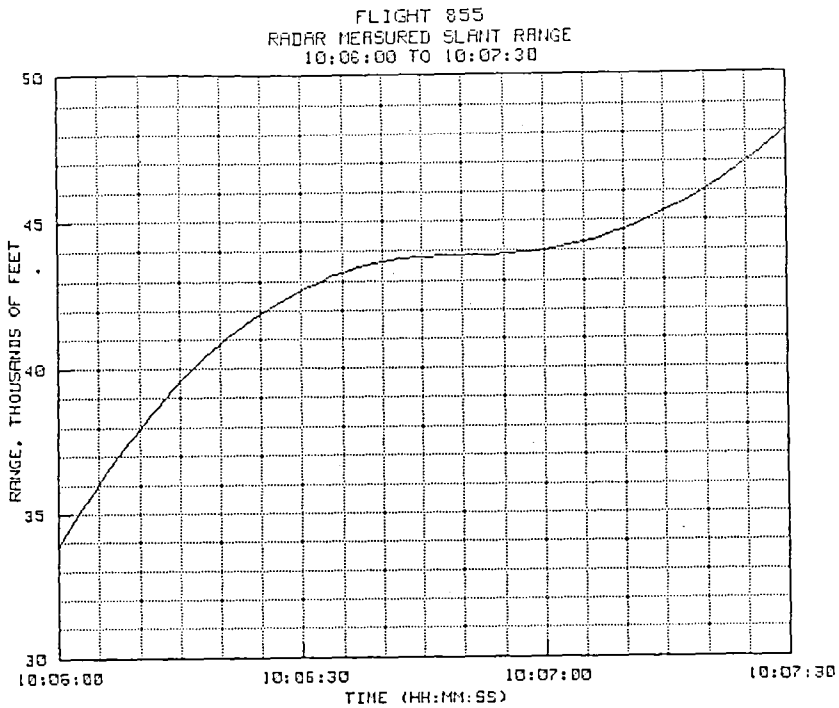

Figure 5-10(e). TP #1 radar-derived slant range.

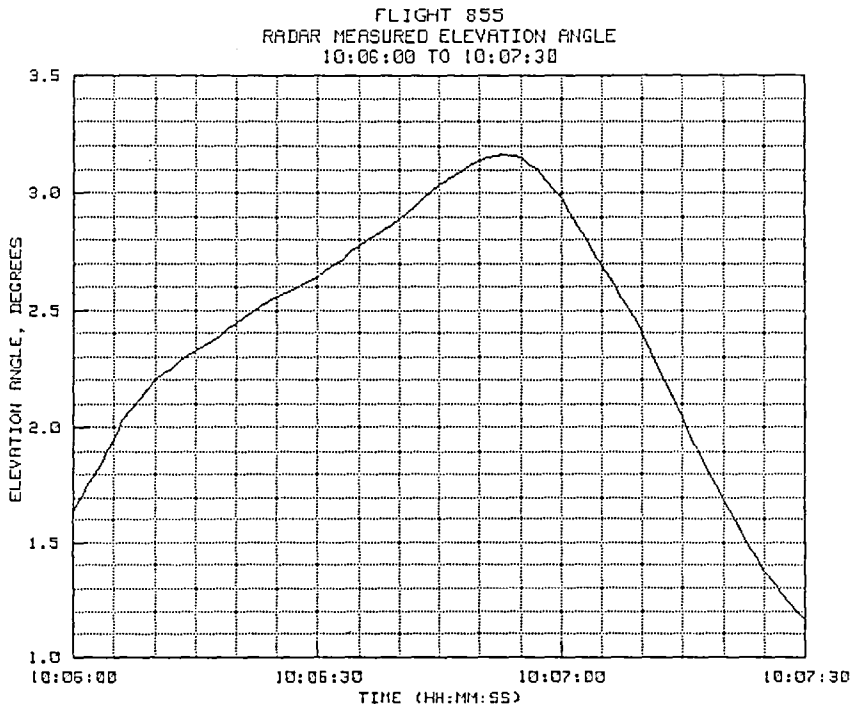

Figure 5-10(f). TP #1 radar-derived elevation angle.

5.2.2 Test Point #2

The time history plots for test point #2 are provided in figures 5-11(a) to 5-11(f). Test point #2 was a climb which started at an altitude of approximately 4000 feet and continued to a level-off at 21,000 feet. The climb was commenced at a slant range of 33,914 feet (5.58 n.mi.) and continued outbound on a general northerly heading until reaching a slant range of 186,931 feet (30.76 n.mi.). Elevation angle at the start of the climb was 2.19 degrees, and at level-off it was 5.35 degrees. During the climb, the radar-derived geometric altitude agreed very closely with the Z-Hp adjusted on-board pressure data. In figure 5-11(a), the solid plot, representing radar-derived altitude, exactly overlays the dashed plot, representing Z-Hp adjusted on-board pressure altitude.

Figure 5-11(b) shows the comparison between radar-derived Mach number and on-board Mach number. Again, short term changes in the on-board Mach number have direct correlation with changes in the radar-derived Mach number, but bias errors of up to 0.015 Mach are present.

No tracking anomalies were noted during this run.

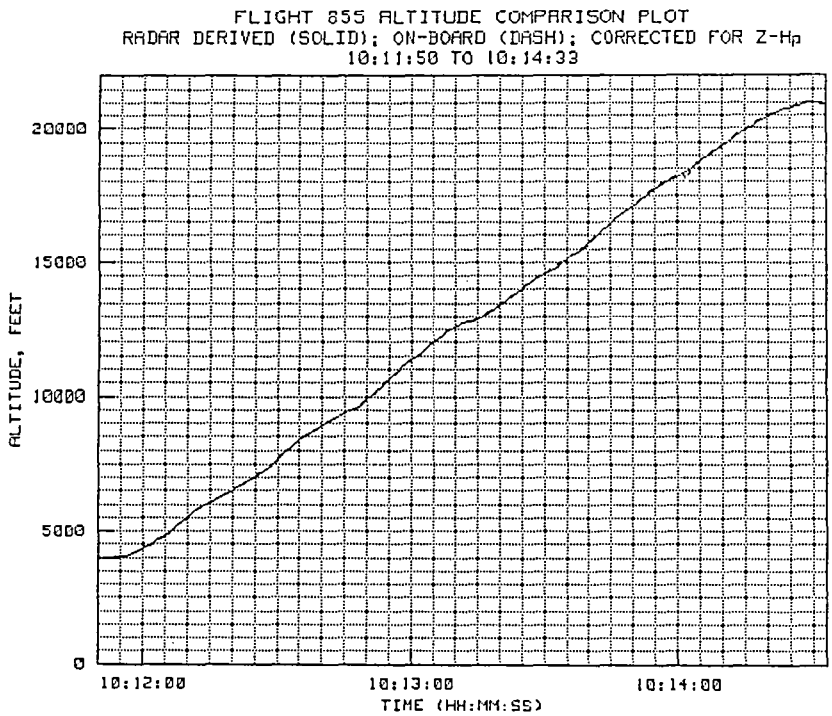

Figure 5-11(a). TP #2 radar-derived and on-board altitude.

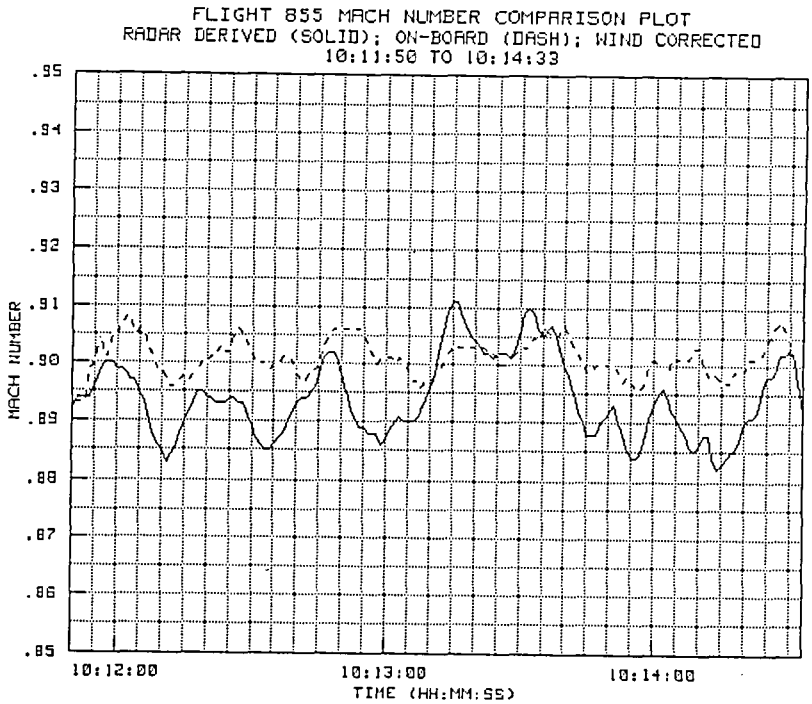

Figure 5-11(b). TP #2 radar-derived and on-board Mach number.

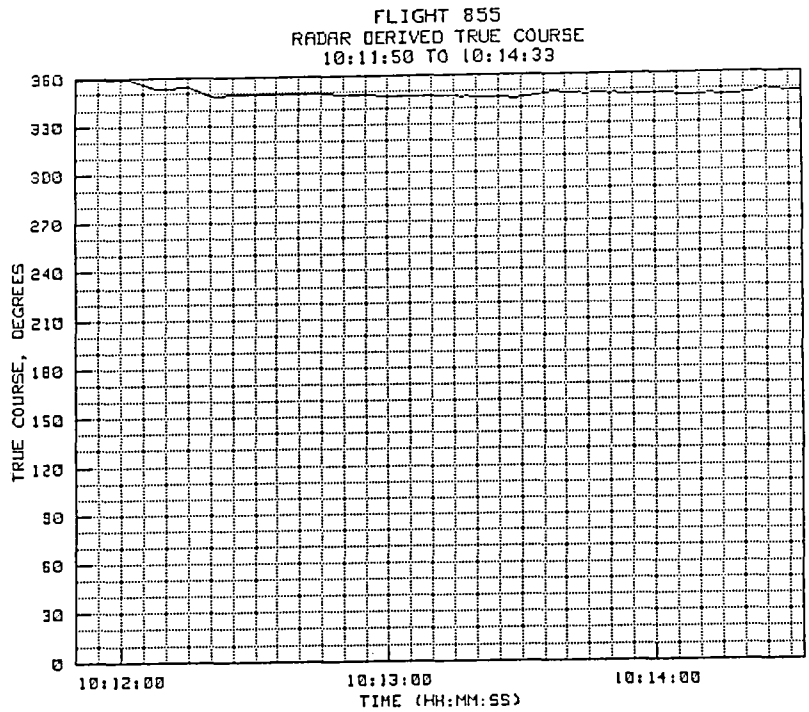

Figure 5-11(c). TP #2 radar-derived true course.

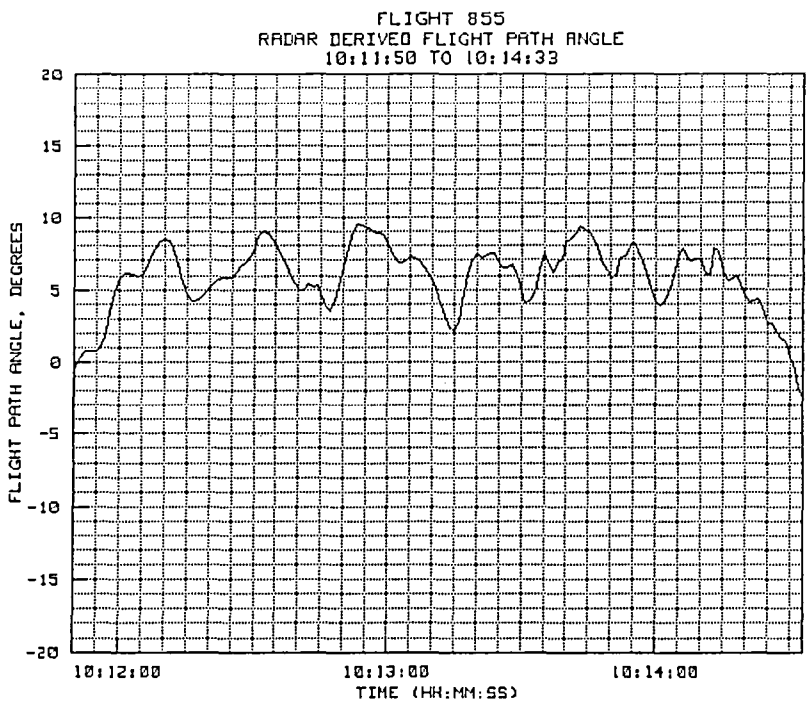

Figure 5-11(d). TP #2 radar-derived flight path angle.

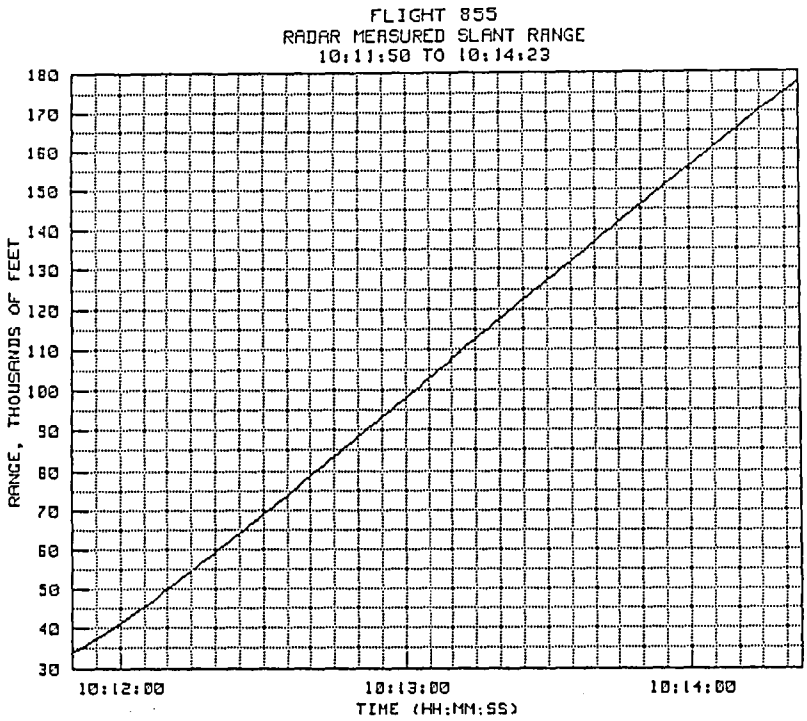

Figure 5-11(e). TP #2 radar-derived slant range.

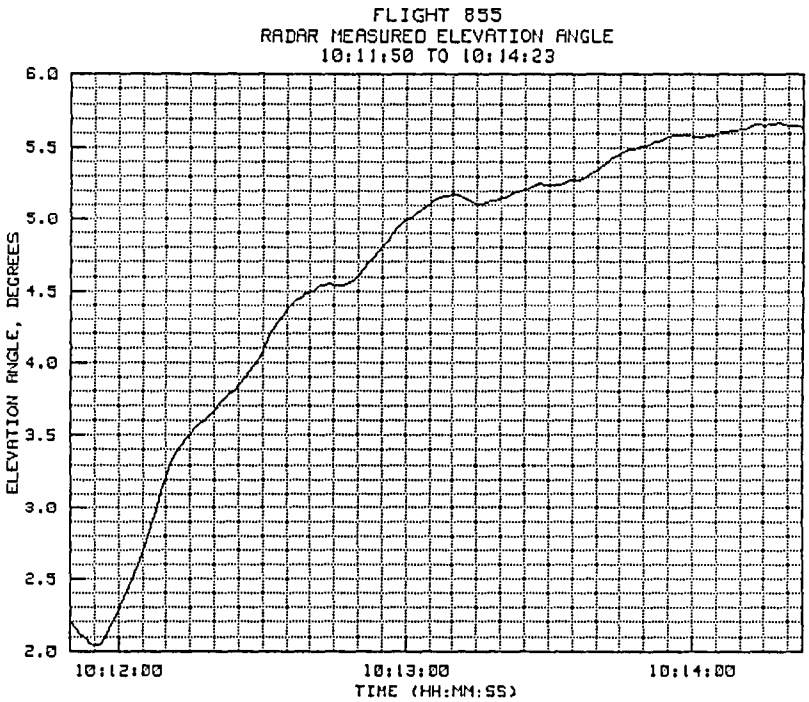

Figure 5-11(f). TP #2 radar-derived elevation angle.

5.2.3 Test Point #3

The time history plots for test point #3 are shown in figures 5-12(a) to 5-12(f). This test point was a left 360 degree turn (with a turn rate of about 4.5 degrees per second) used to test the effect of beacon shielding. The turn was made at slant ranges from about 255,000 feet (42 n.mi.) to about 268,000 feet (44.1 n.mi.). The elevation angle ranged from a high of about 3.13 degrees to a low of about 2.71 degrees. The radar held a solid lock throughout all of the maneuver; however, as shown in figure 5-12(a), the radar data placed the target altitude two to three hundred feet below the Z-Hp corrected pressure altitude. This is consistent with the long range, low elevation angle findings on both of the previous air data calibration flights.

Figure 5-12(b) provides a comparison between the on-board Mach number and the wind-corrected, radar-derived Mach number for the same maneuver. The radar-derived Mach number shows the same general patterns as does the data recorded on-board. However, more noise appears to be present in the radar-derived data, and this is as expected since at ranges of about 260,000 feet (42.77 n.mi.), the LSB granularity of the angle data encoders is equivalent to 12.5 feet of altitude, and the 12.5 foot jumps in the position data seep through the filter into the derived velocity calculations. Again, bias errors of up to 0.015 Mach are present.

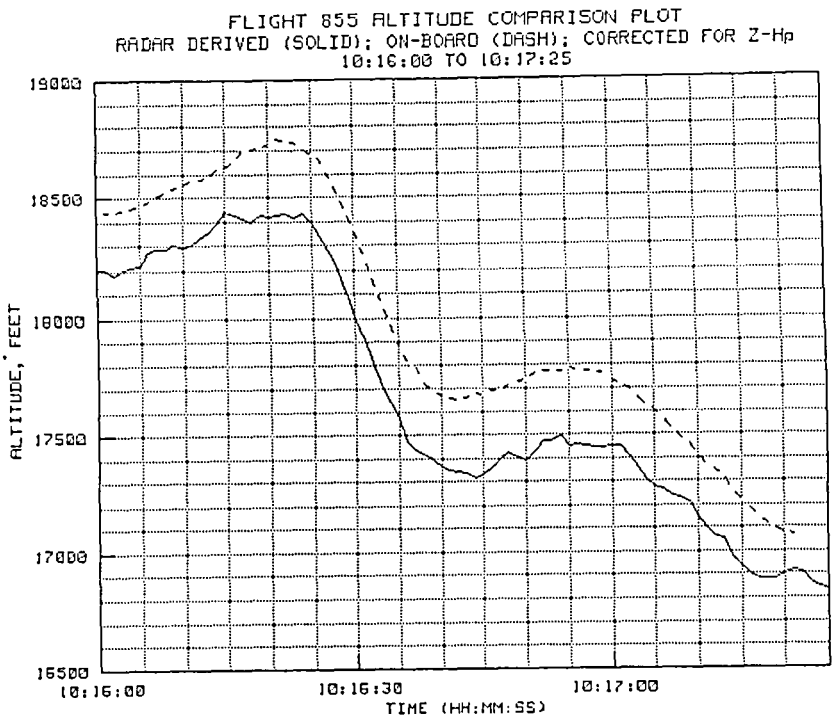

Figure 5-12(a). TP #3 radar-derived and on-board altitude.

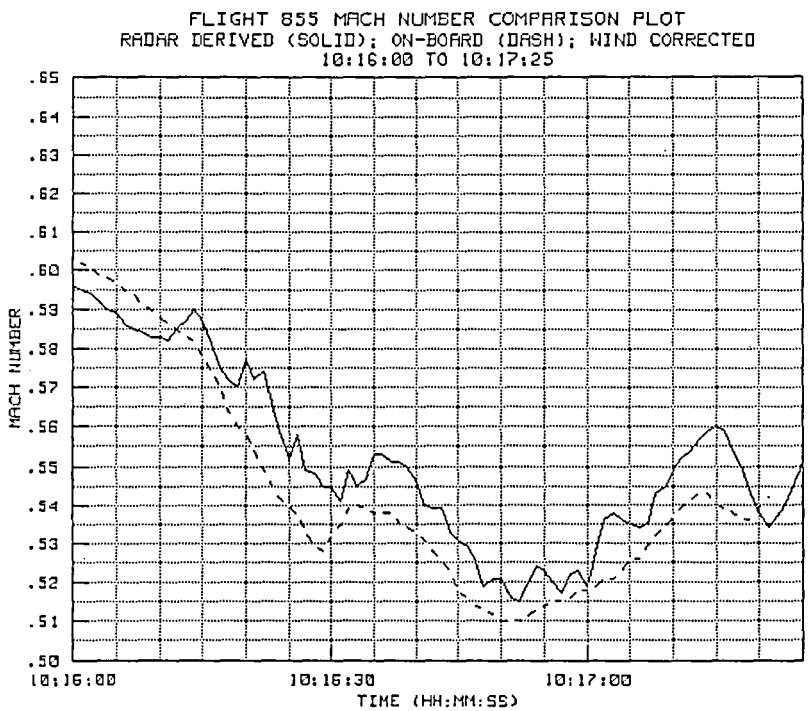

Figure 5-12(b). TP #3 radar-derived and on-board Mach number.

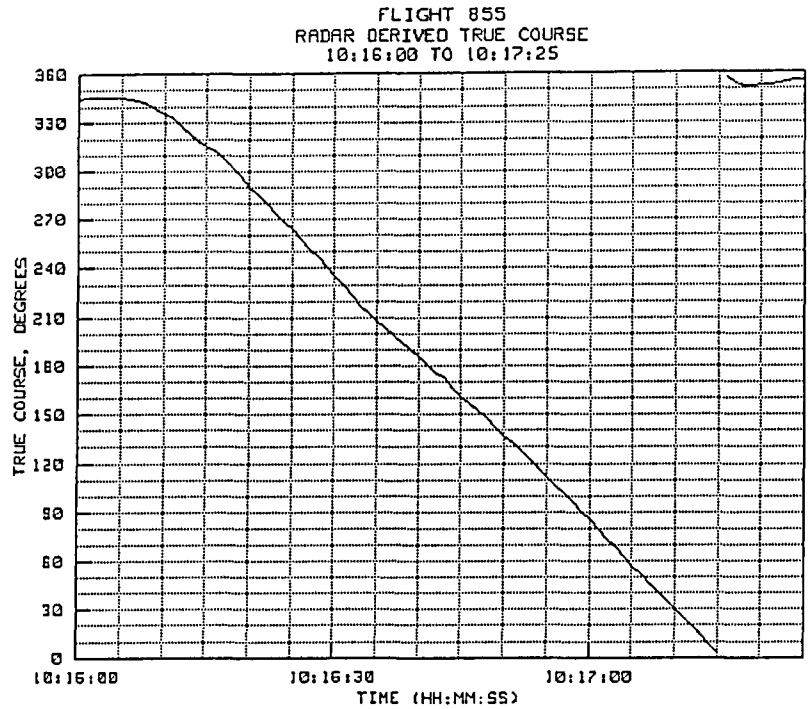

Figure 5-12(c). TP #3 radar-derived true course.

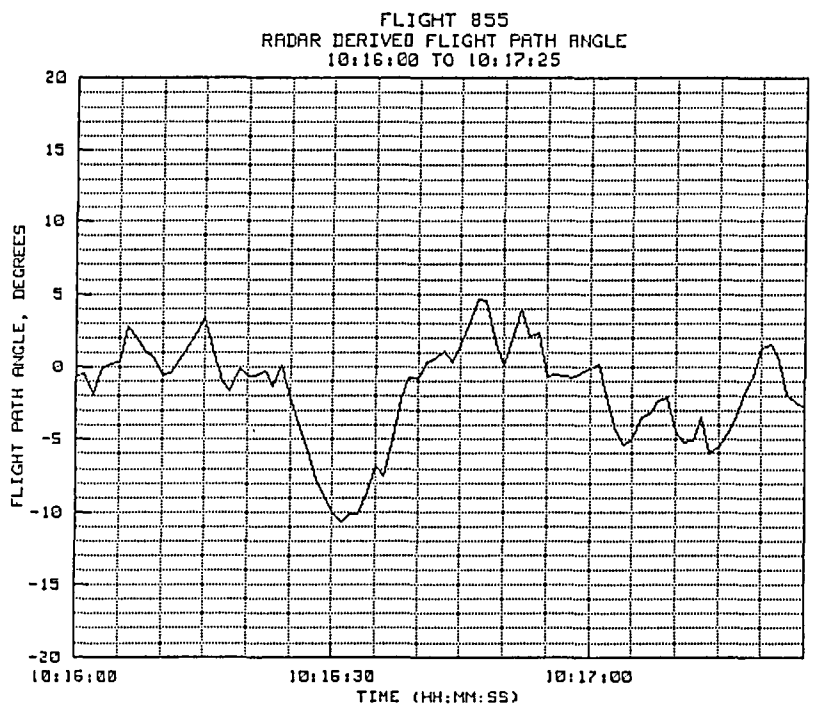

Figure 5-12(d). TP #3 radar-derived flight path angle.

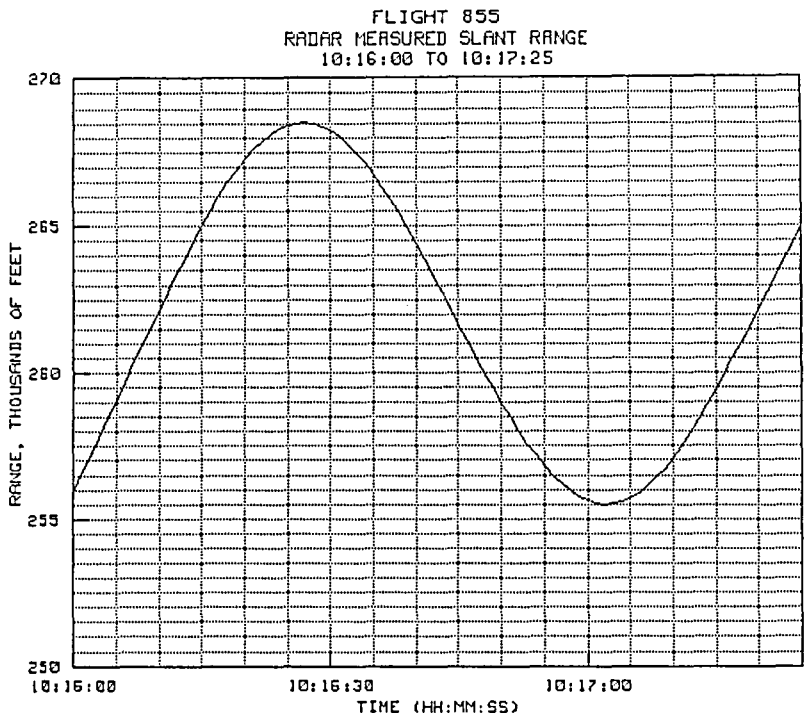

Figure 5-12(e). TP #3 radar-derived slant range.

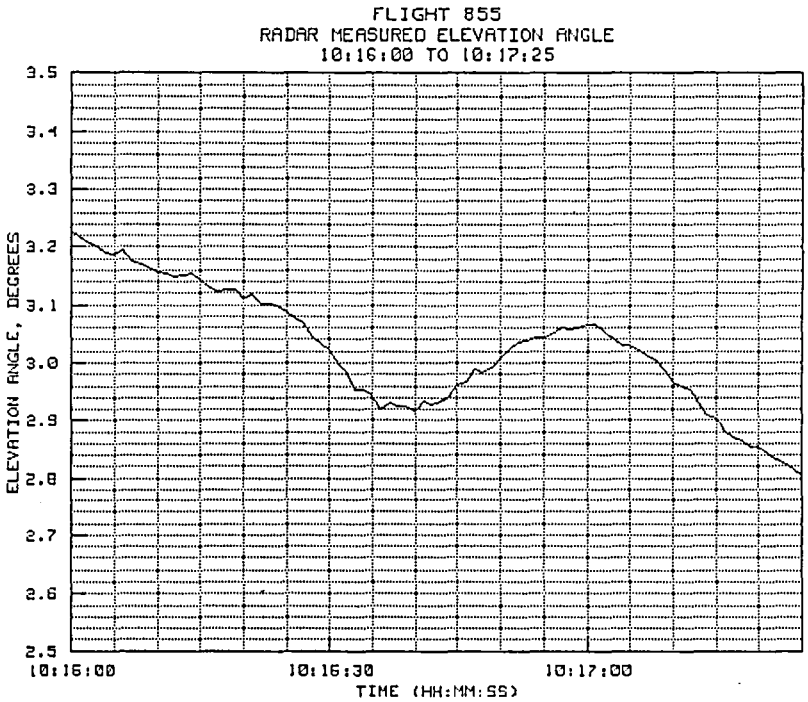

Figure 5-12(f). TP #3 radar-derived elevation angle.

5.2.4 Test Point #4

Time history plots for test point #4 are provided in figures 5-13(a) to 5-13(f). Test point #4 was one of the more important test points performed on flight 855. It was a constant 0.75 Mach survey run at an altitude of 18,350 feet, followed by a turn which is also included in the plots. The run was flown on a southerly heading which yielded a true course of about 166 degrees at the start and 170 degrees at the end of the leg, followed by a rapid 90 degree level right turn started at 10:29:04. The run was started to the north of the radar, at a slant range of 268,382 feet (about 44.1 n.mi.) and at an elevation angle of 2.95 degrees. The near point for the leg occurred at about 10:26:17 when the slant range reduced to 24,410 feet (4.02 n.mi) and the elevation angle increased to 39.88 degrees. The leg continued southward until about 10:29:05 when the right turn was initiated. True course after the turn was about 261 degrees or approximately 90 degrees to the right of the heading held on the survey portion of the leg. The slant range at the turning point was 142,541 feet (23.46 n.mi.) and the elevation angle was 6.07 degrees. Again, the correlation between the on-board altitude and the radar-derived altitude is good, with the exception that the radar-derived altitude developed a bias as the range became greater and the elevation angle became lower. And, again, the radar-computed altitude was low by about the same amount as could be expected from the data from the previous survey runs. In this case, when two points equidistant from the near point (one to the north and one to the south) were picked for a slant range of about 134,500 feet, the difference appeared to be the same, about 45 feet. This would indicate a negligible amount of Z-Hp gradient along the direction of flight, at least as determined by the radar data. At the maximum range and lowest elevation angle, at time 10:20:50, the difference between the two values was about 120 feet. At the near point, the difference in the two values was very close to zero.

The time-history Mach number plot for the same time interval shows the same good correlation between the on-board and radar-derived data, except for differences probably due to wind variability. The radar derived true course indicates that the pilot did an excellent job of holding heading on this run. Just after 10:26:10, a minor course change was observed, after which, at 10:27:25 the course returned to the previous value. Since the greatest bias difference in the Mach number plot appeared over this same segment, it is probable that a slight horizontal wind shear may have occurred at this point in the leg.

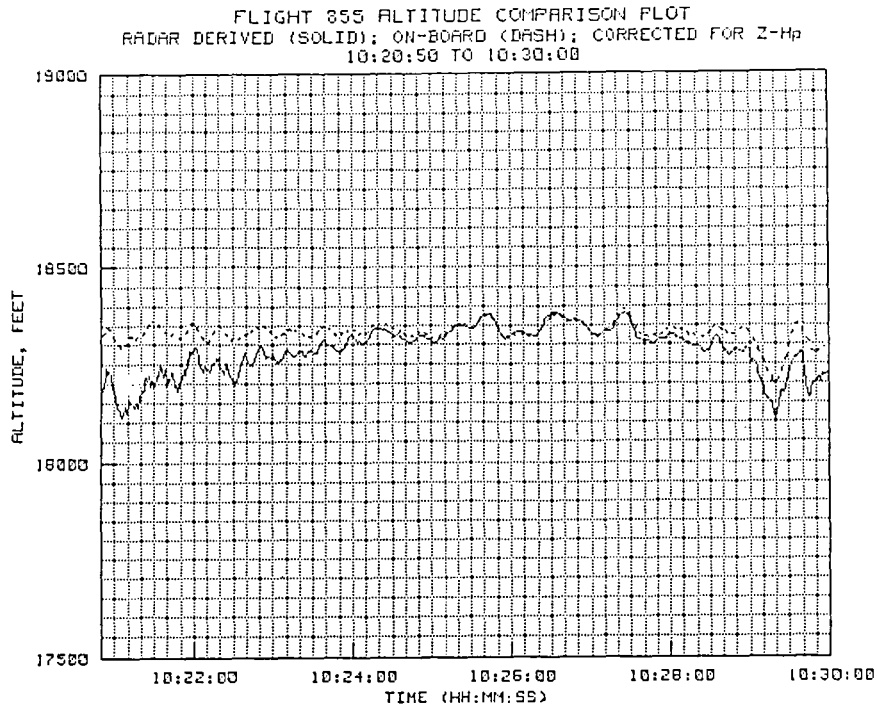

Figure 5-13(a). TP #4 radar-derived and on-board altitude.

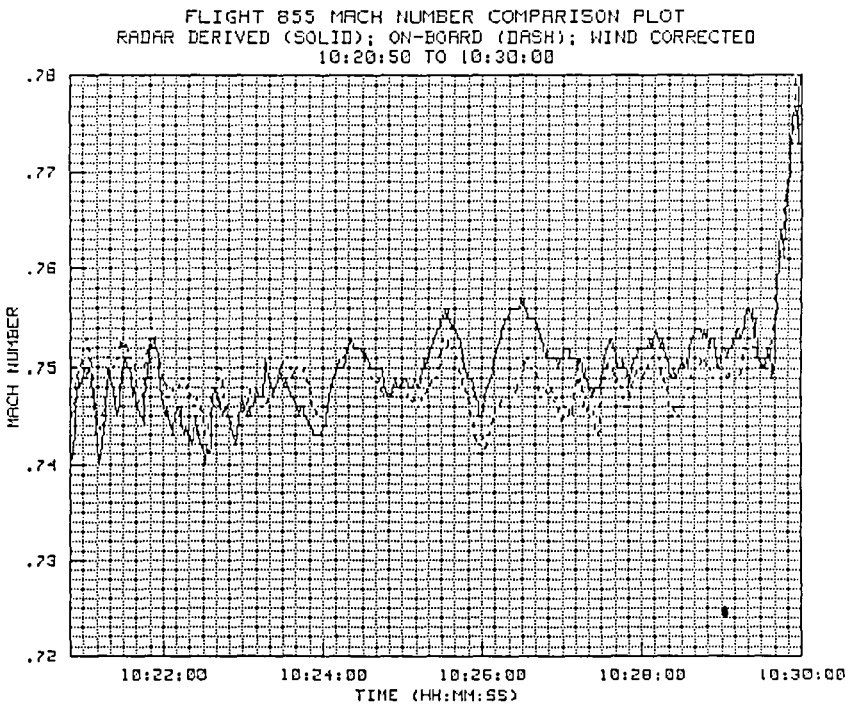

Figure 5-13(b). TP #4 radar-derived and on-board Mach number.

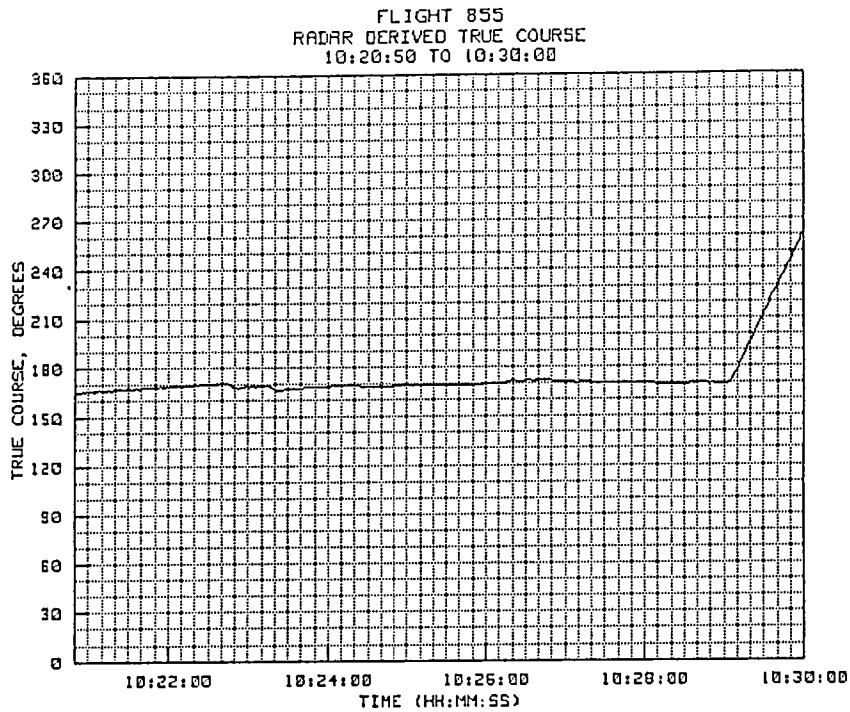

Figure 5-13(c). TP #4 radar-derived true course.

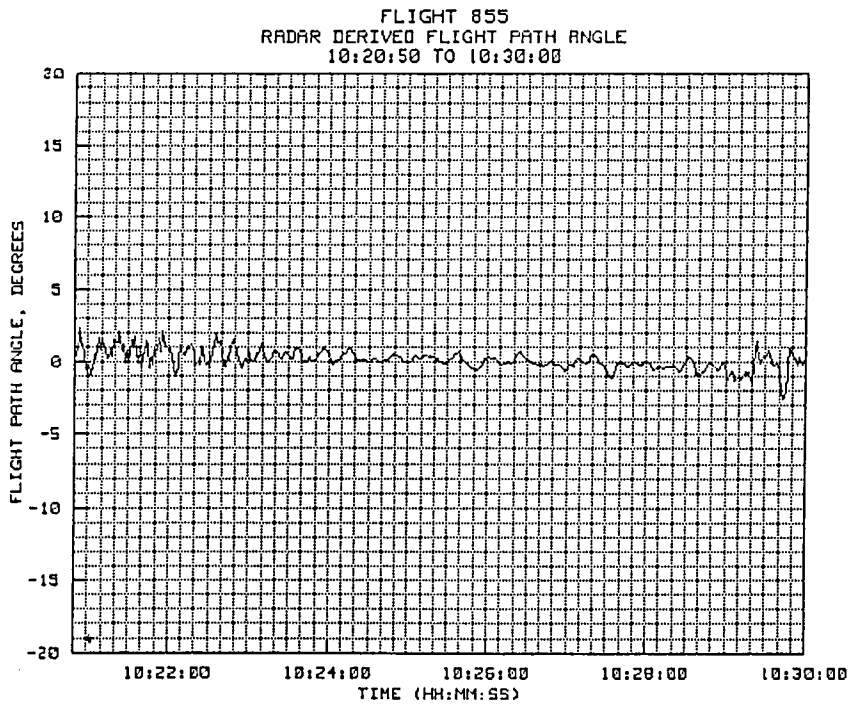

Figure 5-13(d). TP #4 radar-derived flight path angle.

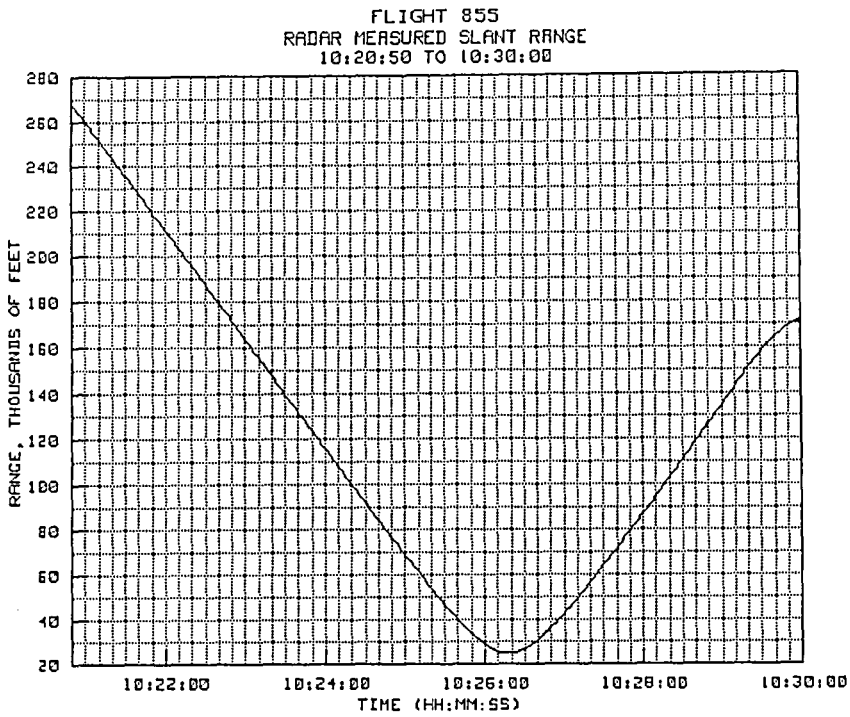

Figure 5-13(e). TP #4 radar-derived slant range.

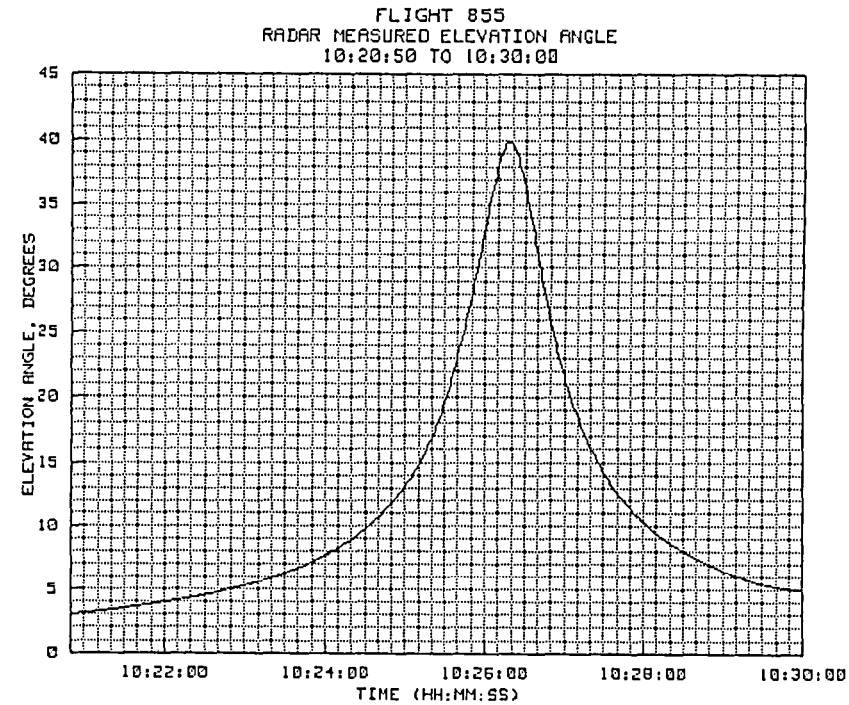

Figure 5-13(f). TP #4 radar-derived elevation angle.

5.2.5 Test Point #5

Time history plots for test point #5 are provided in figures 5-14(a) to 5-14(f). The test point maneuver was a right 360-degree roll, performed to evaluate the ability of the radar to remain on target, in the beacon mode, during maneuvering flight. During the time of the maneuver, the target slant range went from 127,201 feet (20.93 n.mi.) to 152,630 feet (25.12 n.mi.). The elevation angle ranged between about 5 and 7 degrees. As noted in the altiude plot, the pilot pulled the nose of the aircraft up as he started the roll maneuver (about 10:33:50). This caused the aircraft to climb. From the fully inverted point on, the nose fell through, and altitude was lost until achieving a level flight condition again at about 10:34:40.

The radar held lock throughout this maneuver, except that some slight antenna azimuth and elevation biases were apparently present between 10:34:00 and 10:34:40. This behavior is typical of glint error that results from beacon shielding, reflection, or cross polarization effects. From the data plots, it would appear that altitude errors due to these biases were not significant. However, errors in the Mach number calculations (Fig. 5-14(b)), which are much more susceptible to antenna movements, do appear to be large. Also note that the azimuth and elevation noise plots (Figs. 5-27 and 5-28) also show some small noise spikes during this same period.

Numerous observations of spin tests have shown that beacon tracking, during this type of maneuver, is very difficult. Under normal circumstances, if the radar operator knows that the target is about to engage in a radical maneuver, he will select the echo or skin track mode. Although glint effects are present in either mode, they are usually substantially less in a skin track. In short, if the beacon interrogation or return signals are blocked, either by the aircraft structure or by another aircraft between the tracked target and the radar, the beacon track can be expected to be poor and the radar lock-on can easily be lost. Similar effects will occur during maneuvering flight from cross polarization effects or signal blockage, or when reflections from the chase aircraft cause momentary jitter in the radar error signals used to drive the antenna.

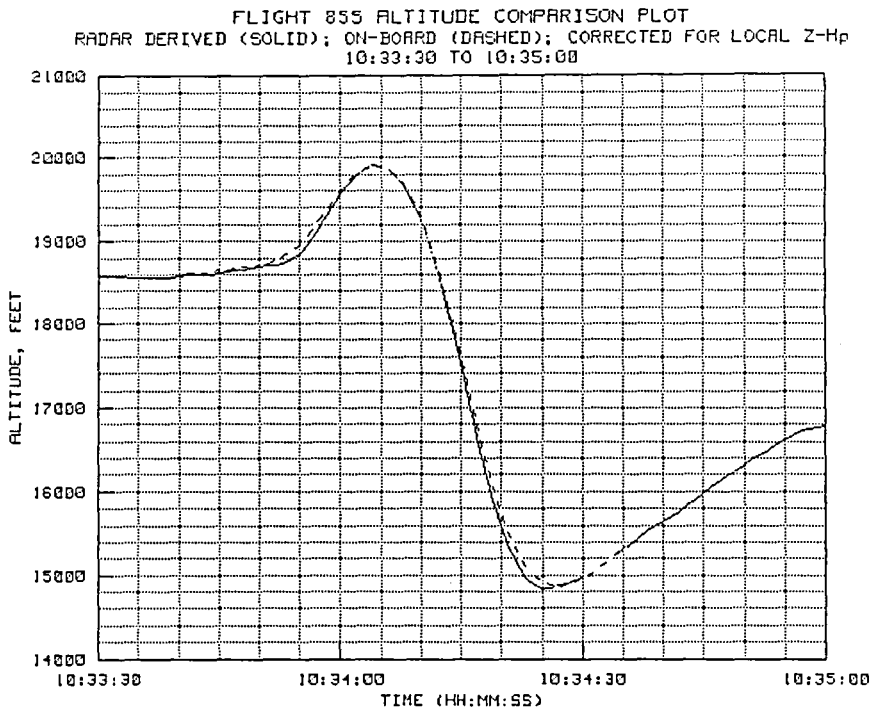

Figure 5-14(a). TP #5 radar-derived and on-board altitude.

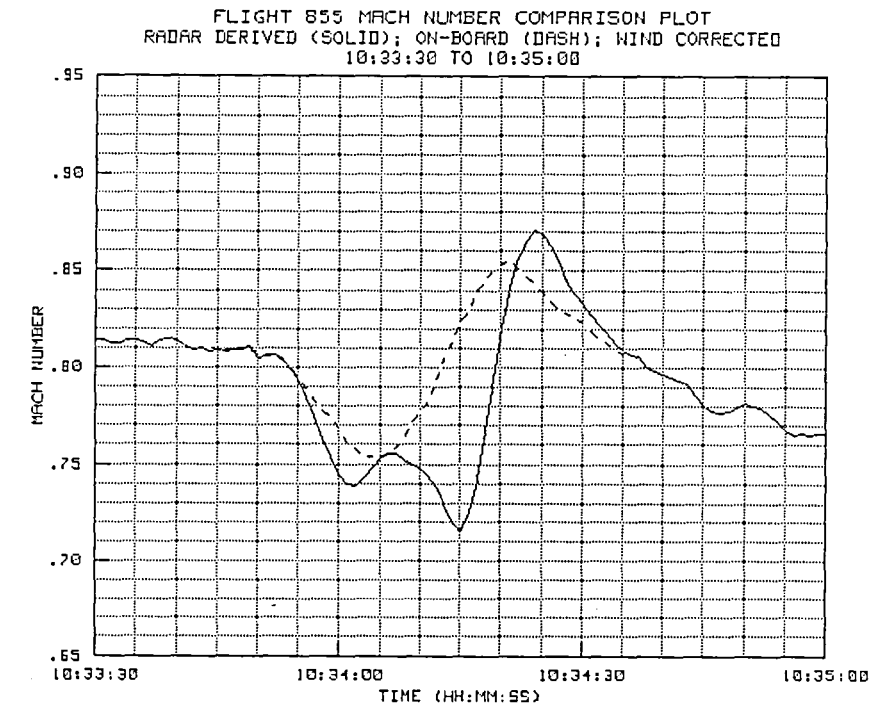

Figure 5-14(b). TP #5 radar-derived and on-board Mach number.

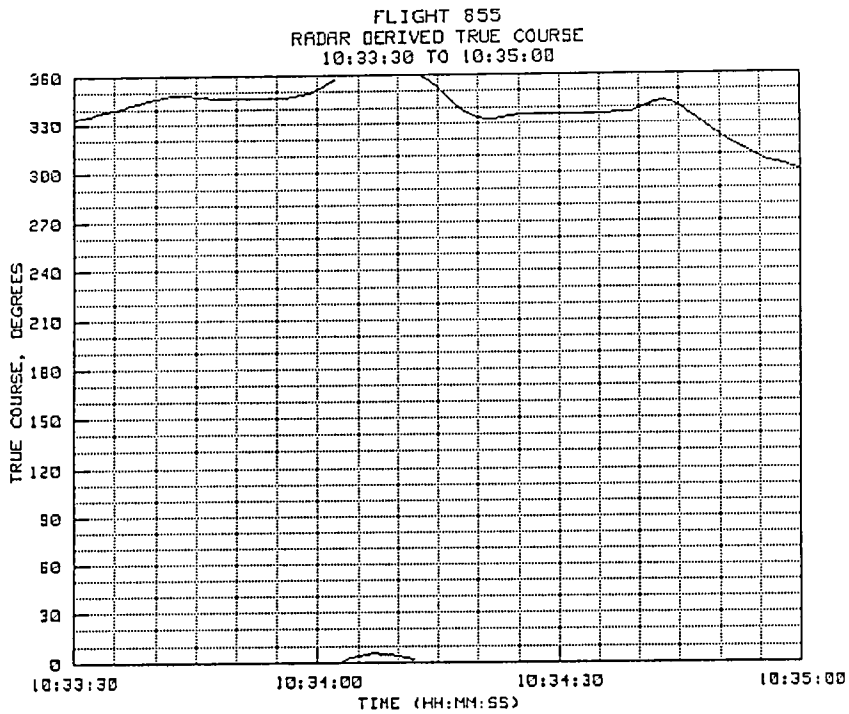

Figure 5-14(c). TP #5 radar-derived true course.

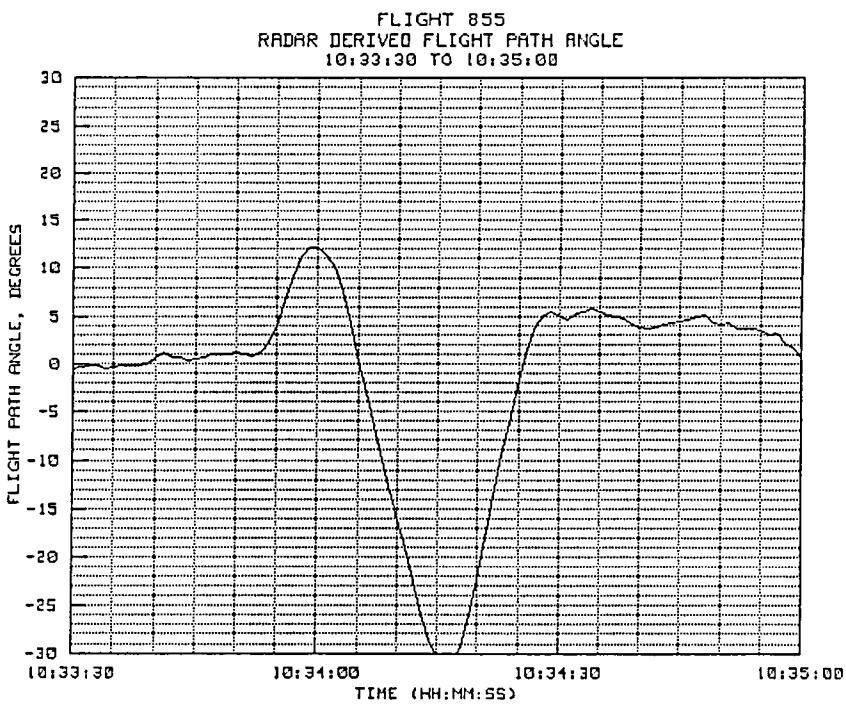

Figure 5-14(d). TP #5 radar-derived flight path angle.

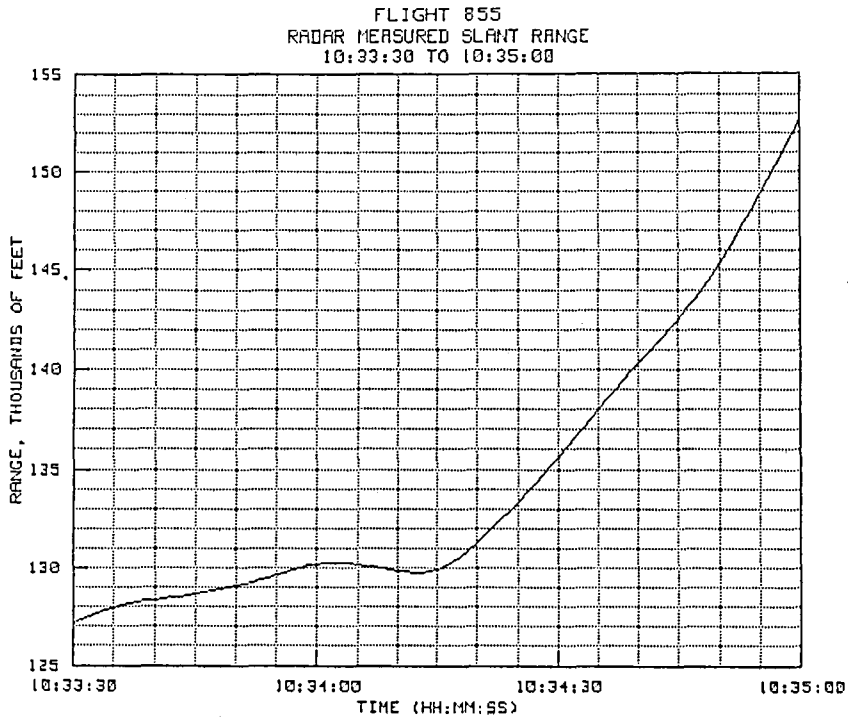

Figure 5-14(e). TP #5 radar-derived slant range.

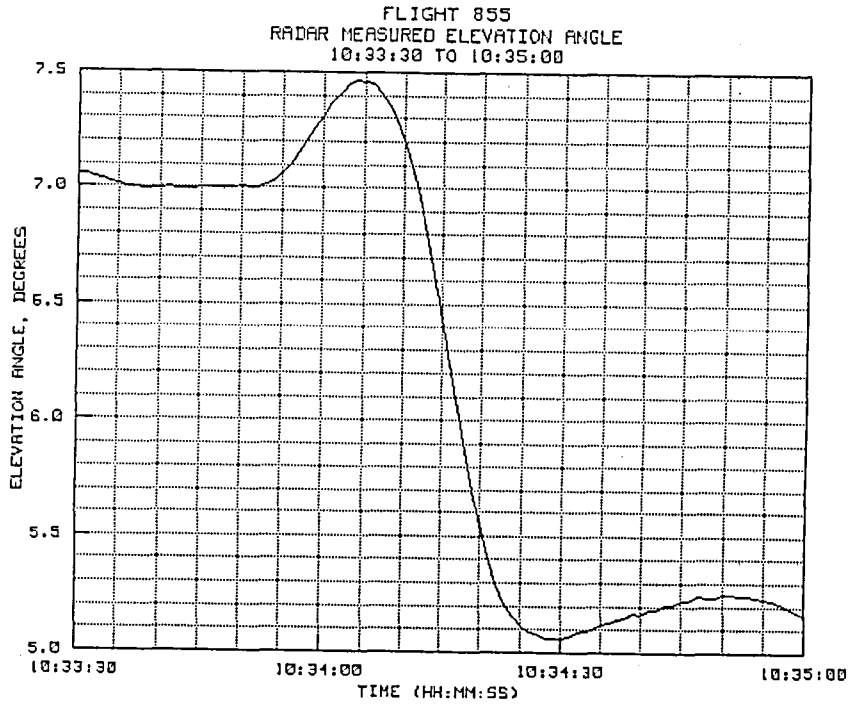

Figure 5-14(f). TP #5 radar-derived elevation angle.

5.2.6 Test Point #6

Time history plots for test point #6 are shown in figures 5-15(a) to 5-15(f). The test point consisted of a left turn with a roll-out on an easterly heading. This was followed by a left roll commenced at about 10:37:00. Slant range for the period covered in the plot is from 182,045 feet (29.96 n.mi.) to 108,264 feet (17.82 n.mi.). During the maneuver, the antenna elevation went from 4.48 degress to 7.49 degrees. No tracking problems were encountered during the turning portion of the maneuver, during which both radar altitude and radar Mach number agreed closely with the on-board data. However; as the pilot pulled up the nose and started the left roll, large azimuth and elevation jumps occurred, eventually causing the radar to go completely off target. As a result, Mach data from about 10:37:10 to the end of the plot was invalid. Altitude data showed large jumps but remained usable except for the short off target period.

Again, there is little need to comment on the results of this test. Beacon tracks require a good signal path between the interrogating radar and the beacon antenna. If anything interrupts this path, or if cross polarization effects are encountered, the track will be erratic, or even lost.

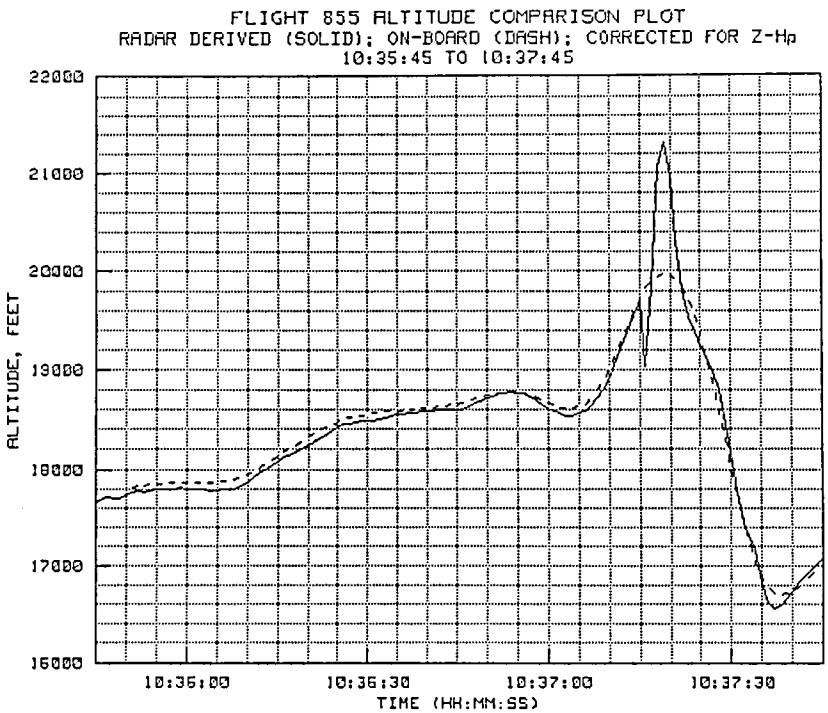

Figure 5-15(a). TP #6 radar-derived and on-board altitude.

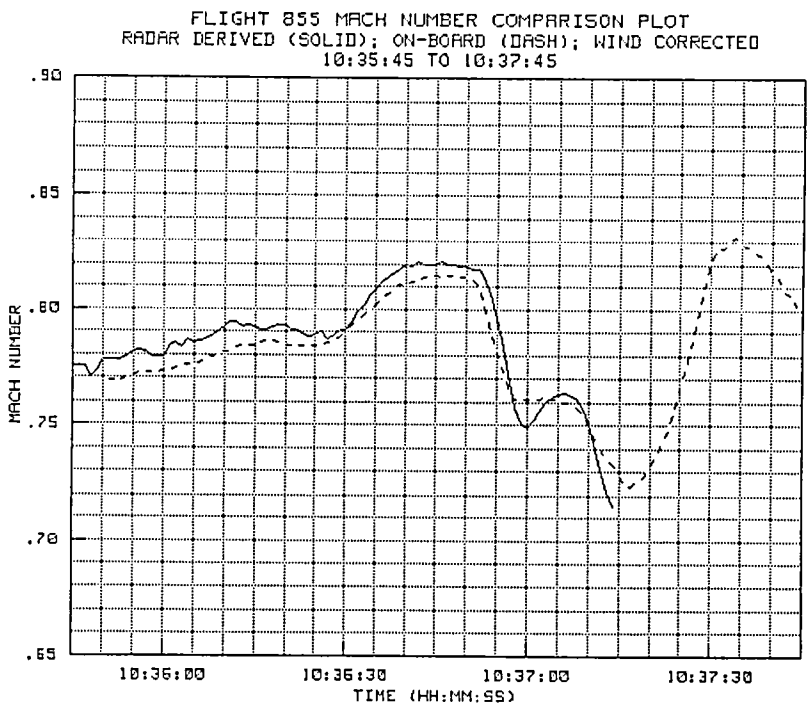

Figure 5-15(b). TP #6 radar-derived and on-board Mach number.

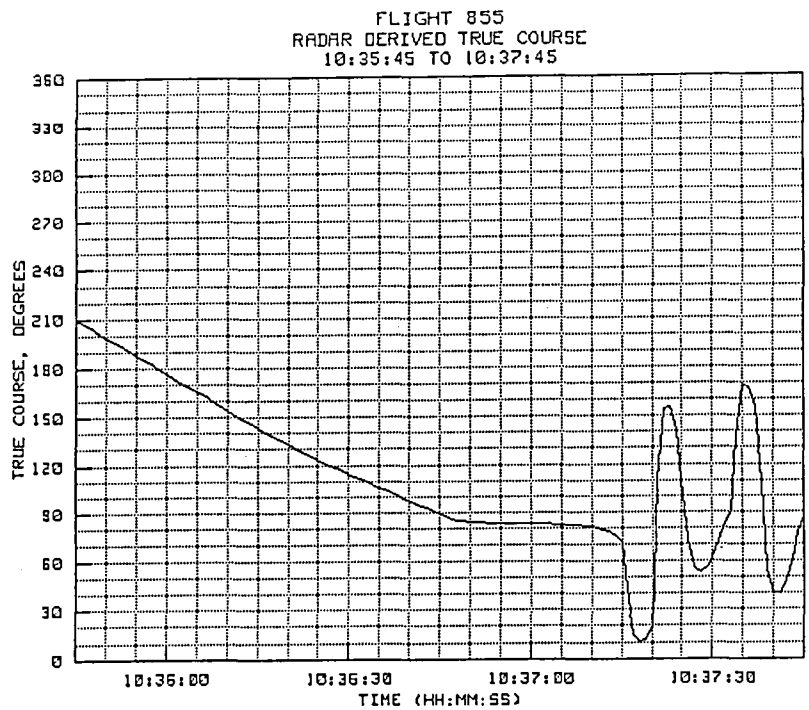

Figure 5-15(c). TP #6 radar-derived true course.

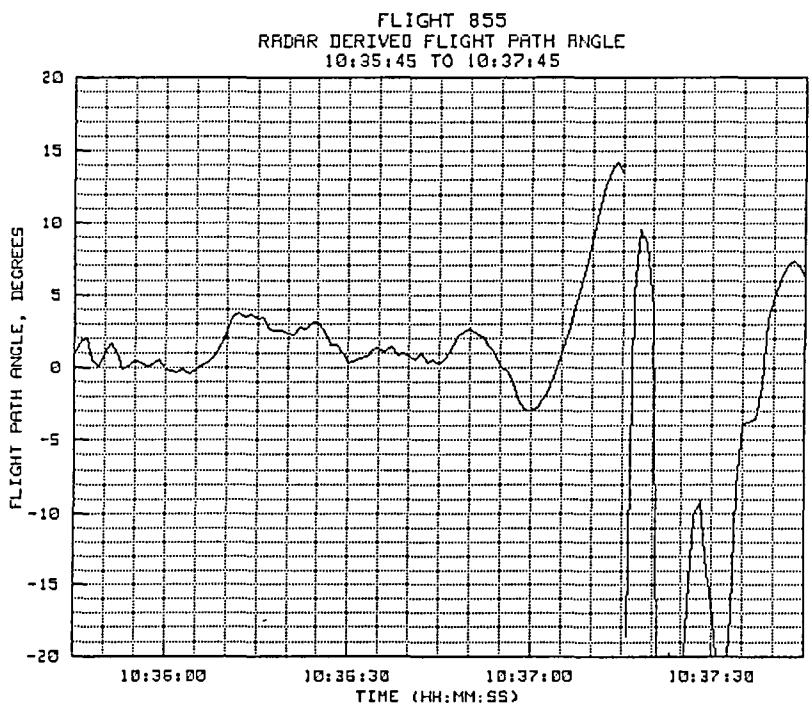

Figure 5-15(d). TP #6 radar-derived flight path angle.

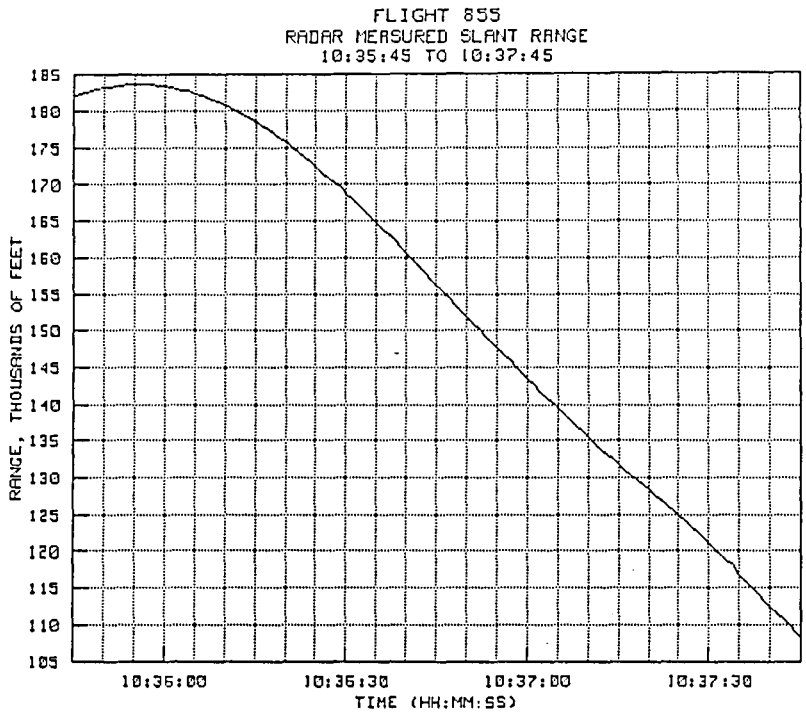

Figure 5-15(e). TP #6 radar-derived slant range.

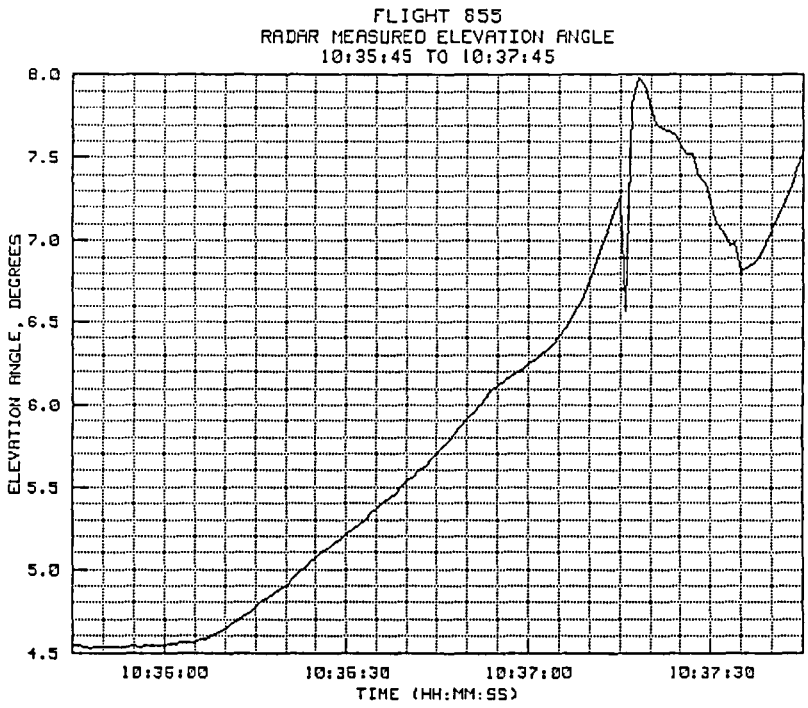

Figure 5-15(f). TP #6 radar-derived elevation angle.

5.2.7 Test Point #7

Time history plots for test point #7 are provided in figures 5-16(a) to 5-16(f). The test point consisted of a cross survey leg flown on an easterly heading, passing the radar at about 10:39:57. At the start of the run the aircraft was 62,490 feet (10.28 n.mi.) to the west; at the end of the run the aircraft was 172,921 feet (28.46 n.mi.) to the east. The run was flown at an altitude of 18,300 feet. The starting elevation angle was 14.44 degrees, the ending angle was 5.05 degrees, and the near pont elevation angle was 43.30 degrees as the aircraft passed about 2.7 miles north of the radar. At the near point, the on-board and radar-derived altitudes agree to within a few feet. However, as the aircraft moved to the east of the radar, the same type of elevation bias as noted on previous survey runs developed. At 10:43:20, just before the pilot started another maneuver, the slant range was 165,046 feet (27.2 n.mi.) and the elevation was 5.21 degrees. At this point, the difference between on-board and radar-derived altitude appears to be 60 feet, about the amount expected from the previous data.

The Mach number plot during this run showed the same type of behavior as seen in previous tests. Good correlation was present in the short term Mach data, but biases as large as 0.01 Mach were present when the aircraft moved to the east.

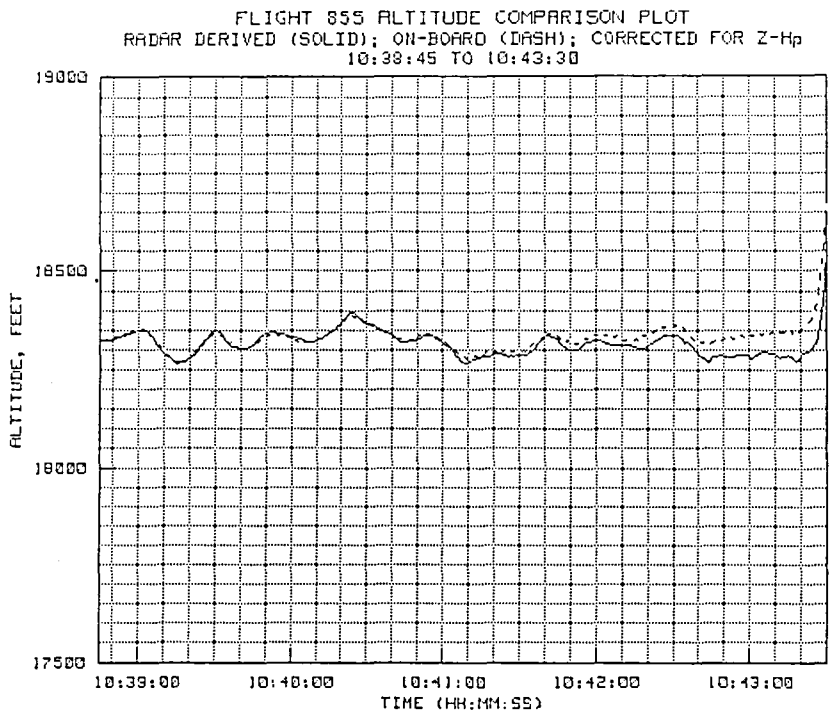

Figure 5-16(a). TP #7 radar-derived and on-board altitude.

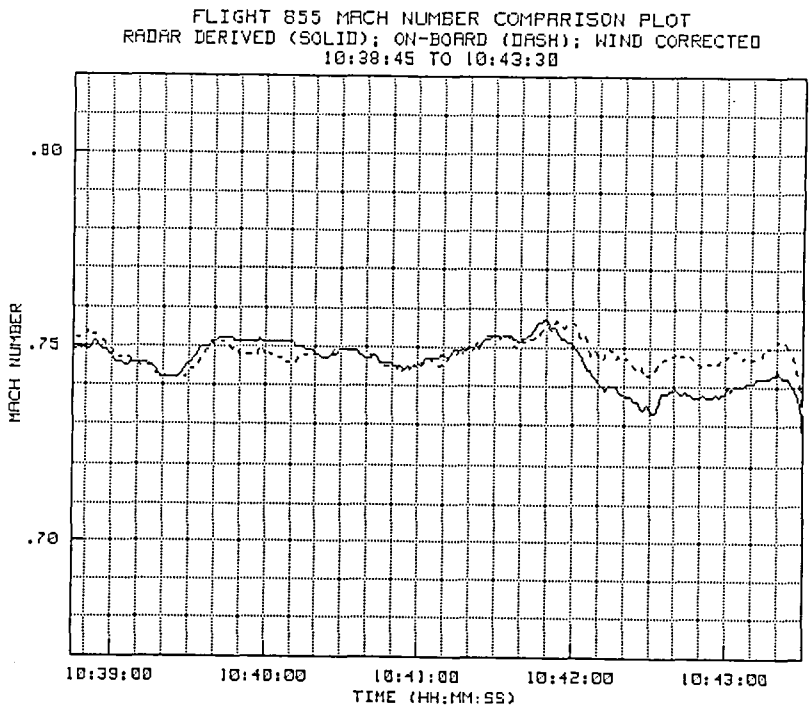

Figure 5-16(b). TP #7 radar-derived and on-board Mach number.

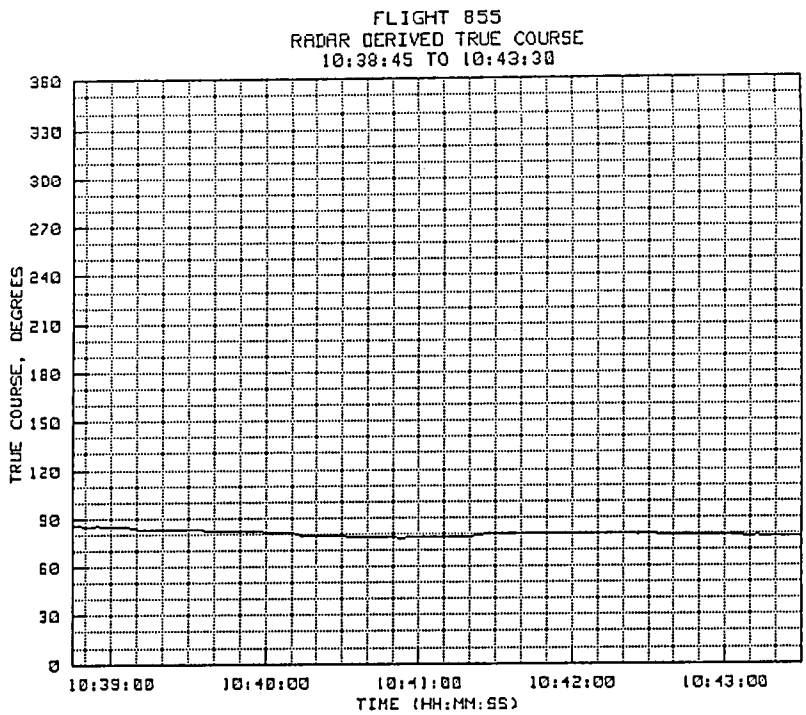

Figure 5-16(c). TP #7 radar-derived true course.

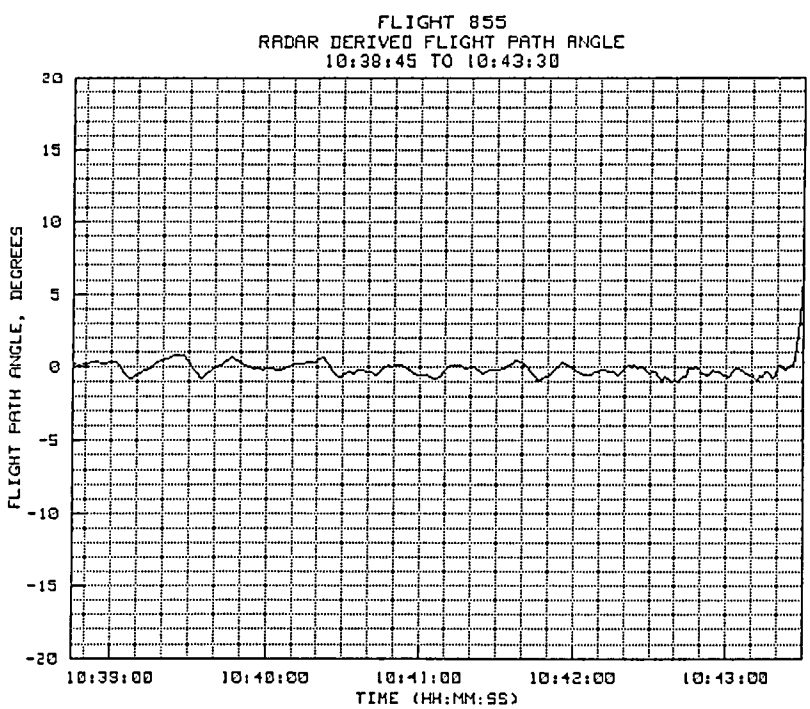

Figure 5-16(d). TP #7 radar-derived flight path angle.

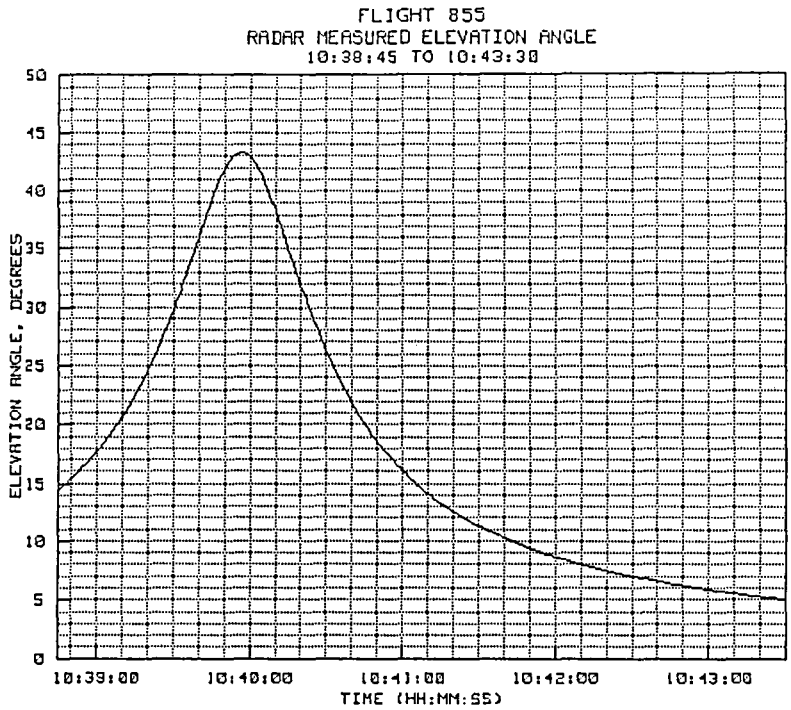

Figure 5-16(e). TP #7 radar-derived slant range.

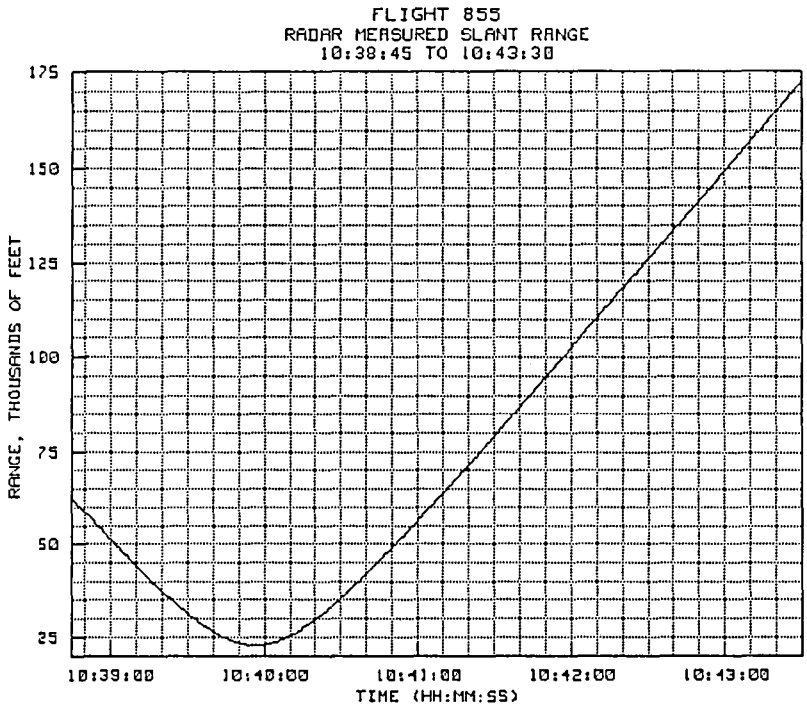

Figure 5-16(f). TP #7 radar-derived elevation angle.

5.2.8 Test Point #8

Time history plots for test point #8 are provided in figures 5-17(a) to 5-17(f). This test point consisted of another roll maneuver. As in the previous cases, position data (altitude) behaved reasonably well throughout the maneuver, but the first derivative (velocity) was highly erratic. This again demonstrates the adverse effect of maneuvering flight on calculations of Mach number made using radar data.

The maneuver was conducted between 26.5 nautical miles and 35.2 nautical miles, at an elevation angle of 5.35 degrees down to 3.54 degrees.

No unexpected information was obtained from this test point.

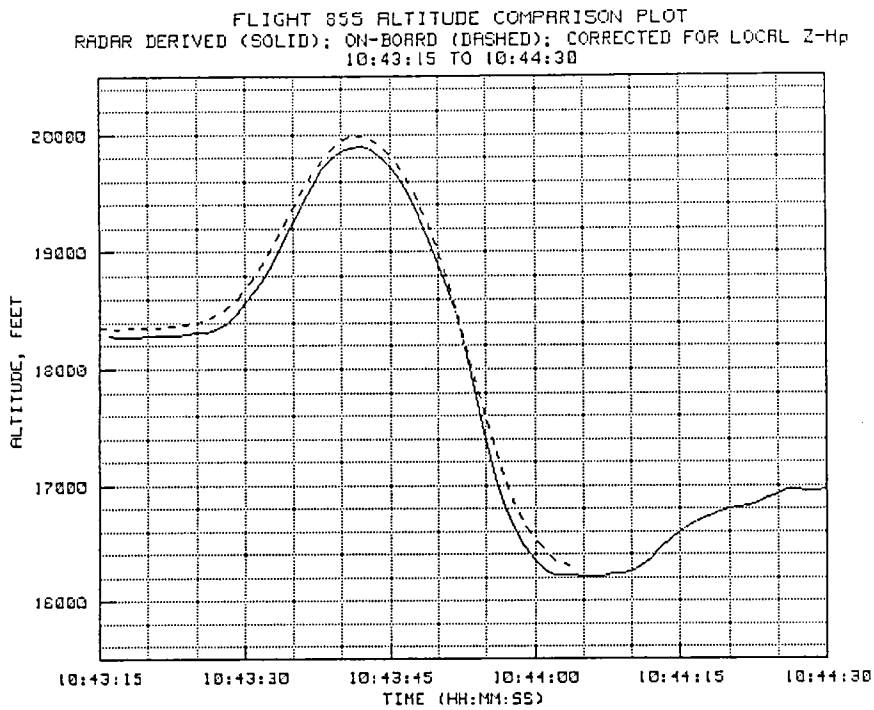

Figure 5-17(a). TP #8 radar-derived and on-board altitude.

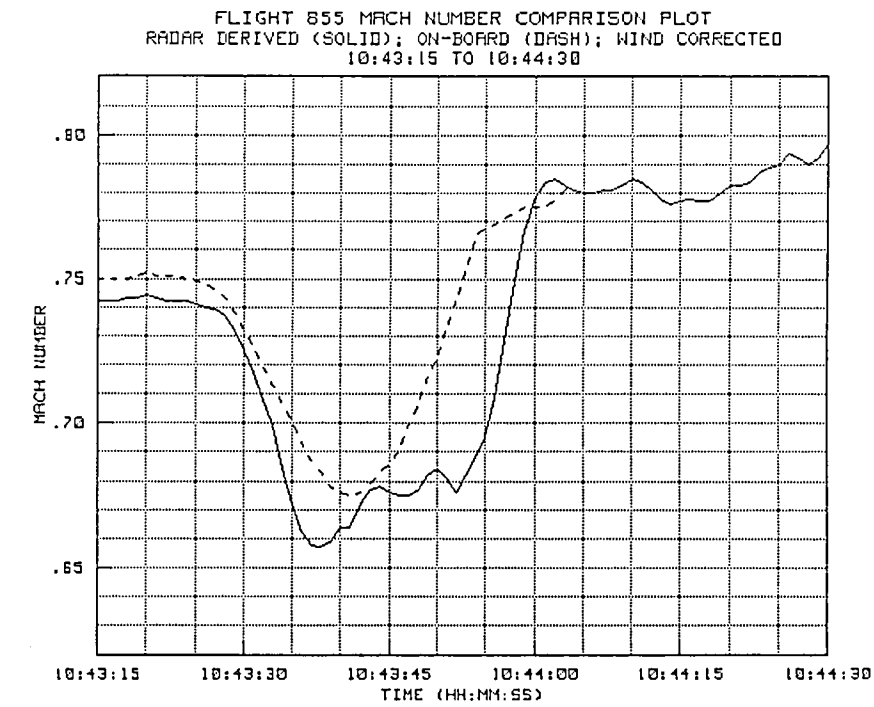

Figure 5-17(b). TP #8 radar-derived and on-board Mach number.

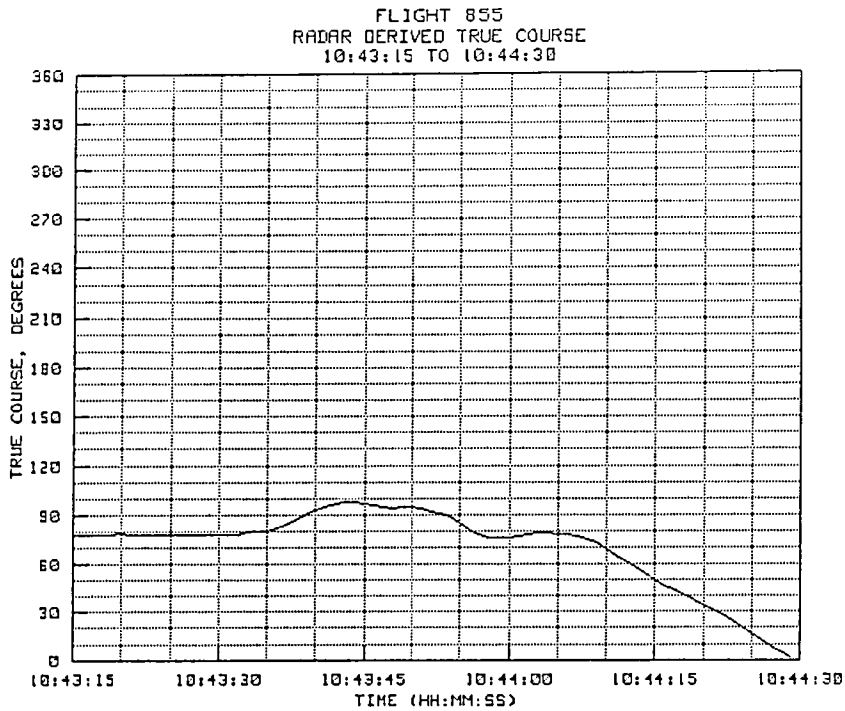

Figure 5-17(c). TP #8 radar-derived true course.

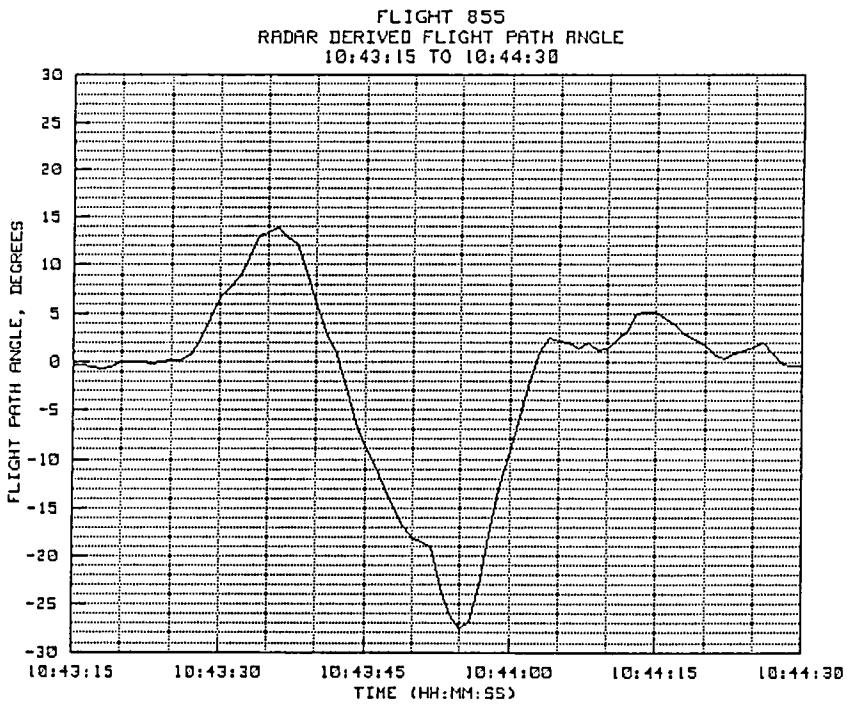

Figure 5-17(d). TP #8 radar-derived flight path angle.

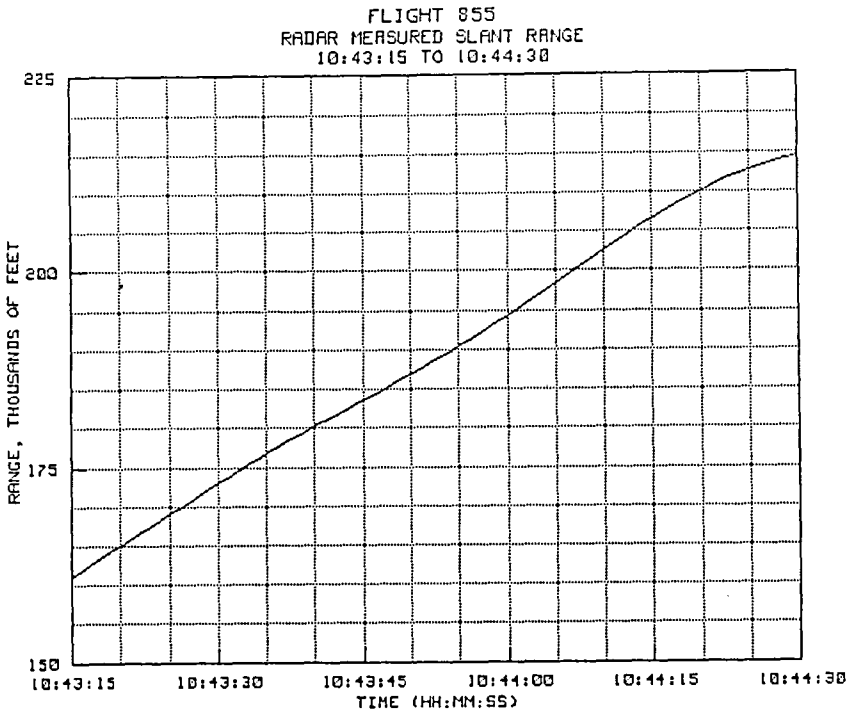

Figure 5-17(e). TP #8 radar-derived slant range.

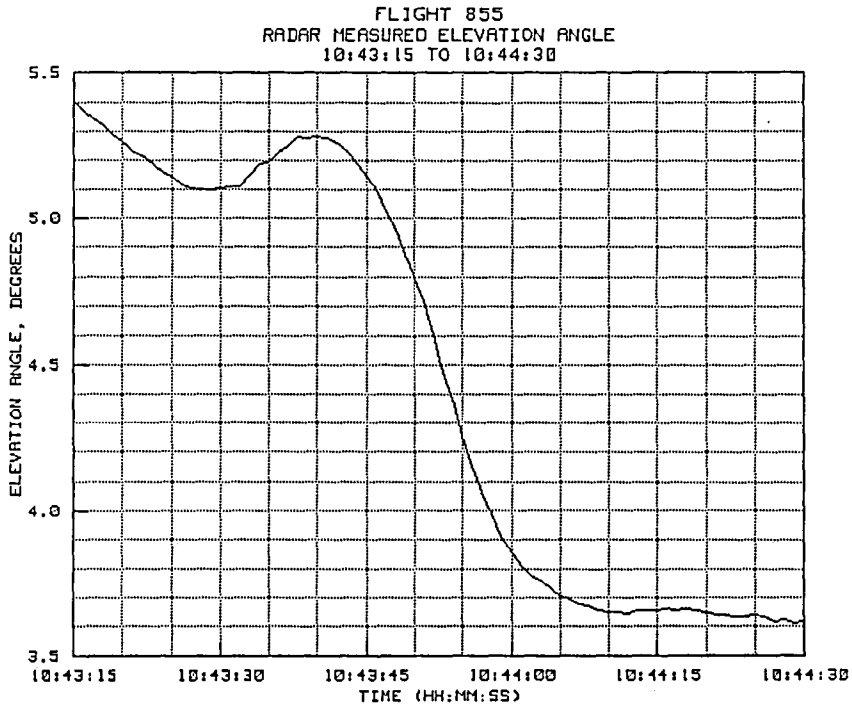

Figure 5-17(f). TP #8 radar-derived elevation angle.

5.2.9 Test Point #9

Figures 5-18(a) to 5-18(f) are time history plots for test point #9. This test point consisted of a maximum rate deceleration followed by a high-g, 90-degree right turn. The maximum rate of deceleration occurred at about 10:48:12 and can be seen clearly in the Mach number time history plot (Fig. 5-18(b)). Over a period of 8 seconds, the Mach was reduced from about 0.97 to about 0.85. A slight overshoot can be seen in the radar-derived data, probably due to a slight amount of servo lag at the lower antenna bandwidth settings normally used.

During the rest of the maneuver (the high-g turn), the radar went off target and the data was invalid from about 10:48:40 until 10:49:05. The off target condition was probably due to beacon shielding as the rapid right turn was commenced. Note that the erratic behavior in the elevation plot is typical of antenna noise response when the true signal return is lost.

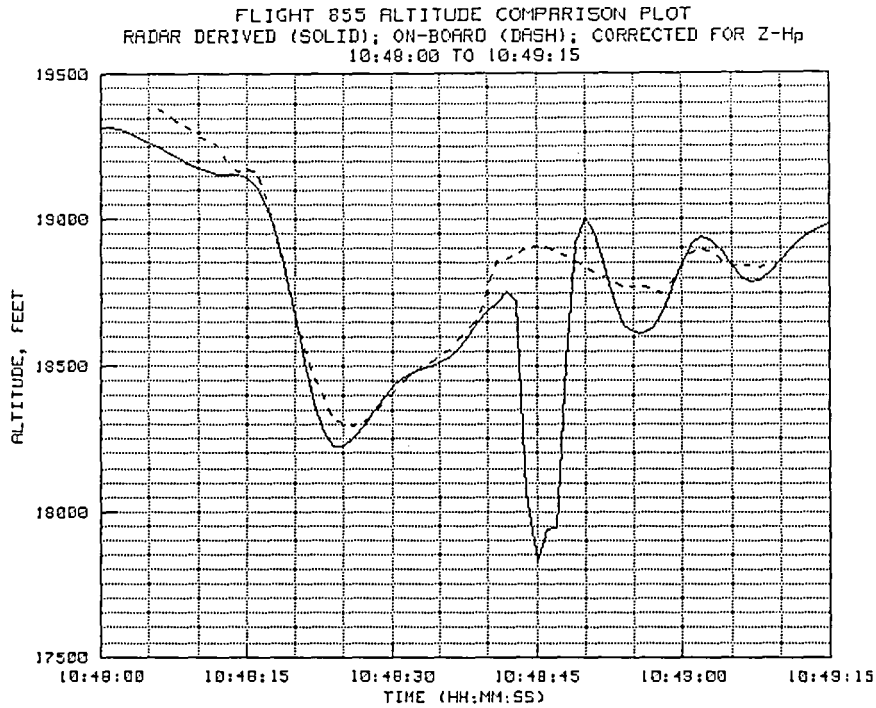

Figure 5-18(a). TP #9 radar-derived and on-board altitude.

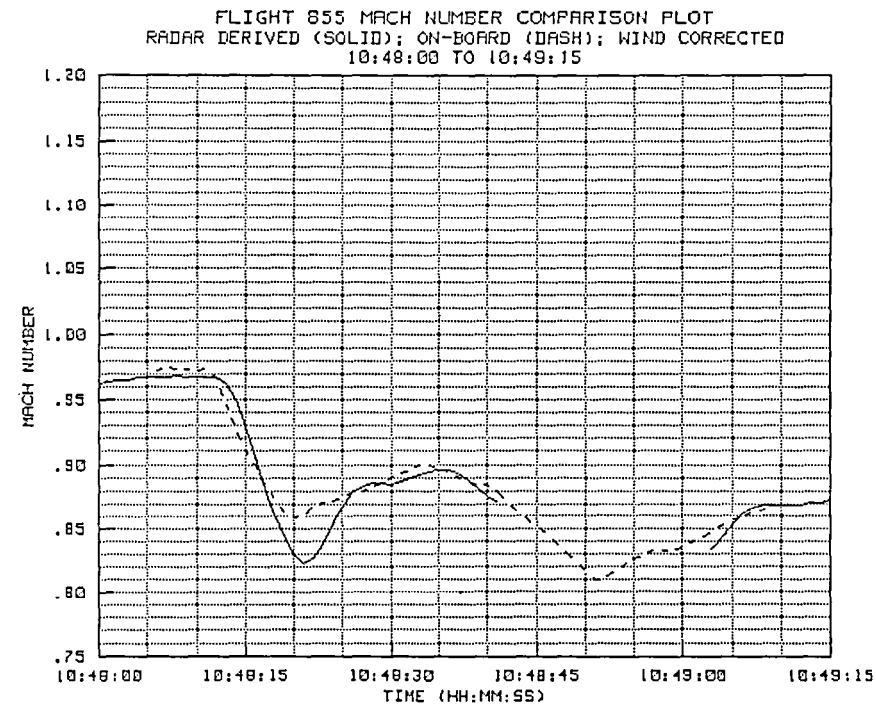

Figure 5-18(b). TP #9 radar-derived and on-board Mach number.

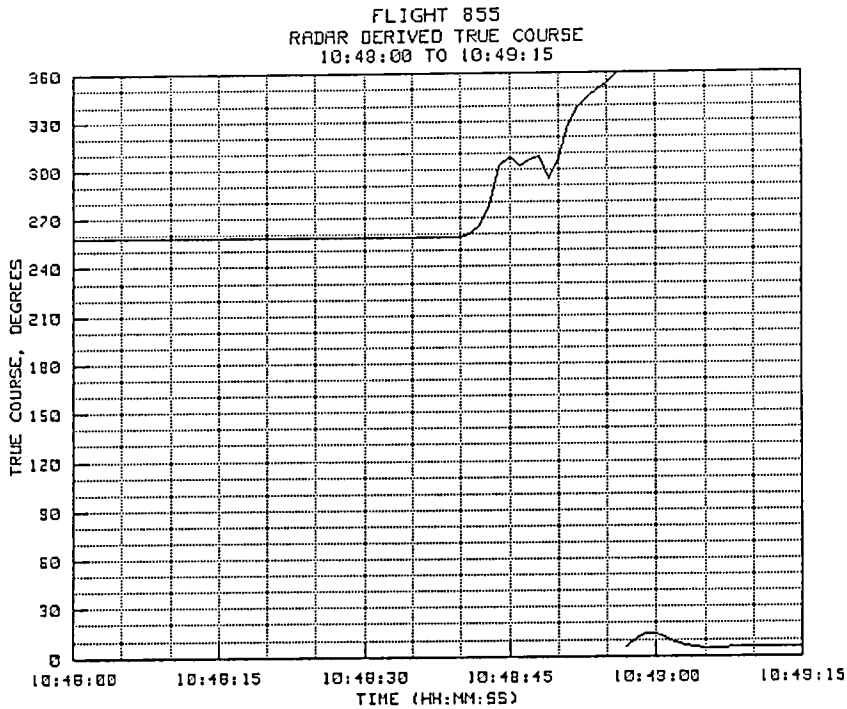

Figure 5-18(c). TP #9 radar-derived true course.

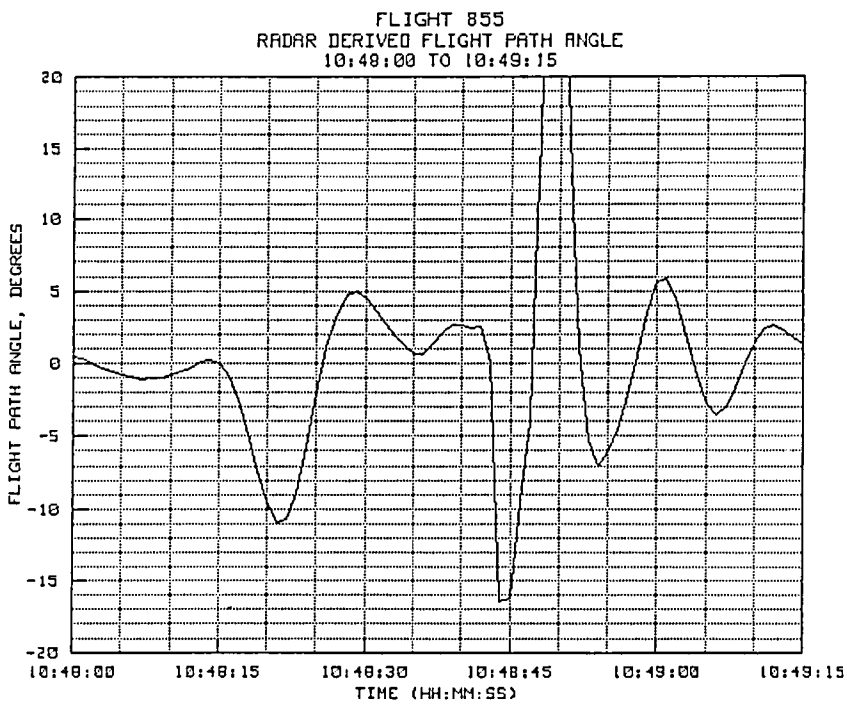

Figure 5-18(d). TP #9 radar-derived flight path angle.

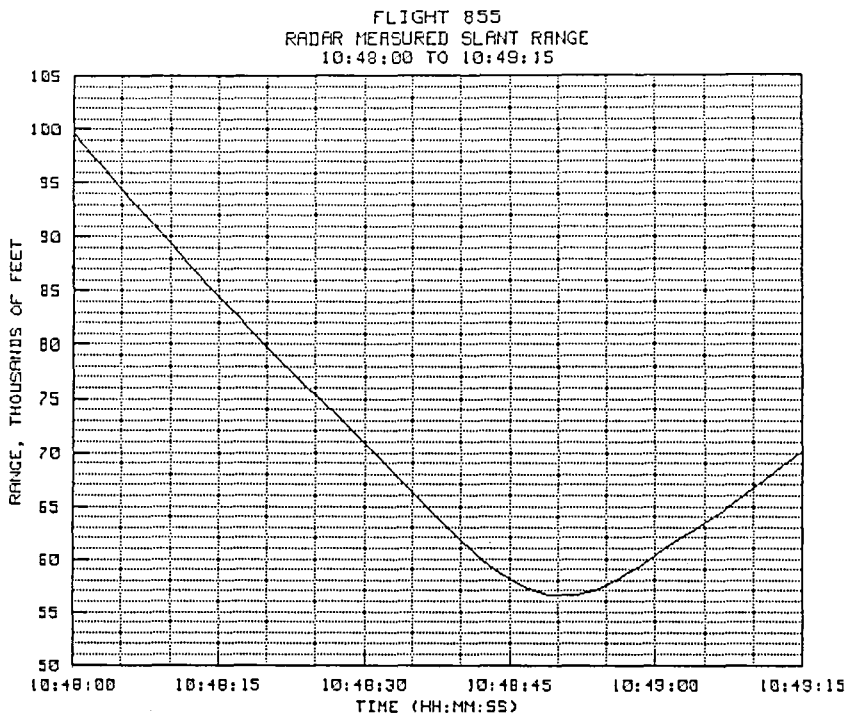

Figure 5-18(e). TP #9 radar-derived slant range.

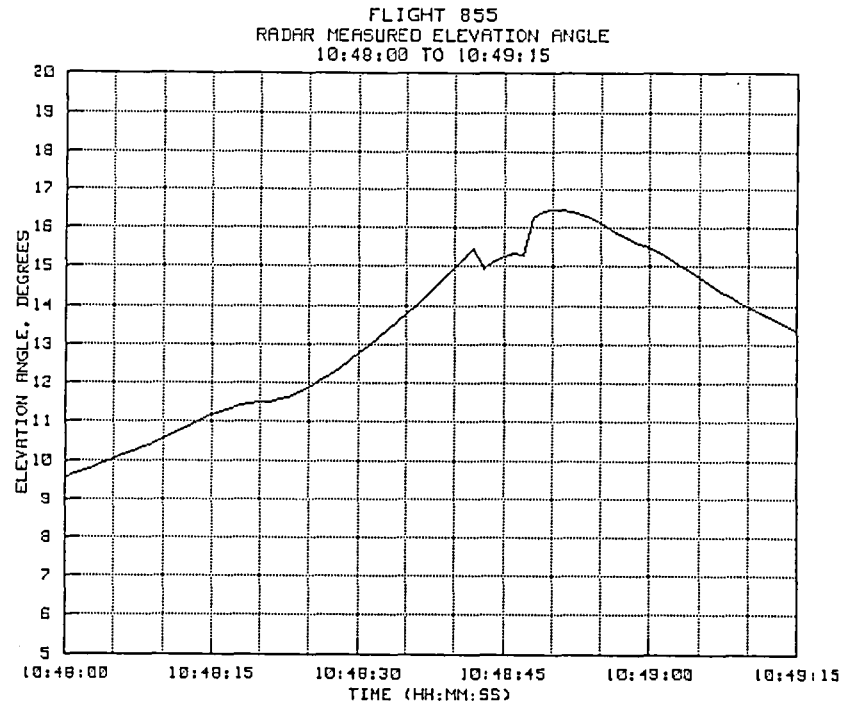

Figure 5-18(f). TP #9 radar-derived elevation angle.

5.2.10 Test Point #10

Time history plots for this test point are provided in figures 5-19(a) to 5-19(f). This test point was a 3-g, 90-degree right turn followed by a 3-g left turn. Reversal time was 10:51:40. Slant range during the maneuver varied between 54,604 feet (8.99 n.mi.) and 41,350 feet (6.81 n.mi.). The radar held lock fairly well throughout the maneuvers, with some angle jumps occurring from 10:51:42 until 10:51:57. Elevation angle throughout the maneuver was moderately high--17.25 degrees at the start and 20.69 degrees at the end of the maneuvers. The altitude plot shows reasonably good correlation with the flight data, in spite of obvious glint conditions during the time period indicated above. However, at the start of the maneuver, the elevation went slightly high, then came back on, and then started oscillating up and down. The derived Mach number went bad as soon as the glint effects started, and remained bad until very near the end of the test point.

Also note that a pull-up was started at about 10:51:10. During this pull-up, a fairly sizeable altitude error developed (about 100 feet). This type of error is usually indicative of a servo lag condition resulting from a low bandwidth setting on the radar elevation channel.

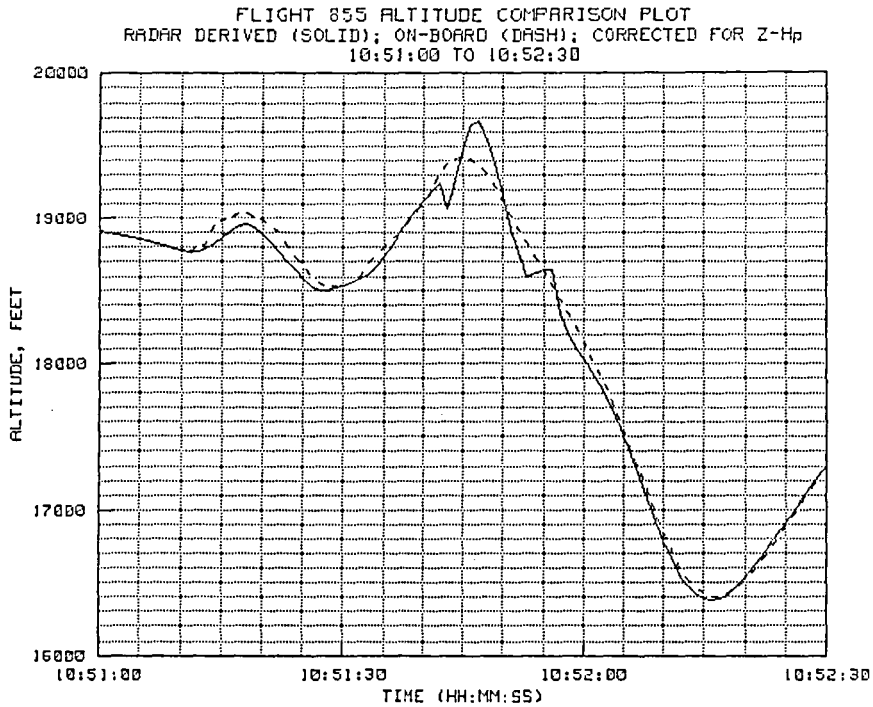

Figure 5-19(a). TP #10 radar-derived and on-board altitude.

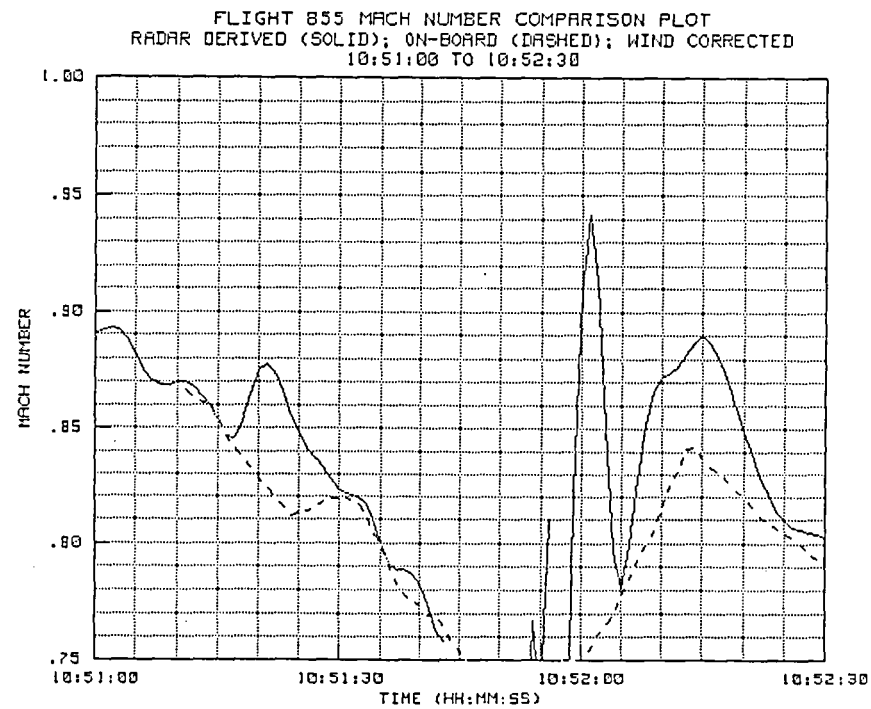

Figure 5-19(b). TP #10 radar-derived and on-board Mach number.

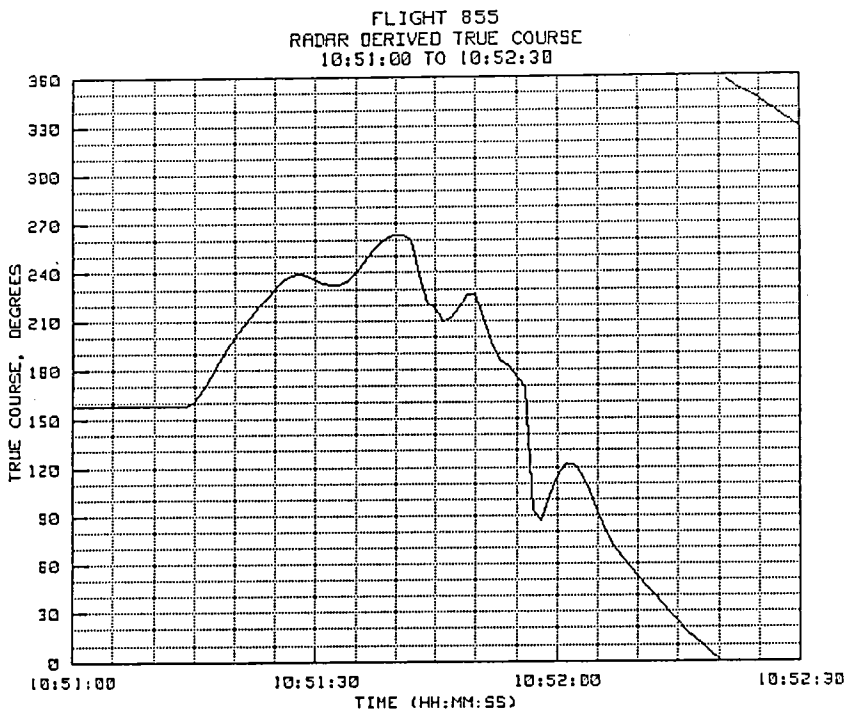

Figure 5-19(c). TP #10 radar-derived true course.

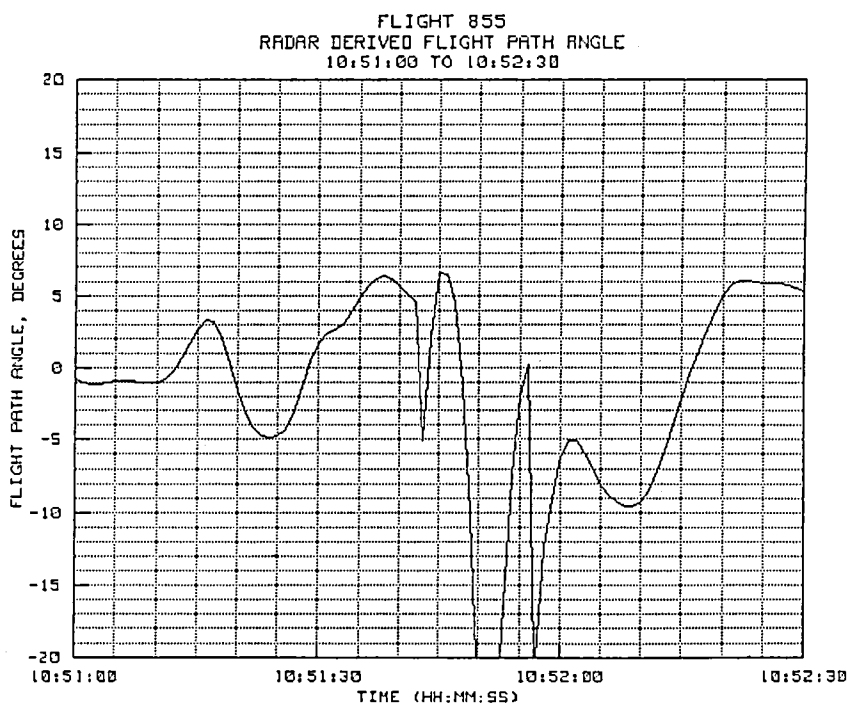

Figure 5-19(d). TP #10 radar-derived flight path angle.

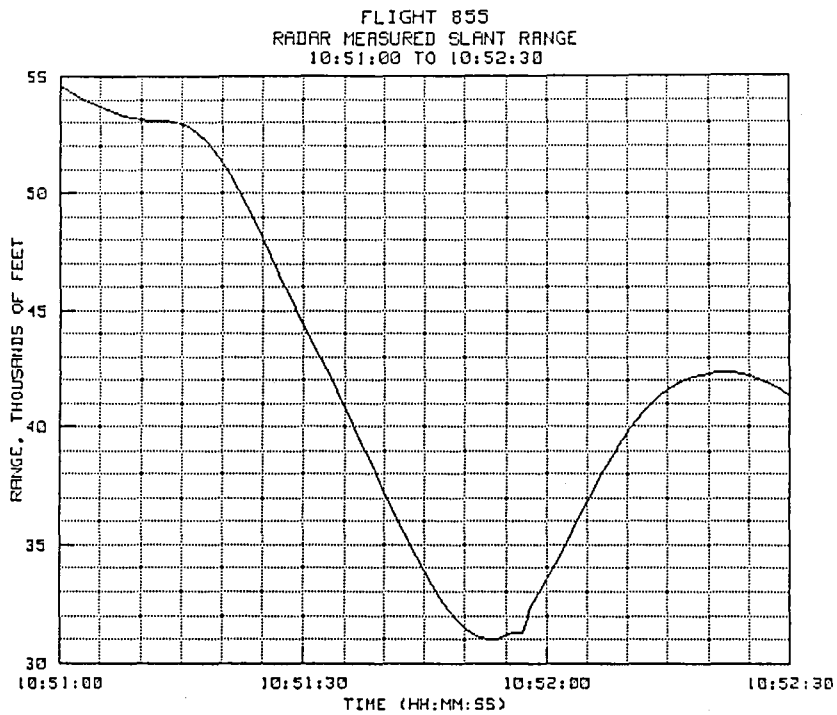

Figure 5-19(e). TP #10 radar-derived slant range.

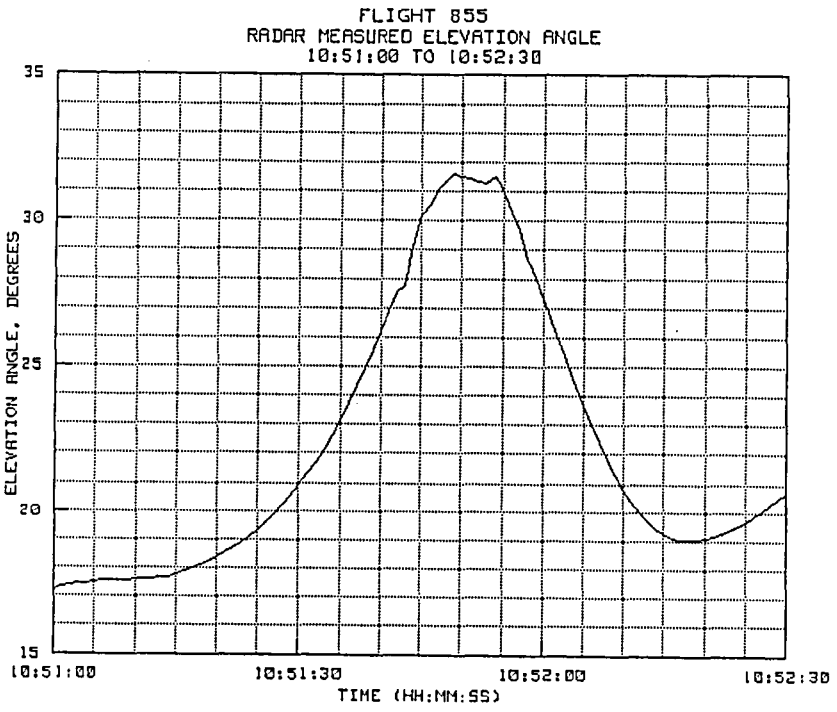

Figure 5-19(f). TP #10 radar-derived elevation angle.

5.2.11 Test Point #11

Time history plots for test point #11 are provided in figures 5-20(a) to 5-20(f). This was another beacon test maneuver consisting of a left 270 degree turn with a 360 degree roll at the end. The turn was started at 10:53:51 and held until about 10:55:10, at which time the aircraft was leveled out on a northerly heading. The roll maneuver was started about 10:56:00. Slant range at the start of the turn was 30,233 feet (4.98 n.mi.) and the elevation angle was 32.87 degrees. Tracking during the turn was reasonably good until about 10:54:50 when antenna oscillations started. These oscillations became very bad about 10:55:00 as the target approached the highest elevation angle, 43.29 degrees. Shortly thereafter the oscillations stopped and a good track was held until the entry into the roll maneuver. At that point the radar went off target.

From figure 5-20(a), a good correlation can be found between the on-board and radar-derived altitude plots, with some jumps occurring at the high-elevation point in the maneuver. A smooth track was then held until just after the pilot pulled the nose up to start the roll maneuver (10:56:09). At that time large angle oscillations occurred.

The Mach number plot also shows good correlation with the short term changes in the on-board data throughout the turning portion of the flight, except for a wind bias of about 0.02 Mach which occurred as the turn went from about 230 degrees to 120 degrees. As soon as the angle oscillations started, the radar-derived Mach number became highly erratic. The derived Mach number stabilized after the high-elevation point was passed and held good until the start of the roll maneuver. From the start of the roll maneuver until the end of the test point, the radar-derived Mach number was unusable.

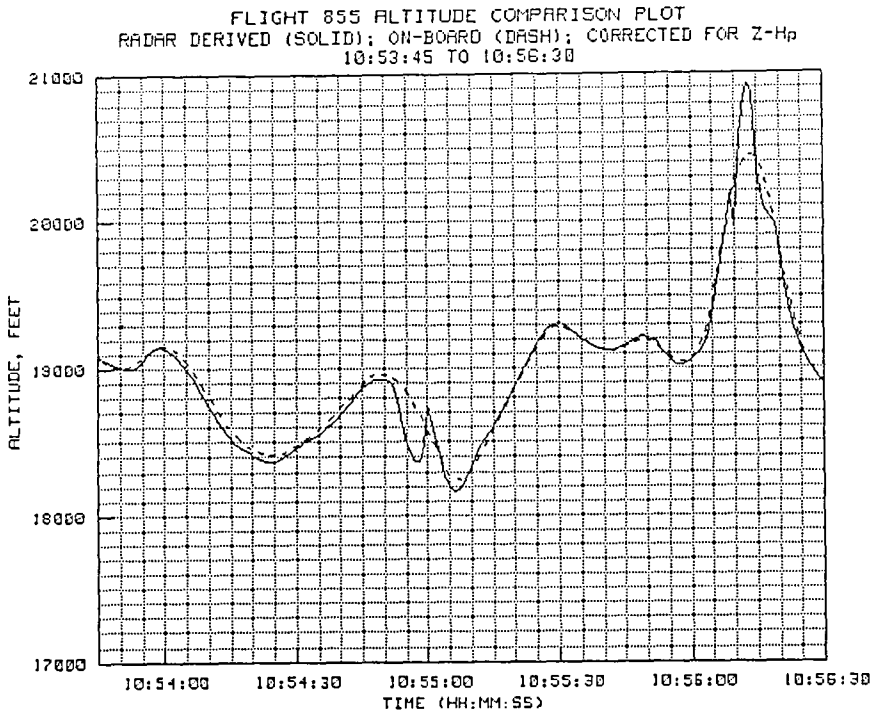

Figure 5-20(a). TP #11 radar-derived and on-board altitude.

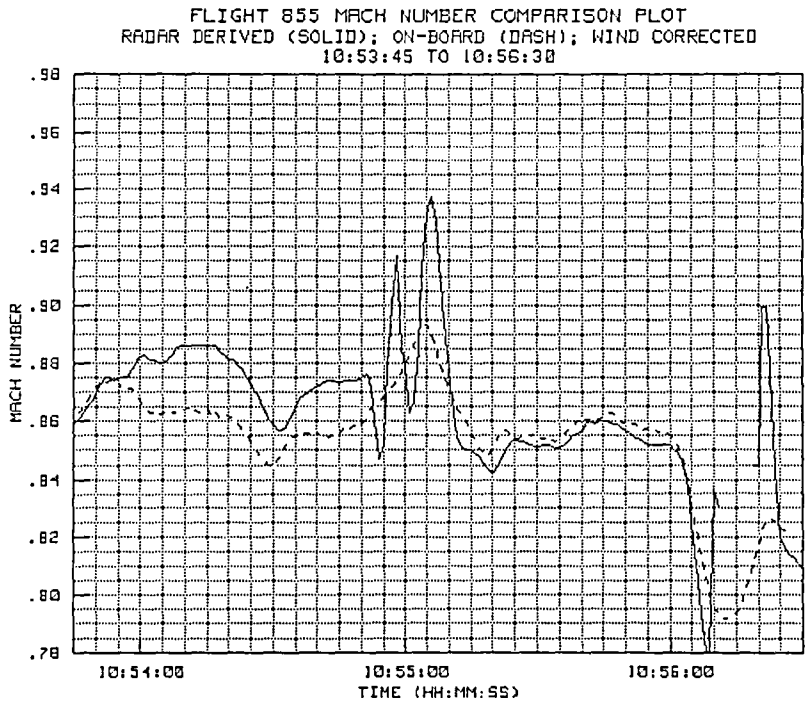

Figure 5-20(b). TP #11 radar-derived and on-board Mach number.

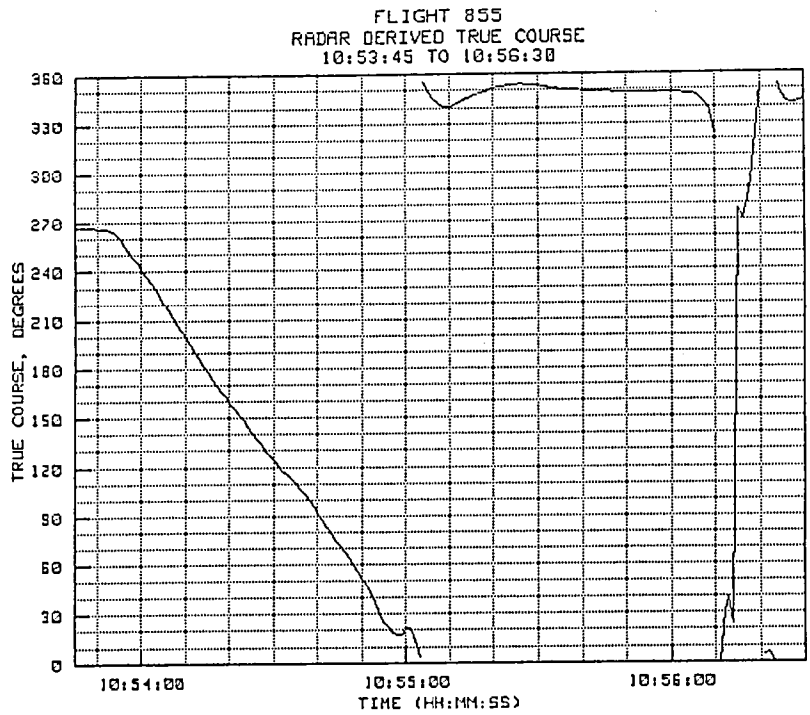

Figure 5-20(c). TP #11 radar-derived true course.

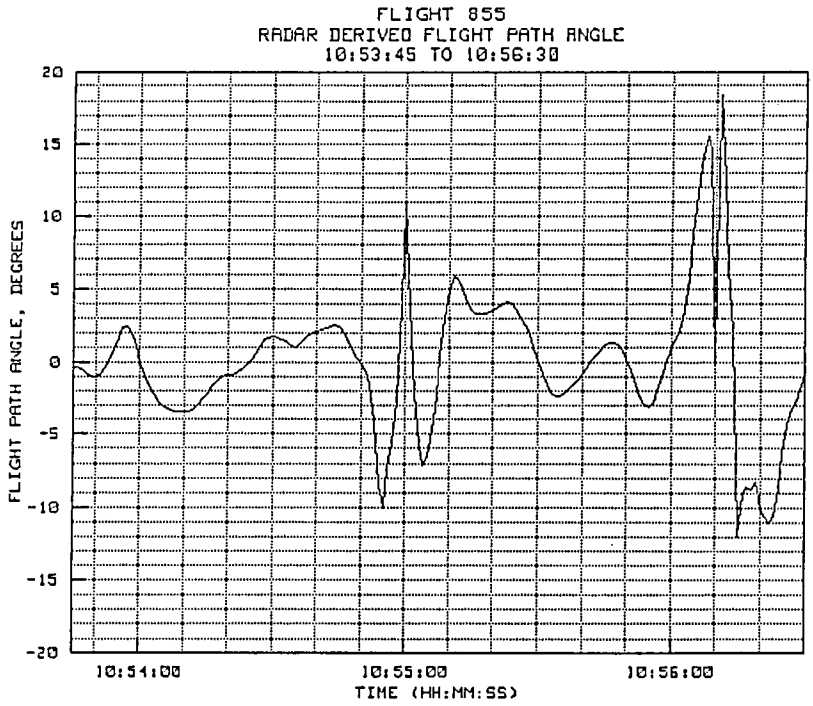

Figure 5-20(d). TP #11 radar-derived flight path angle.

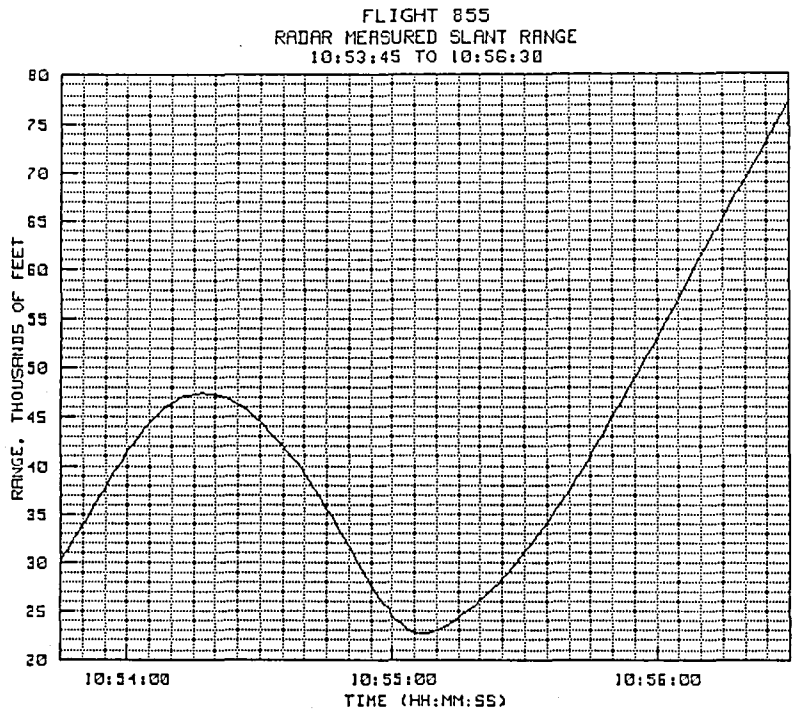

Figure 5-20(e). TP #11 radar-derived slant range.

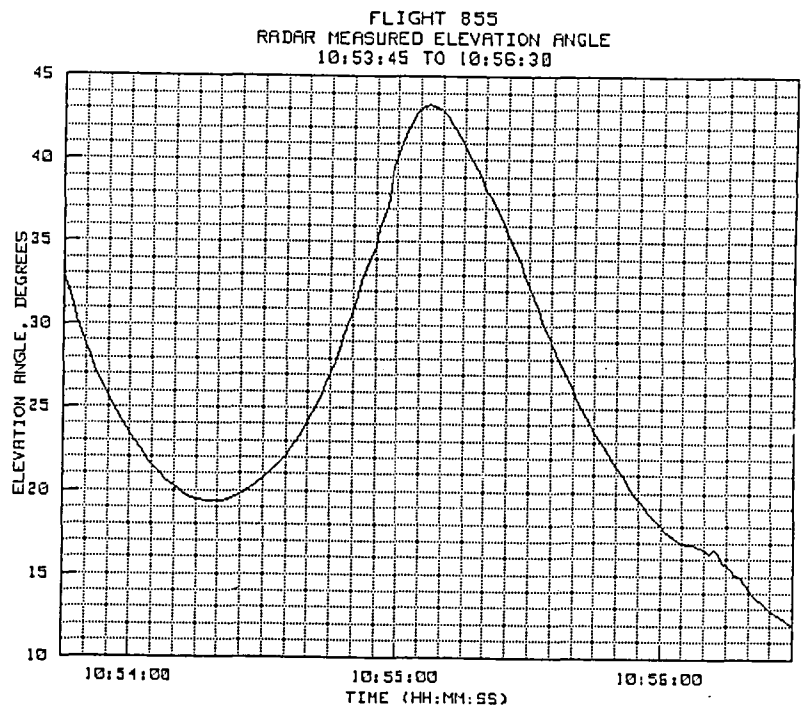

Figure 5-20(f). TP #11 radar-derived elevation angle.

5.2.12 Test Point #12

Time history plots for test point #12 are shown in figures 5-21(a) to 5-21(f). This test point consisted of a high-g 270-degree right turn, followed by a roll maneuver. The slant range at the start of the maneuver was 89,684 feet (14.76 n.mi.) and 92,133 feet (15.16 n.mi.) at the end. The highest elevation angle, 11.81 degrees, occurred at about 10:58:28 when the pilot pulled the nose up to start the roll maneuver. This was an exceptionally good track for the types of maneuvers involved. There was excellent agreement in altitude throughout all of the maneuvers, and the Mach number comparison showed good correlation except for a sizeable bias which appeared to develop at the same time as the start of the high-g right turn. This was probably due to some disturbance in the on-board pressure measurement due to the increased angle of attack. The slight Mach number undershoot at the low peak, about 10:58:28, was probably due to a combination of glint and servo lag. It should be noted that during erratic flight maneuvers, the bandwidth on the angle servo systems is reduced by the operator to minimize the antenna jumps. Under these conditions, there is a tendency for the antenna to lag and overshoot.

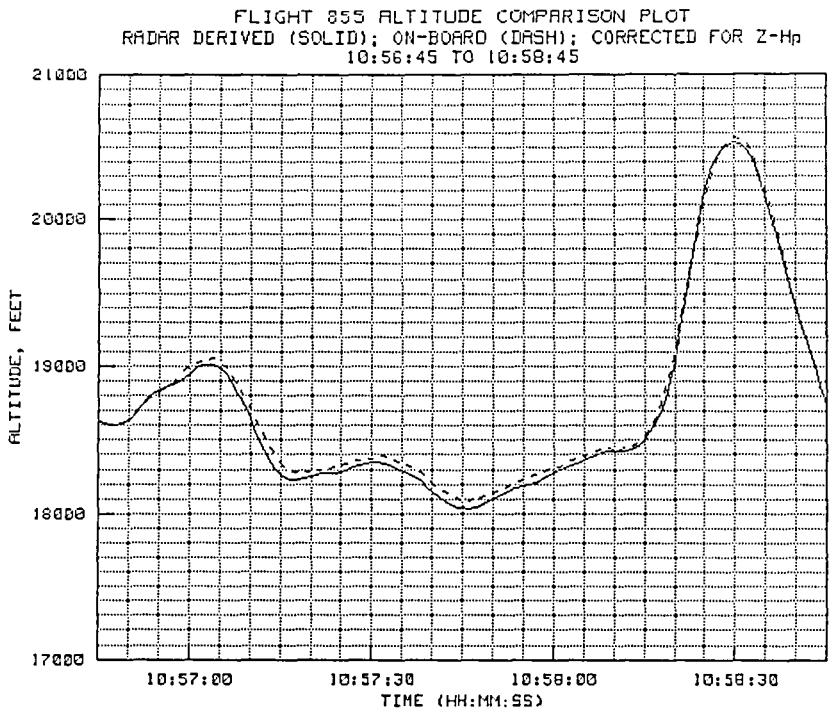

Figure 5-21(a). TP #12 radar-derived and on-board altitude.

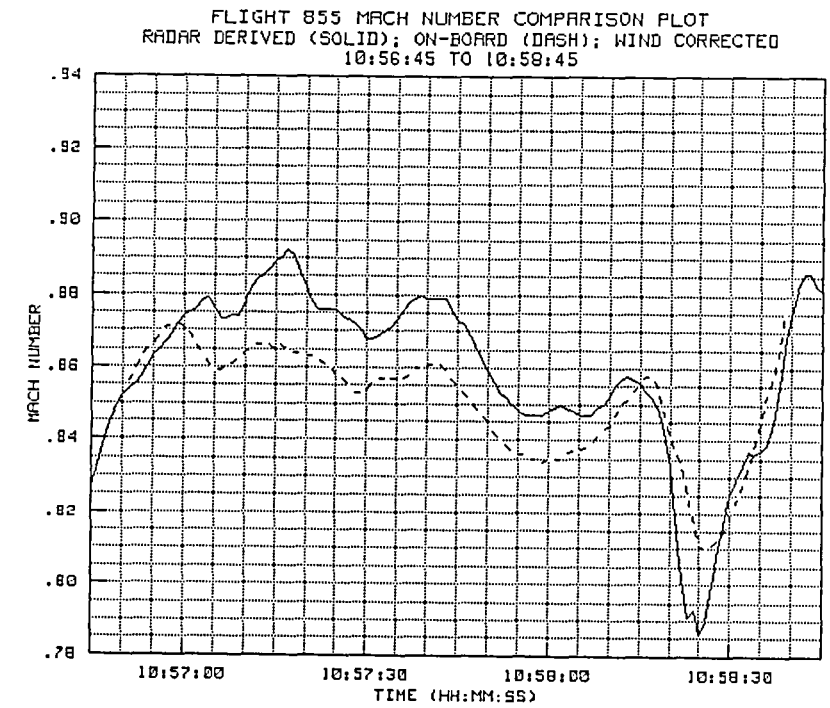

Figure 5-21(b). TP #12 radar-derived and on-board Mach number.

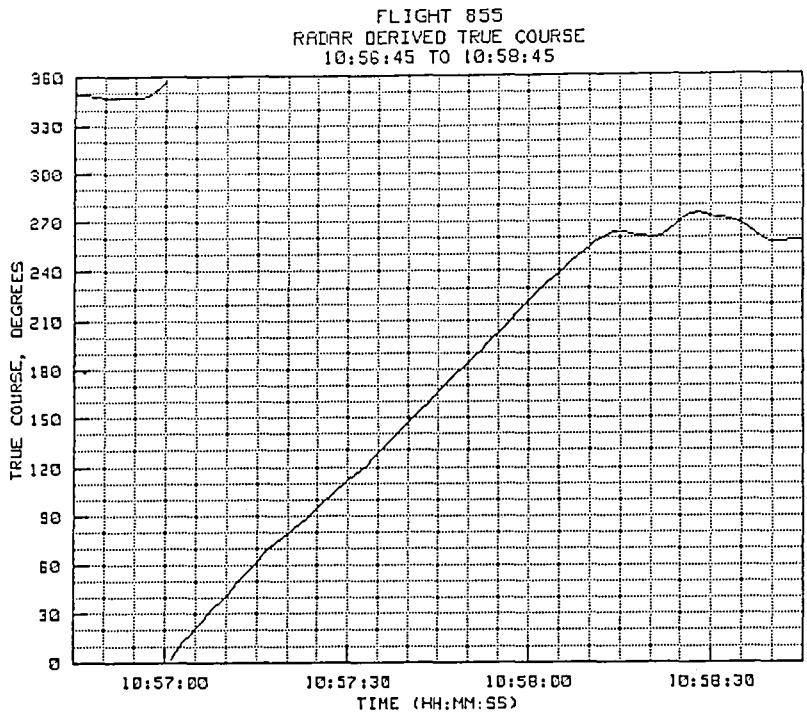

Figure 5-21(c). TP #12 radar-derived true course.

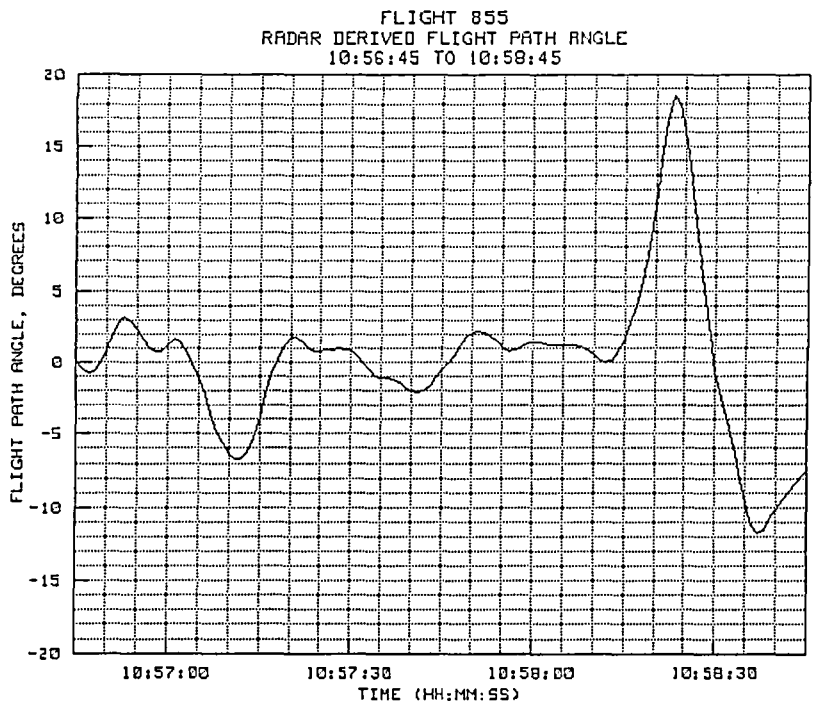

Figure 5-21(d). TP #12 radar-derived flight path angle.

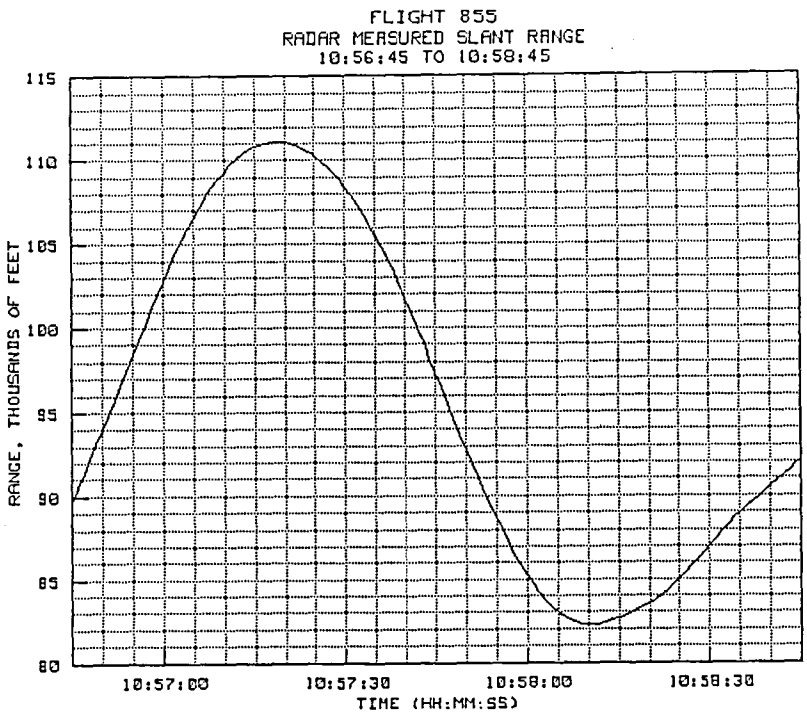

Figure 5-21(e). TP #12 radar-derived slant range.

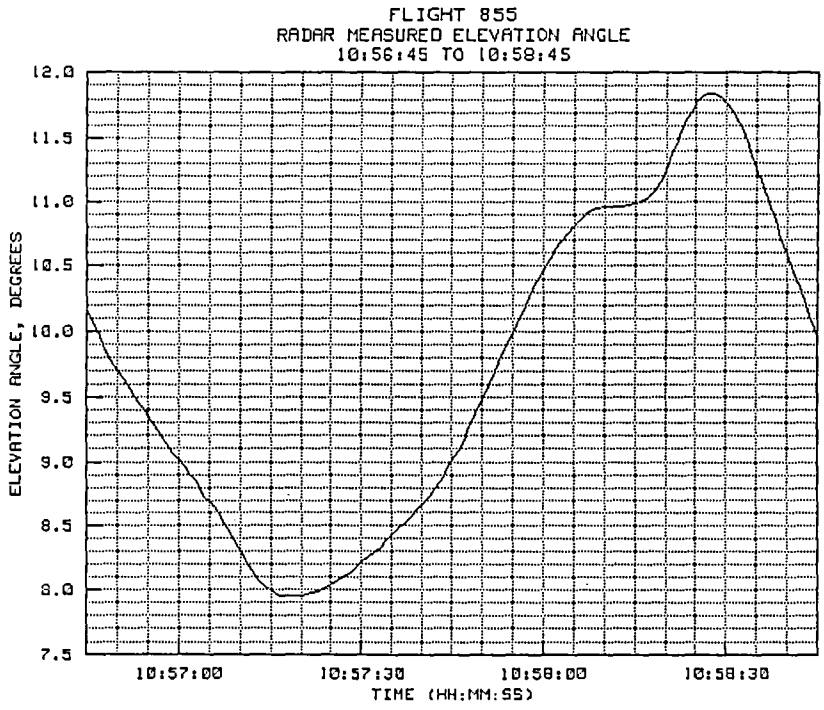

Figure 5-21(f). TP #12 radar-derived elevation angle.

5.2.13 Test Point #13

Time history plots for test point #13 are shown in figures 5-22(a) to 5-22(f). The test point consisted of a constant 0.85 Mach descent from 18,000 feet down to 4000 feet MSL. The descent was made with a constant easterly heading that resulted in a true course that remained between 082 degrees and 084 degrees for the entire leg. The slant range at the start of the descent was 77,742 feet (12.79 n.mi.) and at the end was 81,604 feet (13.43 n.mi.). The point of closest approach occurred at 11:01:00 when the aircraft passed north of the radar at a slant range of 45,843 feet (4.54 n.mi.) at an altitude of about 10,650 feet. The agreement between pressure altitude and radar-derived altitude was excellent throughout this descent, with one plot essentially overlaying the other. The radar altitude did go slightly below the corrected pressure altitude at the level off point by about 20 to 30 feet.

Mach number comparisons during the descent were also good, with the greatest bias error, about 0.02 Mach, occurring while passing about 10,000 feet.

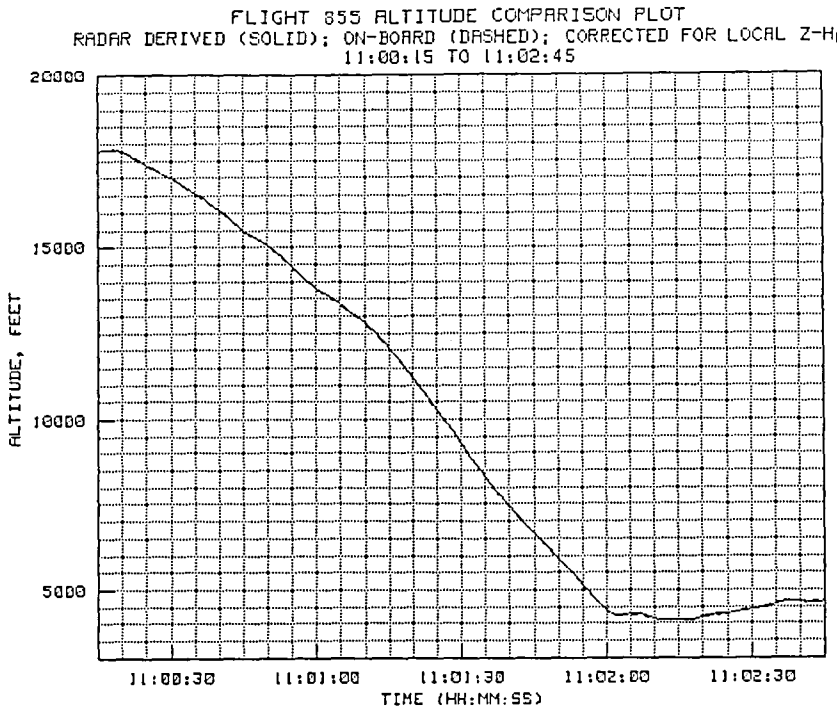

Figure 5-22(a). TP #13 radar-derived and on-board altitude.

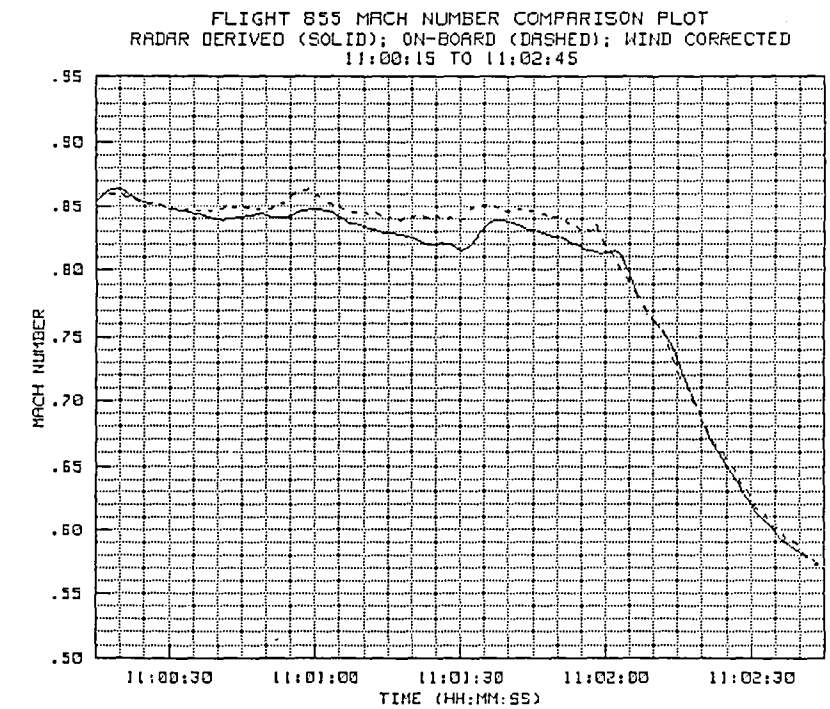

Figure 5-22(b). TP #13 radar-derived and on-board Mach number.

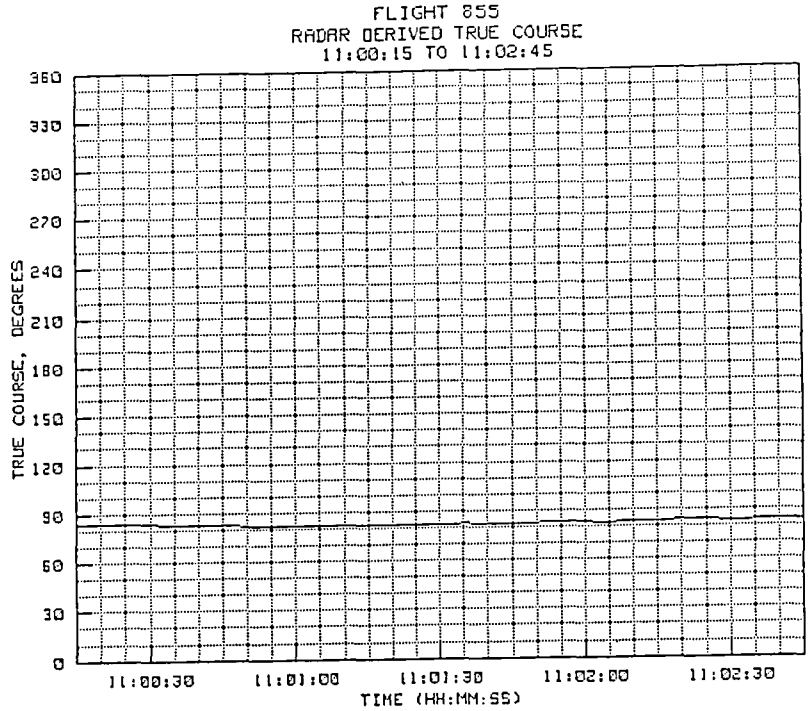

Figure 5-22(c). TP #13 radar-derived true course.

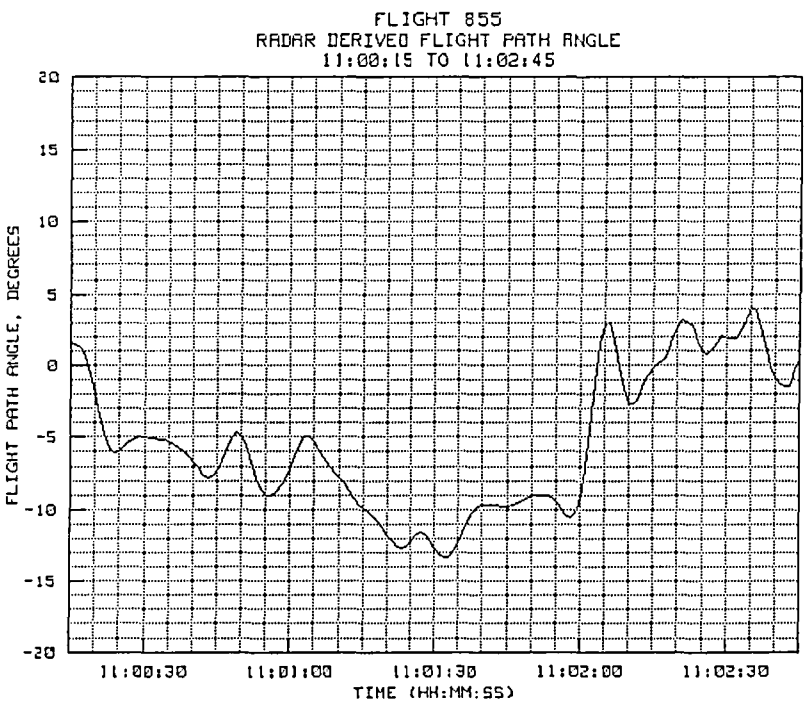

Figure 5-22(d). TP #13 radar-derived flight path angle.

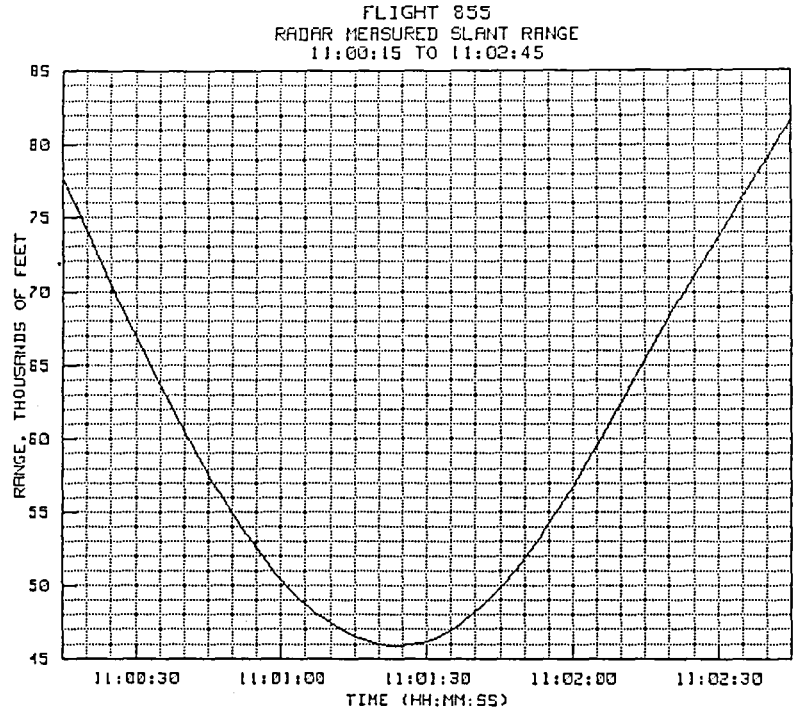

Figure 5-22(e). TP #13 radar-derived slant range.

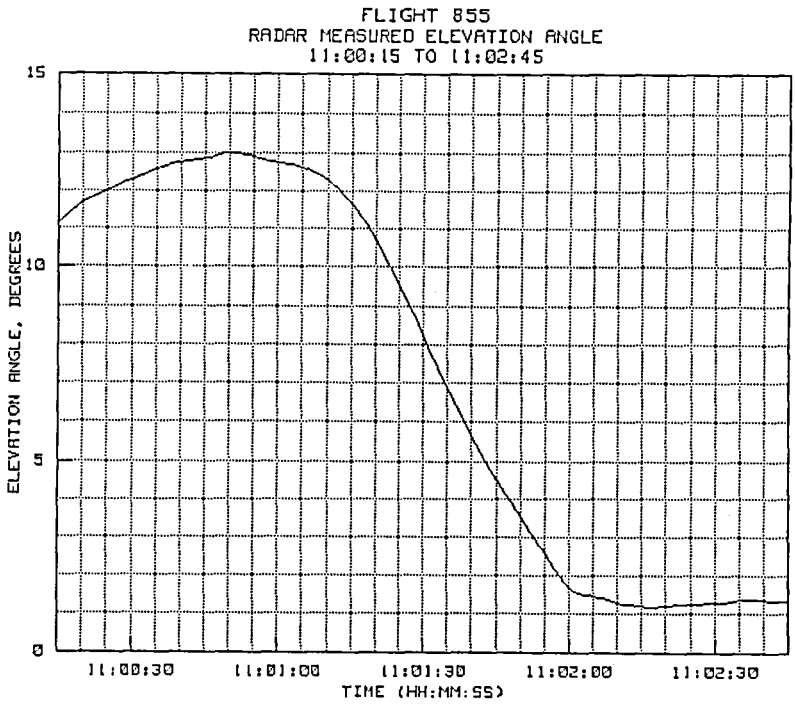

Figure 5-22(f). TP #13 radar-derived elevation angle.

5.2.14 Test Point #14

Time history plots for test point #14 are provided in figures 5-22(a) to 5-22(f). This test point was to have been a short period of trimmed-up, hands-off flight. Unfortunately, this portion of the track occurred after the operator had gone to the AIDED EL rate mode. Neither the operator or the observer realized that this was the case, so the care with which the optical aim point was held on the target may not have been as good as would have been the case if it had been known to be a data point. It was the original intent of this test to attempt to determine which of the movements in the radar were pilot induced, and which were noise induced. However, shortly after the start of the analysis, air data tapes became available so that this question could be better answered by making comparisons between the radar-derived parameters and those recorded on board.

The altitude plot for this test point shows a difference between the radar derived geometric altitude and the Z-Hp adjusted on-board altitude to be on the order of 25 to 30 feet, indicating the possibility of some errors in the lower altitude Z-Hp estimates in combination with some semi-diurnal Z-Hp changes over the period of the flight.

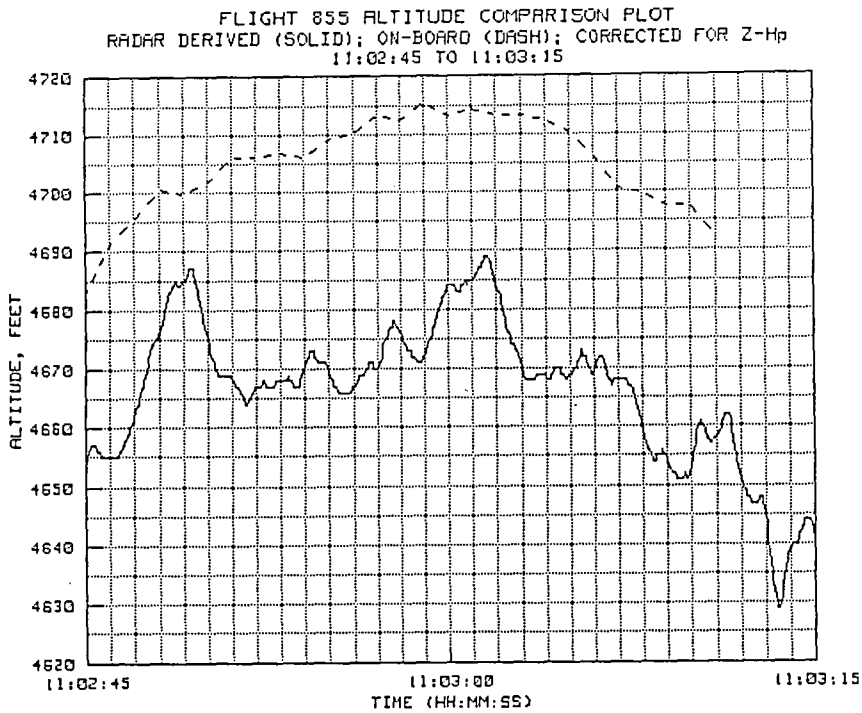

Figure 5-23(a). TP #14 radar-derived and on-board altitude.

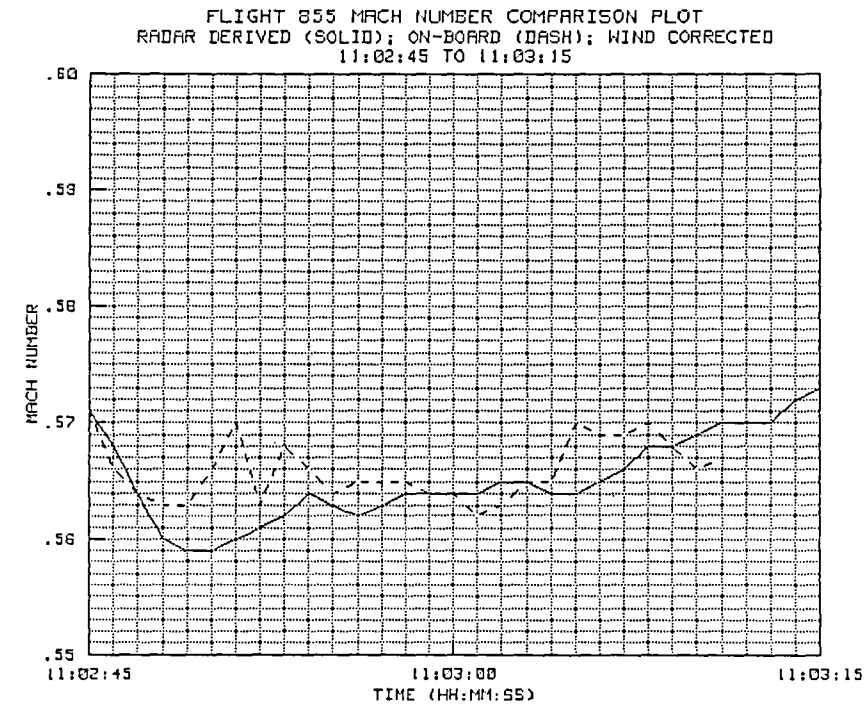

Figure 5-23(b). TP #14 radar-derived and on-board Mach number.

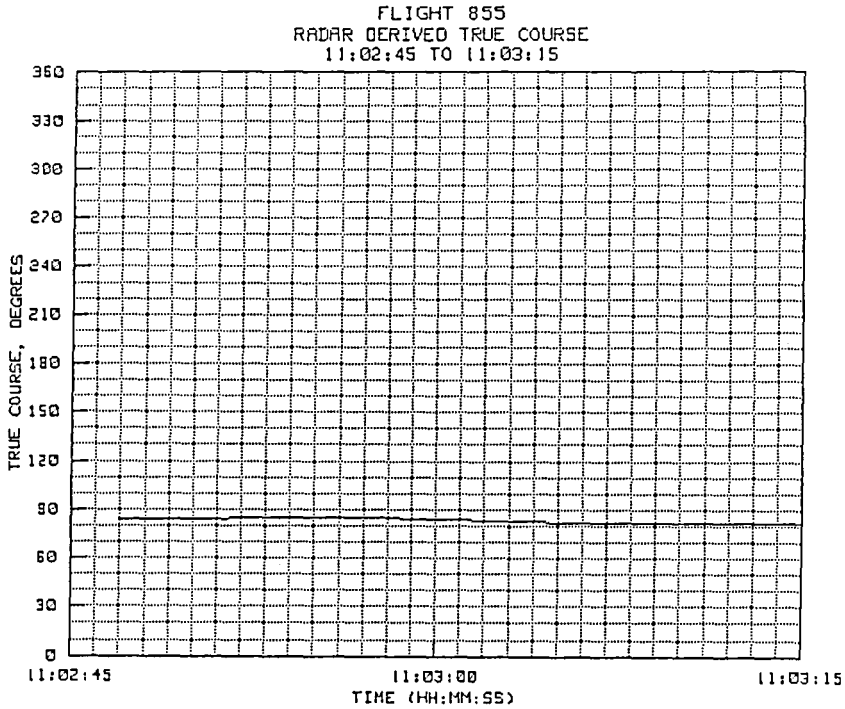

Figure 5-23(c). TP #14 radar-derived true course.

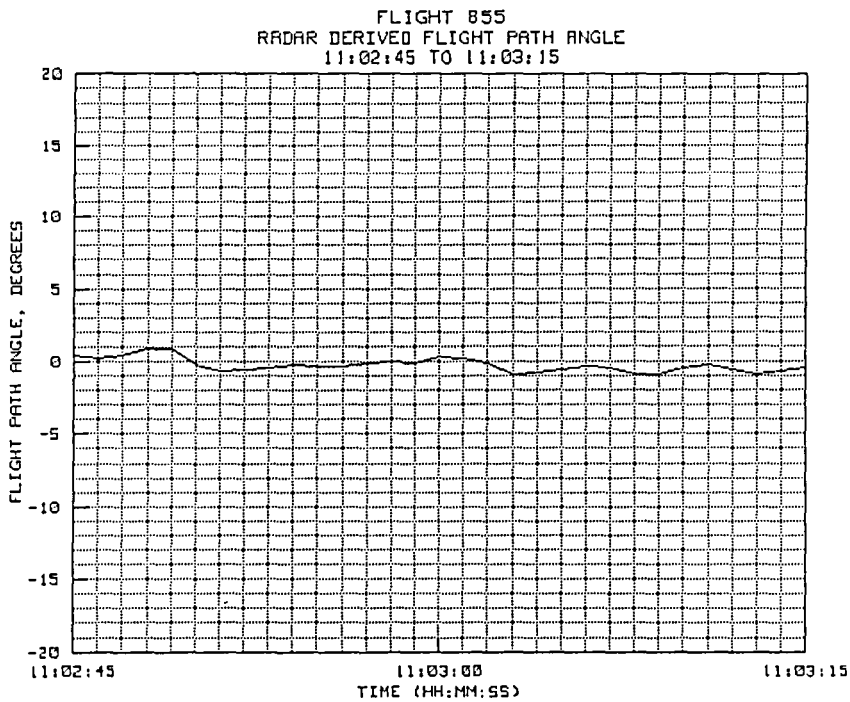

Figure 5-23(d). TP #14 radar-derived flight path angle.

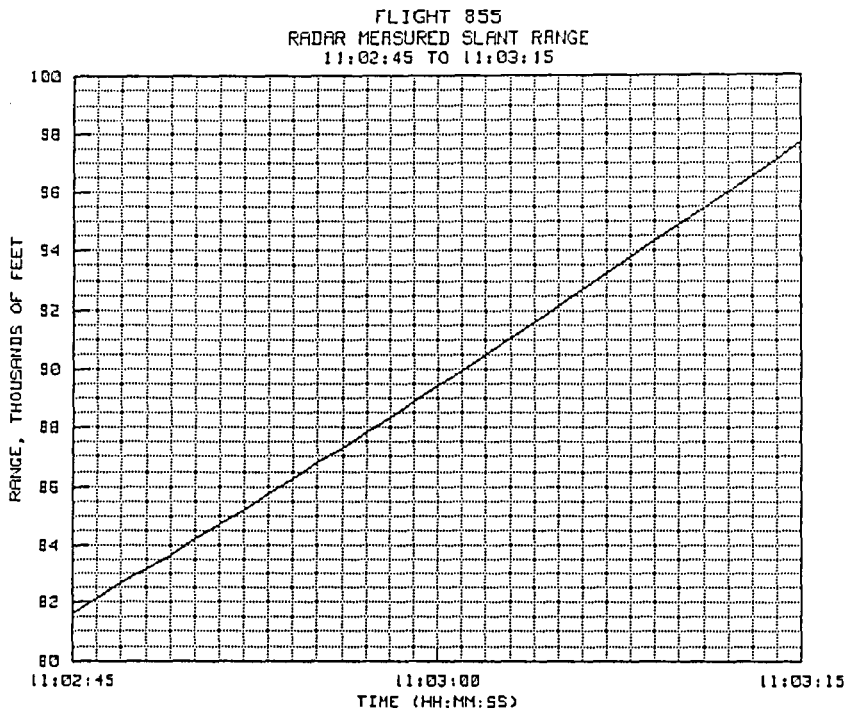

Figure 5-23(e). TP #14 radar-derived slant range.

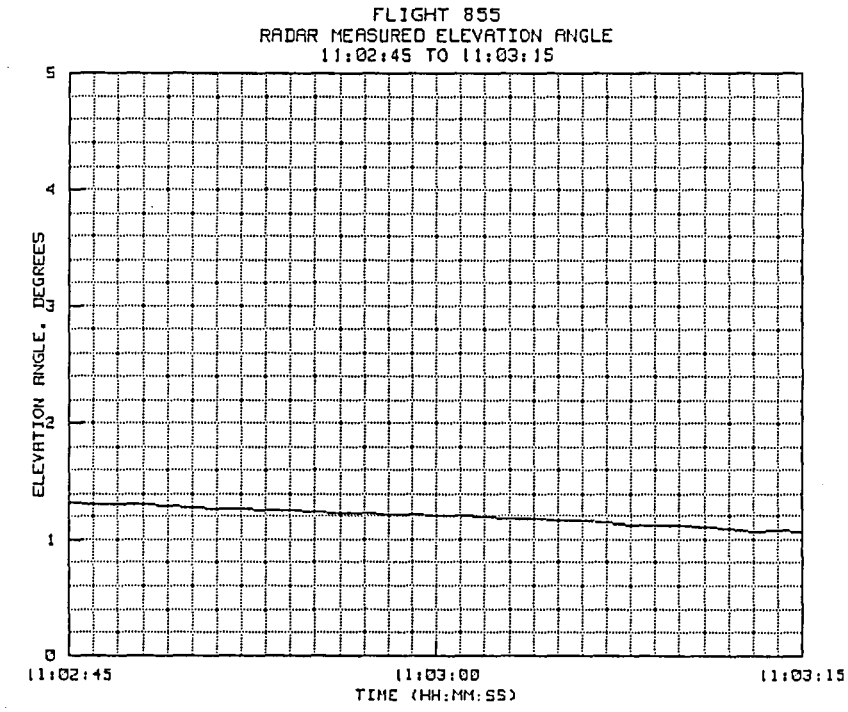

Figure 5-23(f). TP #14 radar-derived elevation angle.

5.3 Analysis of Wind Data for Flight 855

Immediately after the completion of flight 855, a rawinsonde balloon was tracked by the radar. Figures 5-24(a) and 5-24(b) provide plots of both wind direction and velocity as determined from the the radar balloon track (solid lines), the rawinsonde measurements (short dashed line), and the synoptic analysis (long dashed line).

Note that, as was the case for flight 814, the rawinsonde data appear to have more damping than the radar data. However, after analyzing the raw tracking data from the balloon track, and making allowances for the pendulum motion of the radar reflector, it was found that the filtered radar data shown in these figures do provide an accurate representation of the information in the raw radar data. If additional damping were to be used, true wind characteristics would be lost. As noted in the analysis of the data from flight 814, the long tether between the balloon and the weather package (and radar reflector) obviously add some inaccuracies to the measurements because of a significant pendulum motion. However, when wind data from either the rawinsonde computer or from the radar track are applied to the flight data, the variability of the winds appears to mask the differences between the two measurement techniques.

The synoptic winds, shown on the plots as long dashed lines, agree closely with the rawinsonde data. Note that the maximum difference in estimated wind direction, about 22 degrees, occurs below about 10,000 feet. Above 10,000 feet, wind directions from the synoptic analysis and from the rawinsonde measurements agree to within 10 degrees or less. Differences in wind velocities between the synoptic and the local rawinsonde data are also quite small--less than 2 knots at all altitudes.

Figures 5-25(a), 5-25(b), 5-25(c) and 5-25(d) provide comparison plots of radar-derived Mach number using wind data from all three sources. In these plots, the on-board Mach number data is represented by a solid line, the Mach numbers derived using radar balloon track data are represented by a short dashed line, those derived using rawinsonde winds are represented by a long dashed line, and those derived using winds from the synoptic analysis are represented as dotted lines.

The Mach number data shown in figure 5-25(a) uses data from the low level, close-in leg described in section 5.2.1. Altitude on the leg varied from 3320 feet (MSL) at the start to 5060 feet at the high point (10:06:53) and then back down to about 3340 feet at the end of the leg. The radar derived data for this test point should be discarded since a lock-on on the

rawinsonde balloon was not obtained until 5000 feet. In the analysis program, winds for altitudes below the lock-on point are set equal to the values computed at the first consistent lockon. The rawinsonde winds for this leg appear to result in greater Mach number differences than do the synoptic winds. In general, the difference between Mach numbers derived using the latter two wind sources appears to be on the order of 0.004 Mach (about 3 or so knots).

The second comparison plot, shown in figure 5-25(b) contains data obtained during the constant-Mach-number climb described in section 5.2.2. In this case, the target altitude started at about 4000 feet and continued to increase at a fairly constant rate until reaching 21,000 feet at the end of the run. In this plot, Mach number data derived from on-board measurements are shown as a solid line. Data derived from radar, rawinsonde, and synoptic winds are shown as a short dashed, long dashed, and dotted lines, respectively. Mach numbers derived from all three sources show reasonably close agreement, but vary from the on-board Mach measurements by as much as about 0.01 Mach. At the lower levels, the data derived using synoptic winds show a slight advantage (0.003 Mach) over data derived using either radar or rawinsonde winds.

Figure 5-26C shows the same type of comparisons for data taken during a left 360 degree turn described in section 5.2.3. Altitude during the turn ranged from about 18,500 feet at the start down to about 17,000 feet at the end of the turn. Again, Mach number data derived from all three sources appears to match quite closely, however all three of the derived Mach number plots show maximum variations from the on-board Mach measurement of up to nearly 0.02 Mach. Also note that during the wings-level portion of the plot (10:16:00 to 10:16:10) all three derived Mach numbers read about 0.006 Mach below the on-board data. After the start of the turn, all of the derived Mach numbers jumped to and remained at values above those measured on board. However, at the point where the roll out was completed (about 10:17:20), all three derived Mach numbers appeared to again go below the on-board Mach number. This would indicate the possibility of some uncompensated variations in the on-board Mach Number measurements during turning conditions. The turn in this case was carried out at fairly constant turning rate of about 4.5 degrees per second.

The last Mach number comparison plot is for the period from 11:00:15 to 11:02:45. This was a descent from about 17,700 feet to 4000 feet as described in section 5.2.13. The descent was made on an almost constant easterly heading. Again, Mach number data derived using all three wind sources appears to agree closely, except that the radar derived winds

show some very slight advantage at about 11:01:00 and possibly at 11:01:37. However, as in the previous cases, all of the derived Mach numbers show a maximum variation from the on-board data of about 0.025 Mach at 11:01:30 (9300 feet altitude).

Again, it is hard to see any distinct advantage in the wind data from any of the three sources, since all yield results with significant biases from the on-board plots. Considering that this flight was conducted on a very low-wind day, when the winds derived from all three sources could be expected to have reasonably close agreement, it is difficult to see how very accurate Mach number data could be derived from the radar track of a test vehicle on a more typical high-wind day.

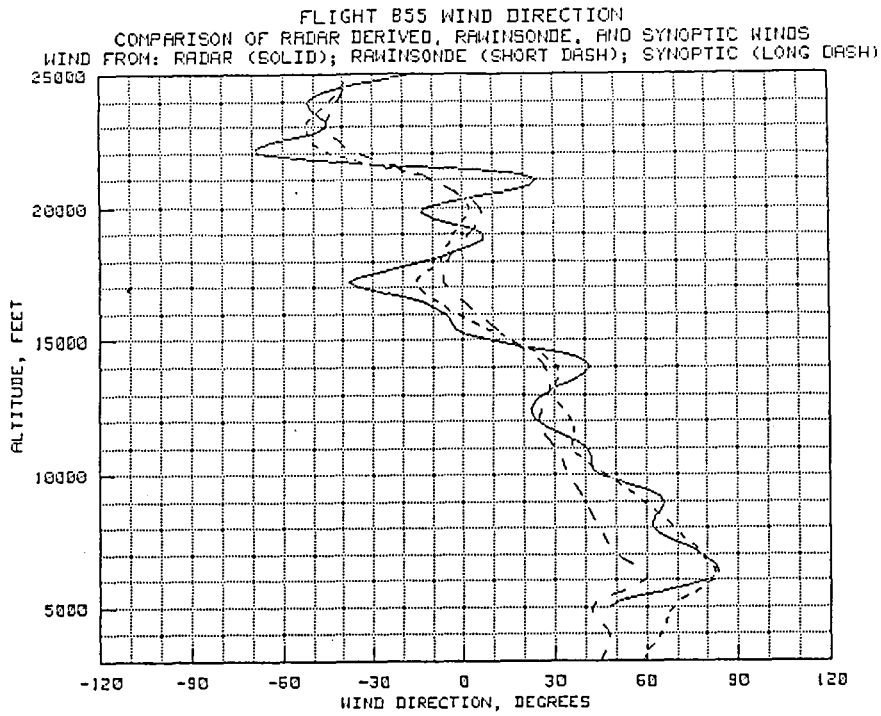

Figure 5-24(a). Flight 855 wind direction.

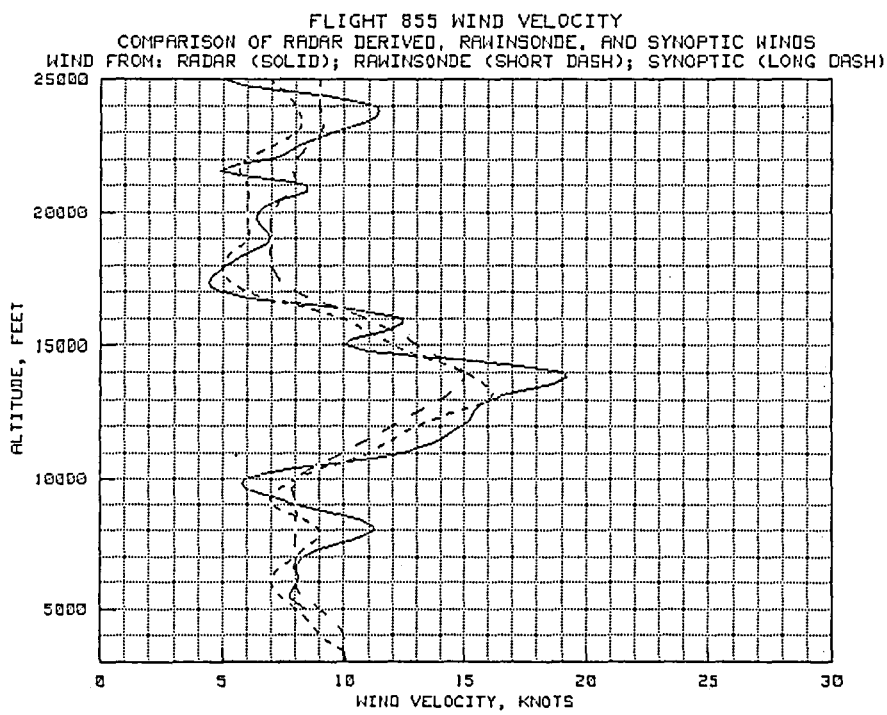

Figure 5-24(b). Flight 855 wind velocity.

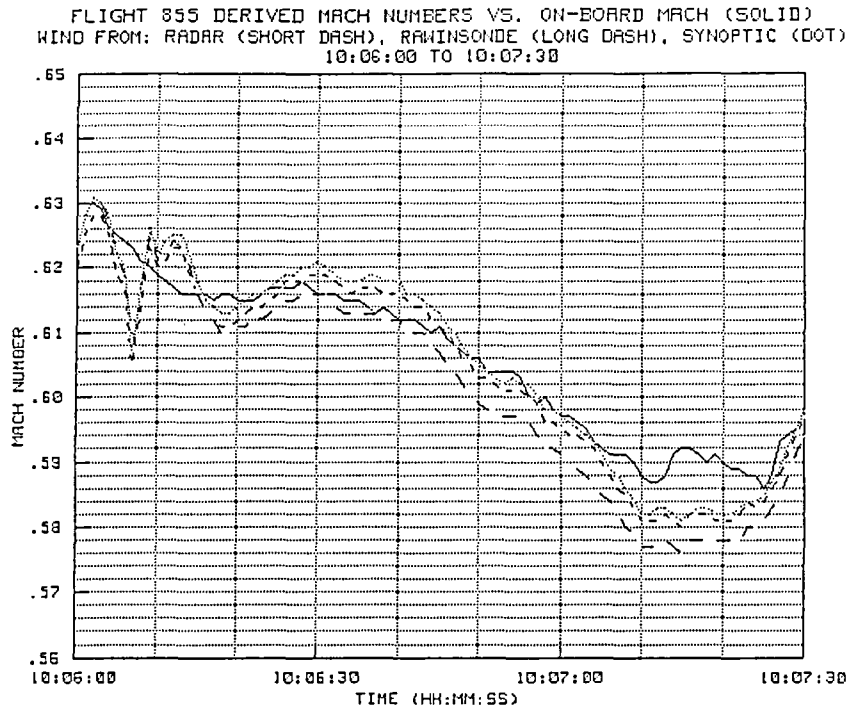

Figure 5-25(a). Flight 855 Effect of wind source on Mach.

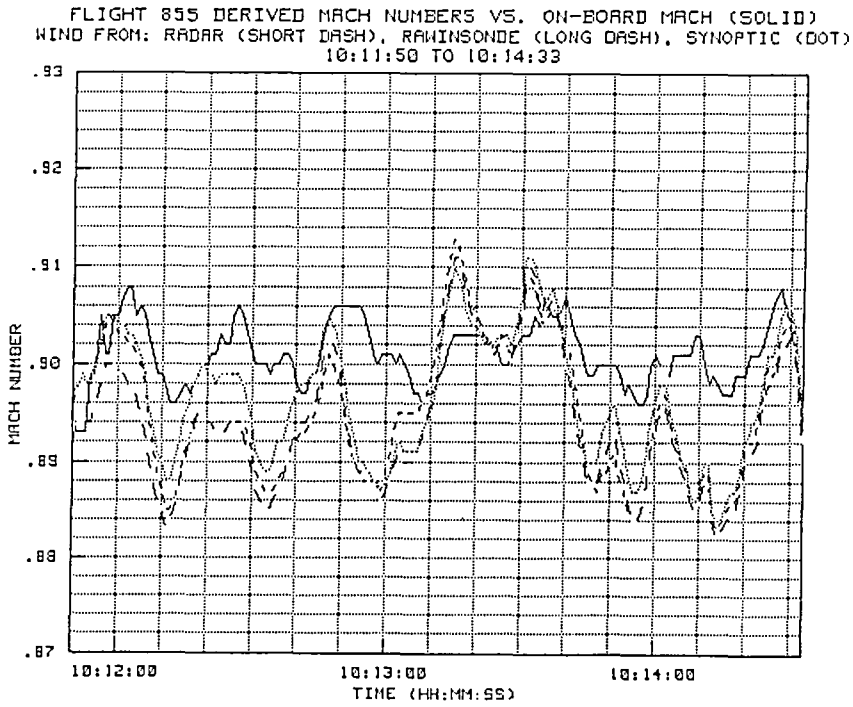

Figure 5-25(b). Flight 855 Effect of wind source on Mach.

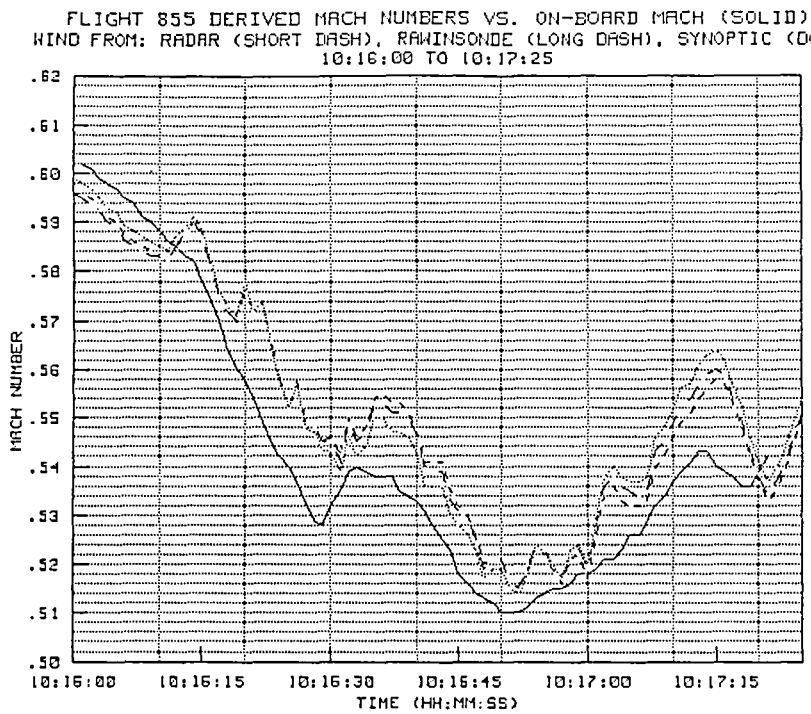

Figure 5-25(c). Flight 855 Effect of wind source on Mach.

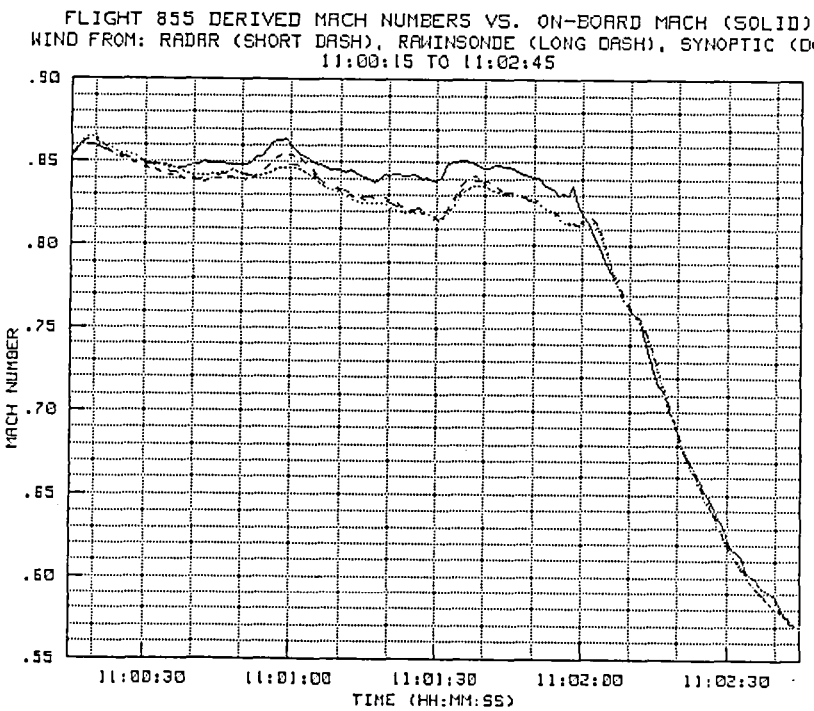

Figure 5-25(d). Flight 855 Effect of wind source on Mach.

5.4 Noise Analysis for Flight 855

Figures 5-26, 5-27, and 5-28 are plots of the one-sigma noise error in the raw range, azimuth, and elevation data from takeoff until landing. Note that the random noise in all of the three channels was one-half an LSB or less at all times except when the radar was off target. These plots show clearly the effects of maneuvering flight on the beacon track. The large noise spike present in all three plots at about 10:37:30 correlates with the noise seen in figures 5-15(a) and 5-15(b) at the time the 360-degree roll maneuver was being performed. Since the noise computation was performed at 100 data point intervals, some offset can be expected between the time the off-target condition occurs and the time at which the spike appears on the noise plot.

A small noise spike appeared in the elevation noise plot at about 10:43:45; however, this was not one of the test points for which on-board altitude and Mach number data were provided. Therefore, no analysis was made.

The next significant noise spike was at 10:48:45, appearing in both the azimuth and elevation channels. Again, this spike was due to a momentary off-target condition apparent in both the altitude and Mach number plots for test point #9. It occurred after the rapid deceleration, just as the high-g turn was commenced. Note that the system held lock through this maneuver so the range remained good, even though the angle data was degraded.

Again, about 10:51:45, a complete off-target condition occurred as another high-g maneuver was being performed. In this case all three channels were affected.

During test point #11, another instance of high-g maneuvering flight, spikes can be seen in all three channels, and on both the altitude and Mach number plots just before 10:55:00. A second off-target condition occurred at the end of the test point, just after 10:56:00, as a roll maneuver was being performed. This also affected all three channels.

A couple more jumps, primarily in elevation, occurred about 10:57:00 and 10:58:30. The first jump occurred during a high-g, 270-degree right turn; the second occurred during a slow roll that concluded the test point.

The noise data contained in figures 5-26 to 5-28 clearly show the need to alert the radar crew prior to any test maneuvers involving unusual aircraft attitudes. Since the maneuvers on this flight were conducted for the expressed purpose of analyzing the beacon track mode of the radar during dynamic flight conditions, no extraordinary measures were taken by

the site crew who, in fact, did not know the test plan. However, under normal circumstances, during test flights involving spin tests, high-g maneuvers, and so forth, the radar would be switched to skin mode just prior to the start of the test point. The skin track, over-all, is more noisy since the radar follows the point of greatest signal return, and this point will wander from the nose to the tail of the aircraft; however, it will generally remain on the target throughout any type of maneuvers. Unfortunately, in skin track, an added problem exists. If a chase aircraft is in the near vicinity while the maneuvers are being performed, the lock will often jump to the chase.

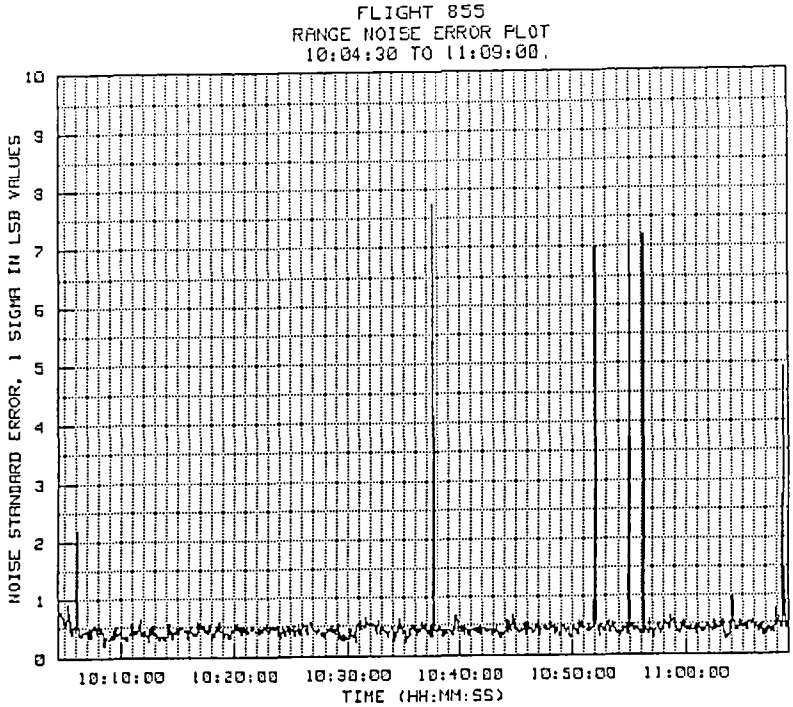

Figure 5-26. Flight 855 range noise plot.

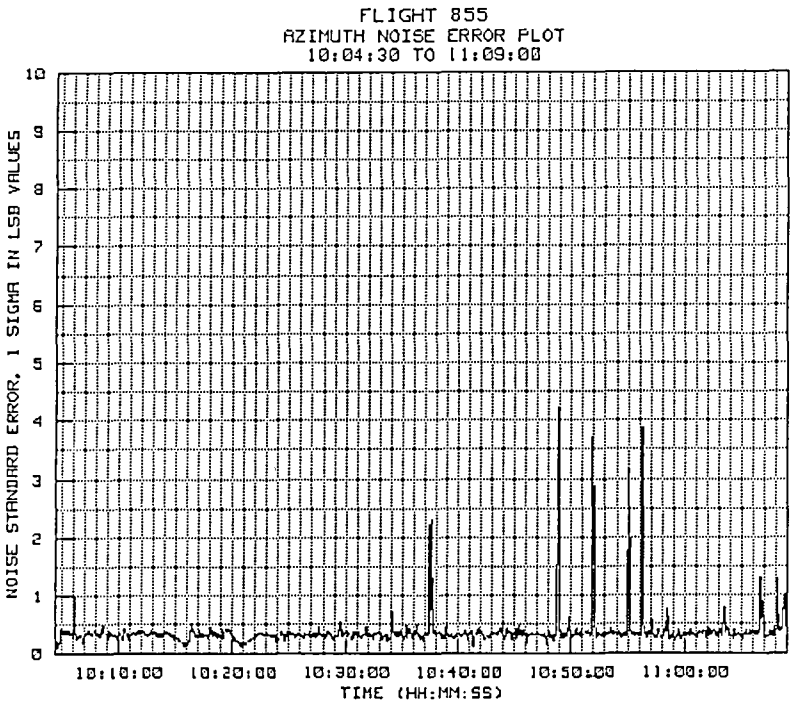

Figure 5-27. Flight 855 azimuth noise plot.

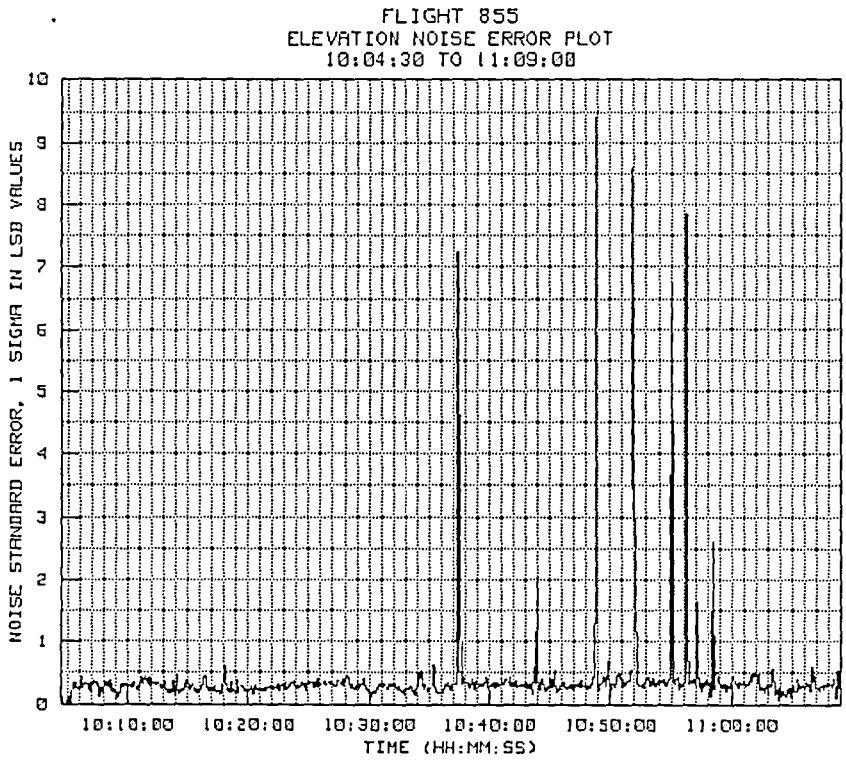

Figure 5-28. Flight 855 elevation noise plot.

5.5 Summary of Results from Flight 855

Flight 855 provided considerably more data for the analysis of the long-range, low-elevation-angle differences present in the data from the previous flights. During test point #3, a 360-degree turn maneuver at a low elevation angle, the radar-derived altitude fell well below the corrected on-board altitude. During test point #4, a north-to-south survey run, the radar-derived altitude was about 120 feet lower than the corrected pressure altitude. Again, on test point #7, a west-to-east survey run, the radar derived altitude was about 60 feet low at the lowest elevation point. At the high elevation points in these runs, the radar-derived and corrected pressure altitudes agreed to within a few feet.

The second finding of consequence from flight 855 was that the beacon tracking mode cannot provide high-quality data during target maneuvers that either shield the beacon from the radar or that provide antenna orientations that create cross polarization effects. During these maneuvers, jumps will occur in both azimuth and elevation. These jumps will degrade the tracking data and often result in an off-target condition. If the radar remains on target throughout the maneuvers, the jumps will degrade the accuracy of the derived altitude data. However, under the same circumstances, the derived Mach number will be totally invalid, and this is to be expected since jumps in either azimuth or elevation that fall below the normal random noise frequencies will pass through the filter and be interpreted as velocity changes. Velocities computed under these circumstances can have error magnitudes of 0.05 Mach or greater.

The wind data from flight 855 substantiates findings from flight 814. Data from radar balloon tracks, rawinsonde measurements, or synoptic analyses may have large variations from the true wind vectors at any given time. Even when wind data is obtained immediately before or after the test flight, large wind differences may still be apparent during in the post-mission analysis of the data. Since winds from radar tracks of rawinsonde balloons correlate reasonably well with data from the rawinsonde measurements, the errors in the wind vectors are probably less due to measurement errors than they are to the variability of the true wind vectors and the spatial offsets between the locations of the measurements and the locations of the test legs.

6.0 AIR DATA CALIBRATION FIGHT 856

Air data calibration flight 856 was flown on 24 August 1984. The pilot was Mr. Ed Schneider, and the aircraft was F-104 tail number 826. Test points for this flight were designed to provide additional information about the low-elevation-angle altitude differences noted on the previous flights, and to provide some comparative data between skin and beacon tracks. Figures 6-1 to 6-3 provide time history plots of the raw range, azimuth, and elevation measurements taken during the course of the flight from 12:33:00 to 13:37:30 PDT.

6.1 Summary of Flight Day Wind and Weather Conditions

The flight day was a classical benign day from the standpoint of pressure-altitude changes, wind speeds, and circulation pattern. Cloud cover consisted of a scattered layer at 20,000 feet AGL. From about 12:55 PDT, some scattered cumulus were observed with bases at 4000 and 10,000 feet; however, no cumulo-nimbus buildups or rain showers were present in the Edwards vicinity.

At flight time, the semi-diurnal surface pressure increase was +52 feet, from a linear interpolation of pressure data between the 1200Z and 2400Z reports on the same day. The applicability of the surface semi-diurnal pressure increase to higher altitudes was tested by synthesizing values for pressure altitude and geometric altitude using the surface pressure and the meteorological analysis of the temperatures aloft. This yielded Z-Hp values which were 23 and 60 feet greater than the linearly interpolated synoptic estimates for 5000 and 10,000 feet. To reflect the semi-diurnal effects, the interpolated Z-Hp profile values were increased by 30 to 50 feet.

At the 850 mb level, the determination of the Z-Hp gradient from an analysis of height contours was somewhat ambiguous. An analysis of surface altimeter settings showed the strongest gradient. Since this flight was intended to obtain low-altitude data within 20 miles of Edwards, the surface analysis results were incorporated into the Z-Hp profile. Measured rates of semi-diurnal Z-Hp change during the flight were nominally -16 feet per hour at the surface.

Psychrometric values and winds aloft for this analysis are provided in table 6-I. Table 6-II contains local synoptic Z-Hp values as well as the adjusted Z-Hp values based on high-angle or short range radar measurements. Figure 6-4 provides plots of both sets of data. Note that at altitudes below about 8000 feet, the synoptic and radar estimates of Z-Hp vary by as much as 50 feet, slightly more than the expected error limits

of 35 feet. Above 8000 feet, the radar estimated values all fall within the expected error limits for the synoptic data.

Because of the need to meet contract deadlines, rawinsonde data, which were available immediately after the flight, were again used to compute both the altitude and Mach number data provided in section 6.2. However, comparisons of winds from the radar balloon track, the rawinsonde measurements, and the synoptic data are provided in the more in-depth wind analysis in section 6.3.

Figures 6-5 shows the takeoff, performed using AIDED EL. The solid line on the plot is the radar derived geometric altitude, the dotted line is the on-board pressure altitude corrected using the radar adjusted Z-Hp values, and the dotted line is the on-board pressure altitude corrected for the synoptic Z-Hp values. No on-board comparison data was provided prior to 12:33:54. The lighted reticule on the TV monitor was used as the reference for the optical track on takeoff. The reticule is periodically adjusted to be as close as possible to the optical aim point on the boresight tower paddle boards. However, very precise adjustments are difficult therefore some small errors may be present even after the calibration. These errors, up to about 6 inches on the paddle boards, could amount to about 5 or 6 feet at the runway range. The radar derived altitude at the point of nose-wheel liftoff (shown by the first event marker at 12:33:47) was computed to be 2294 feet, but video recordings indicated that the center of the reticule at that time was about 1 foot above the canopy, or probably 10 or so feet above the surface of the runway. From that point until just after 12:33:50 the visual track was blocked by a hangar. When again visible, the operator moved the reticule down and onto the approximate location of the aircraft beacon. The main gear broke ground just after 12:33:54 (shown by the second event marker), but the reticule appeared to lag below the true aircraft elevation for a few seconds. Another factor which may contributed to the difference immediately after takeoff may have been the very nose high attitude of the aircraft at that time.

The first airborne Z-Hp check point was taken at time 12:51:30 when the elevation angle was nearly 50 degrees. At this point, the differential for a pressure altitude of 12,000 feet was approximately 555 feet as shown in figure 6-6. The synoptic Z-Hp estimate of 549 feet for this altitude agreed well with radar and on-board comparisons. The next check was performed using altitude data at 13:02:00 when the elevation angle was approximately 25 degrees and the pressure altitude was 25,000 feet. At this point, the difference between the radar-derived geometric altitude and the on-board pressure altitude was 1160 feet as shown in figure 6-7. Again, the Z-Hp

value from the synoptic estimate was within about 23 feet of the radar derived value. Also note that the on-board pressure altitude plot in figure 6-7 shows some erratic behavior at about 13:01:07 and 13:01:35. The cause of the jumps at these times was not determined.

The third check point used was at 13:31:10 when the elevation angle was only 6 degrees, but when the range was just slightly over 4 miles. The pressure altitude at this time was about 5180 feet and the difference between the geometric and unadjusted pressure altitude was about 105 feet. The synoptic estimate of Z-Hp for this same pressre altitude was about 164 feet. The difference, 59 feet, amounts to almost 30 LSB values, indicating a significant error in the lower elevation synoptic Z-Hp estimate, since about 5 minutes later the radar-derived geometric altitude on touchdown showed no appreciable difference from surveyed information.

Figure 6-9 shows the final approach and touchdown. During the approach, the track point remained almost exactly on the location of the beacon until about 13:36:33 when it started to go about 5 to 10 feet low as the aircraft was flared. By about 13:36:38 it was brought back on and held steady on the underside of the fuselage during touchdown (13:36:41). Video recording was stopped after the aircraft passed behind behind a hangar. At touchdown, the radar-derived altitude was 2283 feet, approximately the correct value as estimated from NRP 4.

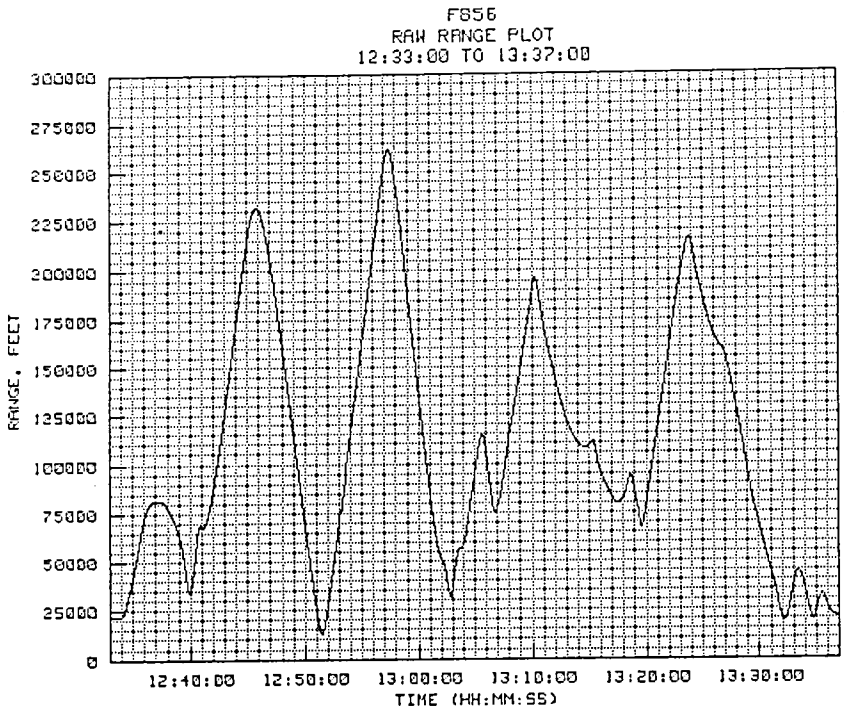

Figure 6-1. Flight 856 radar-derived slant range.

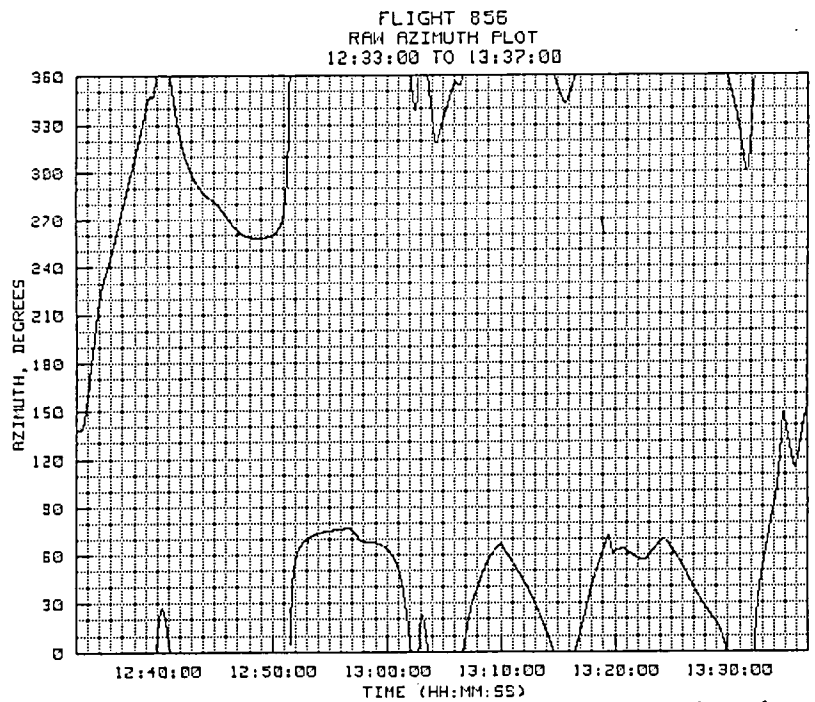

Figure 6-2. Flight 856 radar-derived azimuth angle.

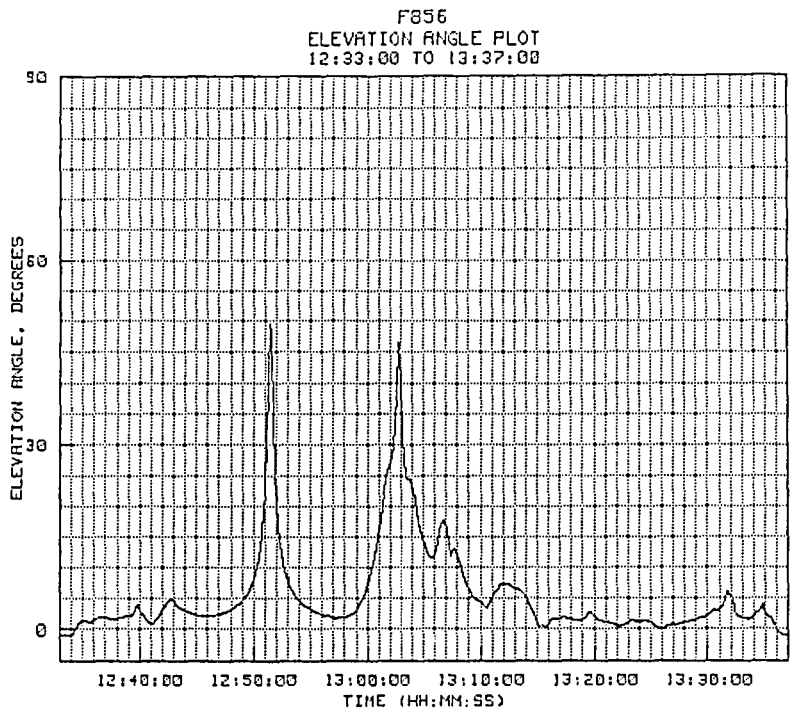

Figure 6-3. Flight 856 radar-derived elevation angle.

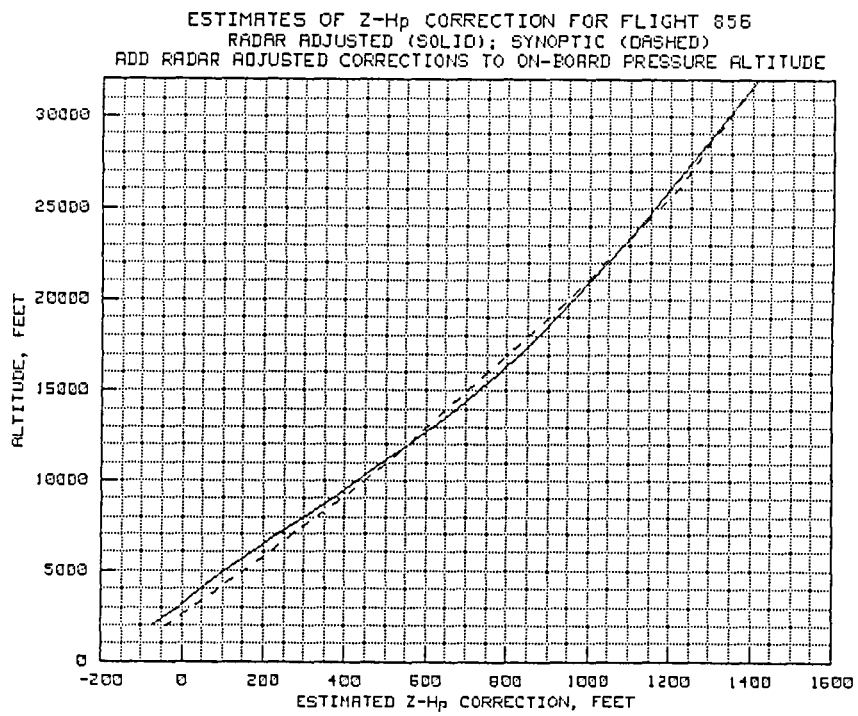

Figure 6-4. Flight 856 synoptic and radar derived Z-Hp plots.

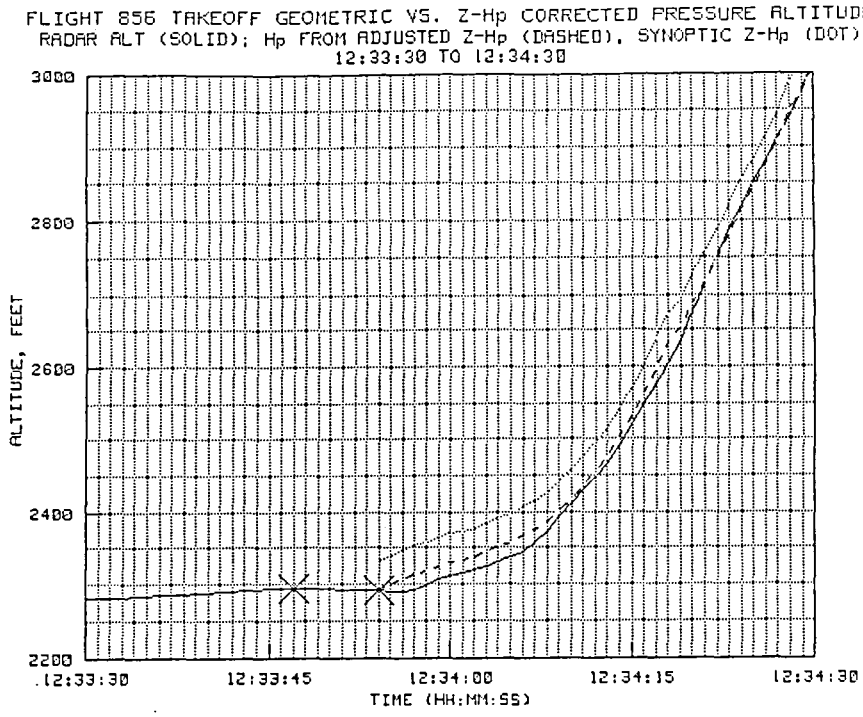

Figure 6-5. Flight 856 geometric altitude on takeoff.

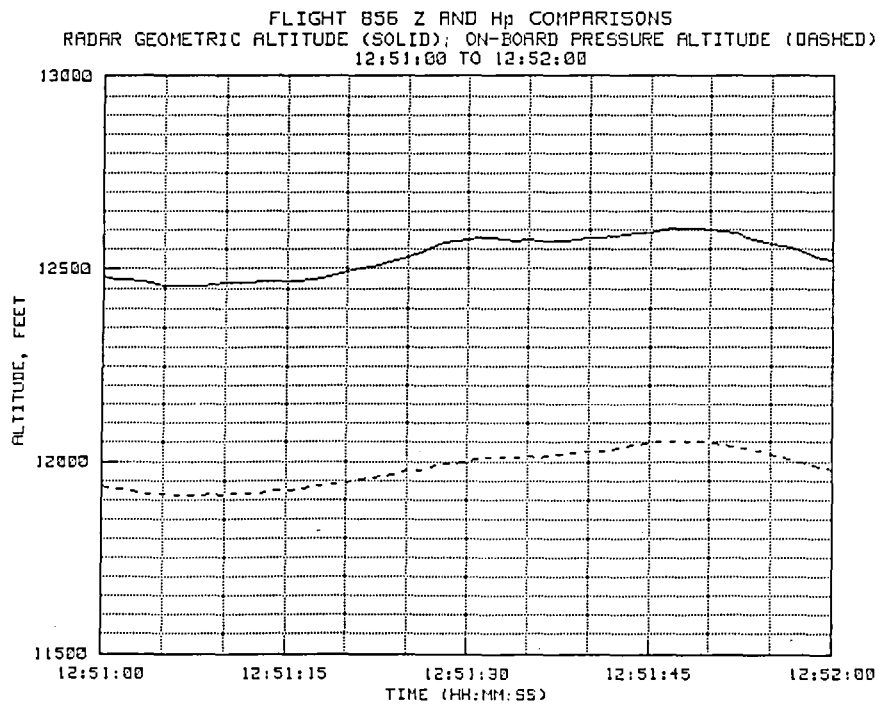

Figure 6-6. Flight 856 Z and Hp comparison at 12,000 feet.

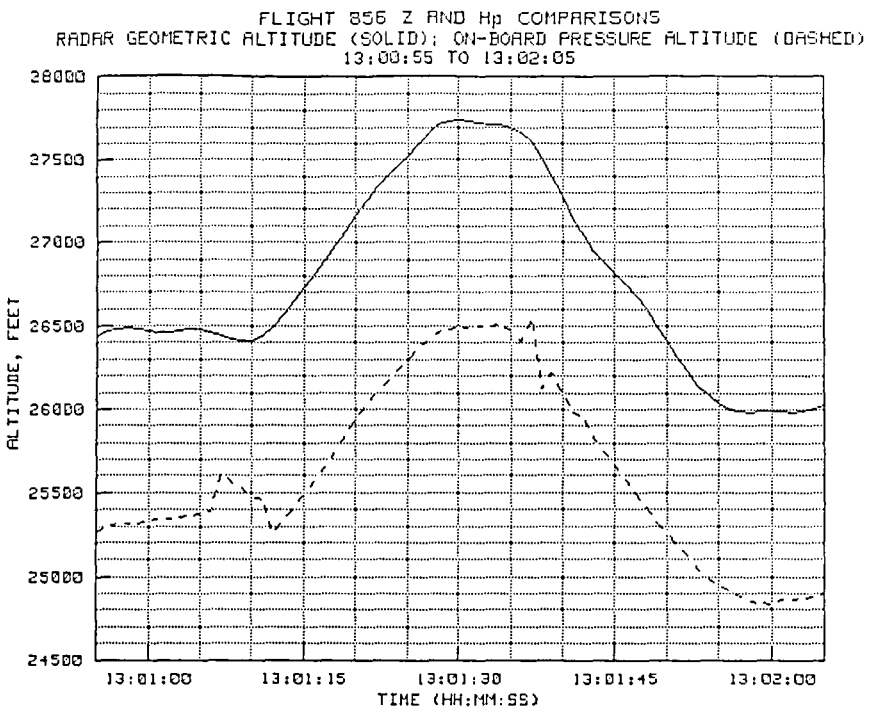

Figure 6-7. Flight 856 Z and Hp comparison at 26,000 feet.

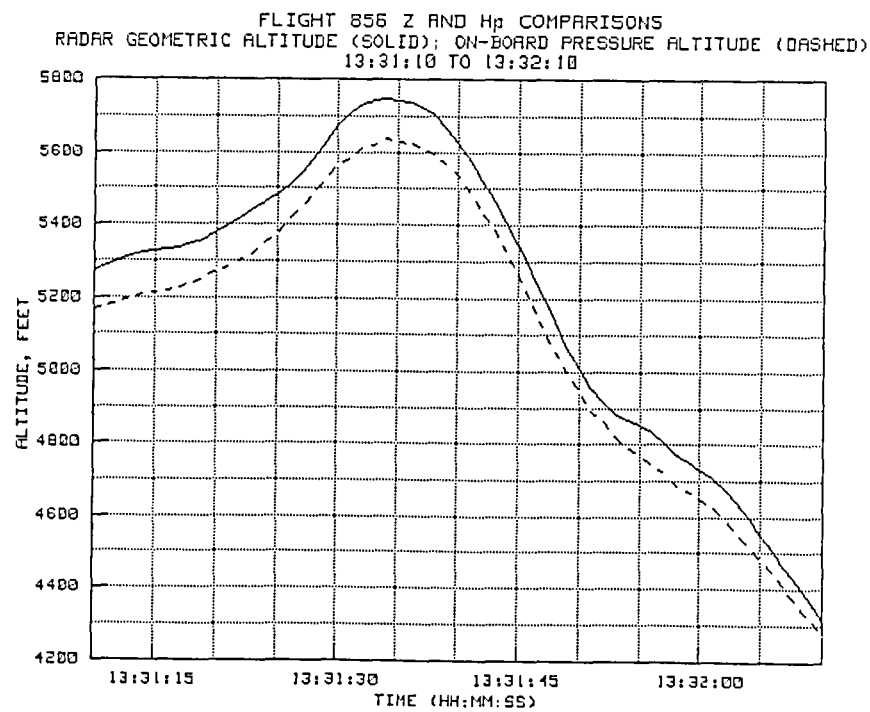

Figure 6-8. Flight 856 Z and Hp comparison at 4500 to 5500 feet.

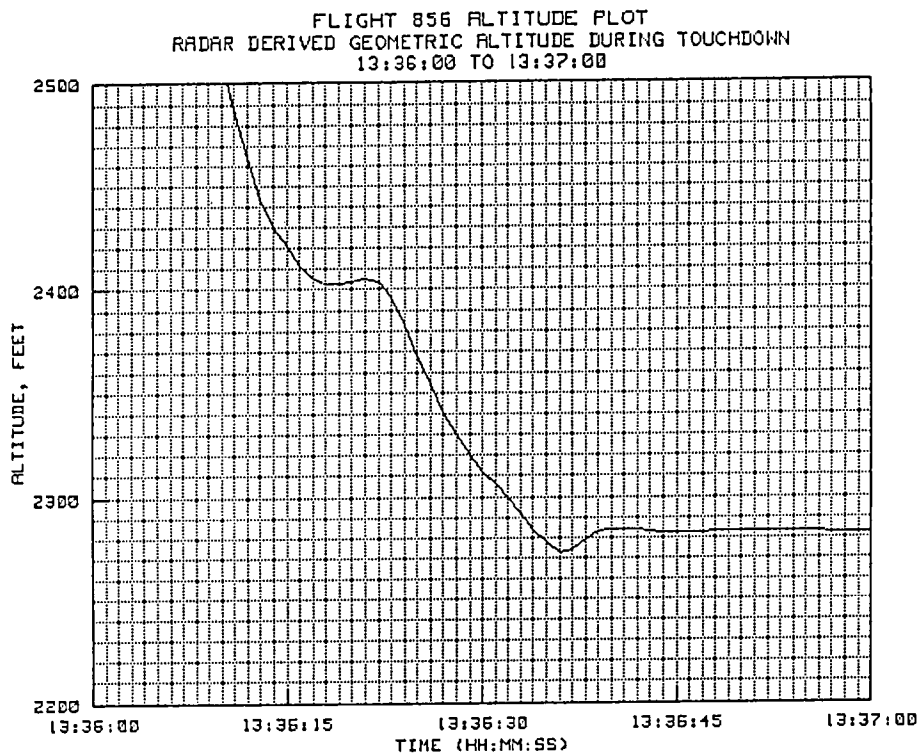

Figure 6-9. Flight 856 geometric altitude on landing.

TABLE 6-I. FLIGHT 856 WEATHER DATA

WEATHER DATA FOR FLIGHT 856

ALTITUDE (FT)	TEMPERATURE (DEG C)	DEW POINT (DEG C)	PRESSURE (MB)	N X 10E6	WIND (DEG/KTS)
2300	34.6	2.2	929.35	262.9	240.0/ 16.0
3000	32.3	2.5	909.85	260.8	224.0/ 16.0
4000	28.9	1.1	879.35	253.3	214.0/ 15.0
5000	26.1	-.3	849.57	245.6	207.0/ 14.0
6000	23.2	-2.1	820.49	237.4	227.0/ 13.0
7000	20.0	-3.2	792.13	230.9	230.0/ 11.0
8000	16.9	-3.6	764.45	225.6	218.0/ 13.0
9000	14.5	-3.4	737.49	220.7	202.0/ 15.0
10000	13.4	-8.6	711.35	207.4	218.0/ 17.0
11000	10.3	-8.1	685.94	203.5	228.0/ 17.0
12000	7.7	-9.0	661.18	197.6	238.0/ 16.0
13000	5.4	-10.1	637.12	191.4	240.0/ 16.0
14000	2.2	-11.2	613.69	186.0	243.0/ 17.0
15000	-.3	-13.9	590.92	178.7	244.0/ 17.0
16000	-2.4	-20.0	568.78	169.5	224.0/ 15.0
17000	-4.0	-23.3	547.34	162.7	198.0/ 17.0
18000	-4.2	-25.7	526.63	155.9	178.0/ 20.0
19000	-6.8	-27.6	506.62	151.0	164.0/ 21.0
20000	-9.3	-29.3	487.18	146.2	171.0/ 19.0
21000	-12.2	-32.0	468.28	141.6	182.0/ 19.0
22000	-14.5	-33.6	449.95	137.0	187.0/ 18.0
23000	-16.7	-35.0	432.18	132.6	193.0/ 18.0
24000	-18.7	-36.5	415.00	128.2	197.0/ 18.0
25000	-21.1	-37.9	398.34	124.0	200.0/ 19.0
26000	-23.8	-39.8	382.20	120.1	202.0/ 20.0
27000	-26.9	-41.9	366.54	116.5	202.0/ 23.0
28000	-29.7	-43.7	351.32	112.8	203.0/ 23.0
29000	-32.2	-45.3	336.60	109.1	203.0/ 23.0
30000	-34.9	-46.9	322.33	105.6	203.0/ 23.0

TABLE 6-II. FLIGHT 856 Z-Hp DATA

Synoptic Z-Hp Data for Flight 856

Altitude (feet)	Syn. Z-Hp (feet)	Radar Z-Hp (feet)	Change in Z-Hp (feet/n.mi.)	Direction of decrease
32,000	+1410	+1412		
31,000	+1378	+1378	0.85	308
30,000	+1347	+1342	0.80	308
29,000	+1313	+1309	0.75	305
28,000	+1282	+1272	0.68	300
27,000	+1248	+1236	0.62	295
26,000	+1218	+1200	0.55	298
25,000	+1183	+1160	0.49	300
24,000	+1125	+1122	0.45	296
23,000	+1081	+1083	0.42	292
22,000	+1039	+1045	0.39	288
21,000	+ 994	+1004	0.37	284
20,000	+ 950	+ 963	0.36	280
19,000	+ 906	+ 921	0.35	280
18,000	+ 850	+ 879	0.35	295
17,000	+ 799	+ 830	0.34	300
16,000	+ 751	+ 784	0.34	305
15,000	+ 700	+ 730	0.33	310
14,000	+ 650	+ 675	0.32	315
13,000	+ 600	+ 615	0.32	310
12,000	+ 549	+ 555	0.31	306
11,000	+ 501	+ 490	0.31	303
10,000	+ 450	+ 430	0.30	300
9,000	+ 387	+ 370	0.31	305
8,000	+ 329	+ 300	0.32	310
7,000	+ 271	+ 237	0.35	330
6,000	+ 213	+ 171	0.40	350
5,000	+ 155	+ 104	0.44	360
4,000	+ 90	+ 45	0.65	005
3,000	+ 28	- 12	0.90	020
2,000	- 35	- 75	1.30	035

Add Z-Hp values to pressure altitude to obtain geometric altitude

6.2 Analysis of Test Points

During flight #856, fifteen test points were successfully completed. The starting and ending times for the data plots covering each of the test points are given below, along with a brief description of the tasks which were performed. Again, since several of the test points were performed concurrently, the test point numbers used in this analysis do not agree with the pilot knee card numbers, but are instead based on a successive numbering of the time segments containing one or more of the original data points.

1. 12:34:00 to 12:39:00 - Takeoff and initiate low-level arc.
2. 12:41:00 to 12:43:00 - 0.9 Mach climb to 12,000 feet.
3. 12:43:00 to 12:47:45 - Westbound set up for survey leg.
4. 12:46:30 to 12:57:00 - 0.68 Mach survey run at 12,000 feet.
5. 12:56:42 to 12:58:00 - Two 90-degree, standard-rate turns.
6. 12:58:00 to 13:01:30 - 0.9 Mach climb to 25,000.
7. 13:00:45 to 13:02:15 - Level acceleration and deceleration.
8. 13:02:00 to 13:04:00 - 2-g level turn and stable point.
9. 13:04:00 to 13:05:15 - 3-g 90-degree turns and stable point.
10. 13:06:45 to 13:08:00 - Push/pull, acceleration and deceleration.
11. 13:11:45 to 13:15:30 - Constant 0.6 Mach descent.
12. 13:21:15 to 13:23:40 - Ridge survey at constant 0.6 Mach.
13. 13:24:30 to 13:26:30 - Valley survey at constant 0.6 Mach.
14. 13:29:30 to 13:31:30 - North to west low level arc.
15. 13:31:45 to 13:32:30 - Constant 0.6 Mach descent to base.

The results of the analysis of specific test points are provided in sections 6.2.1 through 6.2.15.

6.2.1 Test Point #1

The time history plots for test point #1 are provided in figures 6-10(a) to 6-10(f). This time segment includes a short leg from just after liftoff to a point over Rosamond Lake, after which an arcing turn was commenced to the north. The radius of the turn varied from 22,000 feet (3.62 n.mi.) at the start to 81,000 feet (13.33 n.mi.) at 12:37:15, and then back down to 64,260 feet (10.58 n.mi.) at the end of the run. The pilot accelerated from 0.38 Mach after takeoff up to 0.6 Mach at the start of the arc. Mach 0.6 was then held throughout the arcing maneuver. Altitude was about 4000 feet at the start of the arc, increasing to 5500 feet about 12:36:45, and then dropping back to 5200 to 5300 feet from 12:37:50 until the completion of the test point. The elevation angle at the start of the arc was 1.22 degrees, increasing to about 2.22 degrees at the completion of the arc.

Throughout the maneuver, good agreement was obtained between the radar-derived geometric altitude and the on-board pressure altitude corrected using the solid curve in figure 6-4. The largest differences observed were on the order of about 10 to 20 feet for the time from about 12:37:00 until the end of the test point.

The radar-derived Mach numbers also agreed well with the on-board data. All of the short term changes are apparent in the radar-computed Mach number plot. Also note that quite a lot of jitter existed in the on-board measurements, indicative of the usual warm-day, low-level turbulence. Bias differences between the computed and measured Mach numbers ranged up to about 0.01 Mach, depending on heading. This is about the amount expected from the findings on the previous flights.

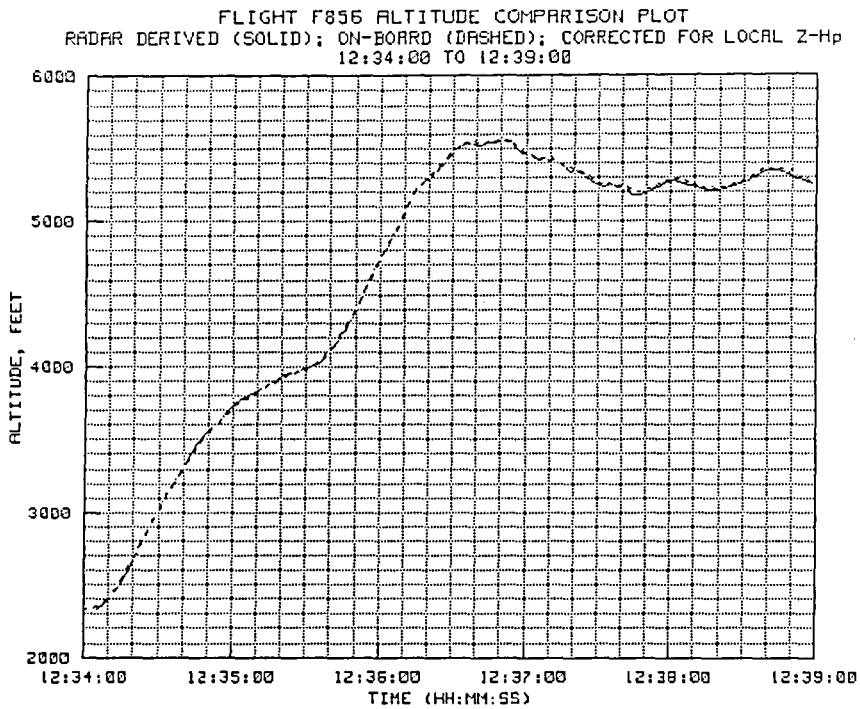

Figure 6-10(a). TP #1 radar-derived and on-board altitude.

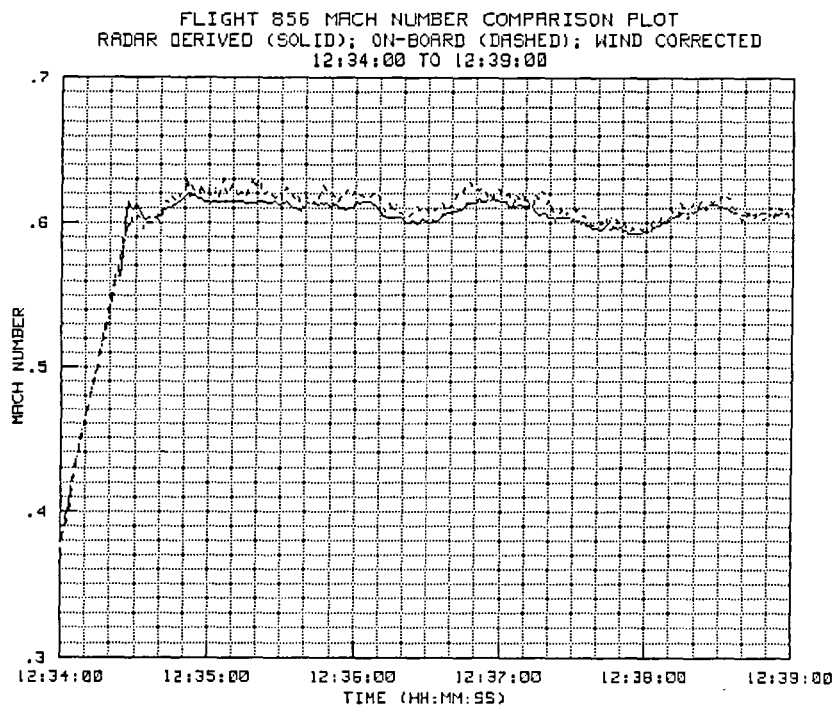

Figure 6-10(b). TP #1 radar-derived and on-board Mach number.

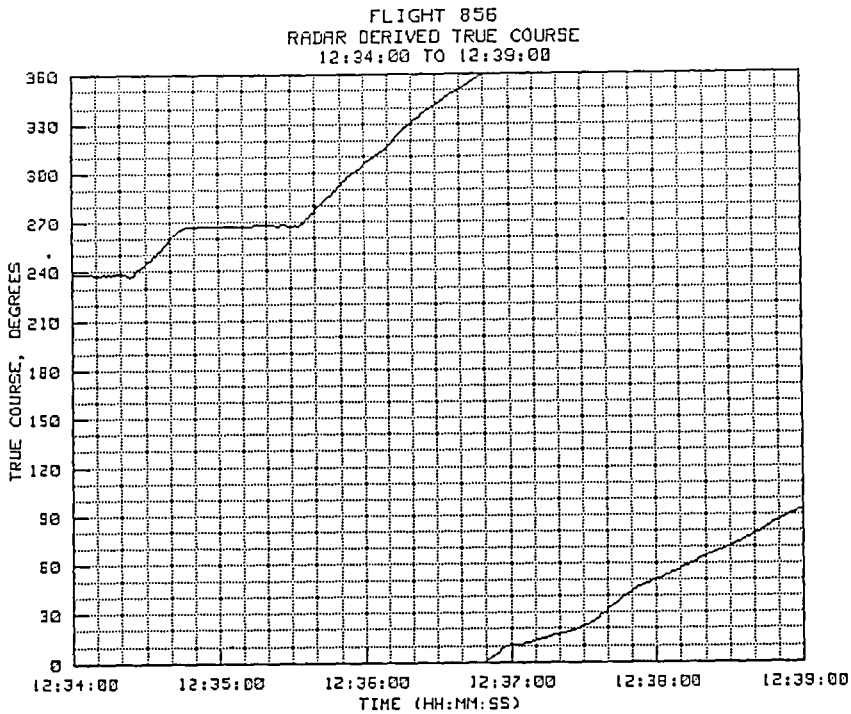

Figure 6-10(c). TP #1 radar-derived true course.

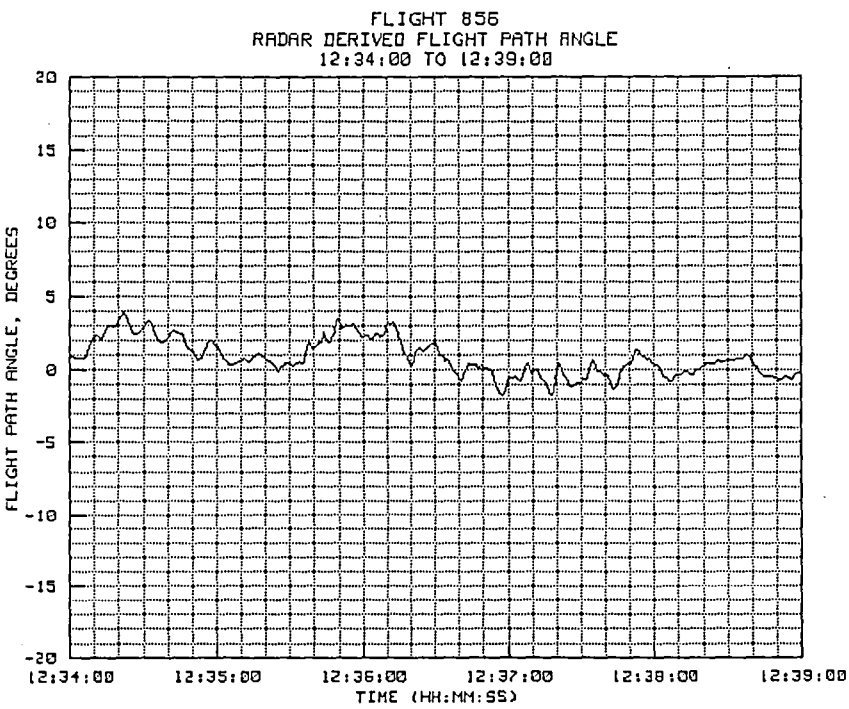

Figure 6-10(d). TP #1 radar-derived flight path angle.

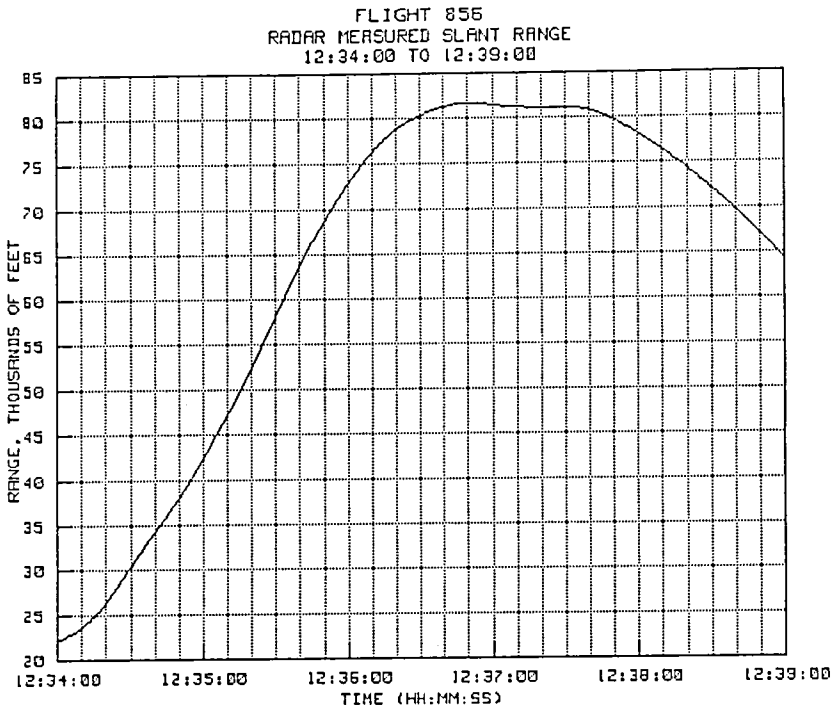

Figure 6-10(e). TP #1 radar-derived slant range.

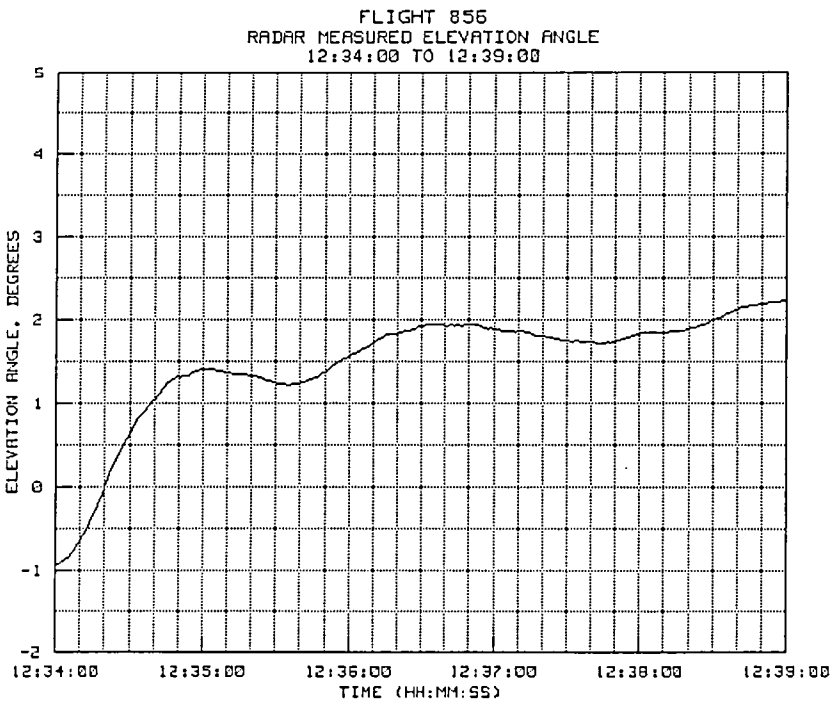

Figure 6-10(f). TP #1 radar-derived elevation angle.

6.2.2 Test Point #2

Time history plots for test point #2 are provided in figures 6-11(a) to 6-11(f). Test point #2 was scheduled as a constant 0.9 Mach climb to 12,000 feet. The climb was made on a westerly heading starting at a slant range of 67,840 feet (11.17 n.mi.) and continuing until level off at an altitude of 13,235 feet and a slant range of 118,990 feet (19.58 n.mi.). Elevation angle at the start of the climb was 0.79 degree, increasing to about 4.93 degrees at level off. Some slight differences between the radar-derived altitude and the pressure altitude can be observed on the plot; however these fall well within the normal range of Z-Hp uncertainty.

The Mach number plot for the climb period showed fairly good agreement at the lower elevations, but developed a significant bias as the aircraft passed about 6000 feet. The bias increased to about 0.01 to 0.02 Mach during the climb and remained about the same until level off. Since only slight heading changes were made during the climb, the bias could be due to differences between the wind vectors from the rawinsonde data and the true winds present at the higher altitudes along the path of the climb. However, note that the Mach number bias started gradually and increased to a maximum in a way that very closely matches the pattern shown in the flight path angle plot (Fig. 6-11(d)). Note that at the same time as the Mach number bias started to increase, the flight path angle started to increase. During the time the flight path angle remained constant at about 6 to 7 degrees, the Mach number bias remained constant at about 0.01 to 0.02 Mach. Then, at level off, when the flight path angle went to zero, most of the Mach number bias disappeared.

This would suggest that the Mach number bias during this climb could have been related to changes in the on-board Mach number measurements caused by the higher angle of attack during the time from about 12:41:40 until 12:42:53.

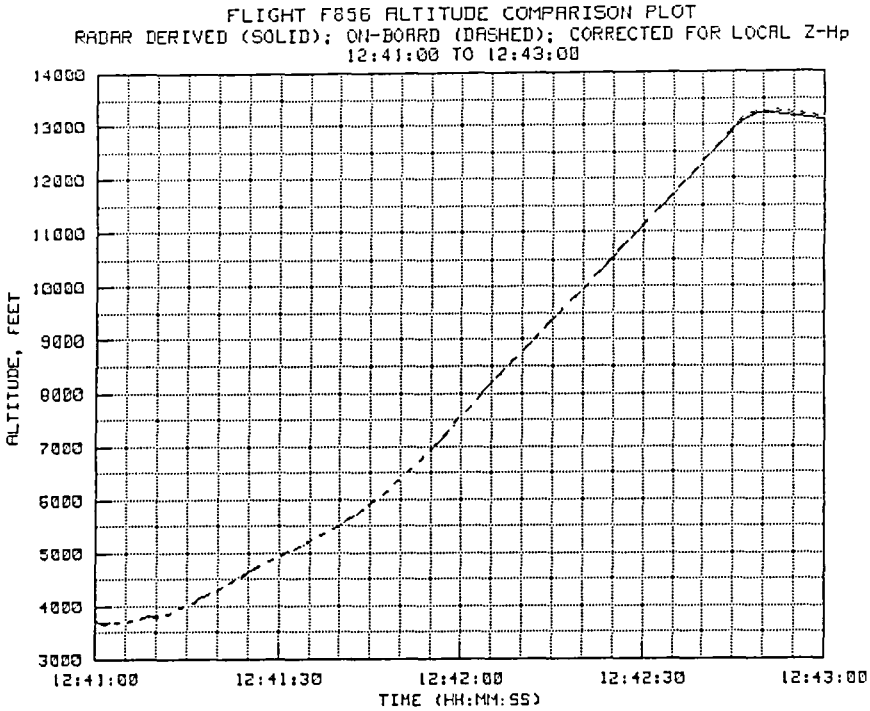

Figure 6-11(a). TP #2 radar-derived and on-board altitude.

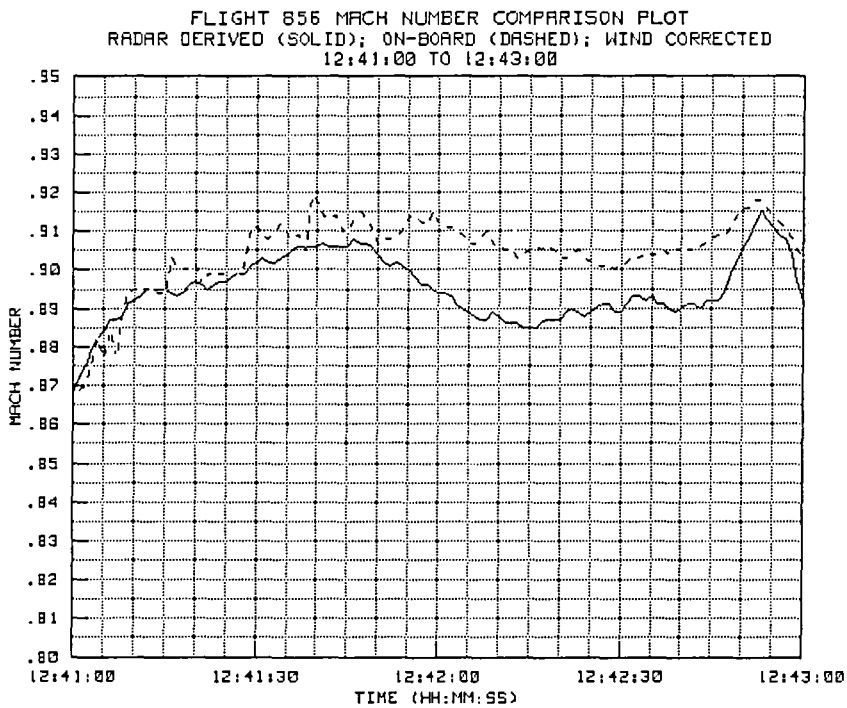

Figure 6-11(b). TP #2 radar-derived and on-board Mach number.

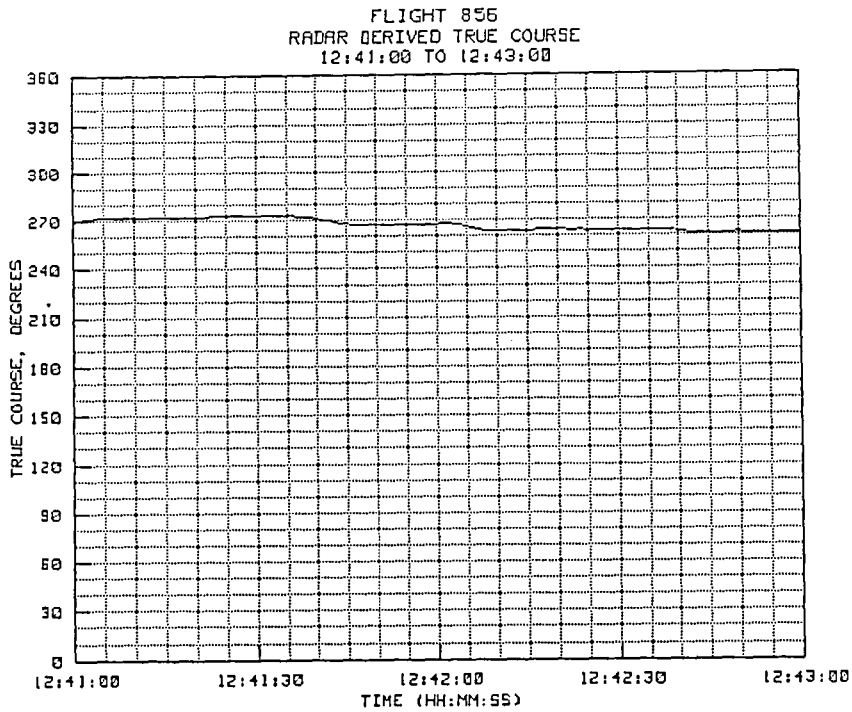

Figure 6-11(c). TP #2 radar-derived true course.

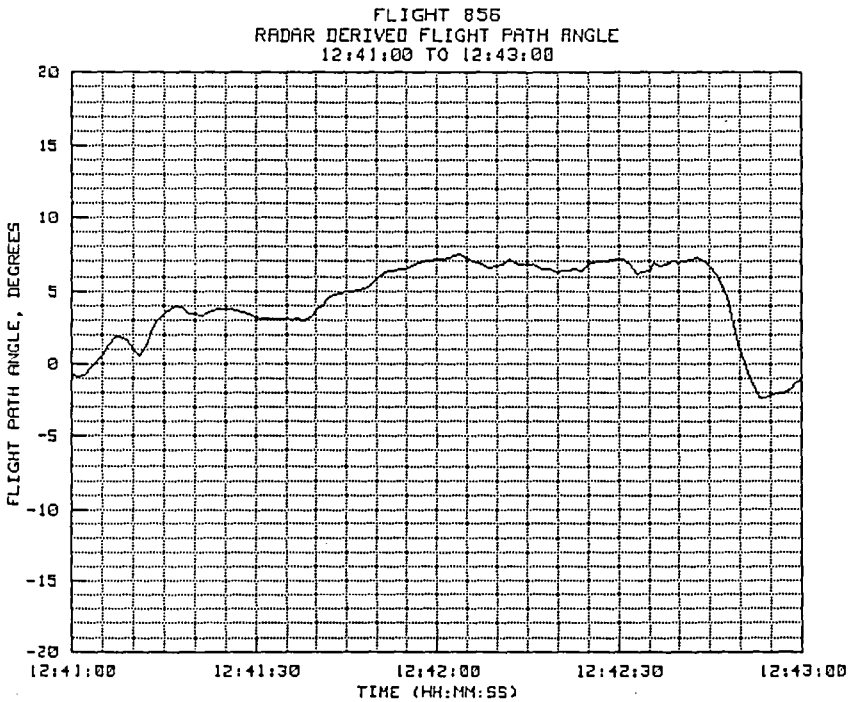

Figure 6-11(d). TP #2 radar-derived flight path angle.

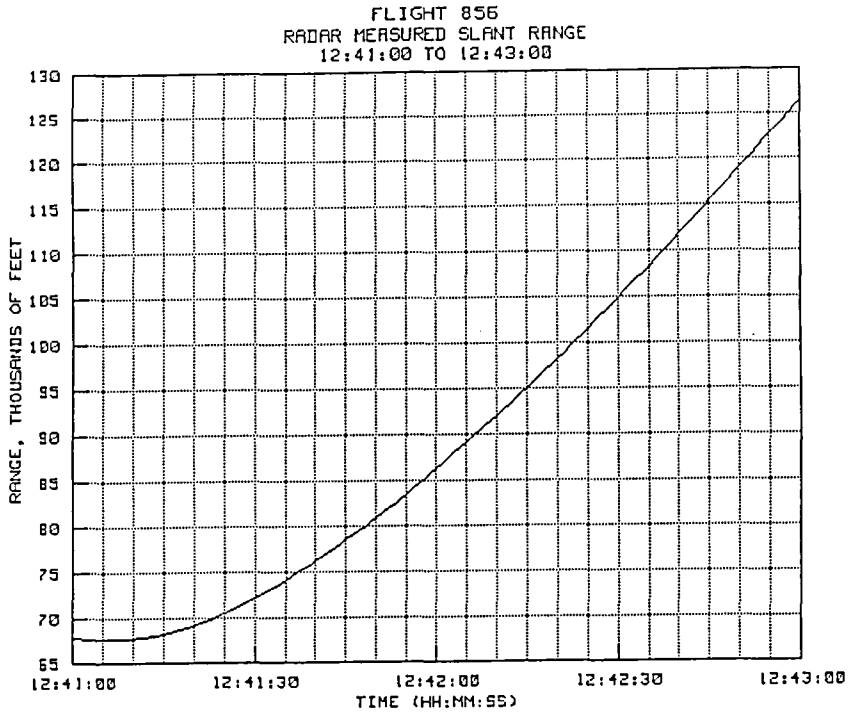

Figure 6-11(e). TP #2 radar-derived slant range.

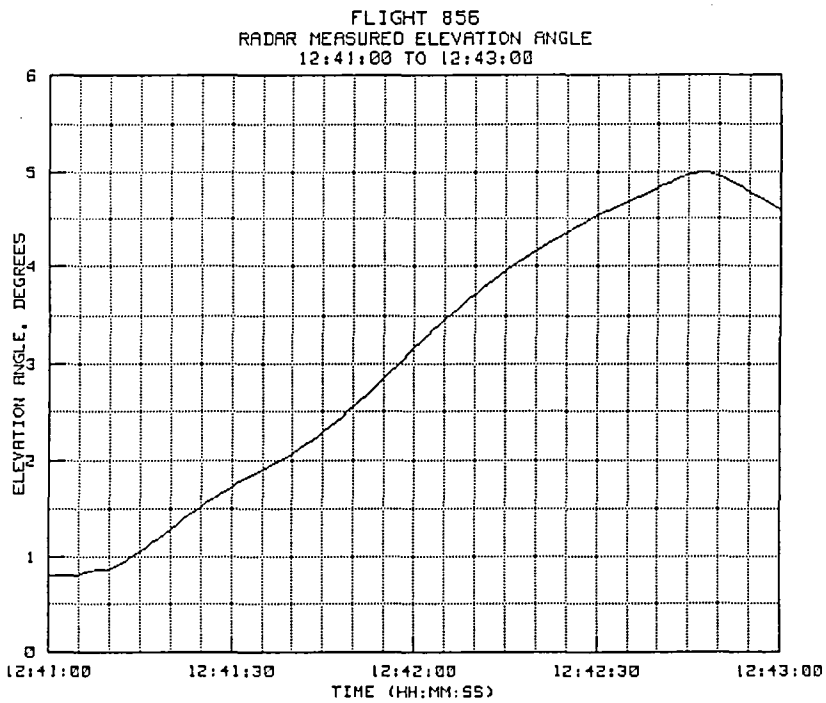

Figure 6-11(f). TP #2 radar-derived elevation angle.

6.2.3 Test Point #3

Time history plots for this test point are provided in figures 6-12(a) to 6-12(f). This test point, the outbound leg used to position the aircraft for the first survey run, was not a scheduled test point; however, since good data was available for the leg, it was analyzed as test point #3. During the time shown in the plots, the pilot adjusted his altitude down to 12,500 feet and continued outbound on a westerly course until approximately 12:45:00 when a left turn was commenced. The left turn was continued around to an easterly heading to align the aircraft along the direction of the supersonic corridor. The slant range at the start of this leg was 126,470 feet (20.81 n.mi.) and the elevation angle was 4.56 degrees. The maximum slant range of about 231,750 feet (38.14 n.mi.) occurred about half way through the turn at 12:45:49. The elevation angle at the maximum slant range point was 2.065 degrees.

The same low-elevation-angle, long-slant-range anomaly as seen previously is clearly visible in the altitude plot. Note that at approximately 12:45:49, the difference between the geometric and pressure-derived altitudes increased to about 100 feet and then reduced somewhat as the aircraft turned inbound and the slant range decreased. The amount of the difference is about the same as would be expected from the previous flights. Also note a spike in the altitude plot at around 12:45:58. This was caused by momentary range noise clearly seen as a sharp line on the range noise plot for this flight. This is believed to have been due to a momentary reflection of the beacon return off the chase aircraft outboard of the target.

Another anomaly can also be observed in the altitude data for the turning portion of the run. Note that the on-board altitude data experienced several jumps between 12:43:00 and 12:44:00. While these were at first thought to be due to a momentary data loss in the on-board system, a more careful analysis indicated the contrary. In fact, this appears to be precisely the same type of bias jump in the on-board pressure altitude data as was observed on test point #4 during flight 811. Note that the data does not drop out but instead jumps back and forth from the current value to a value that is about 300 feet lower. Also note that the same general altitude pattern is present in the upper plot as in the lower plot. This is additional verification that a problem does exist in the airborne transducer or in the airborne data acquisition system; however, it has no impact on this analysis since the anomaly only rarely occurred, and was readily evident when it did occur.

The Mach plot for this test point shows the same typical patterns as previously noted. Short term movements in the on-board Mach number are reflected in the radar-derived Mach number; however some bias is still present. Note that the range noise that caused the spike in the altitude plot at about 12:45:55 also caused a complete loss of Mach data. The 20-pps raw range data for this time period were analyzed and found to have definite noise oscillation of about 50 LSB values (292 feet), spread over about 12 or 13 data samples. This type of anomaly is almost certainly caused by a momentary reflection of the beacon return off the chase aircraft flying about 146 feet (292/2) beyond the tracked aircraft.

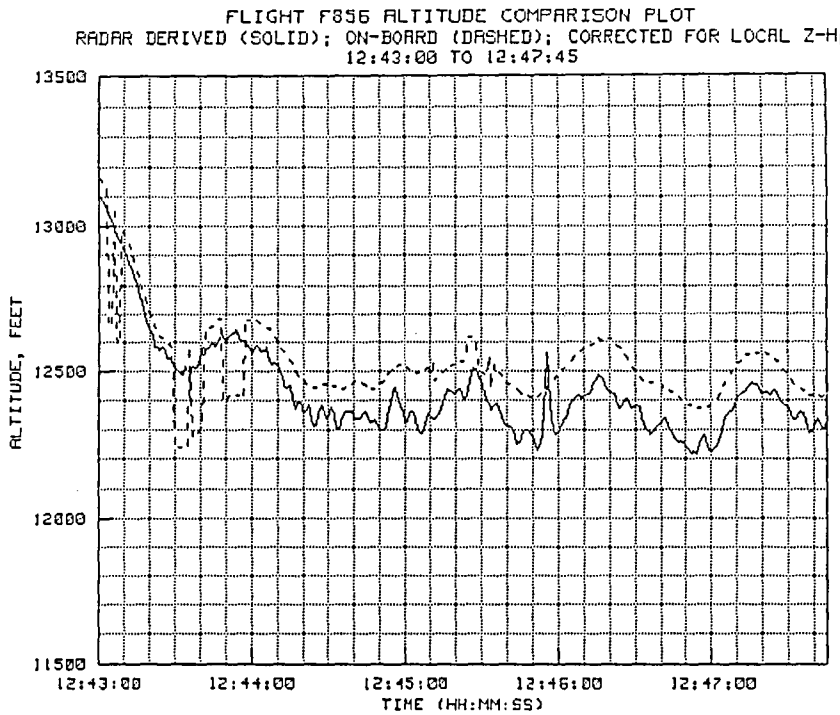

Figure 6-12(a). TP #3 radar-derived and on-board altitude.

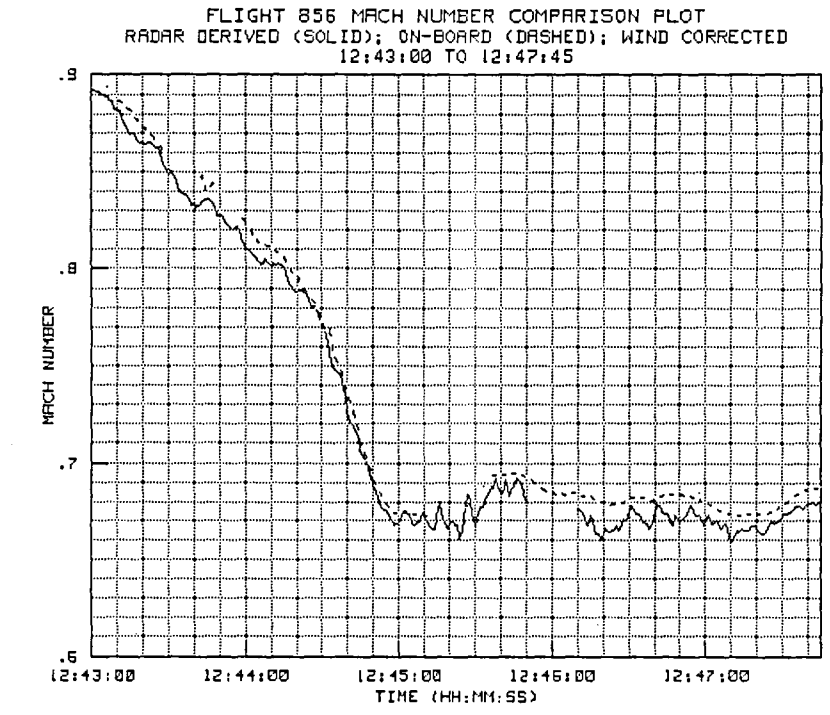

Figure 6-12(b). TP #3 radar-derived and on-board Mach number.

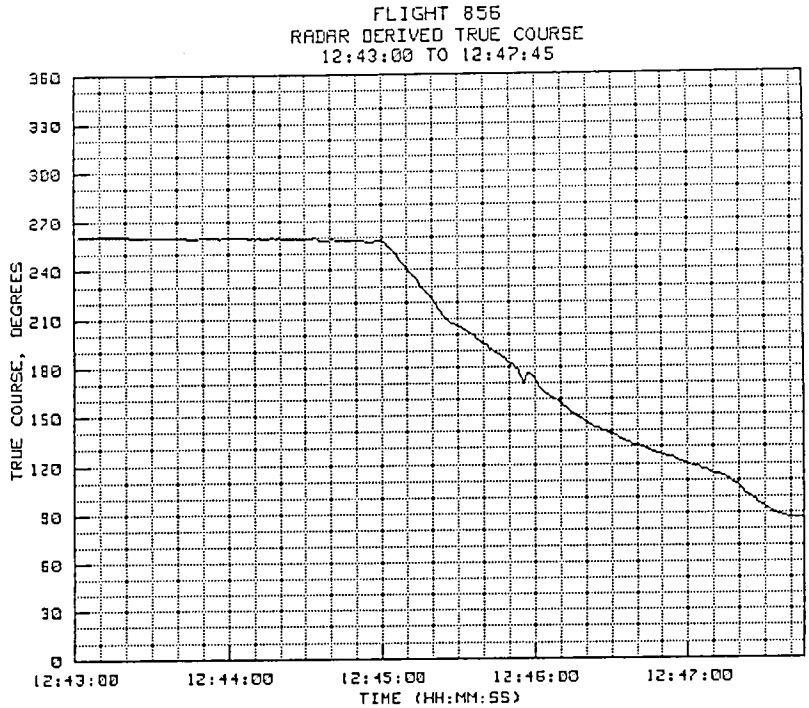

Figure 6-12(c). TP #3 radar-derived true course.

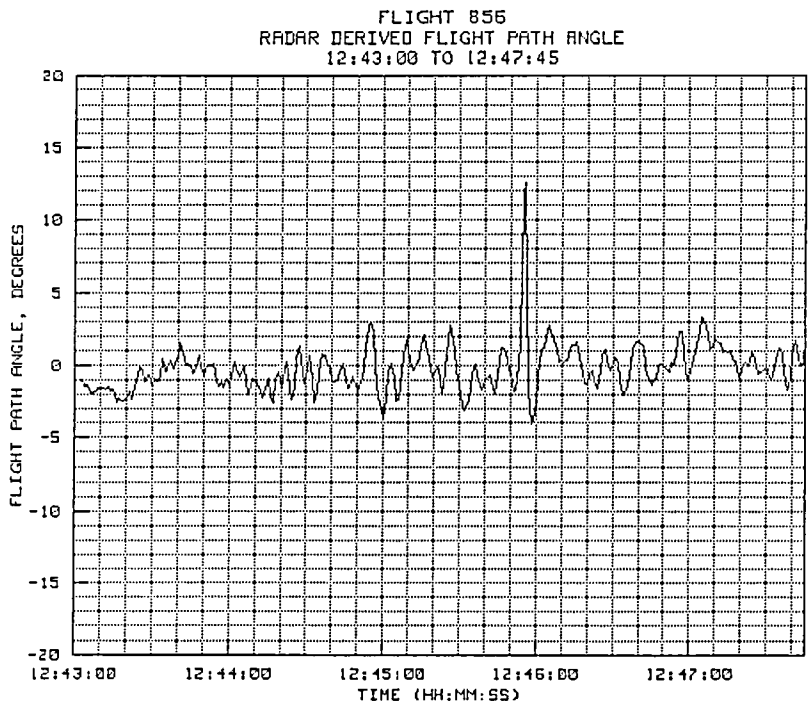

Figure 6-12(d). TP #3 radar-derived flight path angle.

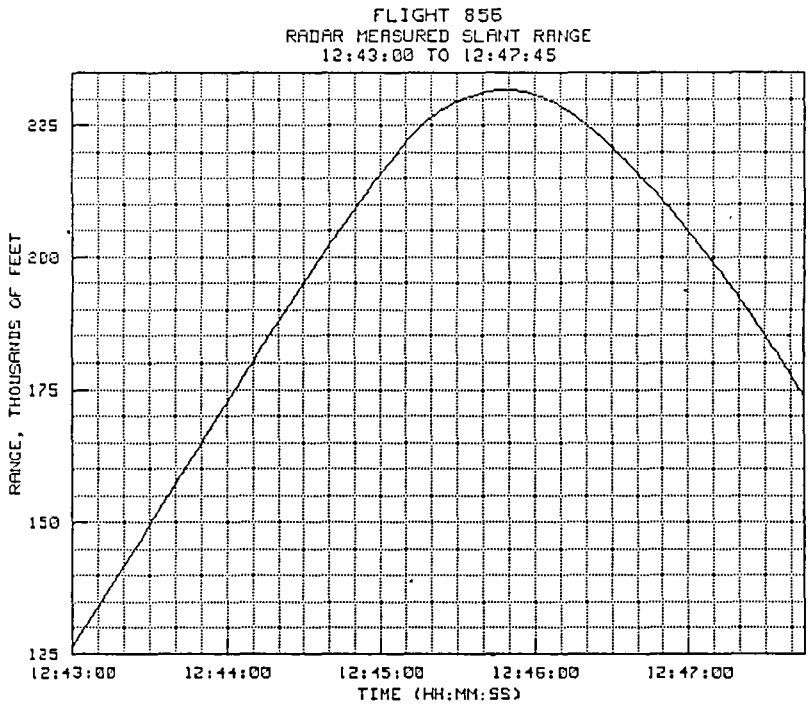

Figure 6-12(e). TP #3 radar-derived slant range.

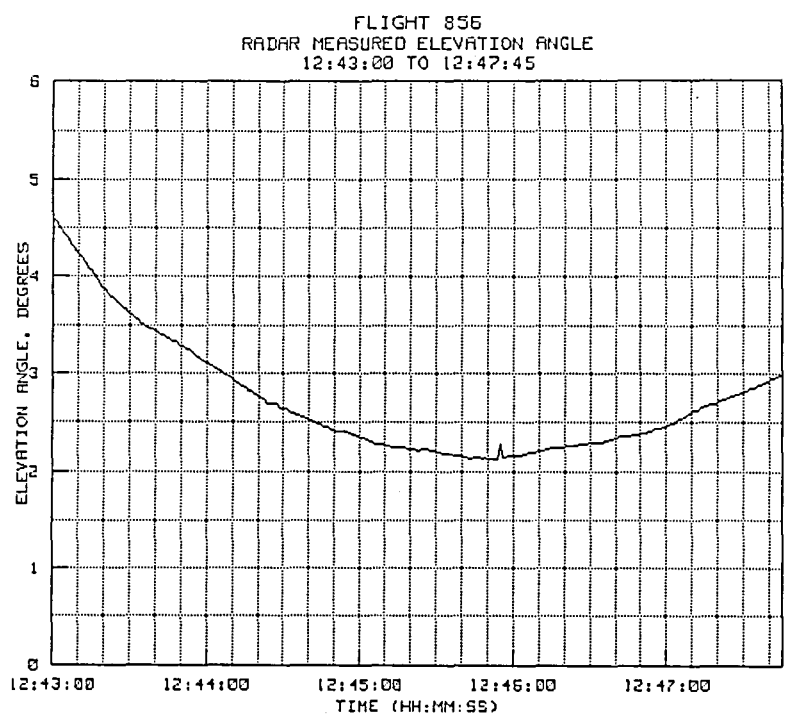

Figure 6-12(f). TP #3 radar-derived elevation angle.

6.2.4 Test Point #4

The time history plots for test point #4 are shown in figures 6-13(a) to 6-13(f). Test point #4 was a survey run flown at a constant 0.68 Mach and at an altitude of 12,500 feet. The slant range at the start of the leg was 221,000 feet (36.37 n.mi.) and the elevation angle was 2.22 degrees. The true course for the run ranged from about 072 degrees to 081 degrees. The high point occurred at 12:51:08 at which time the slant range was 13,008 feet (2.14 n.mi.) and the elevation angle was 49.50 degrees. The slant range at the end of the run was 253,682 feet (41.74 n.mi.) and the elevation angle was about 1.82 degrees. Shortly before 12:49:30, the radar was shifted from the beacon mode to the skin mode, and this point is identified with an event point cross on both the altitude and Mach number plots. Also note that at the switch-over point (beacon to skin), some noise developed in the data, and a short period after the high point was passed, at about 12:53:08, an off target situation occurred. This was believed to be due to a strong momentary skin return from the chase aircraft which caused the radar to transfer lock to a side lobe.

An analysis of the time-history altitude plot indicates the same type of bias difference at the longer-ranges and lower elevation angles. Without considering the effect of the Z-Hp gradient, the difference at the start of the leg was about 88 feet, and near the end of the run, at 12:56:15, it was about 120 feet. The difference at the final time on the plot was not used because a turn was started at 12:56:38 and it was suspected that the change in aspect angle might affect the altitude data. At the near point in the run, the bias difference was essentially zero. No apparent difference can be observed in the altitude plot between the beacon track period and the skin track period. Both have essentially the same type of bias at the longer ranges and lower elevation angles. Taking points equidistant from the near point, and determining the difference in the altitude bias, a Z-Hp gradient along the flight path was computed to be about 0.23 foot per nautical mile of travel, with the pressure altitude moving increasingly above the geometric altitude along the test track. Using this value, the unaccountable difference at the 12:56:15 point would still be on the order of 90 feet.

Also note that there was no appreciable difference in the appearance of the altitude plot at the point where the switch was made from beacon to skin mode, although the gain and bandwidth settings were not yet readjusted. However, the values of computed Mach number shown in figure 6-13(b) did show significantly more noise after the switch-over. During the momentary off-track period, some hasty adjustments were made, and when the relock occurred the Mach data appeared to

have less noise. In any case, when tracking a close-in target in skin mode, the r-f aim point can be seen to move over the full geometric limits of the target; sometimes resting on the fuselage then moving up to the vertical stabilizer. In beacon mode, the r-f aim point remains fairly steady at the location of the beacon antenna on the aircraft. This movement of the aim point in skin mode falls well within the acceptable frequency range of valid pilot and aircraft motions, and it will pass through the filter and manifest itself as variations in the computed Mach number. Therefore, while the large amount of noise in the Mach number plot from the switch-over point until the loss of lock should not be taken as being representative of the amount of Mach number noise to be expected under stabilized skin tracking conditions, it does show the susceptibility of Mach number calculations to even small amounts of measurement noise.

Again notice that a significant amount of Mach number bias existed during the turn at the start of the run until about the same time as the final heading adjustments were completed (about 12:48:40). From that time until the end of the run the radar derived Mach number appeared to match the on-board value, even though the radar-derived Mach was very noisy.

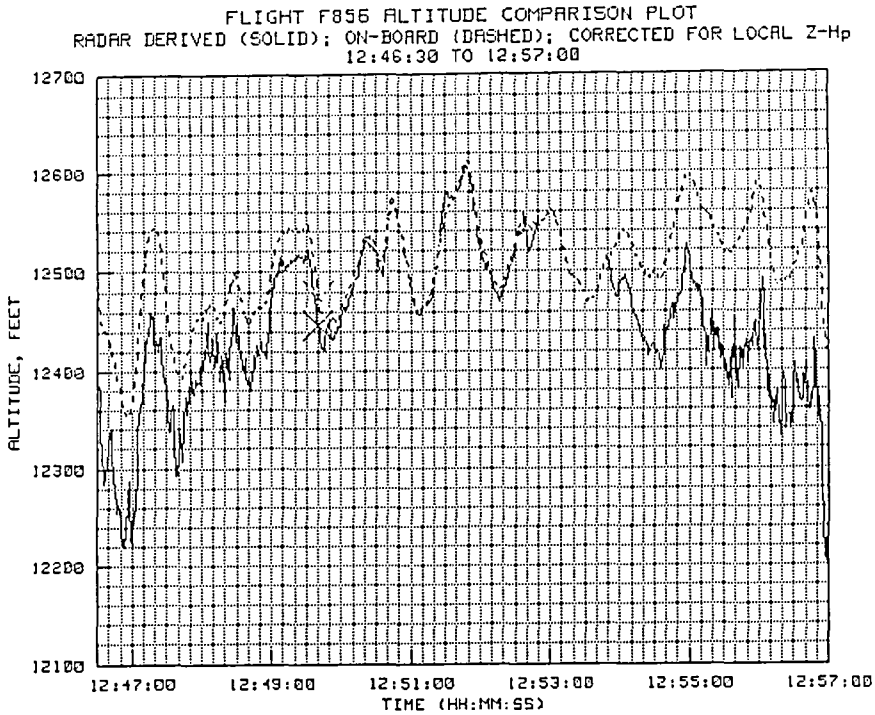

Figure 6-13(a). TP #4 radar-derived and on-board altitude.

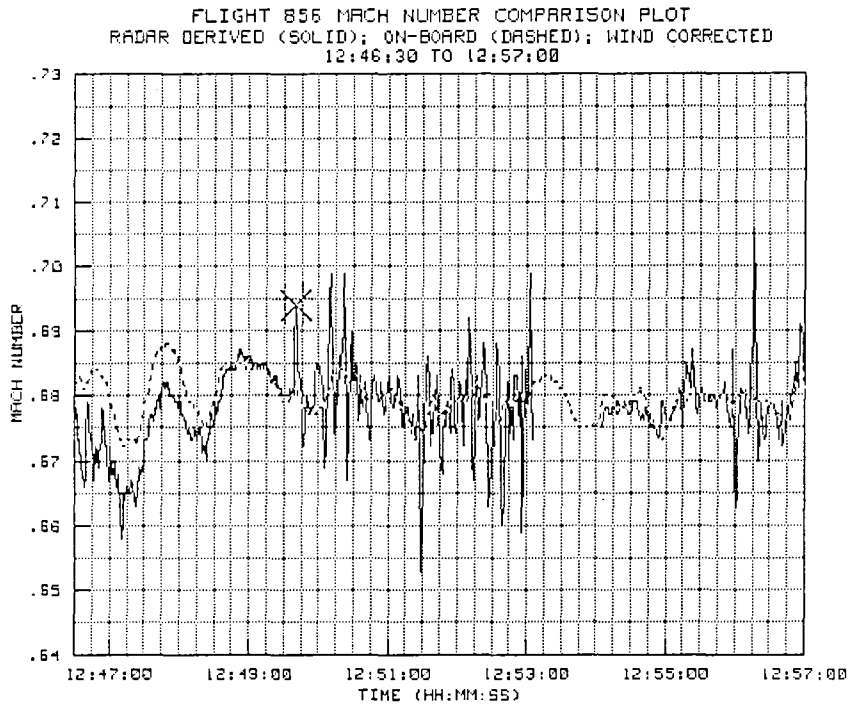

Figure 6-13(b). TP #4 radar-derived and on-board Mach number.

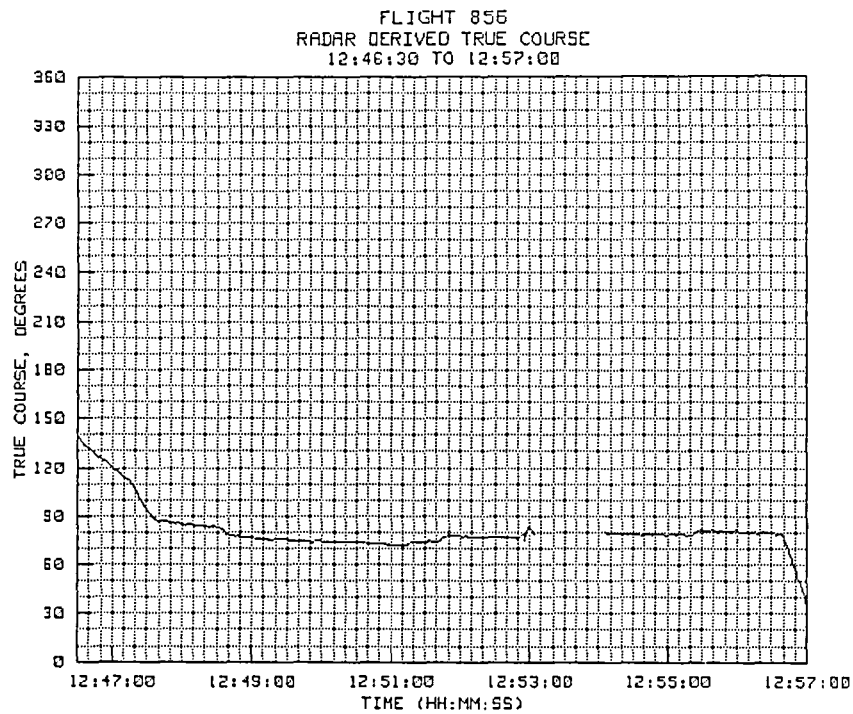

Figure 6-13(c). TP #4 radar-derived true course.

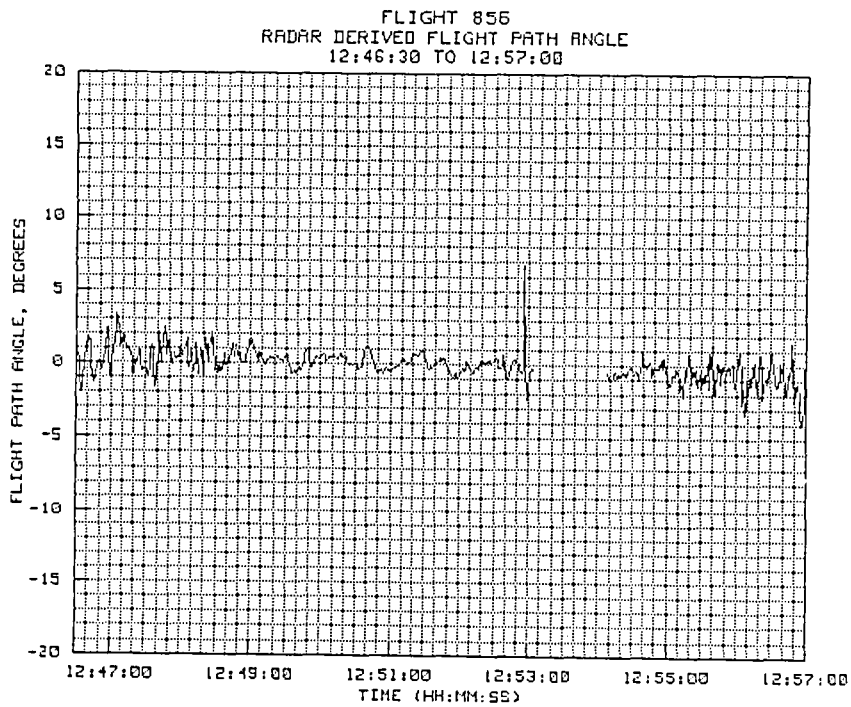

Figure 6-13(d). TP #4 radar-derived flight path angle.

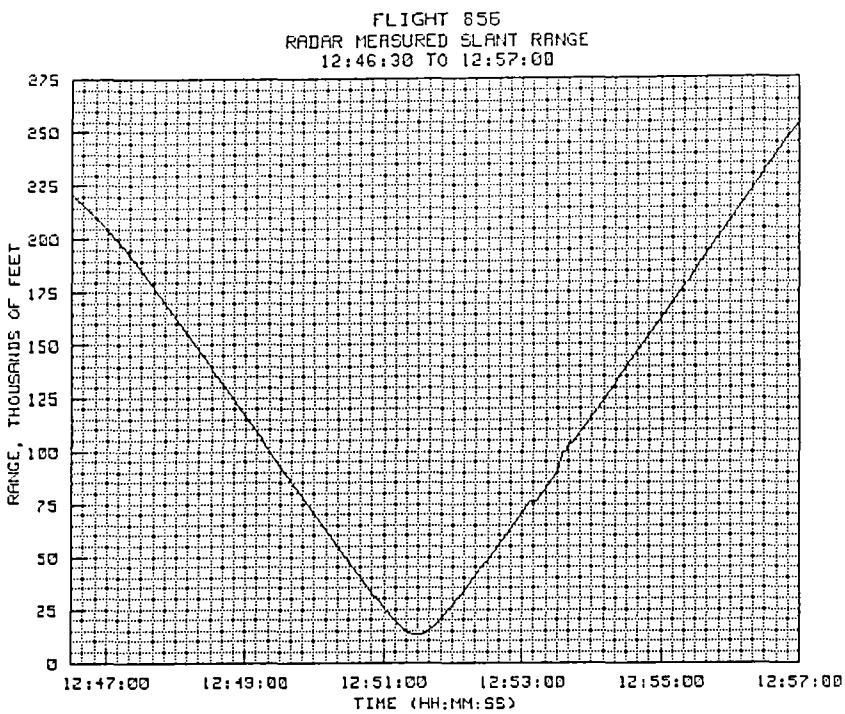

Figure 6-13(e). TP #4 radar-derived slant range.

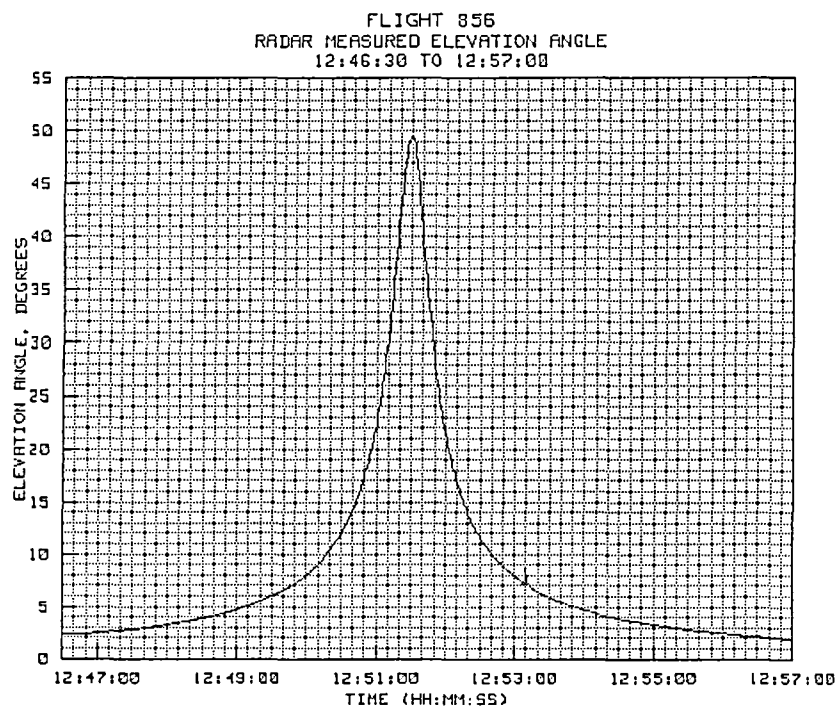

Figure 6-13(f). TP #4 radar-derived elevation angle.

6.2.5 Test Point #5

Test point #5 was planned as two standard-rate 90 degree heading changes at 12,500 feet. The maneuver was actually executed as a single 180-degree left turn from 090 degrees to 270 degrees at about 0.68 Mach. The radar remained in the skin track mode throughout the maneuver which started at a slant range of 240,995 feet (39.65 n.mi.) and at an elevation angle of 1.98 degrees. At the end of the turn, the slant range was 243,521 feet (40.07 n.mi.) and the elevation was 1.93 degrees. The turn was actually made at about 2.5 degrees per second. The time history plots for this test point are provided in figures 6-14(a) to 6-14(f).

This is an important test point, because it shows the performance of the radar in skin track under circumstances in which beacon-track anomalies would have likely occurred. The first thing of importance in the altitude plot (Fig. 6-14(a)) is the amount of difference between the geometric altitude and the corrected pressure altitude, about 150 to 170 feet. With a correction factor applied for the Z-Hp gradient measured along the survey leg, the difference is still about 140 feet as noted for the end of test point #4. Figure 6-14(a) was plotted at a 20 pps rate rather than at a 1 pps rate so that the nature of the oscillations in the radar data could be more closely analyzed. It was found that the antenna was, in fact, oscillating up and down by as much as 12 or 13 LSB values, very likely because of a combination of glint, multipath, and the dynamics of the servo drive system. The period of the oscillations appears to range from about two to ten seconds so that essentially all of the movement passed unaltered through the filter. The 20 pps plot shows that the movements are relatively smooth and reasonably consistent, since 100 data points are plotted between each of the vertical grid lines.

Figure 6-14(b) shows the behavior of the radar computed Mach number for the same period of time. The Mach number plot was prepared from 1 pps data so some of the smoothness of the altitude plot has been lost; however, the Mach number plot in this instance seems to be reasonably good, considering the fact that significant angle oscillations were present. Peak-to-peak excursions in the calculated Mach number throughout the turn were on the order of 0.01 to 0.05 Mach, about the same as for the final level portion of the preceeding survey leg.

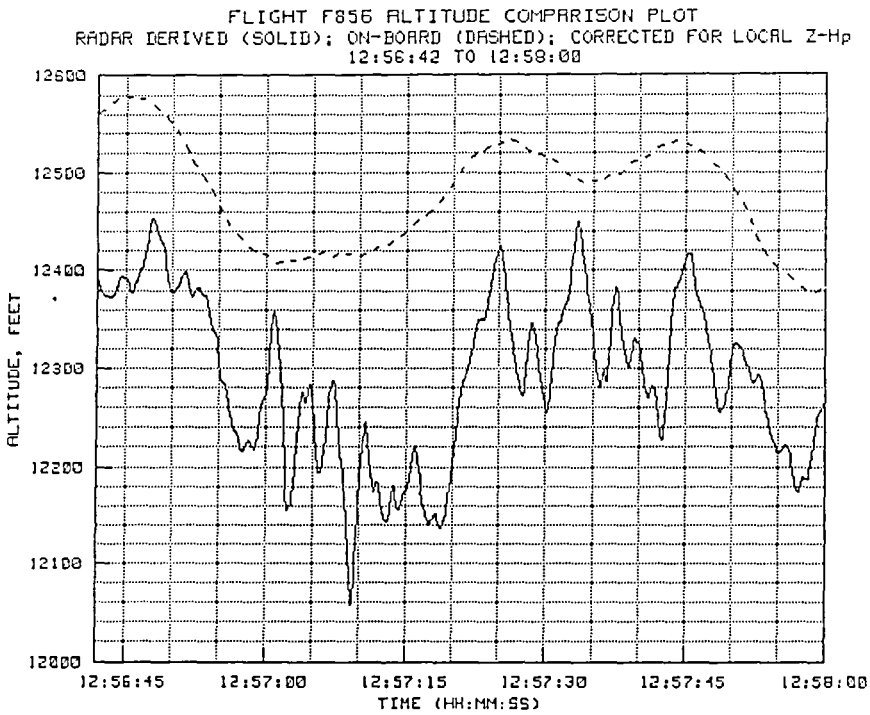

Figure 6-14(a). TP #5 radar-derived and on-board altitude.

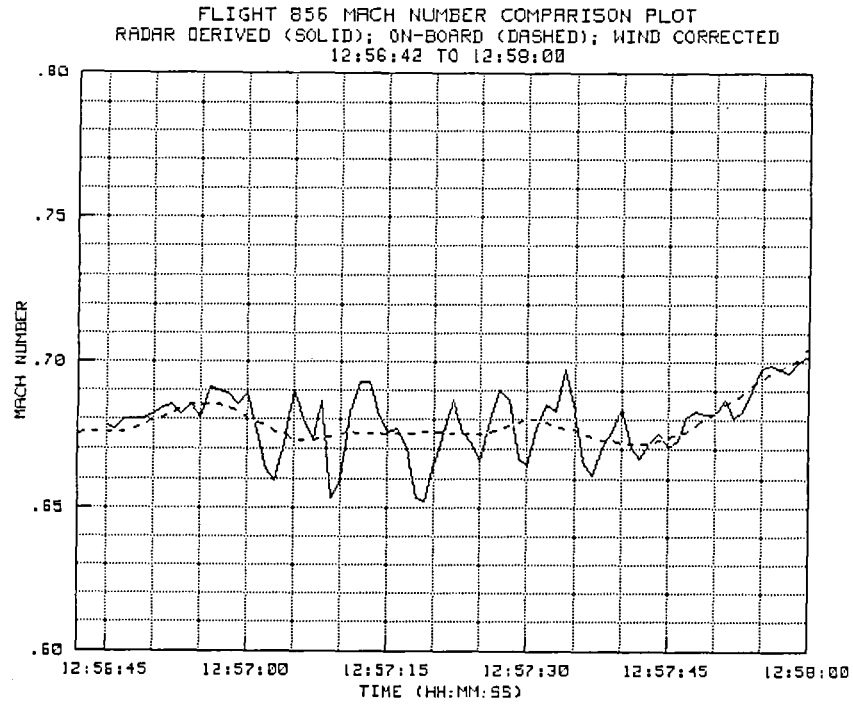

Figure 6-14(b). TP #5 radar-derived and on-board Mach number.

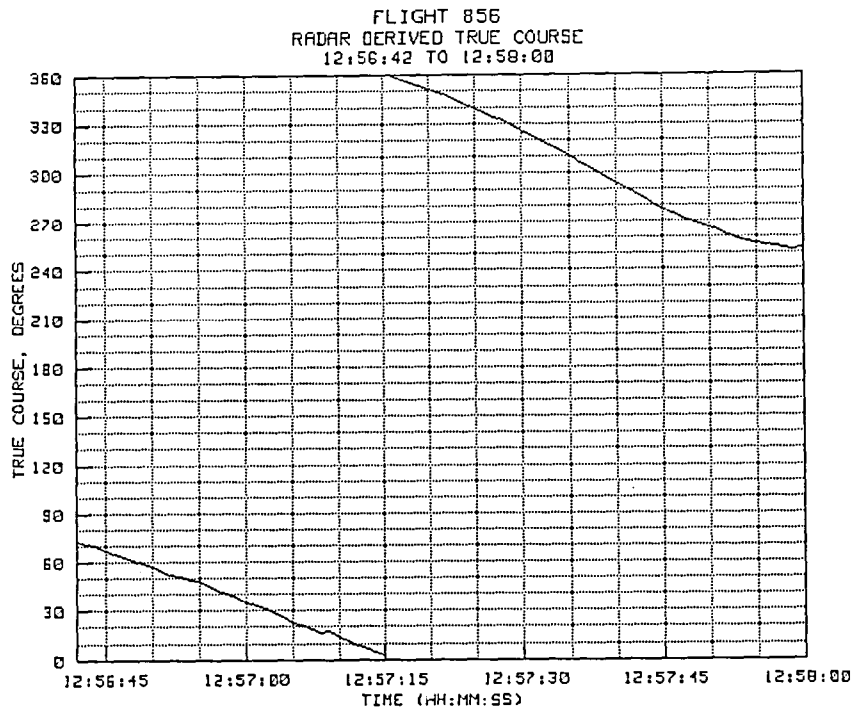

Figure 6-14(c). TP #5 radar-derived true course.

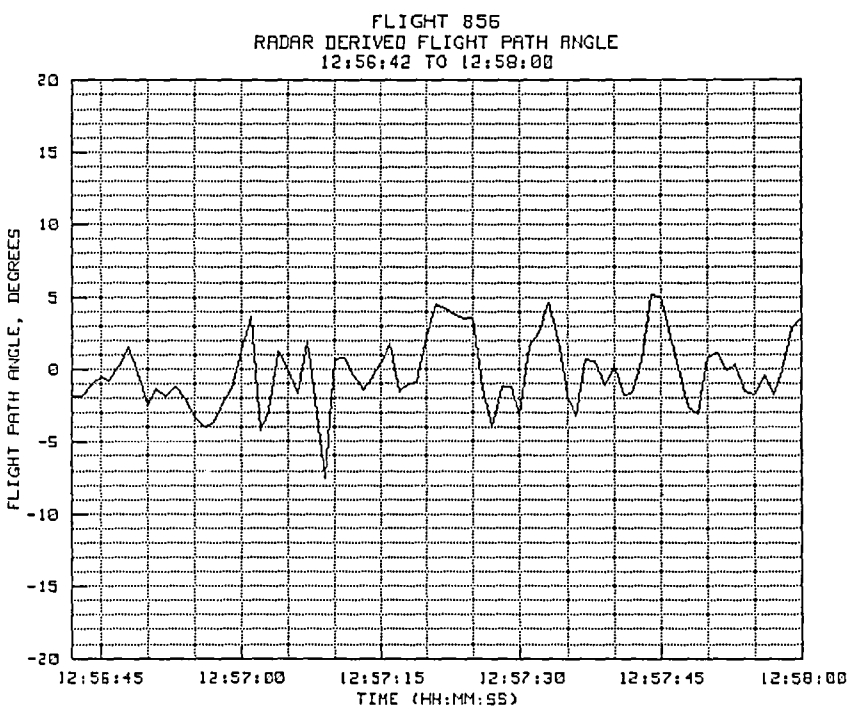

Figure 6-14(d). TP #5 radar-derived flight path angle.

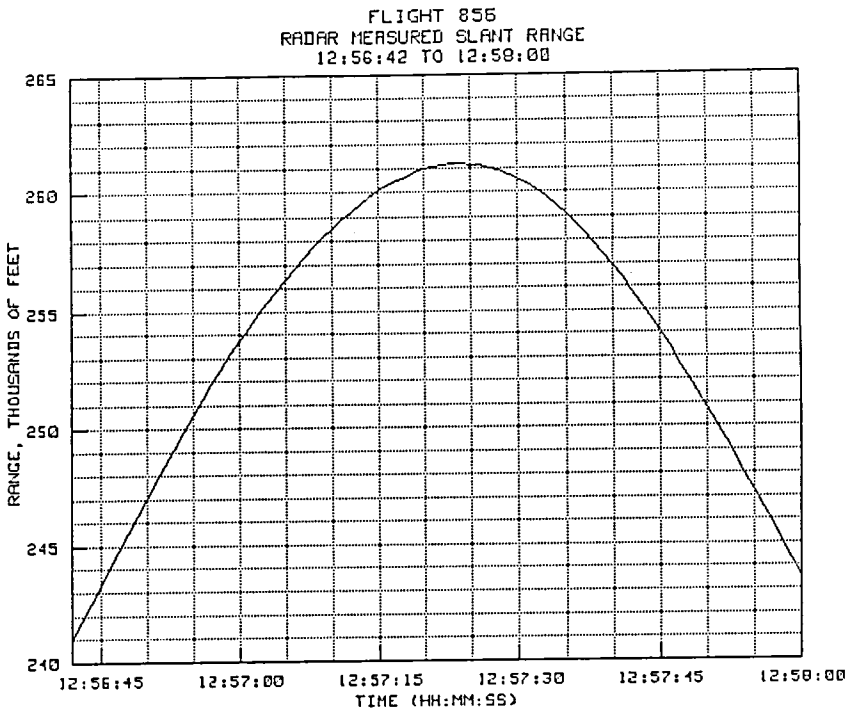

Figure 6-14(e). TP #5 radar-derived slant range.

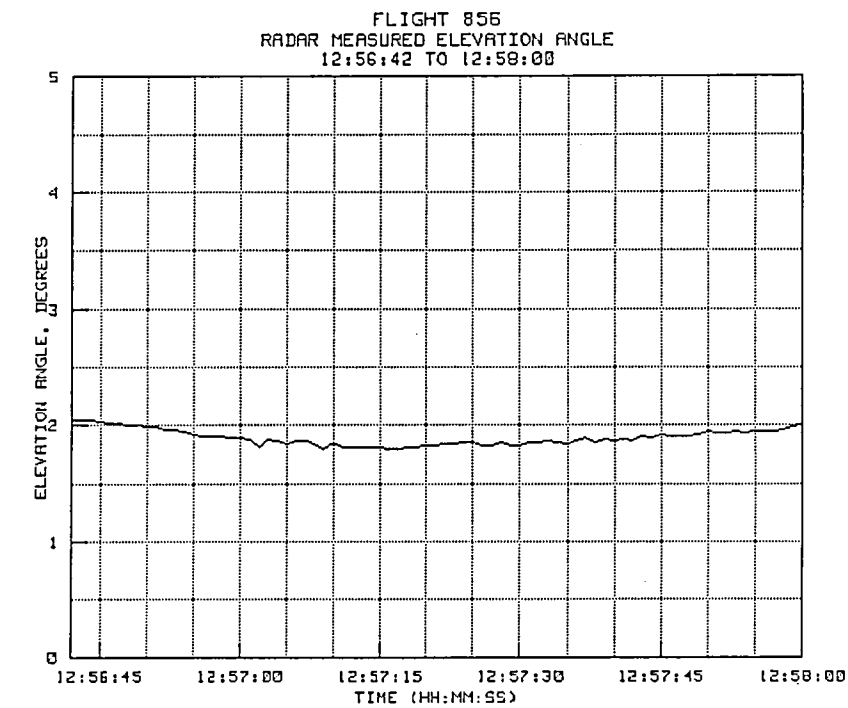

Figure 6-14(f). TP #5 radar-derived elevation angle.

6.2.6 Test Point #6

The time history plots for test point #6 are shown in figures 6-15(a) to 6-15(f). The maneuver consisted of a wings-level, westerly climb from 12,500 feet to slightly over 27,000 feet. At the start of the climb the slant range was 218,980 feet (36.03 n.mi.) and the elevation angle was 2.26 degrees. At the end of the climb the slant range had decreased to 63,715 feet (10.48 n.mi.) and the elevation angle had increased to 23.07 degrees. Although the condensed scale necessary to show the full altitude excursion makes it difficult to read the exact altitude difference at the start of the run, the data shows it to be about 150 feet. This is approximately what would be expected from the altitude behavior during the survey run. As the climb was continued, the difference between the pressure altitude and the geometric altitude became increasingly smaller as would be expected with the decreasing range and increasing elevation angle.

The Mach number during the climb was reasonably well behaved; although the same type of oscillations as previously observed were present in the radar-derived values. Also note that this climb was made at 0.9 Mach, the same as the climb in test point #2. However, in this case, even though the flight path angle was as high or higher than that observed in the data from test point #2, no Mach number bias seemed to develop. Throughout the entire climb the radar-derived Mach number agreed with the on-board data to within about 0.01 Mach.

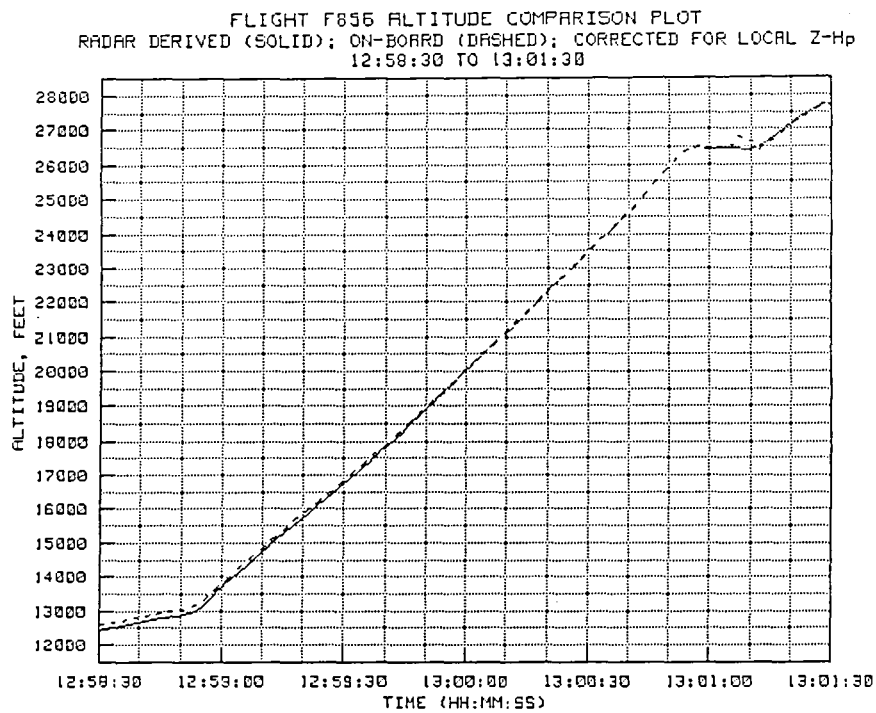

Figure 6-15(a). TP #6 radar-derived and on-board altitude.

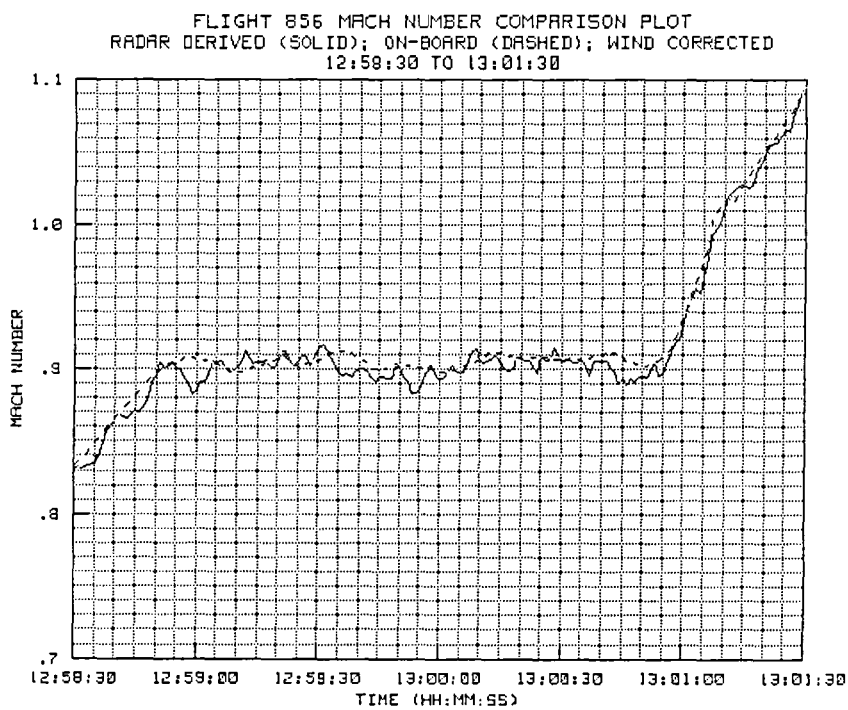

Figure 6-15(b). TP #6 radar-derived and on-board Mach number.

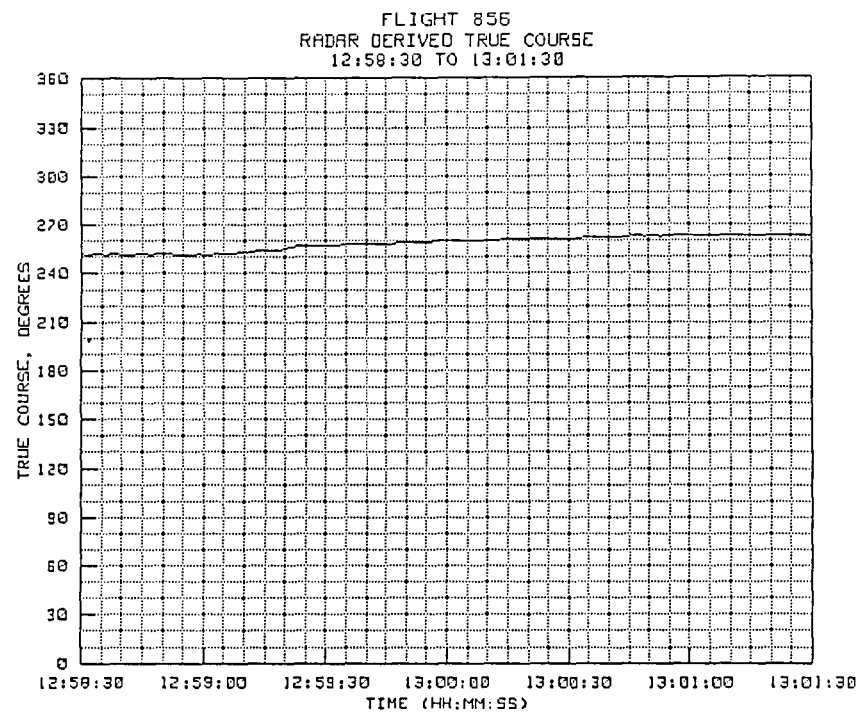

Figure 6-15(c). TP #6 radar-derived true course.

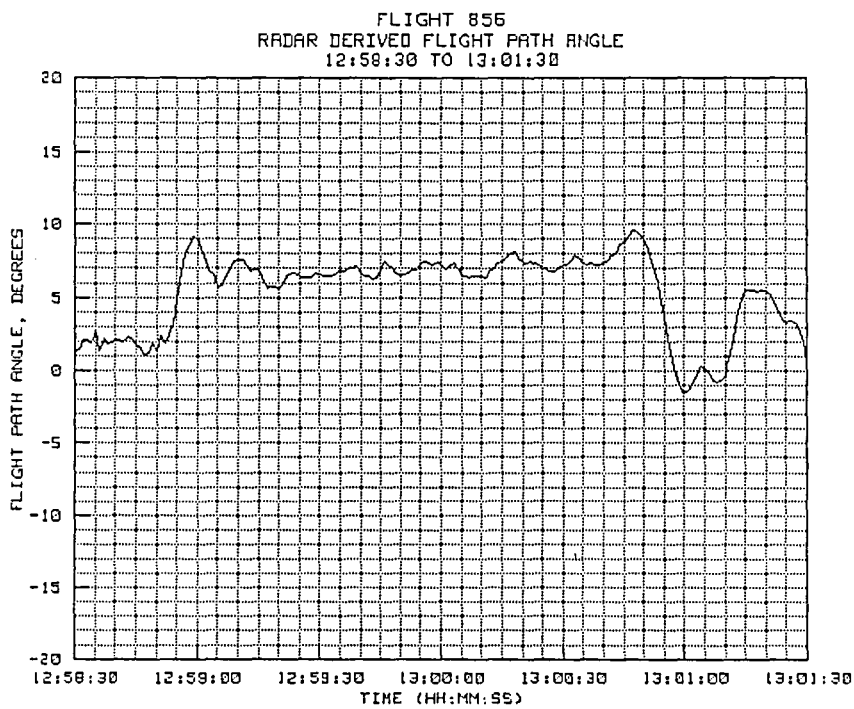

Figure 6-15(d). TP #6 radar-derived flight path angle.

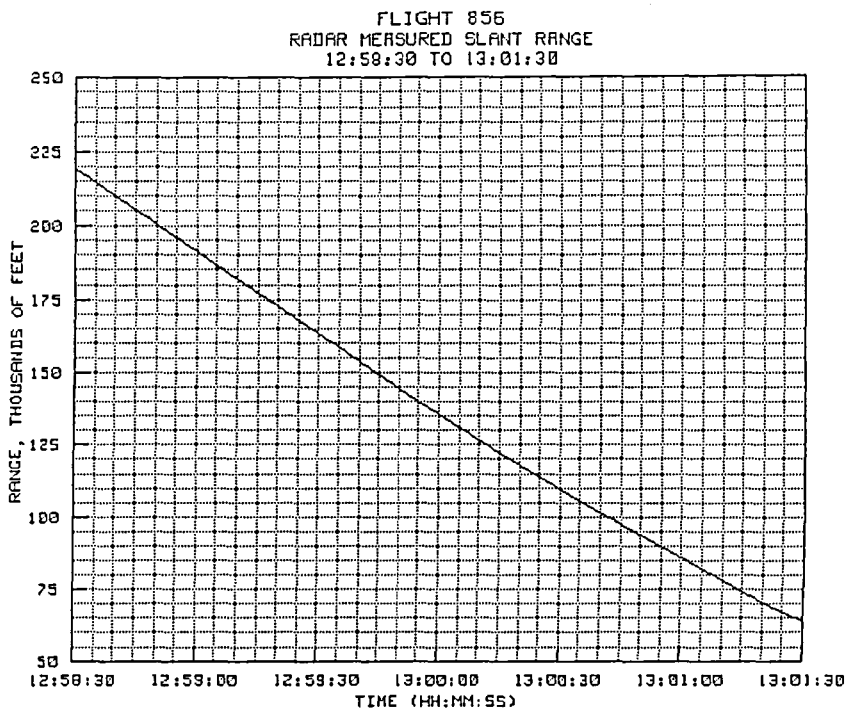

Figure 6-15(e). TP #6 radar-derived slant range.

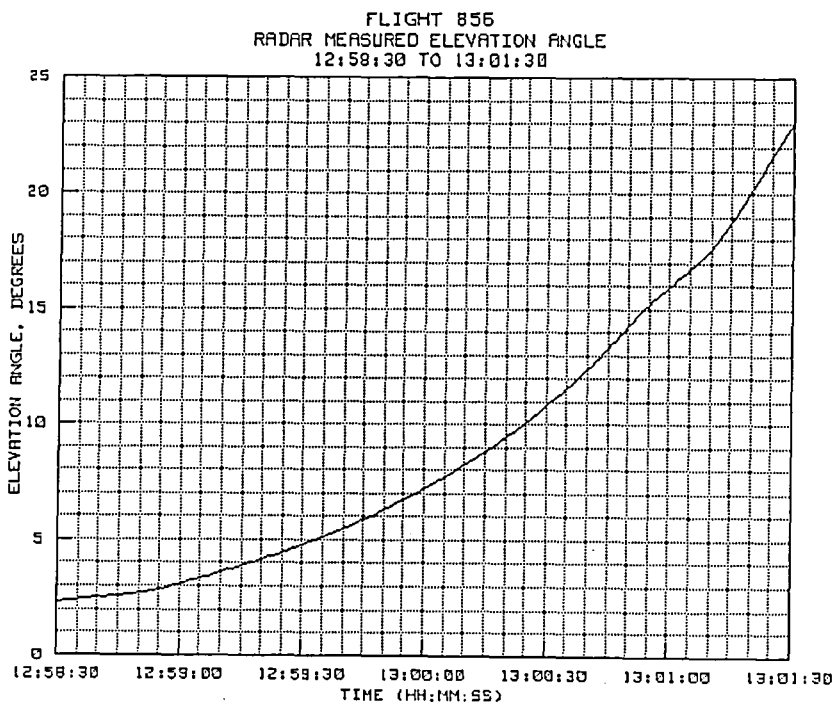

Figure 6-15(f). TP #6 radar-derived elevation angle.

6.2.7 Test Point #7

Time history plots of test point #7 are provided in figures 6-16(a) to 6-16(f). Test point #7 was to have been a level acceleration and deceleration at 25,000 feet; however, the altitude increased by about 2000 feet during the acceleration, and it decreased by almost the same amount during the deceleration. The radar was kept in the skin track mode throughout the leg. The altitude profile is provided in figure 6-16(a), which shows reasonably good agreement between the radar-derived and pressure altitude plots. Jumps can be seen in the on-board data at about 13:01:07 and 13:01:37 due to shock wave effects during the supersonic and subsonic transitions. Slant range at the start of the leg was 97,514 feet (16.05 n.mi.) and the elevation angle was 13.27 degrees. Slant range at the end of the run was 48,504 feet (7.98 n.mi.) and the elevation angle was 29.21 degrees.

The Mach number profile (Fig. 6-16(b)) for this same time segment shows good agreement with the flight data. Some phase shift can be seen in the data at the time the rapid deceleration was started. Bias differences between the radar-derived Mach and on-board Mach number appear to be about the same magnitude as found previously, 0.01 to 0.02 Mach. The most significant thing about this plot is that it does show lag to be present during rapid changes in flight path or airspeed. As noted previously, this was probably due to servo lag present at the lower bandwidth angle settings in combination with some filter lag.

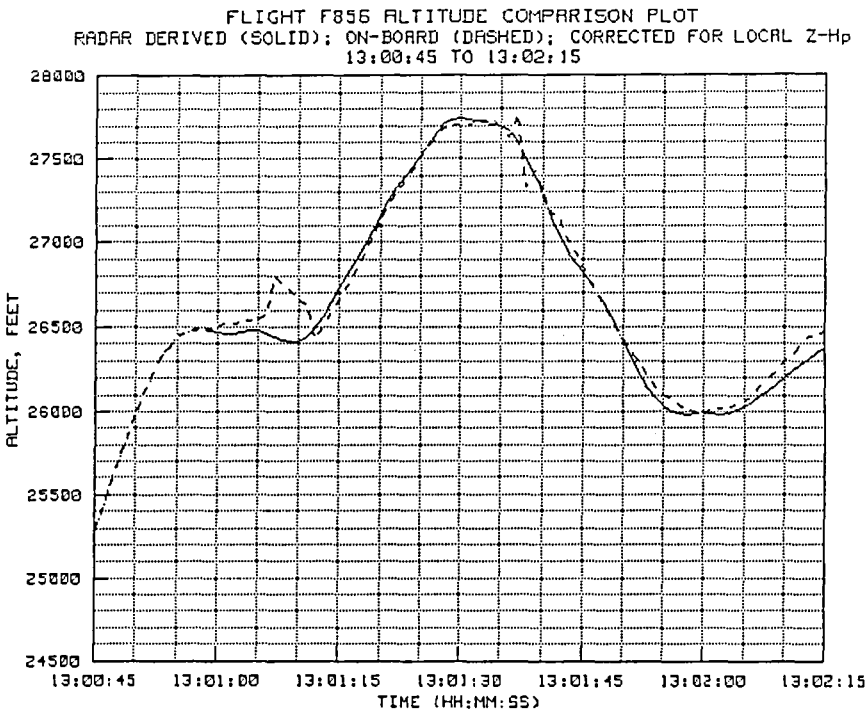

Figure 6-16(a). TP #7 radar-derived and on-board altitude.

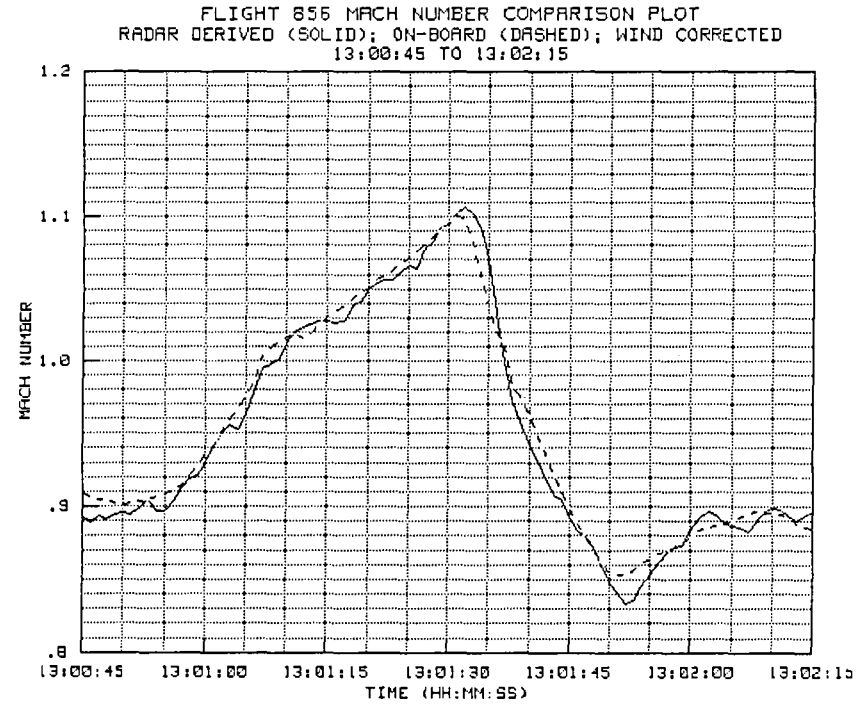

Figure 6-16(b). TP #7 radar-derived and on-board Mach number.

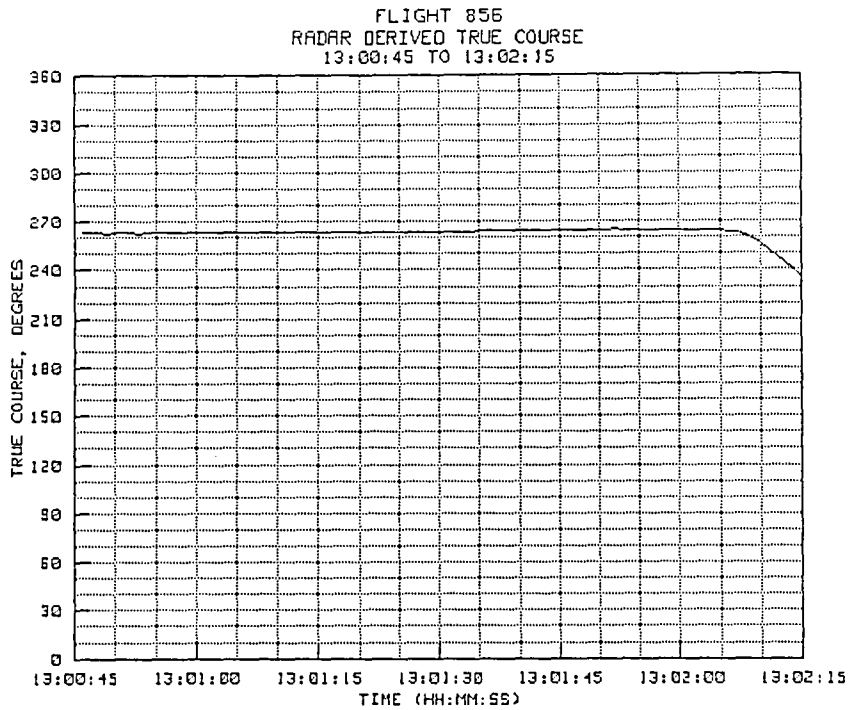

Figure 6-16(c). TP #7 radar-derived true course.

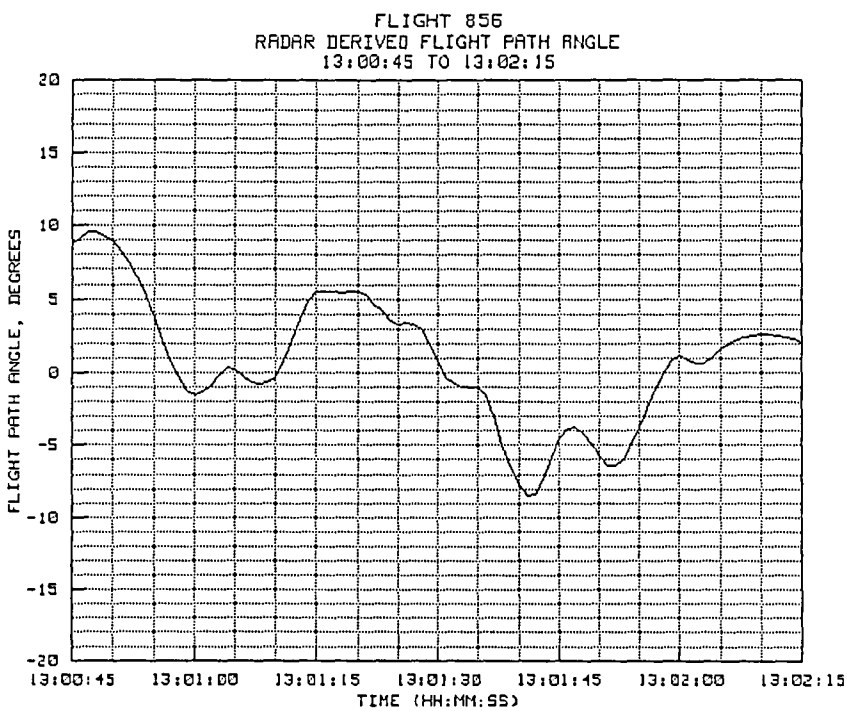

Figure 6-16(d). TP #7 radar-derived flight path angle.

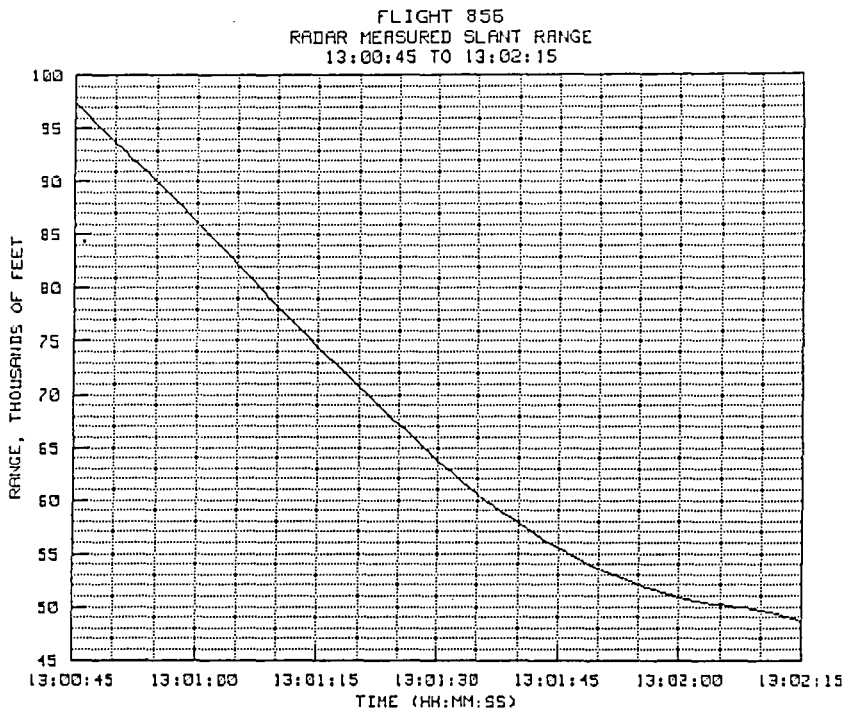

Figure 6-16(e). TP #7 radar-derived slant range.

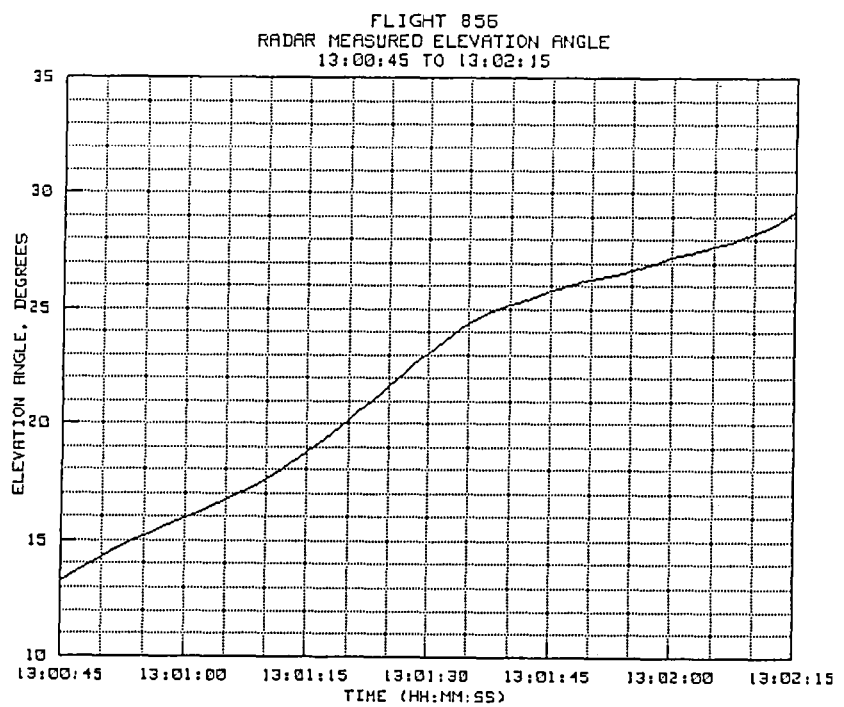

Figure 6-16(f). TP #7 radar-derived elevation angle.

6.2.8 Test Point #8

The time history plots for test point #8 are provided in figures 6-17(a) to 6-17(f).

Test point #8 was a 2-g level turn followed by a stabilized point. The radar remained in the skin track mode throughout this test point. At 13:02:07 a left bank was initiated and held for a complete 360-degree turn. Rollout occurred at 13:03:40. The maneuvers were performed at high elevation angles, starting at 27.20 degrees and ending at 23.46 degrees. Slant range was 50,906 feet (8.38 n.mi.) at the start of the maneuver and 58,852 feet (9.68 n.mi.) at the end. About the time the turn was started, a Z-Hp bias seemed to develop. This bias remained in the altitude data until 13:03:35 when the turn was completed, indicating that the 2-g turn may have affected the on-board pressure altitude readings.

The behavior of the altitude plot for this test point gave rise to some additional scrutiny of the behavior of the derived Mach number. Note that the right turn was initiated at 13:02:07 and completed at 13:03:35. Also note that about 13:02:07, a bias developed between the derived Mach number and the on-board Mach number. The bias remained, in varying degrees, until 13:03:35 when it suddenly vanished, indicating that the 2-g turn may have also affected the on-board Mach number measurement.

These data would indicate that on-board pressure measurements may be very sensitive to various maneuvering conditions, and extreme care must be exercised to insure that any comparisons of high-angle radar derived geometric altitudes and on-board pressure altitude be done at times when the aircraft is in stable flight.

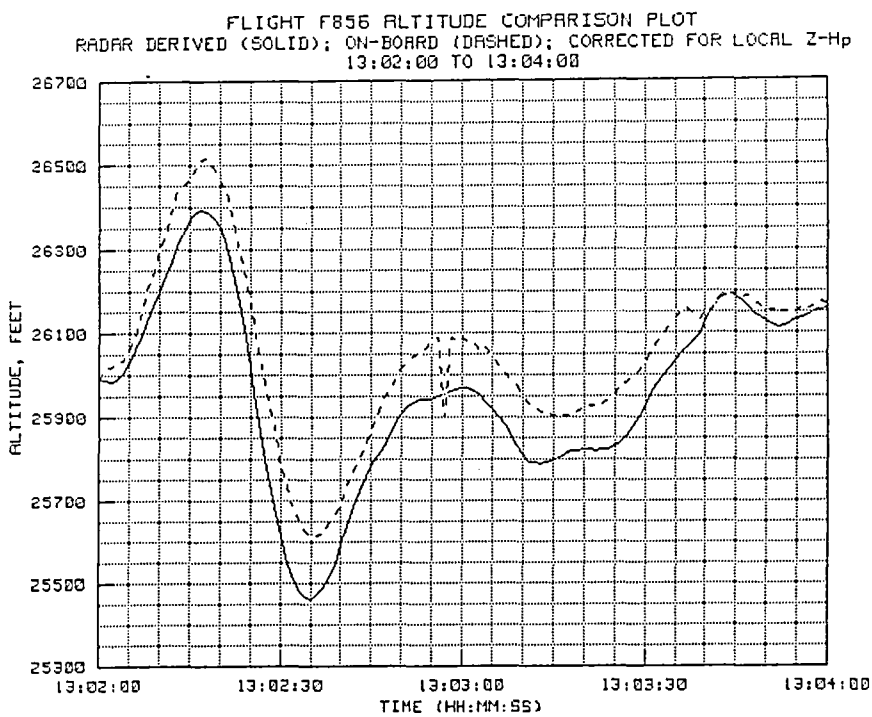

Figure 6-17(a). TP #8 radar-derived and on-board altitude.

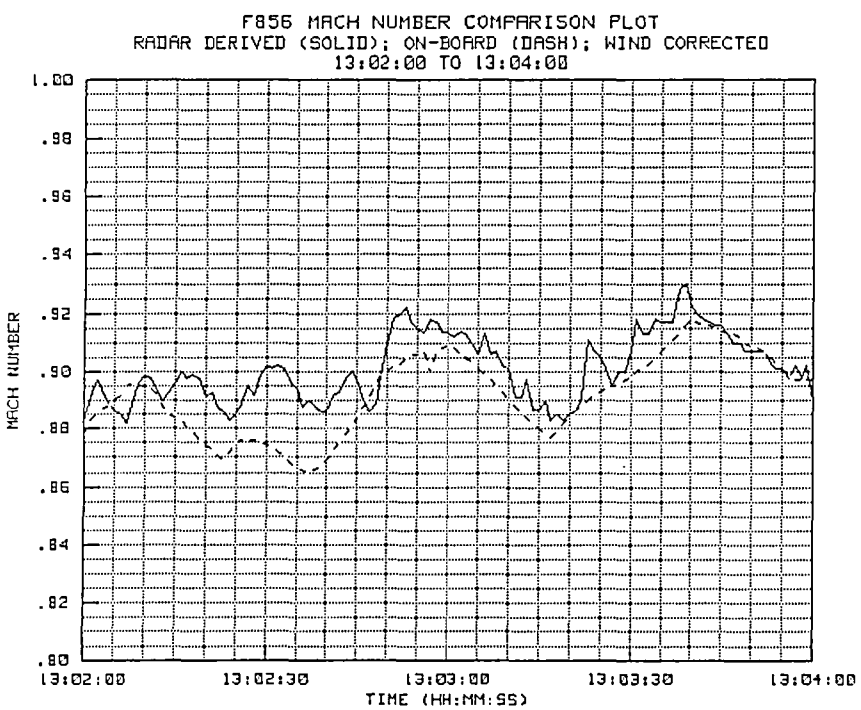

Figure 6-17(b). TP #8 radar-derived and on-board Mach number.

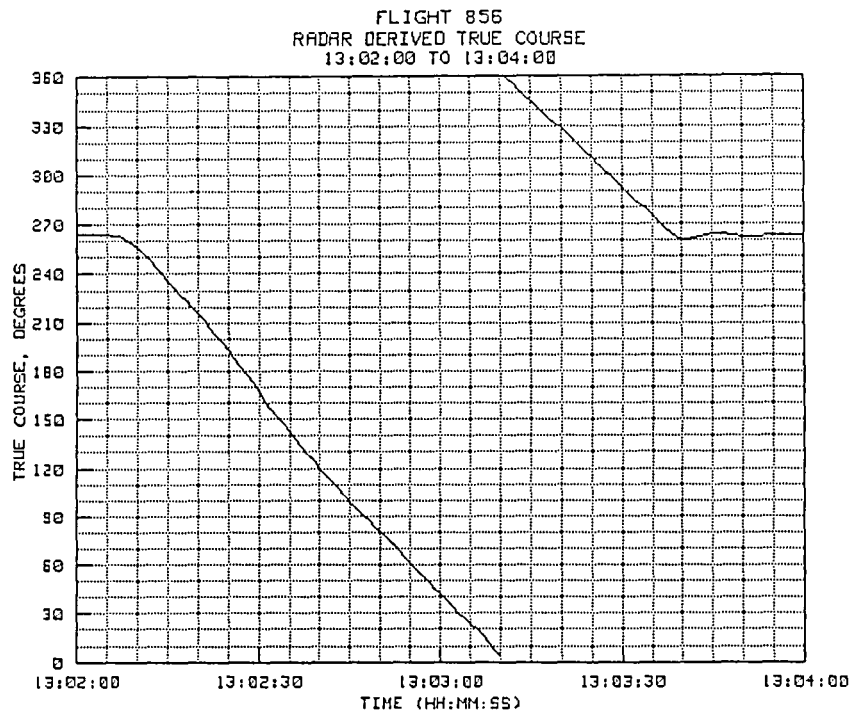

Figure 6-17(c). TP #8 radar-derived true course.

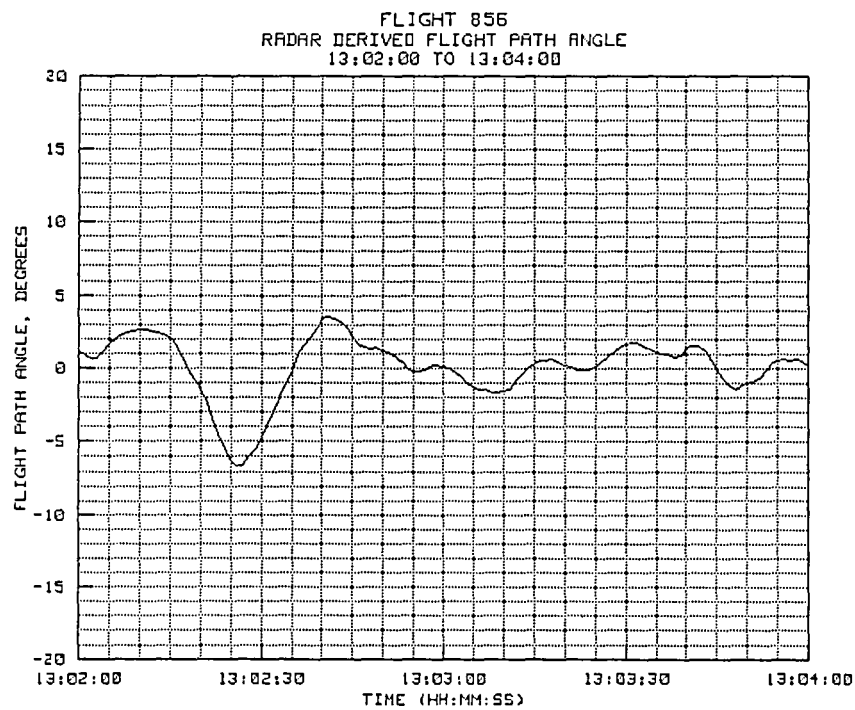

Figure 6-17(d). TP #8 radar-derived flight path angle.

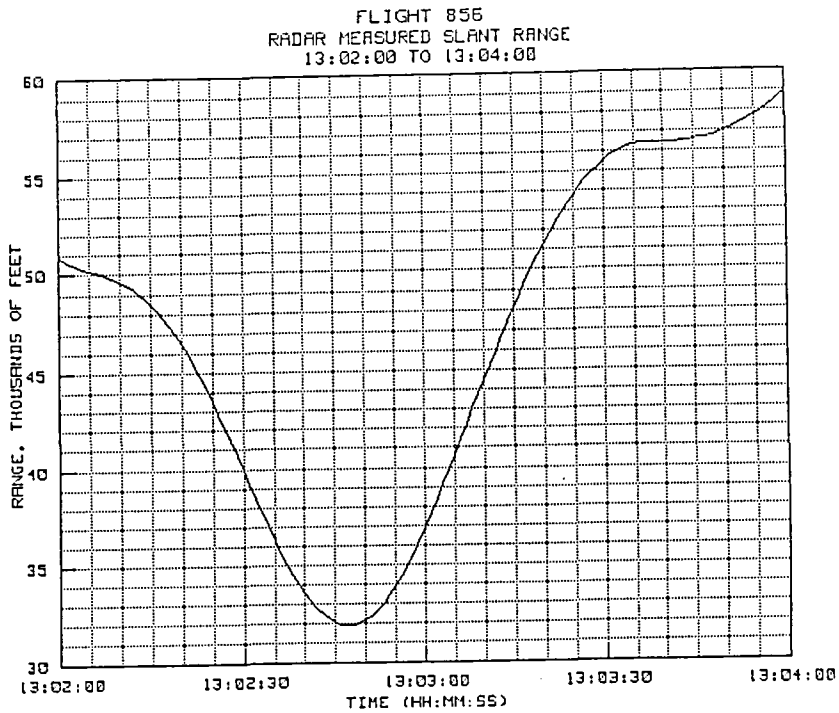

Figure 6-17(e). TP #8 radar-derived slant range.

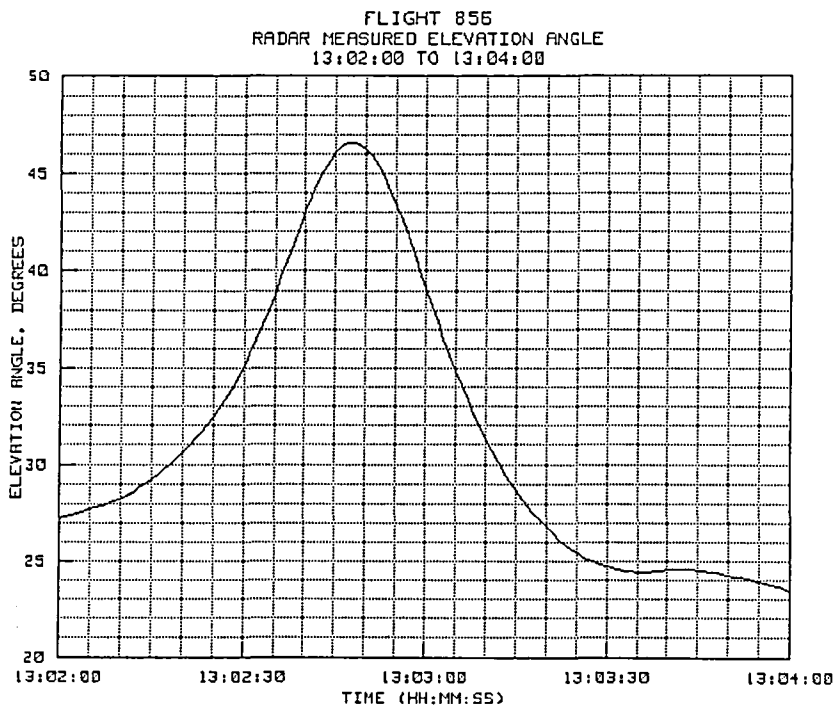

Figure 6-17(f). TP #8 radar-derived elevation angle.

6.2.9 Test Point #9

The data from test point #9 is provided in figures 6-18(a) to 6-18(f). Tracking during this test point was performed in the skin mode, and the data reinforces the findings from test point #8. The test maneuver consisted of one 3-g 90-degree right turn followed by a stabilized point. The elevation angles were again high, ranging from 23.46 degrees down to 12.93 degrees. Altitude for the maneuver varied from 26,000 to 26,650 feet. Slant range started at 58,852 feet (9.68 n.mi.) and ended at 104,291 feet (17.16 n.mi.). The roll into the turn was made at 13:04:15, at which time the Z-Hp bias increased significantly. The bias remained at 100 to 125 feet until the roll out was started at about 13:04:37. It is expected that the g-force was released at the start of the roll out, allowing the on-board pressure measurements to return to normal.

Mach number behavior during this maneuver also revealed some interesting facts. Note that the radar-derived Mach number agreed quite well with the on-board Mach number until 13:04:15, the same time that the roll maneuver was initiated. At that point, a bias error developed and remained in the Mach data until 13:04:42, about the same time as a wings-level attitude was again attained.

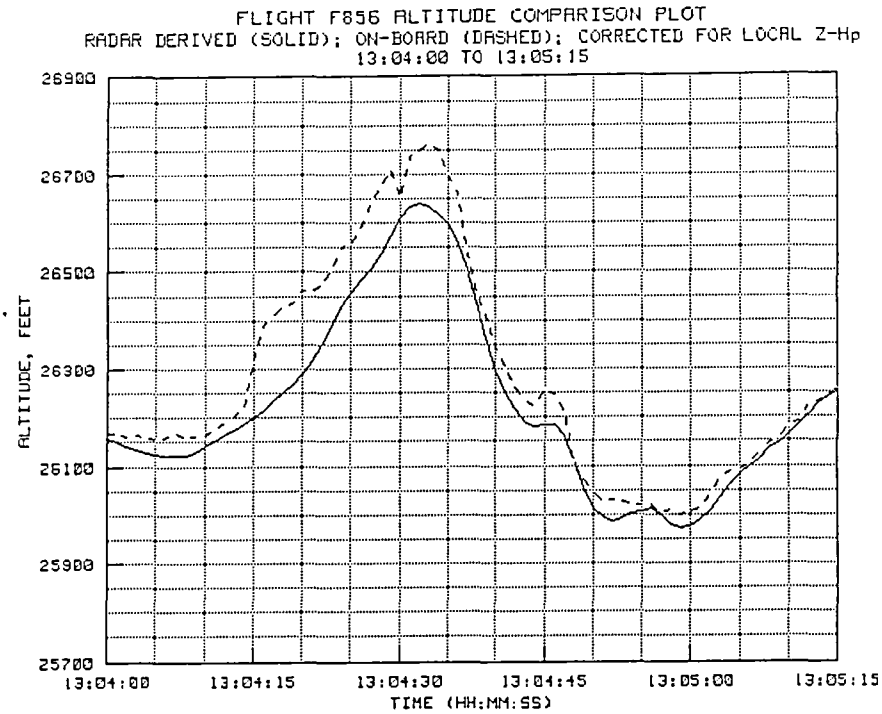

Figure 6-18(a). TP #9 radar-derived and on-board altitude.

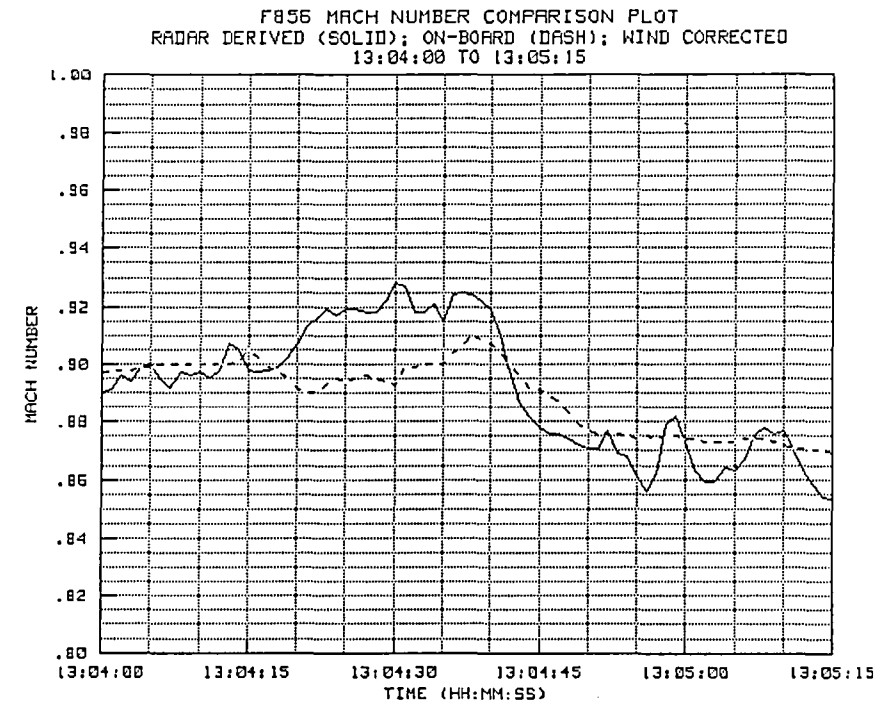

Figure 6-18(b). TP #9 radar-derived and on-board Mach number.

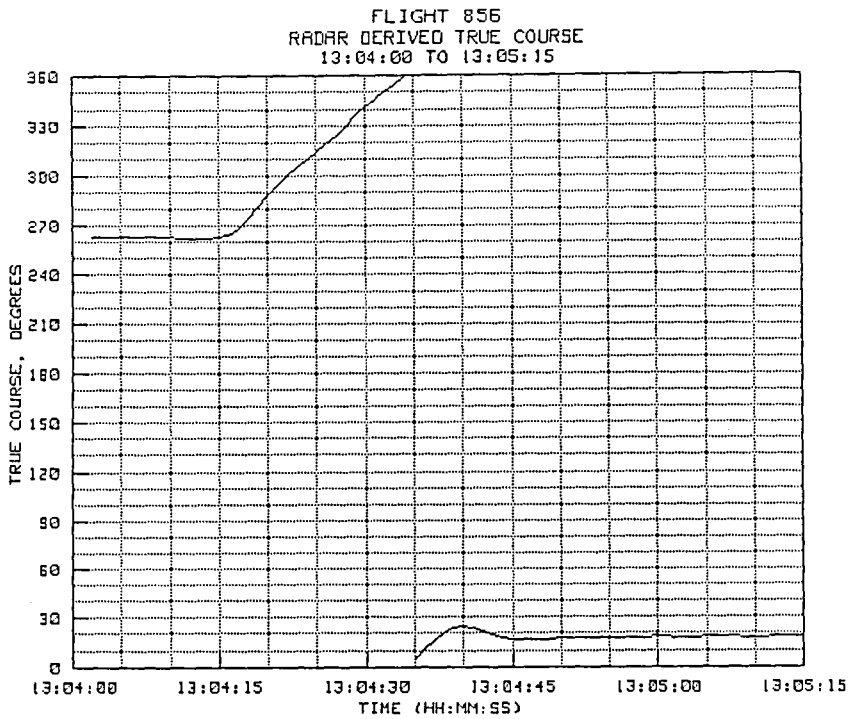

Figure 6-18(c). TP #9 radar-derived true course.

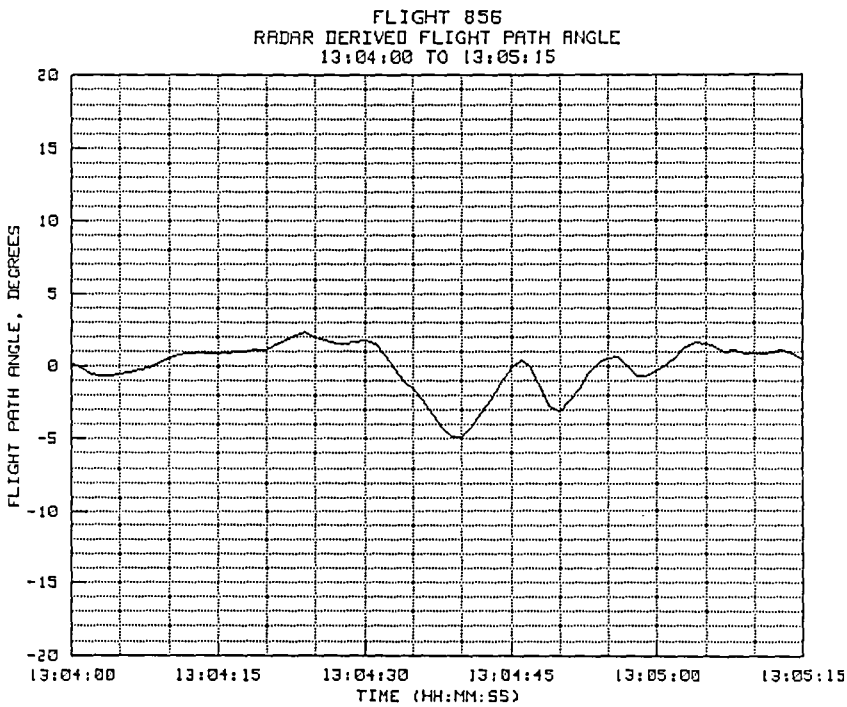

Figure 6-18(d). TP #9 radar-derived flight path angle.

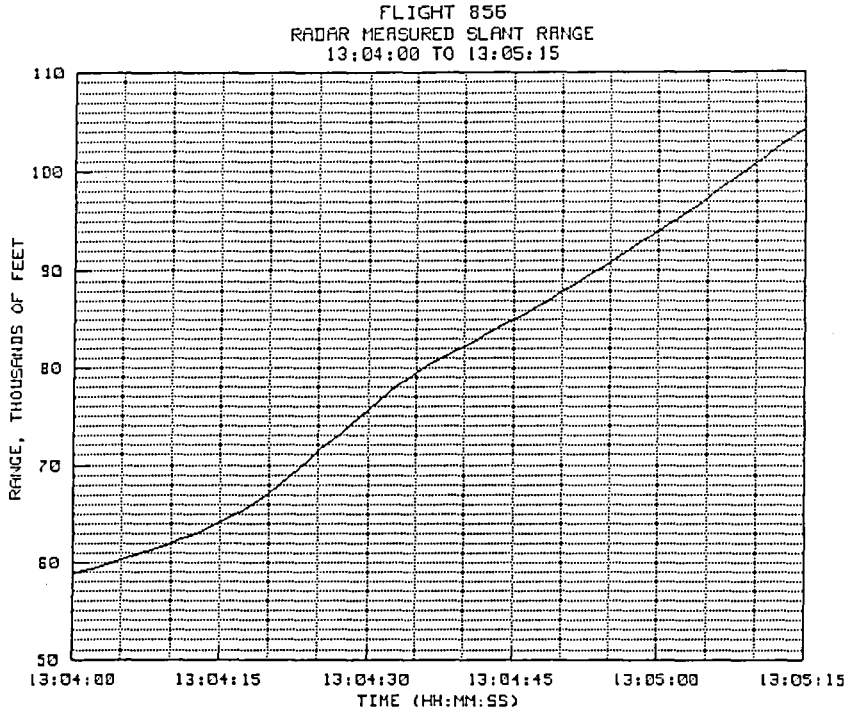

Figure 6-18(e). TP #9 radar-derived slant range.

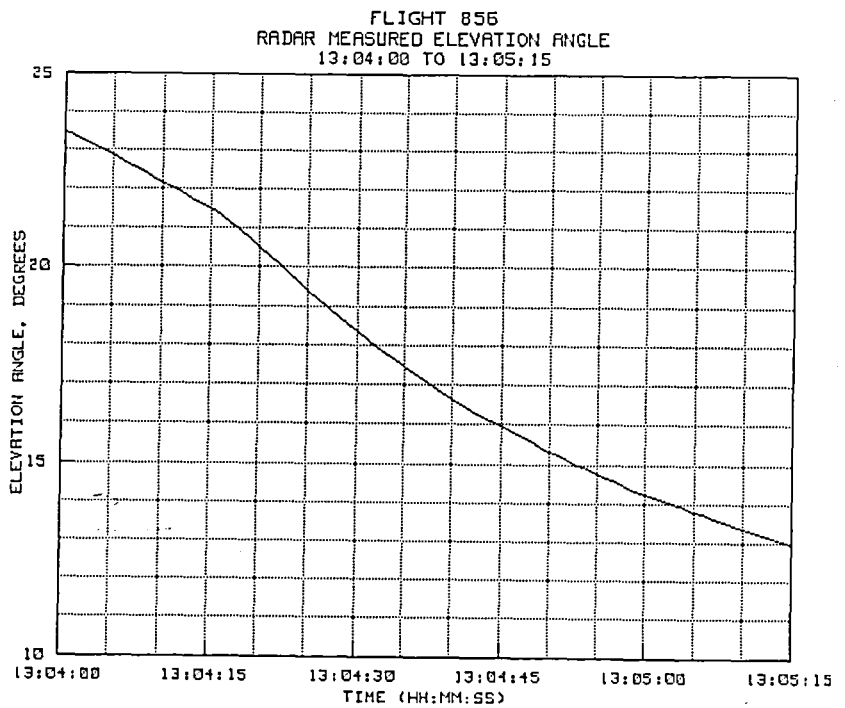

Figure 6-18(f). TP #9 radar-derived elevation angle.

6.2.10 Test Point #10

Prior to test point #10, the radar was returned to the beacon tracking mode. Test point #10 was a push-pull, acceleration-deceleration test started at an altitude of 25,000 feet and 0.85 Mach. Slant range was 74,666 feet (12.28 n.mi.) at the start of the test and 113,520 feet (18.68 n.mi.) at the end of the test. The elevation angle was 17.55 degrees at the start and 11.63 degrees at the end. Data from the beacon mode track are provided in figures 6-19(a) to 6-19(f). Figure 6-19(a) shows the aircraft in a slight descent at the start of the test point. The push over was commenced at 13:07:03, and the round-out at the bottom was started at 13:07:14. A level flight configuration was achieved at about 13:07:43. A spike can be seen in the on-board data at about 13:07:10, the time of the supersonic transition.

The Mach number plot (Fig. 6-19(b)) for this maneuver shows a considerable amount of phase shift and amplitude overshoot. This is primarily due to the magnified effect of pedestal dynamic lag on the first derivative calculation. Future tests might include some rapid acceleration and deceleration maneuvers using different angle bandwidth settings on the radar. It is possible that some on-board pressure anomalies may also be present in the data; however they would probably be masked by the larger amount of servo induced phase shift and overshoot.

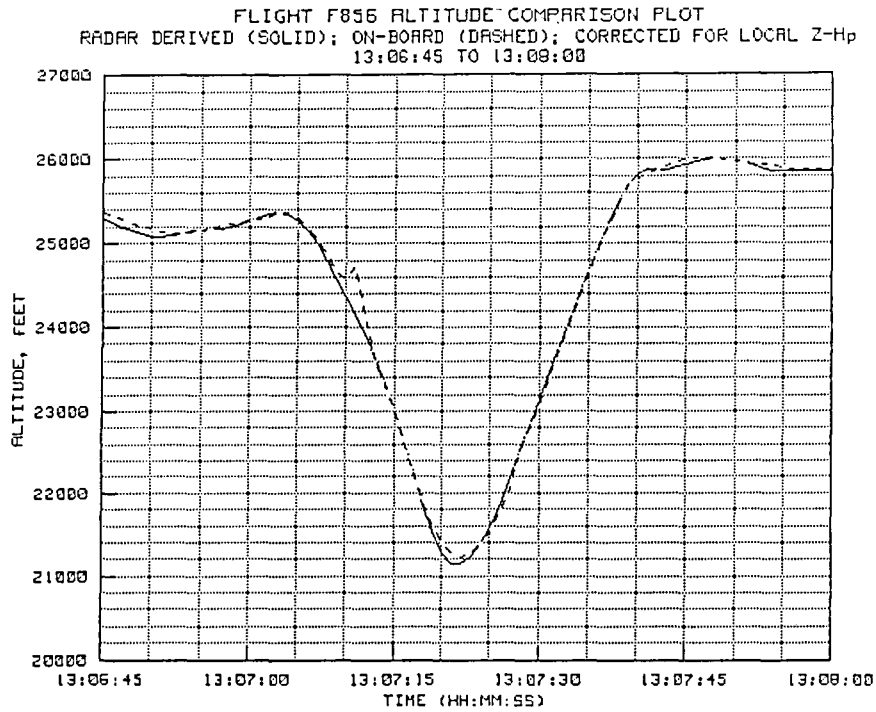

Figure 6-19(a). TP #10 radar-derived and on-board altitude.

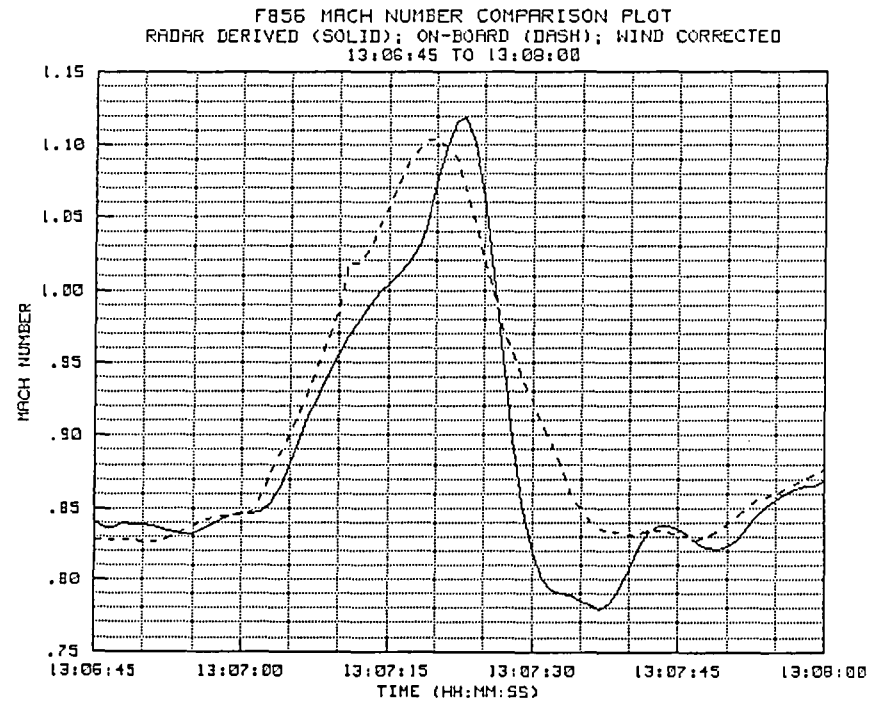

Figure 6-19(b). TP #10 radar-derived and on-board Mach number.

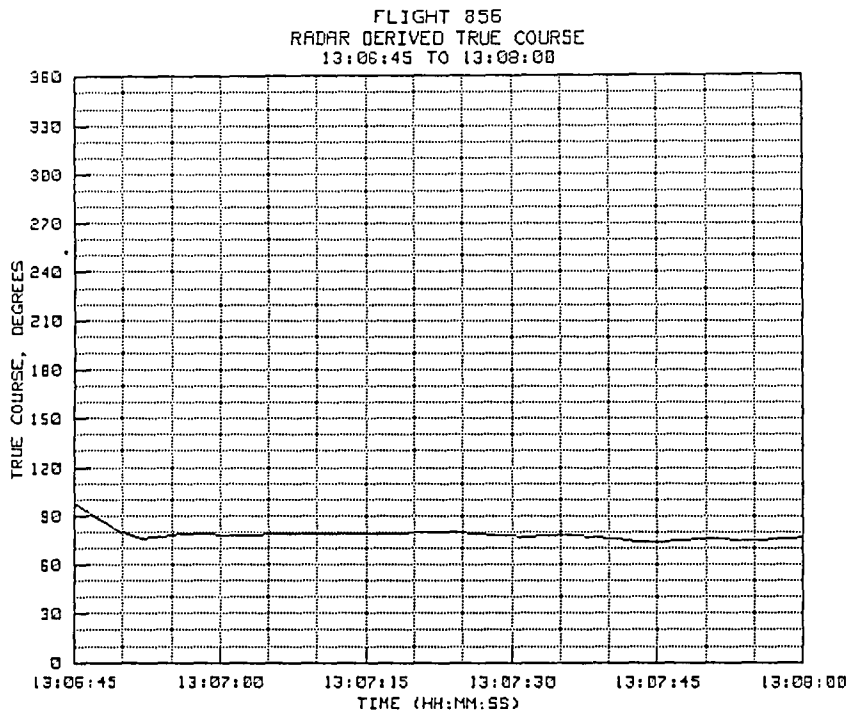

Figure 6-19(c). TP #10 radar-derived true course.

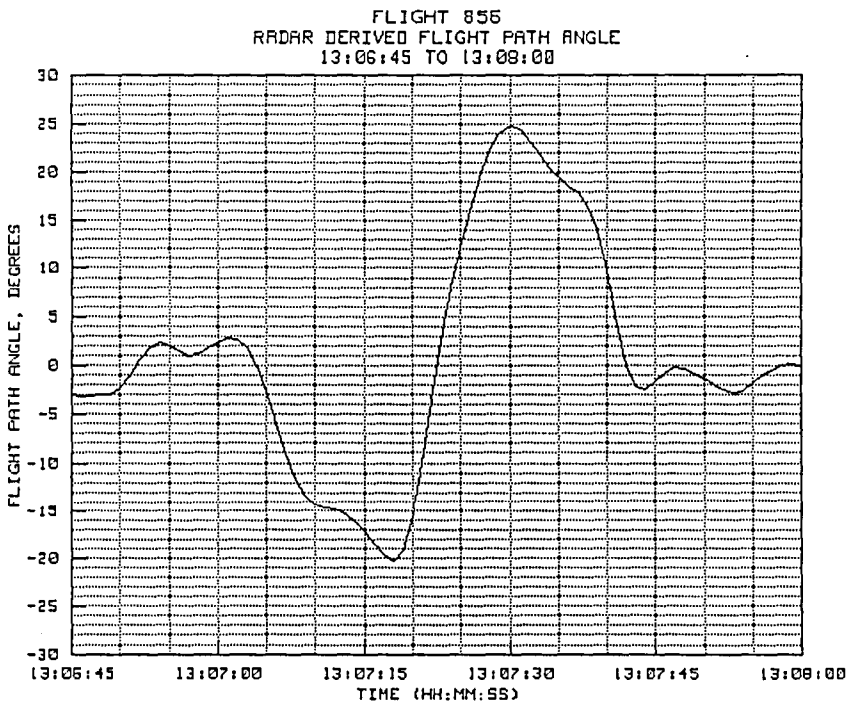

Figure 6-19(d). TP #10 radar-derived flight path angle.

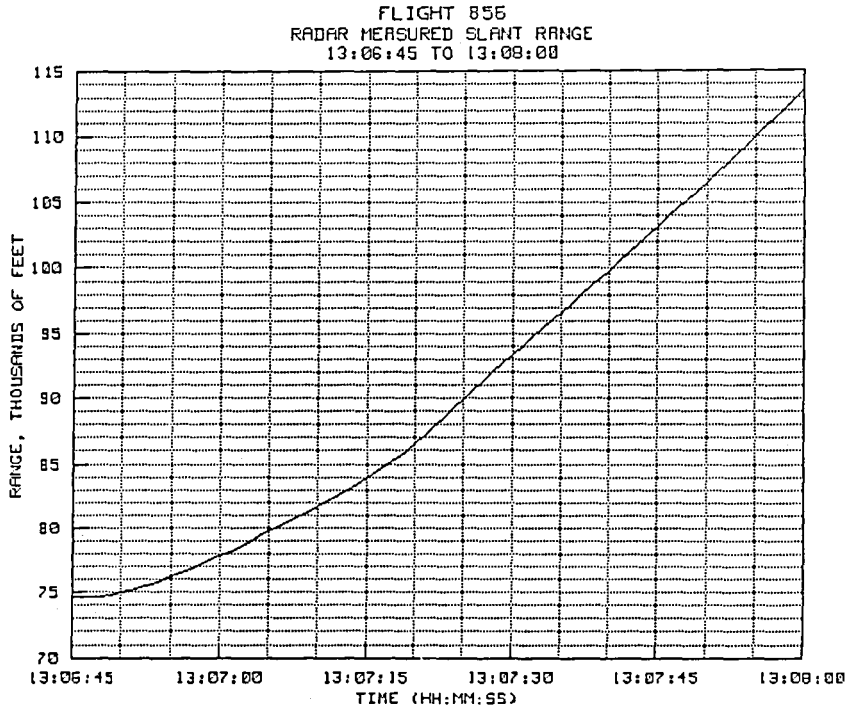

Figure 6-19(e). TP #10 radar-derived slant range.

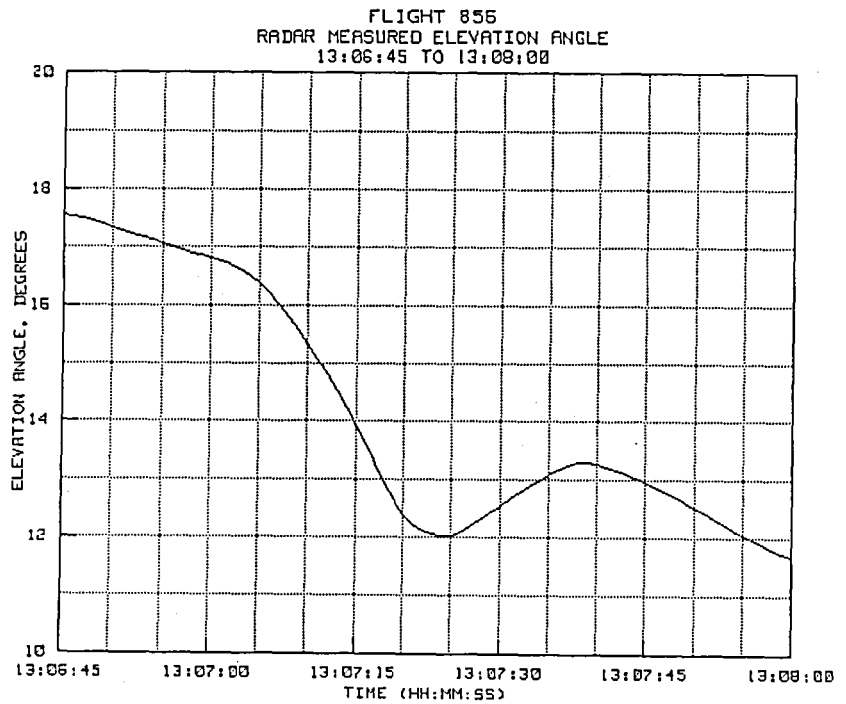

Figure 6-19(f). TP #10 radar-derived elevation angle.

6.2.11 Test Point #11

The time history plots for this test point are provided in figures 6-20(a) to 6-20(f). This test consisted of a constant 0.6 Mach descent from about 22,000 down to 1000 feet above ground level. The leg was started at a slant range of 150,972 feet (24.84 n.mi.) and an elevation angle of 7.21 degrees. The level off occurred at about 108,592 feet (17.87 n.mi.) and 0.5 degrees elevation. The descent was made on a westerly heading with a left turn commenced at the bottom at 13:15:12. Good agreement was obtained in the data throughout the descent, however a minor Z-Hp bias was present. Although it was expected that some bias between the pressure altitude and the radar-derived altitude might be present as the elevation angle lessened, no evidence of this could be seen in these data. Even though the 0.5 degree elevation angle at the level-off point was one of the lowest of the entire series of tests, the range at that time was quite close so that the amount of bias would have been small.

The Mach number plot (Fig. 6-20(b)) indicates a sizeable amount of bias (0.02 Mach) for altitudes between 15,000 feet and level off at about 3500 feet. Also note that the buildup of the bias correlates with the increase in the rate of descent at 13:13:50 as shown in figure 6-20(b). Also significant is the fact that the bias appeared to disappear at about the same time as the level off. This again suggests that, under certain circumstances, on-board Mach number measurements may be susceptible to angle of attack changes. Also note that the radar-derived Mach number lagged the on-board Mach number from about 13:13:50 to 13:15:10. The nature of the plot would indicate that this lag was probably caused by the filter.

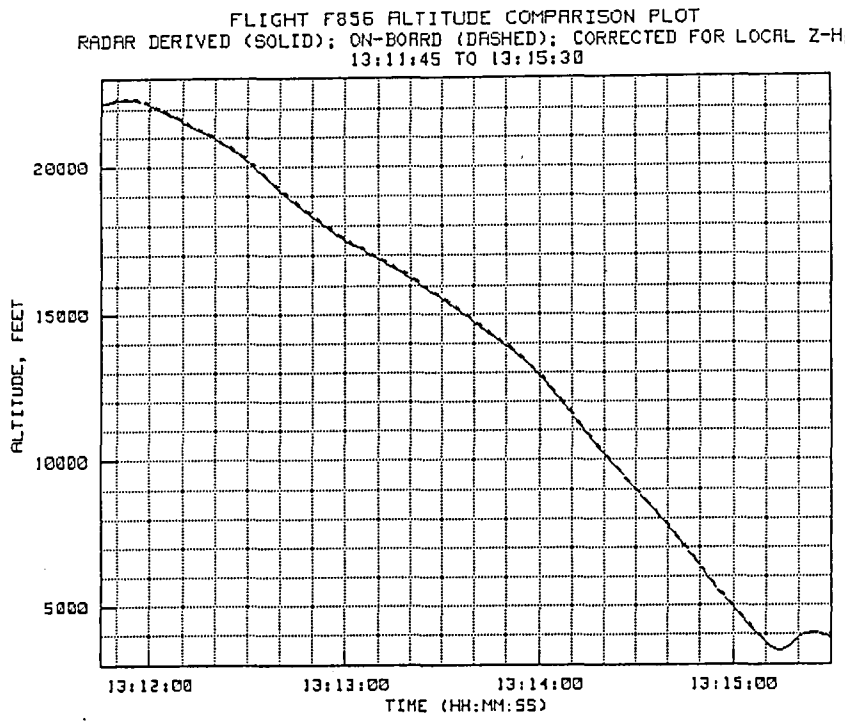

Figure 6-20(a). TP #11 radar-derived and on-board altitude.

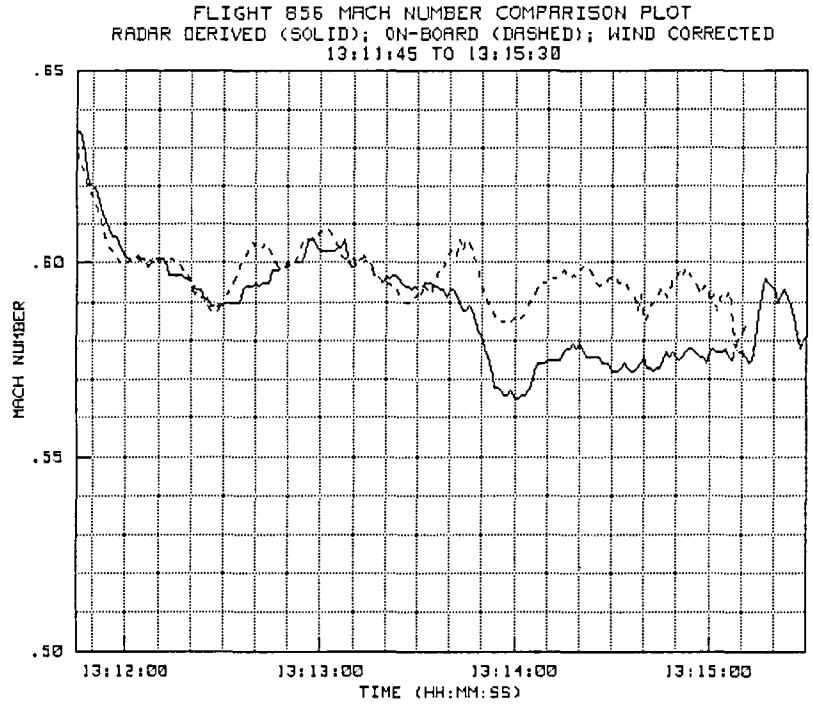

Figure 6-20(b). TP #11 radar-derived and on-board Mach number.

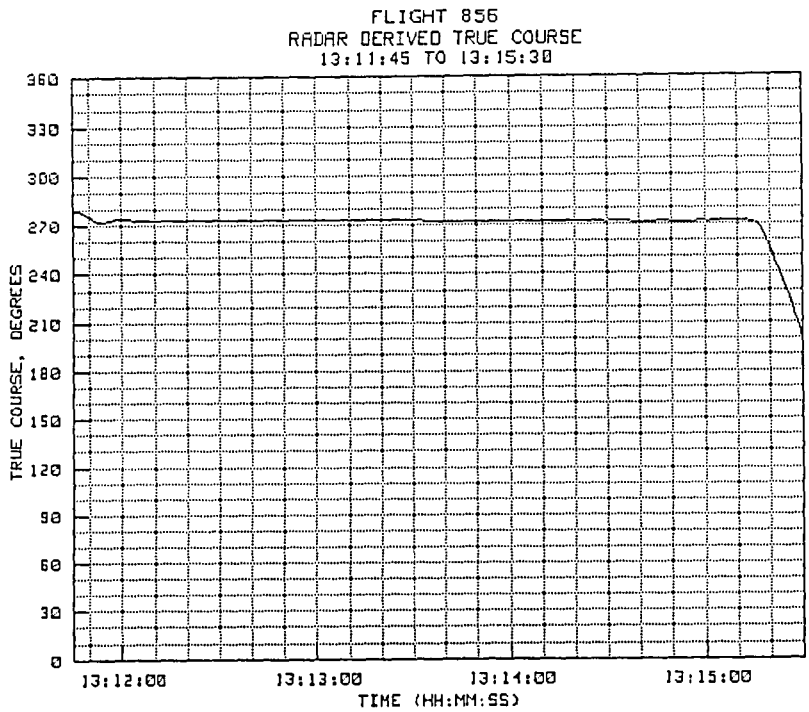

Figure 6-20(c). TP #11 radar-derived true course.

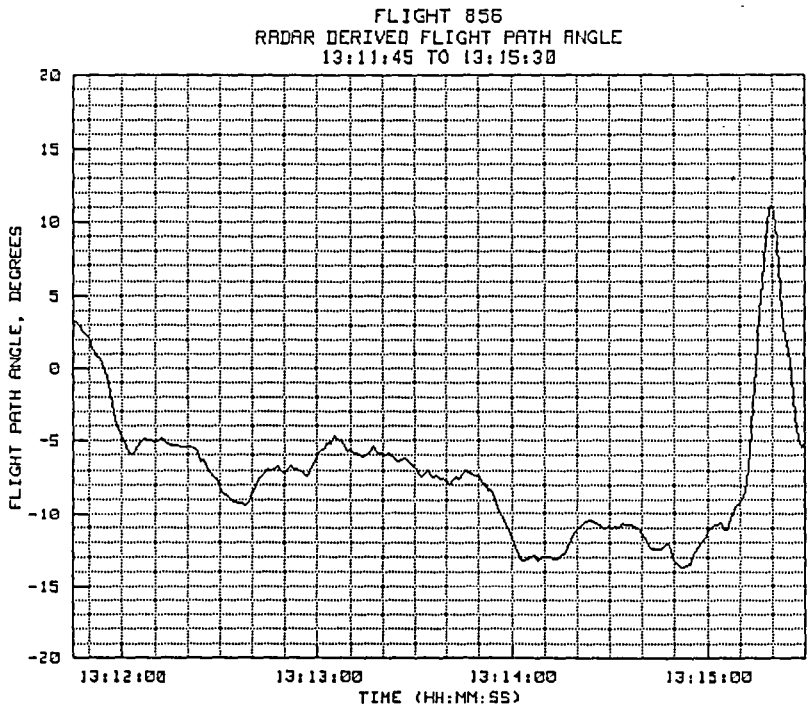

Figure 6-20(d). TP #11 radar-derived flight path angle.

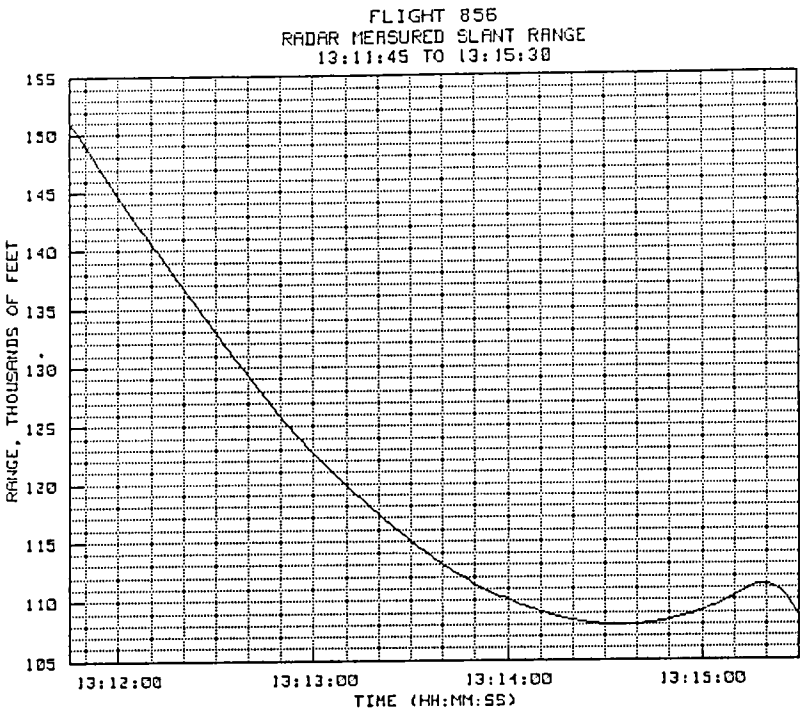

Figure 6-20(e). TP #11 radar-derived slant range.

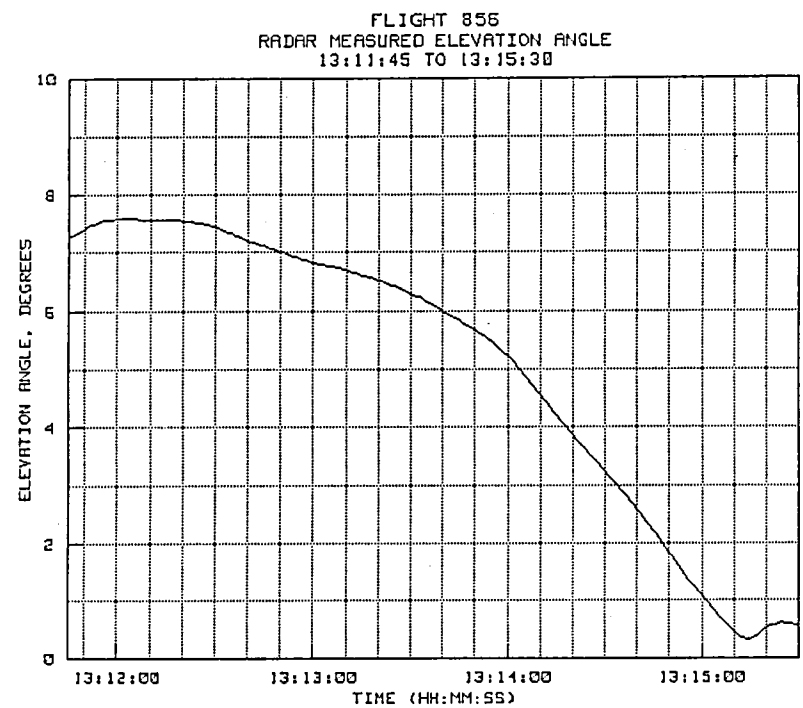

Figure 6-20(f). TP #11 radar-derived elevation angle.

6.2.12 Test Point #12

The time history plots for test point #12 are shown in figures 6-21(a) to 6-21(f). This was a ridge survey run, in which the planned flight path would take the tracked aircraft at a low altitude over Fremont Peak where multipath effects might be observed. The run was started on a true course of about 045 degrees at a slant range of 128,520 feet (21.15 n.mi.) and an elevation angle of 1.03 degrees. Altitude at the start of the run was 5400 feet, and a slow descent was made so that the aircraft would pass over the highest terrain with a clearance of about 1000 feet. As seen from the altitude plot, a relatively good track was maintained on the aircraft as it approached the peak, although some elevation oscillations started to occur as the aircraft approached the higher terrain points. At 13:22:05, the pilot indicated that he was over the peak, and shortly thereafter quite noticeable oscillations began in the elevation channel. Also note that during the period of high oscillations, the rms value of radar-derived altitude seemed to develop additional bias. Prior to reaching the mountain, the on-board altitude was about 40 feet above the geometric value. As multipath effects became greater, causing oscillations in the elevation channel, the rms value of the geometric altitude appeared to decrease somewhat. The aircraft cleared the peak at 13:22:25 and commenced a climb to 8000 feet for the next data point.

The Mach number plots for this test point show very good agreement, considering the amount of antenna movement observed on the video monitor. The momentary oscillation at about 13:21:40 occurred as a result of a noise spike in both the range and elevation channels, probably due to a ground reflection.

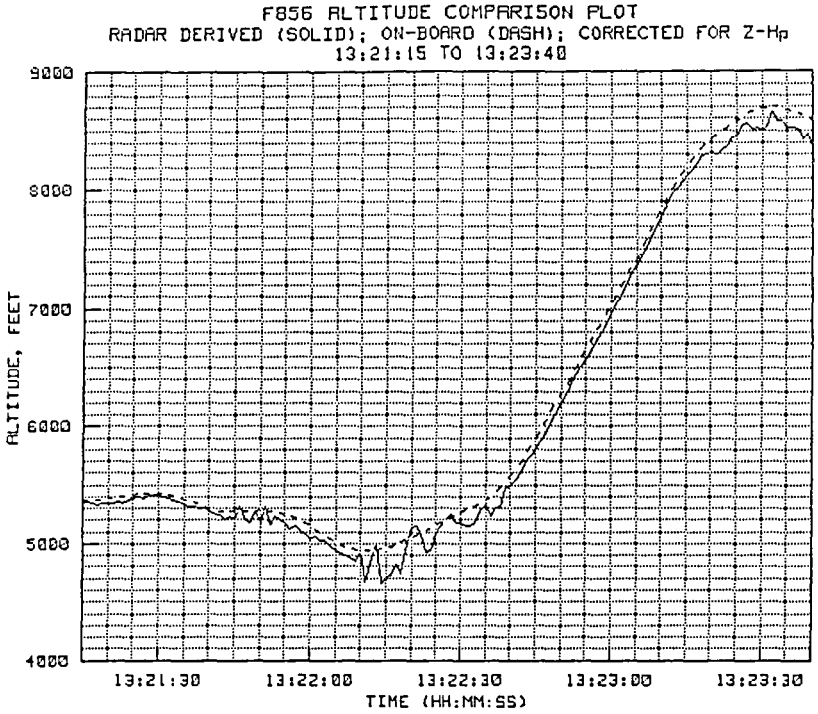

Figure 6-21(a). TP #12 radar-derived and on-board altitude.

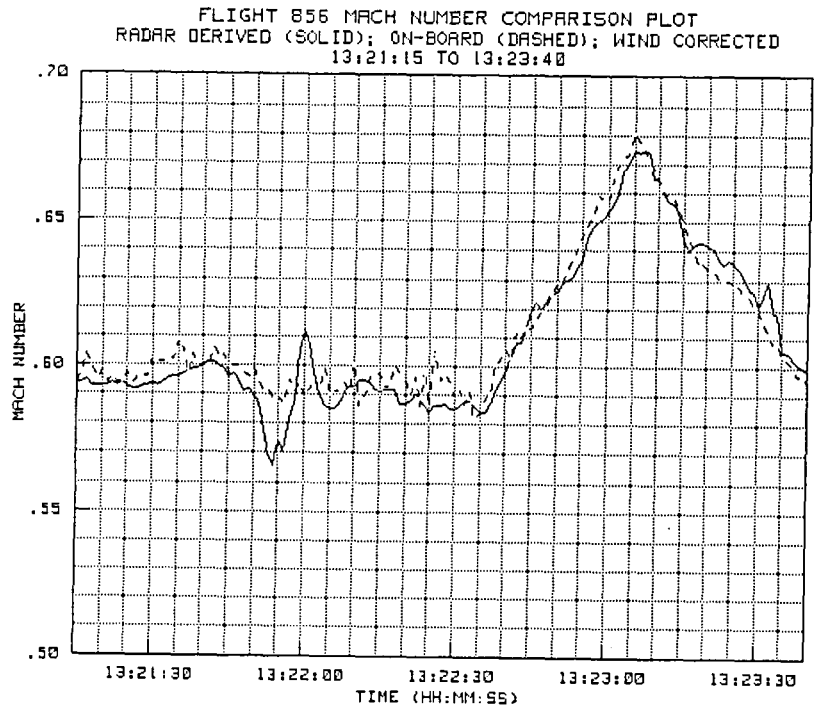

Figure 6-21(b). TP #12 radar-derived and on-board Mach number.

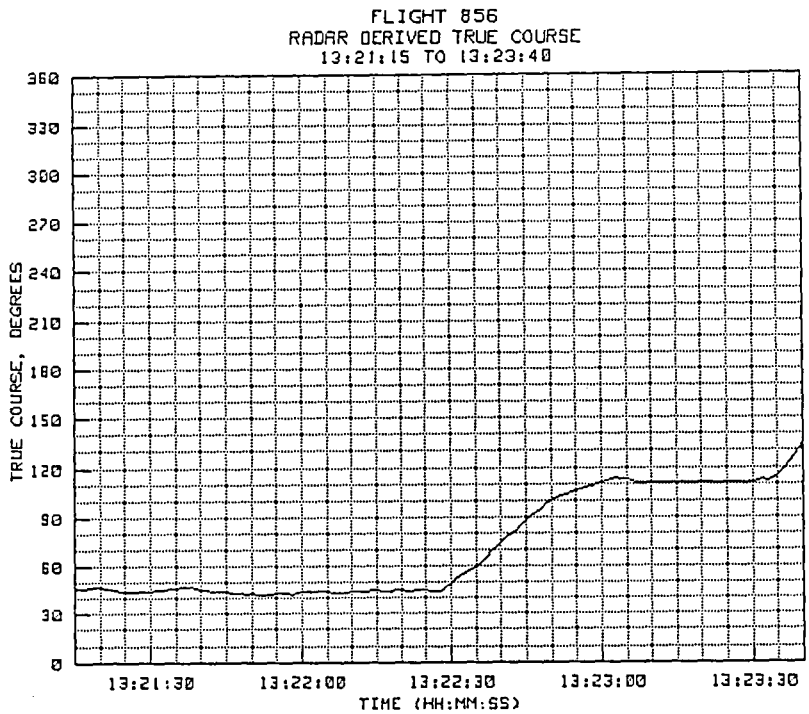

Figure 6-21(c). TP #12 radar-derived true course.

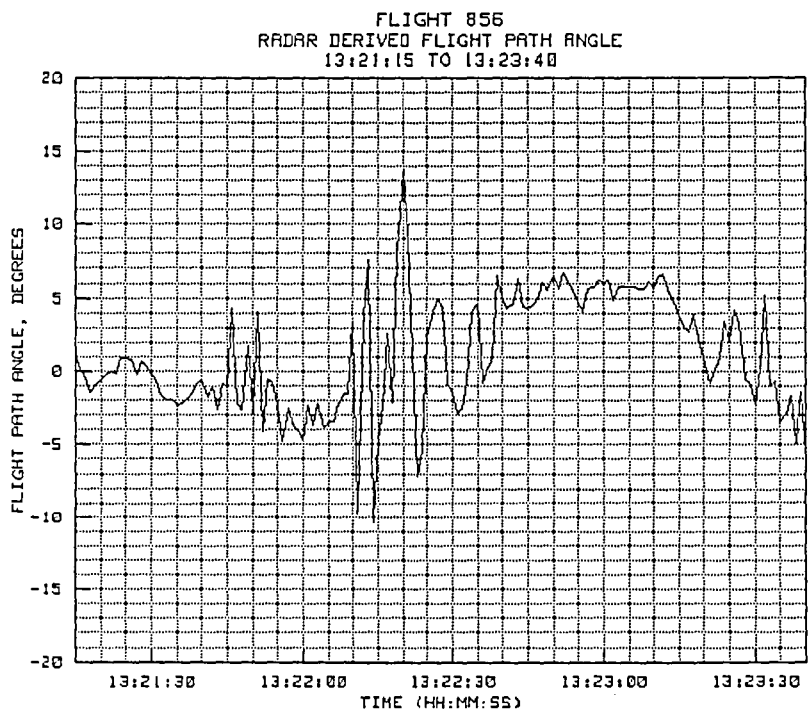

Figure 6-21(d). TP #12 radar-derived flight path angle.

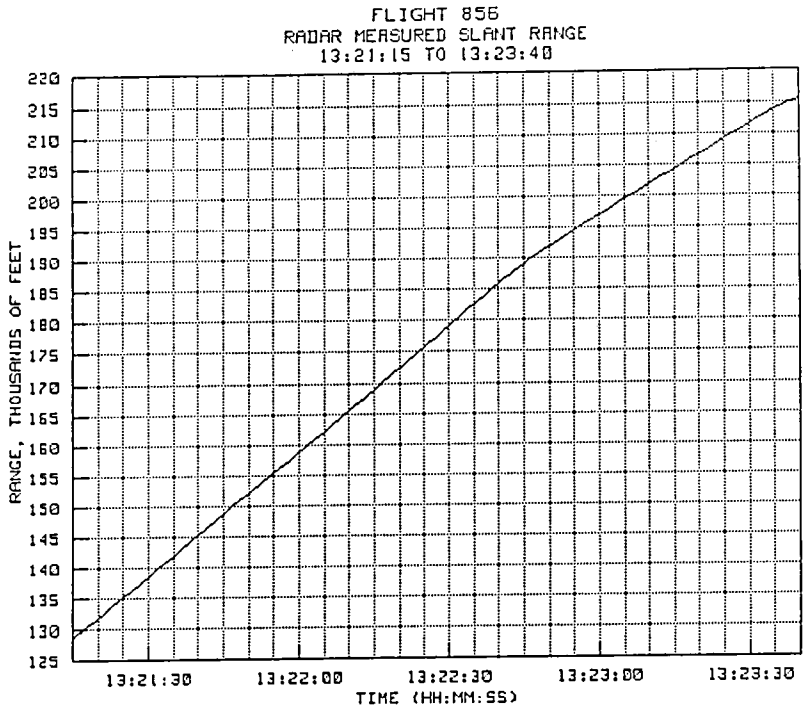

Figure 6-21(e). TP #12 radar-derived slant range.

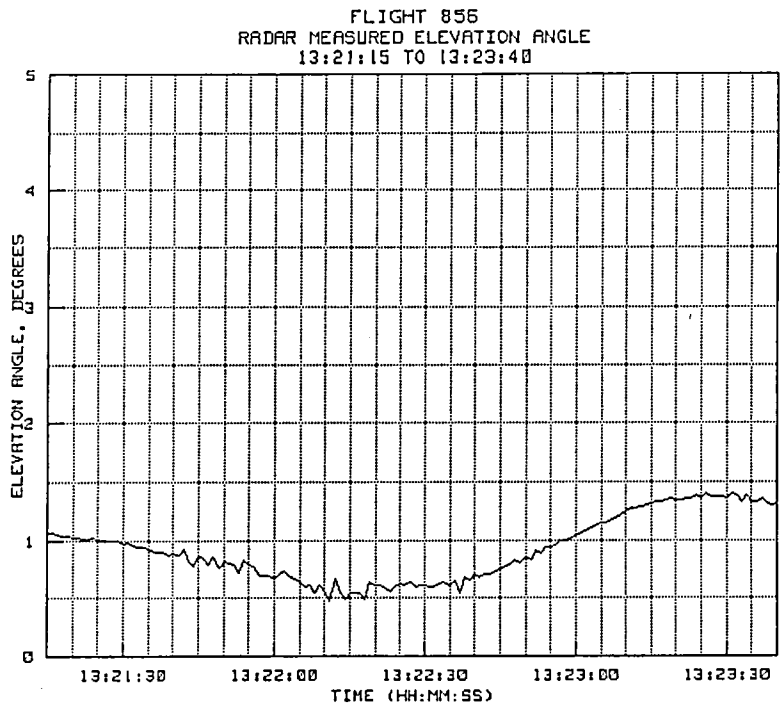

Figure 6-21(f). TP #12 radar-derived elevation angle.

6.2.13 Test Point #13

The time history plots for test point #13 are provided in figures 6-22(a) to 6-22(f).

This test point was a valley run in which the aircraft decreased altitude until line of sight was obscured by terrain blockage. The run was commenced on a heading of 300 degrees at an altitude of 8000 feet. Elevation angle at the start of the run was 1.31 degrees, decreasing to about 0.5 degrees at the time the signal was lost. Slant range at the start of the pass was 198,023 (32.59 n.mi.). A reasonably constant Z-Hp bias could be seen in the altitude data (Fig. 6-22(a)) as the aircraft descended. The bias remained until the signal was abruptly lost as the aircraft flew down the valley and was blocked by the higher terrain to the south. The aircraft emerged from behind the terrain about 13:26:01 and was immediately reacquired by the radar. Note that, at the point of reacquisition, the bias between the radar-derived altitude and the pressure altitude was about the same as for the earlier part of the run.

From this, it appears that there was no Z-Hp bias induced by multipath effects on this leg. A reasonably constant bias was present until the signal was lost, and the same amount of bias was present when the signal was regained. The difference between the preceeding run and this run was in the fact that the signal was lost abruptly and regained abruptly. In the previous test, the signal was allowed to degrade badly, but line-of-sight on the target was never lost.

It should also be noted that, at the point of signal loss, the operator allowed the antenna to coast (rate mode) so that, when the target reappeared, the antenna was reasonably well on-target so that an immediate acquisition could be made. Also note that the radar plots dropped out at the time the ON TGT bit went to a zero value. This was a feature originally included in the plotting program so that only valid on-target data would be plotted.

The Mach number plots for this test point (Fig. 6-22(b)) show reasonably good agreement during the time good line of sight conditions existed. The Mach calculation became erratic at signal loss, and had some oscillatory errors immediately after the track was regained.

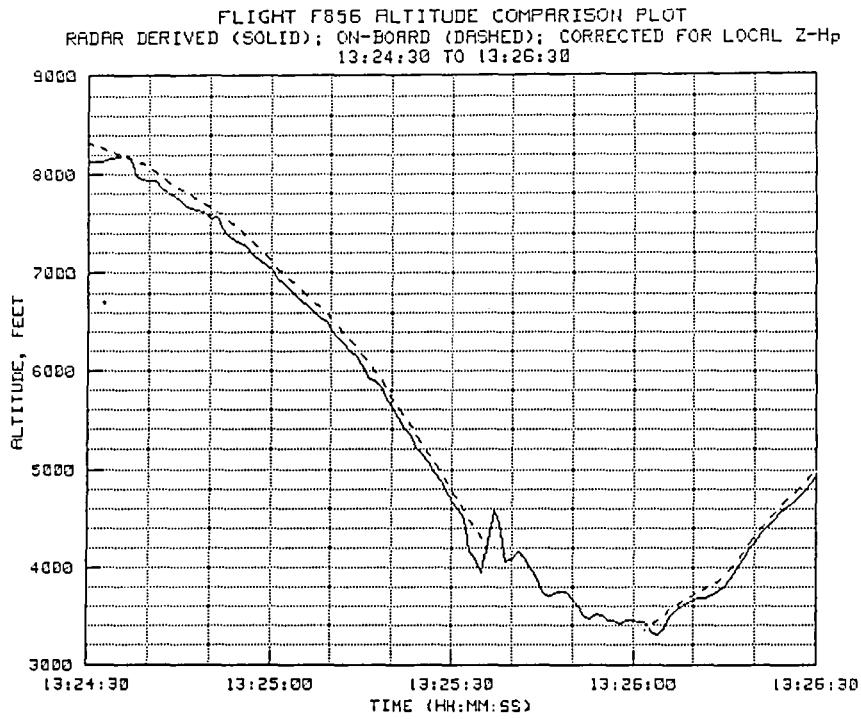

Figure 6-22(a). TP #13 radar-derived and on-board altitude.

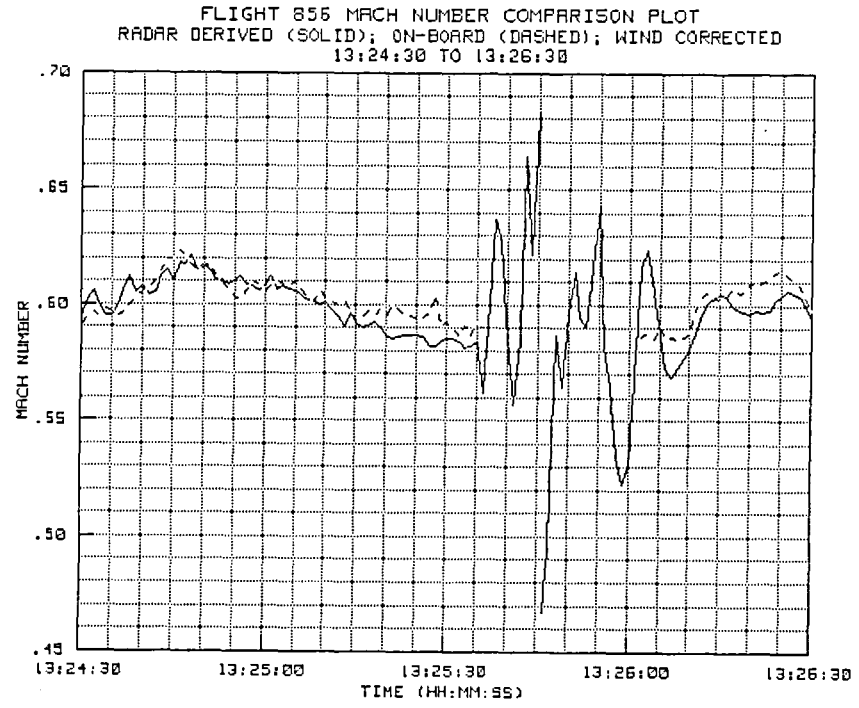

Figure 6-22(b). TP #13 radar-derived and on-board Mach number.

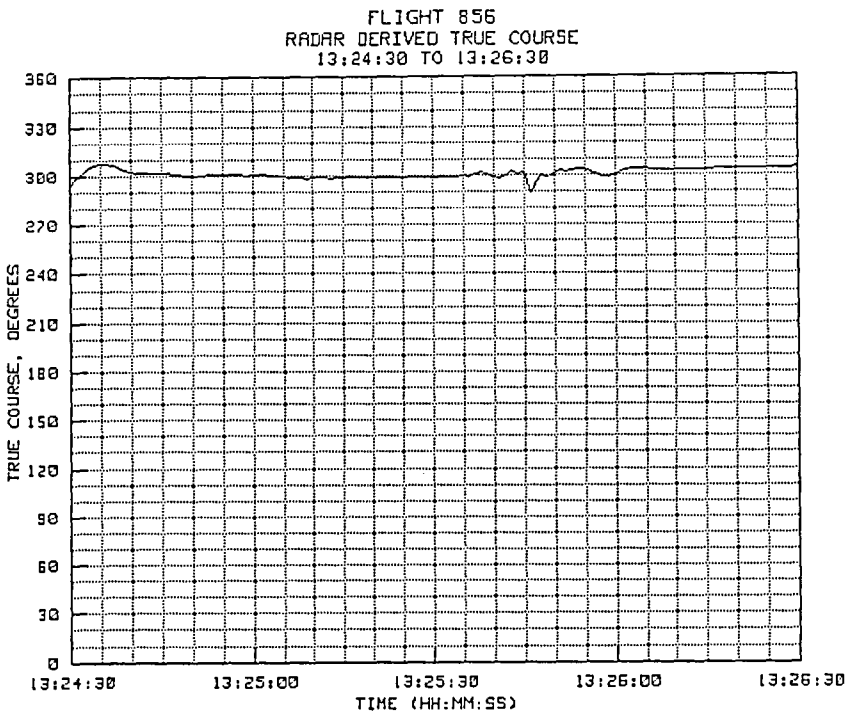

Figure 6-22(c). TP #13 radar-derived true course.

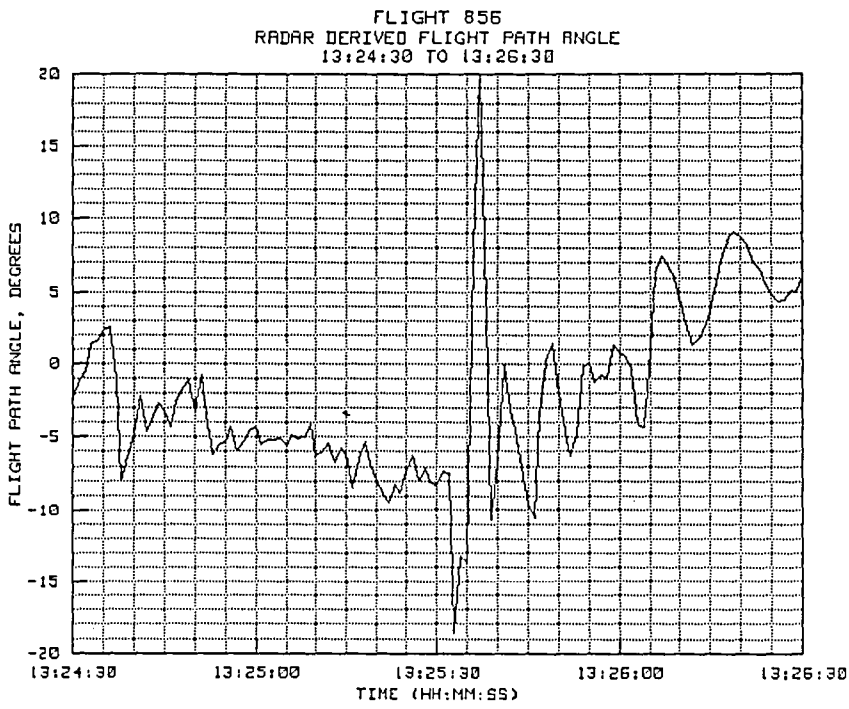

Figure 6-22(d). TP #13 radar-derived flight path angle.

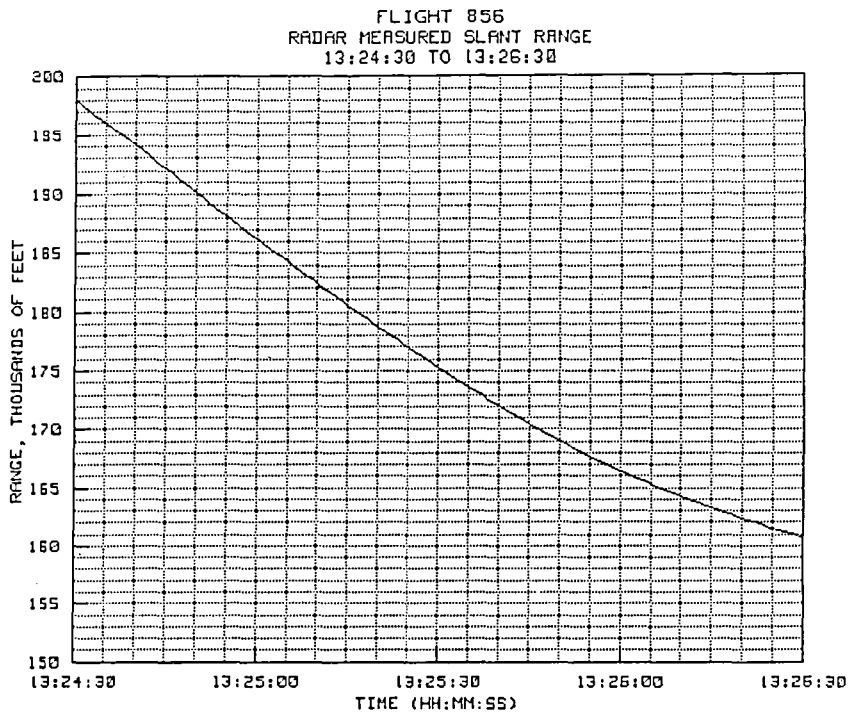

Figure 6-22(e). TP #13 radar-derived slant range.

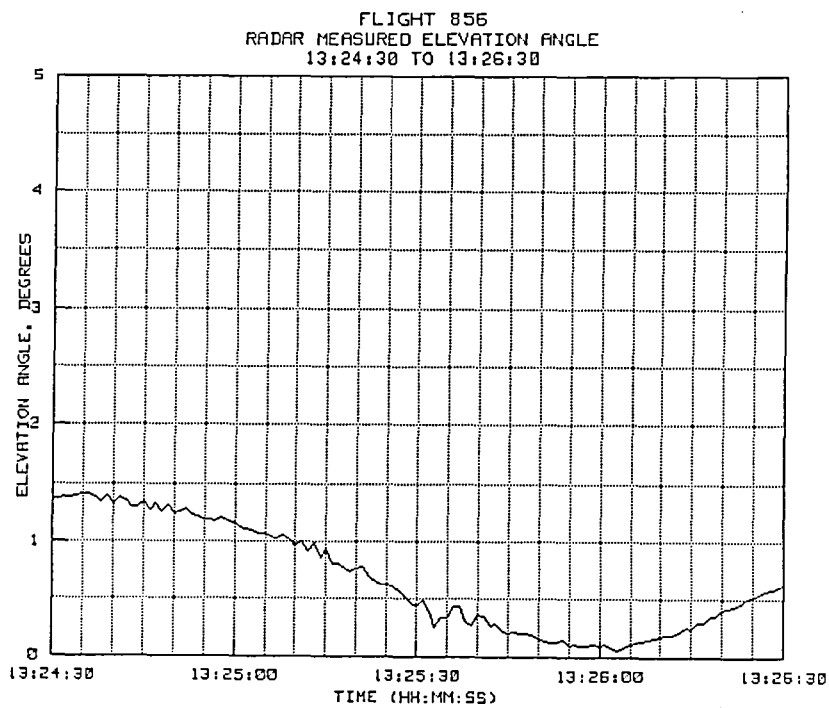

Figure 6-22(f). TP #13 radar-derived elevation angle.

6.2.14 Test Point #14

The time history plots for test point #14 are provided in figures 6-23(a) to 6-23(f). This was an arcing leg during which the aircraft slant range went from 79,797 feet (13.13 n.mi.) down to 34,042 feet (5.60 n.mi.). Elevation at the start of the leg was 2.01 degrees, increasing to 5.02 degrees as the slant range decreased.

The altitude plot appears to have about 10 or 20 foot bias in the Z-Hp correction used to convert pressure altitude measurements to an approximate geometric altitude. This is about the same as bias present in the latter portion of the initial arcing maneuver (test point #1) for an altitude of approximately 5000 feet. Since, in this case, the bias appears to be about constant from about 80,000 to 35,000 feet slant range, it is concluded that the bias is due to an error in estimating the amount of Z-Hp bias for 5500 feet. The radar-adjusted Z-Hp value of about 137 feet is probably about 10 to 20 feet higher than the true value. The unadjusted synoptic estimate of Z-Hp for 5500 feet was about 184 feet which would have yielded a bias of about 60 feet between the two sets of data.

The Mach number plot for the arc also showed close agreement between the radar-derived and on-board data. Again, the effect of low-level turbulence on the on-board pressure measurements can be seen clearly in the dashed line on the Mach plot.

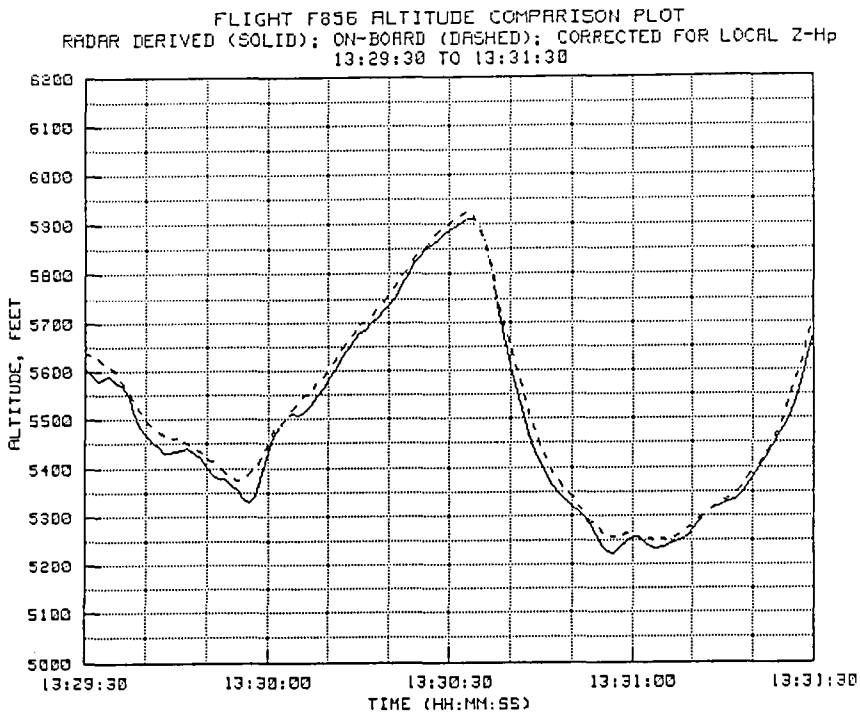

Figure 6-23(a). TP #14 radar-derived and on-board altitude.

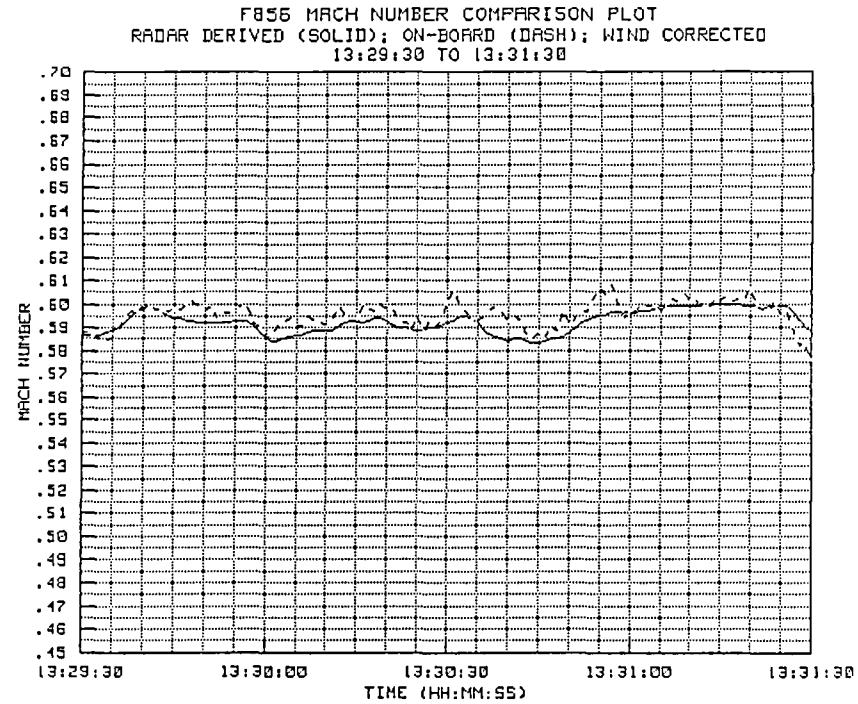

Figure 6-23(b). TP #14 radar-derived and on-board Mach number.

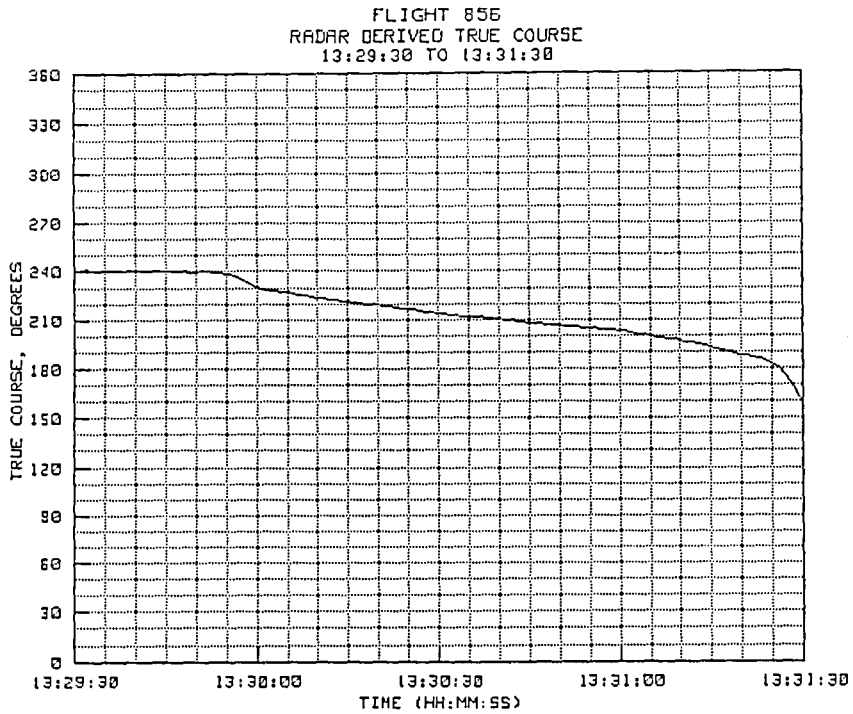

Figure 6-23(c). TP #14 radar-derived true course.

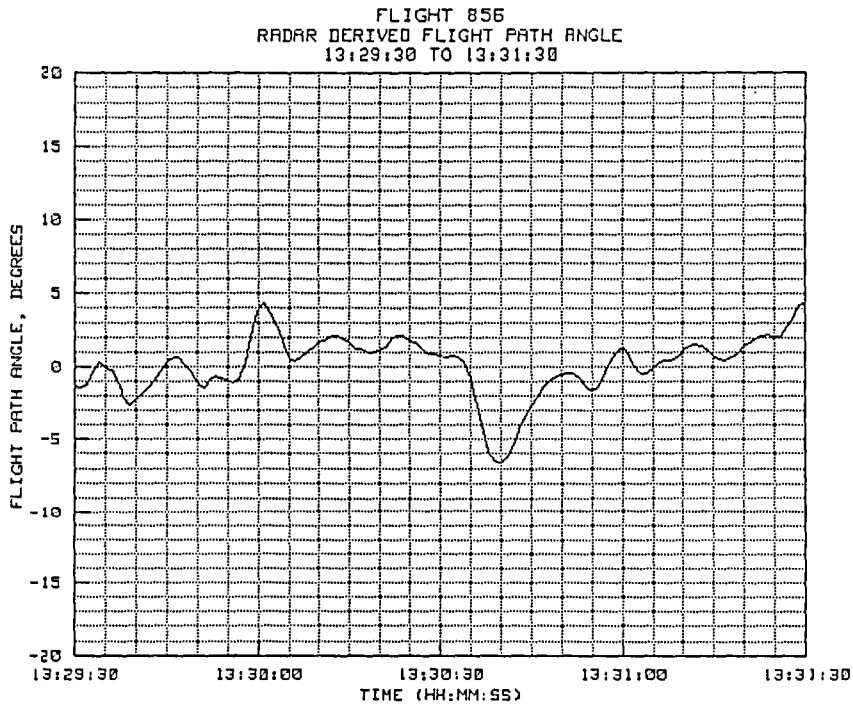

Figure 6-23(d). TP #14 radar-derived flight path angle.

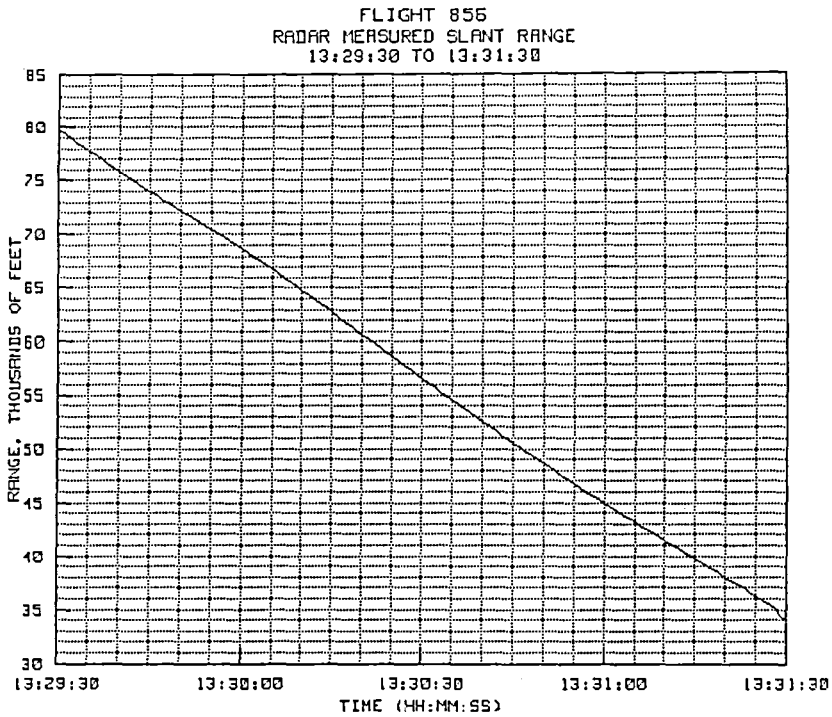

Figure 6-23(e). TP #14 radar-derived slant range.

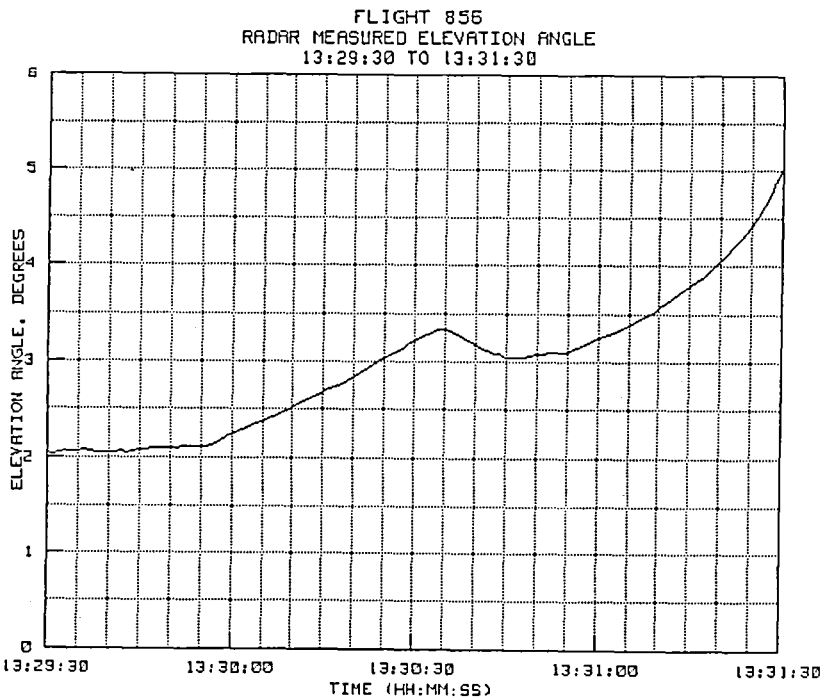

Figure 6-23(f). TP #14 radar-derived elevation angle.

6.2.15 Test Point #15

The time history plots for the last test point are shown in figures 6-24(a) to 6-24(f). All of this track was at very close range, 25,550 feet (4.20 n.mi.) and less. The elevation angle started at 5.99 degrees and steadily decreased to 2.26 degrees. Again, the altitude plot revealed nothing unusual, and the Mach number plot was stable except for a 0.02 difference at the initial turn in. Video recordings showed the track throughout this test point to be excellent, with only very minor (1 to 2 foot) variations in the track point.

Again note that a 10 to 20 foot difference was still present in the altitude data for levels above 4800 feet, even though the target was at about the same slant range as at takeoff. From 4800 feet down to 4000 feet the two altitude measurements appeared to be about the same and then, below 4000 feet, some bias again started to appear. Since the aspect angles were good throughout this test point and the track point was nearly constant, the variations observed on the plot are probably due to errors in the Z-Hp corrections or possibly to some airspeed variations in the on-board measurements.

The touchdown, at 13:36:40 (see Fig 6.9), revalidated the radar-derived geometric value of the runway elevation.

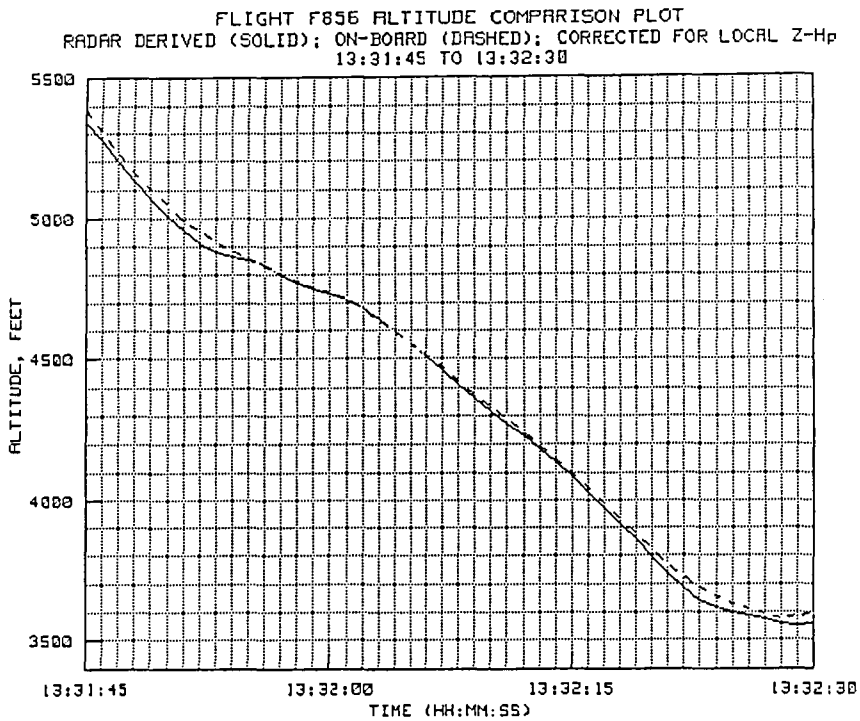

Figure 6-24(a). TP #15 radar-derived and on-board altitude.

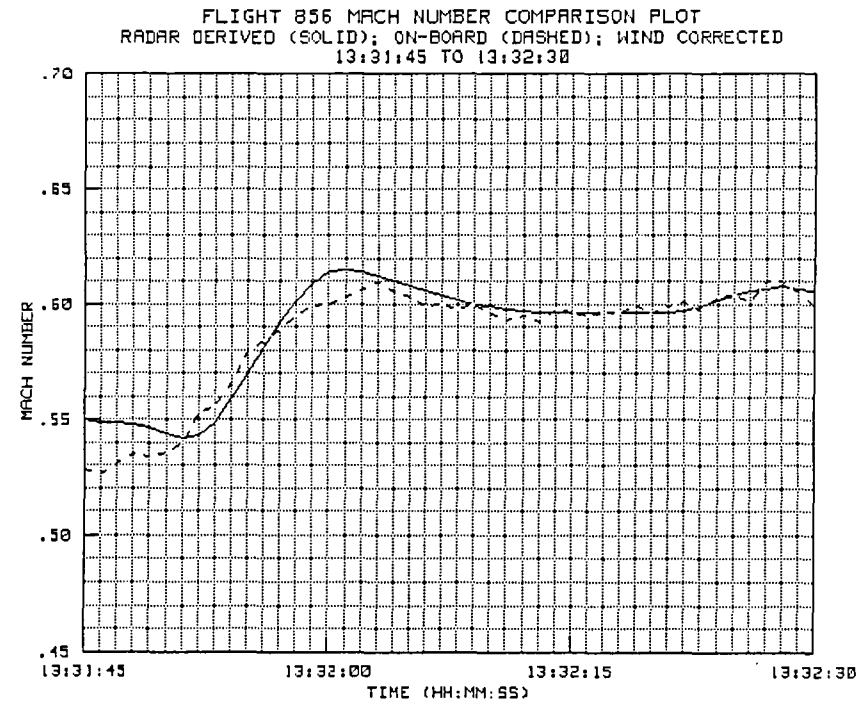

Figure 6-24(b). TP #15 radar-derived and on-board Mach number.

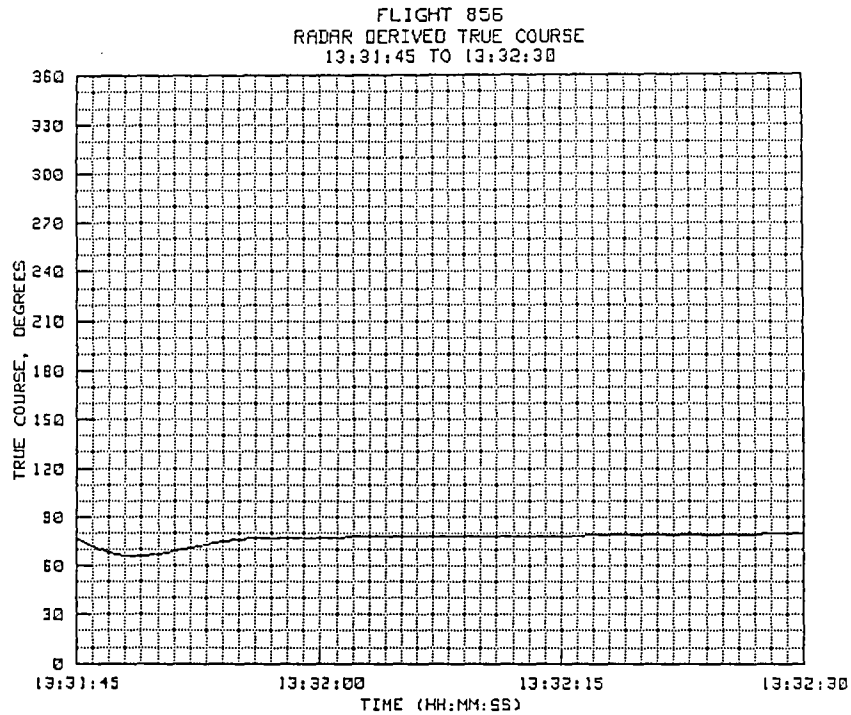

Figure 6-24(c). TP #15 radar-derived true course.

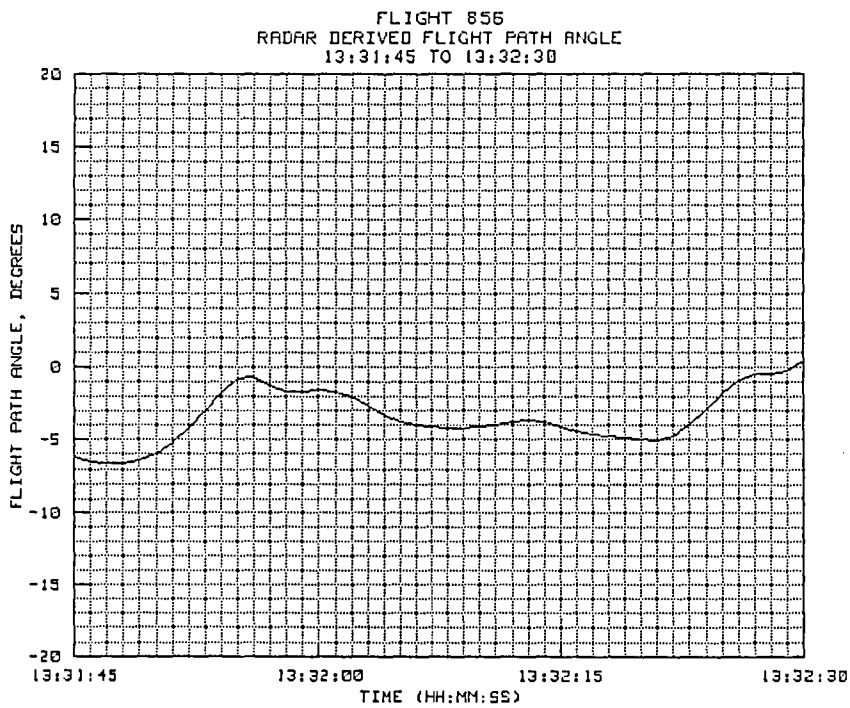

Figure 6-24(d). TP #15 radar-derived flight path angle.

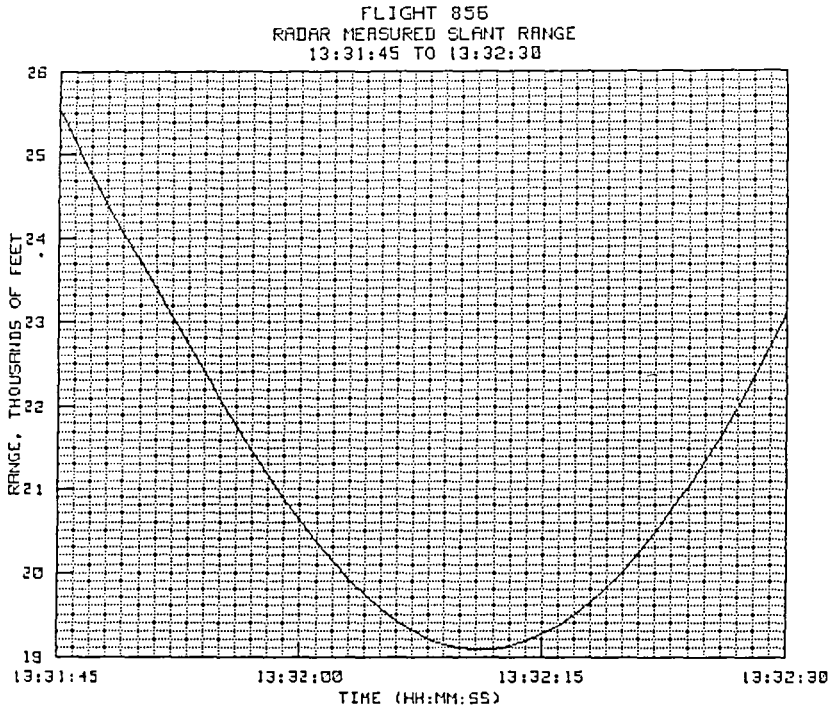

Figure 6-24(e). TP #15 radar-derived slant range.

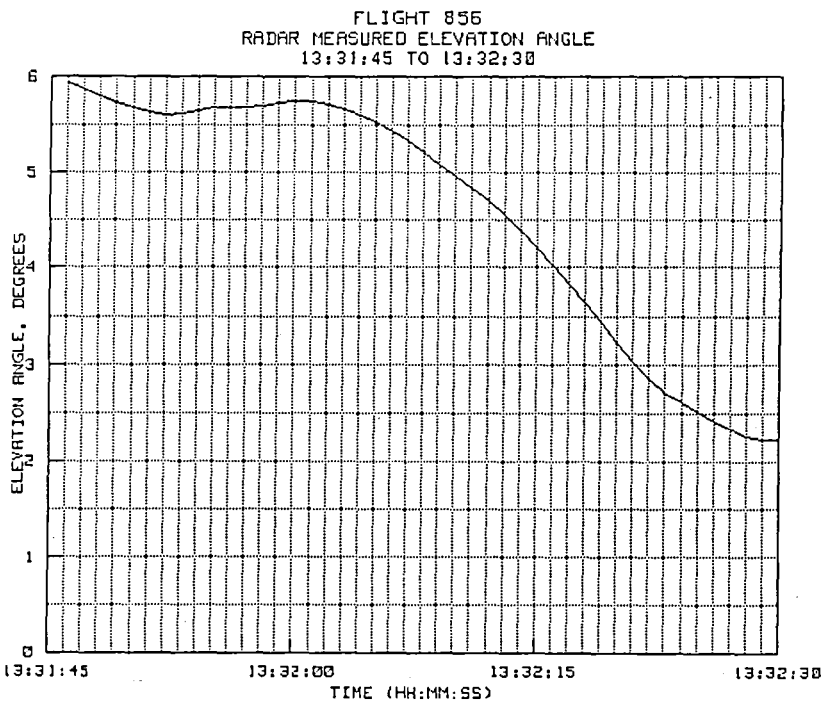

Figure 6-24(f). TP #15 radar-derived elevation angle.

6.3 Analysis of Wind Data for Flight 856

Immediately following the completion of flight 856, a rawinsonde balloon was tracked by the radar. Figures 6-25(a) and 6-25(b) provide plots of wind direction and velocity from both the radar track and the rawinsonde equipment.

Unfortunately, during the launch of the rawinsonde, the radio package struck the ground and the radar reflector broke from the package. Without the radar reflector, there was no passive echo target except for the small electronic package on the rawinsonde. Therefore, a consistent radar lock-on was not achieved until the balloon reached about 7000 feet.

Comparison plots of wind direction and velocity from the three sources are shown in figures 6-25(a) and 6-25(b). Radar-derived Mach number comparisons, using the three wind sources, are provided in figures 6-26 to 6-30.

Figure 6-26 is the portion of test point #1 from 12:35:00 to 12:39:00. During this time the on-board Mach number held between 0.60 and 0.62. Note that it was below the point where winds from the radar balloon track were reliable therefore the short-dashed line should be disregarded. In this case, Mach plots using synoptic and rawinsonde winds are almost identical, and both agree reasonably well with the on-board data. Maximum difference is about 0.01 Mach in the earlier part of the run.

Figure 6-27 shows comparison plots for Mach numbers derived from all three wind sources during a climb from 4000 to 13,000 feet. Below about 6500 feet, both the synoptic winds and the rawinsonde winds yield good Mach results. Above that level, winds from all three sources yielded sizeable errors (0.01 to 0.03 Mach) in the calculations, with no particular source appearing to offer any distinct accuracy advantage. During the climb, no abrupt heading changes were made, however, as noted in the discussion of test point #2, the bias in the radar-derived Mach number appears to correlate with the time the flight path angle exceeded 5 degrees, suggesting the possibility of a bias in the on-board measurement.

Figure 6-28 is a plot of Mach number derived during a 2-g turn described in test point #8. Although some minor target glint effects were present, it does show almost identical results in the Mach calculations from all three wind sources, even though none of the three plots agree well the the on-board data. Note that three Mach number plots are all present, but the last plot made, that for the synoptic data, obscured the other plots during most of the time period.

Figure 6-29 shows Mach number data derived during a roll maneuver at about 26,000 feet. Although the radar measurements suffered from glint effects, all three wind sources yielded Mach number results which were again nearly identical, but none of the three agreed well with the on-board data. As in the previous case, the Mach data from the synoptic winds was plotted last and obscured portions of the other plots. As noted in the discussion of test point #9, the period of high bias occurred during a 3-g turn initiated at 13:04:05 and completed at 13:04:40.

Mach number calculations during part of the test point #11 descent are shown in figure 6-30. During the time shown, the Mach remained fairly constant at 0.6, and the altitude went from 20,000 feet at the start of the plot down to 7000 feet at 13:14:40. Mach number calculations from all sources show the same type of differences as seen in the other plots, even though Mach numbers derived from all three wind sources seem to be relatively consistent. Recall that the period of high-bias coincides with the time the flight path angle went to and remained below -10 degrees, again suggesting a possible effect of angle of attack on the on-board Mach number measurement.

These results again indicate that highly accurate Mach number data cannot be derived from radar measured range, azimuth, and elevation. Even during stable period of flight when no target glint effects are present, the variability of the true wind can cause sizeable errors in the calculations made with wind data derived from radar balloon tracks, rawinsonde measurements, or synoptic data. Unless some technique for instantaneous wind measurement is forthcoming in the future, radar-derived Mach number data appears to be useable only for approximate Mach number calculations.

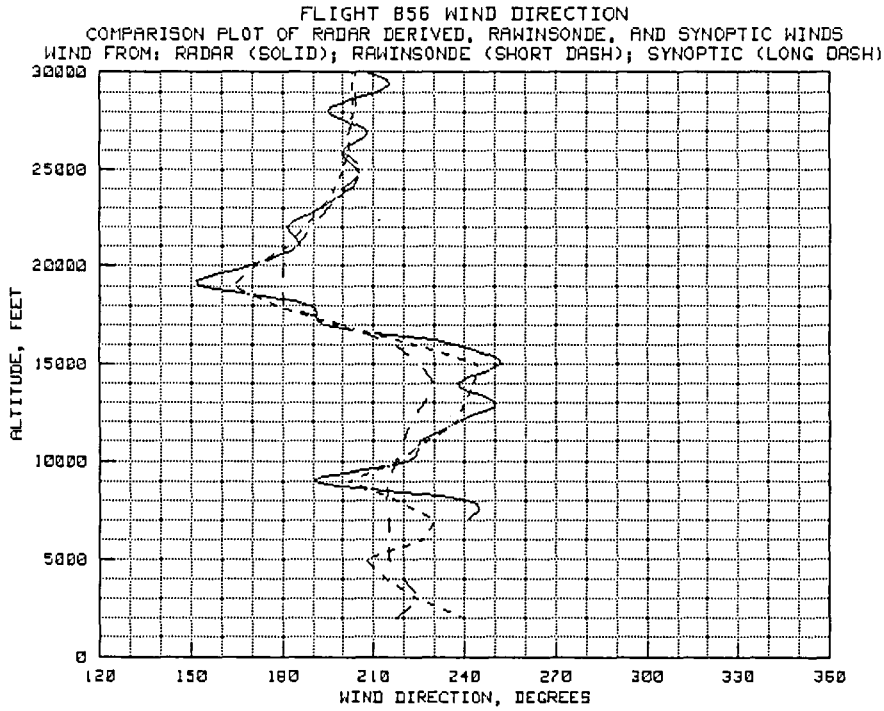

Figure 6-25(a). Flight 856 wind direction.

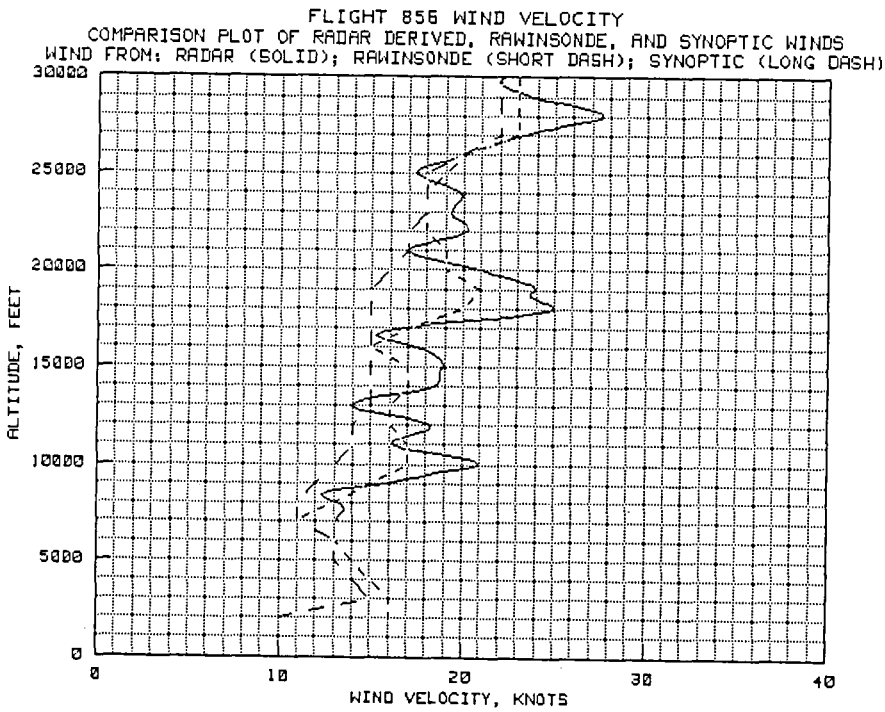

Figure 6-25(b). Flight 856 wind velocity.

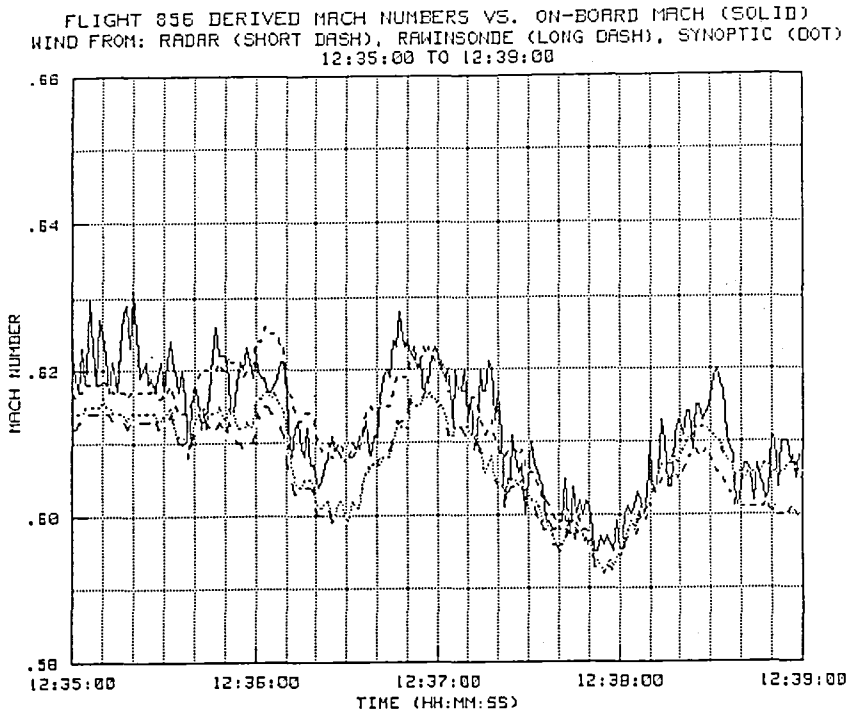

Figure 6-26. Flight 856 Effect of wind source on Mach.

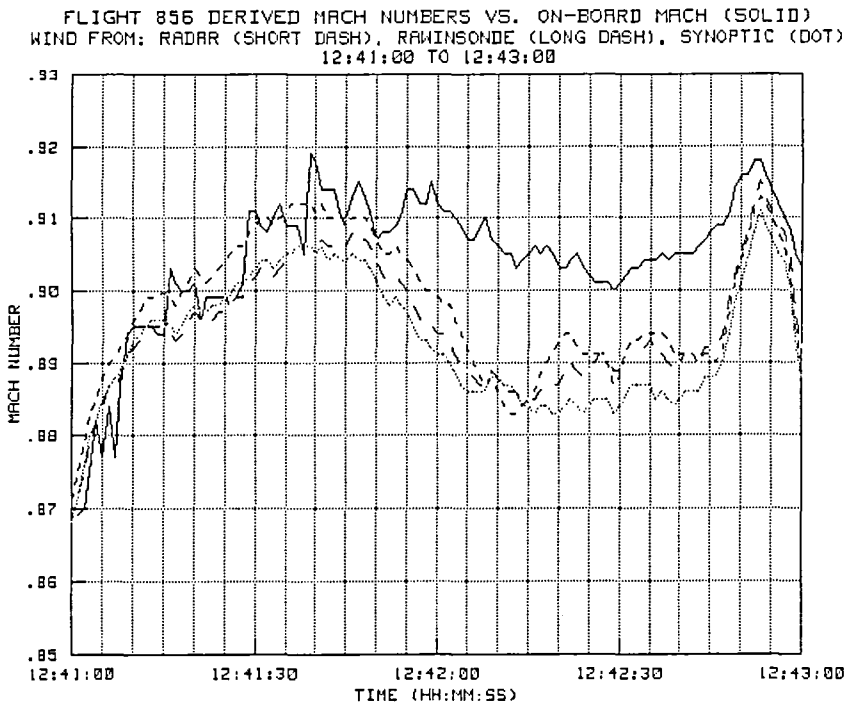

Figure 6-27. Flight 856 Effect of wind source on Mach.

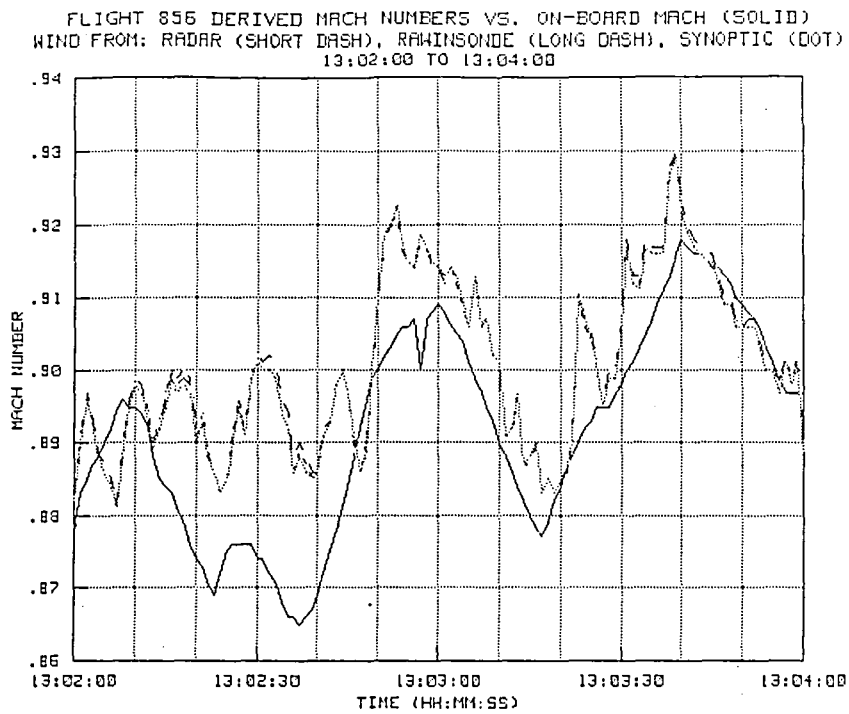

Figure 6-28. Flight 856 Effect of wind source on Mach.

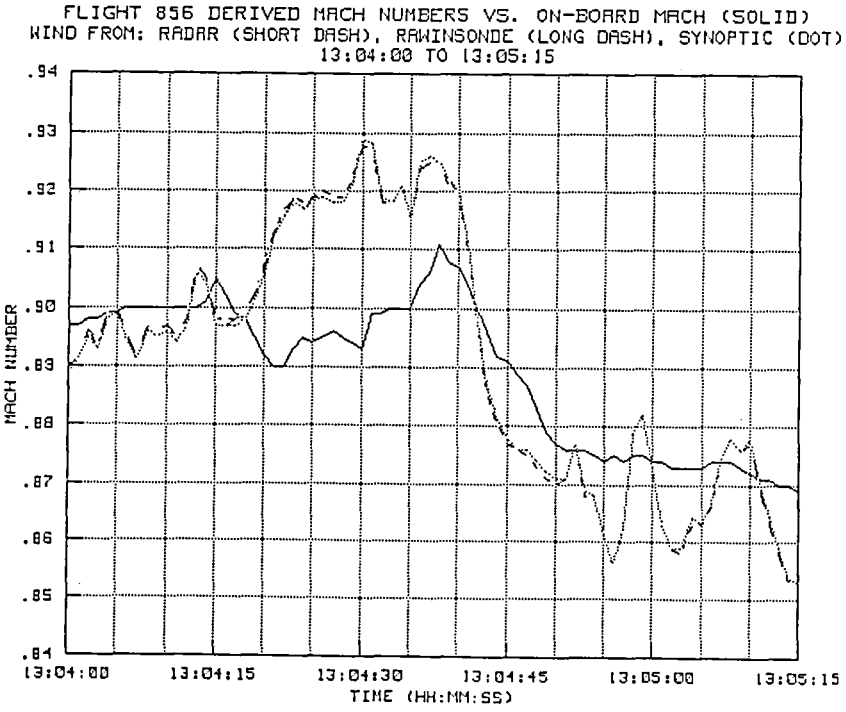

Figure 6-29. Flight 856 Effect of wind source on Mach.

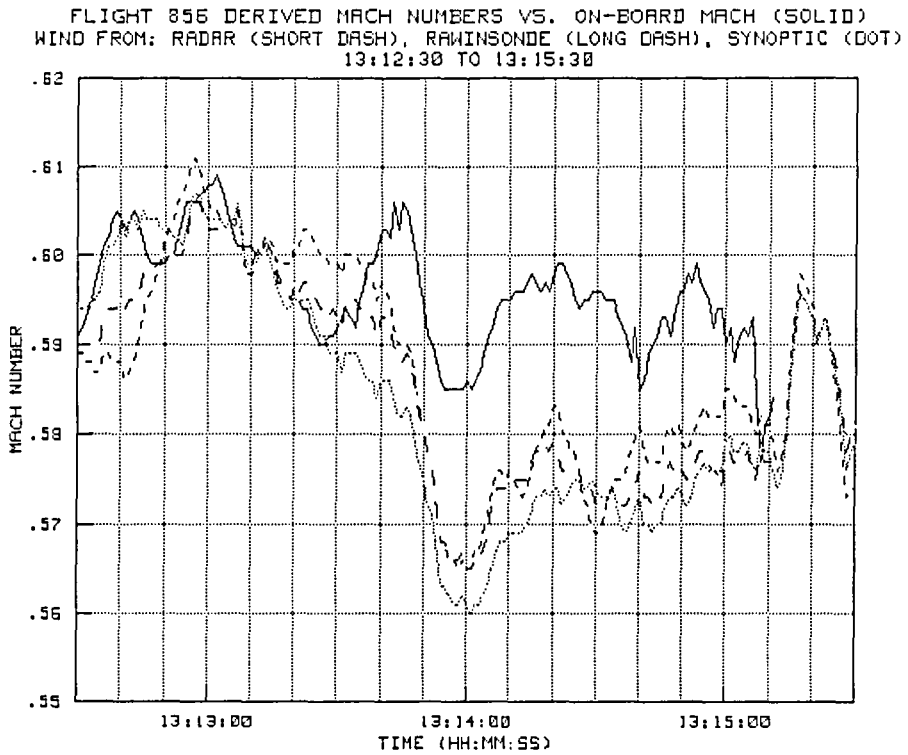

Figure 6-30. Flight 856 Effect of wind source on Mach.

6.4 Noise Analysis For Flight 856

Figures 6-31, 6-32, and 6-33 provide 1-sigma time history plots of the random noise contained in the range, azimuth, and elevation channels.

The large spike seen in the range plot immediately after takeoff occurred at the transition from aided track to full auto track. The spike at 12:46:00, evident only in the range channel, was caused by a momentary reflection of the beacon return off the chase aircraft. The long segment of high noise in all channels about 12:51:00 occurred during skin track when the lock transferred to a target side lobe.

The sharp spikes just after 12:53:00 occurred in skin track and are believed to have been caused by a combination of target glint and momentary chase plane reflections; however, lock was not lost. Noise was also evident in all channels during the 2-g maneuvers of test point #8; however, the noise was sucessfully filtered to the point where the data plots appear normal.

All of the data had low noise content from about 13:04:00 until 13:22:00 when a sharp noise spike is seen in the data from all three channels. This was the point at which the aircraft, on the ridge run, was approaching Fremont Peak and a considerable amount of oscillation could be observed on the radar video monitor. The next spike occurred at 13:25:30, the point of signal loss during the valley run. A final jump in range occurred at 13:36:30, approximately the time when the operator selected the AIDED EL track mode for landing.

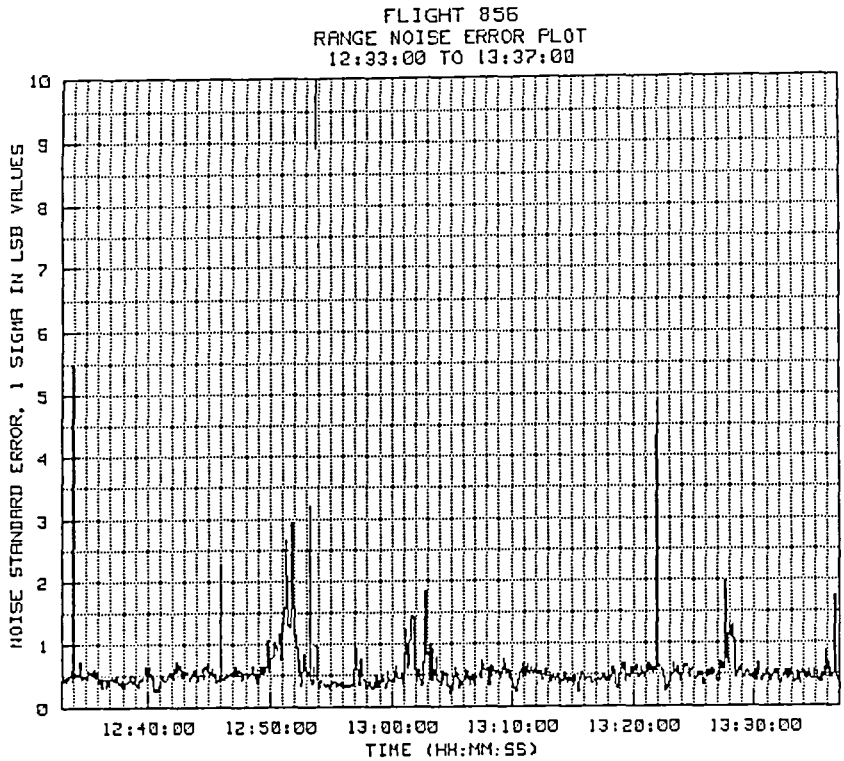

Figure 6-31. Flight 856 range noise plot.

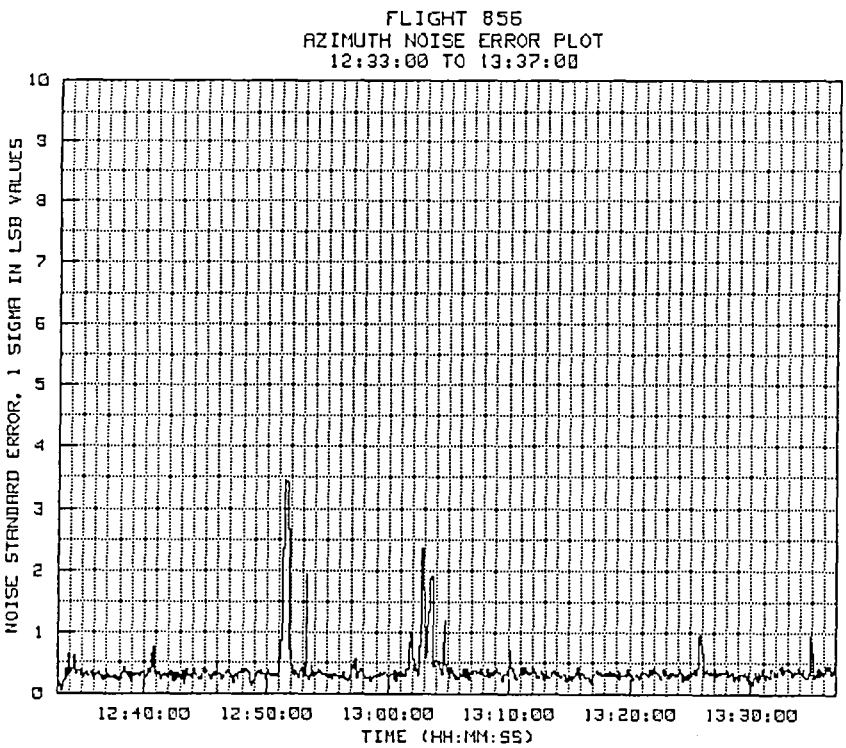

Figure 6-32. Flight 856 azimuth noise plot.

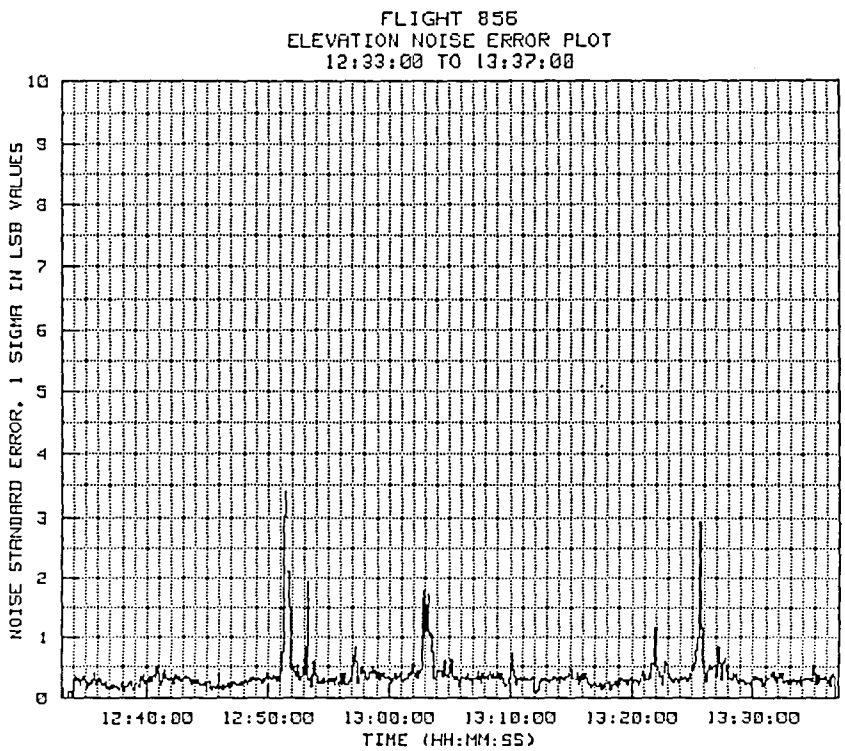

Figure 6-33. Flight 856 elevation noise plot.

6.5 Summary of Results from Flight 856

Flight 856 was flown on a day with benign atmospheric and wind conditions. At the time of the rawinsonde measurements, the surface wind was variable at 16 knots with typical velocities at the upper levels from 15 to 25 knots. Wind direction was west-southwesterly at the surface, shifting to a more southerly direction at about 15,000 feet.

Test points for flight 856 were intended to provide additional information about the low-elevation, long-range anomaly in the altitude derivation, and to provide some comparative data from the skin-tracking mode.

Test point #4 was a survey run which started in beacon mode and ended in skin mode. On this run, the low angle anomaly in the altitude derivation was clearly visible in the data, both during both the beacon track and the skin track, and in essentially the same amounts. As expected, this verified the fact that the problem was not unique to just the beacon tracking mode.

Another result from test point #4 was to demonstrate the effects of aim point movements when in the skin track. At the point where the shift was made from beacon to skin, the noise in the Mach number calculation increased significantly. At the time, the target was at about 10 nautical miles range at an elevation angle of about 8 degrees. At the shift, a marked increase in antenna movement was also observed on the visual monitor. These were fairly rapid movements that were probably due to three causes. First, because of the close range, the angle of the return signal was large allowing the antenna to wander over the large angular span of the target. Second, the chase plane, even though situated beyond the target aircraft, appeared to cause momentary spurious returns that further increased the antenna jitter. Third, the tracking angle was rapidly increasing, and went to a maximum elevation value of just under 50 degrees in about a minute after the switch to skin track. Thus, a combination of glint from the large angular return, jitter from momentary spurious returns from the chase aircraft, and oscillations due to the servo lag conditions at high angles provided ideal conditions for a high level of noise in the Mach number calculations.

A close analysis of the data at the point where the track was lost during test point #4 indicates that the problem was not due to a transfer of lock to the chase aircraft, but rather to a transfer of lock to a side lobe. Since the side lobe condition occurred well after the high point in the track, at a time when the elevation angle was back down to about 7 degrees, it is very probable that both glint (due to the large angle subtended by the target) and the presence of

spurious returns from the chase aircraft both contributed to the transfer of lock to the side lobe. The side lobe condition can be clearly seen in the range plot for test point #4.

Test point #5, a 180-degree standard rate turn, was also tracked in the skin mode. Note that a considerable amount of noise was still present in the Mach data, even though the target was at a much longer range so that the target appeared as more of a point source. At the same time, the elevation angle was quite low (2 degrees and under), so that both multipath and glint problems were considered possible causes. Another possibility considered was frictional effects that occur when the antenna rates are extremely low. The elevation angle during this entire test point changed by only one-half degree from start to finish, so the elevation rates were indeed small.

Test point #6, a wings-level climb to 25,000 feet, was commenced immediately after the turn, and, even at the start of the climb where the elevation angle was still low, the amount of noise in the Mach calculation was less than half as great as in the turn. Therefore, based on this, multi-path effects can probably be ruled out as a major contributor to the noise in the Mach calculations for test point #5. A significant elevation rate was also present throughout all of the climb so that frictional effects, if they were present during test point #5, should have been less during the climb. However, if frictional effects were a major contributor to the Mach noise in test point #5, the same effects would have been observed on other flights when elevation rates were very low, and they were not observed. Thus, noise in the Mach calculations for both test points #4 and #5 can most likely be attributed to glint effects. Thus, while the skin track does not suffer from the beacon shielding effects during the turning maneuvers, it does suffer from target glint and as a result has increased noise in the first derivative (Mach) calculations. However, the antenna is probably less susceptible to off-track conditions that generally occur as a result of shielding and cross polarization during manuevering flight in the beacon mode.

The data from the push-pull acceleration and deceleration in test point #10 showed a considerable amount of dynamic lag to be present if sudden flight path or airspeed changes are made. If the operator were aware that such maneuvers were about to be performed, the antenna bandwidth settings could be increased to provide a faster response to the azimuth and elevation error signals, however no attempt was made to do this during these tests.

During this flight, several periods of high Mach number bias seem to correlate with the onset of high-g conditions or steep climb or descent maneuvers. This suggests the possibility of errors in the on-board measurements during highly dynamic maneuvers.

Finally, it must again be concluded that the use of radar data for Mach number calculations can introduce errors, even during benign day conditions. This is due to (1) variability in the wind and (2) the high susceptibility of the Mach calculations to even slight noise in the position measurements. Furthermore, none of the wind sources analyzed (radar ballon tracks, rawinsonde wind measurements, or synoptic analyses) show any significant accuracy advantage in estimating Mach number from radar-derived ground speed.

7.0 SPACE SHUTTLE 41C, EDWARDS APPROACH AND LANDING

On 13 March 1984, AN/FPS-16 #34 supported the approach and landing of STS-41C at Edwards AFB, California. The reentry was made over the Pacific Ocean and initial acquisition by the NASA radar was made at about 2,300,000 feet (378 n.mi.). At the time of acquisition, designate data was being received from the Vandenberg radars via the DoD acquisition line. The acquisition data was used by the on-site A900 computer system to generate azimuth and elevation drive signals and to position the range gate to the expected target position. When the target first appeared in the acquisition window, the elevation angle was approximately 0.8 degree and the azimuth was 268 degrees. Lock-on was achieved at 13:26:06 GMT. The Shuttle was continuously tracked from the pont of initial acquisition until touchdown, with one off target situation occurring as the vehicle passed directly overhead. The total lapsed time from the initial acquisition to the overhead point was 8 minutes. The total lapsed time including the landing was 12 minutes.

7.1 Analysis of Data from STS-41C Edwards Landing

Figures 7-1 through 7-3 provide the raw range, azimuth, and elevation data, and figure 7-4 provides the true course of the Shuttle from the point of acquisition until touchdown at Edwards. The real-time Kalman filter was used to reduce this data, and the filter constants were selected to provide slightly more damping than that used for analysis of typical aircraft missions.

At first acquisition, the altitude of the target, as shown in figure 7-5(a), was approximately 165,000 feet. The velocity, shown in figure 7-5(b), was about Mach 9.5 or 10,000 feet per second. Both the altitide and Mach number time history plots show the data from immediately after lock-on until overhead to be smooth. However, because the landing track on this mission passed directly over the radar, the lock was intentionally broken at 13:33:58 in order to prevent the antenna from going over the top into plunge. This was accomplished by designating the antenna to the M-3 optics pedestal. This caused the rapid slew from 257 degrees azimuth, around to 80 degrees azimuth. Lock was regained at 13:34:11. However, from the point of reacquisition through the final approach and landing, the presence of the chase aircraft in close proximity to the Shuttle caused an erratic track in all three channels. At 13:37:56 the operator selected the AIDED TRK mode for touchdown. Because of the spurious returns from the chase aircraft from about the time the Shuttle passed the zenith point until touchdown, a great amount of noise was present in the data. Since the skin track mode is not suitable for providing smooth tracking data

when multiple aircraft are operating in close proximity, no further analysis of the noise in the data was made from the zenith point to touchdown.

Since the expanded scale on both the altitude and Mach number time history plots obscured the smaller movements, blow-ups of these plots were made for the period 13:26:30 until 13:28:30. These are provided in figures 7-6(a) and 7-6(b). The altitude scale in figure 7-6(a) spans just 35,000 feet and shows the quality of the radar derived altitude for the period just after initial target acquisition. Note that the altitude data did not settle out until shortly after 13:27:00, but from that point on has about the same general appearance of descent data from the close-in F-104 flights. The Mach number plot for the same period is much smoother, however the total Mach range of the plot is from Mach 6 to Mach 9 so there could still be considerable masking of noise in the Mach number derivations for this period.

Figures 7-7(a) and 7-7(b) are even greater blow-ups of the altitude and Mach number data for the period 13:27:45 to 13:28:00. During this 15-second interval, the altitude went from about 150,700 feet down to 146,400 feet, a change of just over 4000 feet. In the same 15-second time period, the Mach went from just under 7.0 down to 6.7, a change of 0.3 Mach. Considering the fact that the target, at this point, was still in excess of 200 nautical miles from the radar at an elevation angle below 5 degrees, the plots appear to be extremely smooth. It should be mentioned that because of the short time base, the data in figures 7-7(a) and 7-7(b) were plotted at 20 pps intervals instead of the usual 1 pps interval. The smooth behavior of the data during these periods is indicative of the fact that, at these high altitudes, the real-world track of the vehicle is still reasonably smooth and predictable, because of the thinness of the atmosphere.

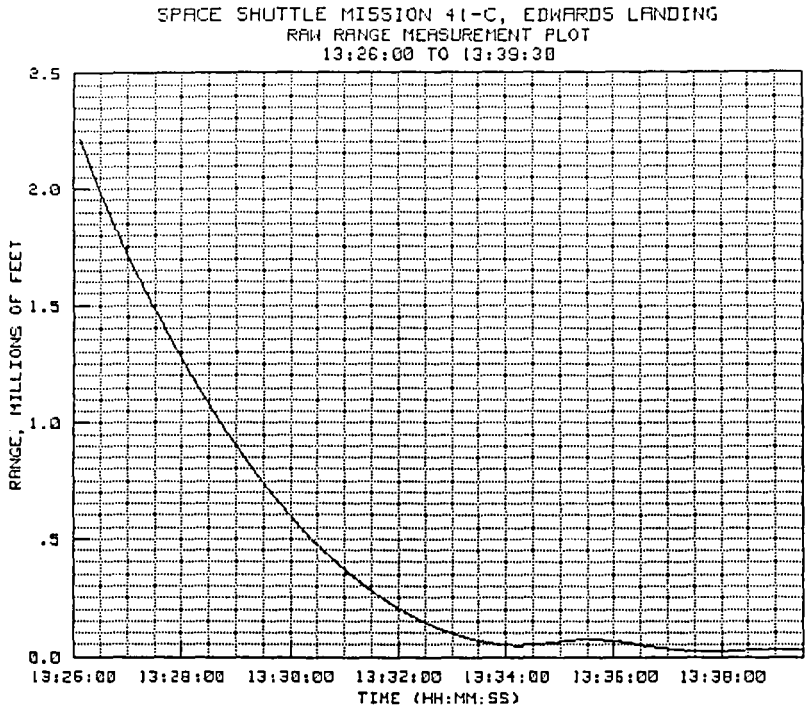

Figure 7-1. STS-41C radar-derived slant range on approach.

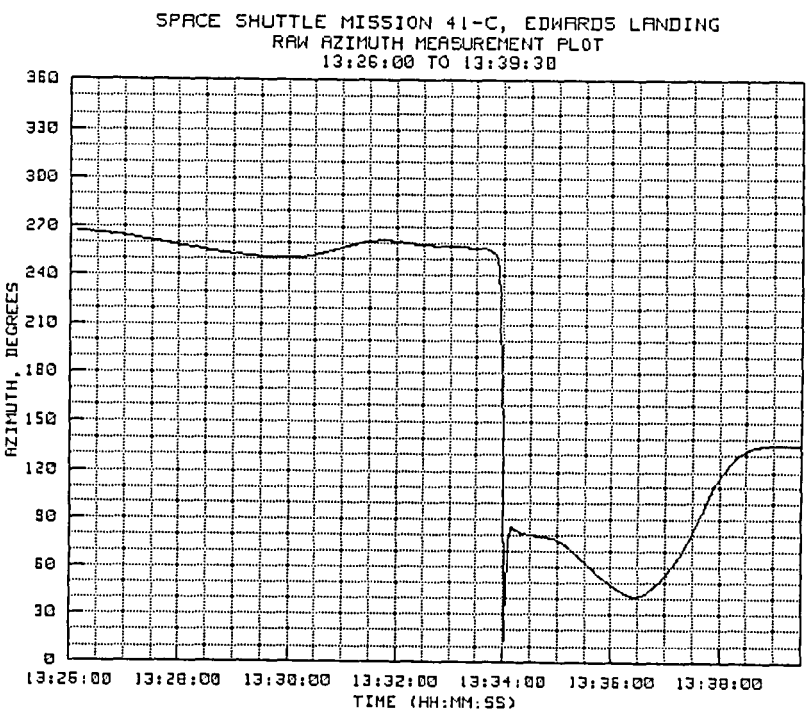

Figure 7-2. STS-41C radar-derived azimuth on approach.

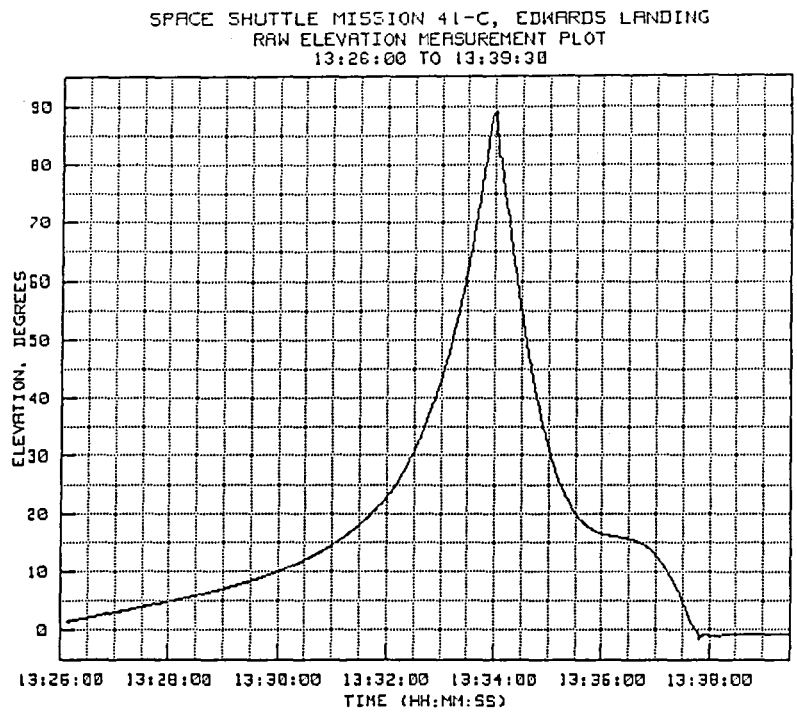

Figure 7-3. STS-41C radar-derived elevation on approach.

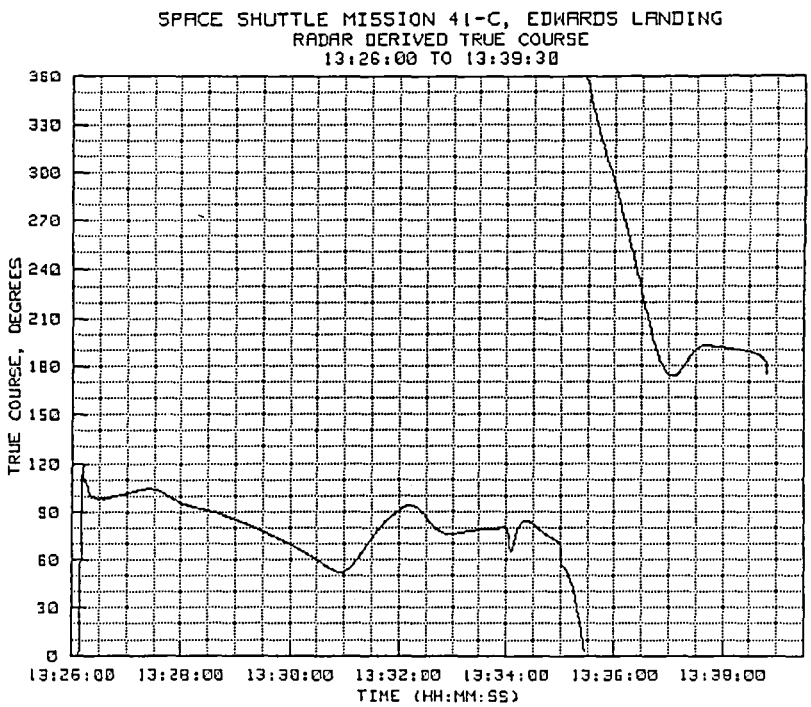

Figure 7-4. STS-41C radar-derived true course on approach.

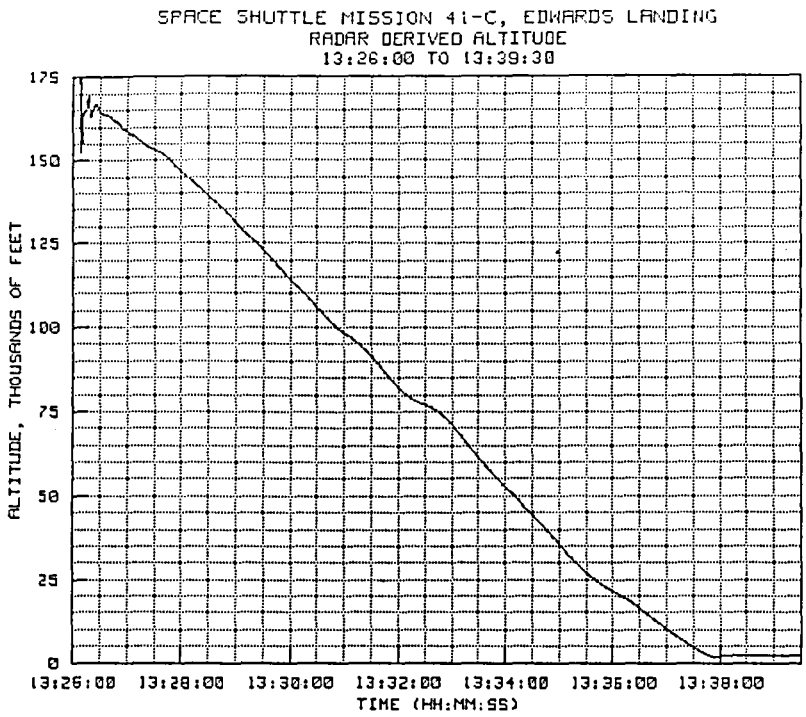

Figure 7-5(a). STS-41C radar-derived altitude.

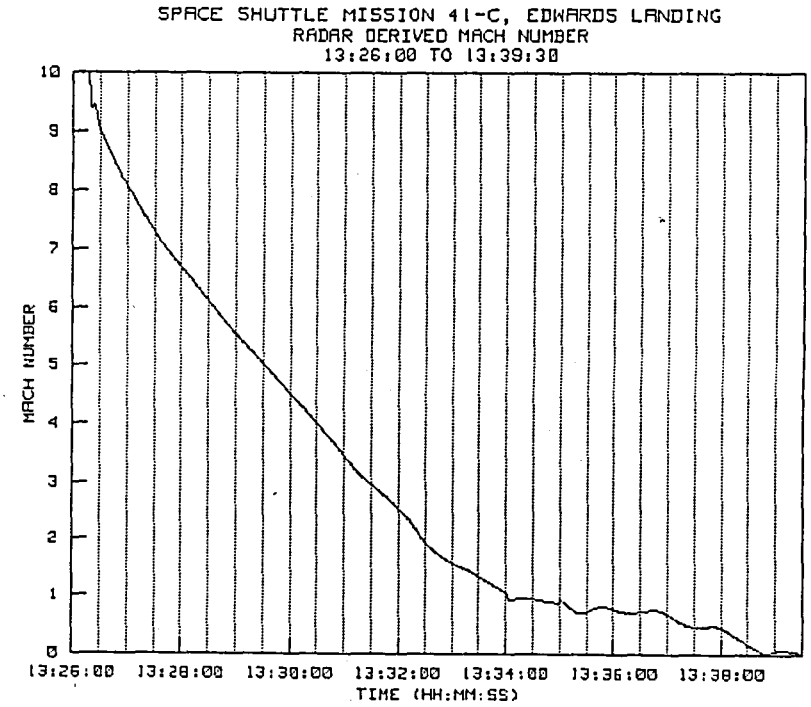

Figure 7-5(b). STS-41C radar-derived Mach number.

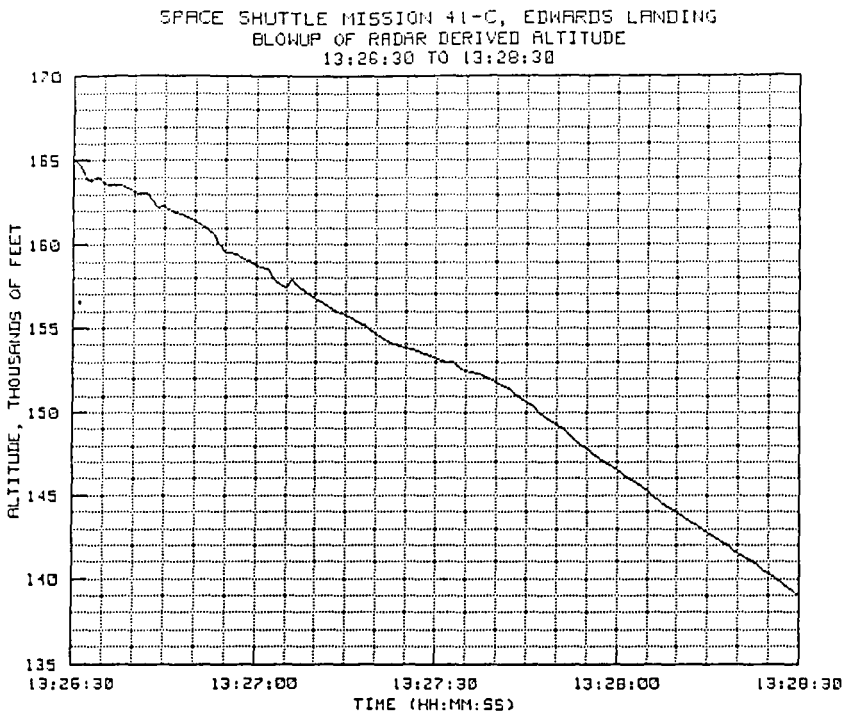

Figure 7-6(a). STS-41C radar-derived altitude blowup.

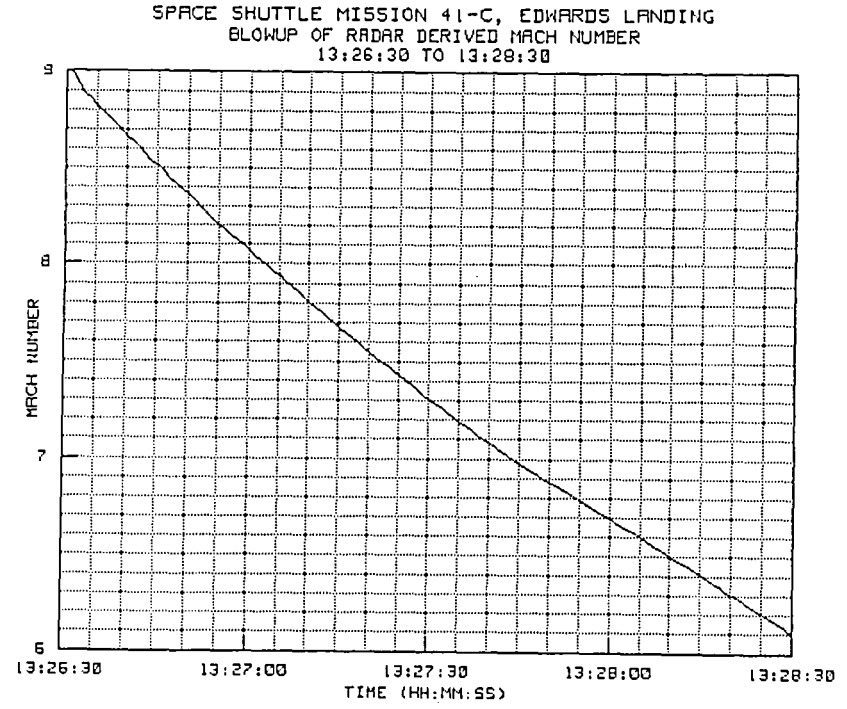

Figure 7-6(b). STS-41C radar-derived Mach number blowup.

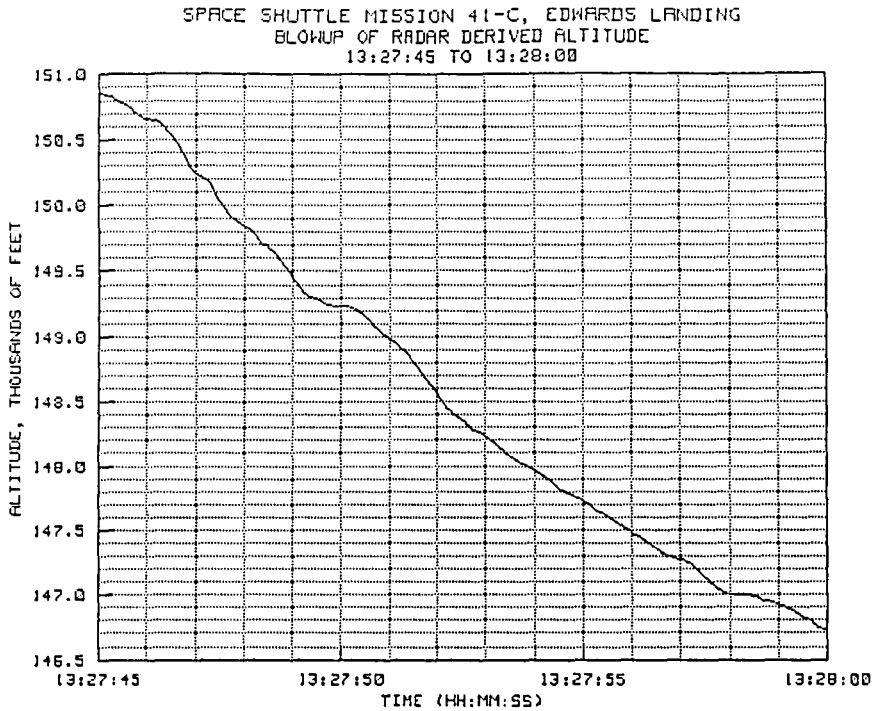

Figure 7-7(a). STS-41C radar-derived altitude blowup.

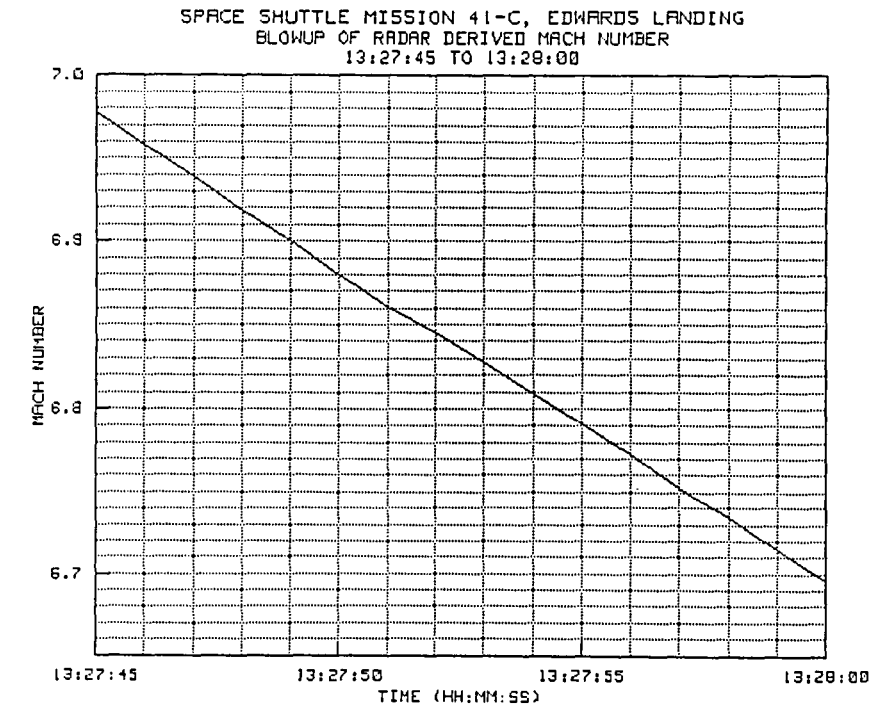

Figure 7-7(b). STS-41C radar-derived Mach number blowup.

7.2 Analysis of Noise in the STS-41C Landing Data

Noise plots for the range, azimuth, and elevation channels are provided in figures 7-8 to 7-10 for the period from initial target acquisition until overhead. Note that the 1-sigma range noise was just slightly higher than 0.5 LSB at the time of acquisition. The noise level then remained around one-half LSB until the target approached the zenith point.

Noise content in both the azimuth and elevation channels was also quite low from shortly after acquisition until the overhead point. At the first acquisition (13:26:05), the target range was still 367 nautical miles and the elevation angle was only 1.49 degrees. The initial 4 LSB 1-sigma azimuth noise decreased to about 1 LSB or less within about 35 seconds after the initial acquisition (range still in excess of 300 n.mi.). The elevation noise took slightly longer, about 65 seconds, for the 1-sigma value to fall below half an LSB value, however the target range at this point was still in excess of 250 nautical miles and the elevation angle was only 3.6 degrees. The noise levels for both angle channels remained very low until about 13:33:00 when both started to increase as the target approached the zenith point. At the zenith point both the azimuth and elevation 1-sigma noise climbed to about 7 LSB values.

To show the excellent manner in which the noise analysis routines derive the amount of random noise in the raw measurement signals, 20 pps first difference plots of the actual range, azimuth and elevation measurements were provided for comparison in figures 7-11 to 7-13. It is planned that, at some future date, the noise algorithms used in this analysis will be programmed into the real-time software on the A900 computer so that the status box on the operator control terminal will continuously display the noise levels in each of the three channels. This will provide the operator with additional information for selecting the proper power, pulse widths, and bandwidths to keep the noise in each of the channels at a minimum.

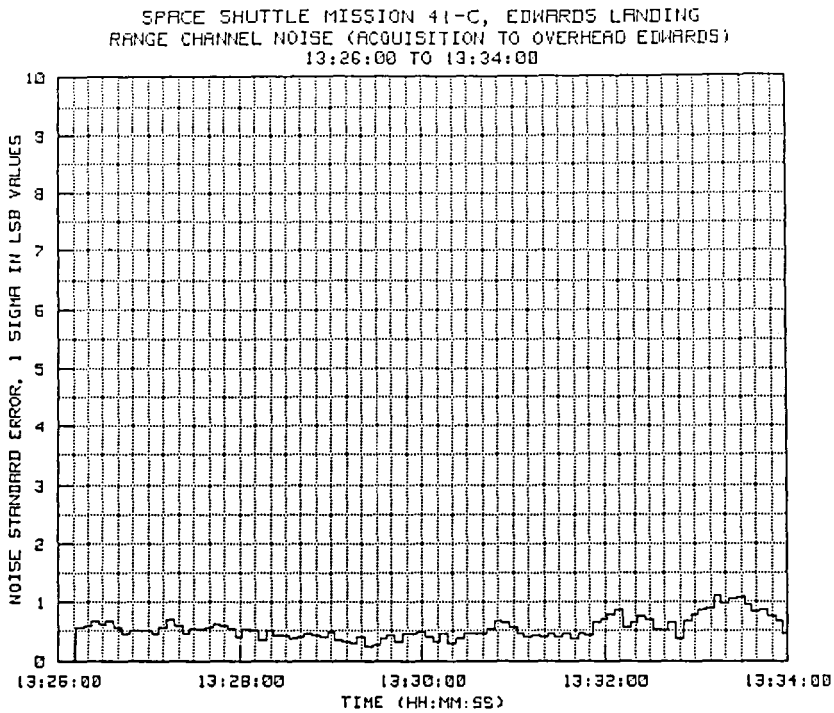

Figure 7-8. STS-41C approach range noise plot.

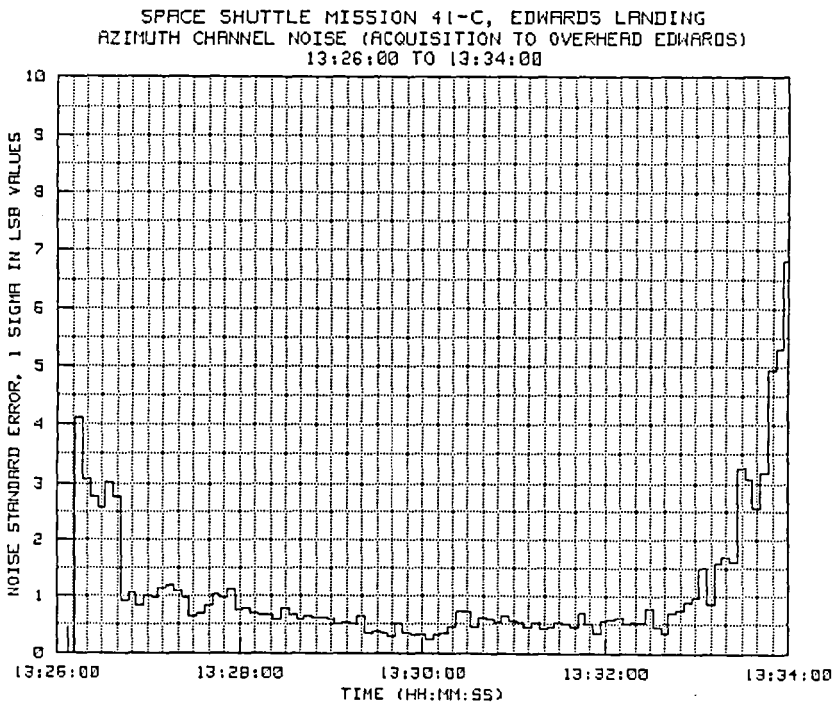

Figure 7-9. STS-41C appproach azimuth noise plot.

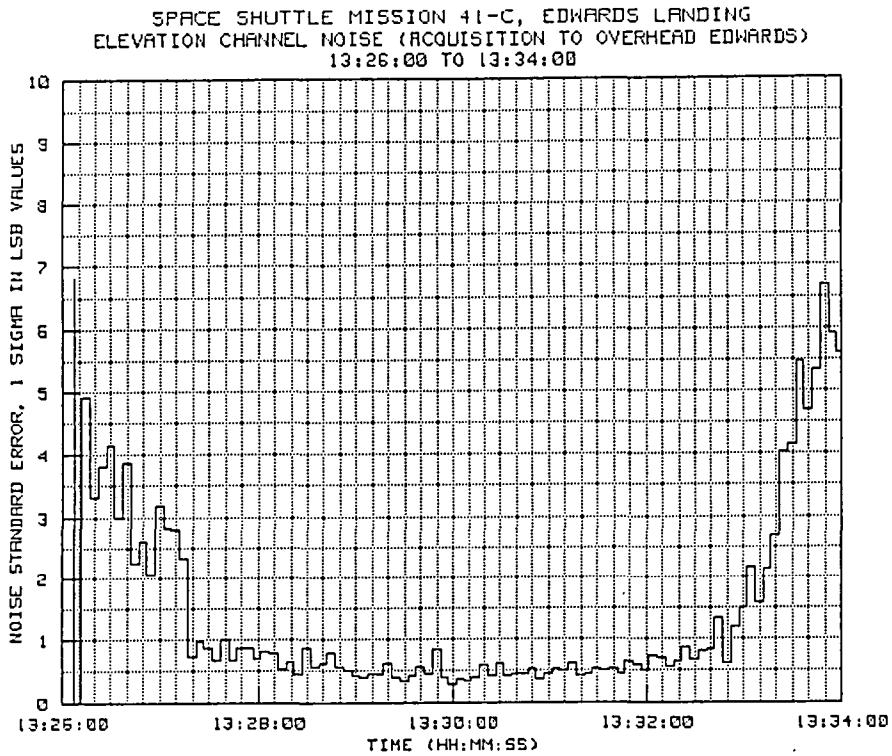

Figure 7-10. STS-41C approach elevation noise plot.

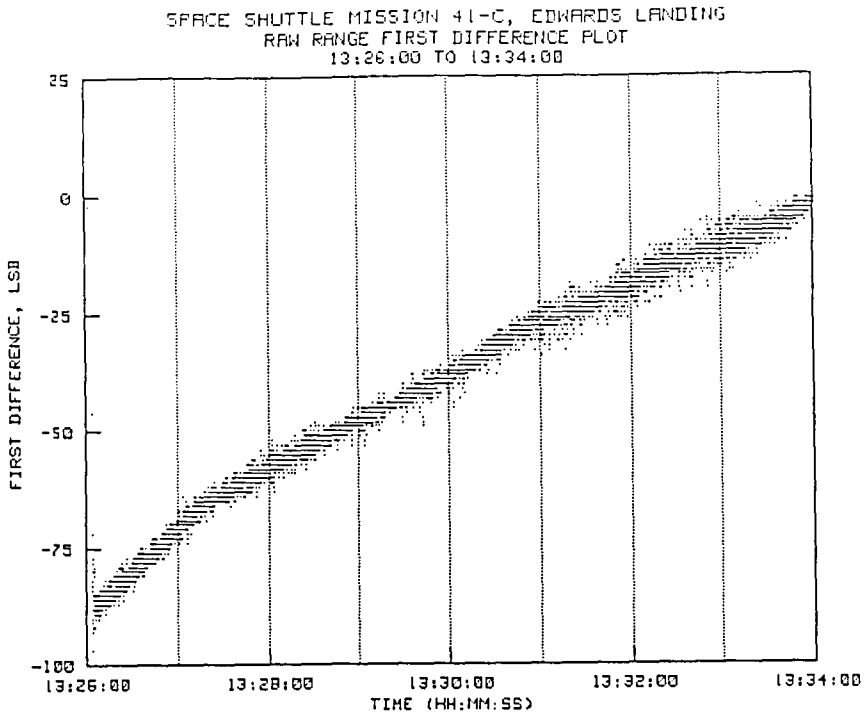

Figure 7-11. STS-41C raw range first difference plot.

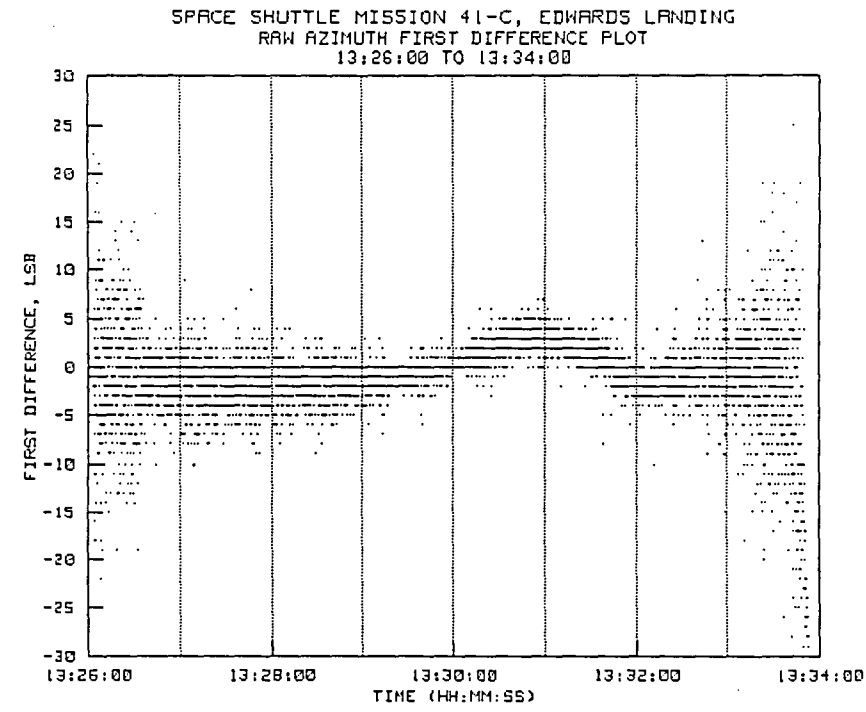

Figure 7-12. STS-41C raw azimuth first difference plot.

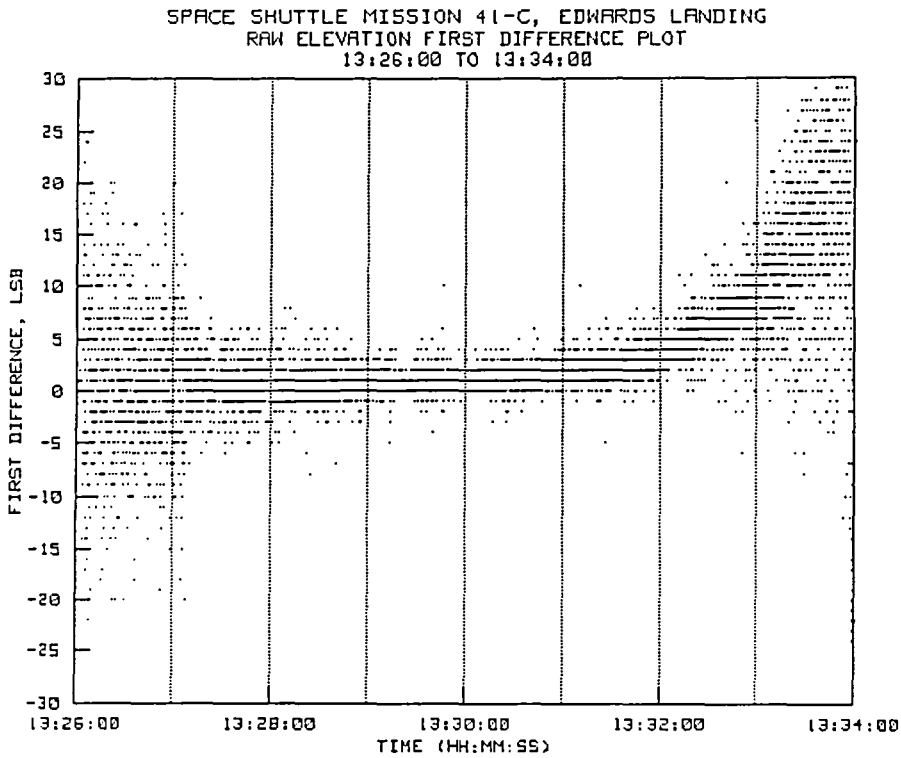

Figure 7-13. STS-41C raw elevation first difference plot.

7.3 Summary of Findings from STS-41C Edwards Landing

The following are considered to be pertinent findings from the skin track made during the STS-41C approach to Edwards.

1. Even at very long range (300 to 400 nautical miles), if the target is at a reasonably high altitude, the signal return from a large target such as the Shuttle can be relatively strong and free from noise, even though at low elevation angles. A cursory examination of signal-to-noise ratios immediately after the track indicated that the radar cross sectional values for the frontal approach generally agreed well with data contained in reference 12.

2. Slightly greater damping was used on the data during the Shuttle approach than used for normal aircraft tracks. This was done to counter the higher levels of noise expected in the data at the point of first target acquisition. This appears to have yielded both altitude and Mach number values that were consistently smooth until the radar was intentionally taken off target at the zenith point.

3. Surprisingly, multipath effects were not a severe problem, even during the very early portion of the track when the elevation angle was only 0.8 degree. However, some very slight noise in the altitude plot can be seen for the period from initial acquisition to about 13:26:30, and multipath effects, along with low signal strength at acquisition, may have contributed to this.

4. The presence of chase aircraft flying close-in during the final stages of the landing can cause the tracking data to become erratic, regardless of the pulse-width, pulse repetition rates, and power combinations set by the operator to minimize these effects. Good skin track data from an instrumentation radar such as the NASA AN/FPS-16 can only be obtained when there are no other interfering targets in close proximity.

8.0 STS-41D, LAUNCH ORBIT (REV 2)

STS-41D launched on 30 August 1984, and the NASA radar was required to track the first orbital pass after the launch.

The STS-41D launch orbit was selected for analysis because it was one in which the range was long and the aspect angles poor so that the returned signal strength was very low. In fact, this track, due to a variety of circumstances, some of which were known and some of which were unknown, had the lowest signal strength and greatest amount of noise of any of the successful orbital tracks recently recorded. Acquisition data for this track was received from the uprange Vandenberg radars via the DoD acquisition line. The antenna angle servos and the radar range gate were positioned by the A900 up until the time that a successful lock-on was achieved at 14:13:08 GMT.

8.1 Analysis of Data From STS-41D Launch Orbit (Rev 2)

At the time of the initial lock-on, the total velocity of the Shuttle was computed to be approximately 24,000 feet per second (about Mach 22.1). The altitude of the target was about 980,000 feet (160 n.mi.). At acqusition the range was slightly over 3,000,000 feet (494 n.mi.) and the elevation angle was 15 degrees. As the pass progressed, the elevation angle increased to a maximum of 16.5 degrees at about 14:13:50 GMT, then decreased steadily to about 3.8 degrees at signal loss. The range at signal loss was slightly over 5,300,000 feet (872 n.mi.).

Figures 8-1 through 8-3 provide raw range, azimuth, and elevation measurement data for the entire pass. Moderately heavy damping was used so that the large amount of random noise in the data would not cause undue jumps in the derived parameters. This is justified on an orbital track since the flight path is generally smooth and predictable, unless on-board rockets are fired to make flight path alterations. Figure 8-4 provides the radar-derived true course of the target from acquisition of signal (AOS) until loss of signal (LOS).

Figure 8-5(a) provides the radar-derived altitude for this mission. Note that considerable noise is present in the data, even with moderately heavy damping. However, the plot scale only goes from 980,000 feet up to 1,000,000 feet so that the spread of 20,000 feet shown on the plot is actually less than the spread shown on some of the air data calibration flights.

Figure 8-5(b) provides the radar-derived total velocity for the pass. Velocity units on this plot are thousands of feet

per second rather than Mach number so as to be consistent with velocity units from inertially derived or radar derived velocities disseminated throughout the worldwide tracking network. Again, significant levels of noise are present even though the data were subjected to moderately heavy smoothing.

In order to show the effect of different filter constants on the derived altitude data, figure 8-6(a) shows the results with normal aircraft damping and figure 8-6(b) shows the same altitude data with very heavy damping. Note that a considerable difference exists between the results with normal damping and moderately heavy damping shown in figure 8-5(a). However, also note that not much difference can be seen between the damping in 8-5(a) and the very heavy damping shown in figure 8-6(b). If heavy damping is used, there is the risk of severe start-up transients if the data has not yet settled. Thus, on very short, high-noise tracks such as this, moderately heavy damping probably offers the best compromise.

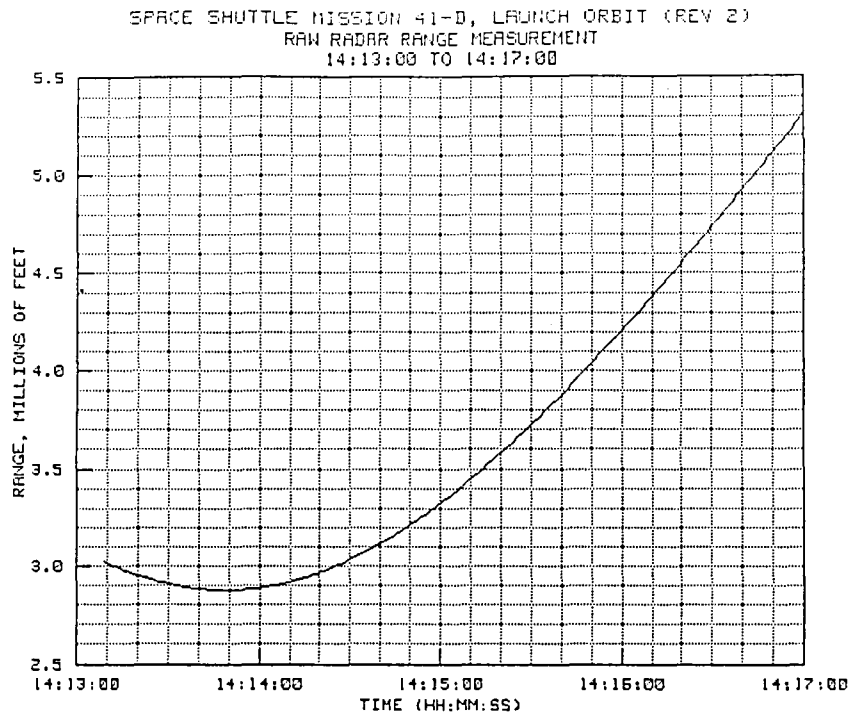

Figure 8-1. STS-41D (Rev 2) radar slant range.

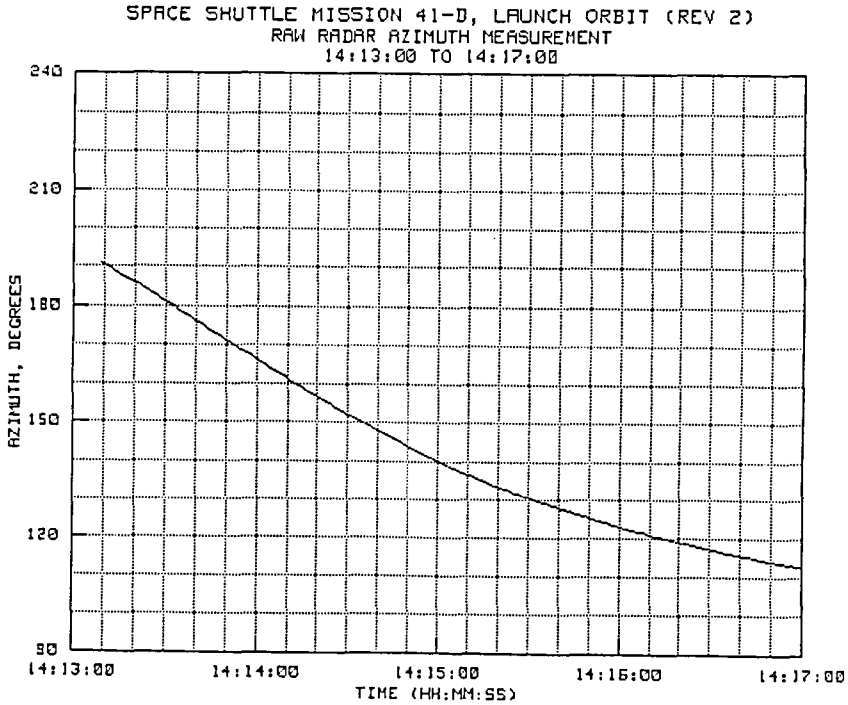

Figure 8-2. STS-41D (Rev 2) radar azimuth angle.

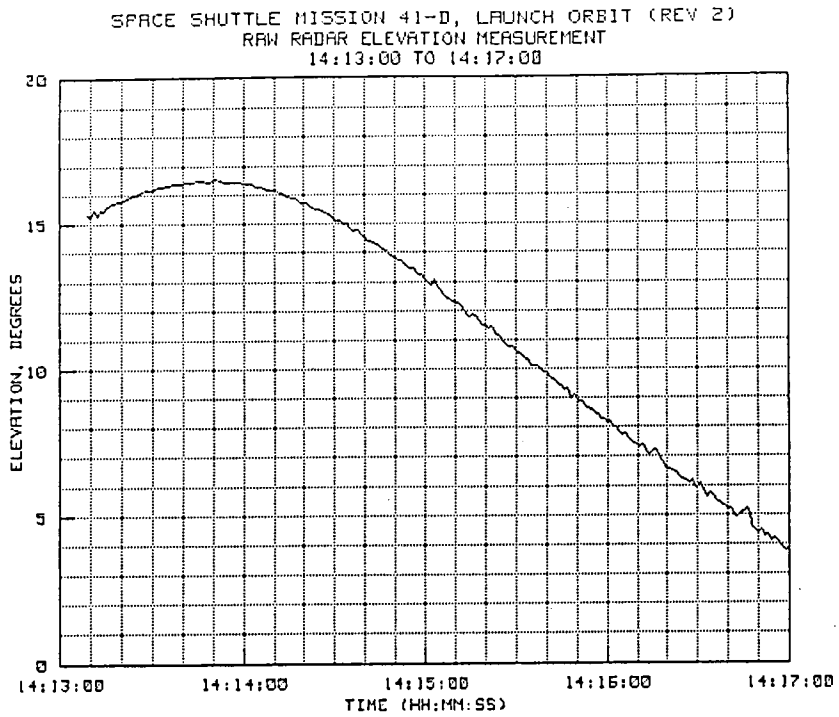

Figure 8-3. STS-41D (Rev 2) radar elevation angle.

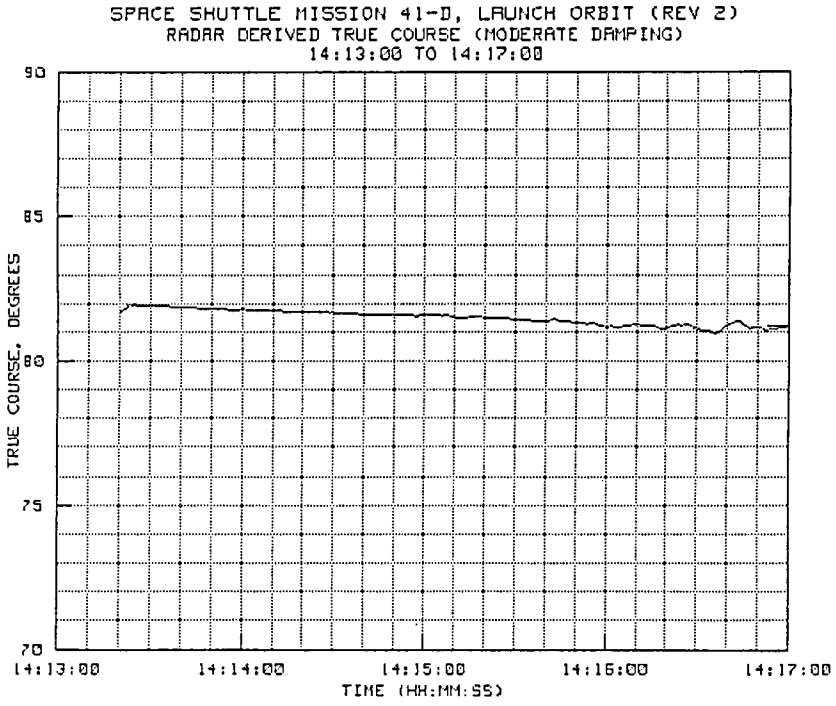

Figure 8-4. STS-41D (Rev 2) radar-derived true course.

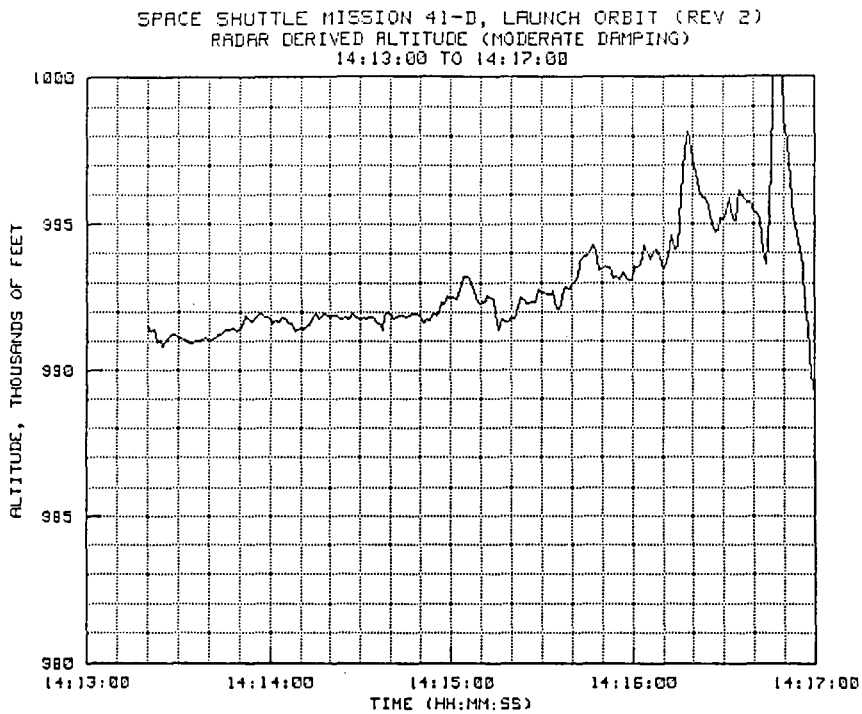

Figure 8-5(a). STS-41D (Rev 2) radar-derived altitude.

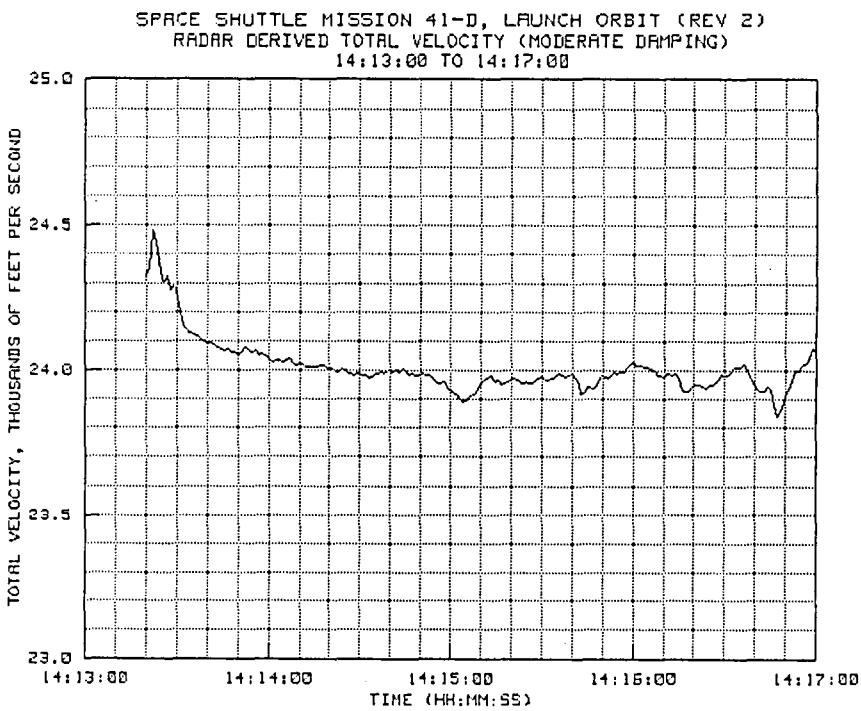

Figure 8-5(b). STS-41D (Rev 2) radar-derived Mach number.

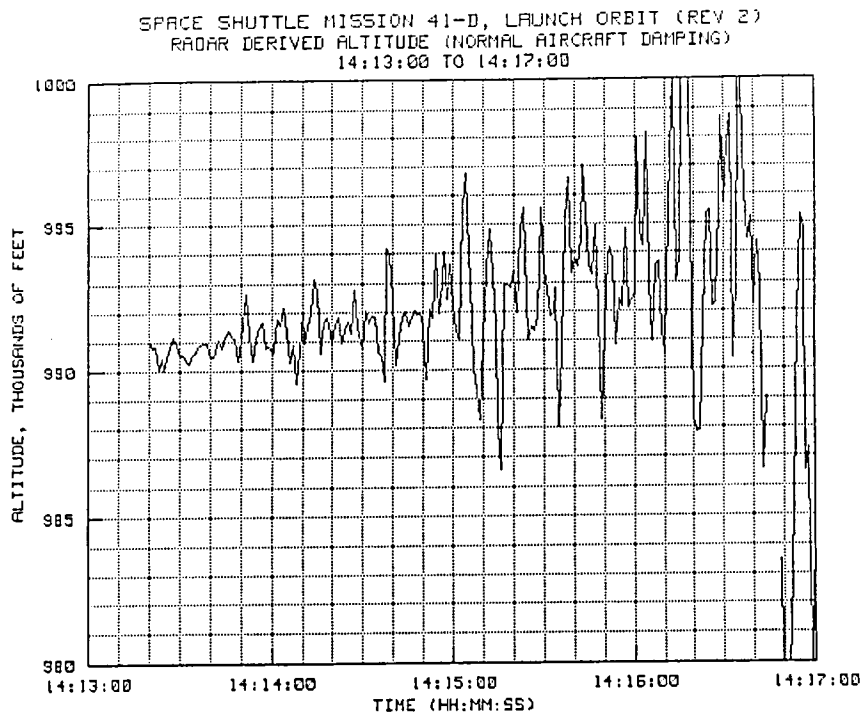

Figure 8-6(a). STS-41D (Rev 2) normal altitude damping.

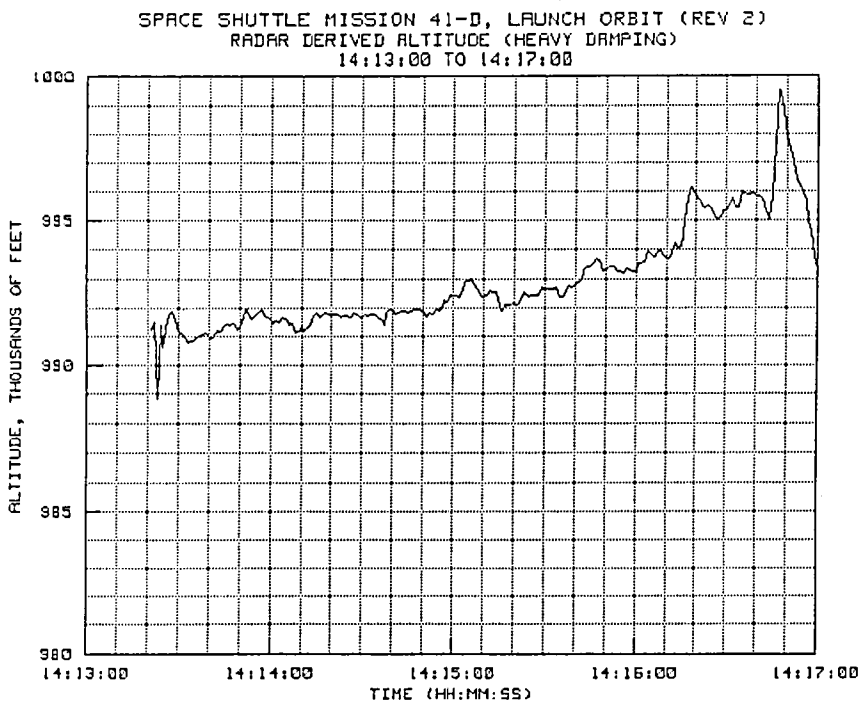

Figure 8-6(b). STS-41D (Rev 2) heavy altitude damping.

8.2 Analsyis of Noise in the STS-41D Launch Orbit (Rev 2)

The noise time history plots for the track are provided in figures 8-7 to 8-9. These plots show one very important feature. Note that the range noise is as low as for any of the close-in portions of the F-104 air data calibration flights. It is about as good as could be expected under even the most optimum tracking conditions. However, the noise in the angle data is extremely high, except near the point of closest approach (PCA) around 14:13:49.

As a general rule of thumb, the amount of dispersion in the measurement data can be considered to fall within plus and minus three 1-sigma values. Thus, for the early portion of the track, just after PCA, the dispersion in the data could be expected to generally range over about 15 to 20 LSB values in azimuth and over about 27 to 43 or so LSB values in elevation with a few points occasionally falling outside these limits.

Figures 8-10 to 8-12 provide first difference plots of the actual measurement data. Note that the noise in both the azimuth and elevation channels is close to that predicted by the noise routines. It might also be mentioned that the signal-to-noise level on this track was about the minimum at which a lock can be maintained.

The reason for the vast difference in the noise levels between the range and angle channels could not be determined; however, further investigation of this condition will be attempted during future orbital tracks.

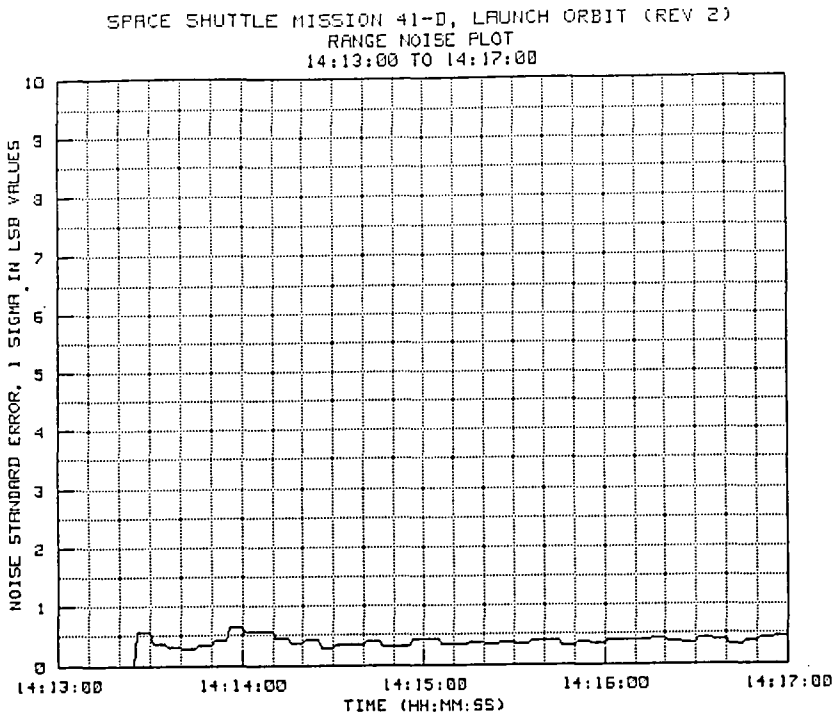

Figure 8-7. STS-41D (Rev 2) range noise plot.

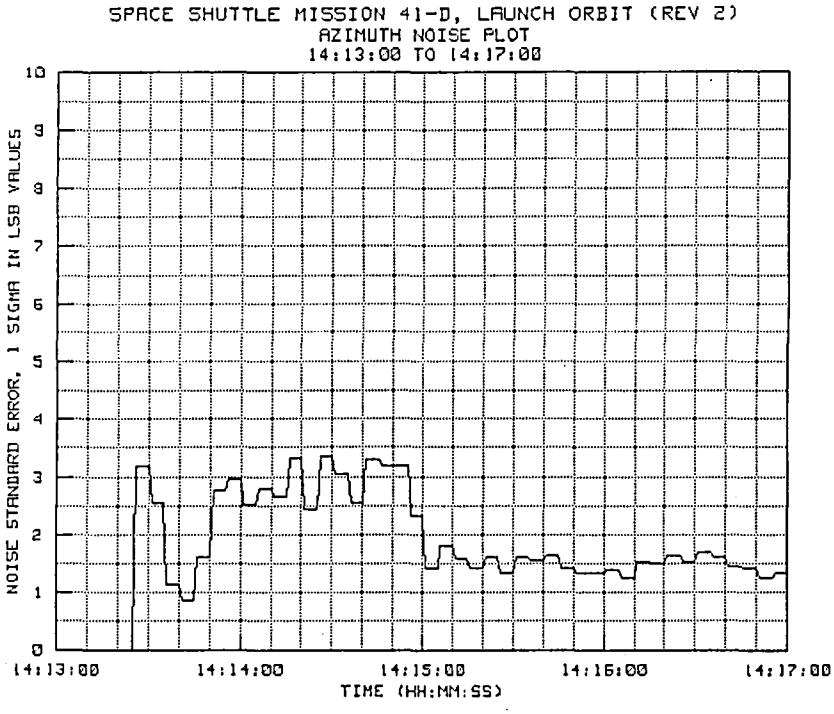

Figure 8-8. STS-41D (Rev 2) azimuth noise plot.

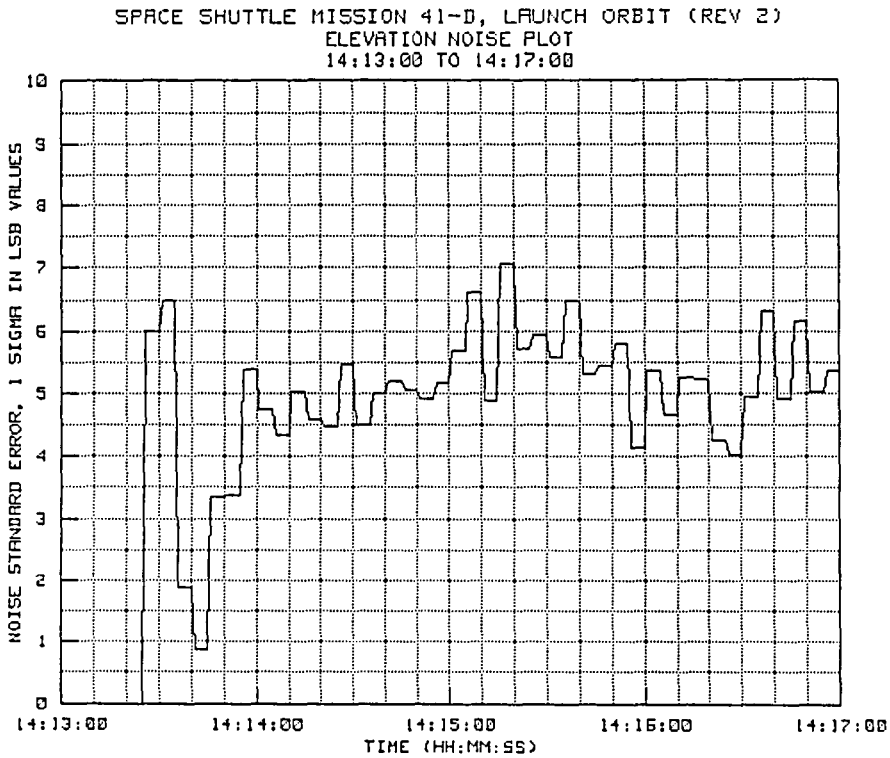

Figure 8-9. STS-41D (Rev 2) elevation noise plot.

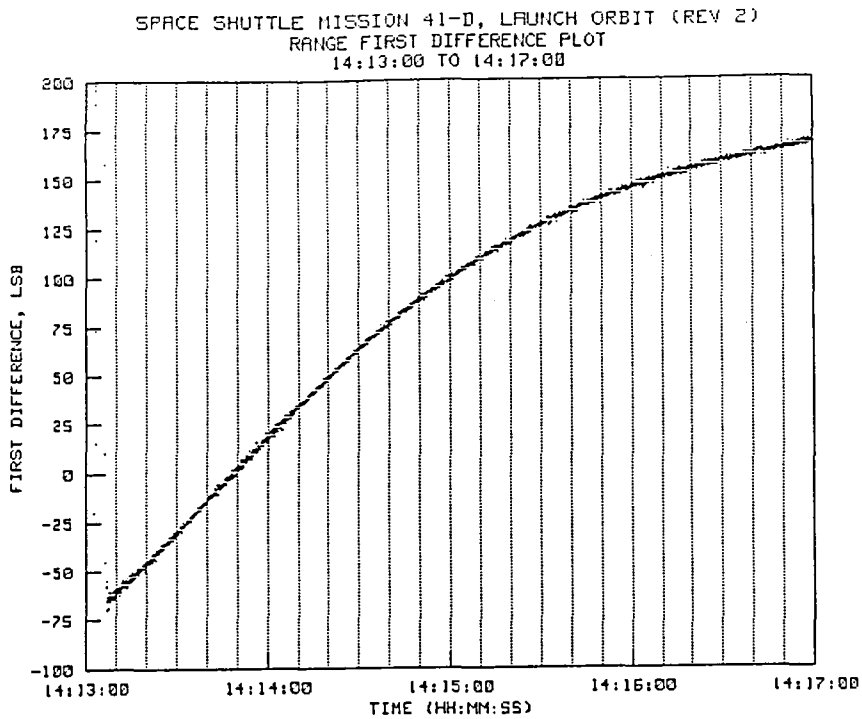

Figure 8-10. STS-41D (Rev 2) first difference range plot.

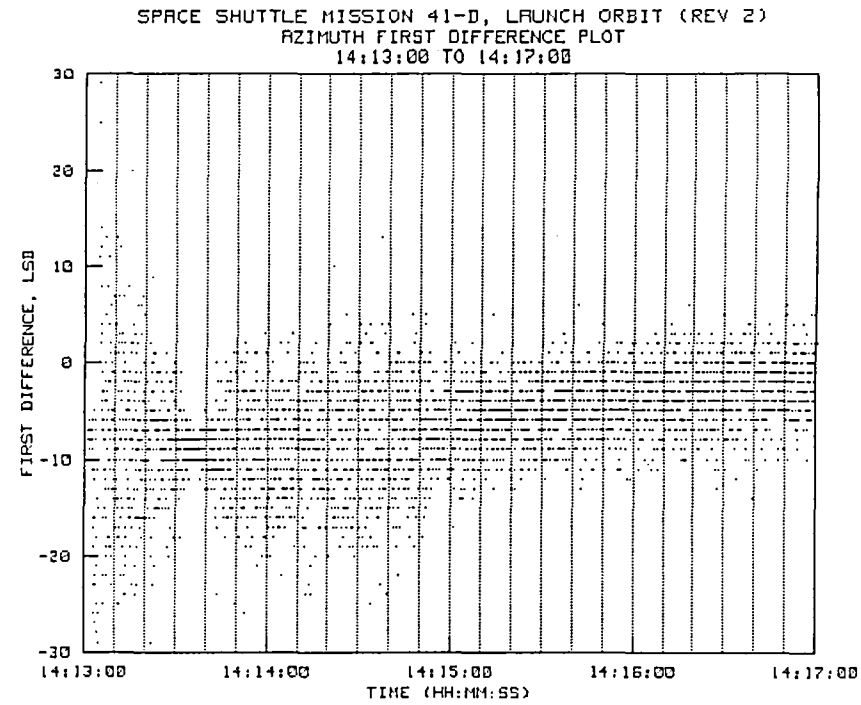

Figure 8-11. STS-41D (Rev 2) first difference azimuth plot.

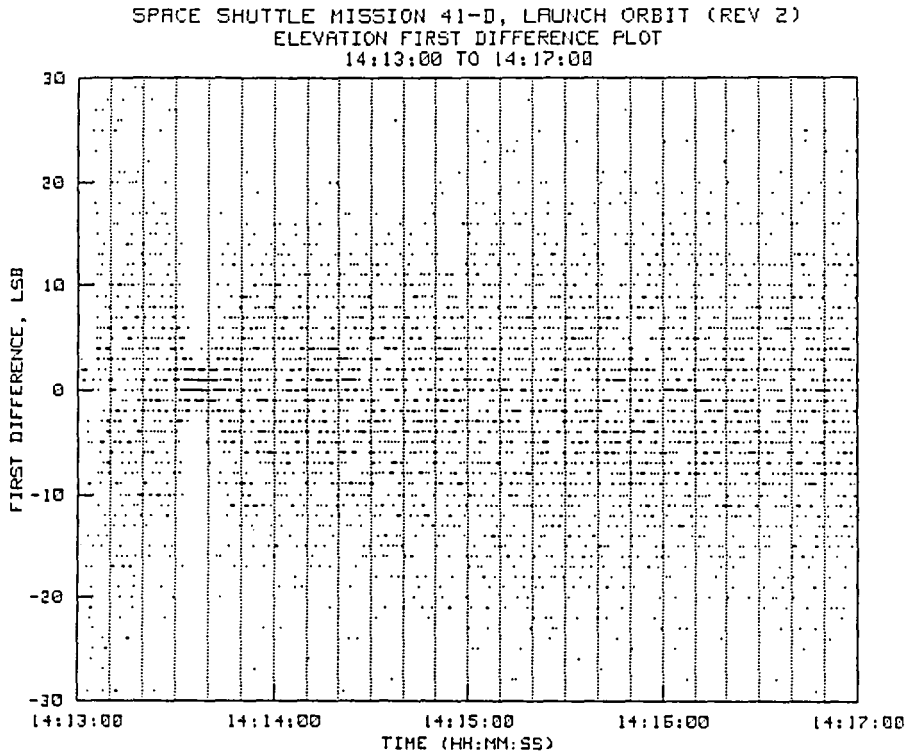

Figure 8-12. STS-41D (Rev 2) first difference elevation plot.

8.3 Summary of Findings From STS-41D Launch Orbit (Rev 2)

Support for orbital tracking missions requires procedures that are considerably different from those used with aerodynamic targets. First, since there is no beacon on many of the orbital objects tracked, the skin mode must be used, and, even though a target such as the Shuttle may be large, the ranges involved can be very great so that the radar must often be operated at the extreme limits of its design capability. Second, the amount of noise in the data can be from 10 to 20 times greater than that present during normal aircraft missions; however since the track is known to be smooth and predictable, much higher damping can be used than feasible for aerodynamic flight. Third, the total on-target time for an orbital track is generally only 5 to 10 minutes, so little time exists for fine tuning the system to optimize the measurements.

Observations of numerous skin tracks on Salute and other space objects lead to the conclusions that, at the time of first signal acquisition, the return from the target may be barely perceptible on the radar scope, and it often fades and reappears several times before a successful lock-on can occur. Thus, for the Shuttle missions, the on-site computer plays a larger role than for the normal aircraft missions. Data from uprange radars is sent to NASA over an acquisition data net. The computer receives this data, decodes the site address from which it is coming, and performs the necessary calculations to position the range gate and angle servos so that, as the target signal strength grows, the target will appear directly within the acquisition gate of the radar.

The following are considered to be pertinent specific findings from the track of the STS-41D launch orbit.

1. Even though the ranges were not extreme and the elevation angles were not as low as on other tracks, a high level of noise was present in both the azimuth and elevation channels, with the elevation noise running about twice as high as that in the azimuth channel. At the same time, the noise in the range channel was as low as could be expected under even the most optimum tracking conditions. The cause of this disparity is not known at the present time, but will be investigated on future orbital tracks.

2. The effect of aspect angle on the signal level is apparent from figures 8-7 to 8-9. Note that around PCA, the noise levels in all channels diminished to what can be considered close to the minimum levels expected under the most optimum tracking conditions. And, even the already low noise level in the range channel shows some improvement at the PCA point. Since range and elevation

angle were not far different at points well before and well after PCA, the sudden improvement in signal quality is probably due to the aspect angle of the target. On other passes, it has been found that, because of the flat surface on the sides and underbelly of the Shuttle, if the aspect angles are such that the impinging angle of the radar strikes normal to one of these flat sides, then a large momentary improvement in the returned signal level will occur. This was also noted in the findings in reference 12.

3. Even under the most adverse noise conditions, filtering techniques can be employed which will derive reasonably good altitude and Mach number data from the noisy raw data measurements. Probably additional improvements to those shown in figures 8-5(a) and 8-5(b) could be obtained with better tuning of the filter. In this regard, future studies should look into the possibility of improving the adaptive filters by automating real-time changes to the filter constants, in addition to the inherent adaptation of the system gain matrix.

4. Additional future study into direct filtering of azimuth and elevation error signals might prove beneficial. At present the operator can observe the error signals on radar console meters and make real-time adjustments to bandwidth, pulse width, and output power to minimize the amount of noise in these signals. Unfortunately, increasing the bandwidth on noisy signals may result in a false sense of security. By increasing the servo gain, it may be possible to cause the antenna to rapidly follow noise transients so that the error levels on the meters look better when, in fact, all that has been done is to transfer the noise to the pedestal itself. More sophisticated filtering techniques in the error feedback loops might possibly result in substantial improvements when high levels of noise are present.

9.0 AN ANALYSIS OF CYBER DATA REDUCTION ALGORITHMS

In order to provide an additional test of the data reduction routines it was decided to review the Cyber radar data reduction program and to make comparisons between the GMD results and Cyber results obtained using the code from the current Cyber listings. Data reduced by the Cyber program was also furnished directly on magnetic tape media so that various types of direct comparisons could be performed.

9.1 Cyber Radar Data Reduction Software

Listings from the Cyber radar data reduction program were obtained and reviewed as part of the analysis task. The Cyber program routines reviewed included:

1. RADATA1: This program reads the control cards, prints out header information, initializes control flags, and calls the various processing subroutines.

2. WILDCYB: This subroutine searches for start time, finds the first good starting interval, eliminates wild points, and stores data on disc.

3. RDRADAR: This subroutine reads radar data tapes formatted in the NASA TACDAC format.

4. RDAFRA: This subroutine reads radar data tapes formatted in the USAF TACDAC format.

5. CALCDK: This subroutine computes the elevation refraction correction; makes E-N-V coordinate conversions; computes geodetic latitude and longitude; computes target altitude, total velocity, Mach number, dynamic pressure, flight path heading and flight path angle, horizontal and vertical velocity components, and atmospheric parameters needed for the various computations; and prints data files (printer and disc).

6. FILSMO: This subroutine performs data smoothing using a low-pass filter.

7. BALOON: This subroutine accepts card deck information containing weather data: geometric altitude, air density, atmospheric pressure, optical index of refraction, dew point, wind direction, wind speed, vapor pressure, relative humidity, and wind shear. It stores the variables in program arrays and stores the weather data from the input cards onto disc.

8. SMOOTH: This subroutine smooths data using a high-pass filter.

9. WEATH: This subroutine contains standard atmospheric temperature and pressure data and provides a printout of rawinsonde weather data or standard atmosphere data, depending on which is used for any specific data reduction. If rawinsonde data are used, the source material is provided by a weather deck.

10. WEIGHT: This subroutine provides weighting factors for the low pass filter.

When the data for a specific mission are to be reduced on the Cyber system, the test engineer provides specific time intervals of interest and the Cyber program reduces the data for those intervals. Reduced data are stored in a master data base file for the specific flight, and a printout of the results is furnished to the requesting engineer. As part of this analysis, a special program was prepared by NASA to provide GMD the following parameters from the Cyber data base.

1. On-board pressure altitude
2. On-board Mach number
3. On-board ambient temperature
4. Free-stream pressure
5. Cyber-derived radar geometric altitude
6. Cyber-derived radar Mach number

From the Cyber listings, programs were prepared to duplicate the Cyber refraction correction calculations. The new program used essentially the same code as contained in the Cyber listings. A similar program was prepared from listings of the NASA Varian (spherical slab) refraction algorithms. This allowed real-time tracking data, recorded at the radar site by the A900 computer system, to be analyzed using the the same refraction method as used on the Cyber, the Varian, or the A900 computers. The GMD software also included printout routines that provided data in exactly the same format as output by the Cyber as well as in a variety of other more abbreviated formats.

9.2 Cyber Calculations of Index of Refraction

During the analysis, it was found that the routine used to compute the r-f index of refraction in the Cyber program did not provide results which matched those from other sources. Closer examination indicated that, while the dry term (based on the contribution of pressure and temperature to the refractive index) provided a low but acceptable value, the wet term (based on the amount of water vapor in the atmosphere) did not provide satisfactory results. In fact, it provided values very nearly zero in all cases. Thus, the refraction correction as computed by the Cyber algorithms is

based on what is essentially optical refractivity in all cases.

While not a part of the contract tasks, it was considered worthwhile to spend some time in attempting to determine what the algorithm should be, since it is the only one known to use dew point temperature in a direct and simple manner to compute the contribution of water vapor to the total refractivity value. With most methods, it is first necessary to compute the partial pressure of water vapor, and then apply the values of water vapor, temperature, and pressure to refractivity equations provided in reference 3 or to similar equations contained in various Inter-Range Instrument Group (IRIG) publications.

It was noted in the Cyber documentation that the refraction method, including the index of refraction computations, were taken from a White Sands Missile Range document (Ref. 10) published in 1958. Therefore, calls were made to White Sands in order to attempt to locate a copy of the source document. This effort proved successful and a copy was obtained. The method used in the Cyber to compute the index of refraction was found on page 2 of the document and it was identical to the algorithm in the Cyber program. However, reference 10 further referenced an earlier 1953 publication (Ref. 13) in regard to the refractivity calculation. when reference 13 was finally obtained, it was found to have essentially the same equations as provided in reference 3, with no mention of the specific algorithm contained in the White Sands document. In fact, reference 13 was written by Smith and Weintraub who provided the same material for the preparation of the Bean and Dutton publication (Ref. 3).

Thus, the effort to find if the Cyber algorithm was, in fact, a valid algorithm, in which a possible transcription error had caused an incorrect relationship to be used, was abandoned.

It might also be noted that a telephone conversation with a member of the trajectory analysis branch at the White Sands Missile Range indicated that the refraction method set forth in reference 10 was no longer used, since it did not have sufficient accuracy to handle orbital tracks. Instead, a recent NASA method had been substituted.

Table 9-I shows the values for r-f, optical, and ruby laser energy for the surface conditions of flights 811, 814, 855, and 856, respectively. The GMD solution uses the Claperon-Clausius equations from reference 4 to compute the partial pressure of water vapor; and; from the partial pressure of water vapor, the temperature, and the total pressure; the r-f index of refraction. The latter calculation is performed by

TABLE 9-I. PSYCHROMETRIC DATA COMPARISON

TEMPERATURE (DRY)	=	17.0000 DEG CELCIUS
DEW POINT TEMPERATURE	=	1.1000 DEG CELCIUS
BAROMETRIC PRESSURE	=	931.8200 MB
SATURATION VAPOR PRESSURE OF WATER	=	19.5672 MB
PARTIAL PRESSURE OF WATER VAPOR	=	6.6868 MB
RELATIVE HUMIDITY	=	34.1734 %
ABSOLUTE HUMIDITY	=	4.9935883 GM/CU METER
R-F REFRACTIVITY (K,K5)	=	0.0002788
R-F REFRACTIVITY (K1,K2,K3)	=	0.0002789
OPTICAL REFRACT (WHITE LIGHT)	=	0.0002533
OPTICAL REFRACT (RUBY LASER)	=	0.0002513

TEMPERATURE (DRY)	=	27.0000 DEG CELCIUS
DEW POINT TEMPERATURE	=	5.3000 DEG CELCIUS
BAROMETRIC PRESSURE	=	932.5100 MB
SATURATION VAPOR PRESSURE OF WATER	=	35.9992 MB
PARTIAL PRESSURE OF WATER VAPOR	=	9.0000 MB
RELATIVE HUMIDITY	=	25.0004 %
ABSOLUTE HUMIDITY	=	6.4971305 GM/CU METER
R-F REFRACTIVITY (K,K5)	=	0.0002784
R-F REFRACTIVITY (K1,K2,K3)	=	0.0002784
OPTICAL REFRACT (WHITE LIGHT)	=	0.0002451
OPTICAL REFRACT (RUBY LASER)	=	0.0002431

TEMPERATURE (DRY)	=	28.8000 DEG CELCIUS
DEW POINT TEMPERATURE	=	16.7000 DEG CELCIUS
BAROMETRIC PRESSURE	=	931.1900 MB
SATURATION VAPOR PRESSURE OF WATER	=	39.9793 MB
PARTIAL PRESSURE OF WATER VAPOR	=	19.1984 MB
RELATIVE HUMIDITY	=	48.0207 %
ABSOLUTE HUMIDITY	=	13.7767807 GM/CU METER
R-F REFRACTIVITY (K,K5)	=	0.0003179
R-F REFRACTIVITY (K1,K2,K3)	=	0.0003179
OPTICAL REFRACT (WHITE LIGHT)	=	0.0002433
OPTICAL REFRACT (RUBY LASER)	=	0.0002413

TEMPERATURE (DRY)	=	34.6000 DEG CELCIUS
DEW POINT TEMPERATURE	=	2.2000 DEG CELCIUS
BAROMETRIC PRESSURE	=	929.3500 MB
SATURATION VAPOR PRESSURE OF WATER	=	55.5205 MB
PARTIAL PRESSURE OF WATER VAPOR	=	7.2350 MB
RELATIVE HUMIDITY	=	13.0312 %
ABSOLUTE HUMIDITY	=	5.0939875 GM/CU METER
R-F REFRACTIVITY (K,K5)	=	0.0002628
R-F REFRACTIVITY (K1,K2,K3)	=	0.0002629
OPTICAL REFRACT (WHITE LIGHT)	=	0.0002382
OPTICAL REFRACT (RUBY LASER)	=	0.0002363

both the two-term and three-term methods contained in reference 3, using the constants of Smith and Weintraub given on page 8 of reference 3. However, using the Cyber algorithm, the r-f refractivity for flight 811 shown as 0.0002789 in table 9-I is computed to be only 0.0002326, which is even less than the optical values shown in the table. For flight 814, the computations using the Cyber method yield a refractivity value of 0.0002393 as opposed to 0.0002784 from Smith and Weintraub. Similar differences are present for the psychrometric data from flights 855 and 856.

It might also be noted that the r-f refractivity values computed by the GMD algorithms agree very closely with r-f refractivity values provided on the rawinsonde printouts. Values from the three methods (given in N-units) are:

Flight #	GMD	Rawinsonde	Cyber
811	278.9	***	232.6
814	278.4	277	239.3
855	317.9	316	237.6
856	262.9	262	232.6

9.3 Direct Comparison of Altitude Computations

Although the results of the r-f refractivity calculation from the Cyber program appears to disagree with results from other well established sources, the refraction correction itself, also from the White Sands document, does yield valid results. In fact, if the same index of refraction is used in the A900, Cyber, and Varian algorithms, then essentially the same results are obtained for aircraft targets until the elevation angles become very low.

Figure 9-1 shows a survey run from flight 811 that has been reduced using all three methods. For this comparison, the gradient refraction solution used only the surface refractivity values so as to be consistent with the other two solution methods. The three plots in figure 9-1 having the lower altitude trend at longer ranges are the A900 gradient solution, represented by a solid line; the Cyber (White Sands) method, represented by a dashed line; and the Varian spherical slab method, represented by a dotted line. The slight differences in the results obtained from the three solution methods is to be expected, since the elevation angle was becoming low at the end of the run, and, as will be shown in the Task II report, both the White Sands method and the spherical slab method fail completely at low elevation angles.

If the method set forth in reference 10 is used to compute the r-f index of refraction, then the result is essentially optical, and the plots would all have a level or slightly

upward trend, more in line with expectations. While this apparently gives better agreement with the flight data than does the standard r-f refractivity, it must nevertheless be discarded since it relies on an untenable assumption that all of the foregone work by scores of experts in this field is wrong.

Figure 9-2 shows the results when a survey run from flight 814 was reduced using the A900, Varian, and Cyber refraction correction methods. Again the on-board data, represented by the longer dashed line, falls well above all three of the other solution methods at the longer ranges and lower elevation angles. As in the previous case, the other three methods yield close results with some slight variations as the range gets longer and the elevation angle gets lower.

Figure 9-3 shows an altitude plot from flight 856 and figure 9-4 shows a similar plot from flight 856. Note that the same trend to compute lower altitude values at the longer ranges and low elevation angles was present in all the flights and with all the refraction correction methods, providing the same refractivity values were used.

9.4 Direct Comparison of Mach Number Calculations

Mach number values contained on the Cyber data tape were used to prepare data plots showing the agreement, or disagreement, between Mach number values computed from the GMD software and from the Cyber radar data reduction program.

Figures 9-5 to 9-8 provide data from the same flight times as used in figures 9-1 to 9-4. Note that no wind correction was made in the Cyber data reduction program, therefore the GMD comparison plots also contain no wind correction. Because of this, the values shown in figures 9-5 to 9-8 will not agree with data shown earlier in the analysis for the same time periods, since the earlier data used flight day atmospheric conditions for the Mach calculations and were wind corrected.

All four figures show good general agreement between the results of the Cyber radar data reduction program and the GMD routines. The Cyber data does however contain more noise, and it was noticed that spikes in the Mach number calculations were more evident in the Cyber data than in the GMD data, probably because of more damping in the GMD filter. Typical spikes can be seen at a time of about 14:58:52 in figure 9-6 and at several obvious times in figure 9-8. At other times, such as for the flight 811 acceleration-deceleration period shown in figure 9-9, the spikes are quite large.

Note that figures 9-5 through 9-9 are computed with no wind correction so that the Mach number values are biased from the true on-board readings.

The solid line on figure 9-9 is the result from the GMD data reduction, and, even though no wild point editing was done, the velocities computed by the program did not show perceptable jumps at these points.

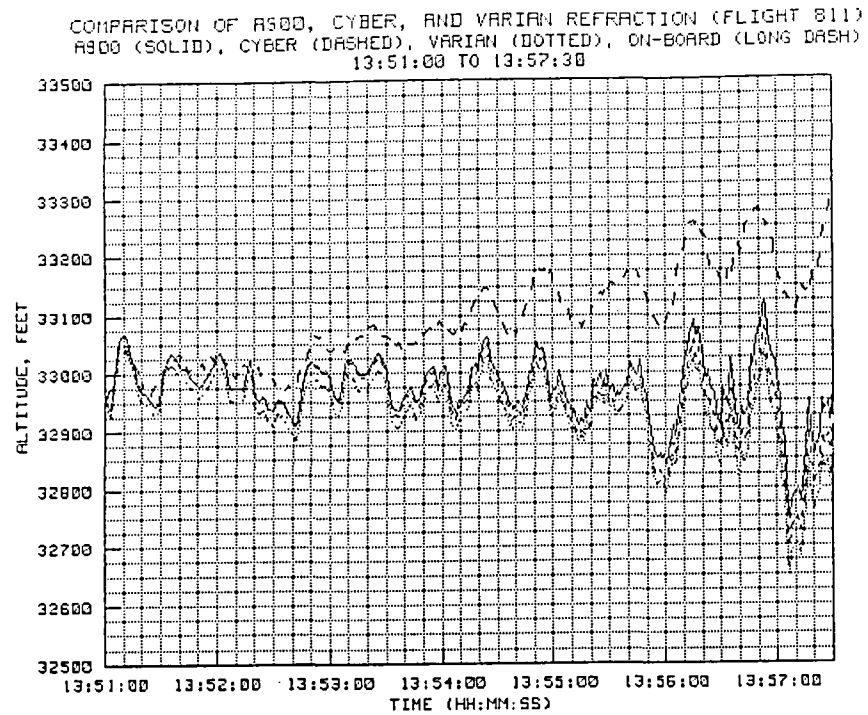

Figure 9-1. Cyber software analysis altitude comparison plot.

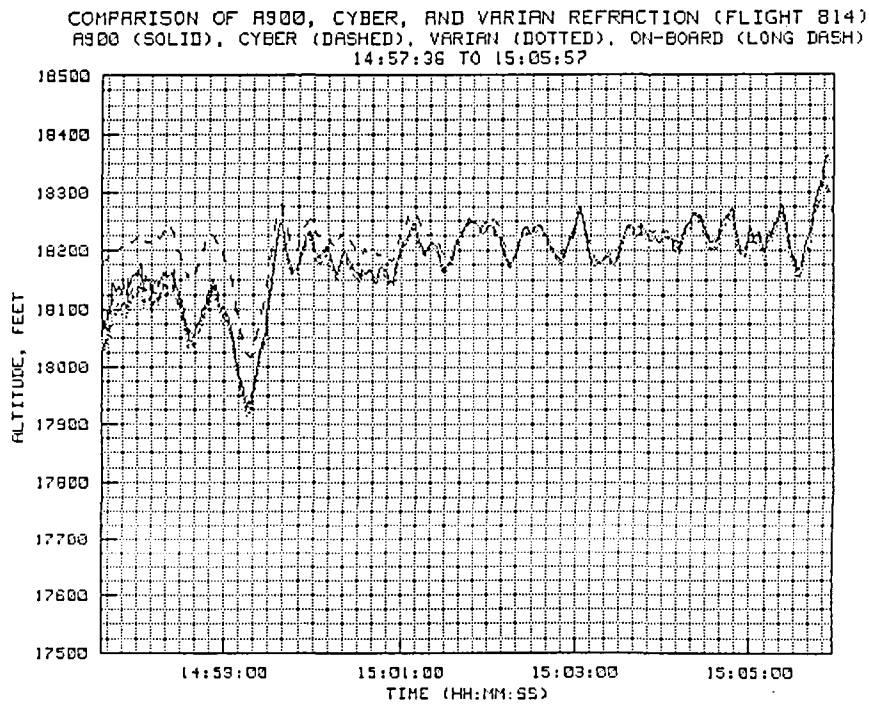

Figure 9-2. Cyber software analysis altitude comparison plot.

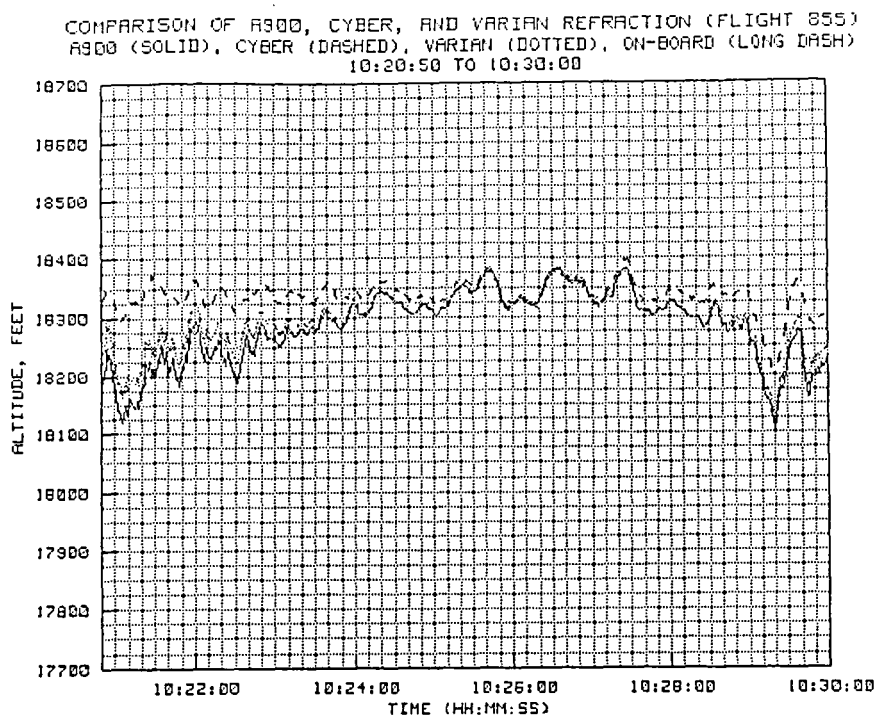

Figure 9-3. Cyber software analysis altitude comparison plot.

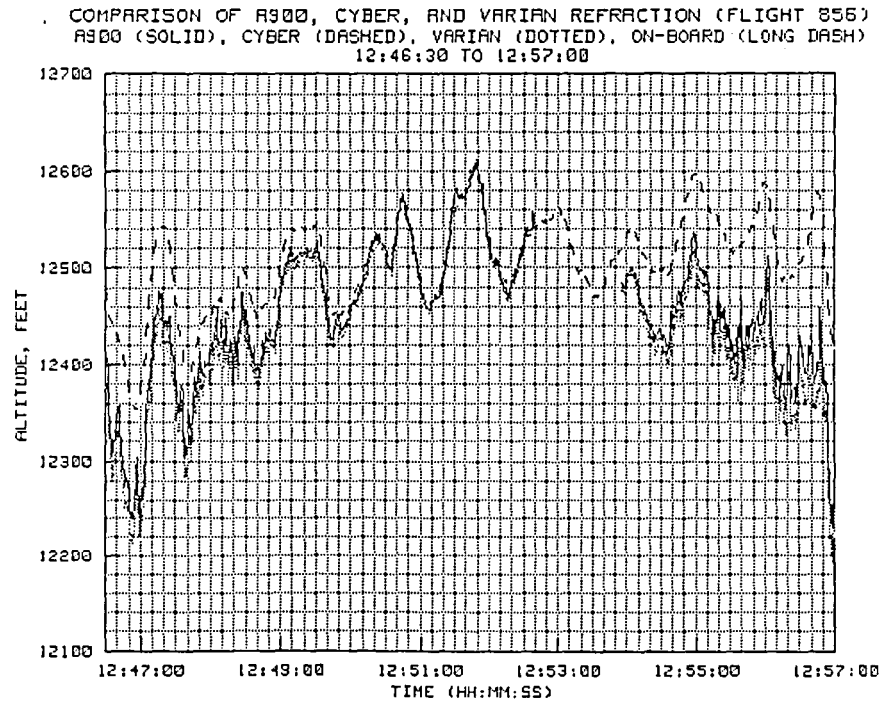

Figure 9-4. Cyber software analysis altitude comparison plot.

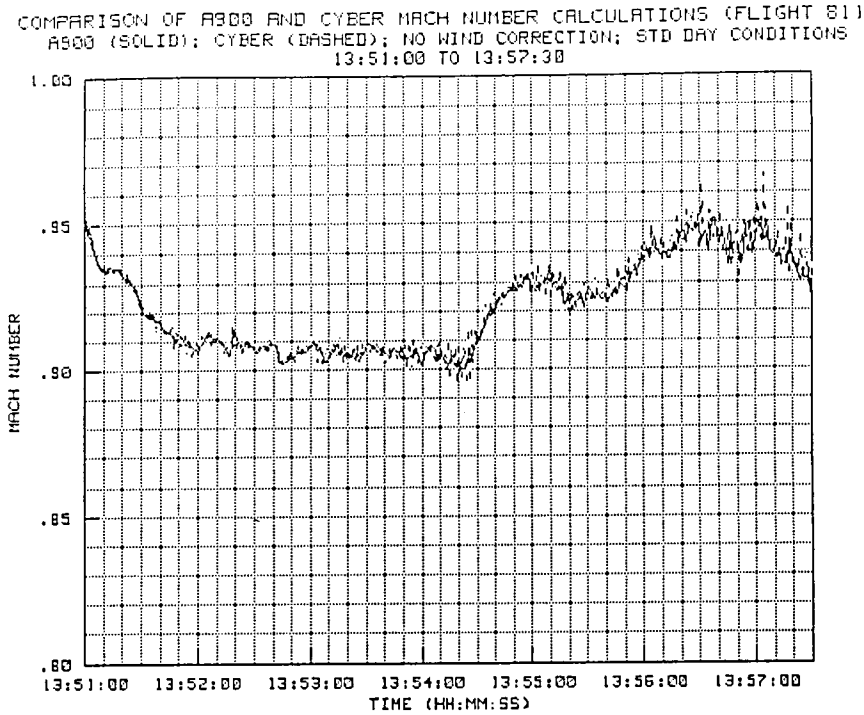

Figure 9-5. Cyber software analysis Mach number comparison plot.

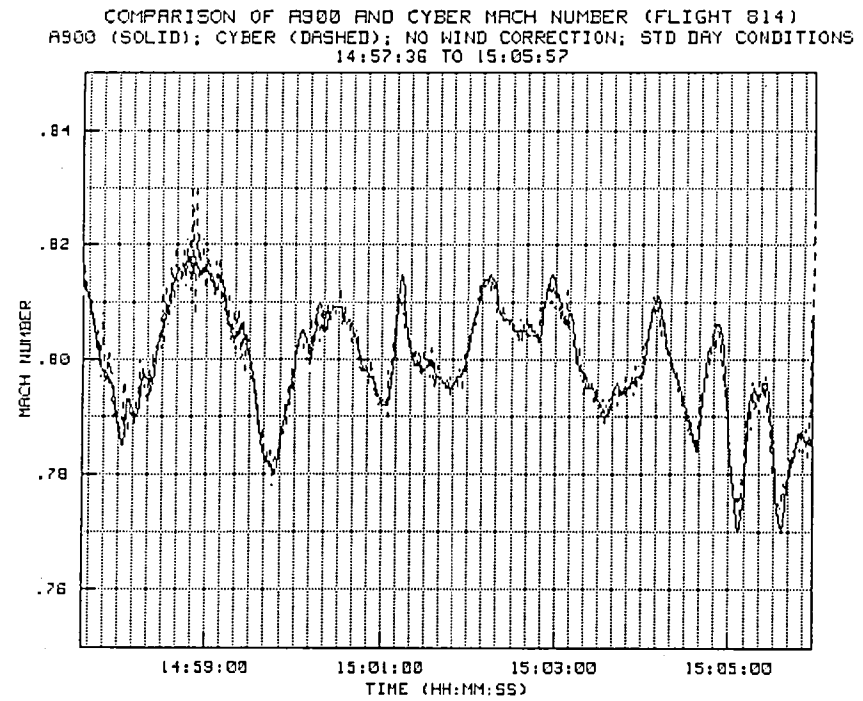

Figure 9-6. Cyber software analysis Mach number comparison plot.

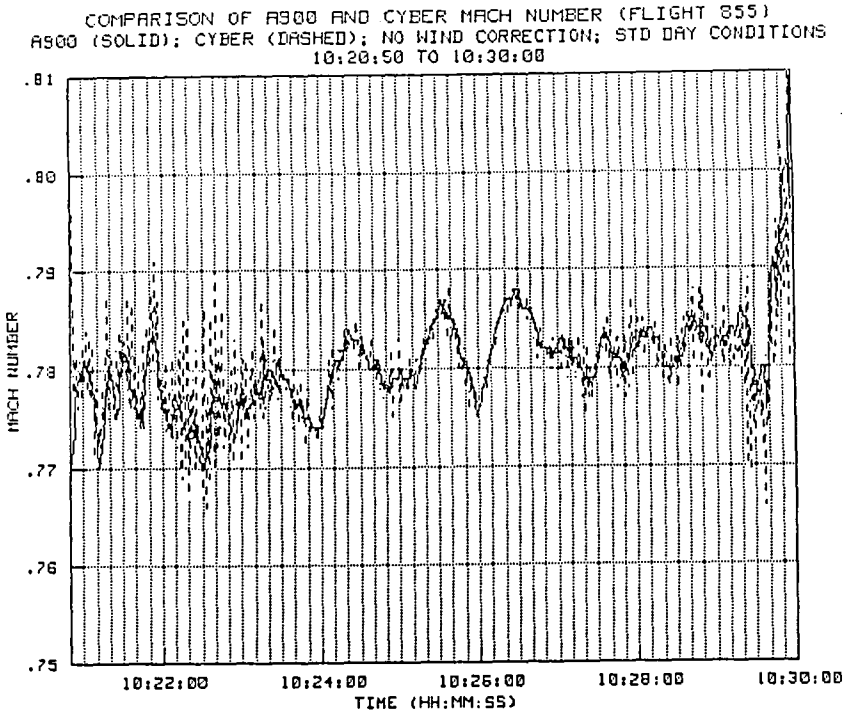

Figure 9-7. Cyber software analysis Mach number comparison plot.

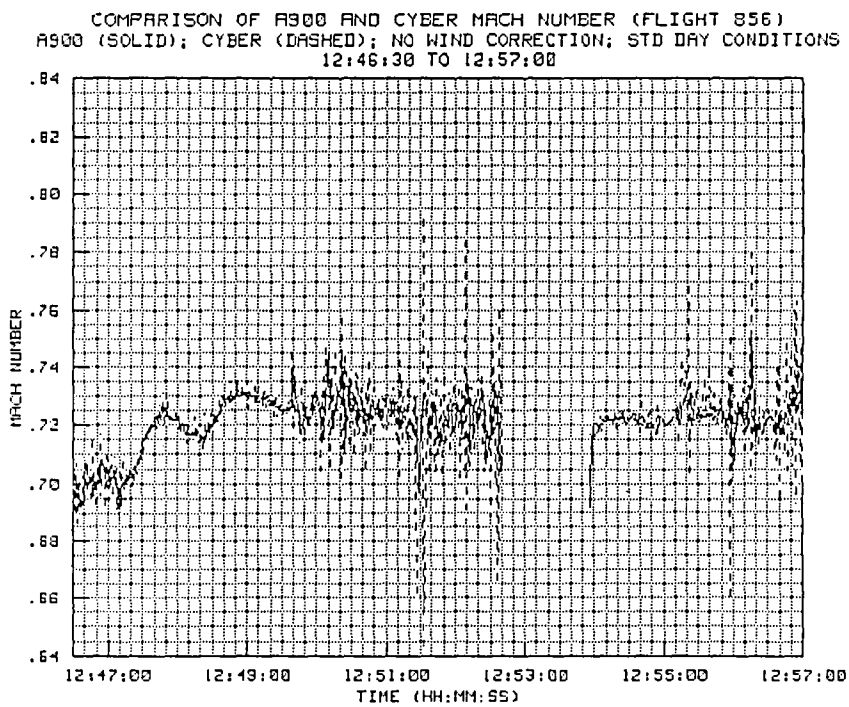

Figure 9-8. Cyber software analysis Mach number comparison plot.

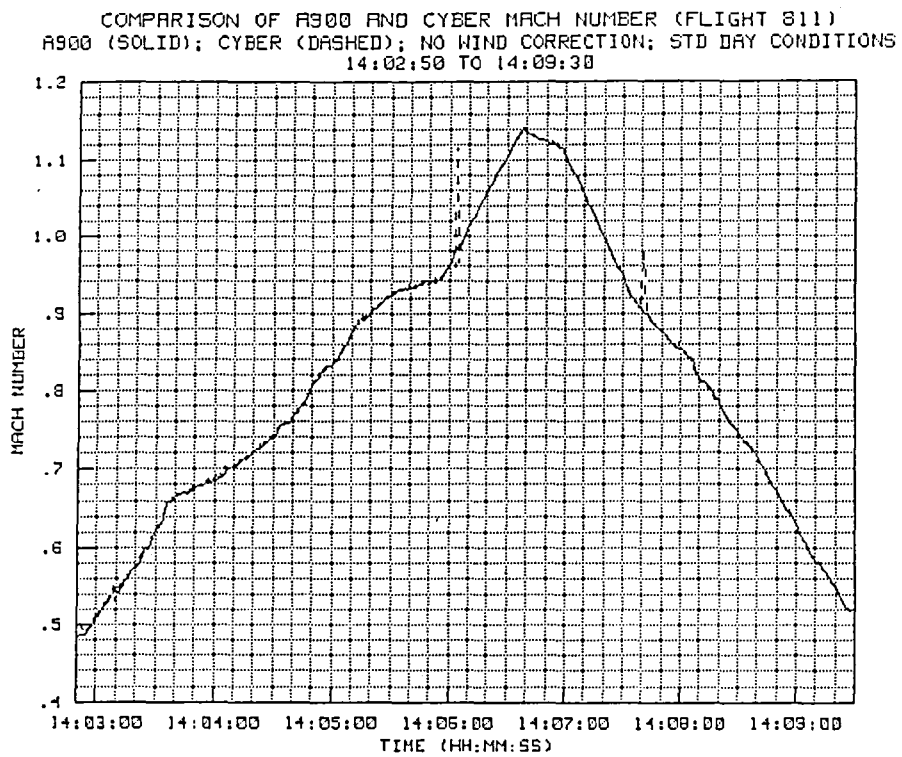

Figure 9-9. Cyber software analysis Mach number comparison plot.

9.5 Results From the Analysis of Cyber Data

The following conclusions may be drawn from the analysis of the data from the Cyber radar data reduction program.

1. The algorithm used to compute index of refraction does not yield values consistent with calculations from reference 3 or from any of the various IRIG documents reviewed. It also does not agree with the r-f refractivity values shown on the rawinsonde printouts. It is the conclusion of this analysis that the equation is incorrect and should be discarded. More appropriate methods for making this calculation are contained in reference 3.

2. The refraction correction method used on the Cyber is known as the Pearson method. It was developed in 1958 as a fast means to obtain reasonably good answers without the need for lengthy processing of atmospheric profile data, and it indeed meets that requirement very well. Running time is probably an order of magnitude less than that required for the Varian solution, and probably two orders of magnitude less than the time required for the A900 solution. And, as shown, if identical values for r-f refractivity are used in the computations, the Pearson method will deliver results that agree well with both the Varian and A900 solutions until the elevation angles become low. However, on the negative side, the solution as implemented on the Cyber performs only the elevation correction, neglecting the range correction provided by both the Varian and A900 methods. And, as will be shown later in this analysis, the results from the Pearson solution does develop extremely large errors at very low elevation angles or very long ranges. However, the method was intended only for target ranges out to about 100 nautical miles and for high elevation angles. It is therefore not suited for reducing any of the Shuttle orbital data or any of the data from the various satellite tracks performed by the NASA radar.

3. The Cyber filter has slightly less damping than what would be considered optimum for the flight profiles examined. Although this noise does not cause undue problems in the altitude results, it can have a detrimental effect on the Mach number calculations, as noted by fairly large spikes in figure 9-9.

Thus, other than for the problem in the calculation of the index of refraction, and in the presence of an occasional Mach number anomaly, the results from the Cyber are in general agreement with the data derived for the same time periods using the analysis software. However, if the radar data reduction programs are to be reprogrammed in the near

future, then the following recommendations would be appropriate:

1. Replace the present refraction correction method with a method designed with a better accuracy to speed tradeoff, since accuracy is really the objective of non-real-time, post-mission processing. In addition, a system should be selected which is capable of reducing data from orbit tracks as well as normal aircraft missions.

2. Consideration should be given to either replacing the present Cyber filtering algorithm with one of those examined in this study or, as a minimum, including one of these filtering techniques as an option. The filters examined in this study consistently provide better handling of aircraft position values and are better suited to handle the varying noise conditions found to be present in the different orbital and aerodynamic tracking situations imposed on the NASA radar.

3. As soon as possible, replace the algorithm used to compute the index of refraction in the Cyber with one that is correct.

10.0 ANALYSIS OF LOW ELEVATION ANGLE ANOMALY

Throughout this analysis, derived altitude was observed to be too low at any time target ranges were long and the elevation angles small. As noted, because of a computational error in the Cyber program, optical instead of r-f refractivity is being used in the NASA refraction correction algorithms. Although, the altitude computed from the Cyber program was found to better match on-board data than did the altitude computed by any of the refraction algorithms (including those used on the Cyber) when the correct values of r-f refractivity were used, the improvement can only be considered coincidental. A wealth of data, both from empirical measurements and from theoretical studies, have substantiated the r-f refractivity constants and equations given in reference 3, and in the many IRIG documents, to be correct.

In attempting to pursue the cause of the anomaly, considerable time was spent reviewing the calibration procedures used on the NASA AN/FPS-16 radar. Tolerances held in the range and azimuth calibrations were very precise and appeared to rule out any significant errors in those channels, and none were noted in this analysis. However, a problem was found in the calibration of the elevation channel. While range and azimuth calibrations can be easily verified on any number of surveyed r-f targets, low-angle multipath effects prevent the same targets from being used for r-f axis elevation checks. This leaves the boresight tower r-f signal source as the sole surveyed checkpoint for the elevation channel. However, even though both the horizontal-vertical (HV) axis of the antenna and the boresight tower feedhorn are surveyed to first-order accuracy, both the normal and plunge mode r-f lock-on readings have always differed from surveyed angles by 3 to 4 LSB values. Because the path between the boresight tower and the antenna passes across the full length of the metal roof of the radar building, the differences have been attributed to multipath. This is believed to be an accurate assessment, since normal and plunge calibrations on the optical targets agree with surveyed information to within less than 1 LSB value.

However, because of the r-f multipath problem, an alternate method was devised for calibrating the elevation channel. Instead of using the r-f signal source as the primary calibration reference, the optical paddle boards were used. The advantage to this procedure was in the fact that, although the optical path was subject to refraction effects, it obviously was not affected by multipath (reflections). However, the trick to this procedure was in finding a way to accurately collimate the r-f and optical axes. To do this, a method was worked out in which an r-f lock-on was established

on a distant aircraft target, which served as a point source for the r-f skin return. With the proper combination of power and bandwidth, the optical track point (the location of the point target on the video monitor) could be established quite closely, generally to within about 1 LSB value. Assuming the difference between optical and r-f refractivity to be small as long as the target was within visual range, the antenna could now be brought back onto the boresight tower so that the optical aim point rested exactly on the center of the paddle board. With the antenna in this position, the surveyed elevation angle to the paddleboards could be accurately set in using the encoder offset switches.

One problem existed with this procedure. Even if the optical aim point could be determined with fairly small tolerances, unless the target was at a high elevation angle, computer simulations indicated a greater difference between the amount of bending in the r-f and optical beams than assumed by this procedure. And, for a target of opportunity to serve as a point source for a skin return, it had to be at a reasonably long range, where the differences between optical and r-f refractivity could become significant. Thus, without compensation for the increased bending in the r-f beam, a bias error would be introduced into the elevation measurement, and this error would cause the radar-derived altitude to read increasingly lower than the true target altitude as the elevation angle became smaller. Note also that the amount of bias introduced by this procedure would be variable depending on the range and altitude of the target used for establishment of the optical aim point. Thus, it might be expected that if this type of error were present, the amount of error could vary with each different calibration.

Shortly after the final test flight, a complete realignment of the radar was accomplished, and the procedures for calibrating the elevation channel were revised. The alignment of the radar included: (1) an accurate pedestal mislevel check and mislevel adjustment, (2) a mechanical calibration of the optical scope system using forward and reverse observations on the boresight tower optical targets, (3) a realignment of the antenna feedhorn assembly to collimate the mechanical and r-f axes of the system, and (4) a precise realignment of the boresight video system using the optical paddleboard targets. The alignment of the mechanical and r-f axes of the antenna was important to assure that the radiation pattern was symmetrical about the r-f axis. This alignment was accomplished by making numerous adjustments to the feedhorn assembly until agreement was obtained between the normal and plunge r-f lock-on points with no encoder bias added. Note that if the r-f radiation pattern is non-symmetrical, then the amount of multi-path pull-down may differ between the normal and plunge modes. However, with a

symmetrical pattern, when the normal and plunge elevation readings match (180-Elp=Eln), then even with significant amounts of multipath, if the amount of encoder non-linearity is small, the elevation calibration should be correct. The results were then roughly checked as before by establishing the optical track point when locked on to a distant target; then checking the optical track point on the boresight paddleboards--after compensating for differences in optical and r-f bending for the particular target range and elevation angle.

It should also be noted that a precision mislevel system is installed on the antenna pedestal, and mislevel checks are are generally performed on a weekly basis. These checks are made during nighttime hours, because solar heating effects can be clearly detected in daytime measurements. Changes in the pedestal mislevel due to solar heating can account for about 1 or possibly 2 bits of error in the elevation angle measurements, however this would not account for the amount of the low-angle altitude errors uncovered during this analysis, and solar heating effects would manifest themselves in different ways depending on the position of the antenna with respect to the sun.

Another possibility considered was an error in the surveyed elevation coordinates of either the boresight tower or the antenna, or both. The boresight tower is located 2,212.44 feet from the feed horn of the radar dish. The amount of angular error observed at the ends of the survey legs was computed to be on the order of 0.021 to 0.025 degree, or about 8 to 10 LSB values. If the differences were due to a survey error, then that error would have to be about 10 to 12 inches in the elevation of either the radar antenna or the feedhorn, or a combination of both. Considering the fact that the tower is about 150 feet high and almost a half-mile from the antenna, a relative elevation error of 10 or 12 inches did not seem outside the realm of possibility. However, numerous angle measurements made by the site crew as a result of this analysis, did not substantiate the hypothesis that a survey error might be present. Rather, optical scope checks on the boresight tower paddle boards of both the NASA and USAF boresight towers showed almost exact agreement with surveyed data.

Also considered was the possibility that the pedestal might have an excessive amount of droop. Since droop is a function of the cosine of the elevation angle, the greatest amount of droop, and hence the greatest altitude error, would be present at the low elevation angles. Two factors immediately ruled out droop as the possible cause. First, droop (sag) error causes the measured elevation to read higher than true elevation, the opposite of the long range anomaly observed

during this analysis. Second, if significant droop were present, it would not only affect the r-f calibrations, but would also be present during optical checks. No measurable droop effects were observed in the normal and plunge mode checks with the optical system. This also ruled out the possibility of any significant encoder non-linearity.

In order to determine how much elevation bias would have to be present in the measurements, data from eight of the test points, all survey legs, were rerun. The amount of elevation bias was adjusted until the data came into reasonable agreement with the Z-Hp horizontal gradient estimated from the synoptic analysis. The results are shown in figures 10-1 through 10-4. Figure 10-1(a) provides the altitude time history plot for test point #3 on flight 811. Note that, in this case, an elevation bias correction of about 10 LSB values brings the plot into reasonably good agreement with estimates using the synoptic Z-Hp horizontal gradient.

Figure 10-1(b) provides a time history altitude plot for test point #4 on the same flight. Even though an anomaly also existed in the on-board measurements during this run, the overall agreement appears to be good. Finally, figure 10-1(c) shows the same type of time history plot for test point #5, the cross-survey leg. Again, the agreement appears much better with the amount of difference between the on-board and radar-derived plots being approximately as predicted by the synoptic data. Thus, assuming the synoptic estimate of the Z-Hp gradient to be reasonably accurate, it is possible that an elevation bias of about 10 LSB values was present in the data from flight 811.

Figure 10-2 provides the revised time-history plot for test point #4 on flight 814. The data from the synoptic analysis for this flight predicted the maximum Z-hP horizontal gradient for 18,000 feet to be 1.02 feet per nautical mile at 017 degrees. The leg was flown on an approximate southerly heading at which the estimated gradient would be about 0.98 feet per nautical mile with the pressure altitude showing a decrease in relation to geometric altitude along the direction of flight. At equidistant points about 29 miles from the near point, this would amount to an asymmetrical altitude difference on the order of about 57 feet. However, the data from test point #4 shows a difference of about 110 feet between the two 29-mile points. If the synoptic data were accurate, this would equate to an elevation bias of about 8 LSB values. The plot in figure 10-2 provides a comparison of local Z-Hp adjusted on-board data and radar-derived data with an 8 LSB elevation correction included.

Figures 10-3(a) and 10-3(b) provide the time history plots for test points #4 and #7 on flight 855, flown under benign day

conditions. Test point #4 was flown on an approximate southerly heading along which the estimated gradient was very nearly zero. In order to match radar-derived altitude to the synoptic estimate approximately 10 LSB values of elevation bias were required in the reduction of the data. With the correction made, the plot shows good agreement with the Z-Hp adjusted on-board pressure data; however, some non-linearity in the horizontal gradient may have been present. Test point #7 from flight 855 was also reduced with corrections for a 10 LSB elevation bias. The leg was flown on an easterly heading at which the synoptic estimate of the Z-Hp horizontal gradient was only 0.27 feet per nautical mile. This would have resulted in an altitude change from the near point to the 150,000 foot range point of only 7 feet which would probably be masked by normal atmospheric variations. The data from test point #7 are shown in figure 10-3(b). Thus, if an elevation bias were the cause of the anomaly, then on the basis of the flight 855 data, the bias would have had to have been about 10 LSB values.

Figures 10-4(a) and 10-4(b) are for test points #3 and #4 from flight 856. Test point #3 was flown on a westerly heading until about 12:45:00 when a left 180 degree turn was commenced. On the westerly portion of the run, the estimated horizontal pressure gradient would have resulted in an pressure altitude change of only 3 or 4 feet, probably too little to detect. However, data shown in figure 10-4(b) is for the portion of test point #4 during which a constant easterly heading was held. Data reduced without an elevation bias correction showed sizeable errors at the low elevation angles. When compensation was made for an elevation bias of 10 LSB values, the radar-derived altitude and on-board pressure data agreed better, however it appears as though the 10 LSB bias compensation might not be quite enough, since the synoptic analysis estimated that the geometric altitude plot would increase with respect to the pressure altitude plot by about 20 feet along the leg. Instead, a decrease of about 20 feet can be seen in the data. Thus, for the data from flight 856 to agree with the synoptic estimate, a elevation bias correction of about 11 LSB values would probably be required.

Thus, assuming the synoptic estimates of the horizontal Z-Hp gradient to be accurate, it would appear that the low elevation angle anomaly could be due to an elevation bias on the order of 10 LSB values. If this were the case, then radar-derived altitudes would be less than the true values. In addition, differences between high-angle geometric and pressure altitude determined from high-angle radar measurements would also be in error. For the case of a target flying at an altitude of 30,000 feet, the difference in pressure altitude and geometric altitude determined from a high-angle track at about 37 degrees elevation angle would

have had an error of about 19 feet. As the elevation angle decreased, the error in the altitude determination would have increased to about 46 feet at a slant range of 100,000 feet, 95 feet at a slant range of 200,000 feet, and 191 feet at a slant range of 400,000 feet. However, the calibration procedures followed during the recent major realignment of the radar, should have eliminated any elevation encoder bias, and this can be determined by analyses of data from future air data calibration flights. If significant bias still remains, then it will be necessary to look elsewhere for the problem.

It is also important to mention that an additional check of the optical axis elevation calibration may be possible in the near future through the use of a "star calibration" program currently in preparation. This will permit high angle optical calibrations using very precise star trajectory data. After the optical axis is calibrated, an r-f axis and optical collimation will then be performed using high-angle orbital tracks on the Space Shuttle during times when the Shuttle is visible on the video monitor. At the higher angles, where the refraction correction is small, accurate adjustments for differences in r-f and optical bending should be easily determined down to within the LSB resolution of the elevation encoders.

Finally, it should be mentioned that for a target at an altitude of 30,000 feet, the altitude error is less than 250 feet for a target slant range of 500,000 feet. Considering that the error appears to be consistent, predictable, and correctable is very encouraging. This is especially true in light of the fact that many authoritative studies have concluded that high accuracy in radar elevation measurements cannot be achieved at very low elevation angles. The errors in radar-derived altitude found in this analysis, even without correction, are probably less than what would be expected from much of the information available on the subject. If, as indicated by the consistency of the error, it can be corrected, then the NASA radar should achieve accuracies that are remarkably good.

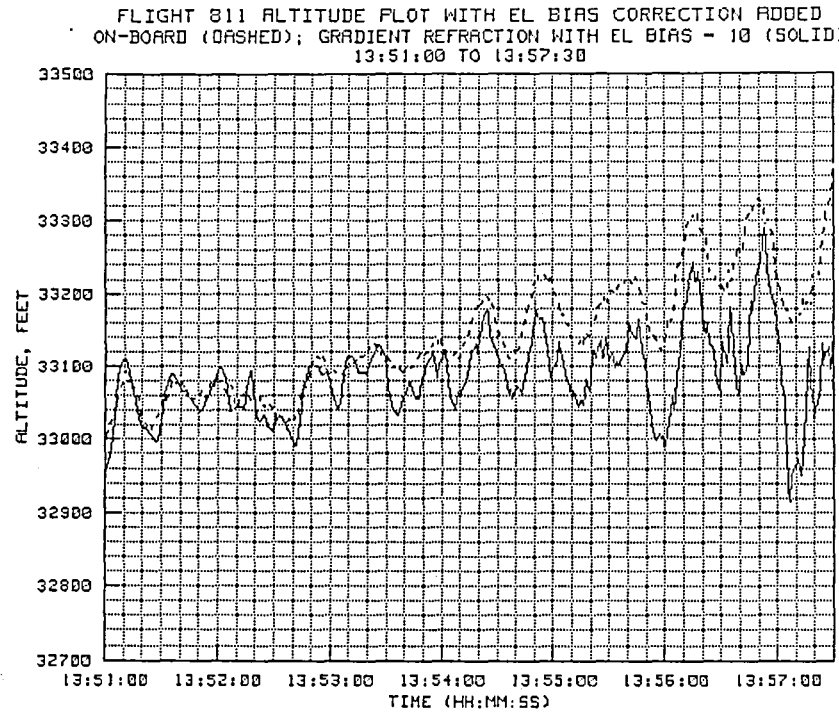

Figure 10-1(a). Flight 811 comparison with bias correction.

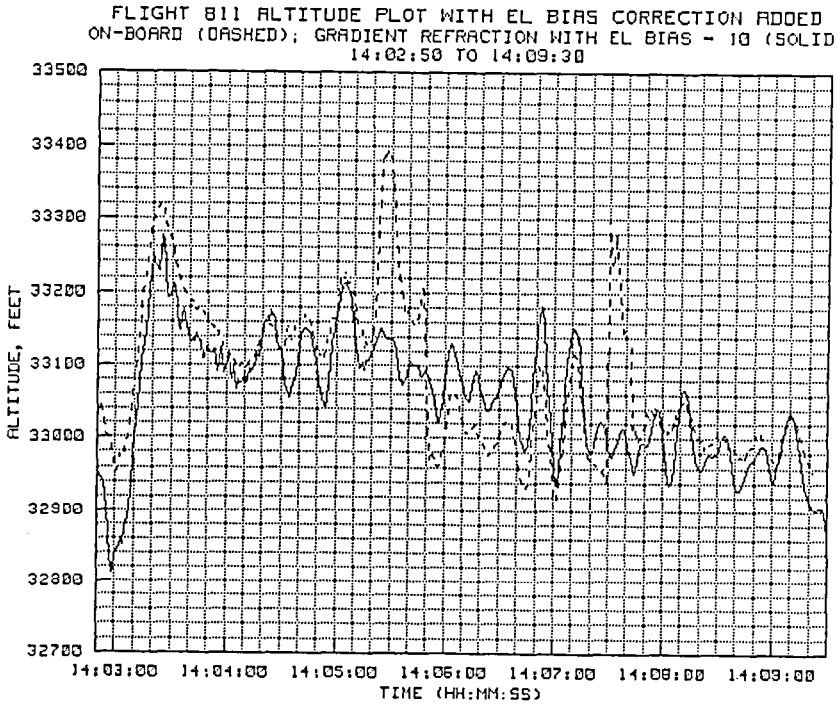

Figure 10-1(b). Flight 811 comparison with bias correction.

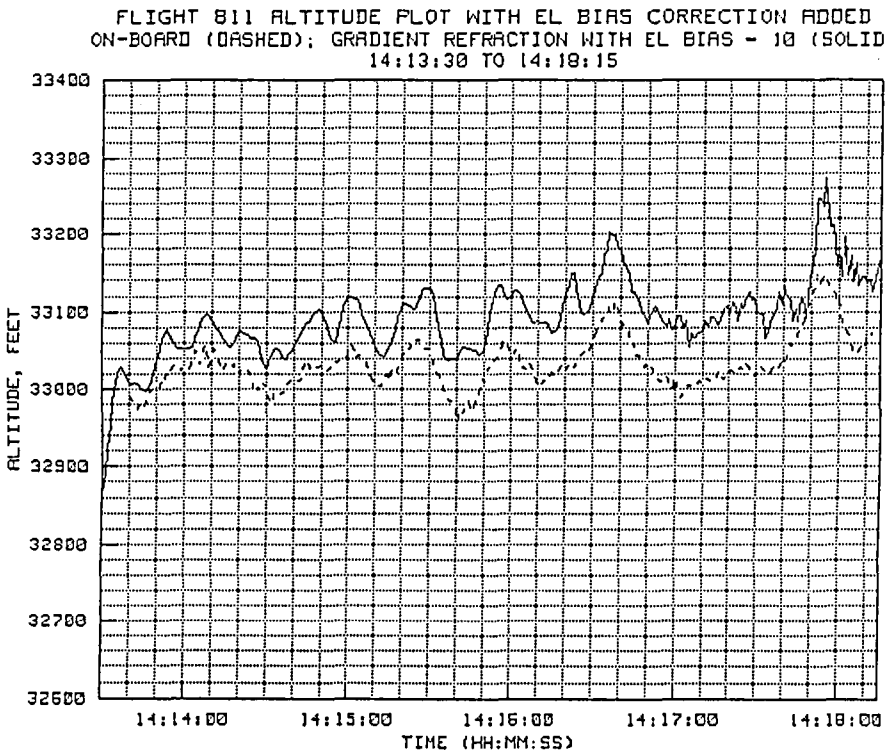

Figure 10-1(c). Flight 811 comparison with bias correction.

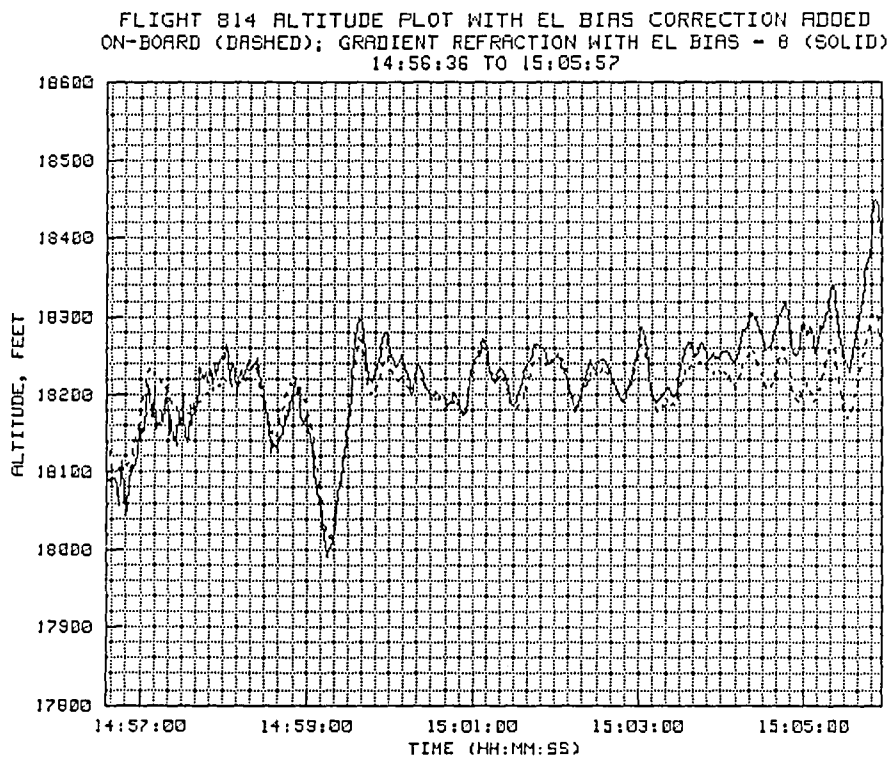

Figure 10-2. Flight 814 comparison with bias correction.

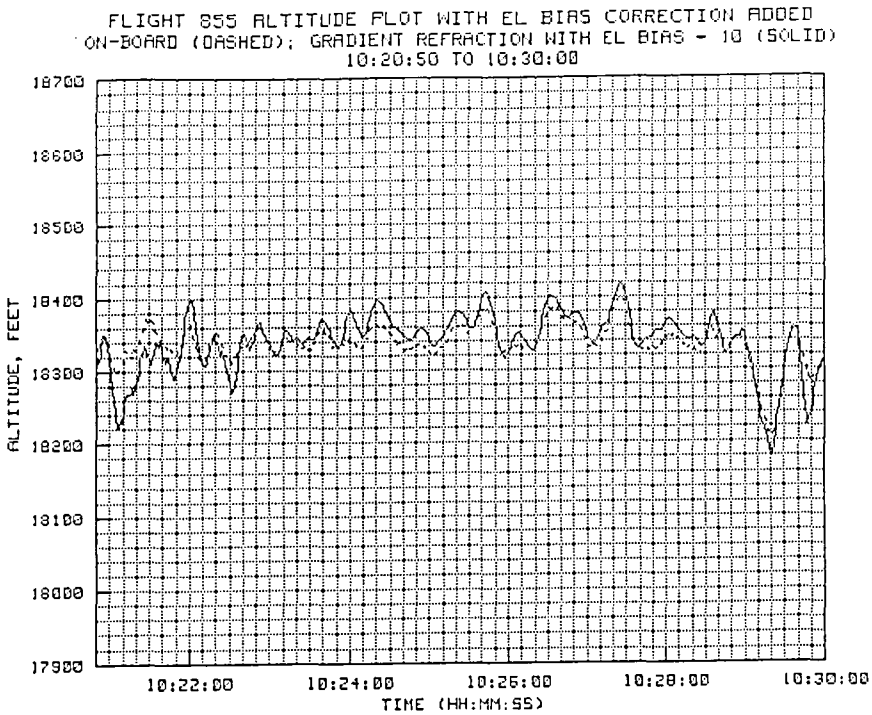

Figure 10-3(a). Flight 855 comparison with bias correction.

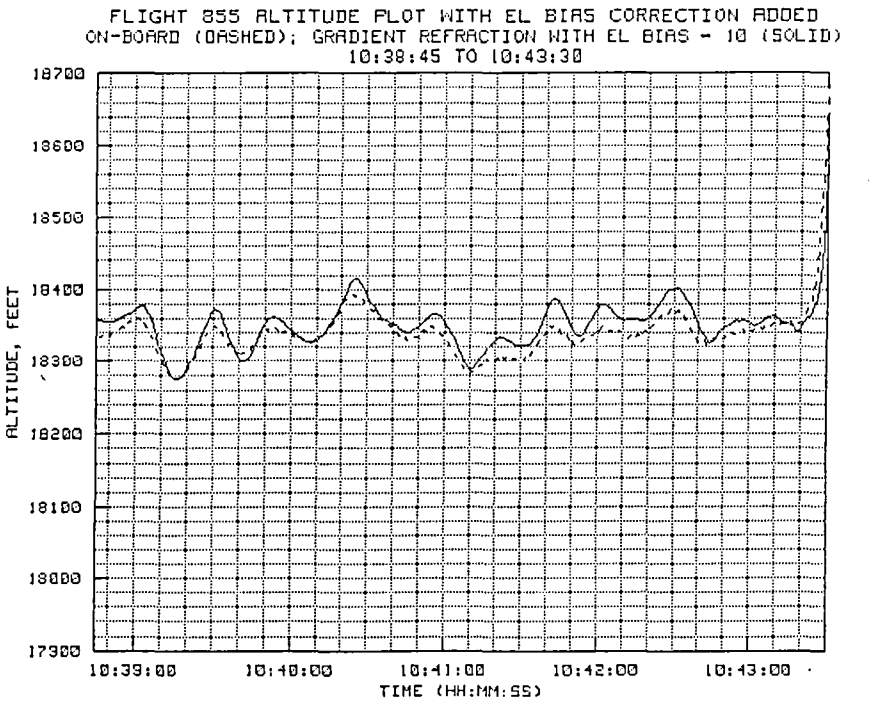

Figure 10-3(b). Flight 855 comparison with bias correction.

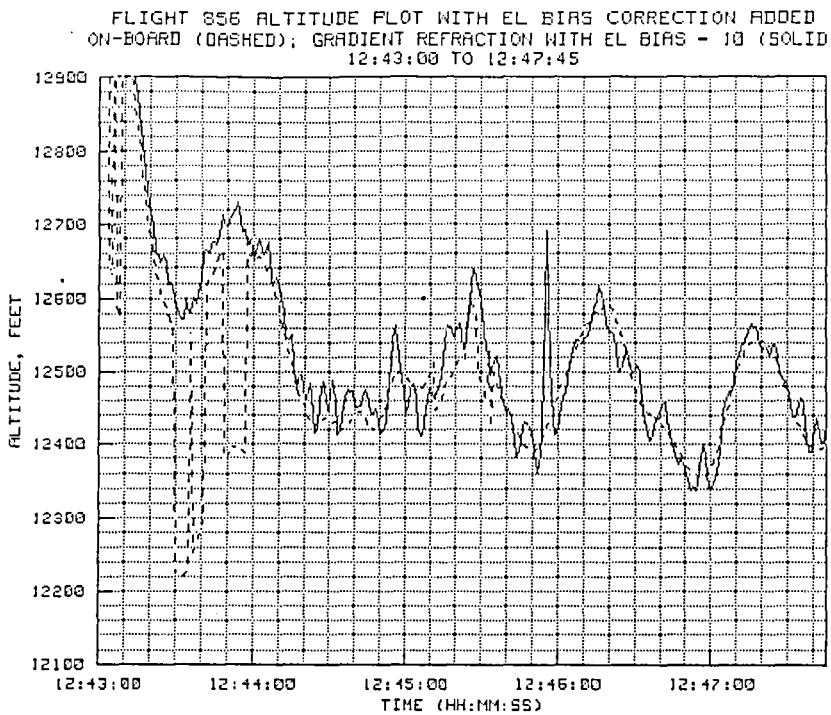

Figure 10-4(a). Flight 856 comparison with bias correction.

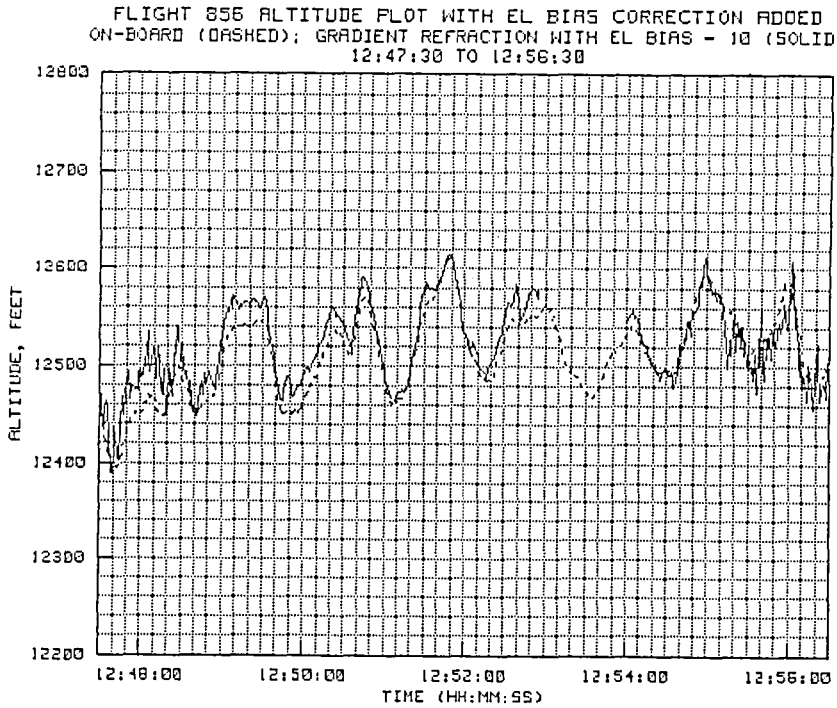

Figure 10-4(b). Flight 856 comparison with bias correction.

11.0 FILTER COMPARISONS

Detailed discussions relating to the performance characteristics of each of the four filters analyzed in this study are provided in appendix C. This section describes the capabilities provided in the GMD software to select and compare different filtering methods and the results of doing so.

When data from any specific mission were to be analyzed, the operator selected the data reduction mode of operation. As part of the many alternative selections provided for data reduction, the operator could select any one of four filtering methods: the real-time Kalman, the 8-state Kalman, the QD filter, or the alpha-beta-gamma filter. After the filter selection was made, the operator was prompted to enter the appropriate filter constants to be used for that specific flight.

A considerable amount of data processing was started immediately after the first flight on April 5. At that time, the real-time Kalman filter from the A900 program was the only filter available, since the other methods were still being adapted to be compatible with the rest of the data reduction software. Thus, many tests were performed using the real-time Kalman filter on data from both flight 811 and 814. The objective of the tests was to provide preliminary data from each of the flights so that data reduction software could be configured to yield the greatest flexibility and the maximum amount of information. Thus, by the time the other filters were adapted to this requirement, a considerable amount of radar data had already been reduced using the real-time Kalman filter. Therefore, to be consistent in the remainder of the data reduction work, the real-time Kalman was used as the primary data reduction filter. After implementation of the other filters, comparisons were then made between the data obtained using the real-time Kalman filter and data obtained using the other three filtering methods.

During the initial stages of the analysis, filtering was performed on the raw measurement parameters (range, azimuth, and elevation) as is done in the real-time software operated on the A900. Subsequently the program was modified to filter range, azimuth, and elevation and X-Y-Z data. This was found to yield slightly smoother values for the X-Y-Z coordinates. With the real-time filter, filtering of the X-Y-Z values also had the advantage of providing, as part of the state vector, both the velocity and acceleration components of the X, Y, and Z coordinates. Since these components were needed as part of the horizontal velocity, vertical velocity, and total velocity calculations, the filtering of X-Y-Z eliminated the

need to separately compute these parameters. It was also found that the velocity and acceleration values obtained directly from the X-Y-Z filter had slightly less noise than those computed from the R-A-E state vector.

The next step in the development of the data reduction package was to investigate the results of eliminating the R-A-E filter entirely, and filtering only the X-Y-Z values. It was found that eliminating the prefiltering of the R-A-E values caused no noticeable change in the output data from the X-Y-Z filter. Thus, without any significant degradation in the quality of the X-Y-Z state vector, the time required for the filtering tasks was essentially cut in half. Therefore, this was the procedure implemented in the data reduction software.

Although the R-A-E filter was not selected for use during the reduction of the data from the six missions analyzed under this contract, it does serve to demonstrate the effectiveness of the filters in processing measurement data having large quantization levels. It should be noted that the NASA radar operates as part of the NASA/DoD worldwide tracking network. Transmission formats are standardized in accordance with requirements established by the Inter-Range Instrumentation Group (IRIG). This facilitates the flow of tracking data throughout the worldwide net. Data sent to the main building is transmitted in the IRIG-I format. Data sent to the USAF and other network sites is in the IRIG-II format. In both of these formats, the value of the least significant bit in the range word is 1.953125 yards. Thus, it is important to understand that, even with on-site filtering, no matter how smooth the data from the filter may be, it is still rounded off to the same LSB level prior to transmission. If, at the receiving site, smooth velocities are to be derived for flight control purposes, then the data must be restored to a continuous rather than discrete form, otherwise the quantitization levels may cause problems in the velocity computations.

Figures 11-1 and 11-2 are first difference plots showing both unfiltered and filtered range data from portions of flight 814. No pre-filtering of the data was done prior to transmission. The quantization levels in the transmitted data are clearly apparent in these plots. Note that the usual 0.5 LSB 1-sigma measurement noise is present in the transmitted data. This means that about 99.9 percent of the data points should fall within plus or minus 3 1-sigma values, or within a total range of 3 LSB's. This is approximately the noise level observed in both the plots. The continuous line is a first difference plot of the same data after filtering. The filter used for this test was the real-time Kalman with moderate damping.

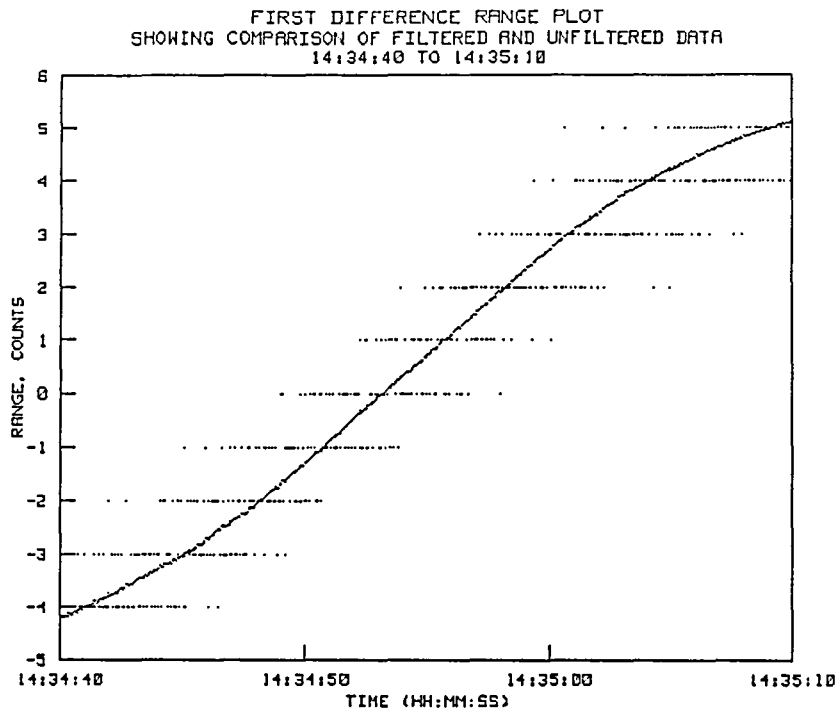

Figure 11-1. Comparison of filtered and unfiltered data.

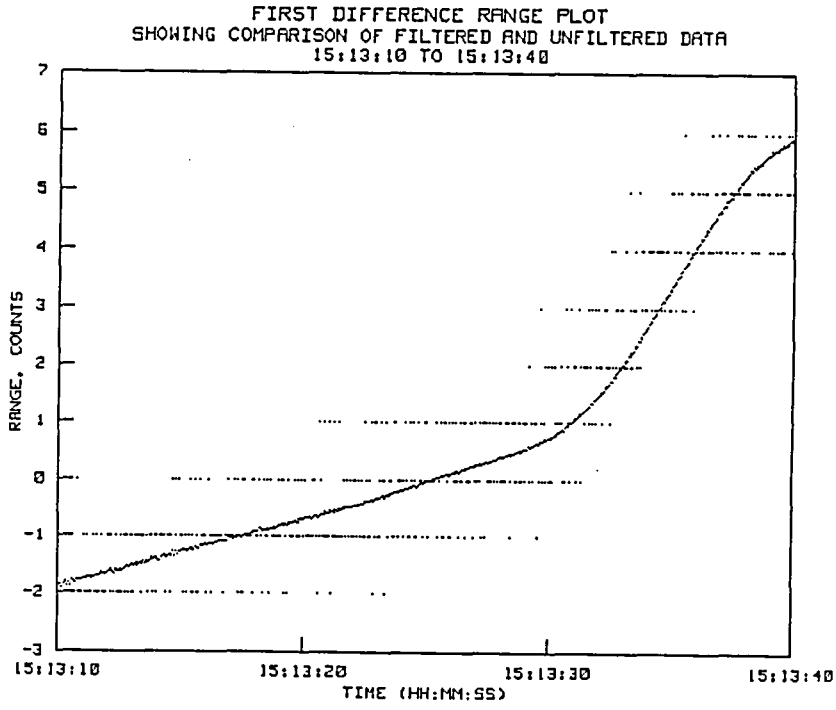

Figure 11-2. Comparison of filtered and unfiltered data.

Although the first difference plot is not exactly the same as velocity, it is close enough to show the need for a high-quality filter in any application were smooth velocity outputs are required. Without filtering, the computed velocity will not only change in steps, it will usually jump back and forth over two or three step levels as does the first differences of the raw data shown in both of the plots. With filtering, there are significant improvements in the results. For example, the 1-sigma noise in the unfiltered data causes 'velocity' jumps of up to 17.5 feet per sample, but the 1-sigma noise in the filtered data causes jumps of only 1 or 2 inches per sample.

Figures 11-3 to 11-6 show altitude data from a typical test point during flight 811. Figures 11-7 to 11-10 show Mach number data for the same time period. In each series of plots, the first figure provides data obtained from the real-time Kalman filter, the second figure provides data obtained from the 8-state Kalman filter, the third figure provides data obtained from the QD filter, and the fourth figure provides data obtained from the alpha-beta-gamma filter. The purpose of these figures is to demonstrate the similarity in the outputs of all three filters. Only very slight differences can be seen between the figures in each of the two sets of plots, and these differences probably could be lessened with some slight adjustments to the filter constants.

These figures are typical of the results from twenty to thirty test points in which the data from all four filters were compared. Even though the QD and alpha-beta-gamma filters are not 'adaptive,' it is hard to detect instances where the results are noticeably different from the adaptive filters.

Both the real-time Kalman and the 8-state Kalman make extensive use of matrix manipulations. Many of these (e.g. a matrix inversion) require a large amount of computational time. Close observation of the matrix elements in these manipulations show that many of the terms in these calculations, while required in a purely mathematical sense, have a negligible effect on the outcome. In fact, in the real-time Kalman filter, when the matrices involved were diagonal, the matrix operations were converted to conventional algebraic form so that unnecessary calculations (e.g. 0 x 0) would be eliminated. This significantly reduced the computational time.

Also noted in the comparison of the different filters was the fact that changes in the filter constants obviously had great effect on the outcome. On the other hand, the adaptive filters did not inherently adjust well to increased noise in the X-Y-Z coordinates as target range increased. Even though

the amplitude of the noise in the raw angle measurements did not change significantly over the normal aircraft tracking ranges, the amplitude of the noise in the derived X-Y-Z values did increase as a function of range. This suggests that the best way to filter position data may be to use a filter with variable noise statistics so that more dependence is placed on the filter dynamics model as the range becomes greater. This could permit the same filter to perform better throughout the normal tracking envelope for aircraft targets, and should also allow the filter to perform well with orbital targets as well. In theory, this feature could be used on any of the four filters examined, however, more study would be required to devise an optimum implementation technique.

Another reason that the adaptive filters did not show significant improvement in the quality of the X-Y-Z data at longer ranges was due to the fact that, in addition to the normal measurement noise, small oscillations in the aircraft trajectory caused slight overshoots in the antenna angle data. That is, some servo lag was present when small pilot inputs were made to keep on a desired altitude or Mach profile. This resulted in position errors of only a few feet when the target was at close range, but, at longer ranges, the same amount of overshoot resulted in position errors many times as great. Since the overshoot errors are essentially bias errors that occur at the same frequencies as the true aircraft movements, they cannot be easily removed by standard filtering techniques.

Thus, if the adaptive filters provide only marginal improvements in the output data, it may be more economical to implement either the alpha-beta-gamma or QD filters in any real-time applications, since they perform well and require only a fraction of the computational time needed by the Kalman-type filters.

One more comment should be made regarding filtering techniques. Since range, azimuth, and elevation are the measurement parameters on the radar, it seems natural to put the filter as close to the source as possible and perform the filtering on the raw range, azimuth, and elevation values. This did not seem to be advantageous in the situations investigated in this analysis. Better results were obtained when X-Y-Z coordinates, computed from raw R-A-E measurements, were filtered. Note that aircraft trajectories, even highly dynamic trajectories, have reasonably smooth X-Y-Z plots. Even during an overhead pass, the X-Y-Z state vectors behave well. On the other hand, azimuth and elevation do not behave well. When the target is directly overhead, azimuth becomes indeterminant, and when a target passes the radar, both the velocity and acceleration in the elevation measurements experience a quick reversal. This makes extrapolations of

the state vector more inaccurate when working in the R-A-E coordinate system than when working in the X-Y-Z coordinate system, especially when the target is at a point where the highest levels of noise are present in the measurements.

It is therefore recommended that single-pass filtering be performed, and that it be performed on the X-Y-Z rather than on the R-A-E coordinates. For real-time applications the alpha-beta-gamma or QD filters appear to be the best selection. For post-mission processing, some marginal improvements may be found when using the Kalman filter.

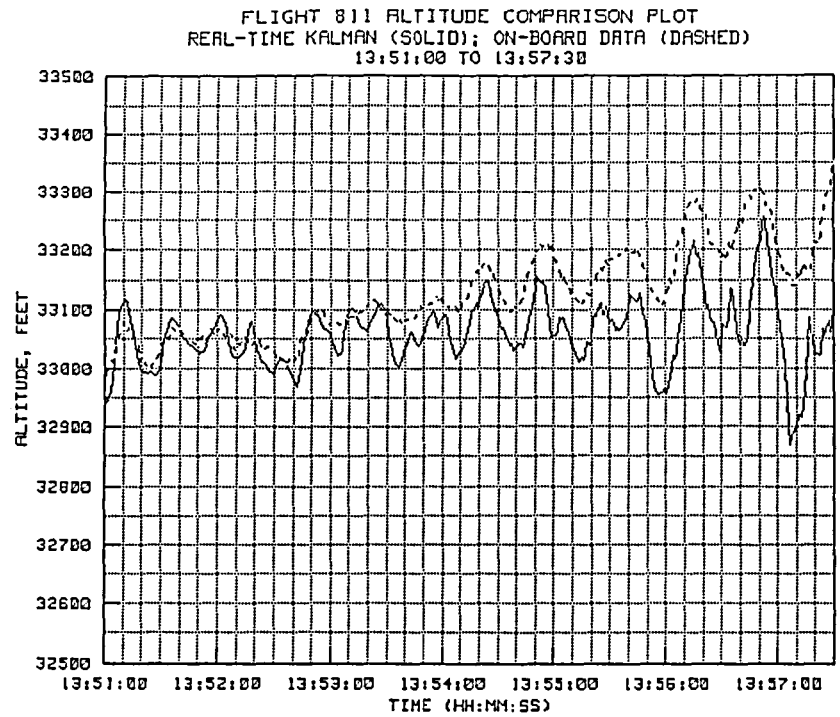

Figure 11-3. Altitude data derived from real-time Kalman filter.

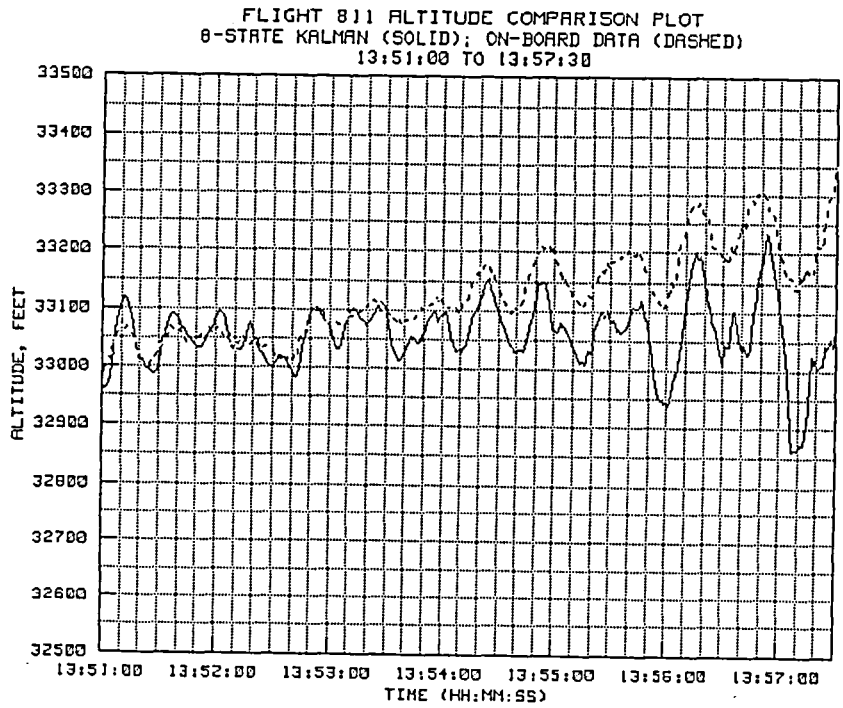

Figure 11-4. Altitude data derived from 8-state Kalman filter.

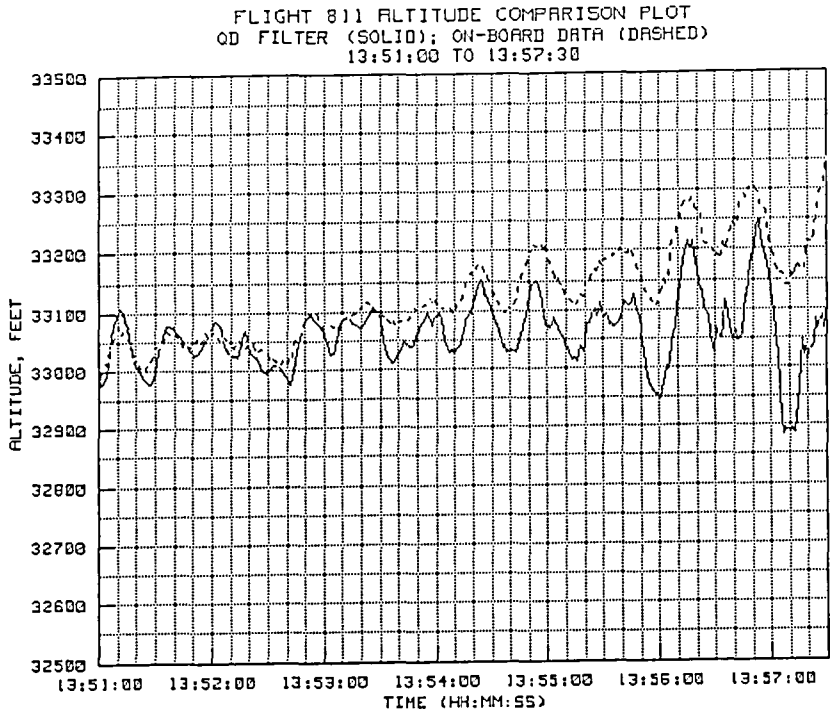

Figure 11-5. Altitude data derived from QD filter.

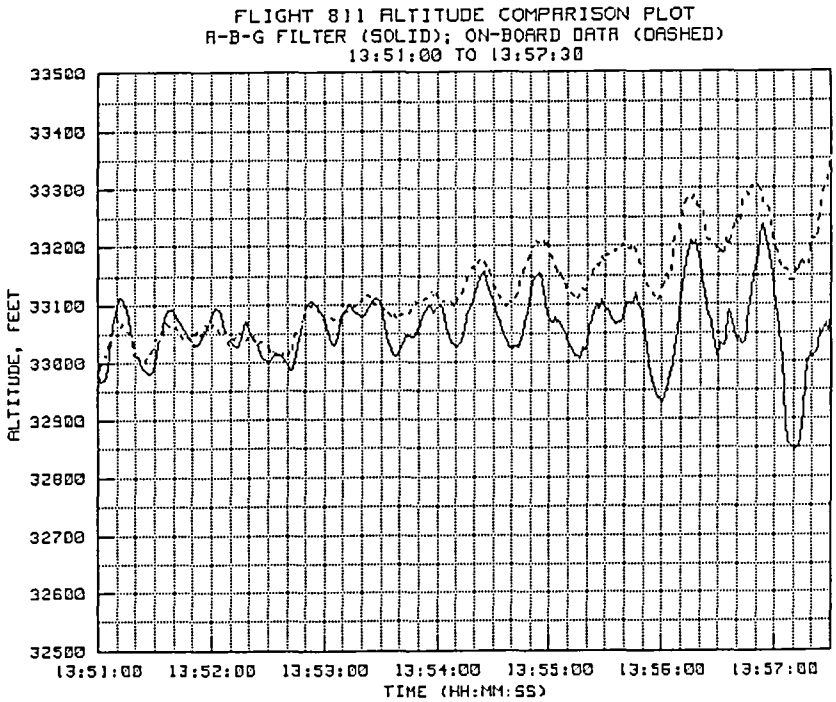

Figure 11-6. Altitude data derived from A-B-G filter.

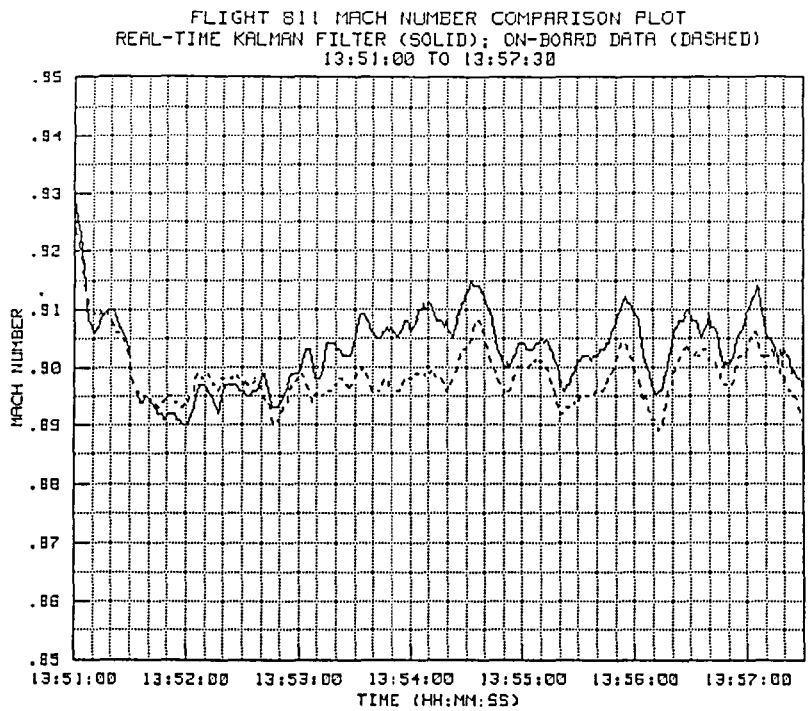

Figure 11-7. Mach number derived from real-time Kalman filter.

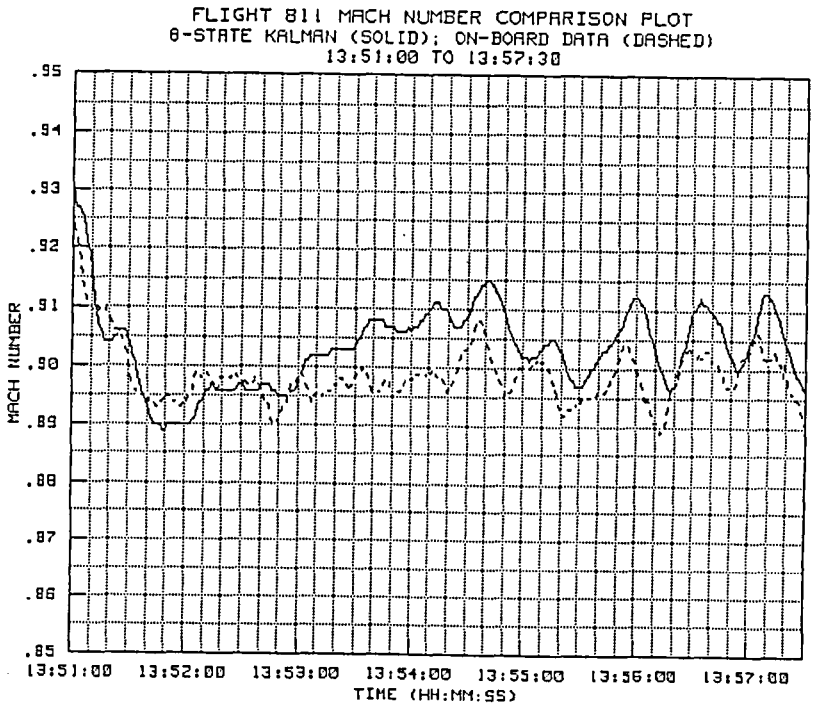

Figure 11-8. Mach number derived from 8-state Kalman filter.

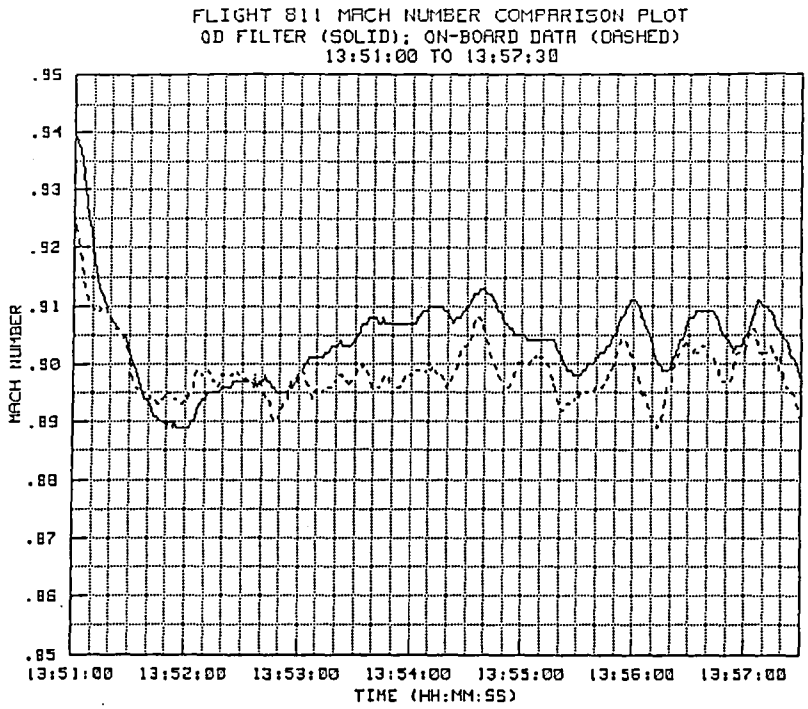

Figure 11-9. Mach number derived from QD filter.

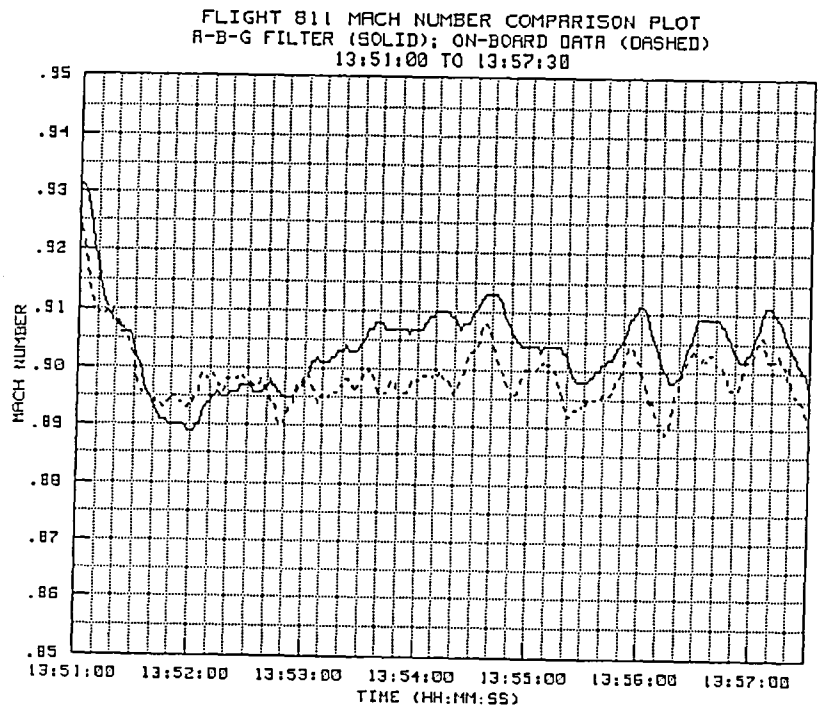

Figure 11-10. Mach number derived from A-B-G filter.

12.0 CONCLUSIONS

This analysis examined the accuracy of radar-derived geometric altitude and Mach number by comparing radar-derived parameters with on-board pressure measurements, after the on-board measurements were corrected for the flight day atmospheric conditions. The two sets of altitude data were 'tied in' through the use of synoptic Z-Hp profiles adjusted to agree with high-angle or short-range radar-derived altitude, which, for aircraft targets, should provide geometric altitude data accurate to within 5 feet. However, the possibility that an elevation bias error may have been present during these tests would increase the margin for error so that high-angle measurements could have had an error of up to 20 feet. Mach data for this analysis were computed using radar-derived velocities adjusted for flight day wind and weather conditions.

For all of the flights analyzed, consistent altitude agreement was obtained for portions of the flight in which the elevation angles were in excess of about ten degrees. During non-maneuvering flight, even minor movements in the on-board pressure altitude were duplicated in the radar-derived data. However, at greater ranges, more noise was present in the altitude data, even though the measurement noise remained about the same. This suggests that the best way to filter radar-derived position data may be to use a filter with variable noise statistics. At longer ranges more dependence should be placed on the filter dynamics model.

Also noted was the fact that a significant error developed in the radar-derived geometric altitude whenever the elevation angles were low. For a target at an altitude of 30,000 feet and a slant range of about 75 nautical miles, the error was about 200 feet, regardless of the refraction method used. A close analysis of the problem indicated that it may have been due to a bias in the elevation data. The exact cause could not be determined during this study; however, when corrections were made for this type of bias, the radar-derived altitude data closely matched the Z-Hp adjusted on-board data for all elevation angles studied. It should be noted that a star calibration program is presently being prepared to check the elevation encoder system on the NASA radar. When this program is completed, it will be possible to detect elevation errors down to the measurement granularity of the system.

Target maneuvers were found to have an adverse effect on both altitude and Mach number calculations. In beacon mode, a poor track will develop whenever shielding, reflection, or cross polarization effects occur. These effects will often cause rapid changes in the apparent target position and can

lead to a complete loss of radar lock. At close ranges in skin mode, the point of maximum return can jump around the surface of the aircraft causing substantial jitter in the position data. At longer ranges where the geometric limits of the target subtend a smaller angle, maneuvering causes less noise. Whenever noise develops in the position data, the first derivative (velocity) becomes even more erratic.

The presence of a chase aircraft can also have adverse effects on both altitude and Mach number data. In beacon mode, turns or other maneuvers often cause the body of the aircraft to block the signal path. When this occurs, the transponder signal received by the radar is weak. Under these conditions, a reflection off the chase aircraft can cause the radar to lose lock. In skin mode, the signal return is subject to considerable glint due to the normal variation in aspect angles. If the momentary return from the chase aircraft is stronger than the return from the tracked aircraft, then the lock can jump to the chase aircraft. Therefore, in order to improve tracking performance in both the skin and beacon modes, the chase aircraft should remain well clear.

Another factor that affects the quality of the track is the power, bandwidth, pulse length, and pulse repetition rate on the radar. This study did not investigate these factors. The analysis assumes the site crew operated the system at settings they perceived to be optimum for the various tracking conditions. In several cases, during maneuvering flight, the effects of servo lag were noted. It is felt that a real-time display of noise levels in the three data channels, along with the normal display of error signals, would allow the operator to better fine tune the radar system.

In this regard, the noise data contained in figures 5-26 to 5-28 clearly show the need to alert the radar crew prior to any test maneuvers involving unusual aircraft attitudes so that appropriate adjustments may be made to provide the best possible track during the maneuver. Even if the operator is monitoring the ground-air communications, the fact that the pilot is on condition and that data is being taken does not provide any warning concerning the nature of the maneuvers about to be performed. Although this problem could be eliminated if the radar personnel could attend the crew briefings, this is often not possible because of heavy operational commitments, including Air Force support missions, which require the presence of all members of the site crew.

All Mach calculations must be corrected for wind. Actual wind, even on benign days, is subject to a large amount of variability in both direction and velocity. As a result,

even when balloon data are available, Mach calculations based on radar measurements are poor at best. Errors of 0.02 Mach are commonplace, and errors up to 0.05 Mach or greater can easily occur on high wind days. During this analysis, Mach number data were derived from the synoptic analysis, from rawinsonde measurements, and from radar balloon tracks. No distinct accuracy advantage was found with data from any of the three sources.

An analysis of the noise content in the range, azimuth, and elevation channels of the NASA AN/FPS-16 radar reveals that the system is well maintained and meets or exceeds the design specifications for the system. The one-sigma noise levels in both the range and angle data are generally less than one-half of the LSB values of the data takeoff devices. However, during orbital tracks, the noise levels increase significantly.

When tracking aircraft targets, occasional spikes are present in the noise data from all three channels. Generally, these noise spikes are caused by momentary blockage of the beacon return, reflections off the chase aircraft, terrain or multipath interference, dynamic lag of the pedestal, or combinations of these effects.

The landing track of STS-41C had exceptionally low noise content for the long ranges involved, and both of the derived parameters, altitude and Mach number, were well behaved from the point of acquisition until the target arrived overhead. The launch orbit of STS-41D, on the other hand, had poor aspect angles. These, in combination with other unknown factors caused a high level of noise in the azimuth channel and even higher noise in the elevation channel. However, the noise plot provided some unanticipated findings. The noise in the range channel was extremely low; about the same as for a close-in aircraft target. The cause of the great difference in noise levels between the range and angle channels could not be explained.

The Cyber radar data reduction algorithms were also reviewed during this analysis. They were found to yield general agreement with data from the GMD data reduction programs, except that the algorithm used for the calculation of r-f refractivity is wrong and should be replaced. Also, both the White Sands (Pearson) refraction correction method currently used on the Cyber and the spherical slab correction method currently used on the Varian yield unacceptable results during low angle, long range tracks. Errors in both of the methods increase as the elevation angle decreases toward the failure point. At the failure point (a function of both range and elevation angle), both solution methods provide

invalid data. The failure point for both solution methods is about the same.

Finally, as far as the overall accuracy of the radar is concerned, if proper data reduction techniques are employed, radar-derived target geometric altitude should be within plus or minus 10 feet for high-elevation angle tracks (35 to 45 degrees) on targets at 35,000 feet and below. If the cause of the low angle altitude error can be found, data for low tracking angles (2.5 to 3.0 degrees) should be within plus or minus 25 feet for the same range of target altitudes. However, atmospheric anomalies on any specific test day could cause the low-angle refraction errors to probably double.

On the other hand, Mach number calculations based on wind-corrected radar data are poor. Normal variability in the wind vectors make accurate derivations impossible. Thus, even on a benign day, errors up to 0.02 Mach can be expected. On a high wind day, errors of 0.05 Mach or greater can be present. During maneuvering flight, derived Mach numbers will be erratic due to target glint effects.

13.0 RECOMMENDATIONS FOR FUTURE STUDY

During the six-month period of performance under this contract, there was insufficient time to conclusively isolate the cause of the low angle anomaly observed in the radar-derived altitude data. Therefore, it is recommended that some future effort be directed toward this end. The fact that the error seems to be consistent and predictable is encouraging since, if that is the case, it is also correctable. It is suggested that future study be performed using cross-survey legs, with tracks performed in both the normal and plunge modes. If possible, a simultaneous track using one of the Air Force radars would also be desirable.

None of the refraction corrections analyzed during this contract are ideal for all purposes. Both the Varian and the Cyber refraction correction methods fail at low elevation angles and long ranges. The GMD gradient method provides high accuracy at all angles and ranges, but requires excessive computational time. If accurate data from radar tracks are to be obtained, it is important that a better technique be devised for accomplishing refraction corrections on both aircraft and orbital missions. Future work in this area might also investigate the feasibility of including the capability to correct for horizontal variations in weather profiles. It is possible that one of the 'exact' solution methods could be improved to yield both speed and accuracy in these calculations.

In many cases during this study, data became erratic during maneuvering flight. Jumps in the data and even complete off-target conditions were observed in the beacon mode when shielding or cross polarization effects occurred. In the skin track, target glint effects were also present under the same conditions. These problems were compounded to some extent by antenna dynamic lag at the lower bandwidth settings needed to "ride through" the periods of poor signal return. Since the antenna movements resulting from these situations occurred well within the normal range of frequencies associated with pilot and aircraft dynamics, it was not possible to remove them from the data by filtering. However, it has been long noted that the actual error signals, from which the servo drive commands are generated, do have some consistent patterns when these conditions occur. Therefore, while post-mission processing techniques cannot detect and remove the erroneous movements, "intelligent" real-time filtering of the actual error signals on the radar might offer some marked improvements in this area.

As noted in the study, multipath affects elevation measurements whenever low-elevation returns pass over the length of the metal roof on the radar building. These

multipath effects appear to be measurable and hence correctable. The on-site A900 computer could be used to provide real-time corrections using stored multipath profile data. In addition, some type of multipath barrier might shield the antenna from returns from reflections occurring at "impossible" elevation angles. If multipath affects signals from boresight tower r-f feedhorn, then it will also affect signals from low-elevation tracks occurring near the same azimuth and elevation angles.

The last survey of the radar pedestal and boresight tower were made in February 1975. This data should be updated as soon as possible. In addition, the triangulation should include the antennas and reference points used by the Air Force radars since both the NASA and Air Force radars often operate as part of single tracking network. In addition, surveyed information should be updated for all of the lakebed r-f targets used by the NASA radar, and this should include vertical as well as horizontal control data in all cases.

14.0 REFERENCES

1. Marvin, C. F.: Psychrometric Tables for Obtaining the Vapor Pressure, Relative Humidity, and Temperature of the Dew Point from Readings of the Wet- and Dry-Bulb Thermometers. Weather Bureau Publication 235, U.S. Department of Commerce, 1941

2. U.S. Standard Atmosphere, 1976. NOAA S/T 76-1562. U.S. Government Printing Office, 1976.

3. Bean, B. R., and Dutton, E. J.: Radio Meteorology. Dover Publications, Inc., 1968.

4. Parish, O. O., and Putnam, T. W.: Equations for the Determination of Humidity From Dewpoint and Psychrometric Data. NASA TN D-8401, 1977.

5. Aldrich, G. T., and Krabill, W. B.: An Application of Kalman Techniques to Aircraft and Missile Radar Tracking, AIAA Journal, Vol. 11, No. 7, July 1973, pp. 932-937.

6. Gelb, A. ed.: Applied Optimal Estimation. MIT Press, 1974.

7. Status of Range Safety Filter Systems. Document 309-77, Range Commanders Council, White Sands Missile Range, N.M., 1977.

8. James, R: Baseline Mathematics and Geodetics for Tracking Operations, NASA CR 163102, 1981.

9. Lear, W. M.: Refraction Corrections for an Exponential Atmosphere, NASA JSC Internal Note 75-FM-60, 1975.

10. Pearson, K. E.: The Refraction Correction Developed for the AN/FPS-16 Radar at White Sands Missile Range, TM 577, U.S. Army Signal Missile Support Agency, 1958.

11. Johnson, D. L.: Hot, Cold, and Annual Reference Atmospheres for Edwards Air Force Base, California (1975 Version). NASA TM X-64970, 1975.

12. Cooper, D. W., and James, R.: Shuttle Orbiter Radar Cross-Sectional Analysis. NASA TM 72870, 1979.

13. Smith, E. K., Jr., and Weintraub, S.: "The Constants in the Equation of Atmospheric Refractive Index at Radio Frequencies," Proceedings of the Institute of Radio Engineers, Vol.41, Nr. 8, pp 1035 to 1037, August 1953.

APPENDIX A

A DESCRIPTION OF THE NASA AN/FPS-16 INSTRUMENTATION RADAR AND FACTORS AFFECTING SYSTEM ACCURACY

1.0 DESCRIPTION OF THE NASA AN/FPS-16 (34) RADAR

The Ames Research Center, Dryden Flight Research Facility supports a wide range of aeronautical test and development programs as well as missions associated with the Space Transportation System (STS). Many of these missions require precise position and velocity data that can only be obtained, in real-time, from ground tracking systems. In order to meet these space positioning requirements, an AN/FPS-16 C-band radar (serial number 34) is installed on Buckhorn Ridge overlooking Rodgers Dry Lake.

The AN/FPS-16 radar was designed specifically for the purpose of obtaining highly accurate trajectory data during guided missile tests. Because of the high-accuracy of the system, it was also found to be extremely useful during various types of flight tests when it was necessary to derive accurate flight path information for real-time control and post-mission analysis purposes.

The AN/FPS-16 radar is classified as a high-resolution, moderate range, mono-pulse system, capable of high-accuracy tracking of objects in flight or in orbit. The operator can select a single pulse output for target echo (skin) tracking or a coded pulse group for beacon tracking. A tunable magnetron transmitter provides 1 megawatt of peak power at any frequency between 5450 and 5825 Mhz. Provisions are made in the microwave section of the radar which allow the operator to reduce the radiated power as the range to the target decreases, or this can be accomplished automatically with a power programmer. Field effect transistor (FET) amplifiers are also provided to improve the signal to noise ratio of the incoming signal at the r-f head when tracking targets with low signal returns. The selection of the FET amplifiers is a discretionary judgement of the operator based on his observation of the range of the target and the level of signal return.

When the system is in operation, a maximum of 40,000 volts is supplied to the transmitter section. The transmitted pulse, generated by the magnetron transmitter, is relayed through high-power wave-guides and other microwave components to a four-horn feed assembly. The feed horn illuminates a 12-foot diameter parabolic reflector which radiates a narrow, sharply

defined signal. The return r-f signal is channeled by the four-horn feed into an r-f comparator which separates the signal into a reference component, an elevation error component, and an azimuth error component. The reference component is the sum of all the other components. These signals are then channeled separately into the tracking section of the receiver. Each error channel amplifies and compares its respective signal with the reference signal to determine the direction and magnitude of the error. The outputs of the azimuth and elevation error channels of the receiver are supplied to the angle tracking section, where they serve as control signals for the azimuth and elevation servo drive systems. Data takeoffs for both the azimuth and elevation channels consist of two-stage 17-bit optical angle encoders with a least significant bit (LSB) resolution of 131072 parts in 360 degrees or 0.00274658203125 degrees per LSB. Bandwidths of both angle servos are adjustable from 0.25 to 5 hertz.

In the NASA radar, the original ranging system has been replaced with an Advanced Digital Ranging (ADRAN) system. This theoretically extended the range tracking capabilities of the radar to 32,000 miles; however, practical limitations are more on the order of 1 to 2 million yards maximum for normal echo targets. The ADRAN equipment includes special circuits to enhance and verify range measurement data and to prevent beacon stealing which results because of the inability of beacon transponders to respond to closely spaced interrogation pulses from different radars. The maximum range rate capability of the ADRAN equipment is in excess of 20,000 yards per second. Bandwidth is selectable from 1 to 15 hertz. Range measurement data from the ADRAN is supplied in 25-bit digital form, with an LSB resolution of 1.953125 yards.

Bandwidth selections for the individual range, azimuth, and elevation channels are operator discretionary. Bandwidth selections are really selections of closed loop gain which increases the response frequencies of the range and angle systems. The specific bandwidth configurations at any given time are based on judgements by the operator based on the strength of the returned signal, the types of maneuvers being tracked, the observed behavior of the error signals, and so forth. During normal tracking operations, all bandwidths are generally set to about 0.5 to 1.0 hertz.

A video camera is mounted on the pedestal reflector. This camera provides real-time video that is displayed on a monitor located above the operator control console. The video display enables the operator to evaluate the tracking performance of the radar, and to optically track the target when at low angles where multipath may prevent the use of the full auto-track capabilities of the system. Aided (manual)

track capabilities are individually selectable for both the azimuth and elevation channels. This permits the operator to use aided track in one channel while auto tracking in the other, or, if conditions warrant, he can select the manual track mode for both channels.

R-f, optical, and mechanical calibrations of the system require the use of a boresight tower. The tower is approximately 150 feet high and has an associated equipment enclosure which houses a signal generator, a pulse generator, attenuator, waveguides, and power supplies. An r-f feedhorn at the top of the tower serves as an r-f signal source used to calibrate the electrical axis of the antenna. The position of the horizontal-vertical (HV) axis of the antenna pedestal and the boresight tower feedhorn are known to first order survey accuracy. In addition to the feedhorn assembly, the tower has optical calibration boards mounted on each side of the feed horn and a zero-elevation reference target mounted on the tower axis. One part of the target is used for alignment of the boresight camera, another is for alignment of the pedestal's mechanical data takeoff devices using a precision optical scope. Measurements are made in both the normal and plunge modes. Guy wires are used to prevent tower movement, and tension in the wires is periodically checked.

The angles from the HV axis to the feedhorn are 202.6882 degrees in azimuth and 0.8444 degrees in elevation. Range to the feedhorn is 675.11 meters.

Additional calibration features include built-in transmitter power measuring equipment, built-in receiver noise figure measuring equipment, built-in frequency monitors for both the transmitter and receiver, built-in four-channel oscilloscope for recording various radar parameters, and a number of data monitoring features programmed into the A900 computer.

The radar has full and continuous 360 degree azimuth coverage and elevation coverage from -10 degrees to +190 degrees. It has a maximum slew speed of 800 mils per second in azimuth and 425 mils per second in elevation. The r-f beamwidth, as measured to -3 dB points, is 1.2 degrees. The antenna is vertically polarized and has a gain of 44 dB. The maximum peak power output of the transmitter is 1 megawatt; however, the antenna and waveguides are designed to accommodate up to 3 megawatts if needed. Measurable pulse to pulse jitter is less than 0.02 microsecond (1 yard), and the stability of the reference oscillator is better than 1 part per million which is equivalent to a maximum scale factor error of 0.5 yards at 500,000 yards. The angle servo bandwidths can be adjusted to respond to frequencies as high as 5 Hz; the range bandwidth can be adjusted to respond to frequencies up to 15 Hertz.

Associated with the radar is a high-speed Hewlett Packard A900 computer. The computer performs a wide variety of data acquisition, control, and enhancement tasks needed to support the real-time operations and calibrations of the radar. Specifically, these tasks include:

1. Control of basic readout and update cycles of the radar.

2. Receipt, decoding, and processing of two streams of incoming acquisition data.

3. Generation of range and angle designate commands for target acquisition.

4. Real-time filtering of raw range, azimuth and elevation data.

5. Real-time pedestal corrections.

6. Real-time refraction correction of tracking data.

7. Formatting and outputting three formatted tracking data streams.

8. On-site recording of real-time tracking data.

9. Control of the antenna and ranging systems during calibrations and alignments.

Included with the A900 computer system are two operator control and display terminals, one 132 megabyte hard disc system, one Datum 9390 time code translator, and one computer-radar interface.

2.0 SOURCES OF ERRORS IN TRACKING DATA

This section summarizes the various classes and types of radar errors which affect the quality of range, azimuth, and elevation measurements. In general, radar errors are classified in four ways:

1. By source as radar dependent, propagation path dependent, and target dependent.

2. By type as random (noise) or systematic (bias) errors,

3. By coordinate as range, azimuth, or elevation errors.

4. By correction responsibility as measurement errors or as data analysis errors.

During this project, all of the above classifications were considered; however, the greatest emphasis was placed on those errors associated with the reduction of data from the user standpoint, rather than the device dependent errors which are the responsibility of the radar site personnel. However, a brief discussion of all of the classes and types of errors is provided in this section to acquaint personnel engaged in the postmission reduction of data with the types and approximate orders of magnitude of errors which can be expected in the various measurement processes.

Also note that noise (random) errors can be determined by an analysis of the radar data alone using various curve fitting and filtering processes, whereas bias errors are most often indiscernable to the user unless comparison data is available from unrelated sources. During this project, data from on-board measurements provided parameters similar to those which were derived strictly from the radar measurements. By using high-angle radar-derived altitude data to calibrate and tie into the on-board pressure altitude data, the necessary ingredient was found to permit bias differences to be isolated with a relatively high degree of accuracy.

This review of error sources will begin with those errors that are generally beyond the control of the user. They consist of both systematic and random errors, in both ground and airborne equipment, that are normally minimized by strict adherence to well established calibration or correction procedures. The effects of certain of these errors (those of a random nature) may be removed by proper processing of the data on a post-mission basis. The effects of errors of a systematic nature, may, if known, be corrected during post-mission processing. Others, that are more a function of proper system maintenance and calibration, will most often not be known and may have significant influence on the accuracy of the data in its

final processed form. Typical of systematic errors which can be corrected on a post mission basis are errors in either the beacon delay settings on the radar or in settings used on the airborne transponder. Other errors, such as those from r-f axis shift, servo imbalance, and so forth are seldom known by the user and generally no provisions are available on a post-mission basis for applying correction factors, even if the presence of the error were suspected.

In this regard, however, personnel from GMD Systems have worked closely with the site crew at the NASA radar site. Extensive calibration and alignment work is done on the radar on a periodic basis, at least monthly and more often when missions are to be supported which depend on tracking data for real-time guidance or post-mission analysis. In addition, daily system checks include those for r-f axis collimation, optical axis collimation, transmitter and receiver tuning, phasing, range calibration, beacon delay, noise figures, power output, and so forth.

2.1 Noise and Systematic Errors Inherent to Tracking Systems

2.1.1 Thermal Noise

Thermal noise errors may be subdivided into the range noise component and the angle (azimuth and elevation) noise component. The range noise component, Sigma(rt), is given in FORTRAN notation as:

```
Sigma(rt)=Rres/SQRT((S/N)*(Prf/Nbw)
```

where Sigma(rt) is the resulting RMS range error, Rres is the range resolution of the system, S/N is the single-pulse signal-to-noise ratio, Prf is the pulse repetition frequency in pulses per second (pps), and Nbw is the ranging system noise bandwidth. For a signal to noise ratio of 20 dB, and with the worst case combination of Prf and Nbw (160 Prf and 15 Hz Nbw) the RMS error is about three feet or 1 LSB value. At the normal operating settings this noise falls to about 1.5 feet or one-half an LSB value for a 20 dB S/N ratio.

The angle noise component due to thermal noise is computed from the FORTRAN equation:

```
Sigma(at) = Theta/(SQRT(2*(S/N)*(Prf/Nbw)))
```

where Sigma(at) is the rms value of the noise measured normal to the line of sight and Theta is the -3 dB half-power antenna beamwidth of the angle servo system. Other parameters are as described above for range thermal noise. Again, using the most commonly used Nbw and Prf settings, the error is on the order of 0.05 mil or about one-half an LSB value for a 20 dB

S/N ratio. However, for a near minimum S/N ratio for acceptable tracking (about 6 dB), the thermal noise can go as high as about 0.25 mils which is equivalent to 5 LSB values.

2.1.2 Servo Noise

The servos themselves can contribute to the overall noise content of a tracking system. The servo noise is dependent on the design of the particular servo electrical and mechanical components as well as on adjustments and the quality of maintenance. Manufacturer's measurements made at numerous field installations have shown that this can vary from 0.01 to 0.03 mils, with the larger values being present at very slow rotations where friction can cause small jumps to occur. For 17-bit encoder systems, such as used on the NASA radar, the maximum error is still less than 0.5 LSB value. However, it should be noted that the NASA radar is on a regularly scheduled depot maintenance program, and periodically undergoes a complete field overhaul. The last such overhaul occurred in the spring of 1984, so, at least from a maintenance standpoint, this type of error should be minimized.

2.1.3 Servo Deflection

Servo deflection errors occur when an unbalanced torque exists around the elevation axis. This can be increased by post-manufacture addition of camera mounts and similar items having a significant amount of mass. In the case of the NASA AN/FPS-16 pedestal, a camera mount was added, however the system was carefully rebalanced after the installation. No other heavy items have been attached to the reflector. Manufacturer measurements have indicated that even with what might be considered as a reasonable torque imbalance, this error will be less than 0.00005 degree, a neglible value.

2.1.4 Dynamic Deflection

Dynamic deflection results from a deformation of the feed horn and reflector structure during conditions of high acceleration. Photo-electric measurements made on production pedestals by the manfacturer have indicated that this error may possibly reach 0.01 mil during conditions of maximum acceleration; however, when any high-acceleration conditions exist, the normal dynamic lag error will far exceed and mask any deflection errors which might be present.

2.1.5 Data Takeoff Noise and Nonlinearity

On the NASA radar, azimuth and elevation data are measured by means of optical encoders. The mechanical linkage uses anti-backlash gearing that is designed to minimize any hysteresis effects. Thus, since the noise in the data takeoff devices

themselves is essentially non-existent, some small errors can still be present if gears become worn or if there is any offset of the encoder about the measurement axis. Manufacturer's measurements, made on various production pedestals and pedestals installed in the field, have revealed this error to be no more than 0.02 mil or less than one-half an LSB value in the worst cases encountered.

2.1.6 Wind Gust Effects

Wind gusts can introduce noise errors in two ways: (1) by causing direct deformation of the antenna support structure, and (2) by forcing the servos off their null positions. In regard to the first of these effects, every mechanical system must be built with tolerances in bearings, gears, and so forth. When pressure is applied in any one direction, some amount of slack will be taken up in bearings and gearing throughout the entire system. In the AN/FPS-16 design, because of the rigid design specification for shipboard use, errors arising from the first condition have been found to be negligible. However, measurable errors can occur from the second effect. With the AN/FPS-16, the worst case condition occurs when the wind vector is approximately 45 degrees from the line of sight, going into the reflector dish. A constant wind torque will cause a servo bias error that is dependent on the angle bandwidth settings and the mean wind velocity. For a 20 knot wind the error will range from 0.01 mil in narrow bandwidth (0.1 Hz) to 0.0001 mil in wide bandwidth. The AN/FPS-16 radar was designed for operation in winds up to approximatley 50 knots. In conditions with a steady state wind of 60 feet per second and gusts of 5 feet per second rms, the errors can range from 0.05 mil in narrow bandwidth to 0.0005 mil in wide bandwidth. However, it is important to note that the NASA radar must sometimes operate in a heavy wind environment, especially during the winter months. Sometimes it is not possible to stop a mission support operation, simply because the winds have exceeded 50 knots. In such cases, minor movements are discernable on the boresight video monitor, and it is expected that movements up to 2 LSB values could occur. Fortunately, these cases are somewhat exceptional. Under normal conditions the antenna would be stowed when wind velocities approached 50 knots.

2.1.7 Boresight Axis Collimation Error

Boresight axis collimation relates to the alignment of the r-f axes with the mechanical axes of the angle data takeoff devices. Reliable procedures have been developed for accomplishing r-f axis collimation. If the geometry of the boresight tower and antenna reflector is good (i.e. free from multipath effects and so forth), then these calibrations should be accurate to within one-half an LSB value (about

0.0014 degree). Even when multipath errors are present in the elevation channel, procedures can be used which sequentially take the antenna back and forth between normal and plunge until the multipath error (as shown between differences in measured angles versus computed angles) is divided between the normal and plunge tower lock-on measurements. On the NASA radar, this procedure appears to yield results that are consistently accurate to under 1 LSB value.

Optical axis collimation: Tracking performance can also be evaluated by collimating the optical axis to the r-f axis so that a track point can be established on the boresight video monitor. In the video system installed on the NASA radar, an illuminated reticle is provided to assist in establishing an optical track point. Unfortunately, the optical reticule can only be adjusted by opening the camera enclosure on the reflector assembly and making mechanical adjustments. These adjustments are very sensitive thereby making it difficult, if not impossible, to obtain a precise alignment. In addition, some movement has been observed in the optical aim point between the normal and plunge modes. This is believed to be due to movements internal to the camera and lens system. Therefore, for observers in the flight control room, the reticule can only be used as an approximate reference for the optical aim point. A more precise aim point is usually established by the site crew directly on the face of the console TV monitor.

It must be noted that optical and r-f axis collimation is only accurate at short ranges where atmospheric refraction effects are slight. At longer ranges, with large targets that remain visible in the optical system, different amounts of bending can be expected to occur in the optical and r-f propagation paths. However, the amount of difference should be the same for normal and plunge tracks, so that checks can be made, for example during balloon tracks, by sequentially locking on in the normal and plunge modes. A computer designate feature is provided in the NASA radar to permit this type of test to be performed.

2.1.8 R-F Axis Shift

When boresight procedures are carried out at a specific frequency, and the antenna transmitter and receiver systems are tuned to another frequency, a shift will occur in the alignment of the r-f axis. This error can be as great as one LSB value in both azimuth and elevation. However, the error can be lessened significantly if the boresight procedures are carried out at the same frequency as used for the tracking mission. Except under very unusual circumstances, the NASA radar is calibrated at the same frequency that is to be used for mission support.

2.1.9 Axis Shift Due to I-F Detuning

Intermediate frequency (i-f) detuning can occur in the local oscilator, or can occur as a result of changes in the signal amplitude. The specifications for the AN/FPS-16 radar require that the AFC system hold the tuning to within 0.1 to 0.25 megahertz. Frequency changes, if no greater than this amount, will result in angular errors that are on the order of 0.01 to 0.02 mil rms (about one-quarter to one-half an LSB value). Changes in signal amplitude can also cause detuning of the i-f amplifiers. Tests performed by the manufacturer indicate that over the dynamic range of 60 dB over the noise level, the rms error due to this effect is 0.008 mil, an insignificant value with 17-bit encoder systems.

2.1.10 Orthogonality Errors

During manufacture, the azimuth and elevation axes are held to within 0.02 mil of exact orthogonality. If an orthogonality error is present, it will manifest itself as an azimuth error which is a function of the elevation angle. If the maximum permissible non-orthogonality is present, the resulting azimuth error will be .02 mil times the tangent of the elevation angle. However, non-orthogonality errors can be corrected by repositioning the mechanical feed horn. This is a very tedious trial and error procedure which would normally only be accomplished during an overhaul cycle or other major pedestal modification or refurbishment. By using feed horn adjustments, the mechanical misalighment can be effectively corrected. In addition, a non-orthogonality correction algorithm is programmed into the existing A900 computer program; however, thus far it has not been used since no opportunity has been presented to measure the amount of misalignment present in the NASA pedestal.

2.1.11 Antenna Droop Error

Gravity forces acting on the feed horn assembly will cause a small droop in elevation proportional to the cosine of the elevation angle. Unless other anomalies are present (such as excessive bearing wear) then the AN/FPS-16 pedestal can be expected to have a maximum droop of 0.3 mil. For the 17-bit encoders used on the NASA radar this error is less than 1 LSB value. However, a correction routine is provided in the A900 computer system to compensate for antenna droop. This routine has not been used to date but may be activated in the future if 19-bit angle encoders are ever installed.

2.1.12 Pedestal Mislevel

On the NASA AN/FPS-16 radar, adjustable legs are provided to permit leveling of the antenna. This is accomplished on a

periodic basis, usually during nighttime hours. As part of the A900 computer system, an automated mislevel feature causes the antenna to be slewed through 360 degrees with stops at each 22.5-degree interval. An inclinometer mounted on the antenna pedestal provides voltages that are proportional to the offset of the inclinometer from the pedestal's vertical axis. At each stopping point, 20 inclinometer readings are taken and averaged. Results are displayed on the operator control console. Thus, the leveling procedure consists of taking an initial set of mislevel measurements, then making the adjustments indicated by the results of the first rotation. After the adjustments have been made, a second rotation is made, and finer adjustments are made. This continues on a trial and error basis until a sufficiently level condition is attained. Without solar heating, the mechanical misleveling procedure can generally accomplish antenna leveling to approximately 0.25 LSB. In order to check the permanently installed mislevel system, an Air Force mislevel measurement system has been used. Agreement between the two systems was within one-quarter of an LSB value.

In addition to the mechanical mislevel features, routines are provided in the A900 computer software to make mislevel corrections. Thus far, this routine has not been used since the mechanical leveling procedures bring the night time level conditions to well within one LSB value.

2.1.13 Solar Heating Errors

Solar heating causes distortion in the pedestal and reflector assemblies of the antenna. This error is measurable in the elevation axis and negligible in the azimuth axis. Solar heating on the AN/FPS-16 can result in errors of up to 1 LSB in elevation, during the hotest parts of the day. Corrections for solar heating are difficult to make because they can change during the course of a mission, since different tracking angles will expose different parts of the antenna and pedestal structure to the most direct rays of the sun. Corrections for solar heating errors, when known, take the same form as mislevel corrections.

At the present time, a study is underway at the NASA radar to determine if strain gauges mounted on the base of the pedestal can detect deflections in the pedestal structure due to solar heating. If so, it is planned that the outputs from an array of strain gauges will be read by the computer in real time and correlated is such a way as to provide a real-time measurement of solar heating. If this can be accomplished, then corrections can be made for varying pedestal heating conditions which may occur during the course of a flight support mission.

2.1.14 Deflection of the Vertical

Deflection of vertical in the vicinity of the NASA radar has been computed by the Defense Mapping Agency's Geodetic Survey Squadron to be -3.96 seconds of arc in the meridional component and 2.62 seconds of arc in the prime vertical component. This results in an overall misalignment between the plumb-bob vertical and the outward normal of the reference spheroid on the order of 4 arc seconds. This translates to about 0.0011 degree or 0.4 angle LSB values.

2.1.15 Beacon Delay Errors

Beacon delay must be set into the ADRAN system to correspond to the delay that is set on the airborne transponder. An attempt is made to have the same beacon delays for most of the test aircraft at Dryden. The amount of beacon delay set into the system can be easily checked by a special feature provided in the NASA radar. This feature allows the operator to lock on to one of several range calibration targets in skin mode. The range readings are taken for a short period of time and averaged. Next the system is switched to beacon mode and again the range readings are taken for a short time and averaged. The difference between the two sets of readings is a function of the amount of beacon delay set into the radar system. Tables can then be used to convert the range difference into a specific beacon delay value, based on the velocity of propagation of r-f energy.

While this procedure will test the amount of beacon delay set in to the radar, it still remains to determine if the airborne beacon delay is also properly set. This is accomplished by having the aircraft taxi over one of several calibration points situated on the runway and ramp areas. While the beacon antenna on the aircraft is situated directly over the calibration point, range measurements are taken and averaged. The range readings should agree with survey distances which are known to first order accuracy (approximately one inch). If a range bias is noted, it is recorded so that appropriate corrections can be made during the post-mission processing. In addition, if any discrepancies are noted, they are reported to the beacon lab for correction. Errors due to beacon delay misadjustments may amount to one or two LSB values in range. However, the error is constant over the tracking range so that corrections may easily be made in the post mission processing operations.

2.1.16 Beacon Jitter

Specifications for newer models of beacons call for jitter to be less than 0.002 microsecond. This corresponds to approximately two feet in range, which is less than one LSB value.

This degree of stability can be determined with beacon test equipment, and it is a part of periodic maintenance checks of the aircraft system.

2.2 Errors Associated with Target Characteristics

The next group of errors to be discussed will be those which arise because of the shape or size of the target, the types of maneuvers that are performed during the mission, the proximity of other aircraft, or the proximity of the test vehicle to the radar tracker. These are errors that can best be avoided by adequate pre-mission briefing of the pilots of test and chase aircraft, and by proper planning of flight paths and maneuvers. Obviously the limitations of the tracker can not dictate the types of maneuvers that will be carried out on a flight test mission. However, if good tracking data is required, then an understanding of the errors can sometime result in mission scenarios that are planned so that good tracking data can be obtained in spite of certain adverse tracking conditions.

2.2.1 Glint and Scintillation

Glint is angle noise that arises from variations in the apparent angle of arrival of skin or beacon returns caused by reflection, shielding, cross polarization and so forth. Scintillation is amplitude noise that is causes by signal modulation by a propellor or rotor, by differing aspect angles, and so forth. Often these two factors work in combination and can greatly degrade the quality of the tracking data. For example, the maneuvering of a target may result in a continuously changing aspect of the beacon antenna with respect to the radar causing the signal to build and fade. It can also occur in either skin or beacon tracks when the range is very short so that the antenna detects more than one lobe in the target return. This condition is especially noticeable when high-angle, close-in tracks are performed in which the pedestal's dynamic lag may cause the antenna to drive slightly off the target so that a side lobe can provide erroneous readings on the azimuth and elevation error channels of the radar. In general, angle glint is directly proportional to the span of the return and inversely proportional to the target range. When glint becomes severe, the center of reflection will not correspond to the center of the target and may, in many cases, be completely off the physical extent of the target.

Glint and scintillation errors are most often observed as anything from slight to very severe angle gyrations in the antenna system, sometimes appearing as if the target were bouncing in the boresight video display. If glint or scintillation conditions persist, then the system will often lose

lock or transfer lock to a target side lobe. With the NASA radar, glint is most difficult to handle when in beacon mode. With the proper angle bandwidths, glint or scintillation that is due to target maneuvering can generally be handled successfully in skin mode, if the target is at sufficient range.

Since glint and scintillation errors often manifest themselves in much the same way, it may be difficult to know which is the cause of the problem, but it is probably not important to know which caused the problem. It is more important to concentrate on how to avoid it. Glint and scintillation errors can sometimes reach a sizeable amount before the situation subsides or a loss of lock results.

2.2.2 Signal Interference Due to Other Aircraft

This condition is most often observed when a chase aircraft is flying in close proximity to the target aircraft. Often when in beacon mode, a slight maneuver may block the return from the tracked vehicle, while a reflection off the chase aircraft remains strong. This can result in angle jumps toward the chase aircraft and often causes a transfer of lock from the main lobe to a side lobe from the tracked vehicle's beacon return.

When in skin track, when even the slightest manuevers are performed, the signal level of the return from the chase aircraft may often exceed that of the tracked target, resulting in a transfer of lock from the tracked target to the chase aircraft. This can even occur when the chase aircraft is reasonably distant from the tracked aircraft. Thus, in all cases where precision tracking data is important to the mission, pilots of chase aircraft should be advised to stay well clear of the tracked aircraft and preferaby at a greater range from the radar than the tracked aircraft.

2.2.3 Dynamic Lag

The dynamic lag of the antenna and servo drive system results when the antenna cannot slew fast enough to keep up with the target. Obviously, this condition can combine with the effects of glint and scintillation to create the same type of error conditions. Normally, dynamic lag is negligible for targets at longer ranges and at low to moderate elevation angles. It becomes very severe for any type of target at very high elevation angles where extreme azimuth movements may be required to remain on target. Dynamic lag can corrupt data during high-speed close-in passes, during very high elevation tracks of maneuvering or non-maneuvering targets, or during high-angle orbital tracks.

2.2.4 Multi-Path Errors

Multipath errors appear primarily in the elevation angle measurements because of reflections from the surface. The rms error due to multipath is given by:

$$Sigma(mp)=Theta*Rho/SQRT(8*As)$$

where Theta is the half-power antenna beam width, Rho is the ground reflectivity, and As is the power ratio of the main-lobe gain to the gain in the sidelobe reflection. Normally, the reflected energy is received at an off-axis angle equal to twice the elevation angle of the target. Cancellation and reinforcement effects make this error cyclic for differing elevation values. The elevation change for one cycle (Deltae) is given by:

$$Deltae = Lambda/(2*H)$$

where Deltae is the cyclic elevation interval, Lambda is the radar wavelength, and H is the height of the center of the reflector above the surface.

The amount of multipath error at two degrees elevation angle is on the order of .05 mils or one LSB. The cyclic interval is on the order of 5 mils or about one-quarter degree. At very low elevation angles the multipath error will cause the antenna to drive down so that the ground returns reinforce the multipath signal and eventually overwhelm the direct return. In this case the antenna will drive into the down stops unless halted by the operator.

During normal takeoffs and landings, the NASA AN/FPS-16 radar has a negative view of the runways. This requires that the elevation channel be manually controlled by the operator. Thus, during takeoff and for a short period thereafter, the system is placed in AUTO AZ and AIDED EL. Also, during the mission, if the target gets to a sufficiently low altitude where multipath starts to affect the tracking performance, the operator will select AIDED EL, provided the target is still within visual range on the boresight optics. Similarly, on landing AIDED EL is selected when the tracking performance starts to degrade.

2.3 Post-Mission Data Reduction Errors

Thus far, the errors which have been described all relate to items which are correctible or avoidable by system calibrations, by various types error compensations or corrections, or by a knowledge of the error causes. Even if a fairly large amount of noise (random) error is still present in the

data, significant improvements can obviously be achieved by proper filtering and curve fitting techniques during the post-mission processing cycle. However, it is possible that the post-mission processing can also introduce errors, and this section briefly describes the major sources of error during the post-mission analysis phase.

2.3.1 Atmospheric Refraction Error

Atmospheric refraction error is probably the largest and most difficult error to eliminate from raw radar tracking data. There are numerous refraction techniques and all suffer from certain flaws which can greatly influence the quality of the tracking data under certain circumstances. Since a study of atmospheric refraction errors was a major part of this project, a separate section will address refraction errors in detail, however, for completeness, they will also be briefly discussed in this section.

As a first step to accomplishing refraction corrections, it is necessary to determine the behavior of the r-f beam as it propagates through the atmosphere. Most of the refraction methods still in use today rely on very simple approximations which, needless to say, do not achieve a high degree of accuracy. For example, during the accuracy evaluations of the AN/FPS-16 radar at RCA Moorestown, an atmospheric refraction equation of the following form was used:

$$Dele = Ns * .001 * H / (TAN(EL) * (H + 35000)) \quad \text{millirad}$$

where Ns is the surface r-f refractive index modulus, H is the target geometric altitude in feet and EL is the measured elevation angle. At about the same time, the White Sands Missile Range developed the Pearson correction method currently used in the NASA Cyber radar data reduction program:

$$Dele = Kle * D / K2e * H \quad \text{mils}$$

where Kle is equal to -Ns*.001*1.02; D is equal to R*cos(EL), the ground range; and H is equal to R*sin(EL), the geometric altitude. K2e is a constant in the range from about 13000 feet to 22,000 feet. It is obtained from a lookup table using Kle as the entry parameter.

Numerous other refraction methods are currently in use. The complexities of these methods range from simple calculations shown above to very time consuming ray-tracing iterative solutions. All refraction methods suffer from certain shortcomings which can include:

1. Failure of the refraction method to compensate for non-standard vertical refractivity profiles.

2. Failure of the refraction method to compensate for non-standard horizontal refractivity profiles.

3. Failure of the method to accurately calculate the refractive index.

4. Excessive computational time requirements for the more complicated solutions.

Over the 150 nautical mile range analyzed in this project, the refraction correction can be as great as 300 LSB values in angle and 75 LSB values in range, for very low elevation angles. Obviously when corrections of this magnitude are involved, much consideration must be given to using a refraction method which best suits the application. For high-angle tracks (above 5 or 10 degrees) the selection is not as critical as for low-angle tracks where even a small percentage error can overshadow all of the rest of the systematic and random errors previously discussed.

3.0 PRACTICAL CONSIDERATIONS

It is important that the relative magnitudes of the various tracking errors be understood so that needless time-consuming computations can be avoided in cases where errors may be below the granularity of the system. Generally, as a rule of thumb, the computational precision of the data reduction system should provide corrections that are at least one order of magnitude better than the measurement accuracy of the system. Therefore, the typical values of bias errors estimated to be present in the NASA AN/FPS-16 radar are provided in table I. Note that these represent the errors that would be present if no corrections were made, except for the best possible manual alignments. All of the errors are compared with the LSB values of the data takeoff devices so that practical decisions can be made regarding the need for additional computer corrections. Also note that, while the A900 computer at the radar site does perform refraction corrections, these corrections are not made in the data sent from the site so that individual users can apply the corrections that best suit their needs.

The value for pedestal mislevel shown in table I is considerably less than that given in other sources. However, the pedestal mislevel at the NASA radar is closely and frequently monitored. If mislevel conditions are present, the site crew carries out the necessary adjustments to bring the total mislevel to within one LSB value.

The same type of reasoning applies to the error from r-f axis shift. Generally this is shown as a value well in excess of

1 LSB unless corrections are made in the data system. However, it is NASA policy to perform r-f collimations whenever the frequencies must be changed. If the antenna is collimated at the frequency at which it is to be used, then this error is usually negligible.

Table I.

Source	Type	Typ. mils	Typ. yards	LSB values
Thermal (Rng)	noise		0.80	0.41
Thermal (Ang)	noise	0.02		1.40
R-f axis shift	bias		(negligible)	
Droop (El only)	bias	0.03		0.61
Orthogonality	bias	0.02		0.41
Mislevel	bias	0.05		1.00
LSB precision	noise	0.03	0.97	0.50
Solar heating	bias	0.05		1.00
Wind force	bias	0.01		0.20
Ant unbalance	bias		(negligible)	
Servo unbalance	bias	0.01		0.20
Dynamic lag (2)	bias	0.01		0.20
Glint (2)	noise	0.00		0.00
Refraction (3)	bias	0.05	3.90	2.00
Vert. deflection	bias	0.02		0.40
Earth model	bias	0.01		0.20

Note 1 For elevation angle of 10 degrees
Note 2 Target at 150 nautical miles
Note 3 Error after refraction correction applied

During the noise analysis conducted as part of this contract, it was found that the NASA AN/FPS-16 radar had considerably less measurement noise than what is considered to be typical by the manufacturer. For airborne targets, operating in beacon mode, the 1-sigma noise in all three channels was found to be under 0.5 LSB.

APPENDIX B

NOISE DATA ANALYSIS TECHNIQUE

1.0 THEORY

The noise data analysis for this contract is based on a technique known as the 'Variate Difference' method. It was applied successfully to a number of engineering problems by William Lear (reference 1). The method is also discussed at length by Kendall and Stuart, 'The Advanced Theory of Statistics' Volume 3 (Ref. 2).

The basic idea behind any error analysis is to identify the source and the relevant characteristics of the errors. In the present application, the errors cannot be observed directly. It is assumed that the data examined consists of two components: signal and noise. A further assumption is made that the 'signal' portion of the data is essentially smooth, that is, the parameter of interest (azimuth, elevation, range, or whatever) is a physical process that is continuous and posesses (at least) a continuous first derivative. The data that is actually observed is assumed to be the sum of this smooth process and noise. The noise is assumed (at least initially) to be independent of the signal, independent of previous noise values, and to have statistical characteristics that change slowly with time. For purposes of estimation, then, the noise characteristics are taken to be constant for some 'short' period of time. The mean value of the error was, in fact, found to be essentially zero in all cases examined. The variance was found to be time-varying. By examining data in five second intervals estimates of the noise variance were produced that show reasonable stationarity within any given interval.

The Variate Difference method is based on the procedure of taking successive differences of a discrete time history of the data under consideration. If the original data consists of an essentially smooth data signal plus additive (independent) noise values then the successive differences will serve to eliminate the signal and accentuate the noise on the process. In the present study the data examined represent position values, the first differences then give a rough estimate of velocity, the second differences an estimate of acceleration, the third differences an estimate of jerk, and so on. From these considerations, then, one would expect that by taking third or fourth differences the better part of the physical process could be accounted for, and only the noise would remain. This turned out to be the case: it was found in the present study that fourth differences were sufficient to isolate a linear combination of the errors. From this, the noise variance can then be estimated. Because the fourth difference of the data, y(t), is a linear combination of the errors, the variance of y(t) is related to the variance of the error terms. Specifically by assuming that the errors are independent, it can be shown that

$$y(t) = \text{sum } (a(i)e(i)),\ i=1 \text{ to } n$$

implies that

$$\text{Variance } (y(t)) = \text{sum}((a(i)^2)\text{var}(e(i))).$$

This is done by writing

$$\text{Variance } (y(t)) = \text{Expected value } ((\text{sum}(a(i)e(i)))(\text{sum}(a(i)e(i))))$$

and noting that if e(i) and e(j) are independent then the expected value of the cross product e(i)e(j) is zero. From the fourth differences we then find both the a(i)'s and the variance of y(t), and as a result, Var(e(i)) may then be found.

Consider the following example. Let f(t)=t and suppose the signal, f(t) is corrupted with additive noise, e(t). A difference table for this case resembles:

t	f(t)	df(t)	$d^2f(t)$	$d^3f(t)$	$d^4f(t)$
0	e(0)				
		1+e(1)-e(0)			
1	1+e(1)		e(2)-2e(1)+e(0)		
		1+e(2)-e(1)		e(3)-3e(2)+3e(1)-e(0)	
2	2+e(2)		e(3)-2e(2)+e(1)		e(4)-4e(3)+6e(2)-4e(1)+e(0)
		1+e(3)-e(2)		e(4)-3e(3)+3e(2)-e(1)	
3	3+e(3)		e(4)-2e(3)+e(2)		e(5)-4e(4)+6e(3)-4e(2)+e(1)
		1+e(4)-e(3)		e(5)-3e(4)+3e(3)-e(2)	
4	4+e(4)		e(5)-2e(4)+e(3)		e(6)-4e(5)+6e(4)-4e(3)+e(2)
⋮	⋮	⋮	⋮	⋮	⋮

and so on.

The fourth difference is seen to have coefficients given by the binomial expansion $(a+b)^4$. Thus the sum of the coefficients squared in this case is 70. This forms the divisor for estimating the variance of the e(t)'s from the variance of the differences, y(t)'s.

2.0 SPECTRAL DENSITY OF THE ERROR

Based on the binomial expansion given above, the fourth difference is given by:

$$y(t) = e(t) - 4e(t-1) + 6e(t-2) - 4e(t-3) + e(t-4).$$

This can be thought of as a difference equation describing the relation of the output, y(t) to the input e(t). Standard Z-transform theory

yields:

$$y(t) = (1 - 4/Z^1 + 6/Z^2 - 4/Z^3 + 1/Z^4)e(t).$$

Letting $Z = \exp(i\omega)$, we have the following expression for the transfer function in the frequency domain:

$$H(\omega) = (1 - 4\exp(-i\omega) + 6\exp(-2i\omega) - 4\exp(-3i\omega) + \exp(-4i\omega)).$$

From this frequency domain transfer function the theoretical power spectral density (PSD) of the fourth differences may then be derived. This theoretical PSD is included with actual PSD's given in figures 1.1 throught 1.9. The actual PSD's were computed for the fourth differences for range, azimuth and elevation quantities on the STS 41D REV 2 data. Figures 1.1 through 1.9 show the PSD computed from the data in two ways. First the PSD is plotted as a step function. The frequency resolution (.2 cycles per second) is apparant in the top PSD. In the plot given at the bottom of each figure, the same information is shown as a continuous quantity. The bottom figure was also further smoothed using a five-point moving average window. The expected PSD for each case was then computed (based on the assumptions enumerated above), and plotted as a dashed line on the bottom plot. Part of the validation of the noise estimation process may then be taken as a comparison of the PSD's estimated from the data with this theoretical PSD.

3.0 ESTIMATION OF PSD'S FOR ERROR ANALYSIS VALIDATION

An extensive error analysis, as outlined above, was completed as part of this contract. Error analysis in this case is dependent upon some understanding of the processes involved as well as an identification of system bias as opposed to system random error. The variate difference method is appealing in that it eliminates system bias from the noise, providing the bias quantity is approximately constant for the time period under consideration.

The error analysis was performed in five second intervals across entire flights. Using the variate difference method with fourth differences, the standard error of the noise on the range, azimuth and elevation was computed and is plotted for a variety of cases. Notice that the error sigma is given in LSB's: this was done to avoid any units dependence, and to make error content estimation independent of parameter estimate. To verify that the error analysis is valid, one would have to have the 'true' values of the range, azimuth and elevation to get the 'true' noise parameters. These quantities are, of course, not available. Some validation is possible, however, by comparing the computed PSD's of the fourth differences with the theoretical values under the assumptions listed above. For this purpose, the fourth-difference PSD's were computed in the following manner. The raw data (100 points at a time) first had the mean subtracted and were then windowed in the time domain with a standard Parzen window. 100 points were used since the error analysis was done in five second intervals.

This modified series was then Fourier transformed using a mixed-radix discrete Fourier transform. This precluded the necessity of extensive 'padding' of the time series to contain a 'power of two' number of points. The modulus of the resulting frequency-domain values was then plotted against frequency. For comparison of the actual and the theoretical, the computed PSD's were further smoothed, as mentioned above, using a five-point (equal weight) moving average window in the frequency domain. This window is the ususal sin(x)/x type of smoothing procedure.

A number of statistical considerations are relevant here. A PSD computed from 100 points may not be a particularly good estimate of the true power spectral density. The standard error of the computed PSD could be as large as the estimate itself. This difficulty is usually circumvented by frequency domain averaging. Such a procedure enhances the stabilty of the PSD estimate but results in less resolution in the PSD. With just 100 points, the frequency resolution (nominally 0.2 cycles/sec) is not all that good to begin with. Averaging PSD's across different time intervals may not yield meaningful results either—the variance of the processes examined is a time varying quantity. Using the Parzen window and a five point moving average does smooth the PSD estimate somewhat, and the frequency resolution is something greater than 0.2 cycles per second. This was judged to be about the best estimate that could be found under the present circumstances.

4.0 COMPARISON OF ACTUAL AND THEORETICAL PSD's

A number of actual and theoretical PSD for STS-41D (Rev 2) are shown in figures 1 through 9. These plots are divided into three parameters (range noise, azimuth noise and elevation noise) and are plotted at five second intervals from 14:13:20 to 14:13:35.

In all three plots the theoretical (expected) PSD is shown as a dashed line. Notice that since the fourth difference is a linear combination of the errors, its PSD is not a 'flat' function. If the PSD of e(t) as opposed to the fourth difference, y(t), were depicted, it would be approximately flat. The first three plots (Figs. 1 to 3) show the actual and expected PSD's for the range error.

In all cases, good agreement was obtained between the general shape of the actual and the estimated PSD's. The PSD's estimated from the data tend not to rise as smoothly as the theoretical PSD's, but this is to be expected. An estimate of the PSD made from 100 points, even with substantial smoothing, will be fairly 'rough.' One consistent point worthy of note is that in two cases shown for the range error analysis, there seems to be a 'lower than expected' power in the vicinity of 7 and 9 cycles per second. This may be the result of the integral data values (LSB's) that were used in the analysis. In any case, the range error noise is seen to be fairly small in this instance, and generally follows the expected shape of the theoretical PSD.

Similar plots for the azimuth error analysis are presented in figures 4 through 6. Once again, it is seen that the computed PSD's generally follow the expected shape of the theoretical PSD's. The PSD's over time intervals 14:13:25 through 14:13:30 and 14:13:35 agree particularly good. This suggests that the error analysis for these times is likely to be very good. When the actual PSD lines up that well with the theoretical PSD the underlying assumptions made for the analysis are likely to have been met. Notice that the power level for the azimuth noise PSD's is slightly higher in the first two plots than in the range noise case. The third plot (14:13:30-14:13:35) is of the same magnitude as the range errors.

The elevation error analysis (Figs. 7 to 9) demonstrates, by far, the worst agreement between theoretical and actual PSD's. The general shape of the expected PSD can still be found, but the agreement is not as good as in the cases plotted for range and azimuth. This is to be expected, as the elevation noise is clearly the greatest from both a data analysis standpoint and also from the radar system performance vantage. The first two plots demonstrate considerable elevation error noiseμ the third (14:13:30-14:13:35) is more in line with the results of the previous cases. This analysis serves to indicate, in yet another manner, the inherent difficulties with the elevation channel.

The overall impression that the theoretical and actual PSD plots leave is that the noise error analysis is fairly accurate. Even considering that the actual estimates were made from as few as 100 data points, the agreement between actual and theoretical is generally good. In terms of quantifying radar system space positioning accuracy, the PSD's provide a method to validate the underlying assumptions made for the error analysis. When there is good agreement between the actual and expected PSD's the error analysis is likely to yield excellent results in determining the levels of random noise that are corrupting the space-positioning information.

5.0 REFERENCES

1. Lear, W. M.: Noise Statistics of Skin Tracking With the FPS-16 Radar at NASA/FRC. NASA Rept. No. 27054-6010-TU-00, 1975.

2. Kendall, M., and Stuart, A.: The Advanced Theory of Statistics, vol III, 3rd ed. Hafner Press, New York, 1976.

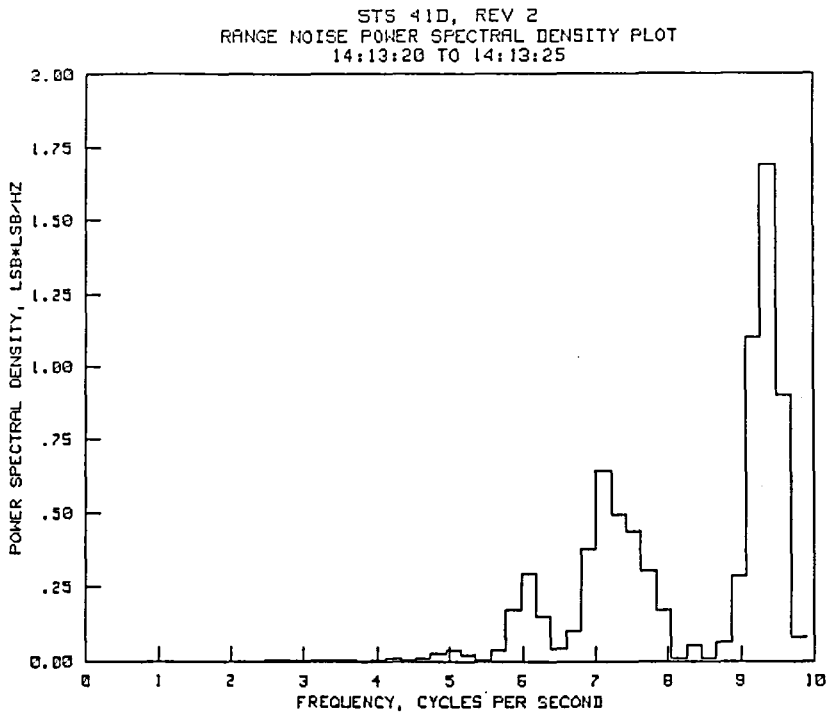

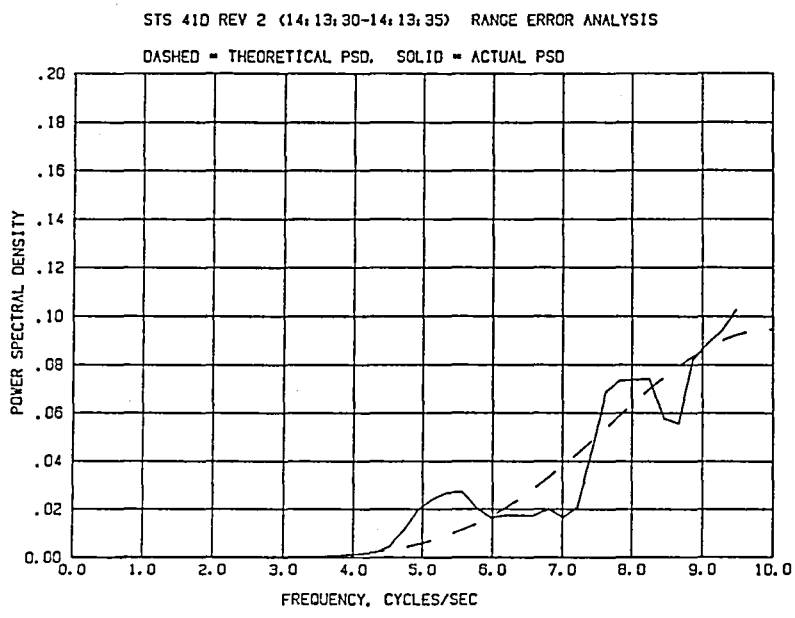

Figure 1. Range power spectral density plot (14:13:20 to 14:13:25)

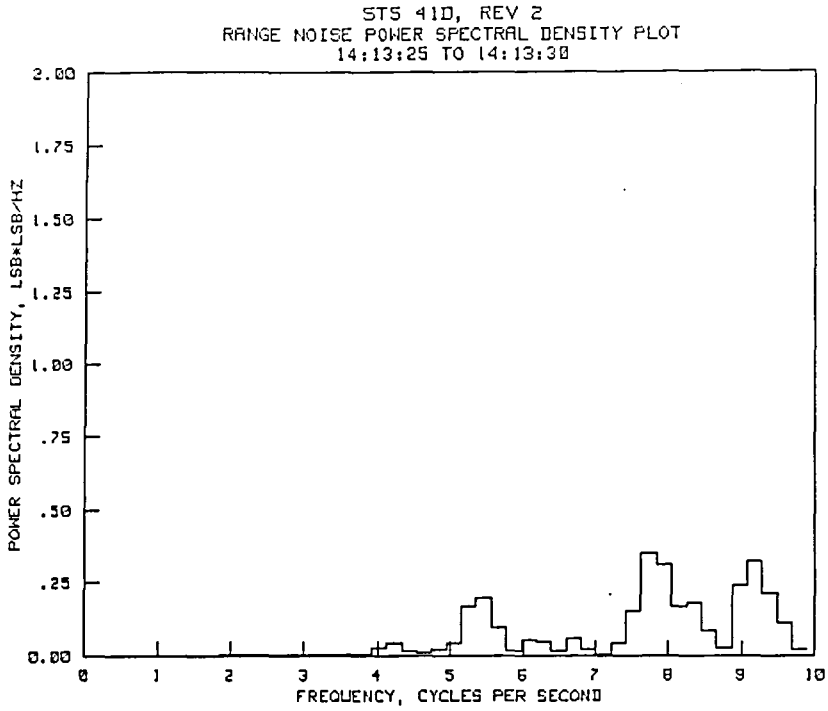

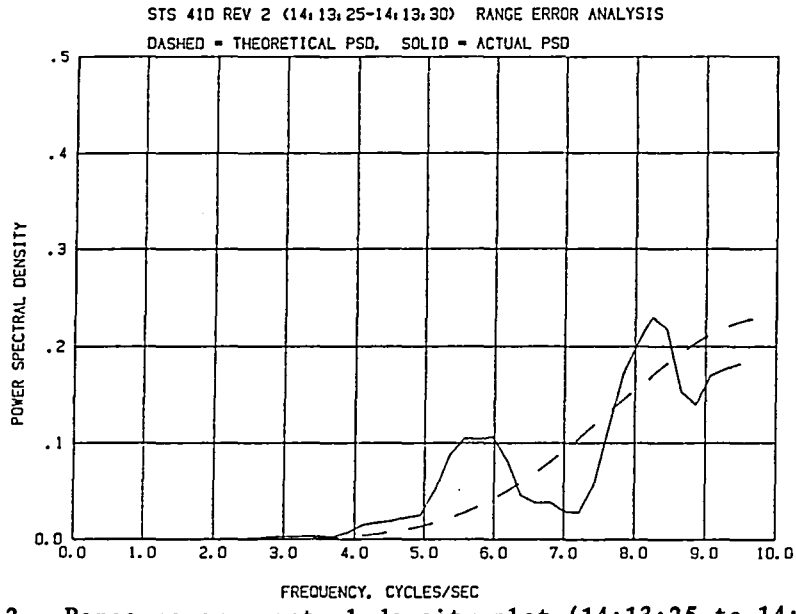

Figure 2. Range power spectral density plot (14:13:25 to 14:13:30)

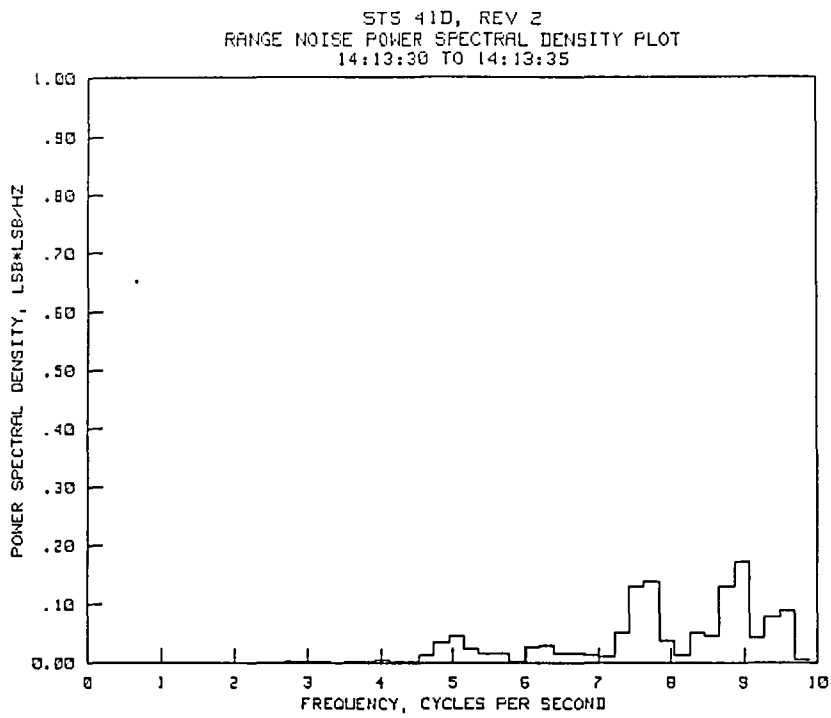

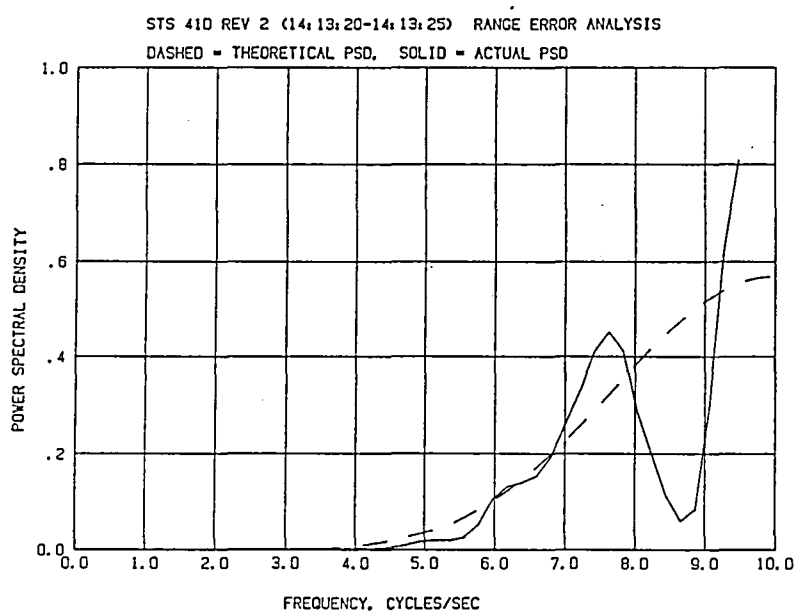

Figure 3. Range power spectral density plot (14:13:30 to 14:13:35)

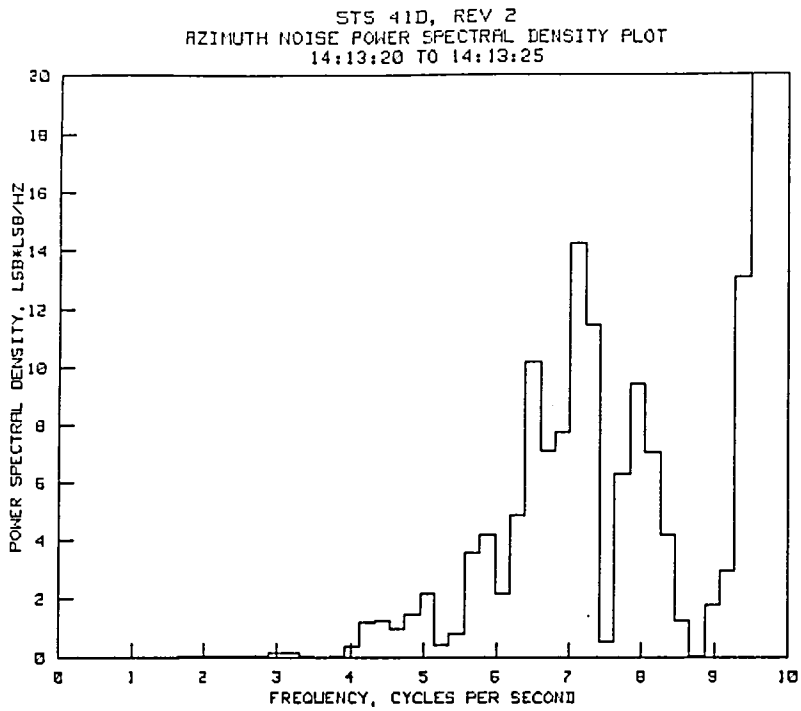

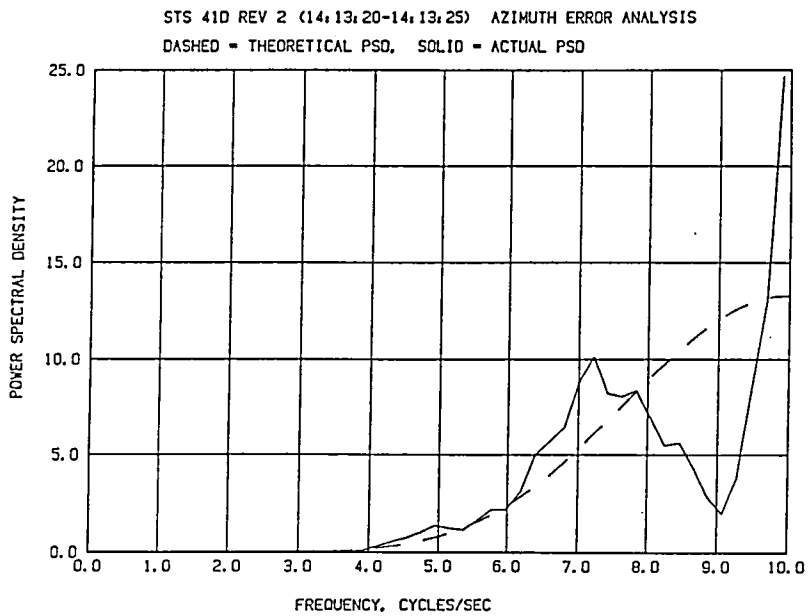

Figure 4. Azimuth power spectral density plot (14:13:20 to 14:13:25)

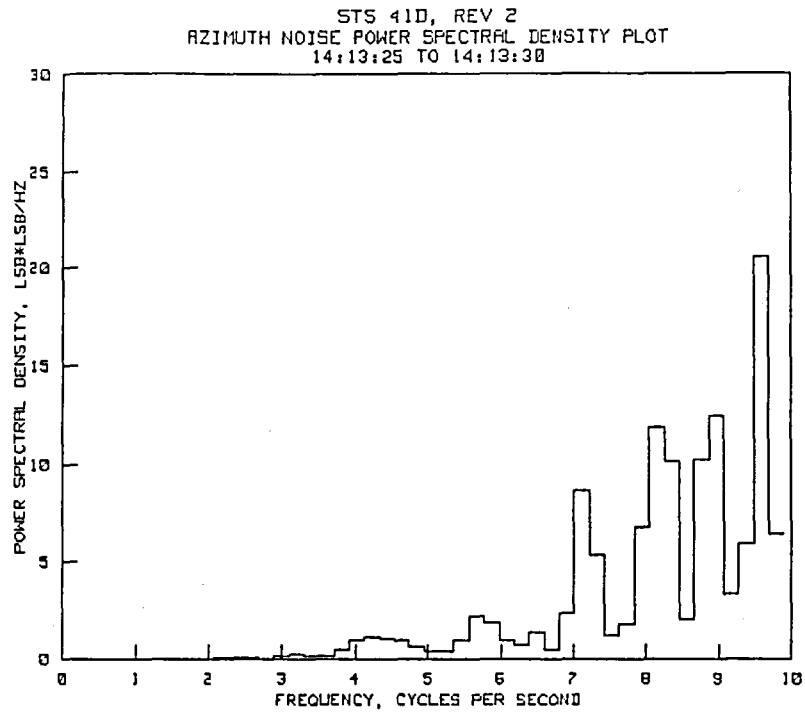

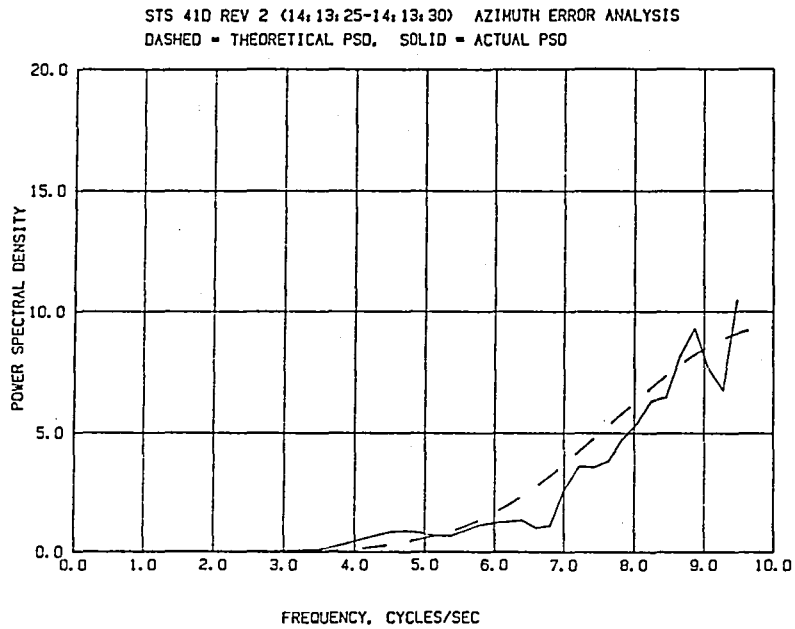

Figure 5. Azimuth power spectral density plot (14:13:25 to 14:13:30)

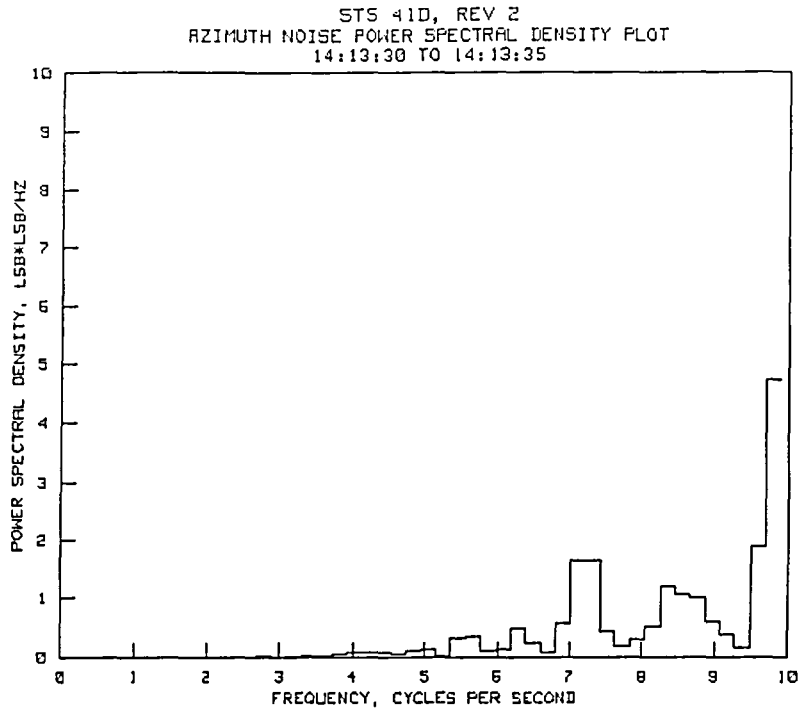

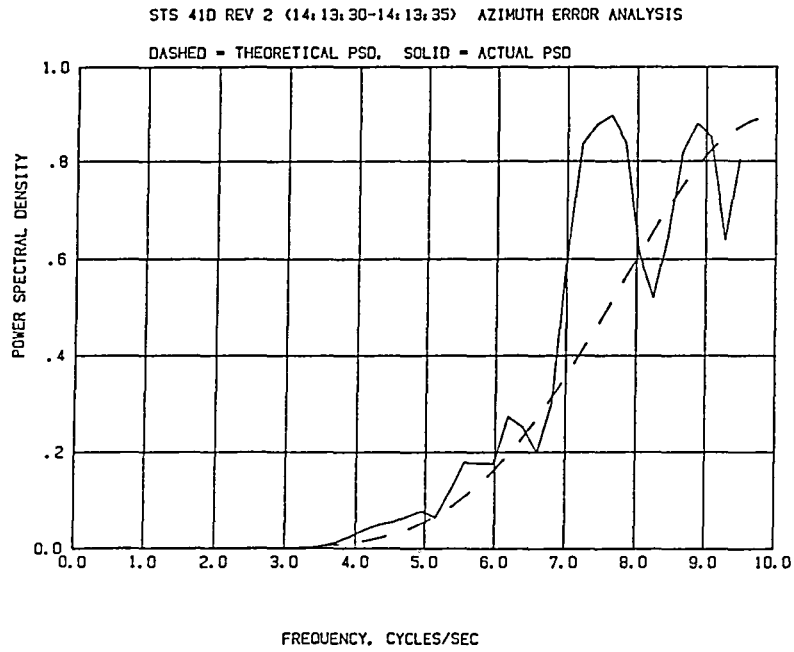

Figure 6. Azimuth power spectral density plot (14:13:30 to 14:13:35)

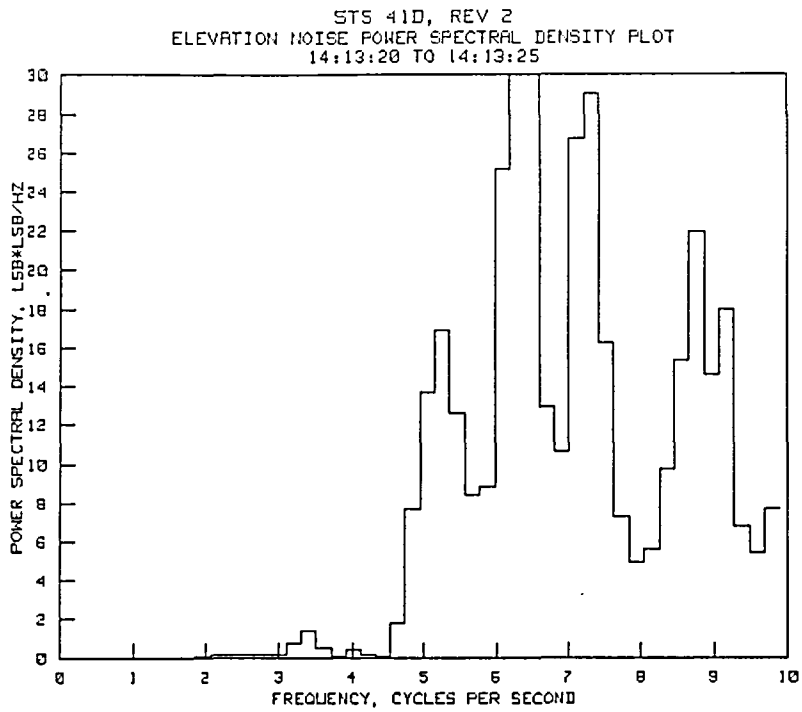

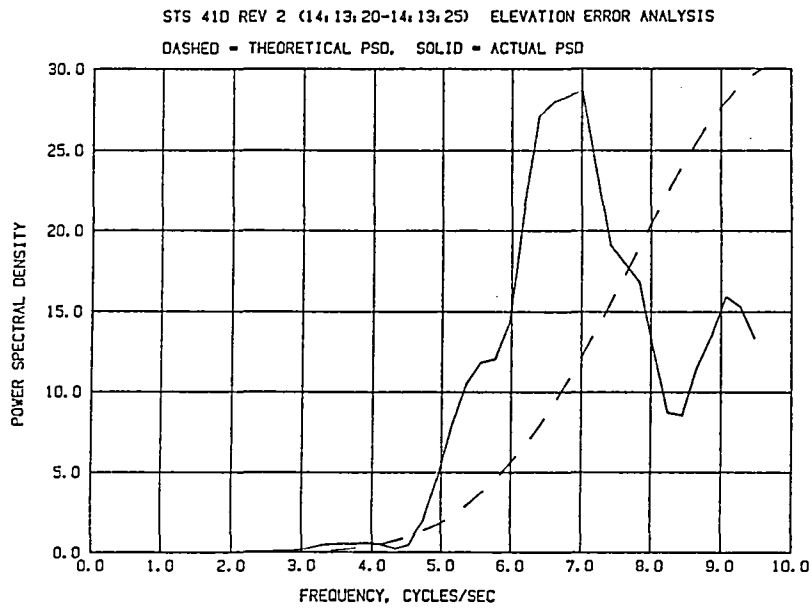

Figure 7. Elevation power spectral density plot (14:13:20 to 14:13:25)

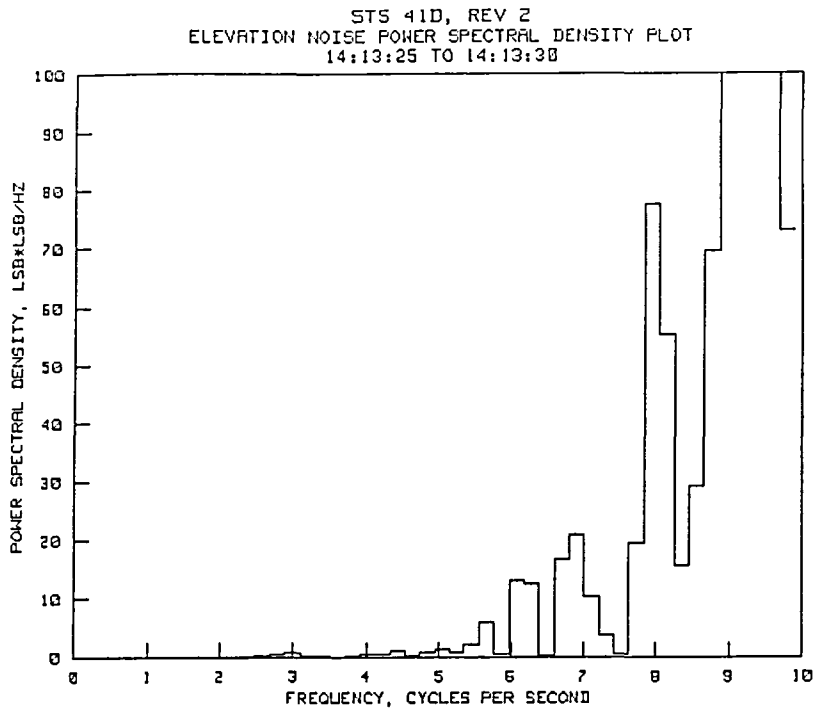

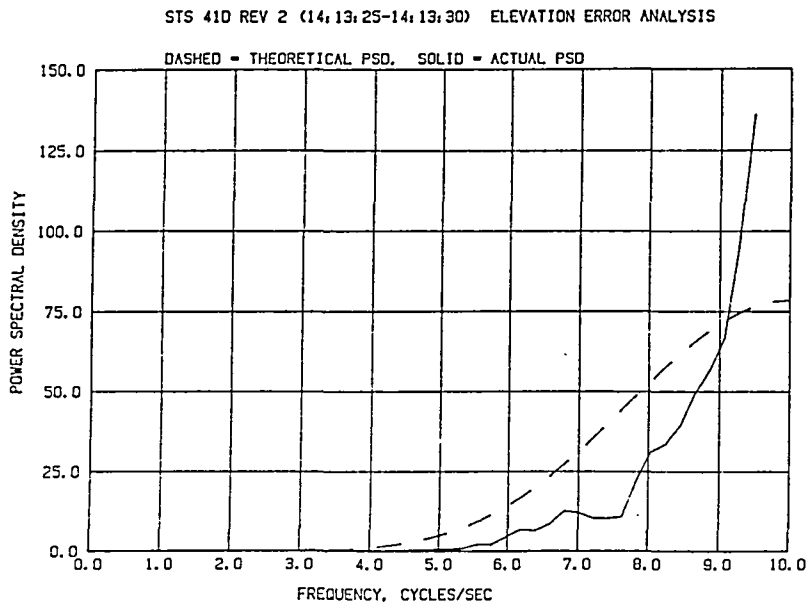

Figure 8. Elevation power spectral density plot (14:13:25 to 14:13:30)

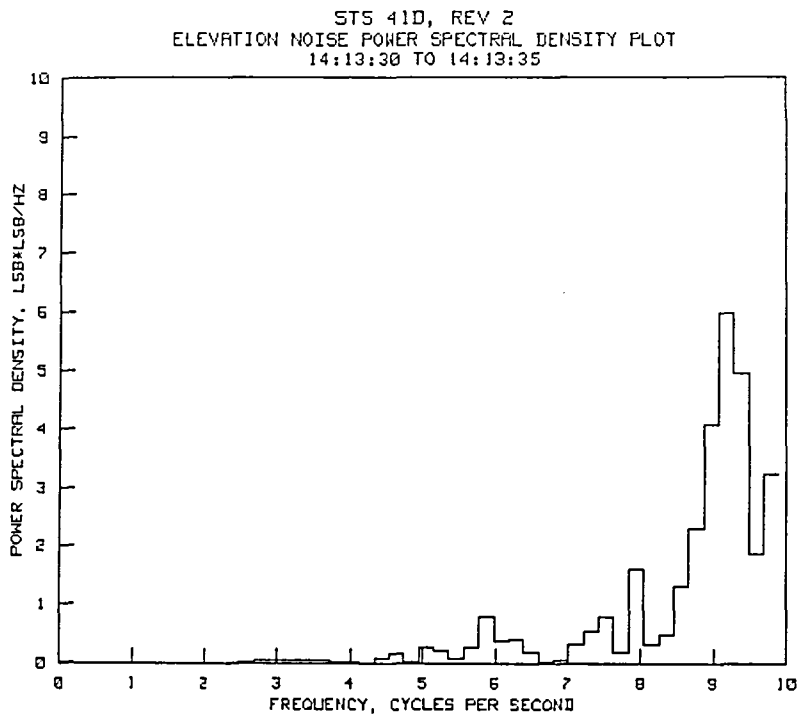

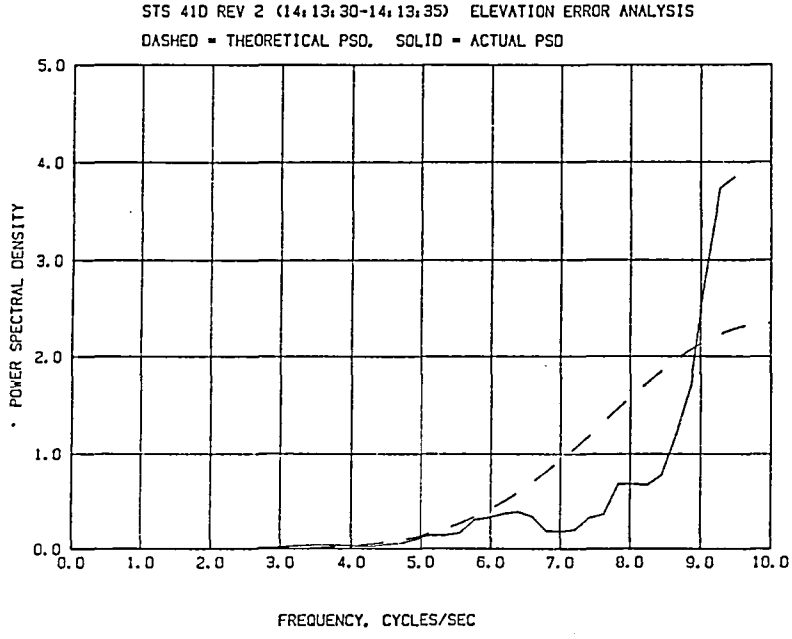

Figure 9. Elevation power spectral density plot (14:13:30 to 14:13:35)

APPENDIX C

AN ANALYSIS OF FILTERING TECHNIQUES

1.0 FILTERING ALGORITHMS FOR PROCESSING RADAR DATA

This section of the documentation presents a discussion of the filtering algorithms used in the processing of radar data. The filtering algorithms used are: 1) Discrete-time Kalman, 2) The QD, and 3) The Alpha-Beta-Gamma filters. Throughout most open literature, these filtering algorithms are generally regarded as the most appropriate for determining aircraft position, velocity, acceleration and attitude parameters from (noisy) measurement data. In the present study, the measurement data consist of radar-generated estimates of aircraft position as a function of time.

As a matter of introduction to the various filtering techniques, each of the three procedures listed adopt a 'state-space' approach to the problem of determining aircraft position and velocity as a function of time. The state-space approach formulates the unknown 'state-vector' of aircraft parameters, and uses a 'predictor-corrector' approach to estimating those parameters. The two equations used in this approach can best be described as 1) a state dynamics equation, and 2) a measurement equation.

The state dynamics equation uses a set of equations of motion for the aircraft to predict what the values of the state vector will be at the time the next measurement is made. The actual estimate of the aircraft state vector is then a function of what was observed and what was expected. The measurement equation expresses the observed measurement as a linear combination of the state vector.

In this study two separate formulations of the discrete-time Kalman filter were used: a three-state and an eight-state version. The three-state Kalman filter works in polar coordinate form: the aircraft position in range, azimuth and elevation are taken as the measurements and also form the components of the state vectors. Range, azimuth and elevation are assumed to be independently varying quantities with independent errors: a state vector of position, velocity, and acceleration is formulated for each of the three measurements and the usual 'Newtonian' physics model relating acceleration, velocity and position is used to determine the state dynamics equation. In the eight-state Kalman filter (adopted from a version used at Wallops Island Tracking Station) the state vector consists of aircraft position and velocity parameters in a radar-centered X-Y-Z coordinate system along with total (aircraft) acceleration and the tangent of aircraft bank angle. The state dynamics equation in the eight-state Kalman filter couples the X-Y-Z parameters through the assumption of aircraft coordinated-turn dynamics (constant bank angle and acceleration) between data points. The tangent of the aircraft bank angle is a component of the state

vector and, as such, is not measured, but rather is estimated from the aircraft position and velocity, using the dynamics for a coordinate turn.

The QD and Alpha-Beta-Gamma filters are similar to the Kalman filters in that they also formulate the aircraft position and velocity estimation problem in a state-space manner. Both of these filters use an X-Y-Z coordinate system and, like the three-state Kalman fiter, assume that the state dynamics are unrelated between time points and use position velocity and acceleration in each of the three axes. Unlike the Kalman filters, the QD and Alpha-Beta-Gamma filters employ a fixed gain: the measurement contribution to the state vector estimate always carries the same weight: with the Kalman filter the measurement contribution to the state vector estimate varies.

1.1 Three-State Kalman Filter.

The three-state Kalman filter formulates the aircraft parameter estimate by assuming that the aircraft position satisfies a linear differential equation (given by the equations of motion as indicated above) driven by a noise-corrupted observation vector. In this case the observation vector can be either aircraft range, azimuth and elevation or the radar-centered cartesian coordinates east, north, and vertical (E-N-V).

It can be shown that the error covariance matrix of the optimal estimate of the aircraft state vector satisfies a matrix Riccati equation. A basic part of the Kalman filter implementaton is the update of the state-vector covariance matrix based on the solution of the matrix Riccati differential equation. The Kalman filter is a linear, time-varying, discrete-time version that provides a least-mean-square-error estimate of a discrete-time signal (the aircraft state vector) based on noisy measurements. The Kalman filter is characterized by an adaptive (time varying) weighting of the measurement information. This weighting changes as the error covariance matrix indicates how well (or how poorly) the present data matches the predicted aircraft state parameters.

The three-state Kalman filter implemented for this study is essentially the version presented in reference 1. Estimates of the three position corrdinates (and hence, aircraft altitude and velocity) are defined by a state vector for each of the three (radar related) parameters. The discrete Kalman filter is then used to produce estimates of the 'true' (uncorrupted with noise) postion and velocity parameters.

The state vector used for each of the quantities being filtered is:

$$X = (x \ , \ x' \ , \ x'')^T$$

The transition process is a 3x3 state transition matrix:

$$\begin{bmatrix} x \\ x' \\ x'' \end{bmatrix} = \begin{bmatrix} 1 & t & t^2/2 \\ 0 & 1 & t \\ 0 & 0 & 1 \end{bmatrix} \begin{bmatrix} x \\ x' \\ x'' \end{bmatrix}$$

The following summarizes the processing steps.

State extrapolation:

$$x(n+1)=PHI*x(n).$$

Covariance extrapolation:

$$P = PHI*P*PHI' + Q.$$

Kalman gain:

$$K = P*H'*(H*P*H' + R)-inv.$$

State update:

$$X = X + K*(Z-H*X).$$

Covariance update:

$$P=(I-K*H)*P.$$

These are the standard Kalman filter equations, and they are predicated upon the following state dynamics and measurement equations.

State dynamics:

$$X = PHI*X + E$$

where cov(E) = 0.

Measurement:

$$Z = H*X + G$$

where cov(G) =R.

The bulk of this derivation is found in the reference 1.

1.2 Eight-State Kalman Filter

The eight-state Kalman filter used for this contract is one that has been implemented at the NASA Wallops Station. The basic details of the filter are described in reference 2. The radar measurements used are the standard range, azimuth and elevation that have been transformed to cartesian coordinates. The origin for the cartesian coordinate system is the radar location. The X and Y components lie in the horizontal plane, with Y directed north and X directed east. Z completes the right-handed set and is directed upward along the local vertical. The eight-state Kalman filter assumes input and output are in this coordinate system.

Consider an aircraft velocity vector as shown below. Resolving this velocity vector into the cartesian coordinate system yields:

$$Xa' = V\cos(\theta)\sin(psi),$$

$$Ya' = V\cos(\theta)\cos(psi),$$

$$Za' = V\sin(\theta)$$

where Xa, Ya, and Za are the aircraft cartesian coordinates (that is with origin at the aircraft center of gravity). This aircraft coordinate system translates with the aircraft, but does not rotate. Xa, Ya, and Za remain parallel to X, Y, and Z at all times.

Differentiating these equations with respect to time yields:

$$Xa'' = V'\cos(\theta)\sin(psi) + psi'V\cos(\theta)\cos(psi) - \theta'V\sin(\theta)\sin(psi)$$

$$Ya'' = V'\cos(\theta)\cos(psi) - psi'V\cos(\theta)\cos(psi) - \theta'V\sin(\theta)\cos(psi)$$

$$Za'' = V'\sin(\theta) + \theta'V\cos(\theta)$$

Because of the high measurement rate of the radars (20 points per second) reasonable aircraft dynamic behavior indicates that the assumptions of constant acceleration (V' = 0), constant glideslope angle (θ) and constant bank angle (phi) between data points is probably not far from correct.

Assuming the dynamics of a coordinated turn:

$$psi = (g/V)\tan(phi).$$

Notice that 0 is the glideslope angle and psi is the bank angle. Then this yields:

$$X'' = \frac{V'X'}{V} + g\ \tan(phi)\ \frac{Y'}{V}$$

$$Y'' = \frac{V'Y'}{V} - g\ \tan(phi)\ \frac{X'}{V}$$

$$Z'' = \frac{V'Z'}{V}\ .$$

Where g is gravitational attraction, and the prime (') indicates the derivative with respect to time. Note that the above equations involving X, Y and Z are correct in either cartesian coordinate system. This system of equations represents a vector state equation of the desired form.

$$X(t+1) = F(X(t))X(t)$$

Where F(X(t)) is the state transition matrix. This continuous state representation can be made discrete for arbitrary delta-t to arrive at the following matrix state transition equation:

$$
\begin{bmatrix} X \\ Y \\ Z \\ X' \\ Y' \\ Z' \\ V' \\ \tan(phi) \end{bmatrix}
=
\begin{bmatrix} X1 \\ X2 \\ X3 \\ X4 \\ X5 \\ X6 \\ X7 \\ X8 \end{bmatrix}
=
\begin{bmatrix}
1 & 0 & 0 & dt & 0 & 0 & \frac{X4(dt)^2}{2V} & \frac{gX5(dt)^2}{2V} \\
0 & 1 & 0 & 0 & dt & 0 & \frac{X5(dt)^2}{2V} & \frac{-gX4(dt)^2}{2V} \\
0 & 0 & 1 & 0 & 0 & dt & \frac{X6(dt)^2}{2V} & 0 \\
0 & 0 & 0 & 1 & 0 & 0 & \frac{X4(dt)}{V} & \frac{gX5(dt)}{V} \\
0 & 0 & 0 & 0 & 1 & 0 & \frac{X5(dt)}{V} & \frac{-gX4(dt)}{V} \\
0 & 0 & 0 & 0 & 0 & 1 & \frac{X6(dt)}{V} & 0 \\
0 & 0 & 0 & 0 & 0 & 0 & 1 & 0 \\
0 & 0 & 0 & 0 & 0 & 0 & 0 & 1
\end{bmatrix}
*
\begin{bmatrix} X1 \\ X2 \\ X3 \\ X4 \\ X5 \\ X6 \\ X7 \\ \tan(phi) \end{bmatrix}
$$

where

$$V = \text{total velocity} = (X4^2 + X5^2 + X6^2)^{1/2}.$$

The transition matrix is evaluated at each time point and assumed to be constant for small time periods. This is a linear Kalman filter as opposed to an extended (non-linear) filter. This was found to produce excellent results by both GMD and the NASA Wallops Station (reference 2). The inclusion of tan(phi) as an element of the state vector significantly improves the accuracy of the state dynamics model when the filter is applied to tracking data from maneuvering aircraft. The implementation of the filter was done by the U-D factorized form, developed fully in reference 3. This particular formulation was implemented because it enhances filter stability (particularly when the magnitudes of elements of the state vector are all quite different) and reduces the amount of computation. This is especially relevant when a single-precision implementation is considered.

1.3 The QD filter

The QD filter implemented for this contract is a version of the filter developed at the White Sands Missile Range in the 1960's. Versions of this filter have been applied to a variety of radar tracking problems. The significant aspects of the QD filter appear to be its minimal computational time, and the use of an 'equivalent' n-th order polynomial type of curve-fit for smoothing.

Given a set of data points that are taken at equal time intervals the second order QD filter for sequential filtering of these data are described as follows. The QD filter is a recursive, predictor-corrector alogrithm. The formulation is done as follows:

$$\bar{x}''(n+1) = \tilde{x}''(n)$$

$$\bar{x}'(n+1) = \tilde{x}'(n) + dt\ \tilde{x}''(n)$$

$$\bar{x}(n+1) = \tilde{x}(n) + dt\ \tilde{x}'(n) + ((dt^2)\ \tilde{x}''(n))/2$$

The first of these equations asserts that acceleration is assumed to be constant between observations. The second indicates that velocity is based on previous velocity plus acceleration, and the third that position is given by previous position with present velocity and acceleration.

Notice that the quantities with the bar over them are the predicted: those with the tilde over them are the values estimated in the previous step.

The prediction formulas are the standard equations of motion that are used in the three-state Kalman filter as well. They are a Taylor series truncated for a second degree fit. The corrections of the predicted values are then based on the difference between the observed and predicted data values. This is accomplished as follows:

$$dx = \bar{x}(n+1) - x(n+1)$$

and the correction equations are:

$$\tilde{x}''(n+1) = \bar{x}''(n+1) + k1\ dx$$

$$\tilde{x}'(n+1) = \bar{x}'(n+1) + k2\ dx$$

$$\tilde{x}(n+1) = \bar{x}(n+1) + k3\ dx$$

Where, once again, the quantities with a bar are the predicted values, and the quantities with the tilde are the current estimates of the parameter. The correction coefficients k1, k2, and k3 are designed to minimize the error of the current estimate. The above formulas prescribe the computational procedure of the second order QD filter. Notice that these formulas use the estimates computed in the previous step as well as data from a present measurement. This is the recursive nature of the QD filter. As a result, the QD filter requires some form of initialization. That is, initial estimates of the parameters being estimated must be provided. The most common approach is to compute the initial estimates from the first few data points with a conventional least squares method or some other (comparable) algorithm. It can be shown that the QD formulas are equivalent to a constrained least squares (CLS) filter applied to M given data values with estimates determined for the most recent data value (m=M). In the CLS filter, intercept and slope constraints are applied at the oldest value of the data under consideration (i.e. at m=0). This means that the polynomial fit to the M data points in the least squares sense must also contain the estimates of the true value and the corresponding first derivative at the span point m=0. Under these constraints in the second order filter, the

predicted data value and its derivative can be obtained with the truncated Taylor series:

$$\bar{x}'(n+1) = \bar{x}'(n-M+1) + M\ dt\ \bar{x}''(n-M+1)$$

$$\bar{x}(n+1) = \bar{x}(n-M+1) + M\ dt\ \bar{x}'(n-M+1) + (M\ dt)^2\bar{x}''(n-M+1)/2$$

Where the subscript n-M+1 corresponds to m=0 in the filter span and x(n-M+1) and x'(n-M+1) are the constraints which were computed in the preceeding step as x(n-M+2) and x'(n-M+2). Since x(n-M+1) and x'(n-M+1) are fixed, only x''(n-M+1) can be adjusted to make the formula for predicted position fit the M data values in the least squares sense. Let dx be the required correction, then,

$$\bar{x}''(n+1) = \bar{x}''(n+1) + d^2x$$

Since the second derivative (acceleration) is taken to be constant for the second order QD filter, and by applying this correction to the prediction formulas above, we obtain the following estimates.

$$\tilde{x}'(n+1) = \bar{x}'(n-M+1) + M\ dt\ \bar{x}''(n-M+1)+d^2x)$$

$$\tilde{x}(n+1) = \bar{x}(n-M+1) + M\ dt\ \bar{x}'(n-M+1) + \frac{(M\ dt)^2}{2}(\bar{x}''(n-M+1)+dx)$$

Subtracting these two formulas from the two previous formulas yields:

$$x'(n+1) = x'(n+1) + M\ dt\ d^2x$$

$$x(n+1) = x(n+1) + \frac{(M\ dt)^2dx}{2}$$

The values of the gain factors are given by:

$$d^2x = k1\ dx$$

$$k2 = M\ dt\ k1, \text{ and}$$

$$k3 = \frac{(M\ dt)^2k1}{2}$$

From the first of the above three expressions involving k1, k2, and k3, it is apparant that k1 must first be developed as a function of M, the corresponding CLS span. That is,

$$k1 = k1(M)$$

When M is specified, then k1 is determined by the polynomial expression

$$k1 = 60M^2 / (10M^3 + 33M^2 + 23M - 6)$$

Note that the actual formulas implemented for the QD filter do not contain the constraint terms x(n-M+1) and x'(n-M+1). The recursive nature of the filter allows us to eliminate the need to carry these terms along.

$$\tilde{x}'(n) = \bar{x}'(n-M+1) + (M-1)dt\ \bar{x}''(n-M+1)$$

combined with

$$\tilde{x}(n+1)=\bar{x}(n-M+1) +(M-1)dt\ \bar{x}'(n-M+1) + \frac{(m-1)^2(dt)^2\bar{x}''(n-M+1)}{2}$$

yields an expression involving only x''(n-M+1) and this term is assumed to be constant between observation points. Higher order QD filters could be developed, but for most aircraft tracking problems using filters with order greater than two does not significantly improve the filter performance.

The White Sands Missile Range reports that the best results are obtained when the filter span is set somewhere between 17 and 46 points. Under conditions of higher accelerations, shorter filter span values seem to be more appropriate: when there is very little acceleration present, larger values of the filter span give maximum smoothing.

1.4 Alpha-Beta-Gamma Filter

The Alpha-Beta-Gamma (ABG) filter, like the other filters implemented for this contract is formulated in terms of a state vector. The elements of the state vector are position, velocity and acceleration in each of the three axes. This is identical to the initial formulation of the QD filter, and is the same axes system used in the eight-state Kalman filter. The prediction part of the filter is given by the usual equations of motion:

$$\hat{x}''(n+1) = \tilde{x}''(n)$$

$$\hat{x}'(n+1) = \tilde{x}'(n) + dt*\tilde{x}''(n)$$

$$\hat{x}(n+1) = \tilde{x}(n) + dt*\tilde{x}'(n) + \frac{dt^2\tilde{x}''(n)}{2}$$

Processing in the ABG filter is broken into two parts: the initialization portion (or 'expanding memory portion') and the normal processing mode ('fading memory portion'). The expanding memory portion of the processing is done to initialize the filter—once this has been accomplished, the second processing mode is employed. Both processing modes use the state transition indicated above. The only real difference between the processing mode is the manner in which the parameters α, β, and γ are computed. For the initialization portion of the filtering algorithm, the three parameters are computed as a function of the number of data points processed (n=0,1,2,...). For the actual filtering portion of the algorithm, these parameters are a function of a

control parameter, theta. In each case:

$$e(n) = x(n) - \hat{x}(n).$$

And the current state vector is given by

$$\tilde{x}''(n) = \hat{x}''(n) + (2\gamma/dt^2)*e(n)$$

$$\tilde{x}'(n) = \hat{x}'(n) + (\beta/dt)*e(n)$$

$$\tilde{x}(n) = \hat{x}(n) + \alpha*e(n).$$

During the initialization portion of the filtering process, the gain coefficients are given by:

$$\alpha = 3(3N^2+3N+2)/((N+3)*(N+2)*(N+1))$$

$$\beta = 18(2N+1)/((N+3)*(N+2)*(N+1))$$

$$\gamma = 30/((N+3)*(N+2)*(N+1))$$

These values of alpha, beta and gamma are used up until some value, M. At that point the procedure for computing the three filter gains is changed to:

$$\alpha = 1-\theta^3$$

$$\beta = 3*(1-\theta)^2(1+\theta)/2$$

$$\gamma = (1-\theta)^3/2$$

where theta is specified by the user, $0 <= \theta <= 1$. The closer to 1 that theta is chosen the smoother the filter output will be. Theta determines the weight given to past data and as such, controls the tradeoff between dynamic response and noise suppression. A relatively large value of theta produces good noise suppression, but yields poor dynamic response. A relatively small value of theta gives good dynamic response, but has low noise suppression. There are a variety of pocedures for selecting the switching point of the filter: the one selected for this contract is

$$M = (4.463 + (\theta - 0.9)(4.7850 - 4.463)/0.99)/(1 - \theta)$$

2.0 FILTER PERFORMANCE

In this section some of the performance characteristics of each of the filters is discussed. The filters under consideration are the 'Real Time' (3-state Kalman, range, azimuth and elevation filtered independently), the 8-state Kalman filter (with state transition matrix taken from a Wallops Island tracking routine) a QD filter and an Alpha-Beta-Gamma tracker. Each of the filters was used to filter first a step function, and then some randomly generated noise that had predominantly

higher frequency content. The difference equation that generated this 'violet' noise is

$$Y(t) = e(t) - .9e(t-2)$$

where the e(t)'s are random, normally distributed with mean zero and standard deviation sigma. Notice that the variance of Y(t) is variance (e(t)) + .81 x variance (e(t-2)). Since the same process was used for all the e(t)'s this amounts to var(Y(t)) = 1.81 x var(e(t)). The variance of e(t) was chosen so that 1.81 x var(e(t)) is 0.5 LSB's. This corresponds to the noise that was observed for most of the flight data collected. When the filters were evaluated using random (colored) noise as input, the noise was filtered for approximately one minute prior to the time plotted. This was done to allow the filter time to 'settle down.'

2.1 Step Response Function

Each filter was used to filter the X-coordinate when the input for that coordinate was a step function. From 22:00:00 to 22:00:30 a fixed value of 50 feet was input. At 22:00:30 the input was changed to 500 feet. This input of 500 feet was maintained throughout the balance of the plot (to 22:01:00). On each of the figures shown, 3.1 through 3.3, the filter performance for a single filter with 3 different initialization conditions is given. In general the dashed line represents the case where filter parameters were selected to give the most smoothing, the solid line the case to give the best dynamic tracking ability.

2.1.1 Real-Time Kalman Filter

Figure 1 shows the results of the real-time Kalman filter tracking performance when the X-coordinate step function was used for input. Notice that the Y and Z coordinate input values for this case were zero. The 3-state Kalman filter was set up with variance noise values for the plant equation (state dynamics) taken to be 0.01 foot, 0.0001 foot and 0.000001 foot. In each case the measurement noise variance was taken to be 1000 feet. The first condition thus corresponds to saying that the one-sigma error contamination in the state dynamics model is 0.1 foot and the measurement one-sigma error contamination is something just over 30 feet. This is shown on the plot as the solid line. Notice that this filter tracks fairly well: it is subject to some overshoot and a slight bit of 'ringing', but is back 'on track' within 4 seconds. The plots are made at one second intervals. The actual filtering was done at 20 samples per second. The maximum of the overshoot appears to be about 80 feet. The fairly good tracking performance of this particular set-up suggests that it may not do as well at smoothing rough data as other filters. When the state dynamics error variance is reduced to 0.0001 (0.01 foot, one sigma) the filter interprets variation off of the predicted position as being mostly noise. This condition is shown as the dotted line on figure 3.1. The overshoot appears to be approximately comparable to that of the previous case (maximum overshoot of about 90 feet) but the 'recovery' period takes longer, about 9

seconds in this case. The 'ringing' evident in this filter likewise overshoots a little more than the previous case. By ascribing the observed error to the measurement rather than to the dynamics (position), this filter will give a smoother estimate of position than does the first implementation.

The final case shown on this figure is the case where the error variance of the state dynamics is given to be 0.000001. This corresponds to a one sigma error of 0.001 foot. The filter response is exactly as one would expect. There is considerably more overshoot than in either of the previous two cases, and the filter recovery time is longer (about 17 seconds). This case is shown as the dashed line on the figure. This filter would perform best in terms of data smoothing.

2.1.2 Eight-State Kalman Filter

The eight-state Kalman filter performance is shown in figure 2. Three cases are shown for this filter as well. In the first, the state dynamics error variances were taken to be 0 feet for the position estimate, 0 feet per second for the velocity, and 0.1 feet per second-squared for the acceleration, and an error variance of 1 for the tangent of the roll angle. The measurement error variance was taken to be 10 feet, 100 feet and 10000 feet for each of the three cases shown. The eight-state Kalman filter allows for coupling among the axes filtered (X, Y, and Z). For this case, the X coordinate was used as the step input and the Y and Z coordinates were taken to be zero. Because of this coupling through the roll angle, filter performance in this case could be evaluated under a variety of aircraft conditions. To compare this filter to the others considered in this study, however, it was assumed that the aircraft position was 'on the X axis.'

In the first case, the filter shows overshoot of about 90 feet. It takes six or seven seconds to recover from the step input. This filter exhibits fairly good tracking characteristics, and at the same time is not too bad in terms of data smoothing. The remaining two cases for this filter show the effects of using greater values for the variance of the measurement error. There tends to be less overshoot, and the recovery time (the time it takes for the filter to recover the correct X position, 500 feet) is approximately the same for all three cases.

2.1.3 Alpha-Beta-Gamma Filter

The alpha-beta-gamma filter is a tracking algorithm that has been around for quite a while. It is similar to the Kalman filters in that it does an extrapolation of aircraft position and adjusts the 'state' estimate by a multiple of the difference between the measured and 'expected' positions. The principal difference between this and a Kalman filter is that the alpha-beta-gamma tracker has fixed gain. Kalman filters dynamically adjust the gain to minimize the mean squared error of the state vector. The parameter theta is used to determine how much (fixed) gain will be used in the smoothing process. The parameter theta varies between zero and one. The closer to zero that theta is, the more

heavily the error term is weighted. Figure 3 shows how the alpha-beta-gamma tracker does on the step function for theta values of .91, .94, and .98. As one would expect, the value of .98 gives the most overshoot and longest recovery time. Theta equal to .98 gives less weight to the difference between the expected and observed aircraft position. As a result, the aircraft position is more a function of the dynamics model than of the data. This contributes to a smoother estimate of position, but also gives more overshoot. The cases that show filter performance for theta of .91 and .94 show less overshoot and faster recovery time, as one would expect. As would also be expected, these filters will not smooth as well as the theta equal to .98 case will. Performance of this 'fixed gain' filter, (as well as that of the other fixed gain filter, the QD algorithm) is surprisingly good.

2.1.4 QD Filter

The QD filtering algorithm is similar to the alpha-beta-gamma tracker in that it, too, is a fixed gain filter. The QD algorithm is set up as a recursive filter that uses a specified amount of recent information most heavily. Like the other filters discussed, it does a state variable extrapolation to estimate present aircraft position. The 'filtered' state variable estimate is given by the predicted state vector corrected by a weighted amount of the discrepancy between the expected and the observed values. Figure 4 shows how well this filter performs when a step function is used as input. In this plot three initialization parameters are used: spans of 20, 40, and 60. The spans correspond to how much of the recent past is used in filtering the present point. As would be expected, when a longer span is used, more smoothing occurs, and there is more 'overshoot' for the span equals 60 case than in the other cases. Notice that even when the smoother case is used, the overshoot is only about 50 feet (as compared to almost 100 feet with the other filters). The recovery time for this particular step function is a respectable eight seconds or less.

2.2 Filter Performance for Noise Input

Each of the filters considered in this report were also evaluated by allowing each to filter a random noise signal. The random noise was generated to have more middle and high frequency content than low. This may be thought of as 'violet' noise. The difference equation use to generate this noise is given above, and, as also mentioned above, the standard error of the noise was set to correspond to a 0.5 LSB range value. Figures 5 through 8 show filter performance for each of the filters with this noise as input.

2.2.1 Real-Time Kalman Filter

The real-time Kalman filter performance for this input is shown in figure 5. Superimposed on all plots of filter output for this noise input is every twentieth noise point. It should be noted that the same noise sequence was used for each filter and for each case. A perfect filter would show no overshoot when given a step input, and would

produce a straight line (value equal to zero) from time 22:00:00 to 22:01:00 for these plots.

The real-time Kalman filter was used to filter the random colored noise with the same set-up parameters that were used with the step function input. The error variance in the measurement equation was taken to be 1000 feet, and the error variances in the plant (state dynamics) equation were taken to be .01, .0001, and .000001. The real-time Kalman filter performs exactly as one would expect. When the state dynamics error variances are taken to be .01, the filter is more disposed to tracking changes in the data (noise in this case). When the error variance in the plant equation is considerably smaller, the filter performs better. Notice that the solid line in figure 8.1 deviates from the zero position by only about one-half a foot for the entire time period. This is the setup that exhibited the greatest overshoot in the previous graph. Even in the worst case for this filter, (error variance of 0.01) the maximum error deviation appears to be about two to three feet. Selection of the appropriate filter parameters would depend on the type of data to be filtered. Under conditions of extreme maneuvering, relatively larger values of the error variance for the plant equation would be appropriate: under conditions of less maneuvering (high altitude, or very fast, for example), relatively smaller values of the error variance would be appropriate.

2.2.2 Eight-State Kalman Filter

The eight-state Kalman filter performance in terms of filtering the colored noise is shown (for the same cases considered in the step function) in figure 6. The general performance characteristics of this filter are not unlike those of the real-time Kalman. The greatest variability occurs when the variance of the noise in the measurement equation is smallest. This is exactly what one would expect. Telling the filter that the errors in the measurement have a variance of ten feet as opposed to 1000 feet says that the measurement is more reliable in the first case. The eight-state Kalman filter's worst performance in this case is something on the order of three to four feet. The trace that is closest to zero (corresponding to a measurement error of 10000 feet) represents the case where the filter does best: the maximum error is about 1 foot.

2.2.3 Alpha-Beta-Gamma Filter

Figure 7 shows how the alpha-beta-gamma filter performs when filtering the colored noise. The filter parameters are the same as those that were used when filtering the step function. As indicated above, the case of theta equal to 0.98 gives the 'smoothest' performance. The maximum error appears to be on the order of one-half foot. Even when the cases of theta equal to 0.91 or 0.94 are considered, the maximum error is only about 2 feet. The alpha-beta-gamma filter apparently does a very good job at filtering—both from the standpoint of step response and to noise input.

2.2.4 QD Filter

The QD filter performance with the colored noise input is given in figure 8. This filter also does well on noise. The filter parameters are span equal to 20, 40 and 60, just as was done with the step input. The QD filter performs almost as well as does the alpha-beta-gamma filter in this case. The maximum error appears to be about 2 feet (when span equals 20) and the maximum smoothing case (span equal to 60) is within one foot of the correct value for the entire time interval. The 'maximum smoothing' case for the alpha-beta-gamma filter is more aesthetically pleasing than that of the QD filter. Because both filters work on the same principal, it is possible to specify equivalent values for the theta and span parameters. That is, for each span value, there is some value for the parameter theta that would yield an alpha-beta-gamma filter equivalent to the specified QD filter. As a practical matter, then, choosing between these two filters is largely a matter of preference for the name.

3.0 REFERENCES

1. Gelb, A. ed.: Applied Optimal Estimation. MIT Press, 1974, Boston, Mass.

2. Aldrich, G. T., and Krabill, W. B.: An Application of Kalman Techniques to Aircraft and Missile Radar Tracking, AIAA Journal, Vol. 11, No. 7, July 1973, pp. 932-937.

3. Bierman, G.: Discrete Sequential Estimation. Academic Press, 1977, New York.

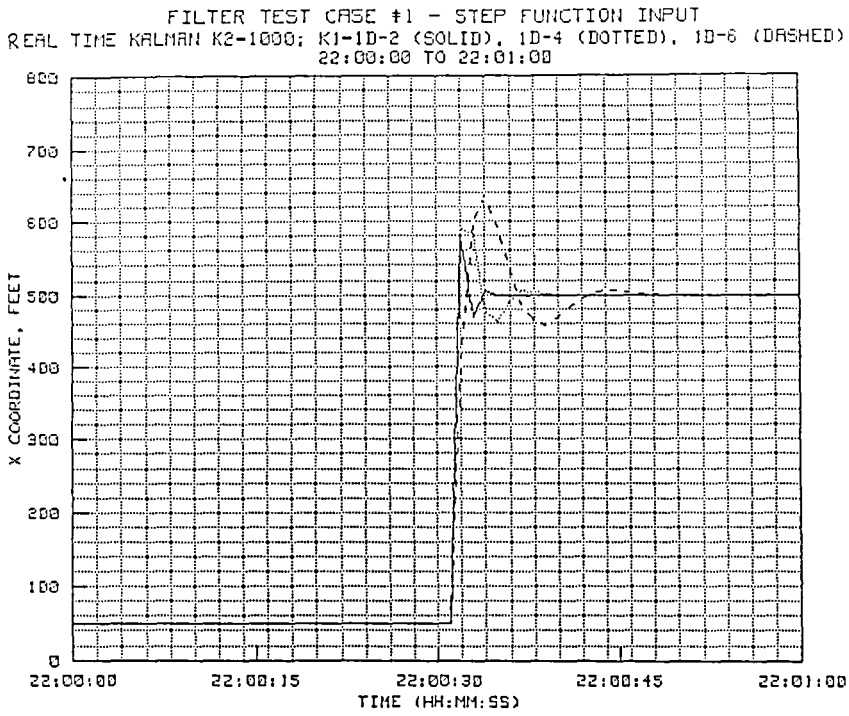

Figure 1. Real-time Kalman filter response to step input.

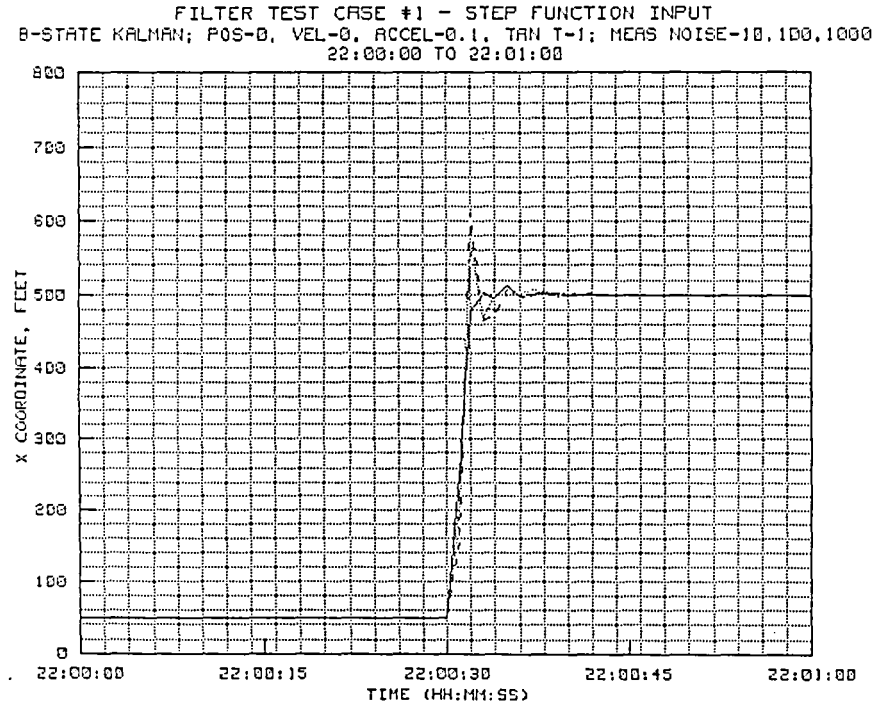

Figure 2. Eight-state Kalman filter response to step input.

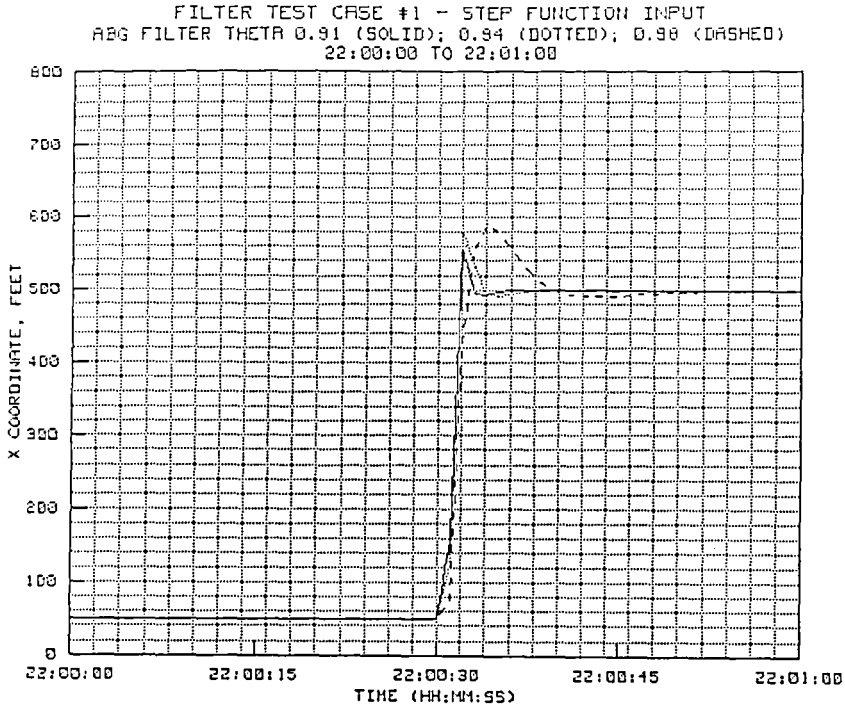

Figure 3. Alpha-Beta-Gamma filter response to step input.

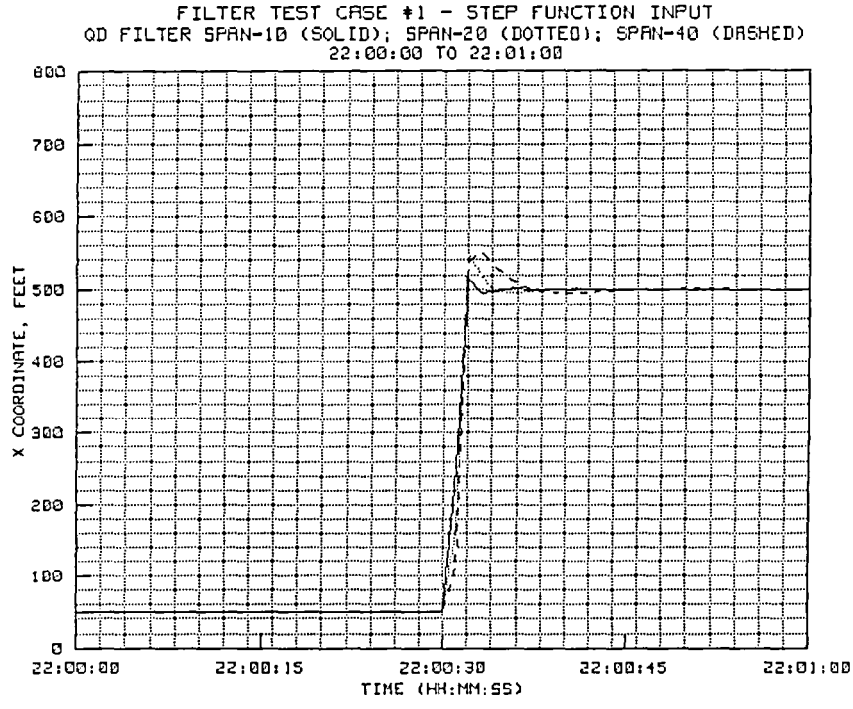

Figure 4. QD filter response to step input.

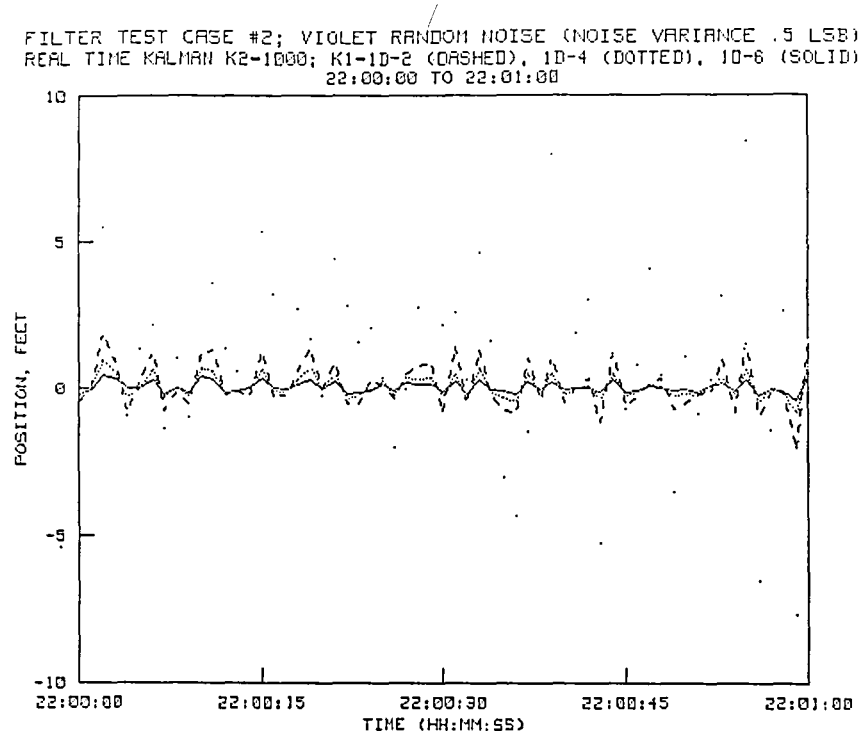

Figure 5. Real-time Kalman filter performance with random noise.

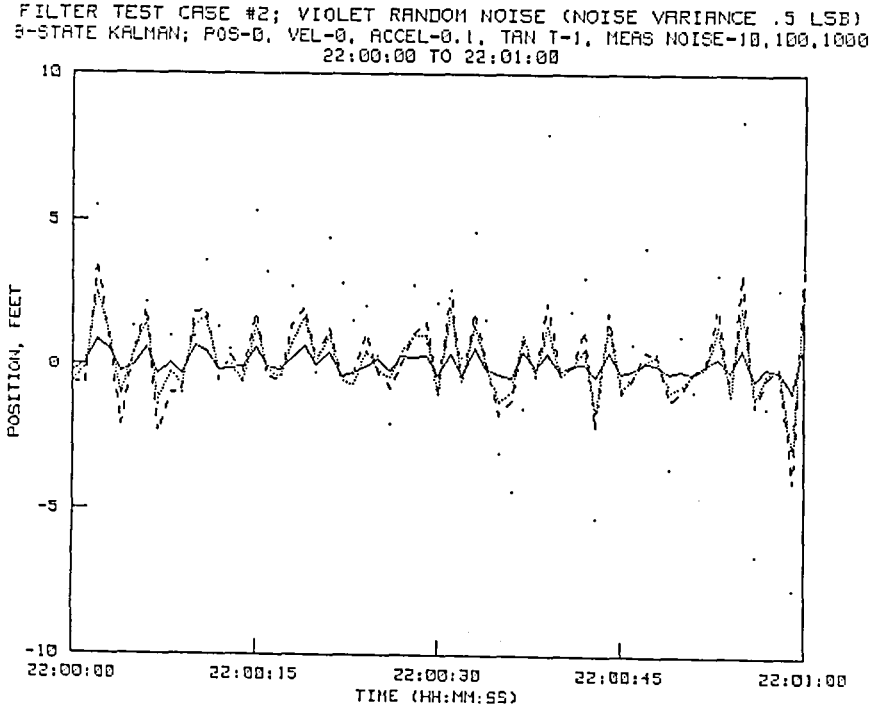

Figure 6. Eight-state Kalman filter performance with random noise.

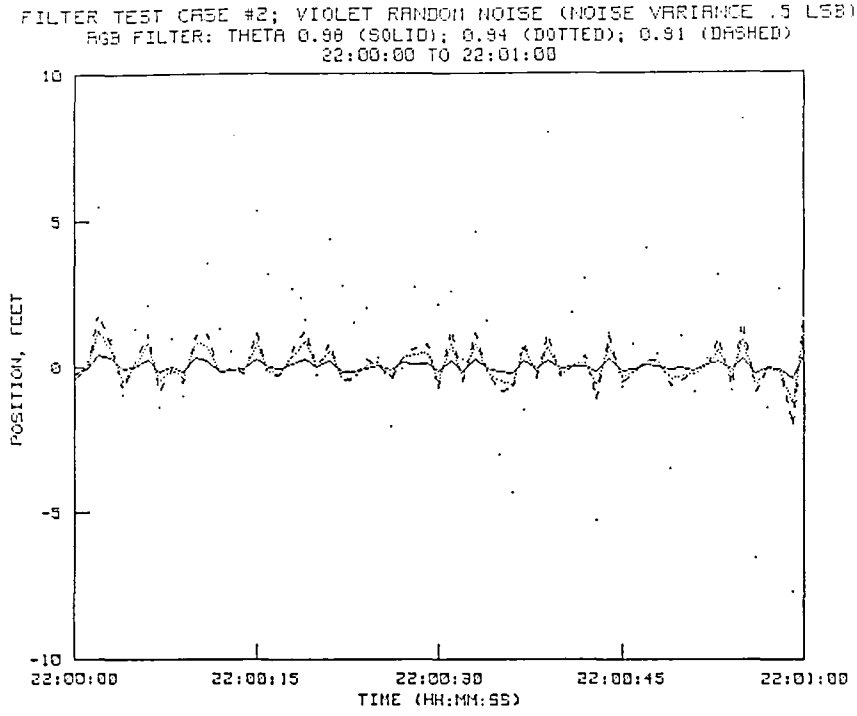

Figure 7. Alpha-Beta-Gamma filter performance with random noise.

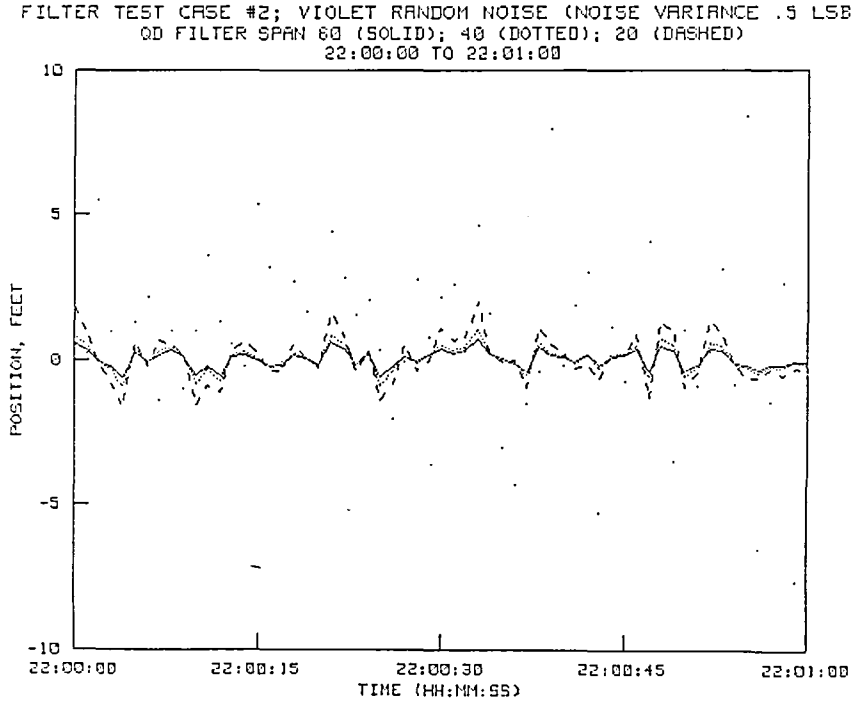

Figure 8. QD filter performance with random noise.

1. Report No.	2. Government Accession No.	3. Recipient's Catalog No.
NASA CR-166616		

4. Title and Subtitle	5. Report Date
Mathematical Analysis Study for Radar Data Processing and Enhancement Part I: Radar Data Analysis	August 1985
	6. Performing Organization Code
7. Author(s) Robert James and James D. Brownlow	8. Performing Organization Report No. H-1287
	10. Work Unit No. RTOP 506-51-11
9. Performing Organization Name and Address GMD Systems 45303 N. Twenty-third St. West Lancaster, California 93534	11. Contract or Grant No. NAS2-11491
	13. Type of Report and Period Covered Contractor Report — Final
12. Sponsoring Agency Name and Address National Aeronautics and Space Administration Washington, D.C. 20546	14. Sponsoring Agency Code

15. Supplementary Notes

NASA Technical Monitor: Terry J. Larson, NASA Ames Research Center, Dryden Flight Research Facility, Edwards, California 93523-5000.

16. Abstract

A study was performed under NASA contract to evaluate data from an AN/FPS-16 radar installed for support of flight programs at Dryden Flight Research Facility of NASA Ames Research Center. The purpose of this study was to provide information necessary for improving post-flight data reduction and knowledge of accuracy of derived radar quantities. Tracking data from six flights were analyzed. Noise and bias errors in raw tracking data were determined for each of the flights. A discussion of an altitude bias error during all of the tracking missions is included. This bias error was defined by utilizing pressure altitude measurements made during "survey flights." Four separate filtering methods, representative of the most widely used optimal estimation techniques for enhancement of radar tracking data, were analyzed for suitability in processing both real-time and post-mission data. Additional information regarding the radar and its measurements, including typical noise and bias errors in the range and angle measurements, is also presented. Part I of this report is an analysis of radar data; part II is a discussion of the modeling of propagation path errors.

17. Key Words (Suggested by Author(s))	18. Distribution Statement
Atmospheric refraction Data filtering Radar calibration Radar systems Tracking data processing	Unclassified — Unlimited STAR category 17

19. Security Classif. (of this report)	20. Security Classif. (of this page)	21. No. of Pages	22. Price*
Unclassified	Unclassified	377	A17

*For sale by the National Technical Information Service, Springfield, Virginia 22161.

End of Document